

Im Fachbereich Physik der Freien Universität Berlin eingereichte
Dissertation. Doctoral Dissertation at the Freie Universität Berlin.

Ultrafast Electron Dynamics in Low-Dimensional Materials

by

Patrick S. Kirchmann



Freie Universität Berlin 2008

Bibliografische Information der Deutschen Nationalbibliothek

Die Deutsche Nationalbibliothek verzeichnet diese Publikation in der Deutschen Nationalbibliografie; detaillierte bibliografische Daten sind im Internet über <http://dnb.d-nb.de> abrufbar.

ISBN 978-3-86853-035-3

This work was done between September 2004 and November 2007 in the group of Professor Dr. Martin Wolf at the Physics Department of the Freie Universität Berlin.

Patrick S. Kirchmann
Berlin, in November 2008

An electronic version (PDF) of this doctoral work is available on the dissertation server of the Freie Universität Berlin at <http://www.diss.fu-berlin.de>.

1st referee: Prof. Dr. Martin Wolf
Freie Universität Berlin

2nd referee: Prof. Dr. Karsten Horn
Fritz-Haber-Institut der Max-Planck Gesellschaft

3rd referee: Prof. Dr. Thomas Fauster
Friedrich-Alexander-Universität Erlangen-Nürnberg

Day of Defense: 9th of February 2009

The cover image shows an artistic alienation of the photoemission intensity of a Pb/Si(111) wedge as function of Pb coverage and binding energy. The original data is presented in Fig. 5.4

© Verlag Dr. Hut, München 2009
Sternstr. 18, 80538 München
Tel.: 089/66060798
www.dr.hut-verlag.de

Die Informationen in diesem Buch wurden mit großer Sorgfalt erarbeitet. Dennoch können Fehler nicht vollständig ausgeschlossen werden. Verlag, Autoren und ggf. Übersetzer übernehmen keine juristische Verantwortung oder irgendeine Haftung für eventuell verbliebene fehlerhafte Angaben und deren Folgen.

Alle Rechte, auch die des auszugsweisen Nachdrucks, der Vervielfältigung und Verbreitung in besonderen Verfahren wie fotomechanischer Nachdruck, Fotokopie, Mikrokopie, elektronische Datenaufzeichnung einschließlich Speicherung und Übertragung auf weitere Datenträger sowie Übersetzung in andere Sprachen, behält sich der Autor vor.

1. Auflage 2009

A human being should be able to change a diaper, plan an invasion, butcher a hog, conn a ship, design a building, write a sonnet, balance accounts, build a wall, set a bone, comfort the dying, take orders, give orders, cooperate, act alone, solve equations, analyze a new problem, pitch manure, program a computer, cook a tasty meal, fight efficiently, die gallantly. Specialization is for insects.

Lazarus Long in *Time Enough For Love*

Abstract

This work investigates the ultrafast electron dynamics in low-dimensional materials using femtosecond time- and angle-resolved photoemission techniques. In low-dimensional materials, the electronic wave functions are confined to one and two dimensions, (1D) and (2D). This electron confinement can lead to (i) quantum size effects, where the physical properties of a solid state material depend decisively on the size of the considered system, and to (ii) many-body phenomena, where electron-electron correlation and coupling to other excitations such as phonons can result in the formation of broken-symmetry ground states like charge density wave (CDW) or superconducting phases. Besides the fundamental scientific significance, low-dimensional materials become increasingly important with the advent of nanotechnology. In this work, several well-defined prototypical quasi-2D and quasi-1D model systems have been studied.

The quantized band structure and electron dynamics of the occupied and unoccupied quantum well states (QWSs) in the quasi-2D model system Pb/Si(111) have been investigated with two-photon photoemission (2PPE) and photoemission spectroscopy (PES) directly in the time domain. The general trend of the hot electron lifetimes in the *unoccupied* QWS is confirmed to be governed by Fermi liquid theory. To describe all observed population decays quantitatively, the quantized electronic system has to be taken into account since the simultaneous population decay and build-up in two adjacent QWSs favors inter-subband scattering from the higher lying into the lower lying state. The investigation of the dynamics of the highest *occupied* QWS in Pb/Si(111) with time-resolved PES revealed an ultrafast electronic stabilization due to the excitation of electron-hole pairs that induce a sudden change of the screening of the ion cores and displacively excite a coherent phonon mode in the film direction. Potential anisotropies of the hot electron lifetimes of self-assembling metallic quasi-1D nanowires in 4×1-In/Si(111) were investigated using time-resolved 2PPE and a novel position-sensitive electron time-of-flight technique, which was developed as part of this work for efficient angle-resolved photoemission studies of low-dimensional materials with anisotropic band structure. Finally, collective excitations of the electron and lattice system in the prototypical quasi-1D CDW compound TbTe₃ have been explored with time- and angle-resolved PES. The temperature-, fluence- and k -dependence of the transient band structure in the CDW nesting region at the Fermi level reveals an oscillation of the valence band, which is assigned to the excitation of the amplitude mode of the CDW phase of TbTe₃. At the highest fluences investigated, the charge-ordered CDW melts within 100 fs, evidenced by the ultrafast closing of the CDW gap in the band structure at the Fermi level and the transient recurrence of a nearly free electron dispersion.

Deutsche Kurzfassung

Diese Arbeit untersucht die ultraschnelle Elektronendynamik in niedrig-dimensionalen Materialien mit Femtosekunden zeit- und winkelaufgelösten Photoemissionstechniken. In niedrig-dimensionalen Materialien sind die elektronischen Wellenfunktionen auf ein und zwei Dimensionen beschränkt, (1D) und (2D). Diese Einschränkung der Elektronen kann dazu führen, dass es (i) zu größenbedingten Quanteneffekten kommt, bei denen die physikalischen Eigenschaften eines Festkörpers entscheidend von der Systemgröße abhängen, und (ii) zu Vielteilchen-Phänomenen, bei denen Elektronen-Elektronen-Korrelation und die Ankopplung an andere Anregungen wie Phononen zur Bildung von Grundzuständen mit gebrochener Symmetrie wie etwa Ladungsdichtewellen (*charge density waves*, CDWs) oder supraleitenden Phasen führt. Neben der grundlegenden wissenschaftlichen Bedeutung gewinnen niedrig-dimensionale Materialien mit dem Aufkommen der Nanotechnologie zunehmend an Bedeutung. Mehrere wohldefinierte, prototypische quasi-2D und quasi-1D Modellsysteme wurden in dieser Arbeit untersucht.

Die quantisierte Bandstruktur und Elektronendynamik der besetzten und unbesetzten Quantentrogzustände (*quantum well states*, QWSs) in dem quasi-2D Modellsystem Pb/Si(111) wurde mittels Zwei-Photonen Photoemissionspektroskopie (2PPE) und Photoemissionspektroskopie (PES) direkt in der Zeitdomäne untersucht. Die allgemeine Tendenz der heißen Elektronen-Lebensdauern in den *unbesetzten* QWSs folgt der Theorie der Fermi-Flüssigkeiten. Um alle beobachteten Bevölkerungszufälle quantitativ zu beschreiben, muß die quantisierte elektronische Struktur berücksichtigt werden, da der gleichzeitige Populationszerfall und -aufbau in zwei benachbarten QWSs Inter-Subband Streuung vom höher liegenden in den tiefer liegenden Zustand nahe legt. Die Untersuchung der Dynamik des höchsten *besetzten* QWSs in Pb/Si(111) mittels zeitaufgelöster PES ergab eine ultraschnelle elektronische Stabilisierung durch die Anregung von Elektronen-Loch Paaren, die eine plötzliche Änderung der Abschirmung der Ionenkerne induzieren und eine kohärente Phononen-Mode in der Filmrichtung anregen. Potenzielle Anisotropien der Lebensdauer heißer Elektronen in sich selbst-organisierenden metallischen quasi-1D Nanodrähten in 4×1-In/Si(111) mittels zeit- und winkelaufgelöster 2PPE untersucht. Dazu wurde ein neuentwickeltes Spektrometer für positions-empfindliche Elektronen Flugzeit-Spektroskopie angewandt, das im Rahmen dieser Arbeit für effiziente winkelaufgelöste Photoemissionsstudien von niedrig-dimensionalen Materialien mit anisotroper Bandstruktur entwickelt wurde. Die kollektiven Anregungen des Elektronen- und Gittersystems in dem quasi-1D CDW-Material TbTe₃ sind mit zeit- und winkelaufgelöster PES analysiert worden. Die Temperatur-, Fluenz- und *k*- Abhängigkeit der transienten Bandstruktur im Verschachtelungsbereich der CDW am Fermi-Niveau offenbart eine Schwingung des Valenzbandes, die der Anregung der Amplituden-Mode der CDW-Phase von TbTe₃ zugeschrieben wird. Bei der höchsten untersuchten Fluenz schmilzt die CDW-Phase innerhalb von 100 fs, was durch das ultraschnelle Schließen der CDW-Bandlücke am Fermi-Niveau und die transiente Rückkehr einer quasi-freien Elektronendispersion angezeigt wird.



Contents

Abstract	I
Deutsche Kurzfassung	III
1 Introduction and Motivation	1
2 Theoretical Background	7
2.1 Quantum Size Effects in 2 Dimensions	8
2.1.1 General Properties of Quantum Wells	8
2.1.2 Quantum Well States of Pb/Si(111)	10
2.1.3 Quantum Size Effects in Pb/Si(111)	16
2.2 Charge Density Waves	19
2.2.1 Peierls Transition	19
2.2.2 Collective Excitations	24
2.2.3 A Tunable CDW System: RTe ₃	26
2.3 Electron Dynamics in Reduced Dimensions	32
2.3.1 Inelastic Electron-Electron Scattering	33
2.3.2 Inter- and Intra-Subband Scattering	38
2.4 Photoelectron Spectroscopy	40
2.4.1 The 3-Step Model of Photoemission	42
2.4.2 The 1-Step Model of Photoemission	43
2.4.3 Angle-Resolved Photoelectron Spectroscopy	44
2.4.4 Two-Photon Photoelectron Spectroscopy	45
2.4.5 Time-Resolved Two-Photon Photoemission	48
2.4.6 Analytic Description of the Population Decay	50
2.4.7 Time- and Angle-Resolved Photoemission Spectroscopy	53
3 Experimental Details	57
3.1 Laser Setup	58
3.1.1 Generation and Amplification of fs-Laser Pulses	59
3.1.2 Pulse Incoupling	59
3.1.3 Pulse Characterization	61
3.2 Ultra High Vacuum Chamber	65
3.2.1 Conventional Time-of-Flight Electron Spectrometer	68
3.2.2 Data Acquisition	69
3.2.3 Data Analysis	70
3.3 Sample Preparation	74
3.3.1 Preparation of Ultrathin Epitaxial Metal Films	74
3.3.2 Preparation of TbTe ₃	82

4	Position-Sensitive Electron Time-of-Flight Spectrometer	85
4.1	Design Considerations	86
4.1.1	Hardware Implementation	88
4.1.2	Principle of Operation	90
4.1.3	Time-of-Flight Analysis	91
4.1.4	Energy and Momentum Resolution	93
4.1.5	Delay-Line Anode	94
4.1.6	Trajectory Simulations	96
4.2	Software Implementation	100
4.2.1	The <code>cEvent</code> Class	100
4.2.2	<code>Igor Pro</code> and <code>LabView</code> Front Ends	103
4.2.3	Reconstruction of Multihit Events	104
4.3	Performance of the pTOF Spectrometer	108
4.3.1	Comparison to Conventional TOF Spectrometer	112
4.3.2	Discussion of the Multihit Capability	113
	<i>Conclusions</i>	116
5	Ultrafast Dynamics in Quantized Pb/Si(111) Bands	117
5.1	Structure of the Occupied QWS	120
5.1.1	Workfunction Oscillations	124
5.1.2	Substrate Contributions	130
5.2	Structure of the Unoccupied QWS	133
5.3	Overview of the Quantized Pb/Si(111) Band Structure	140
	<i>Conclusions</i>	145
5.4	Ultrafast Electron Dynamics of the Unoccupied QWS	146
5.4.1	Coverage Dependence of the Schottky Barrier	148
5.4.2	Population Decay Times	150
5.4.3	Coverage Dependence of the Decay Times	153
5.4.4	Comparison to Fermi Liquid Theory	157
5.4.5	Interband vs. Intraband Scattering	163
5.4.6	Substrate Contributions	167
	<i>Conclusions</i>	171
5.5	Ultrafast Dynamics of the Occupied QWS	172
5.5.1	Simulation with the 2-Temperature Model	173
5.5.2	Coherent Phonon Modes in Pb/Si(111)	178
5.5.3	Population Decay in the Unoccupied Bands	181
	<i>Conclusions</i>	184
6	Electron Dynamics in In/Si(111)	185
6.1	Ground State Properties of 4×1-In/Si(111)	186
6.2	Experimental Details	189
6.3	Time- and Angle-Resolved 2PPE	191
	<i>Conclusions</i>	200

7	Time- and Angle-resolved Photoemission of TbTe₃	201
7.1	Equilibrium Bandstructure of TbTe ₃	205
7.2	Excitation of Collective Modes	207
7.2.1	Excitation of the CDW Amplitude Mode	208
7.2.2	Assignment of the Frequencies	211
7.2.3	Ultrafast Melting of the CDW State	213
7.2.4	Analysis in k -space	215
	<i>Conclusions</i>	220
8	Conclusions and Outlook	221
A	Abbreviations	225
B	Free Electron Gas	227
C	Landau Theory of Fermi Liquids	231
D	Optical Bloch Equations	237
E	Generation and Amplification of fs-Laser Pulses	239
F	Parameters for the pTOF-Software	247
G	Experimental Equipment	251
	Publications	281
	Academic Curriculum Vitae	285
	Acknowledgements	287

List of Figures

2.1	Quantum size effects	8
2.2	Wave functions in 1D quantum well	8
2.3	Phase-accumulation model	9
2.4	Unit cell and band structure of Silicon	11
2.5	Unit cell, band structure and Fermi Surface of Pb	12
2.6	Schottky Barrier	14
2.7	Quantized band structure of Pb/Si(111)	15
2.8	ARPES spectra for 10 ML Pb/Si(111)	16
2.9	Magic island heights in Pb/Si(111)	17
2.10	Peierls metal-to-insulator phase transition	20
2.11	Dimensionality and temperature dependence of the response function	22
2.12	Fermi surface nesting in 2D	23
2.13	Temperature dependence of the Peierls gap at k_F	24
2.14	Collective excitations of the CDW state	25
2.15	Dispersion of phase and amplitude mode of the CDW phase	25
2.16	Lanthanide-Tellurium crystals and lattice parameters	26
2.17	CDW phase transition temperature and gap size in $R\text{Te}_3$	27
2.18	Structure and Fermi surface of $R\text{Te}_3$	29
2.19	Fermi surface nesting in $R\text{Te}_3$	30
2.20	Feynman diagram of e-e scattering event	33
2.21	e-e interaction in lowered dimensions	34
2.22	e-e scattering in 3D	35
2.23	Comparison of FLT for 3D and 2D	37
2.24	Inter- and intra-subband scattering processes	38
2.25	Escape depth of photoelectrons	41
2.26	1- and 3-Step model of photoemission	43
2.27	Conservation of parallel electron momentum	44
2.28	Excitation mechanisms in 2PPE	46
2.29	Energy scales in 2PPE	47
2.30	Pump-probe sequence of 2PPE	48
2.31	Time-resolved two-photon photoemission	49
2.32	3- and 4-level system	51
2.33	Limiting Cases of a 4-Level System	52
2.34	Time-resolved photoemission	54
3.1	Femtosecond laser system	58
3.2	Pulse Incoupling	60
3.3	Typical beam profiles	62
3.4	Typical laser spectra	63
3.5	UHV chamber	65

3.6	Sample holder and sample boats	66
3.7	Slanted sample post	67
3.8	Convictional electron TOF spectrometer	68
3.9	Electronic signal processing	70
3.10	Potential gradients between sample and spectrometer	71
3.11	Effective k_{\parallel} -acceptance	72
3.12	Silicon 7×7 reconstruction	74
3.13	Cutting and Mounting of the Si Samples	75
3.14	7×7 -Si(111) preparation	76
3.15	LEED image of the 7×7 -Si(111) reconstruction	77
3.16	$(\sqrt{3}\times\sqrt{3})R30^{\circ}$ -Pb/Si(111) reconstruction	78
3.17	LEED image of β - $(\sqrt{3}\times\sqrt{3})R30^{\circ}$ -Pb/Si(111) reconstruction	79
3.18	Preparation of smooth Pb wedges	80
3.19	LEED image of 10 ML Pb/Si(111)-(1 \times 1) film	81
3.20	Phase diagram of Gd_xTe_y	82
3.21	Preparation of $TbTe_3$	83
3.22	Microscope images of different $TbTe_3$ samples	84
4.1	pTOF design	88
4.2	Impedance matching	89
4.3	ARPES geometry	91
4.4	TOF analysis	92
4.5	Energy and momentum resolution	94
4.6	Position encoding with delay line	95
4.7	Numerical electron trajectory simulations	96
4.8	Electron trajectories at the aperture	98
4.9	Electron trajectories at the MCPs	99
4.10	Working principle of the <code>cEvent</code> class	101
4.11	Relation of sample and pTOF coordinate system	102
4.12	Single vs. multihit detection	105
4.13	Position dependence of the time-sum	106
4.14	Position-resolved TOF spectra	108
4.15	Angle-resolved photoelectron spectra	109
4.16	Dispersion of the Cu(111) surface state	110
4.17	Effective mass of the Cu(111) surface state	111
4.18	Comparison to conventional TOF spectrometer	112
4.19	Distribution of multihit events	113
4.20	Space and time correlation functions	114
5.1	Photoemission spectra of Pb/Si(111)	120
5.2	Lorentzian fit of the PES spectra	122
5.3	QWS binding energies	123
5.4	Photoemission spectra of Pb/Si(111)	125
5.5	Work function oscillations	127
5.6	Modeling the work function oscillations	129
5.7	Modulation of binding energies of Si states	131

5.8	Fit the 2PPE spectra	133
5.9	Background correction of the 2PPE spectra	134
5.10	Photon energy dependence	135
5.11	Coverage dependence of the exponential background	136
5.12	Background subtracted monochromatic 2PPE spectra	136
5.13	Quantized Pb/Si(111) band structure I	140
5.14	Quantized Pb/Si(111) band structure II	142
5.15	Ultrafast electron dynamics in QWSs	147
5.16	Background subtraction and surface photovoltage	149
5.17	Pump-induced surface photovoltage	149
5.18	Time-resolved 2PPE of 8 ML Pb/Si(111)	150
5.19	Fitting of a 3- and 4-level system	152
5.20	Time-resolved 2PPE for odd and even coverages	154
5.21	XC traces for odd and even coverages	155
5.22	Coverage dependence of the decay constants	155
5.23	Comparison to FLT	158
5.24	Predictive power of FLT	161
5.25	Comparison of spectral linewidth and reciprocal lifetime	162
5.26	2D plot of Pb/Si(111)	164
5.27	Intra-subband scattering	166
5.28	Substrate contributions	168
5.29	Energy dependence of τ_B	169
5.30	tr-ARPES of 10 ML Pb/Si(111)	172
5.31	Thermalization of hot carriers	174
5.32	Temperature transient in the 2TM	175
5.33	Comparison of transient energy and peak shift	177
5.34	Coherent binding energy oscillation in Pb/Si(111)	178
5.35	Displacive excitation of coherent phonons	181
5.36	Population decay in luQWS	182
6.1	Model of the 4×1 -In/Si(111) reconstruction	186
6.2	Surface band structure of 4×1 -In/Si(111)	187
6.3	Quasi-1D Fermi surface of 4×1 -In/Si(111)	188
6.4	LEED image of 4×1 -In/Si(111)	189
6.5	Fluence dependence of the 4×1 -In/Si(111) spectra	191
6.6	2PPE spectrum and XC traces of 4×1 -In/Si(111)	193
6.7	Evaluation schemes in angle- and time-resolved 2PPE	195
6.8	Lifetime maps I	196
6.9	Lifetime maps II	197
6.10	Asymmetry of the lifetimes	198
7.1	Experimental ARPES geometries	203
7.2	Access to the Brillouin zone	204
7.3	Equilibrium Bandstructure of TbTe_3	206
7.4	Tight binding model of RTe_3	207
7.5	tr-ARPES of TbTe_3 at low fluence	209

7.6	Frequency evaluation at low fluence	210
7.7	Fluence dependence of frequencies	212
7.8	tr-ARPES of TbTe ₃ at high fluence	213
7.9	Frequency evaluation at high fluence	214
7.10	k -dependent excitation of TbTe ₃	215
C.1	Electron-electron scattering	231
C.2	Electron-electron scattering in 3D	233
C.3	Electron-electron scattering in 2D	234
E.1	Femtosecond laser system	239
E.2	Spectroscopic properties of Ti:Sa	240
E.3	Mode-locking	240
E.4	Kerr-lens mode-locking	241
E.5	Second order non-linear optical processes	243

1 Introduction and Motivation

Why Study Low-Dimensional Materials?

Modern technology creates an insatiable demand for faster processor speeds, greater computing and storage capabilities, and improved functionality of integrated semiconductor devices. Over the last 40 years, this increasing demand was likewise anticipated and accommodated by Moore's Law [Sch97], which predicts a doubling of the transistor density of an integrated circuit every 18 months. Accordingly, Moore's Law forecasts an exponential decrease of the size of transistor structures, shrinking the size of functional structures into the nm length scale. Although Moore's Law was repeatedly challenged over the last years [Pee00], to date, the worlds smallest transistor features linear structure sizes of 45 nm and employs Hafnium-infused high- k metal oxide gates [Int08]. For the year 2022, the International Technology Roadmap for Semiconductors [ITRfS07] predicts structure sizes of < 10 nm and < 1 nm thickness of the metal oxide gate layer. Beyond this point, the emerging technology of self-assembling functional structures in the nm regime might provide control on even smaller length scales [Bar05]. Also, innovative technologies for photovoltaic light conversion employ thin-film structures [Lin04] or dye-sensitized solar cells [Naz93], where the relevant processes of carrier excitation and charge separation occur at few atom thick semiconductor interfaces.

All these developments lead inevitably into a nanoscale regime, where the quantum nature of matter has to be considered. The macroscopic physical properties of a low-dimensional solid state material can be dominated by quantum mechanical effects, because the symmetry of the electronic structure is reduced from three dimensions (3D) to two dimensions (2D) or one dimension (1D) due to an anisotropic atomic bonding equivalent to a spatial confinement of the electronic wave functions. Such an electron confinement can result in a discontinuous change of the macroscopic physical properties as function of the system size, so-called quantum size effects (QSEs). Moreover, the electron confinement in low-dimensional materials can lead to many-body phenomena, where a strong electron-electron (e-e) correlation and a significant electron-phonon (e-ph) coupling result in the formation of broken-symmetry ground states like charge density wave (CDW) or superconducting phases. These technologically important aspects of low-dimensional materials are intimately linked to questions that are of fundamental physical significance. A recent report of the Office of Science of the Department of Energy in the USA identifies the following five grand challenges in basic energy sciences [Fle07]:

1. Control material processes at the level of atoms.
2. Design and perfect the directed synthesis of new forms of matter with tailored properties.
3. Understand and control the remarkable properties of matter that emerge from complex correlations of atomic and electronic constituents.

4. Master energy and information on the nanoscale to create new technologies with capabilities rivaling those of living things.
5. Characterize and control matter away - especially far away - from equilibrium.

In fact, this thesis work addresses several of these fundamental challenges with the investigation of the ultrafast non-equilibrium dynamics in low-dimensional materials where a strong correlation of atomic and electronic properties is observed. Explicitly, several well-defined model systems with a low-dimensional electronic structure such as ultrathin epitaxial metal films and self-assembling metallic nanowires were investigated with femtosecond time- and angle-resolved photoemission techniques at the crossover regime from 3D to 2D and 1D. Before introducing the low-dimensional model systems studied in this work, the next section gives an overview of the experimental concepts.

Time- and Angle Resolved Photoemission

Why Employ Femtosecond Time-Resolved Photoemission?

Many fundamental microscopic scattering processes such as e-e or e-ph scattering in solids are governed by strong interactions and hence occur on an ultrafast timescale ranging from attoseconds to picoseconds. This fact requires the appropriate tools to explore the relevant time and energy scales on which the fundamental processes of interest take place. Time-resolved photoemission spectroscopy (PES) techniques are based on a pump-probe approach and provide a tool for the study of transient non-equilibrium states in the femtosecond (fs) regime directly in the time domain. These methods are well-suited to obtain information about the fundamental quasi-particle scattering dynamics that ultimately determine the non-equilibrium properties of a material.

Conventional angle-resolved photoemission spectroscopy (ARPES) is a long-standing technique that has contributed significantly to the understanding of the electronic ground state properties of solid state materials in the last decades [Hüf95, Dam03] since it provides direct access to the single particle spectral function in reciprocal k -space and thus enables a comprehensive analysis of the band structure. In a time- and angle-resolved photoemission spectroscopy (tr-ARPES) experiment, the ground-state of a system is optically excited by an intense fs pump laser pulse and the transient evolution of *occupied* part of the band structure is monitored by direct photoemission with a time-delayed probe laser pulse. This approach permits direct access to the transient band structure in k -space, adding significant information on the collective excitations of a system that can hardly be inferred from the spectroscopic analysis of the electronic ground state alone. This brings novel insights into the energy relaxation dynamics of occupied electronic states and their coupling to other quasi-particles such as phonons and magnons [Bov07].

The well-established method of time- and angle-resolved two-photon photoemission (2PPE) spectroscopy [Fau95, Pet97b, Wei02b, Zhu04, Güd05] permits the efficient characterization of the *unoccupied* part of the band structure. 2PPE experiments employ ultrashort laser pulses to transiently populate unoccupied electronic

states above the Fermi level. The use of ultrashort fs laser pulses allows a natural implementation of a pump-probe scheme to monitor the energy and momentum relaxation of the excited electron population directly in the time domain.

Comparing the time-resolved methods of 2PPE and ARPES, the excitation densities that are usually employed in 2PPE are in the order of $\ll 10^{-2}$, whereas the strong pump pulse in tr-ARPES can excite a significant fraction of up to 10% of the valence electrons near the Fermi level. Accordingly, for 2PPE a single particle picture applies where excited electrons present perturbations that do not interact with each other. In this case, the unoccupied bands are unaltered by the optical excitation and present a fixed stage for the electron dynamics. In contrast, the higher excitation densities created in tr-ARPES can induce collective phenomena as, for example, the electronic screening is abruptly changed. Such correlated processes affect the band structure itself and turns it into a transient quantity.

Position-Sensitive Electron Time-of-Flight Spectrometer

An integral part of this work was the development and implementation of a novel position-sensitive electron time-of-flight (pTOF) spectrometer, which determines both in-plane electron momenta of the photoemitted electrons along with their kinetic energy. The capability to simultaneously detect both in-plane electron momenta presents a considerable improvement of the existing imaging concepts established in photoemission spectroscopy [Spe, Roe] and facilitates the study of the electron dynamics in low-dimensional materials with a regularly anisotropic band structure. The investigations of asymmetries in the hot electron lifetimes in the quasi-1D band structure of 4×1 -In/Si(111) presents the application of the developed pTOF technique to the time- and angle-resolved study of hot electron dynamics.

Low-Dimensional Model Systems

Ultrathin Epitaxial Lead Films: Pb/Si(111)

Ultrathin epitaxial films of the *sp*-band metal Pb on Si(111) present a quasi-2D model system where the electronic wave functions are efficiently confined to the metal film by the global bandgap of the semiconducting substrate. The electron confinement in the metal film breaks the periodicity along the surface normal and forms quantum well states (QWSs) occurring at discrete energies in the occupied and unoccupied parts of the quantized band structure. The orientation bandgap on metal surfaces also facilitates electron confinement and results in QWSs that present interesting model systems for the study of QSEs in 2D [Pag99, Oga02, Dil04, Oga04, Weg05, Mat06, Mat08]. The system Pb/Si(111) has been studied intensively by scanning tunneling microscopy (STM) [Ote02], PES [Upt04b, Dil06] and density functional theory [Wei02a], since it exhibits a rich variety of pronounced QSE. Among these are the preference of "magic" island heights [Zha98, Hup01] due to electronically assisted growth, also observed in the formation of the "devils-staircase" phases [Hup03], oscillations of the transition temperature of the superconducting state [Guo04] as well as oscillations in the direction and magnitude of the Hall effect [Vil02]. All these properties sensitively depend

on the film thickness such that a change of coverage by 1 monolayer (ML) translates into variations of these quantities. The reported oscillation period of 2 ML can be directly linked to the modulation of the electron density at the Fermi level due to the quantization of the $6p_z$ Pb bulk bands. In this respect the system of Pb/Si(111) may be regarded as a prototype for the observation of QSE in a quasi-2D material. The electronic structure of Pb/Si(111) is readily controlled by the film thickness, which qualifies it as an ideal candidate for the investigations of the hot electron dynamics at the crossover from 3D and 2D.

The hot electron lifetimes in *sp*-band metals are governed by inelastic e-e scattering processes and in general well-described by Fermi liquid theory (FLT), which considers the electronic screening of the quasi-particle interactions as well as the phase space available for scattering [Pin66]. FLT predicts a quadratic scaling law of the inelastic e-e scattering Γ of the excited quasi-particle, $\Gamma \propto \xi^2$, with respect to the excess energy above the Fermi level $\xi = E - E_F$. As the dimensionality of the electronic system is lowered, competing effects contribute to a change of the quasi-particle lifetime. On the one hand, the screening in lower dimensions is less effective and thus the strength of the screened Coulomb interaction increases, leading to more intense scattering. On the other hand, the energy and momentum space that is available for e-e scattering decreases with the dimensions of the electron system and hence the scattering rate reduces. For a 2D electron gas, FLT predicts a logarithmic correction to the quadratic scaling law of the inelastic scattering rate [Giu05].

This work investigates the inelastic e-e scattering rates in the *unoccupied* QWSs of Pb/Si(111) with time-resolved 2PPE spectroscopy. The dynamics of *occupied* QWSs are studied with time-resolved PES. The hot electron dynamics in ultrathin quasi-2D metal films raises many interesting questions: How well is the quantized electronic structure captured by the current theoretical models? Is FLT applicable to such ultrathin metal films, and if so, is an explicit consideration of the quasi-2D symmetry required? How does the electron confinement in the substrate influence the hot electron decay due to electron transfer? How are the microscopic scattering processes affected by the quantized band structure? Is it possible to launch a collective excitation in the ultrathin *sp*-metal film with intense fs laser pulses?

Self-Assembling Metallic Nanowires: 4×1 -In/Si(111)

The self-assembling metallic Indium nanowires on the 4×1 reconstructed In/Si(111) surface [Bun99, Kum00] realize a quasi-1D model system that allows to extend the study of the dimensionality dependence of the hot electron lifetimes into the regime of highly anisotropic 1D band structures. The anisotropic coupling of the electronic wave functions with respect to the high-symmetry directions of the atomic chains gives rise to a strongly anisotropic, essentially 1D topology of the band structure in 4×1 -In/Si(111), which becomes manifest in a Peierls metal-to-insulator phase transition at lower temperatures [Yeo99, Gal01, Sun08]. With respect to the lifetimes of hot electron distributions, one might expect significantly longer lifetimes perpendicular to the nanowires due to decreased wave function overlap and phase space normal to the atomic chains resulting in inefficient e-e scattering [Rüg07].

This thesis work presents a time- and angle-resolved 2PPE study of possible anisotropies of the hot electron lifetimes in $4\times 1\text{-In/Si(111)}$. The hot electron dynamics in quasi-1D metallic nanowires poses problems such as: How large are the scattering rates of hot electrons in such linear metallic structures? How are the hot electron lifetimes distributed in k -space? Is the structural anisotropy reflected in the k -dependence of the hot electron lifetimes? How much do the substrate bands contribute to the electron dynamics in such metallic nano-structures?

Prototypical Charge Density Wave Compound: TbTe_3

The prototypical CDW compound TbTe_3 is a quasi-1D model system that is particularly suitable for the study of emerging collectivity in low-dimensional materials with strongly correlated phononic and electronic degrees of freedom. TbTe_3 is a binary metal compound that crystallizes in a layered structure [Ru06b], where the wave function overlap along the high-symmetry directions of the quadratic Te planes results in the diamond-shaped electronic structure of the valence band [Lav05]. At low temperatures, TbTe_3 undergoes a Peierls metal-to-insulator transition into a CDW phase, which is driven by a coupled instability of the electron and lattice system and the near perfect nesting of the Fermi Surface [Grü94]. The opening of a bandgap at the Fermi level due to a strong coupling of the electron and lattice degrees of freedom and minimization of the total energy is observed by angle-resolved photoemission spectroscopy [Gwe98, Bro04, Gar07, Bro08]. From the theoretical point of view, the CDW formation is based on a divergence of the Lindhard response function at the Fermi level that occurs in quasi-1D materials [Grü94, Mal05, Joh08]. This CDW phase transition and the corresponding structural and electronic changes have also been studied by various experimental techniques such as electron diffraction [DiM95], x-ray diffraction [Kim06, Ru08], STM [Fan07] and Raman spectroscopy [Lav08].

The collective dynamics of the coupled electron and lattice system in RTe_3 are addressed with a time- and angle-resolved PES study of the occupied band structure of TbTe_3 in the vicinity of the Fermi wave vector. Here, several fundamental questions are of interest: Is it possible to optically excite an coupled electron and lattice dynamics in the CDW phase that can directly be followed in k -space? Can the intense laser pulse trigger a phase transition from the insulating CDW phase to the metallic state? What is the signature for an ultrafast phase transition in k -space? How long does it take to melt the frozen-in CDW phase and how does the e-ph coupling contribute to such a non-equilibrium dynamics?

2 Theoretical Background

This chapter introduces the fundamental theoretical concepts for the present work on the ultrafast electron dynamics in low-dimensional solids.

First, the discussion focuses on the occurrence of quantum size effects (QSEs) in quasi-2D ultrathin epitaxial metal films. Here, the formation of discrete quantum well states (QWSs) due to the broken periodicity along the surface normal leads to a confinement of the electronic wave functions in the metal film [Chi00, Mil02b]. In general, the QWS and their influence on the macroscopic physical properties are well described by a particle-in-the-box model. After specifying the characteristic features of the QWSs in Pb/Si(111), the manifold of QSE observed in Pb/Si(111) is introduced. The quantized band structure in Pb/Si(111) leads to pronounced QSEs such as the occurrence of "magic" island heights [Zha98, Hup01], the modulation of the work function [Kir07], surface reactivity [Ma07], and superconductivity transition temperature [Guo04].

Secondly, the Peierls metal-to-insulator phase transition is considered. In low-dimensional electronic systems anisotropic band structure with quasi-2D or 1D symmetry are regularly encountered [Grü94]. Such band structures allow to nest certain regions of the Fermi Surface (FS) with a single perturbation vector, resulting in the opening of a bandgap at the Fermi level and a doubling of the periodicity of the unit cell. The resulting charge density wave (CDW) phase presents a coupled instability of the electron and lattice system that is governed by the divergence of the Lindhard response function at low temperature. After the discussion of the collective excitation modes of the CDW phase, the quasi-2D CDW model system of TbTe₃ [Bro04] is introduced.

The understanding of the microscopic electron scattering processes that redistribute and equilibrate the excess energy on an ultrafast timescale, is discussed in the context of Fermi liquid theory (FLT) [Pin66]. The study of low-dimensional electronic systems requires the consideration of the dimension dependence of the electron scattering processes, which is detailed in appendices B and C. Finally, the theoretical foundations of photoemission spectroscopy (PES), which is the principle research method employed in this thesis work, are presented. Here the emphasis lies on femtosecond time- and angle-resolved two-photon photoemission (2PPE) and time- and angle-resolved photoemission spectroscopy (tr-ARPES).

2.1 Quantum Size Effects in 2 Dimensions

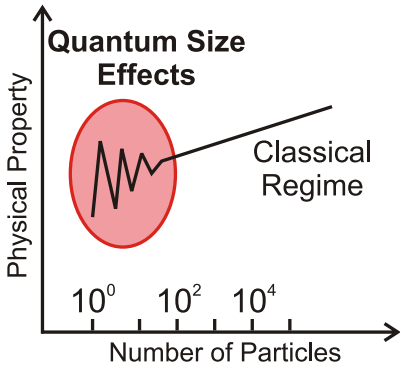


Figure 2.1: Quantum size effects occur for small particle numbers.

Many macroscopic physical properties are linked to the electronic band structure like resistance, reflectivity, work function and reactivity to name just a few. For a large ensemble of particles these properties change continuously when the particle number is changed. When the number of particles involved reaches the quantum limit such that the spatial extent of the system is of the order of the particles de-Broglie wavelength QSEs become manifest in discrete, discontinuous changes of the physical properties as depicted in Fig. 2.1.

2.1.1 General Properties of Quantum Wells

A favorable experimental approach to observe such QSEs are quantum wells of ultra-thin metal films with only a few monolayers (MLs) thickness. When the electrons of a metal are confined to a 2D film with a few Å height, the extent of the electronic wave functions is comparable to the Fermi wavelength of metals [Kit04, Ash76, Web08]. QSEs become observable as the electrons are confined in the direction perpendicular to the film by potential barriers at the interfaces. The resulting standing electron waves give rise to 2D QWSs, which occur only at discrete energies and wave vectors along the film direction [Chi00, Mil02b].

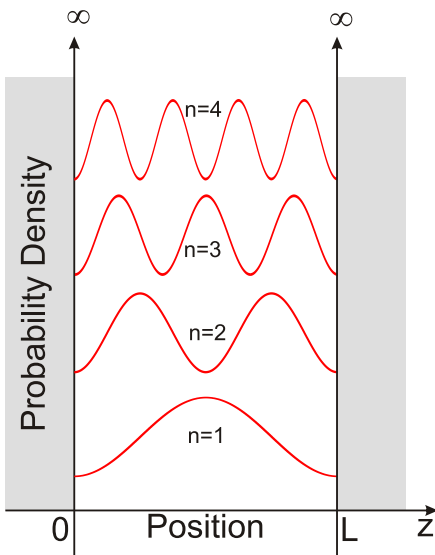


Figure 2.2: Probability distribution $|\Psi|^2$ of the first four particle-in-the-box wave functions along the z -axis.

The particle-in-the-box model is the simplest approximation [Nol04] to describe the eigen-functions Ψ and eigen-energies E of the QWSs in the z -direction normal to the surface [Chi00, Mil02b]. The particle-in-the-box model cannot be expected to be quanti-

tatively exact or account for all QSEs, however it can give an intuitive access to the problem and emphasizes the fundamental importance of the QWSs for the occurrence of QSE. The potential for a well of width L is assumed to be constant for $0 \leq z \leq L$ and infinite elsewhere, as shown in Fig. 2.2. Then the wave vectors k_n are quantized with integer quantum number n , the eigen-functions are standing sinusoidal waves and the eigen-energies scale with n^2 :

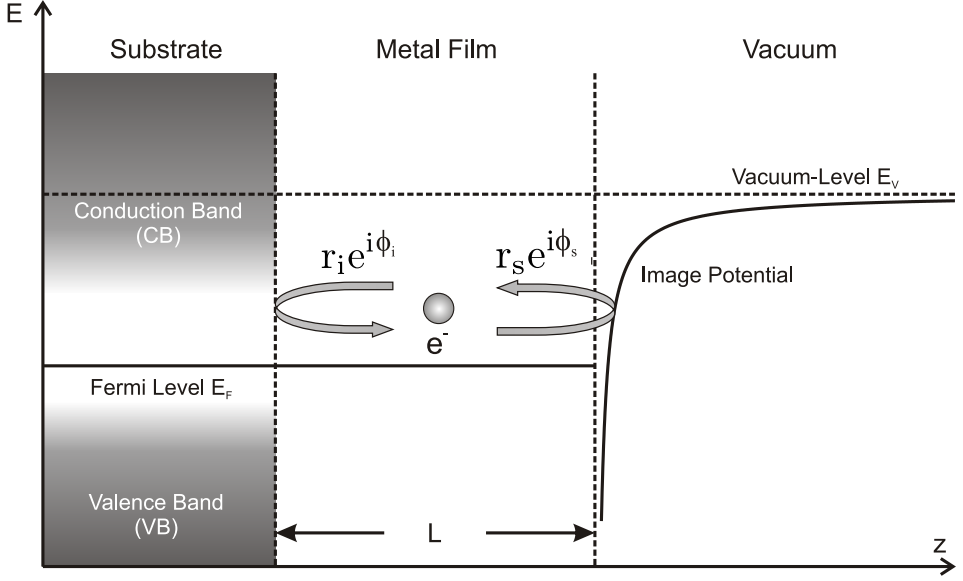


Figure 2.3: Phase-accumulation model. The confined electron accumulates a phase according to its energy in each round trip in the well. The reflectance and the phase shift at the interface and the surface are given by r_i, ϕ_i and r_s, ϕ_s , respectively.

$$(2.1) \quad k_n = \frac{n\pi}{L} \quad , \quad \Psi \propto \sin\left(\frac{n\pi z}{L}\right) \quad , \quad E = \frac{\hbar^2 k_n^2}{2m_e} = \frac{\hbar^2}{2m_e} \left(\frac{n\pi}{L}\right)^2 \quad .$$

The phase-accumulation model allows to take more realistic, i.e. finite and rounded potential boundaries into account [Chi00]. This facilitates the comparison to experiments on real model systems, which present a substrate and vacuum interface. The phase-accumulation model takes this into account by introducing a phase shift ϕ upon reflection at the interfaces to the wave function [Ech78], which decays exponentially into the vacuum and substrate. The allowed wave vectors, which result in constructive interference for one round trip in the well, are given by the Bohr-Sommerfeld rule:

$$(2.2) \quad \oint p dz = \hbar \oint k dz = 2\pi n \hbar \quad \Rightarrow \quad 2k\Theta d + \phi_s + \phi_i = 2\pi n \quad .$$

The total film thickness $L = \Theta d$ is expressed in terms of the ML coverage Θ and the inter-plane distance d of the film. The phase shifts at the film surface and the film-substrate interface are given by ϕ_s and ϕ_i , respectively. This is illustrated in Fig. 2.3, where an electron accumulates a phase $\phi = pz$ according to its momentum p in the well. Constructive interference and standing waves occurs for an accumulated phase of $2\pi n$.

The phase shifts at the interfaces are generally energy-dependent and determined by the model potential at the respective interface. The image potential (IP) at the film-vacuum interface can be described as in [Oga05]:

$$(2.3) \quad V_{\text{IP}} = -\frac{e_0^2}{4\pi\epsilon_0} \frac{1}{4z} \quad ,$$

which is created by the polarization in the metal surface due to an electron in front of the surface [Jac99]. The corresponding phase shift is then approximated by [McR79, McR81, Mil02b, Oga05]:

$$(2.4) \quad \phi_s = \pi \left(\sqrt{\frac{3.4}{E_V - E}} - 1 \right) \quad ,$$

where E_V denotes the vacuum energy in units of eV.

The substrate, which supports the ultrathin films in the experiments, must exhibit a bandgap to confine the electrons in the direction toward the substrate. This can be an Shockley-inverted (orientation) bandgap [Sho39] in case of a metal substrate or a global bandgap in case of a semiconductor or insulator. The approximation of such a bandgap within this so-called two-band-model yields for the phase shift [Smi85, Luh02, Oga05]:

$$(2.5) \quad \phi_i = \text{Re} \left[-\arccos \left(2 \frac{E - E_L}{E_U - E_L} - 1 \right) \right] + \phi_0 \quad .$$

E_L and E_U denote the lower and upper edge of the bandgap, respectively. The constant phase offset ϕ_0 is in general unknown and represents a fit parameter. Electronic states, which are degenerate with substrate bands, are not truly confined to the film as they extend into the bulk crystal and thus are termed quantum well resonances (QWRs) [Chi00].

Interestingly, Chulkov et al. describe a hybrid approach that combines the simple intuitive notion of the rigid, infinite potential boundaries with the phase shift of the wave function experienced in a well with finite boundaries [Oga05]. The starting point is relation (2.1), in which the width of the well L is replaced by an effective width $L' = L + \delta$. This takes the penetration of the wave function into bulk and vacuum into account, which effectively widens the well by δ . The effective penetration δ is related to the phases upon reflection at the interfaces (equations (2.4) and (2.5)) and hence an energy-dependent quantity. This approach delivers results similar to the phase accumulation model.

2.1.2 Quantum Well States of Pb/Si(111)

The following paragraphs introduce some fundamental properties of the Si substrate and the Pb adsorbate as well as of metal/semiconductor interfaces before focusing on the QWSs in more detail.

The semiconducting Si(111) substrate with its global bandgap facilitates the electron confinement to the metal film. This point is of major importance for the study

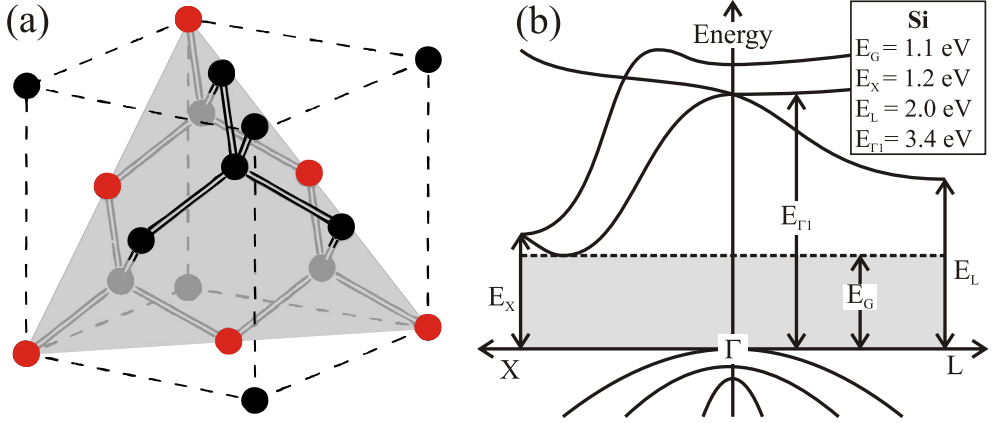


Figure 2.4: (a) Unit cell of Si. The 111-surface plane is indicated as gray-shaded area and exhibits a 3-fold symmetry. (b) Band structure of Si along the Γ -X and Γ -L directions [Che89]. The gray shaded area indicates the global bandgap of Si.

of ultrafast electron dynamics in supported ultrathin films. Time-resolved studies on QWSs in Ag/Fe(001) [Oga02] revealed excited electron lifetimes of ≤ 9 fs although sharp QWSs were observed and indicated a high degree of spatial confinement. This can be understood by the influence of orientation bandgap that facilitates confinement only at the Γ -point. In outer regions of k -space, however, unoccupied bands of the metal substrate exist, which can present an efficient decay channel. The lifetimes of 5 – 150 fs determined in the present work emphasize the importance of electron confinement in a global bandgap for time-resolved studies.

Silicon crystallizes in diamond structure with a lattice constant of $a_0 = 5.43$ Å [Kit04, Web08] as shown in Fig. 2.4(a). The next neighbor distance amounts to $a_{nn} = \sqrt{3}a_0/4 = 2.351$ Å; the next neighbor distance in the [111] lattice plane is given by $a_{nn}^{[111]} = a_0/\sqrt{2} = 3.84$ Å. The truncation of the crystal leaves one unsaturated dangling bond per three surface atoms, see Fig. 2.4(a), because of the directional alignment of the covalent bonds in semiconductors. These dangling bonds are saturated by a $(\sqrt{3} \times \sqrt{3})R30^\circ$ -Pb/Si(111) reconstruction as described in chapter 3.3.1. The reconstructed surface serves as smooth wetting layer with only minor corrugations and allows to grow epitaxial Pb films on Si(111).

The indirect bandgap in Si amounts to $E_G = 1.11$ eV at room temperature, whereas the direct bandgap at the Γ -point is 3.4 eV [Kit04] as sketched in Fig. 2.4 (b) along the Γ -X and Γ -L directions. The optical excitation in the experiments on Pb/Si(111) are in the range of 2 eV such that only multiphoton absorption or phonon assisted excitation of carriers are possible. The bandgap therefore not only maximizes the electron confinement but also minimizes the scattering of excited electrons into the QWS compared to substrates with orientation bandgap.

The metallic Lead adsorbate is a fourth main group metal with $Z = 82$ and electron configuration $[\text{Xe}]4f^{15}5d^{10}6s^26p^2$, which provides 4 valence electrons, $6s^2 + 6p^2$. Pb can be regarded as a quasi-free electron metal with sp -bands that

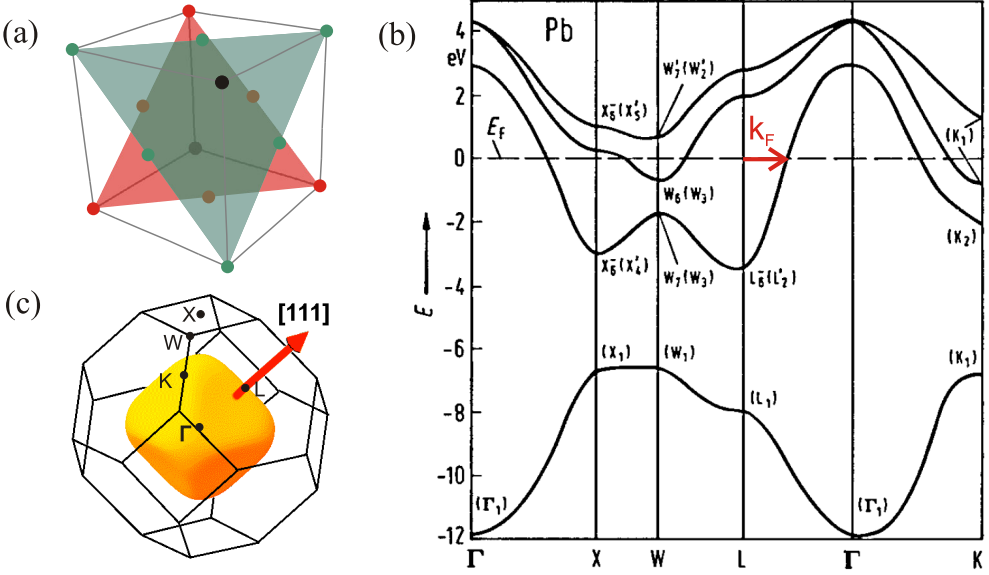


Figure 2.5: (a) The fcc unit cell of Pb contains 4 atoms. Two adjacent (111) crystal planes with inter-plane distance $d_{[111]} = 2.86 \text{ \AA}$ are indicated. (b) The band structure of Pb is shown along high-symmetry directions. (c) The first Brillouin zone of Pb with high symmetry points marked. The relevant Fermi vector k_F parallel to the $[111]$ direction is given in (b) and (c). [Lan76, Hor84]

disperse through the Fermi level making it attractive as a simple metallic model system. Pb crystallizes in a densely packed cubic fcc structure with a lattice constant of $a_0 = 4.95 \text{ \AA}$ [Kit04, Web08] as sketched in Fig. 2.5 (a). The epitaxial growth of Pb on Si(111) defines the inter-plane distance along the $[111]$ direction in Pb as the height of 1 ML

$$(2.6) \quad d_{[111]} = a_0 \frac{1}{\sqrt{3}} = 2.86 \text{ \AA} \equiv 1 \text{ ML} \quad .$$

The next neighbor distance in the $[111]$ lattice plane is given by $a_{nn}^{[111]} = a_0/\sqrt{2} = 3.50 \text{ \AA}$. In general, the significant lattice mismatch of the Si substrate and the Pb adsorbate of 8.8% presents a problem for the growth of epitaxial films, which is overcome by introducing an intermediate $(\sqrt{3} \times \sqrt{3})R30^\circ$ -Pb/Si(111) reconstruction that serves as wetting layer.

The $6s$ and $6p$ valence electrons of Pb form two hybridized bands, which are separated by a low-lying sp -bandgap at $4 - 7 \text{ eV}$ below E_F . The completely filled s -band at $12 - 7 \text{ eV}$ does not contribute to the electronic structure around E_F . The half-filled $6p_z$ -band that disperses along L- Γ becomes quantized in an ultrathin film and forms the QWSs.

Exact knowledge of the Fermi vector k_F along the quantization direction L- Γ is required for the precise understanding of periodicity of the QWSs in Pb/Si(111). The literature value from measurements of the De-Haas-van-Alphen effect is given by

$k_F = 1.59 \text{ \AA}^{-1}$ [And65]. Since the $6p_z$ -band is back-folded from the second Brillouin zone with the band bottom at the L-point it is necessary to consider the back-folded p -like Fermi vector $k_F^{L\Gamma}$ and not the s -like measured from the Γ -point [Wei02a] as indicated in Fig. 2.5(b). Using the inter-plane distance d_{111} for the back-folding the Fermi vector k_F and the Fermi wavelength λ_F are calculated to:

$$(2.7) \quad k_F^{L\Gamma} = k_F - \frac{\pi}{d_{111}} = 0.49 \text{ \AA}^{-1} \quad \Leftrightarrow \quad \lambda_F^{L\Gamma} = 12.8 \text{ \AA} \quad .$$

The electron density in Pb, which will be important for the discussion of the electron dynamics, is determined by the number of 4 valence electrons per Pb atom and the lattice constant a_0 . In 3D the density is given by $n^{(3D)} = 13.2 \cdot 10^{28} \text{ m}^{-3}$, in 2D by $n^{(2D)} = 3.77 \cdot 10^{19} \text{ m}^{-2}$. This corresponds to a density parameter of $r_s^{(3D)} = 2.30$ and $r_s^{(2D)} = 1.74$ for 3D and 2D, respectively, see appendix B. Pb has a high electron density, resulting in an efficient screening and facilitates the comparison with theory, see chapter 2.3.1 and appendix C.

A Schottky barrier [Sch38, Mot39] is formed in a metal/semiconductor interface due to the alignment of the interfacial Fermi levels E_F^{IF} of metal and semiconductor at the interface. This is shown schematically in Fig. 2.6 for the case of a p-semiconductor and a low work function metal, which is the relevant case for Pb/p-Si(111). The Fermi level alignment is associated with a charge transfer across the interface, which creates a space charge region and thus leads to band bending at the interface [Iba90, Mön01].

The sign and amount of the transferred charge is closely related to the strength of the intrinsic chemical bonding of the metal and semiconductor species at the surface. Generally the bonding of metals to semiconductors is so strong that already minute (0.001 ML) metal coverages determine the charge transfer and the band bending in the semiconductor. Hence, the Fermi level is pinned with respect to the semiconductor bands and does only depend on the metal species itself, not on the metal concentration [Iba90, Mön01].

For a low work function metal on top of a p-semiconductor, as in Pb/p-Si(111), the charge transfer proceeds from the metal to the semiconductor. The metal states serve as donors and free holes in the p-type valence band (VB) act as acceptors. The holes in the metal are efficiently screened within the first atomic layer and the surface polarization does not perturb the metallic bands close to the surface. The charge transfer hence only affects the band bending in the near surface region of the semiconductor. The excess electrons combine with free holes in the p-semiconductor to form a hole depleted space charge region. The spatial extend of the space charge region in the semiconductor is governed by Poisson's equation and can be estimated to be mesoscopic with typical dimensions of $0.1 - 1 \mu\text{m}$.

The charge redistribution creates an electric field perpendicular to the surface, which shifts the vacuum level as well as the valence band edge (VBE) and conduction band edge (CBE). The electric field in the space charge region can facilitate the charge separation of electron-hole (e-h) pairs that have been optically excited across the bandgap. In this sense, the Pb/Si(111) surface serves as a simple photovoltaic device [Bac76, Mön01]. In the 2PPE measurements this results in a surface photo voltage (SPV) shift of the spectra as discussed in chapter 5.4.1.

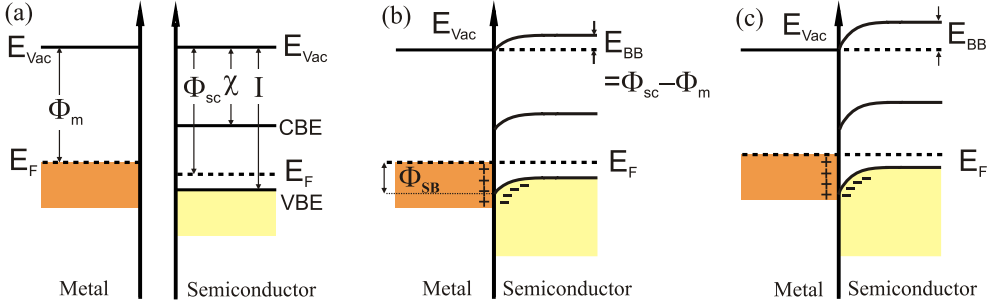


Figure 2.6: Schottky contact at a metal/p-semiconductor interface. (a) Before contacting the vacuum levels E_V are aligned and the Fermi levels E_F differ by the work function difference $E_{BB} = \Phi_{sc} - \Phi_m$. (b), (c) Upon contacting electrons flow from the metal to the semiconductor, which recombine with the free holes in the CB of the semiconductor and creates a hole-depleted surface charge region. In the Schottky-Mott model the amount of charge transfer and so the band bending are determined by the work function difference E_{BB} . (b) shows a Schottky contact for large work function and (c) for a smaller work function, which leads to smaller and larger band bending, respectively.

The electric field presents an effective barrier for holes that propagate from the semiconductor to the metal and hence serves as a diode, see Fig. 2.6. In the Schottky-Mott picture [Sch38, Mot39, Iba90, Mön01] the barrier height Φ_{SB} for a p-semiconductor is given by:

$$(2.8) \quad \Phi_{SB} = E_F - E_{VBE} = I - \Phi_M = E_{BB} + (I - \Phi_{SC})$$

E_{VBE} denotes the VBE at the interface, I the ionization potential of the semiconductor, Φ_M and Φ_{SC} the work functions of metal and semiconductor, and $E_{BB} = \Phi_{SC} - \Phi_M$ the band bending. It has been shown experimentally that this model is oversimplified as it neglects interface states like metal-induced gap states (MIGS) that reduce the dependence on the metal work function significantly [Iba90, Mön01]. The principle mechanism of charge transfer at metal/semiconductor junctions, however, can be qualitatively understood with the Schottky-Mott model. This will be important for the discussion of the coverage dependence of the SPV in Pb/Si(111), which is modulated by the work function oscillations, see chapter 5.4.1.

The quantized Pb/Si(111) band structure is shown schematically in Fig 2.7(a) for a Pb film with thickness d . The substrate band structure is depicted in Fig. 2.7(b) along the in-plane Γ -M and the out-of-plane Γ -L directions. Well-defined QWSs are expected for the gray shaded area of the Si total bandgap. This is in contrast to states, which are degenerate with bands of the Si crystal, that develop broad and diffuse QWRs. In the Γ -M direction in the surface plane a quasi-free electron dispersion is expected that gives rise to 2D parabolic bands, $E \propto k_{||}$.

One very important characteristic in quantum well systems is the periodicity of the QSE modulations as function of film thickness. The periodicity is directly linked to the ratio of inter-plane distance and Fermi wavelength in the quantization direction. As the occurrence of new QWSs at E_F is responsible for the variation of the physical

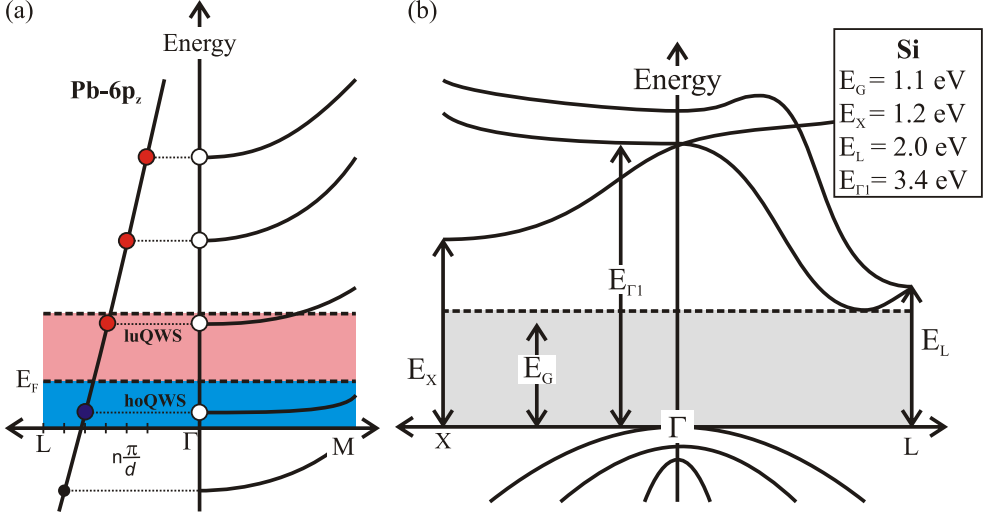


Figure 2.7: (a) Quantized band structure of Pb/Si(111). The $6p_z$ band in Pb is quantized along the L- Γ direction and forms discrete 2D QWSs that are delocalized in Γ -M direction. The states which fall into the global bandgap of the Si substrate (b) give rise to well-defined QWSs, whereas the states, which are degenerate with Si bulk bands form diffuse QWRs.

properties the coverage difference $\Delta\Theta$ for the Fermi level crossing of two subsequent states is evaluated from equations (2.2), (2.6) and (2.7):

$$(2.9) \quad \Delta\Theta = \frac{\lambda_F}{2d_{[111]}} = \frac{\pi}{k_F d_{[111]}} = 2.24 \text{ ML} \quad .$$

For every 2.24 ML increase of film thickness a QWS crosses E_F and becomes occupied. If, for example, the highest occupied quantum well state (hoQWS) is far from E_F for an *odd* coverage Θ then it will be close to E_F for an *even* coverage $\Theta + 1$ and so on. The nearly integer relation of inter-plane distance $d_{[111]}$ and Fermi wavelength λ_F results in pronounced 2 ML *odd-even* oscillations of the density of states (DOS) at E_F . This is the driving force for the oscillatory changes of the physical properties with each ML step like the superconductivity transition temperature [Guo04], workfunction [Kir07], surface reactivity [Ma07] and many more observed in numerous experiments [Jak71, Jal88, Jal92a, Jal92b, Bud00, Pfe00, Yeh00, Su01, Cha02, Ote02, Pfe02, Vil02, Wei02a, Czo03, Jia03, Czo04, Upt04b, Upt04a, Zha05, Ma06, Jia07, Zha08].

Microscopically, only integer ML coverages can exist. The difference of $\Delta\Theta - 2 = 0.24 \text{ ML}$ creates a slight shift of the QWS binding energies, which becomes manifest in a beating pattern. The relation $4 \times \Delta\Theta = 4 \times 2.24 \text{ ML} \approx 9 \text{ ML}$ predicts a 9 ML beating period, which is observed in numerous experiments [Upt04b, Zha05, Jia07, Kir07]. After 4 QWSs have crossed E_F , the beating of the odd-even behavior switches the coverage with a QWS close to E_F from *odd* to *even* and visa versa.

Fig. 2.8 shows the exemplary angle-resolved photoemission spectroscopy (ARPES) intensity of 10 ML Pb/Si(111) along the Γ -M direction in comparison to a density

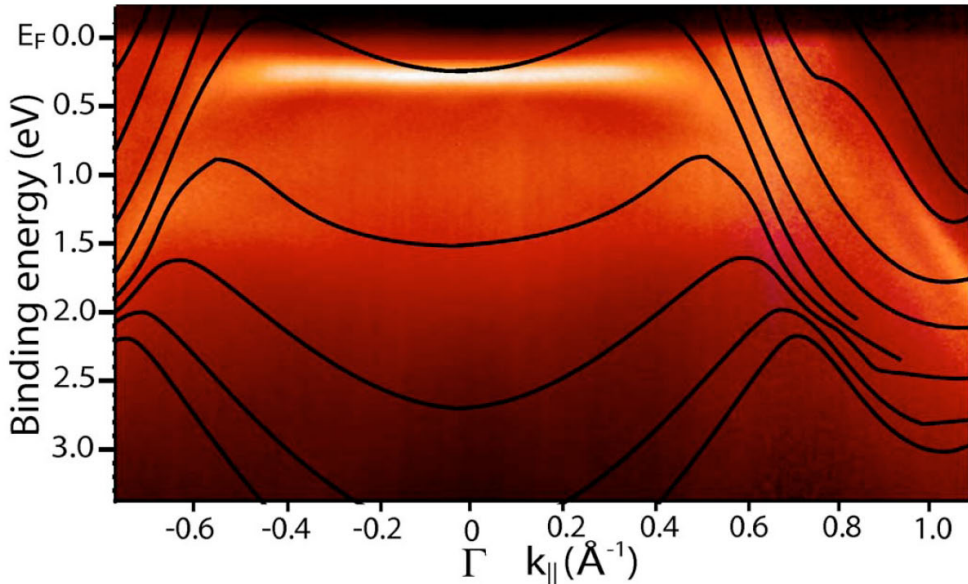


Figure 2.8: ARPES intensity of 10 ML Pb/Si(111) along the Γ -M direction in comparison to a DFT slab calculation (solid lines). The highest occupied quantum well state ~ 200 meV below E_F exhibits a sharp peak due to the confinement in the global Si bandgap. However, this states is anomalously localized in the lateral film direction with an effective mass $m^* = 8 m_e$. The origin of this effect is still debated in literature [Upt05, Dil06].

functional theory (DFT) slab calculation [Dil06]. The confinement of the metal electrons by the global Si bandgap explains the different line shapes and intensities for the confined hoQWS at $E - E_F = -0.2$ eV and the degenerate hoQWS+1 at $E - E_F = -1.5$ eV.

The major observation in Pb/Si(111), however, is the pronounced difference of many physical properties for adjacent coverages. A change of the coverage by 1 ML results in drastic changes of the physical properties of Pb/Si(111) and the characteristic *odd-oven* 2 ML oscillation period as reviewed in the next chapter. These features distinguish Pb/Si(111) as an excellent model system for the study of QSEs.

2.1.3 Quantum Size Effects in Pb/Si(111)

Ultrathin lead films on silicon have been studied with numerous surface sensitive techniques like ARPES, scanning tunneling microscopy (STM) and scanning tunneling spectroscopy (STS). These studies reveal that Pb/Si(111) can in fact be regarded as *the* 2D model system for the observation of QSEs. This section reviews the extensive theoretical and experimental literature and emphasizes the fundamental importance of the quantized band structure with its 2D QWSs as the driving force of *all* QSEs in Pb/Si(111).

The work function and surface reactivity are fundamental properties of metal surfaces. An early theoretical work to study QSEs in ultrathin metal films was a self-consistent study of a jellium slab in vacuum [Sch76]. Schulte as well as Feibelmann et al. [Fei83, Fei84] predicted oscillations of the work function with the period of the Fermi wave vector along the quantization direction. The oscillations are driven by the periodic occurrence of QWSs at E_F and the associated surface dipole due to the modulated spill out of electrons [Smo41, Lan70, Lan71]. It took, however, almost thirty years of advances in surface preparation techniques to observe these work function oscillations [Pag02]. In the present work such work function oscillations in Pb/Si(111) have been observed and could be directly linked to the DOS observed by PES [Kir07].

Conductivity experiments [Jak71, Jal88, Jal92a] were the first to observe QSEs in Pb/Si(111) as pronounced oscillations of the conductivity. These were attributed to the quantization of the electronic band structure perpendicular to the film. Further temperature and coverage dependent studies [Pfe00, Pfe02] indicate that a smooth - because annealed - Pb/Si interface facilitates the observation of QSEs. Furthermore, Jaloehowski et al. [Jal88] observed oscillations in the reflection high energy electron diffraction (RHEED) intensity with 2 ML period, which indicate a bilayer growth mode that is also driven by the quantized electronic structure.

Magic island heights, preferred cluster heights or bilayer growth modes manifest such an electronically driven growth. Preferred island heights have been first theoretically predicted for Pb/Si(111) by Zhang et al. [Zha98]. First STM [Bud00, Su01] and combined low energy electron diffraction (LEED) experiments [Hup01, Cha06] ob-

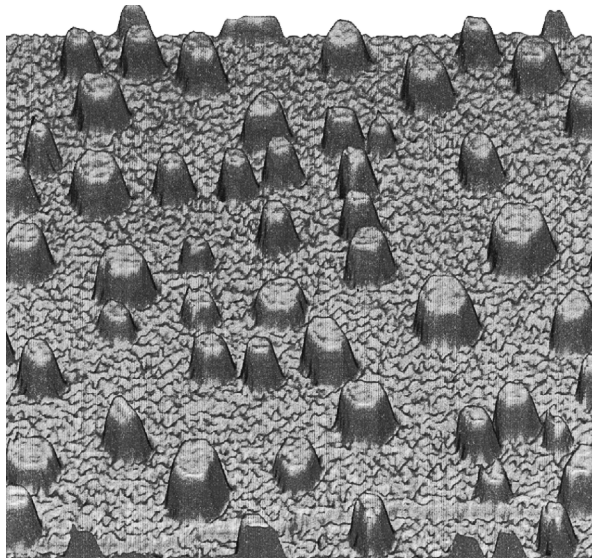


Figure 2.9: Topographic STM Image of the "magic" island heights of 3 ML Pb deposited on Si(111). Taken from [Hup01].

served the preference of certain so-called "magic" island heights for 3, 5, 7 ML above the wetting layer. Here, the growth conditions allow a complex interplay of diffusion and electronic repulsion due to the discrete QWSs. The magic heights reflect the minimization of the electronic energy when the hoQWS is far from E_F [Ote02]. Furthermore, surface x-ray diffraction (SXRD) studies [Czo03, Hon03, Czo04] and DFT calculations [Oga04] for Pb on Cu(111) confirm this interpretation and identify the quantized band structure as origin of the preferred island heights. The film stability was also studied with PES [Man02, Upt04b, Upt04a, Zha05], where only films with a hoQWS far from E_F are stable with respect to annealing. Similar effects were also observed in Ag/Fe(001) with photoemission [Luh01].

Devils Staircase phases are another aspect of an electronically driven growth mode that leads to self-assembling surface structures. For a 2D system a multitude of theoretically infinitely many different surface reconstructions are realized within a very small coverage window. In fact, Pb/Si(111) is one of the best realizations of such a behavior in 2D. In the coverage range of 1.2 – 1.3 ML more than a dozen different reconstructions were observed by STM [Hup03, Yak04, Ste06].

Even more quantum size effects are observed in Pb/Si(111). These are the modulation of the superconductivity transition temperature reported by Guo et al. [Guo04], which is closely related to the modulation of the electron-phonon (e-ph) coupling strength [Zha05]. Also, the magnitude and sign of the Hall coefficient [Vil02] is modulated with 2 ML period. Again, these QSEs are driven by the quantized bands and the resulting oscillatory DOS at E_F . The wealth of QSEs studied under equilibrium conditions as well as the comprehensive understanding of the decisive role of the QWSs establish Pb/Si(111) as a highly attractive model system for the study of ultrafast electron dynamics and their dimensionality dependence at the crossover from 3D to 2D.

2.2 Charge Density Waves

Density waves are broken symmetry ground states that can form at low temperatures in low-dimensional materials or in metals with high densities of states at the Fermi level $n(E_F)$. The strong and anisotropic electron-electron (e-e) and e-ph coupling results in CDWs with a spatially modulated electron density¹. The charge-ordered CDW phase is a type of coupled electronic-lattice instability that often competes with other low-temperature ground state phases such as superconducting phases. The transition to the ordered state is driven by the condensation energy $\sim n(E_F)\Delta^2$. The order parameter Δ is defined as the energy gap for single-particle excitations opened by the phase transition.

The fundamental concept of the CDW formation involves a periodic modulation in the density of the electronic charges with a characteristic spatial distortion \vec{r} that does not transform according to the symmetry group describing the ionic positions. The driving force of this coupled electron-lattice instability is the reduction of the kinetic electron energy as a consequence of a spontaneous periodic modulation of the crystalline lattice with an appropriate (often incommensurate) wave vector \vec{q} in reciprocal space.

The reason for a given material to develop a CDW is the so-called nesting of the Fermi surfaces of a low-dimensional material, which results in a diverging response of the electron system to a lattice perturbation at the Fermi wave vector k_F . Many low-dimensional materials exhibit anisotropic Fermi surfaces with pronounced nesting vectors that result in CDWs. Well-known examples are transition metal dichalcogenides like NbSe₃ and TaSe₃, transition metal bronzes like K_{0.03}MoO₃, and quasi-1D organic conductors like Bechgaard's salt TTF and Krogmann's salt KCP. The concept of a nesting vector for the formation of CDW state and its implications for the band structure are discussed in the following sections.

2.2.1 Peierls Transition

The transition to the CDW state is often termed a Peierls metal-to-insulator transition [Pei29, Pei30a, Pei30b, Frö54, Pei55] because at least part of the Fermi surface is gapped out and can not be regarded as metallic anymore. This section presents the basic CDW mechanism for the idealized example of a chain of atoms in 1D [Grü94].

The simplified description by a 1D chain of atoms with parabolic band dispersion up to the zone boundary and uniform charge density ρ according to the nearly free electron gas (NFE) approximation, see Fig. 2.10(a), captures the essential physics of the metal-to-insulator transition. This simplified model provides an intuitive access to coupled electron-lattice dynamics of the CDW compound TbTe₃ discussed in chapter 7. The atomic chain is presumed to be ideally metallic with a half filled band. Thus k_F is located in the middle of the Brillouin zone far away from the zone boundary. The perturbation of the coupled electron and lattice system with a distortion of

$$(2.10) \quad q = 2k_F$$

¹The discussion of spin density wave (SDW) phases with a spatially modulated spin density is beyond the scope of the present work.

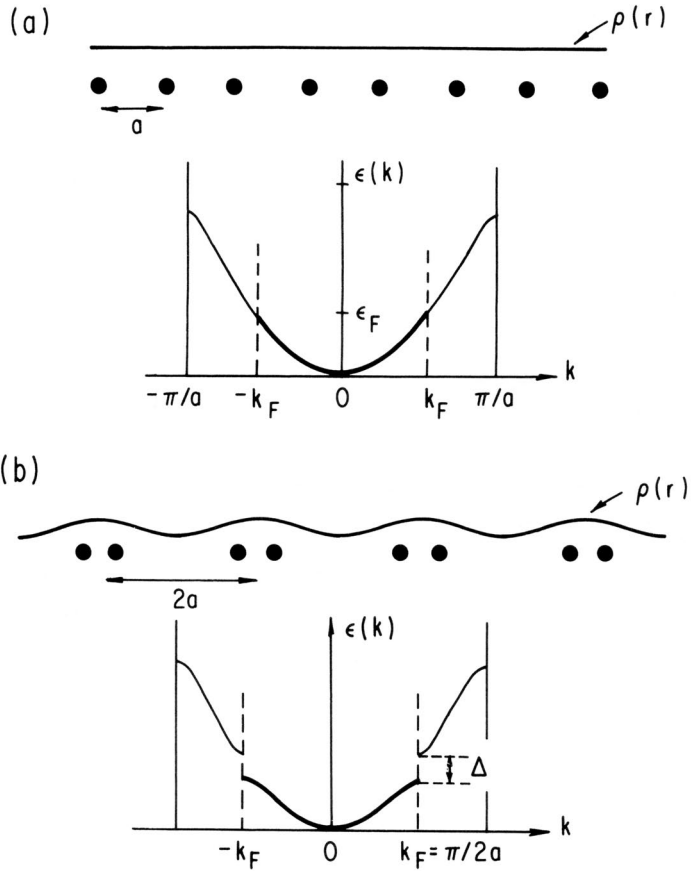


Figure 2.10: Peierls metal-to-insulator phase transition. (a) Idealized metallic 1D atomic chain with half filled band and k_F far away from the zone boundary. The charge density ρ is constant above the phase transition temperature and the lattice periodicity is given by a . (b) The doubling of the lattice periodicity to $2a$ due to a distortion with $q = 2k_F$ results in modulated charge density. Accordingly, new bandgaps open up at $\pm k_F$ and result in an insulating electronic structure. After [Grü94].

results in a Peierls instability: New bandgaps open at the Fermi surface, $\pm k_F$, because of the doubling of the crystal periodicity, as sketched in Fig. 2.10(b). Thus, the bands are gapped out at $\pm k_F$ and the electronic system becomes insulating. Since the group velocity vanishes in at the Brillouin zone boundary, $v_{\text{group}} = \partial E / \partial k = 0$, the wave function in the zone boundary are standing waves and result in a spatially modulated electron density:

$$(2.11) \quad \Delta \rho(x) \propto \Delta \cos(2k_F x + \varphi) \quad , \quad \lambda_0 = \frac{\pi}{k_F} \quad .$$

The period of the modulation $\lambda_0 = \pi/k_F$ is exactly the same as the original distortion.

The density modulation can be regarded as a macroscopically populated, frozen-in lattice distortion with the CDW wave vector q . The e-ph coupling is also reflected in a renormalization of the phonon spectrum in the CDW state, known as Kohn-anomaly [Koh59, Wol62], such that the phonon dispersion exhibits a dip at $q = 2k_F$.

The physical mechanism for the CDW is the nesting of the Fermi Surface (FS) due to a coupling with the perturbation vector $q = 2k_F$. In 1D, the FS is very simple: it consists of two points at $\pm k_F$ and a wave vector $q = 2k_F$ can perfectly nest these two points, resulting in a bandgap. The Peierls transition can be understood as coupled instability of electron and lattice degree of freedom minimizing the total free energy:

$$(2.12) \quad \text{MIN} = E_{\text{electronic}} + E_{\text{lattice}} \quad .$$

Clearly, the impact of the FS nesting mechanism on a given band structure depends on the dimensionality of the coupled electron and lattice system, which shall be discussed in the context of the linear response theory.

The Lindhard response function $\chi(\vec{q})$, some times known as general susceptibility, governs the CDW mechanism with its pronounced dependence on dimensionality and temperature [Lin54, Grü94]. $\chi(\vec{q})$ describes the response of a nearly free electron gas to a periodic perturbation potential

$$(2.13) \quad \phi(\vec{q}) = \int d\vec{r} \phi(\vec{r}) e^{-i\vec{q}\cdot\vec{r}}$$

with the perturbing wave vector \vec{q} . The induced charge density

$$(2.14) \quad \rho_{\text{ind}}(\vec{q}) = \chi(\vec{q}) \phi(\vec{q})$$

is proportional to the potential and the Lindhard response function as is given by

$$(2.15) \quad \chi(\vec{q}, T) = \int \frac{d\vec{k}}{(2\pi)^d} \frac{f(T, \vec{k}) - f(T, \vec{k} + \vec{q})}{E(\vec{k}) - E(\vec{k} + \vec{q})} \quad .$$

The quantity $f(T, \vec{k})$ describes the electron distribution and introduces a temperature dependence of the response function. The dependence on the dimensionality d applies to the integration itself and the divergence of the denominator for $E(\vec{k}) = E(\vec{k} + \vec{q})$.

The induced charge density will itself cause an induced variation in the potential at the same wave vector due to a redistribution of the electrons:

$$(2.16) \quad \phi_{\text{ind}}(\vec{q}) = -g \rho_{\text{ind}}(\vec{q}) \quad .$$

Here g is the electron-phonon coupling constant², which is assumed to be independent of q and a small quantity in this weak-coupling analysis. Proceeding further, the external perturbation potential ϕ_{ext} and the internal, induced potential ϕ_{int} are substituted for ϕ in equation (2.14) and yield:

$$(2.17) \quad \rho^{\text{ind}}(\vec{q}) = \chi(\vec{q})[\phi_{\text{ext}}(\vec{q}) + \phi_{\text{ind}}(\vec{q})] \quad .$$

²The dimensionless e-ph coupling constant is defined by $\lambda = g^2 n(E_F) / (\hbar\omega^2 k_F)$.

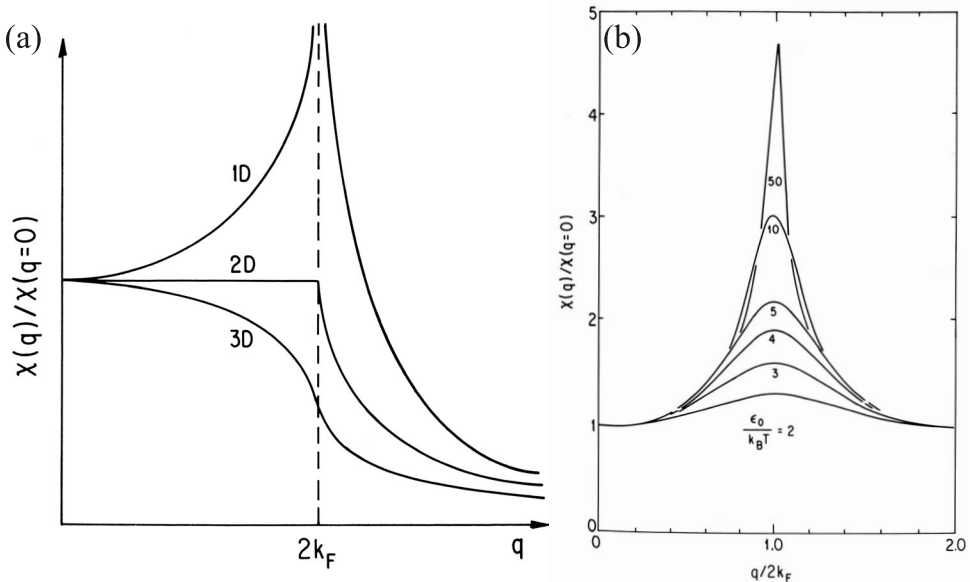


Figure 2.11: (a) Dimensionality dependence of the response function $\chi(q)$ at $T = 0$ K normalized to the value at $q = 0$. The response function varies smoothly at $2k_F$ for a 3D system. In 2D, the first derivative exhibits a discontinuity at $2k_F$, whereas the response of a 1D system diverges at $2k_F$. (b) Temperature dependence of the normalized response function. A significant response is only expected for sufficiently low temperatures $k_B T \ll \epsilon_0$. After [Grü94].

This leads to the mean field induced charge density

$$(2.18) \quad \rho^{\text{ind}}(\vec{q}) = \frac{\chi(\vec{q}) \phi_{\text{ext}}(\vec{q})}{1 + g\chi(\vec{q})},$$

which suggests an instability of the charge density due to a divergence for $g\chi = -1$. Since the e-ph constant g is typically a small number, the actual formation of a CDW requires a large negative value of the general susceptibility. A large value of χ can be realized in materials where large portions of the FS are nested by a single wave vector q as this leads to divergence of the denominator in equation (2.15).

The Fermi surface nesting is closely related to the dimensionality dependence of the response function χ in equation (2.15), as discussed in Fig. 2.11(a). A smooth variation of the response at $2k_F$ is expected for a 3D system, also a 2D system presents a continuous change of the response, whereas the response of a 1D system diverges at $2k_F$. Exactly this divergence of the response function is the driving force for the formation of the CDW phase in low dimensional materials.

Focusing on the case of 2D electron systems that occur in layered materials, two limiting cases for the FS nesting can be distinguished. For an isotropically interacting 2D electron system, the FS is a circle of diameter k_F , as depicted in Fig. 2.12(a). A

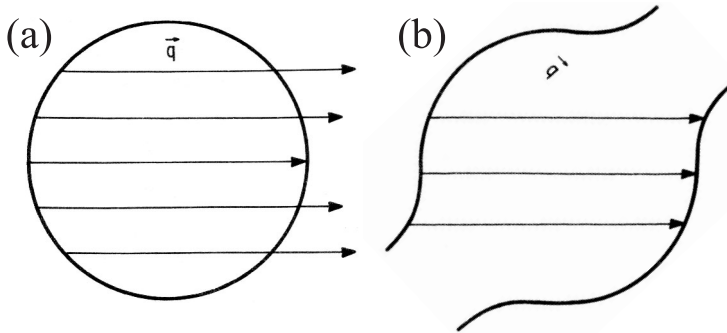


Figure 2.12: (a) Imperfect FS nesting in case of isotropic two-dimensional coupling resulting in a circular 2D FS. (b) Almost perfect FS nesting in a system with highly anisotropic coupling that results in a quasi-1D FS [Grü94].

single perturbation wave vector of $q = 2k_F$ can only nest two single points on the FS, which results in a negligible change of the response function χ . In contrast, an electronic system with anisotropic coupling exhibits also an anisotropic band dispersion. This results in a quasi-1D FS as shown in Fig. 2.12(b). This quasi-1D FS can be nested to a significant extent by a single wave vector, resulting in a large response $\chi(q = 2k_F)$ to the perturbation.

Consequently, materials with (i) a layered structure and (ii) anisotropic in-plane interaction, which results in a layered quasi-1D electron gas, are of interest for the study of the CDW formation. One prominent example is the Lanthanide Tri-Telluride series $R\text{Te}_3$ to which TbTe_3 belongs. The $R\text{Te}_3$ series exhibits a wealth of CDW phenomena as will be discussed in section 2.2.3.

The temperature dependence of the response function is introduced by the distribution function in equation (2.15). In case of $T = 0$, as discussed in Fig. 2.11(a), the response function in 1D diverges at $q = 2k_F$ and reaches an infinite value. The actual temperature dependence, however, renders the response to be finite at $2k_F$:

$$(2.19) \quad \chi(2k_F, T) = -e_0^2 n(E_F) \ln \frac{1.14\epsilon_0}{k_B T}$$

Here, ϵ_0 is an arbitrarily chosen energy cutoff, usually $\epsilon_0 = E_F$. The temperature dependence of the response function is shown in Fig. 2.11(b), where a strong response is only observed for sufficiently low temperatures $k_B T \ll \epsilon_0$.

The Bardeen-Cooper-Schrieffer (BCS) theory [Bar57a, Bar57b] can be applied to the CDW phase transition as the condensation of Cooper pairs due to a coupling of a lattice distortion to the electronic system and a minimization of the total energy is closely related to the CDW phase transition [Grü94]. BCS theory provides explicit expressions for the relation of the order parameter Δ and mean field phase transition temperature

$$(2.20) \quad 2\Delta = 3.52 k_B T_{\text{CDW}}^{\text{BCS}}$$

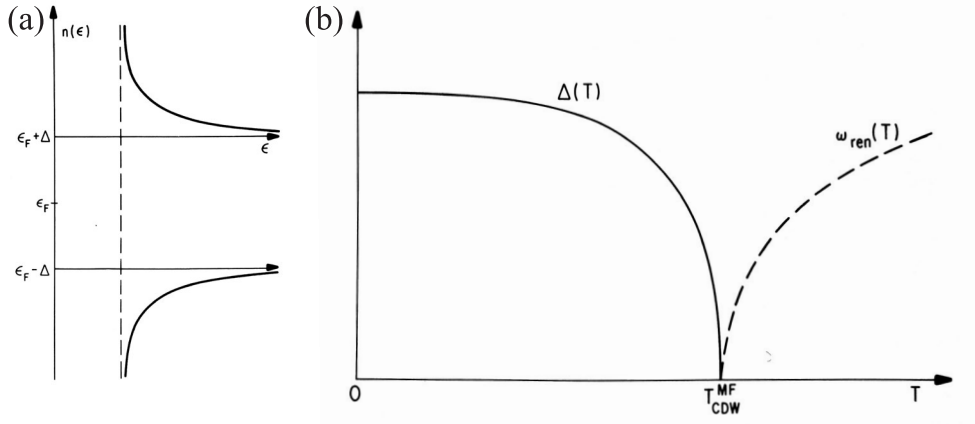


Figure 2.13: (a) Idealized DOS at k_F for the CDW phase. The full bandgap 2Δ for single particle excitations scales linearly with the phase transition temperature. (b) Temperature dependence of the order parameter Δ . After [Grü94].

as well as for the CDW phase transition temperature

$$(2.21) \quad k_B T_{\text{CDW}}^{\text{MF}} = 1.14 \epsilon_0 \exp\left(\frac{-1}{gn(E_F)}\right),$$

which depends exponentially on the electron density $n(E_F)$ and the strength of the e-ph coupling g . The order parameter Δ is defined as the CDW gap around E_F . Fig. 2.13(a) depicts the DOS around E_F for the gapped CDW state. Fig. 2.13(b) shows the temperature dependence of the order parameter itself with its well-known signature for BCS behavior:

$$(2.22) \quad \frac{|\Delta(T)|}{|\Delta(0)|} \propto \sqrt{1 - \frac{T}{T_{\text{CDW}}^{\text{MF}}}}.$$

2.2.2 Collective Excitations

The basic mechanism of the CDW formation, as sketched in the previous section, is founded on the coupling of electron and lattice degrees of freedom and the minimization of the total energy. In the framework of the second quantization, the CDW ground state is a coherent superposition of various e-h pair states. The emergence of the CDW phase thus is a collective phenomenon and one of the fundamental properties of such a strongly correlated material. Directly linked to this collective interaction in the CDW ground state is the question of the collective excitation modes of the CDW state. The investigation of these collective excitations can be accomplished with tr-ARPES, which measures the temporal evolution of the single-particle spectral function, as detailed in chapter 2.4.7.

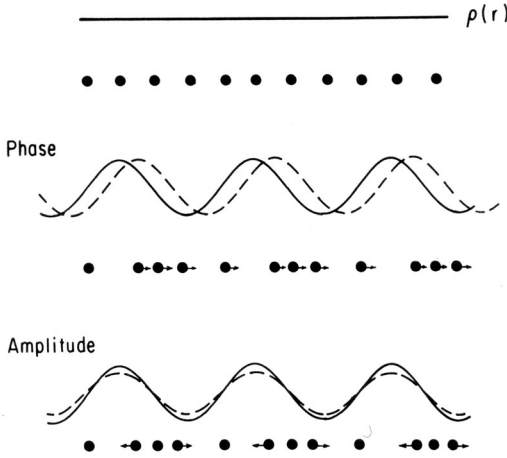


Figure 2.14: Collective excitations of the CDW state. Top: Phase shift of the modulated electron density ρ with respect to the CDW groundstate modulation. Bottom: Amplitude modulation of the CDW. After [Grü94].

The collective excitations are treated in the long-wavelength limit of the Ginzburg-Landau theory. Here, the order parameter is a complex quantity $\Delta = |\Delta|e^{i\phi}$ with amplitude and phase. Returning to simple 1D atomic chain from Fig. 2.10 two collective excitations modes of the coupled electron and lattice system are expected. These collective excitations are (i) the phase mode (phason) and (ii) the amplitude mode (amplitudon). In real space, the phason can be viewed as a unidirectional shift of the ion core positions resulting in a shift of the CDW with respect to the underlying lattice without change of the magnitude of the charge modulation ρ , as depicted in Fig. 2.14. The amplitudon modulates the amplitude of the lattice distortion itself, which in turn leads to a change of the CDW amplitude and thereby also to a modulation of the gap size Δ .

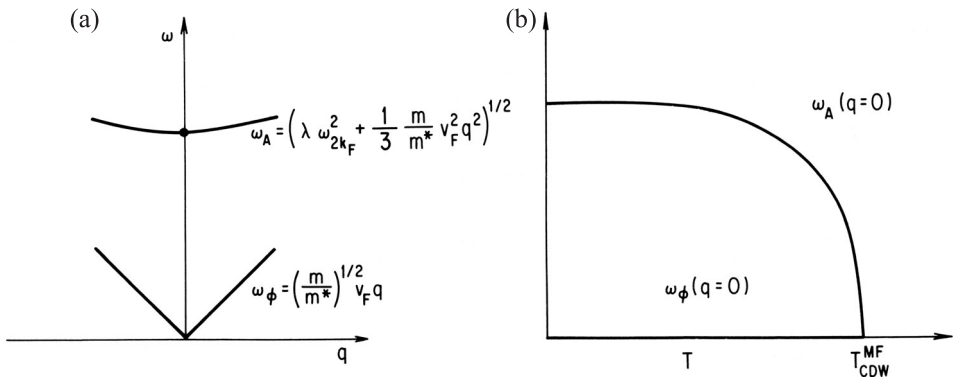


Figure 2.15: (a) Dispersion of the CDW phase $\omega_\phi(q)$ and amplitude mode $\omega_A(q)$ [Lee74]. Here, λ is the dimensionless e-ph coupling constant². (b) Temperature dependence of ω_ϕ and ω_A for $q=0$. Only the amplitudon exhibits a temperature dependence. After [Grü94].

La	Ce	Pr	Nd	Pm	Sm	Eu	Gd	Tb	Dy	Ho	Er	Tm	Yb	Lu
hex	fcc	hex	hex			bcc	hcp	hcp	hcp	hcp	hcp	hcp	hcp	hcp
4.418	4.385		4.358		4.335	4.58	4.320	4.308	4.302	4.288	4.285	4.275		

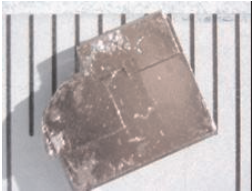
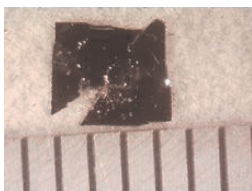

		
R-Te₃ R=Y, La-Sm, Gd-Tm	R₂-Te₅ R=Y, La-Sm, Gd-Ho	R-Te₂ R=Y, La-Sm, Gd-Tm

Figure 2.16: Photographs of several Lanthanide-Tellurium crystals [Fis08]. The small ticks on the scale denote mm. The Lanthanide Tritelluride series belongs to a whole family of binary alloys with different oxidation states of the Lanthanide. The upper panel denotes the lattice constants in Angström along the $R\text{Te}_3$ series [Vil91, Ru08].

The dispersion of the two fundamental collective excitation modes with quasi-momentum is sketched in Fig. 2.15(a). The phase mode $\omega_\phi(q)$ is the excitation of an acoustic, low-energy mode with linear dispersion around $q \approx 0$. The amplitude mode $\omega_A(q)$ is the optical, high-energy excitation mode of the system, which shows only a weak dispersion. The frequency of the amplitude mode shows an explicit temperature dependence in the long wavelength limit $q = 0$, as sketched in Fig. 2.15(b), and follows the BCS relation of equation (2.22), whereas the phason frequency is constant up to the phase transition temperature.

For the discussion of the tr-ARPES measurements on TbTe_3 in chapter 7, the amplitude mode is most important as it modulates the magnitude of the CDW itself and thus the order parameter $|\Delta|$ as a function of time. The modulation of $|\Delta|$ is localized in the CDW nesting region and provides a clear experimental signature in the transient spectra.

2.2.3 A Tunable CDW System: $R\text{Te}_3$

For the tr-ARPES experiments, TbTe_3 was carefully chosen for numerous reasons. TbTe_3 belongs to the Tritellurides series $R\text{Te}_3$ of prototypical CDW compounds, whose physical properties can be quasi-continuously tuned by variation of the Lanthanide R. $R\text{Te}_3$ are layered (2D) materials which are grown via binary melt as described in [Ru06b] and summarized in chapter 3.3.2.

The CDW in $R\text{Te}_3$ was first observed by DiMasi et al. by transmission electron microscopy [DiM95]. The ground state properties of the CDW phase have been studied with various techniques like heat capacity, susceptibility, and electrical resistivity measurements [Ru06b], variable temperature x-ray diffraction [Mal05, Ru06a, Ru08], Raman scattering [Sac06, Lav08], STM [Fan07] and ARPES. Especially, high-resolution ARPES provides valuable information on the exact size, position and symmetry of the CDW gap [Bro04, Shi05, Gar07, Bro08] by analysis of the single particle spectral function $A(\vec{k}, E)$ in the frequency domain, see chapter 2.4.3.

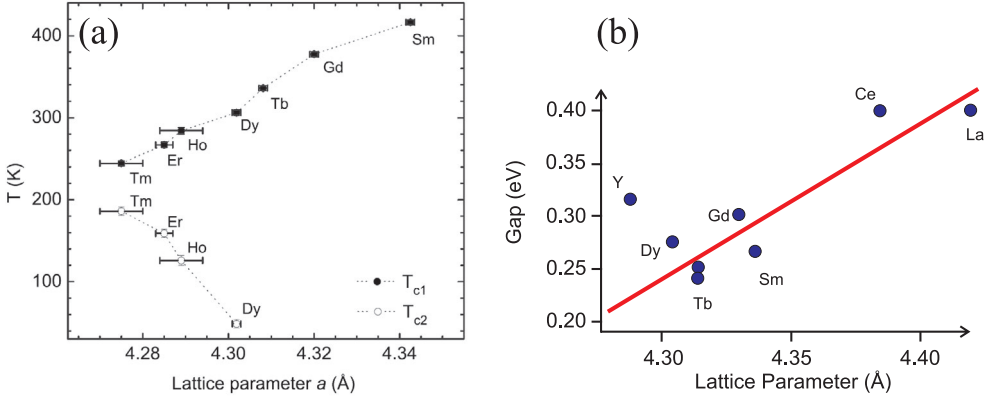


Figure 2.17: (a) CDW phase transition temperature in $R\text{Te}_3$ from conductivity measurements [Ru08]. The heavier Lanthanides exhibit a second CDW bandgap at very low temperatures. (b) Gap size in $R\text{Te}_3$ from ARPES measurements [Bro08]. Clearly, both properties scale with the lattice parameter.

The tunability of the lattice parameter (Fig. 2.16) due to substitution of the Lanthanide R in the binary metal $R\text{Te}_3$ results in a quasi-continuous variation of the wave function overlap. The wave function overlap determines the electron density at the Fermi level $n(E_F)$, which is also termed chemical pressure. According to equations (2.21) and (2.20), the increasing chemical pressure $n(E_F)$ raises the phase transition temperature and enlarges the energy gap Δ . Fig. 2.17 shows the CDW transition temperature extracted from conductivity measurements [Ru08] and the gap size [Bro08] as function of the Lanthanide R . The pronounced gap of several $\Delta = 100$ meV and the CDW phase transition temperature can be tuned by substitution of R within $T_{\text{CDW}} = 100 - 400$ K.

Qualitatively, the variation of T_{CDW} and Δ as function of the substituent R is understood by the influence of the chemical pressure $n(E_F)$: As one moves from the lighter to the heavier elements in the Lanthanide series, see Fig. 2.16, the lattice parameter decreases because of the well-known Lanthanide contraction³. This results in an increasing wave function overlap equivalent to an increasing electron density $n(E_F)$, which in turn leads to a rising T_{CDW} and Δ .

A quantitative comparison to the BCS results, however, reveals a significant deviation of the transition temperature. In case of TbTe_3 , the BCS phase transition temperature is calculated from the gap size of 240 meV [Bro08] and equation (2.20) to be $T_{\text{CDW}}^{\text{BCS}} = 1600$ K. This is about 5 times more than the experimental value of $T_{\text{CDW}}^{\text{exp}} = 336$ K [Ru08]. The significantly lower phase transition temperature can be rationalized by the observation that only part of FS are gapped out and thermal fluctuations hamper the CDW formation. Both effects result in a lowering of T_{CDW} .

³Any given compound of the rare earths is very likely to crystallize with the same structure as any other rare earth. However, the lattice parameters become smaller and the crystal denser as the compound proceeds across the series. This contraction of the lattice parameters is known as the lanthanide contraction, which originates from an increasing screening of the core electrons with increasing number of $4f$ -electrons

The crystal structure and band dispersion of RTe_3 are closely related, and well described in a tight binding (TB) model with 2D symmetry that facilitates the experimental analysis of the equilibrium properties [Bro04, Shi05, Gar07, Bro08]. The RTe_3 crystal structure, as shown in Fig. 2.18(a), is RTe_3 is weakly orthorhombic with space group $Cmcm$ [Mal05, Mal06, Ru08, Ru06b] and constructed from the basic building block of a square Te plane and a buckled RTe slab. The small orthorhombic distortion of the Te square shrinks from $a = 4.405 \text{ \AA}$ and $c = 4.420 \text{ \AA}$ in LaTe_3 to $a = 4.302 \text{ \AA}$ and $c = 4.304 \text{ \AA}$ in DyTe_3 [Ru06a, Ru08]. In the RTe_3 crystal one RTe slab resides between two largely decoupled Te planes. Two of these building blocks are stacked up along the b -axis. Here, the usual convention is used where the b -axis is perpendicular to the Te square in the (a, c) plane that is parallel to the Te planes. The experimental values for RTe_3 are $b = 25.7 \text{ \AA}$ and $a \approx c = 4.3 \dots 4.5 \text{ \AA}$ [Ru06a, Ru08].

Since the planar square net of Te atoms is rotated by 45° with respect to the RTe slab and has only half the area, two different unit cells in real space are used: The larger 3D unit cell is defined by the R atoms of the buckled slab (green in Fig. 2.18), whereas the smaller 2D unit cell is given by the square Te plane (purple). For the description of the band structure in reciprocal space, see Fig. 2.18(c), this results in a larger 2D Brillouin zone corresponding to the Te square, which is rotated by 45° with respect to the smaller 3D Brillouin zone. The 3D Brillouin zone is based on the R atoms of the slab and defines the reciprocal in-plane vectors $a^* = 2\pi/a$ and $c^* = 2\pi/c$.

The band structure can be calculated using the linear muffin-tin orbital method (LMTO) [Lav05], which reveals 18 bands between $E - E_F = 2 \text{ eV}$ and -6 eV . These bands correspond to three Te $5p$ orbitals from each of the 6 Te per unit cell. However, only 4 bands cross E_F , which are derived from the $5p_x$ and $5p_z$ Te orbitals in the (a, c) plane. These 4 bands form the VB and are well isolated from other bands. Thus, the shape of the FS is solely determined by the Te $5p$ orbitals. The calculated and measured band dispersions are well reproduced by a much simpler 2D TB model of the in-plane Te $5p$ orbitals. The TB model considers only two perpendicular chains of $5p_x$ (red) and $5p_z$ (blue) orbitals, as depicted in Fig. 2.18(b). The coupling constants t_{\parallel} and t_{\perp} describe the parallel and perpendicular coupling with respect to the chains. In this calculation the size (a, c) of the 3D unit cell are the only parameters that explicitly depend on the Lanthanide substituent R. Assuming a perfectly square Te plane and neglecting the coupling of p_x and p_z as well as inter-plane coupling along the b -axis yields the dispersion relations in the (a, c) plane:

$$(2.23) \quad \begin{aligned} E_x(k_x, k_z) &= -2t_{\parallel} \cos \frac{2(k_x + k_z)}{a} - 2t_{\perp} \cos \frac{2(k_x - k_z)}{a} - E_F \\ E_z(k_x, k_z) &= -2t_{\parallel} \cos \frac{2(k_x - k_z)}{a} - 2t_{\perp} \cos \frac{2(k_x + k_z)}{a} - E_F \end{aligned} .$$

The Fermi level $E_F = -2t_{\parallel} \sin(\pi/8)$ is fixed by the band filling, which amounts to $5/8$ electrons per Te p orbital [Bro08]. The TB coupling constants are adjusted to reproduce the LMTO calculation [Lav05], which is accomplished for $t_{\parallel} = -1.9 \text{ eV}$ and $t_{\perp} = 0.35 \text{ eV}$. The two Te planes in RTe_3 are distinguishable, see Fig. 2.18, which is not described within the TB model and lead to two sets of so-called bilayer split bands that are not shown in Fig. 2.18(c) and Fig. 2.19.

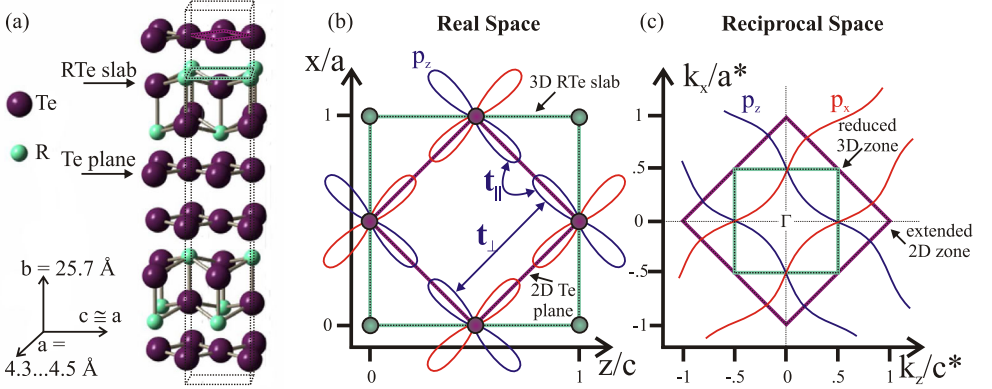


Figure 2.18: (a) The crystal structure of $R\text{Te}_3$ [Ru06b] is composed of square Te planes and buckled RTe slabs. Note that the b -axis in the space group Cmcm of $R\text{Te}_3$ is perpendicular to the Te plane with $b = 25.7 \text{ \AA} \gg a \approx c = 4.3 \dots 4.5 \text{ \AA}$ [Ru06a, Ru08]. (b) Real-space model of the square-planar Te sheet with 2D (purple) and 3D (green) unit cells of the Te planes and the RTe slab, respectively. The Te p_x (red) and p_y (blue) orbitals and the coupling within the TB calculation are indicated. (c) FS calculated in the TB model. The extended 2D and reduced 3D Brillouin zone are indicated. The small perpendicular coupling $|t_{\perp}| \ll |t_{\parallel}|$ results in two sets of quasi-1D bands and an almost rectangular FS.

The FS calculated in the TB model is shown in Fig. 2.18(c) in an extended and reduced zone scheme. Since the TB bands are constructed from only one Te plane, they have the periodicity of the larger 2D Brillouin zone and are folded back with respect to the smaller 3D Brillouin zone, as depicted in Fig. 2.19. Due to anisotropic coupling, $|t_{\text{para}}| \ll |t_{\text{para}}|$, each chain of Te $5p$ orbitals results in quasi-1D band. The presence of *two* $5p$ orbital chains results in the 2D FS that is constructed from two independent orbital chains.

The LMTO calculation and the TB model agree very well to high-resolution ARPES data [Bro04, Bro08] for the band dispersion around E_F . The intensity of the back folded bands is very small, which reflects the small 3D coupling of the system. Specifically, the excellent description of the in-plane Te $5p$ orbitals indicates a weak coupling to the RTe slab and underlines the 2D character of $R\text{Te}_3$ compounds. The TB model does not capture the coupling of the p_x and p_z orbital chains to each other. This inter-chain coupling leads to an avoided crossing of the p bands and thus splits the FS into an inner square and 4 outer electron pockets. The inner square is located in the reduced 3D zone, the four electron pockets are situated in the tips of the extended 2D zone, (not shown in Fig. 2.18(c) and Fig. 2.19, see [Bro08]). For an introductory discussion of the nesting-driven CDW formation in $R\text{Te}_3$, however, the inter-chain coupling can be neglected.

The FS nesting in $R\text{Te}_3$ is discussed on the basis of the TB model and the resulting quasi-1D band structure. The experimentally determined perturbation vector $q_{\text{CDW}} = (0, 0, 2/7)$ is an unidirectional lattice distortion [Kim06, Fan07]. The STM measurements on CeTe_3 [Kim06] and TbTe_3 [Fan07] suggest that q is incommensu-

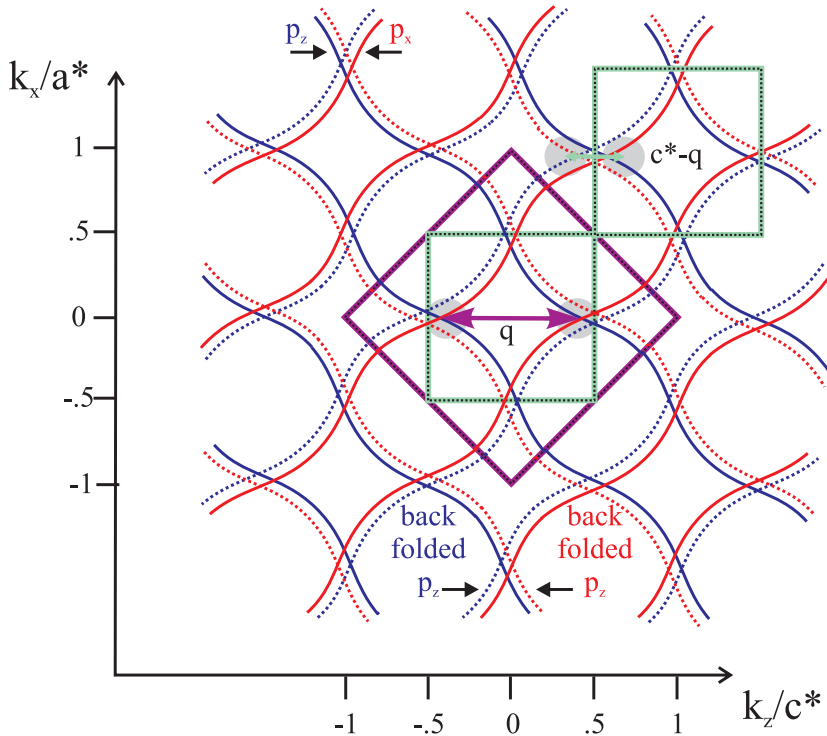


Figure 2.19: Fermi surface nesting vector q in RTe_3 and TB bands as in an extended zone scheme. The dashed bands indicate the back folding into the 3D zone. The nesting vector q is given in the larger 2D (purple) and smaller 3D (green) Brillouin zones. The resulting Peierls gaps in the FS are indicated by gray shaded areas.

rate. Much more so, temperature-dependent SXRD on RTe_3 reveal that the CDW wave vector q_{CDW} remains incommensurate over the entire measured temperature range [Ru08, Grü94]. Previous ARPES experiments on RTe_3 [Bro04, Bro08, Gwe98] reveal that sections of the FS that are nested by the distortion vector q_{CDW} are indeed gapped. The perturbation vector is of similar magnitude and oriented in the same direction, along the c -axis throughout the RTe_3 series. The FS nesting along the c^* -axis is depicted in Fig. 2.19 in extended and reduced zone schemes. The distortion vectors q and $c^* - q$ in the extended and reduced Brillouin zone scale linearly with the reciprocal lattice vector c^*

$$(2.24) \quad q_{\text{CDW}} \approx \begin{cases} \frac{5}{7} c^* & \text{extended zone scheme} \\ c^* - q = \frac{2}{7} c^* & \text{reduced zone scheme} \end{cases}$$

The preference of the c -axis over the a -axis observed in the unidirectional CDW phase transition in RTe_3 is surprising since the FS exhibits an almost perfect 4-fold in-plane symmetry, see Fig. 2.18(c), and one might expect a bidirectional CDW phase transition along both axes.

The CDW formation is driven by the minimization of the total energy. The ionic deformation by q during the CDW transition increases the lattice energy. This energy increase is overcompensated by the electronic response for this particular deformation q that lowers the electronic contribution to the total energy and results in the CDW phase being the ground state at low temperatures. This coupled electron-lattice instability can only lead to a phase transition if spontaneous perturbations occur that introduce small spontaneous distortions. If such a spontaneous perturbation results in a large response of the electronic system this in turn increases the initial distortion and drives the phase transition [Grü94]. Metaphorically speaking, the spontaneous perturbations allow the system to "explore" the total energy space and seek the configuration of minimal energy.

The unidirectional CDW in RTe_3 thus indicates that the observed nesting vector q_{CDW} corresponds to the largest possible response $\chi(q_{\text{CDW}})$ of the electronic system to the lattice distortion. Accordingly, the system exhibits a CDW phase transition in the direction of the largest response at low temperatures. The small orthorhombic distortion in RTe_3 distinguishes the a^* and c^* -axis and might account for the unidirectional behavior due to an effectively stronger response. A LMTO calculation of the response function for the undistorted lattice corroborate this interpretation since the two peaks along the a^* are smaller than the peaks along the c^* [Ru08]. It turns out that a bidirectional so-called "checkerboard" phase with two perpendicular distortion vectors competes with the unidirectional "stripe" phase [Yao06, Fan07] for the heavy Lanthanides. In the "checkerboard" phase a second bandgap in the perpendicular direction is observed for very low temperatures [Ru08], see Fig. 2.17(a). The authors argue that for sufficiently large values of the e-ph coupling, only the wave vector q along c^* is favored due to a larger response $\chi(q)$ and an unidirectional CDW is observed. Essentially, a single wave vector along the c^* -axis gaps out the FS so efficiently that not enough of the FS is left for a simultaneous ordering in the perpendicular a^* direction. Moreover, a recent theoretical investigation of FS nesting driven CDW formation in RTe_3 suggests that also nesting at energies below and above E_F as well as k -dependent e-ph coupling plays a role in the CDW formation [Joh08]. Nevertheless, the simple theoretical picture of the FS nesting presented in Fig. 2.12 may be applied to the RTe_3 family where the CDW formation is driven by the FS nesting in the vicinity of E_F along a *single* perturbation wave vector q .

Summarizing, the RTe_3 family is a good example for a nesting driven CDW in a quasi-1D band structure. The layered crystal structure results in square Te planes that are largely decoupled from buckled RTe slabs. Hence, the band structure around E_F is well described by a 2D TB model, which is based on two independent chains of $5p_x$ and $5p_z$ orbitals of the Te plane. The FS nesting and the CDW formation can be described within the relatively simple TB model. The excellent agreement of theory and ARPES experiments [Lav05, Bro04, Moo08] for RTe_3 family is ideal to extend the ARPES measurements into the time domain and directly address questions regarding collective excitations and even an ultrafast melting of the frozen-in CDW phase.

2.3 Electron Dynamics in Reduced Dimensions

This section discusses the elementary scattering processes of quasi-particle excitations in a solid that will be analyzed by time-resolved 2PPE in chapter 5 and 6 before turning to the implications for electron systems confined in reduced dimensions. The central quantity is the decay rate Γ of an excited quasi-particle (electron or hole) in the frequency domain. According to [Ech00, Ech04, Pit04, Chu06a] there are several different contributions to the total decay rate:

$$(2.25) \quad \Gamma = \Gamma_{e-e} + \Gamma^{1e} + \Gamma_{e-ph} + \Gamma_{e-def} \quad .$$

Inelastic Electron-Electron Scattering Γ_{e-e} is the most important contribution in metals for large excitation energies $E - E_F \gg k_B T$. Hot electrons scatter with cold electrons close to E_F and simultaneously create an electron-hole pair. The equal masses of the scattering partners gives rise to an large energy transfer, which creates a distribution of scattered secondary electrons. The redistribution of energy and momentum is observed as decay of the excited quasi-particle population.

Elastic Electron-Electron Scattering Γ^{1e} changes the electron momentum but not the energy. The elastic scattering therefore contributes to the line width via dephasing and can induce a population decay by electron scattering to substrate bands.

Electron-Phonon Scattering Γ_{e-ph} is the rate of phonon absorption or emission and dominates the temperature dependence of equation (2.25). The transferred energy typically amounts to a few meV and a large change of parallel momentum can occur such that electrons scatter to different $k_{||}$ momenta in the final state. The energy transfer to the lattice subsystem dominates for low excitation energies $E - E_F \ll k_B T$.

Electron-Defect Scattering Γ_{e-def} describes the transfer of energy and momentum due to scattering with imperfections of the crystal structure, such as defects, impurities and potential corrugations at interfaces. This scattering process can be approximated to be a quasi-elastic redistribution of momenta.

In this work, quasi-2D ultrathin epitaxial metal films and quasi-1D self-assembling metallic nanowires on semiconductor substrates are studied with 2PPE at excited state energies of $E - E_F \geq 0.1$ eV. Therefor, the condition $E - E_F \gg k_B T$ is well fulfilled at temperatures of $T = 100$ K corresponding to $k_B T = 9$ meV and the major contribution to the decay rate is expected from inelastic e-e scattering Γ_{e-e} [Pin66, Ech00, Ech04, Pit04, Chu06a].

2.3.1 Inelastic Electron-Electron Scattering

This discussion focuses (i) on a weak perturbation regime in the limit of single particle excitations⁴, (ii) the low temperature approximation $k_B T \ll E - E_F \ll E_F$ and (iii) the limit of high electron density. The high density limit gives rise to an efficient screening corresponding to a weak interaction, which justifies the perturbation treatment a posteriori. The inelastic e-e scattering is described within a system of interacting Fermions, the Fermi liquid. The foundation of this approach is the Landau theory of Fermi liquids, in short FLT [Qui58, Pin66].

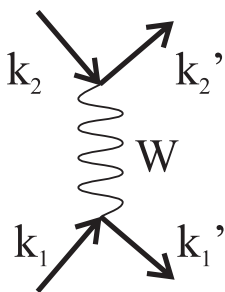


Figure 2.20: Feynman diagram of electron k_1 scattering with electron k_2 due to the screened Coulomb interaction W .

Starting point is a single excited electron with momentum \vec{k}_1 and excess energy $\xi_1 = E_1 - E_F$ above the Fermi level E_F , where $E_1 = \hbar^2 k_1^2 / (2m)$ is the energy in the NFE approximation with effective mass m . This hot electron scatters with a cold electron of momentum \vec{k}_2 and energy $E_2 = \hbar^2 k_2^2 / (2m)$ in the Fermi sea, as sketched in Fig. 2.20. The screened Coulomb interaction W mediates the scattering process, which must conserve energy and momentum:

$$(2.26) \quad \begin{aligned} \vec{k}_1 + \vec{k}_2 &= \vec{k}_1' + \vec{k}_2' \\ &= (\vec{k}_1 + \vec{q}) + (\vec{k}_2 - \vec{q}) \quad \text{and} \end{aligned}$$

$$(2.27) \quad \begin{aligned} E_1 + E_2 &= E_1' + E_2' \\ &= (E_1 + E_q) + (E_2 - E_q) \quad . \end{aligned}$$

The decay of the excited electron k_1 involves the creation of two quasi-particle k_1' and k_2' , and a quasi-hole k_2 . The transferred momentum is given by q and the amount of energy relaxation by $E_q = \hbar^2 q^2 / (2m)$. The Pauli principle requires the initial state k_2 to be occupied and the final states k_1' k_2' to be unoccupied. Following FLT, the decay rate due to e-e scattering Γ_{e-e} is given by a Golden Rule like expression with the same structure as the collision integral [Pin66]:

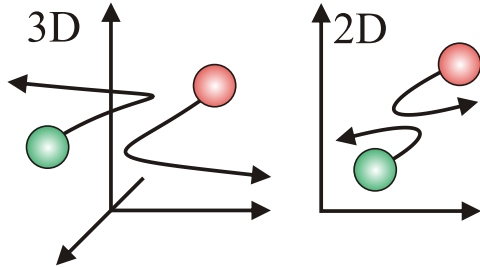
$$(2.28) \quad \begin{aligned} \Gamma_{e-e} &= \sum_{\text{final states}} \underbrace{w(\vec{k}_1, \vec{k}_2, \vec{k}_1', \vec{k}_2')}_{\text{transition probability}} \underbrace{\delta(\vec{k}_1 - \vec{k}_1' + \vec{k}_1 - \vec{k}_2')}_{\text{momentum conservation}} \\ &\times \underbrace{\delta_{\sigma_1 + \sigma_2, \sigma_1' + \sigma_2'}}_{\text{spin conservation}} \underbrace{\delta(E_1 - E_1' + E_1 - E_2')}_{\text{energy conservation}} \underbrace{n_{k_2} [1 - n_{k_1'}] [1 - n_{k_2'}]}_{\text{particle number conservation}} \quad , \end{aligned}$$

where the split-off delta functions emphasize the conservation of momentum k , spin σ , energy E and the number of particles n , respectively.

The transition probability w is proportional to the energy phase space Ω , which is available for scattering, and the square of the screened Coulomb interaction W^2 in a second order perturbation approach. Both quantities, Ω and W are dimension dependent, however, with opposed effects: Ω decreases with increasing dimensionality of the electron system participating in the scattering of excited electrons. The interaction strength W , however, is expected to increase with reducing the dimensionality as the screening reduces and thus the electrons in a system with reduced dimensions scatter more intensely as visualized in Fig. 2.21.

⁴In fact, this is the case in the 2PPE experiments where the relative density of excited states is $\ll 1\%$. In the tr-ARPES experiments, however, excitation densities of $> 1\%$ can be reached where the single particle approximation may break down.

Figure 2.21: Cartoon of the e-e scattering in 3D with maximum degrees of freedom. Spatial confinement reduces the screening and enhances the e-e interaction in 2D. After [Him02].



Specifically for 2D quantum well systems, this implies competing effects for the e-e scattering rate. On the one hand, the phase space available for scattering increases with film thickness. On the other hand, the DOS at E_F is periodically modulated by the occurrence of new QWS as the well grows wider, which in turn leads to a change of screening. The well-defined QWS with tunable band structure makes Pb/Si(111) an interesting model system for the study of the competing effects of phase space and screening in reduced dimensions and the implications for the electron dynamics in confined structures.

Electron-Electron Scattering in 3 Dimensions

In 3D, the phase space is a sphere, filled with electrons to k_F . The phase space Ω available for scattering is given by spherical shells that scale with the excess energy ξ due to energy conservation. The transferred momentum is determined by momentum conservation such that a typical scattering process in 3D involves two electrons that are well separated by $2k_F$ in phase space, see Fig. 2.22. Further approximation of a linear dispersion around E_F , which is equivalent to a constant DOS, yields another factor of $\xi \propto q$ for the k -dependence. Therefore, the scattering rate is expected to scale with ξ^2 in 3D, the prefactor is determined by W and thus ultimately by the electron density n that influences both the phase space and the screening.

Quinn et al. [Qui58, Pin66] were the first to explicitly calculate the e-e scattering rate for a NFE metal within the random phase approximation (RPA) and the limiting case of high electron density⁵:

$$(2.29) \quad \Gamma_{e-e}^{(3D)} = \frac{1}{\tau_{e-e}^{(3D)}} = a^{(3D)} n^{-5/6} \xi^2 \quad \text{with } a^{(3D)} = \text{const}$$

The constant prefactor $a^{(3D)}$ is derived in appendix C.

Numerous experiments on 3D electron systems like Cu [Sch94, Her96, Kno96, Pet97b, Kno98b] indicate the general validity of the ξ^2 scaling law following (2.29) as predicted by 3D FLT. However, more detailed investigations [Oga96a, Ger01] reveal that already for rather simple metals like Cu, which are dominated by NFE-like sp -bands, deviations in the prefactor $a^{(3D)} n^{-5/6}$ occur. The description in (2.29) breaks down completely when transition metals with localized d -bands like Ta are considered [Kno96]. Here, an explicit consideration of the band structure is required, which can not be provided by the FLT. Finally, transport effects due to diffusive and ballistic

⁵The 3D electron density $n = n^{(3D)}$ is measured in units of m^{-3} .

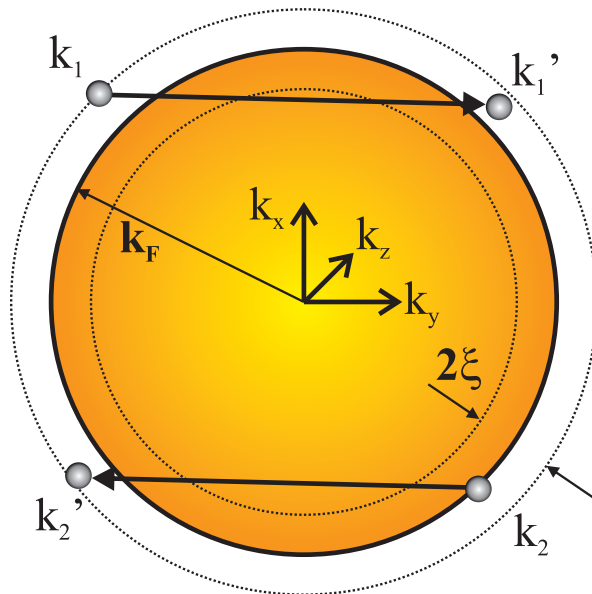


Figure 2.22: Typical e-e scattering process in 3D. An excited electron \vec{k}_1 scatters with an electron \vec{k}_2 in the Fermi sea. This creates two quasi-particles \vec{k}_1' and \vec{k}_2' , and one quasi-hole \vec{k}_2 . Energy conservation constricts the phase space available for scattering to a spherical shell of thickness 2ξ .

electron transport [Aes00] have to be taken into account for bulk single crystals. These transport contributions were clearly identified in a thickness dependent study [Lis04b] of thin Cu films on Si with ~ 10 nm thickness.

First principle methods can take the band structure of the crystal or the surface explicitly into account and thereby overcome the limitations of FLT. One method is the *GW*-approximation [Cam99, Cam00, Ech00, Lad03, Ech04, Pit04, Zhu05, Chu06a, Mön06], which is summarized in appendix C. The basic idea is as follows: Since the quasi-particle states are not eigen-states of the system, the quasi-particle energy is complex and the imaginary part is a measure of energy and momentum transfer to the Fermi sea. The probability of scattering between two electrons is constrained by energy and momentum conservation, and the phase space. The *GW*-approximation projects the imaginary part of the self-energy onto the excited state and sums over the phase space of initial and final states. This allows the explicit consideration of the band structure with, for example, surface states and orientation bandgaps.

One limitation for realistic first principles calculations is the computational cost that arises for structure with large unit cells or complex structured interfaces. This limitation also applies to Pb/Si(111), which requires consideration of the underlying wetting layer as well as the substrate. The large number of electrons with a complicated interface still hinders the *ab-initio* treatment of the electron dynamics in Pb/Si(111) [Chu08].

Electron-Electron Scattering in 2 Dimensions

The e-e scattering rate in 2D is determined by the increase of the screened Coulomb interaction W and a simultaneous decrease of the phase space. The detailed derivation of the e-e scattering rate in 2D and a discussion of the partially discordant theoretical literature [Cha71, Giu82, Qia05, Qia06] is given in appendix C. The result can be summarized with⁶:

$$(2.30) \quad \Gamma_{\text{e-e}}^{(2D)} = \frac{1}{\tau_{\text{e-e}}^{(2D)}} = a^{(2D)} \frac{\xi^2}{n} \ln\left(\frac{n}{\xi}\right) \quad \text{with } a^{(2D)} = \text{const} \quad .$$

Identical to the 3D case, the e-e scattering rate scales with ξ^2 . The logarithmic correction $\ln \xi^{-1}$ as well as the different dependence of n can be understood from the different structure of the screened Coulomb interaction in 2D. In 3D, the screened Coulomb interaction scales with $W(k) \propto 1/(k^2 + k_s^2)$, where k_s is the Thomas-Fermi screening vector that is determined by the electron density. In 2D, the screened interaction is approximated by $W(k) \propto 1/\sqrt{k^2 + k_s^2}$, which yields a logarithmic term from the integration over the final states.

Fig. 2.23 quantitatively compares the lifetime due to e-e scattering as expected within FLT for 2 and 3 dimensions, following the recent theoretical study of Qian et al. [Qia05, Qia06]. The lower panel in Fig. 2.23 shows the energy-dependence of the inelastic electron lifetimes $\tau_{\text{e-e}}$, which exhibit only a subtle dimension dependency. The overall trend is governed by the ξ^2 scaling law and the \ln term gives only a small correction that is important for excitation energies close to E_F . The upper panel in Fig. 2.23 focus on the small lifetime difference expected for 2 and 3 dimensions. The 2D lifetime $\tau_{\text{e-e}}$ is significantly smaller than the 3D lifetime for energies $\xi < 0.8$ eV. The differences of several 10 fs should allow identification of such a 2D behavior. In contrast, the 2D lifetime is expected to be larger than the 3D case for energies $\xi > 0.8$ eV. This difference, however, amounts only to a few fs and is hard to detect.

Up to now, only a few metallic quantum well systems like Ag/Fe(001) have been investigated in time-resolved 2PPE experiments [Oga02, Mat08]. Remarkably, the observed lifetimes in Ag/Fe(001) of < 9 fs are a factor 10 smaller than predicted by FLT and do not scale with ξ^2 although the sharp QWS indicate a high degree of confinement. This observation can be attributed to the presence of an orientation bandgap in the metal substrate, which presents unoccupied states in the outer regions of k-space. Thus, efficient quasi-elastic decay channels into the substrate become available and reduce the observed hot electron lifetimes, in which case the comparison to FLT could be misleading. Metallic Yb(111) quantum wells on W(110) were also studied with STS [Weg05]. The analysis of the linewidth Γ indicates 3D behavior, which can be described with the electron density of Yb. Semiconducting quantum well structures were studied with time-resolved optical pump-probe measurements [Kai01], which, however, reveal no explicit 2D behavior but show the 3D ξ^2 scaling law as well. Clear deviations from the 3D FLT were only observed in the semi-metal graphite [Xu97, Moo01], which can understood in terms of a layered 2D electron gas [Haw87] and peculiarities of the Graphite band structure [Moo01].

⁶The 2D electron density $n = n^{(2D)}$ is measured in units of m^{-2} .

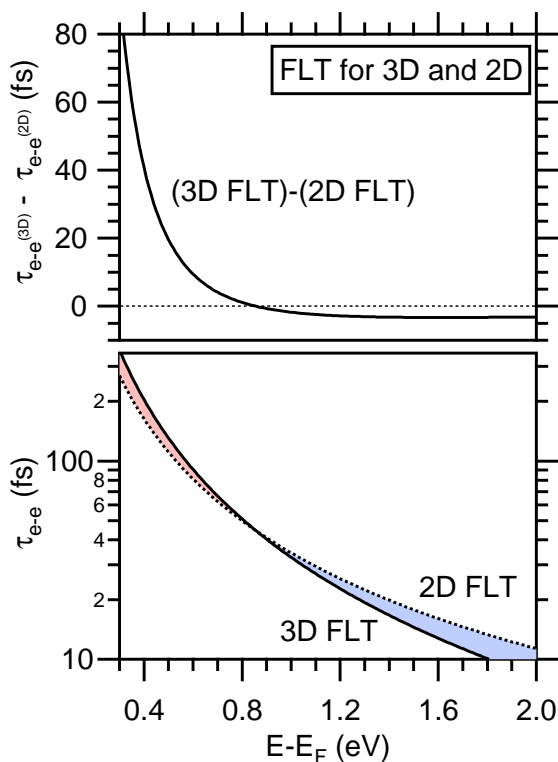


Figure 2.23: FLT prediction for Pb in 3 and 2 Dimensions. Significant differences are only encountered at small excess energies $\xi = E - E_F$ where the decay in 2D is faster than in 3D due to the ln-term in (2.30). The upper panel plots the difference of the scaling laws in 3D and 2D. These features depend only slightly on the electron density and present an fundamental metallic property.

Electron-Electron Scattering in 1 Dimension

There are only few theoretical investigations of e-e scattering in 1D metal structures [Lut61, Lut63] because the 1D Fermi liquid is a peculiar construction that exhibits several instabilities. It is instable with respect to a lattice perturbation, which can result in a Peierls metal-to-insulator transition with a breakdown of the FS and formation of a gapped CDW state [Grü94], as discussed in chapter 2.2. Furthermore, an ideally 1D Fermi liquid is expected to show exotic phenomena such as spin-charge separation in the quasi particle spectrum [Lut61, Med92, Voi95, Zac98]. In this so-called Tomonaga-Luttinger liquid, the charge is carried by holons and spinons are carriers of the spin. The experimental proof for such phenomena in highly confined quasi-1D metal structures, however, still remains a challenge [Seg99, Los01].

Nevertheless, Luttinger predicted a linear scaling of the inelastic e-e scattering rate with the excess energy ξ in 1D [Lut61] :

$$(2.31) \quad \Gamma_{e-e}^{(1D)} = \frac{1}{\tau_{e-e}^{(1D)}} = a^{(1D)} \xi \quad \text{with } a^{(1D)} = f(n) \quad .$$

There exist only a first time-resolved study [Rüg07] and a transport measurement [Teg05] of quasi-1D self-assembling nanowires on Si(557) [Seg99, Los01], which do not discuss the scaling law (2.31). Interestingly, the linear scaling behavior $\Gamma \propto \xi$ is also predicted [Haw87] and observed [Xu97] for layered electron gas systems such as graphite.

2.3.2 Inter- and Intra-Subband Scattering

The discussion of the inelastic e-e scattering was based on FLT, which, by definition, does not take the band structure into account. In fact, the only adjustable parameter in the discussion of the FLT is the electron density n , which is not a free parameter but fixed by the number of valence electrons and the lattice structure. This consideration evidences that FLT may be able to describe general trends of the electron dynamics but the details of the scattering processes have to be inferred from the band structure.

The elementary scattering processes of hot electrons have been extensively investigated by time-resolved 2PPE for image potential states (IPs) on clean and adsorbate covered noble metal surfaces [Fau95, Pet97b, Zhu04, Fau07]. These studies reveal two scattering processes that describe (i) scattering and energy relaxation of hot electrons within the *same* band (*intra*-band scattering) and (ii) scattering to a *different* band (*inter*-band scattering). Although IPS and QWS differ profoundly in many physical aspects, the fundamental scattering mechanisms, which are governed by concepts of wave function overlap and alike, might be relevant for a QWS system.

These two fundamental scattering processes occurring in well-defined subbands are illustrated in Fig.2.24. The left panel depicts the dispersion of the Pb $6p_z$ band along the quantization direction L- Γ . The resulting quantized QWSs form delocalized subbands in the surface plane as shown in the center panel of Fig. 2.24. The right panel sketches the step-like increase of the DOS with the appearance of higher lying QWSs. The central panel focuses on the inter- and intra-band scattering mechanisms in the lowest unoccupied quantum well state (luQWS) leading to energy relaxation of excited electrons and thereby to a decay of the excited state population.

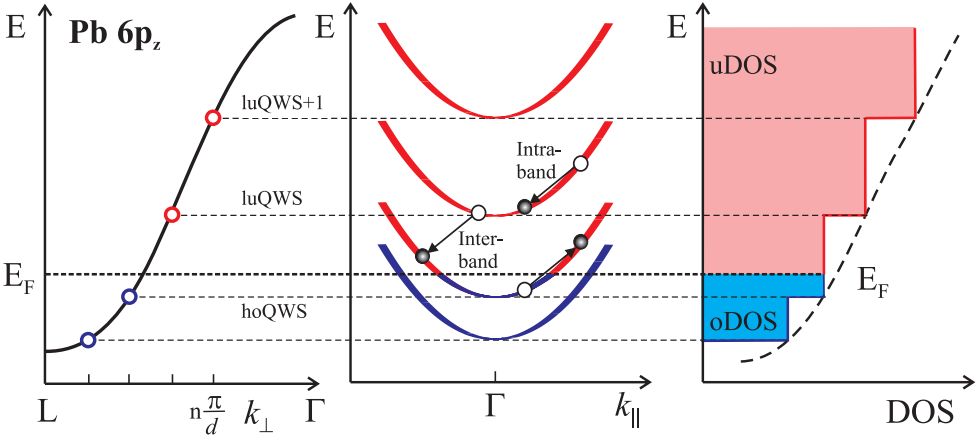


Figure 2.24: Inter- and intra-subband scattering processes in discrete subbands. Left: quantization of the $6p_z$ Pb band along the L- Γ direction. The highest occupied QWS (hoQWS) and the lowest unoccupied QWS (luQWS) are indicated. Center: Inter-subband scattering luQWS \rightarrow hoQWS with creation of an e-h pair due to energy and momentum conservation. Intra-subband decay within the luQWS band creates an e-h pairs as well. Right: The density of states (DOS) evolves in a step-like fashion in a 2D electron system. The (un)occupied DOS (uDOS/oDOS) are marked in red and blue.

The *inter*-subband relaxation in the luQWS is characterized by scattering to unoccupied parts of the hoQWS band at outer regions of k -space, $\text{luQWS} \rightarrow \text{hoQWS}$. According to the transferred energy, this scattering process can be elastic as well as inelastic. The *intra*-subband relaxation occurs within the same luQWS subband and decreases the parallel momentum of the excited electron, which relaxes toward the band minimum at Γ , $\text{luQWS}(k_{\parallel} \neq 0) \rightarrow \text{luQWS}(k_{\parallel} = 0)$. Both decay processes involve the creation of a e-h pair in the hoQWS band due to the conservation of energy and momentum.

Time- and angle resolved 2PPE allows to monitor the excited state population directly in k -space and can thus discriminate inter- and intra-band scattering [Hot00, Ber01, Ber02, Rot02, Wei02b, Bog04a, Rot04, GR05, Kir05, Fau07]. Considering the excited state population of the luQWS at the band minimum, the inter-band decay leads to population decay with a time constant determined by the coupling strength and available phase space. In contrast, the intra-band decay leads to a delayed rise of the excited state population at the band bottom since the relaxation toward the band bottom requires the time given by the intra-band scattering rate. A k -dependent analysis can thus identify the intra-band scattering channel by a decrease of the delayed rise with increasing parallel momentum. If more QWSs than the lowest lying are populated, the decay can be more complicated and involve the subsequent decay into several states. Nevertheless, the underlying fundamental scattering processes are given by the inter- and intra-band relaxation.

2.4 Photoelectron Spectroscopy

In this work, the structure of electronic states is investigated with photoemission spectroscopy (PES), which measures the distribution of momentum and kinetic energy of electrons emitted by the photoelectric effect [Ein05]. angle-resolved photoemission spectroscopy (ARPES) is best suited to study the single particle spectral function $A(k, E)$ of metals and semiconductors directly in k -space [Kev92, Hüf95]. ARPES is a well established technique⁷ and one of the most yielding and direct probes of the electronic band structure of materials in terms of their single-particle spectral function $A(E, \vec{k})$ [Hüf95, Rei05, Dam03]. Recent advances in the study of such important phenomena as electron correlation in high- T_C Cuprates [She95, Dam03] underline its fundamental importance for the understanding of the solid state.

PES is based on the photoelectric effect, where photons with energy $h\nu$, which exceeds the metal work function Φ , emit photoelectrons with kinetic energy

$$(2.32) \quad E_{\text{kin}} = h\nu - \Phi - (E_i - E_F) \quad .$$

The binding energy E_i with respect to the Fermi level E_F is thus reflected in the kinetic energy of the outgoing electrons. This allows to map out the electronic band structure because PES conserves the in-plane (parallel) momentum k_{\parallel} , as will be shown in section 2.4.3. Thus the PES intensity is given by

$$(2.33) \quad I(\vec{k}_{\parallel}, E) = M f(E, T) A(\vec{k}_{\parallel}, E) \quad ,$$

with transition dipole matrix element M , the Fermi-Dirac distribution f and single particle spectral function $A(k, E)$, which is directly connected to the Greens function

$$(2.34) \quad A(\vec{k}, E) = \frac{1}{\pi} \text{Im}(G(\vec{k}, E)) = \frac{1}{\pi} \frac{\Gamma}{(E - E_i)^2 + \Gamma^2} \quad .$$

The second term specifies the spectral function for the case of a single quasi-particle peak with binding energy E_i and intrinsic linewidth Γ .

Many-body effects in PES occur due to the strong and long-range Coulomb interaction of electrons in a solid. The quasi particles may be visualized as "naked" electrons that are "dressed" by a polarization cloud. This results in a short-range screened interaction and a quasi particle spectrum with renormalized eigen-energies

$$(2.35) \quad \Sigma = \text{Re}(\Sigma) + i \text{Im}(\Sigma) \quad ,$$

where the real part $E_i = \text{Re}(\Sigma)$ gives the binding energy in the screened potential. The imaginary $\Gamma = \text{Im}(\Sigma)$ part is equivalent to the natural line width and gives rise to an exponential decay of the wave function amplitude with a time constant $\tau = 1/\Gamma$, as discussed in the context of the electron dynamics in section 2.3.1. The tr-ARPES studies on TbTe_3 actually analyzes the time-dependent spectral function $A(k_{\parallel}, E, \Delta t)$ according to equations (2.34) and (2.35) by observing transient changes of the amplitude, position and width of the single particle spectral function.

⁷Nobel prize 1981 to Kai M. Siegbahn "for his contribution to the development of high-resolution electron spectroscopy".

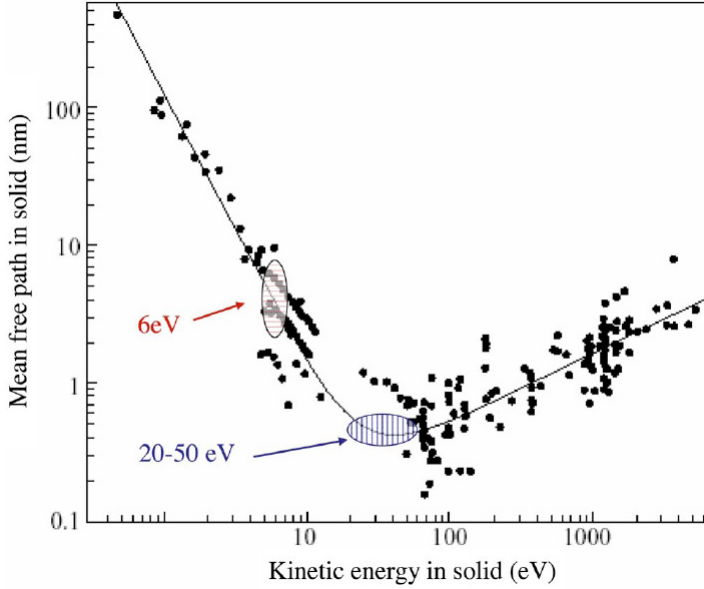


Figure 2.25: The "universal curve" of the mean free path of electrons that determines the escape depth of the photoelectrons. After [Sea79, Kor07].

The **sudden approximation** assumes that the photoemission process, which connects the initial N particle to the final $N-1$ electron state, occurs much faster than it takes the electronic system to relax the excited electronic state. This assumption is closely related to Koopmans' theorem [Koo34, Sch03]

$$(2.36) \quad E - E_F = -\epsilon \quad ,$$

where the measured ionization energy $E - E_F$ equals the negative orbital energy ϵ of the N -particle state as given in a self-consistent Hartree-Fock approximation. In reality electron correlation, usually calculated by post Hartree-Fock methods, relaxes the excited $N-1$ particle state and results in so-called final state effects on the measured energies. However, the corrections arising (i) from rearrangement or relaxation of the orbitals are comparable to (ii) the corrections from electron correlation but of opposite sign, which explains the success of Koopmans' theorem. The validity of the sudden approximation has been questioned at very low kinetic energies, however, recent photon energy dependent investigations seem to confirm its validity [Kor06].

The **surface sensitivity** of ARPES is a result of the finite escape depth of electrons in solids [Sea79, Zan88]. The mean free path, as shown in Fig. 2.25, is in first approximation material independent and a function of the kinetic energy in the solid, which exhibits a minimum of a few Å escape depth at $E_{\text{kin}} \approx 20-50$ eV. In the experiments discussed here, the kinetic energy is ≤ 6 eV and the mean escape depth amounts to ~ 10 Å. Thus, electronic features of both the sample bulk and the surface can be observed in these experiments.

Space charging in photoemission experiments, especially with pulsed light sources such as a lasers, puts an upper limit on the achievable count rates. The Coulomb repulsion of photoelectrons, which are simultaneously emitted by a strong field, can result in spectral broadening at all kinetic energies due to deceleration of slow and

acceleration of fast electrons, and a distortion of the trajectories. The space charge effect [Gil90, Pet92, Rif93] is determined by the electron density ρ

$$(2.37) \quad \rho \propto \frac{I}{\Delta t A} \quad ,$$

which is proportional to the light intensity I and reciprocal to the duration of the light pulse Δt and the illuminated area A . Since the ultrashort laser pulses are the foundation of the time-resolved studies, they can not be scarified and only an increase of the illuminated surface area can reduce the electron density. However, this is only feasible for homogeneous samples like metal single crystals and can not be applied to the wedged and thus inhomogeneous Pb/Si(111) samples (chapter 3.3.1) or the relatively small TbTe₃ samples (chapter 3.3.2).

2.4.1 The 3-Step Model of Photoemission

A detailed description of the photoemission process requires the consideration of all initial and final states and thus is a complicated many-body phenomenon. There exist, however, phenomenological approaches like the 3- and 1-step model of photoemission, as depicted in Fig. 2.26. The 3-step model [Ber64b, Ber64a] separates the photoemission process into three distinct parts:

1. Localized excitation of the electron from the initial to the final state in unoccupied bands above the vacuum level. The transition is vertical in the band structure due to the small photon momentum.
2. Transport of the photoelectron to the surface. Here, scattering processes such as e-e or defect scattering alter the electron momentum and energy, which contributes to the background of the photoemission signal. The transport induces the energy-dependent mean free path and determines the surface sensitivity of the photoemission process to 5 – 100 Å [Sea79], see Fig. 2.25.
3. Emission of the electron into the vacuum and propagation in the vacuum to the detector. The momentum component parallel to the surface k_{\parallel} is conserved due to the small momentum of the photon, whereas the perpendicular component k_{\perp} is altered by the work function.

According to the 3-step model, the photoemission current

$$(2.38) \quad I(k_{\parallel}, E_{\text{kin}}) = T(E_{\text{kin}}) M_{if} D(E_i) D(E_f) \times \int_0^{\infty} dz f(T, E_i) A(k_{\parallel}, E_i) e^{-z/z_0}$$

is determined by the distribution function f , the DOS in the initial and final state, E_i and E_f , respectively, the transition matrix elements M_{if} , a transmission function T , and the mean escape depth z_0 [Sch03]. The different energy scales are linked via equation (2.32).

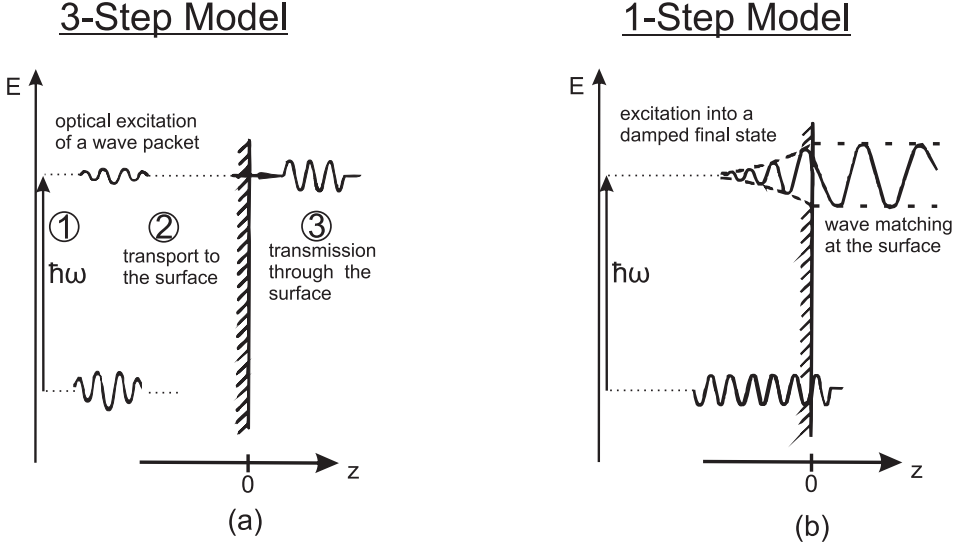


Figure 2.26: (a) 3-step model of photoemission: (1) optical excitation of a wave packet that (2) propagates to the surface and (3) emits an electron into the vacuum. (b) 1-step model: The optical field couples a Bloch-state, which resides in the crystal, to an quasi-free inverse LEED state, which is located in the vacuum but decays exponentially into the bulk. [Hüf95].

2.4.2 The 1-Step Model of Photoemission

The 1-step model [Pen76] allows a more detailed and integrated description of the photoemission process. This model can be depicted as the optical coupling of a Bloch wave inside the crystal to plane wave states in the vacuum, which decay exponentially into the bulk crystal, see Fig. 2.26(b). This can be interpreted as the time-reversal of an electron impinging on the metal surface with an energy-dependent penetration depth. For that reason these final states are also termed time-reversed or inverse LEED states $\Psi_{\text{LEED}}(E_f)$ [Feu78, Mah70a, Mah70b] and the photo current is given by [Sch03]:

$$(2.39) \quad I(k_{\parallel}, E_{\text{kin}}) \propto \sum |\langle \Psi_{\text{LEED}}(E_f) | W | \Psi_i \rangle|^2 A(k_{\parallel}, E_i) \quad .$$

The operator $W = \vec{A} \cdot \vec{p} + \vec{p} \cdot \vec{A}$ describes the interaction of the electrons with the vector potential \vec{A} of the light field. Perturbation theory in first order of \vec{A} and the dipole approximation $\vec{A} = A_0 \vec{e} e^{i\vec{k} \cdot \vec{r}} \approx A_0 \vec{e}$ yields

$$(2.40) \quad W = A_0 \vec{e} \cdot \nabla = A_0 (E_f - E_i) \vec{e} \cdot \vec{r} \quad ,$$

where \vec{e} is the polarization vector of the light wave with amplitude A_0 . E_i and E_f are the initial and final state energies, respectively.

2.4.3 Angle-Resolved Photoelectron Spectroscopy

The photoemission process conserves the parallel momentum⁸ as long as the photon energy is significantly smaller than the electron rest energy $m_e c^2$ and no scattering in the final state occurs. Fig. 2.27 depicts the transmission of an electron at the solid-vacuum interface. The work function of the metal results in a so-called escape cone, which is an apparent increase of the work function with increasing emission angle. For $k_{\parallel} \neq 0$, part of the energy is carried away by the parallel momentum and can not contribute to the perpendicular component k_{\perp} to overcome the work function [Hüf95, Bis06].

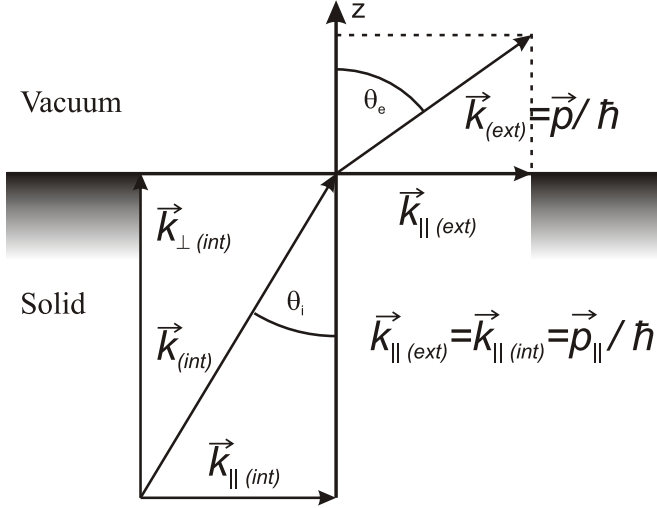


Figure 2.27: Photoemission of an electron with angle Θ_e conserves the momentum component parallel to the surface k_{\parallel} , which thus is accessible by angle-resolved detection. The perpendicular component k_{\perp} is altered by the work function and generally not conserved.

Measuring the photoemission intensity as function of kinetic energy and photoemission angle allows to map out the in-plane band structure as function of in-plane momentum:

$$\begin{aligned}
 (2.41) \quad k_{\parallel}(\Theta_e, E_{\text{kin}}) &= \sin \Theta_e \sqrt{\frac{2m_e}{\hbar^2} E_{\text{kin}}} \\
 &= 0.5123 \text{ \AA}^{-1} \text{ eV}^{-1/2} \sin \Theta_e \sqrt{E_{\text{kin}}} \quad .
 \end{aligned}$$

The angle-resolved detection results in detailed informations about the dispersion of the electronic states. State-of-the-art photoelectron spectrometers, compare to chapter 4, enable a simultaneous and thus very efficient detection of the energy *and* momentum distribution, resulting in comprehensive pictures of the band structure.

⁸The momentum p is, strictly speaking, only proportional to the wave vector k , $p = \hbar k$. For the sake of simplicity, this distinction is omitted in this work and the wave vector k is treated as momentum.

2.4.4 Two-Photon Photoelectron Spectroscopy

The equilibrium band structure is very successfully studied with direct photoemission, which, however, can hardly supply information about non-equilibrium processes or unoccupied parts of the band structure. The unoccupied bands may be accessed with inverse photoemission spectroscopy (IPES) [Smi88], where monochromatic electrons are injected into unoccupied states that relax via emission of photons. However, IPES suffers from the low cross section of the radiative decay channel and a limited energy resolution. Also, it does not allow to directly address the physics of non-equilibrium processes in the time domain. Since its first experimental description⁹ [Lau77, Wau77] 2PPE spectroscopy has matured in the last 20 years [Gie85, Gie87, Sch91, Pad92] to a very powerful tool for the characterization of the unoccupied band structure of clean and adsorbate covered metal surfaces [Fau95, Pet97b, Ge98, Mil02a, Wei02b, Ech04, Zhu04, Fau07].

In the 2PPE process photons with energies below the work function promote electrons from initial states below the Fermi level E_F into unoccupied intermediate states above the Fermi level. Absorption of a second photon overcomes the sample work function and electrons are photoemitted into final states above the vacuum level E_{vac} where the photoemission spectrum is observed. Moreover, the use of ultrashort laser pulses in 2PPE allows a natural implementation of a pump-probe scheme to monitor the energy and momentum relaxation of the excited electron population directly in the time domain. This time-resolved 2PPE scheme employs a pair of time-correlated pulses that are overlapped on the sample and thus give rise to a time-correlated 2PPE signal.

Excitation Mechanisms

The two step nature of the 2PPE process allows several different excitation mechanisms of the intermediate state k as sketched in Fig. 2.28.

(a) Resonant excitation occurs when the energy difference of initial state i and intermediate state k coincides with the pump photon energy $h\nu_{\text{pump}} = E_i - E_f$. In general, resonantly pumped intermediate states lead to exaggerated peaks in the 2PPE spectrum.

(b) Non-resonant excitation populates the intermediate state k via inelastic scattering from another intermediate state. This excitation scheme is typical for a continuous spectrum of initial states and dispersing states, which allow an excitation over a wide range of k_{\parallel} and may result in subsequent inter- and intraband scattering process.

(c) Photoemission via virtual intermediate states arises from the transient second order polarization in the presence of the strong laser fields used in 2PPE. It can be visualized as simultaneous absorption of two photons.

⁹The 2PPE process is a second order phenomenon that requires considerable field strength and thus has only become feasible with the advent of ultrashort sub-ps laser sources in the late 1970's.

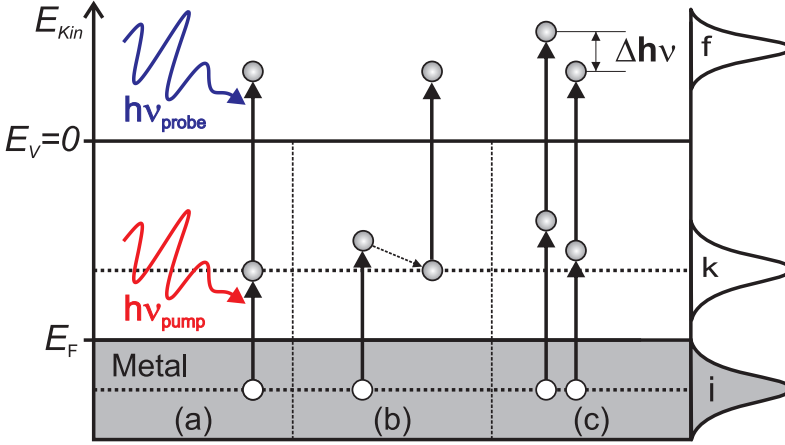


Figure 2.28: Excitation mechanisms of 2PPE involving discrete initial, intermediate and final states, i , k and f , respectively. (a) Resonant excitation, (b) Non-resonant excitation, (c) Photoemission via virtual intermediate states.

The independent variation of the pump and probe photon energies $h\nu_{\text{pump}}$ and $h\nu_{\text{probe}}$, respectively, enables a clear identification whether a peak in a 2PPE spectrum stems from an initial, intermediate or final state in the 2PPE process:

Initial State i The kinetic energy of electrons from occupied initial states i , which are photoemitted via virtual intermediate states, scales linearly with both the pump and probe photon energy.

Intermediate State k The kinetic energy of electrons that are photoemitted from real intermediate states k is independent from the pump photon energy and scales linearly with probe photon energy.

Final State f The final state energy is, by definition, independent of pump and probe photon energy.

Energy Scales in 2PPE

The different origin of peaks in a 2PPE spectrum requires a careful consideration of the appropriate energy scale to describe the binding energy of a given state. This is explained in Fig. 2.29, which shows two unoccupied intermediate states, and the low- and high-energy cutoffs at the vacuum and Fermi edge, respectively. The position of the secondary edge (a) is generated by scattered, secondary electrons that have just enough energy to overcome the work function. The electrons at the Fermi edge (c) are photoemitted from states near E_F via virtual intermediate states and thus have the highest possible energy in the spectrum. The width of the spectrum from its secondary edge $E_{\text{kin}}^{(S)}$ to the Fermi edge $E_{\text{kin}}^{(F)}$ and the sum of photon energies allows to

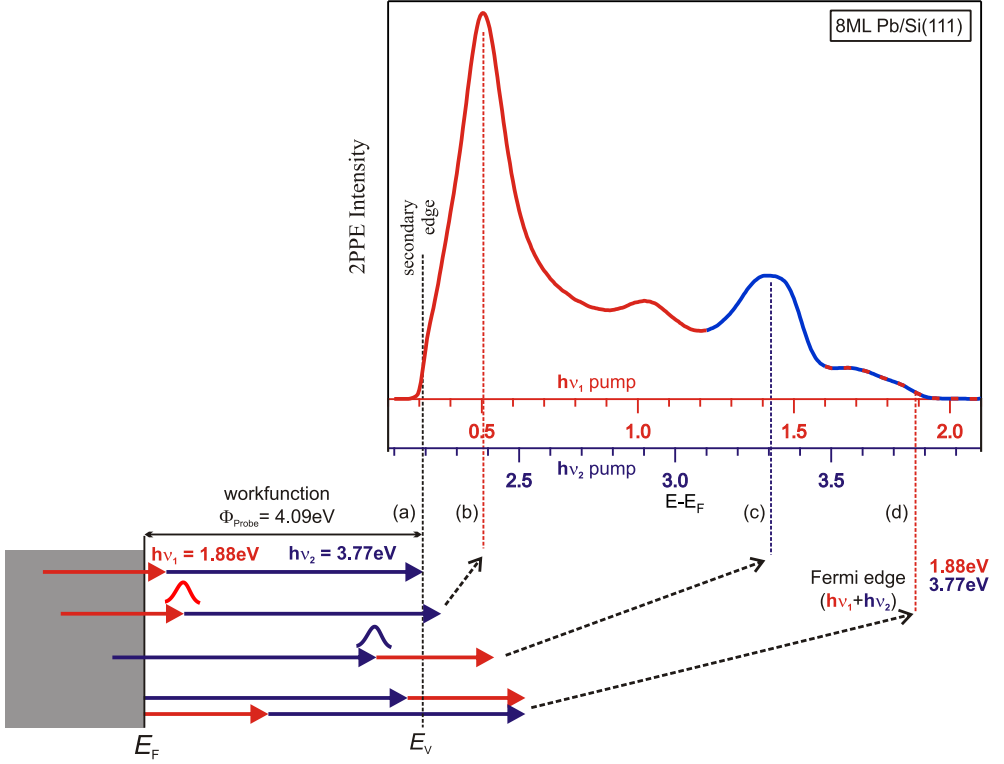


Figure 2.29: Energy scales in 2PPE together with excitation mechanism and appropriate energy scales. Several features are highlighted (a) Low-energy cutoff at the so-called secondary edge. (b) Two intermediate states pump with visible light (VIS), $h\nu_1$ and probed with ultraviolet light (UV), $h\nu_2$. (c) Intermediate state pumped with UV. (d) High-energy cutoff at the Fermi edge.

accurately determine the sample work function:

$$(2.42) \quad \Phi = h\nu_1 + h\nu_2 - \left[E_{\text{kin}}^{(F)} - E_{\text{kin}}^{(S)} \right]$$

Determination of the correct binding energy of an intermediate states peak requires knowledge by which of the 2PPE pulses ($h\nu_1$ or $h\nu_2$) the state is pumped and probed. The sequence of pump and probe pulse can be determined by the photon energy dependence observed in the kinetic energy of the intermediate state peak. Independently, the pump-probe sequence can be inferred from time-resolved 2PPE measurements, see next section. The 2PPE spectrum discussed in Fig. 2.29 exhibits an intermediate state peak at $E - E_F = 0.5$ eV, populated by the visible (VIS) laser pulse $h\nu_1$ (red), and one intermediate state at $E - E_F = 3.3$ eV, pumped by the ultraviolet (UV) laser pulse $h\nu_2$ (blue). Both these energy scales are linked to the (common) Fermi edge (red and blue), as the energy difference of E_F and the high-energy cutoff must equal the pump photon energy on the appropriate intermediate energy scale $E - E_F$. The appropriate binding energy scales referenced to E_F and

the vacuum level E_V for an initial and intermediate state peaks at kinetic energy $E_{\text{kin}} = P$ are given by the following expressions:

$$(2.43) \quad \begin{aligned} E_i - E_F &= P - E_{\text{Kin}}^{(F)} \\ E_k - E_F &= h\nu_{\text{pump}} + P - E_{\text{Kin}}^{(F)} \\ E_k - E_V &= P - E_{\text{Kin}}^{(S)} - h\nu_{\text{probe}} \end{aligned}$$

2.4.5 Time-Resolved Two-Photon Photoemission

To investigate the population dynamics of transiently populated intermediate states, the pump-probe delay Δt is varied by changing the optical path length. The time-correlated¹⁰ 2PPE yield as function of intermediate state energy $E - E_F$ (vertical axis) and pump-probe delay Δt (horizontal axis) is shown in an exemplary "2D-plot" in Fig. 2.31.

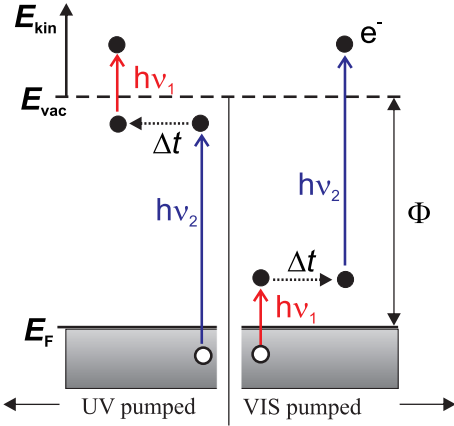


Figure 2.30: Sequence of pump and probe pulses. For positive delays Δt , the VIS pulse, $h\nu_1$, precedes the UV pulse, $h\nu_2$.

inhibits the lowest unoccupied quantum well state (luQWS) as well as an image potential state (IPS). Their population dynamics are discussed in the bottom panel. The cross correlation (XC) traces are shown in the bottom panel and were obtained by integration over the energy windows indicated by the color bars on the left hand side. The population of the luQWS decays toward positive delays indicating a VIS-UV pump-probe sequence. In contrast, the IPS decays to negative delays because of the reversed pump-probe sequence. The XC traces are described with appropriate rate equation models (solid lines), see next section. The laser pulse duration as well as the time zero delay are inferred from a fit of a sech^2 function to the hot electron distribution near E_F . There, the lifetime of the intermediate states may be neglected, which results in the measurement of the laser auto correlation (AC) function as detailed in the next section.

¹⁰An uncorrelated background originates from 2PPE solely from the pump and probe pulse (typically a few % at time zero), which is measured separately and subtracted from the 2D-plots.

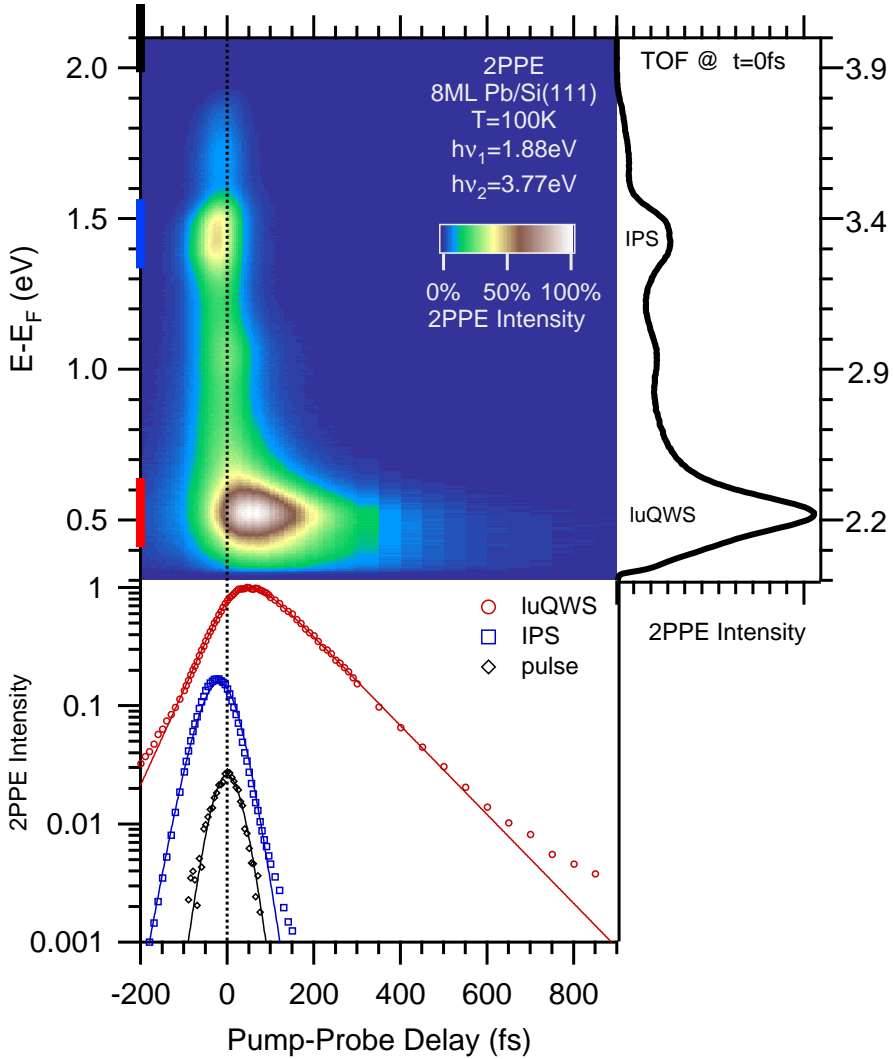


Figure 2.31: Center: 2PPE yield of 8 ML Pb/Si(111) as function of intermediate state energy (vertical axis) and pump-probe delay (horizontal axis) in a false color representation. The left axis is valid for positive pump-probe delays and denotes the intermediate state energy $E - E_F$ for VIS ($h\nu_1$) pumped states. The right energy axis refers to the intermediate energy scale for UV ($h\nu_2$) pumped states and thus is appropriate for negative pump-probe delays. Right: 2PPE spectrum from a vertical cut between -110 and 200 fs. The lower lying peak at $E - E_F = 0.6$ eV originates from the lowest unoccupied QWS (luQWS), which is pumped with $h\nu_1$. The higher lying peak arises from an image potential state (IPS), which is pumped with $h\nu_2$. Therefore its binding energy $E - E_F = 3.3$ eV is given by the left energy axis. The small feature at $E - E_F = 1.1$ eV stems from a neighboring coverage and is not discussed here. Bottom: Cross correlation (XC) traces for luQWS, IPS and the hot electrons at the Fermi edge, from which the time-zero of the pump-probe delay and the laser cross correlation is inferred by a fit of a sech^2 (solid line). The XC traces were obtained from 200 meV wide horizontal cuts as indicated by the color bars on the left.

2.4.6 Analytic Description of the Population Decay

The description of the transient population of an excited continuum of metal states is complicated and can hardly be done within analytical models. The quantization of the band structure and the formation of discrete QWS in Pb/Si(111), however, allows to discuss a discrete 3-level system consisting of initial, intermediate and final state.

Such an optically coupled 3-level system is described by the optical Bloch equations [Lou83], which enable a full quantum-mechanical description including effects of a coherent polarization, which is relevant for resonant excitation conditions [Her96, Kno98a, Wol99, Bog02, Bog04b]. This approach requires exact knowledge of the dephasing parameters of the system, which have to be extracted from linewidth measurements and are not accessible by analysis of the population decay only.

In case of a non-resonant excitation, which can be realized by the choice of excitation photon energies, the optical Bloch equations simplify to a set of classical, coupled rate equations:

$$(2.44) \quad \dot{n}_i = -|V_{ik}(t, \tau)|^2 n_i + \Gamma_1 n_k$$

$$(2.45) \quad \dot{n}_k = |V_{ik}(t, \tau)|^2 n_i - |V_{kf}(t, \tau)|^2 n_k - \Gamma_1 n_k$$

$$(2.46) \quad \dot{n}_f = |V_{kf}(t, \tau)|^2 n_k .$$

The optical Bloch equations and the derivation of the rate equations is detailed in appendix D. The population densities of the initial state i , the intermediate state k and the final state f are denoted by n_x . The probabilities for the transition $x \rightarrow y$ in the presence of the optical field are given by $|V_{xy}|^2$ and the pump-probe delay by τ .

Γ_1 is the inelastic scattering rate from the intermediate to the ground state, $k \rightarrow i$. After decay of the optical excitation ($V_{xy} = 0$), Γ_1 describes an exponential decay of the intermediate state population. In an ideal metal, without defects and electron-phonon coupling, the inelastic decay rate is assumed to be equivalent to the inelastic e-e scattering rate $\Gamma_1 = \Gamma_{e-e}$.

For sufficiently small excitation densities, n_i can be approximated as constant and $|V_{kf}(t, \tau)|^2 n_k$ can be neglected. Integration yields the 2PPE response function for the intermediate state k

$$(2.47) \quad I_k^{2\text{PPE}}(\tau) \propto \int \int dt' dt'' I_1(t') R_k(t'' - t') I_2(t'' - \tau) .$$

Here, $I_1(t)$ and $I_2(t)$ denote the transient envelopes of the pump and probe laser pulses and $R_k(t)$ the response function of the intermediate state k . Using the definition of the XC function of both laser pulses [Rul98]

$$(2.48) \quad F_{XC}(t) = \int dt' I_1(t) I_2(t - t') ,$$

which is equivalent to a convolution of both laser pulses, finally yields for the 2PPE response as function of pump-probe delay τ

$$(2.49) \quad I_k^{2\text{PPE}}(\tau) \propto \int dt F_{XC}(t - \tau) R_k(t) .$$

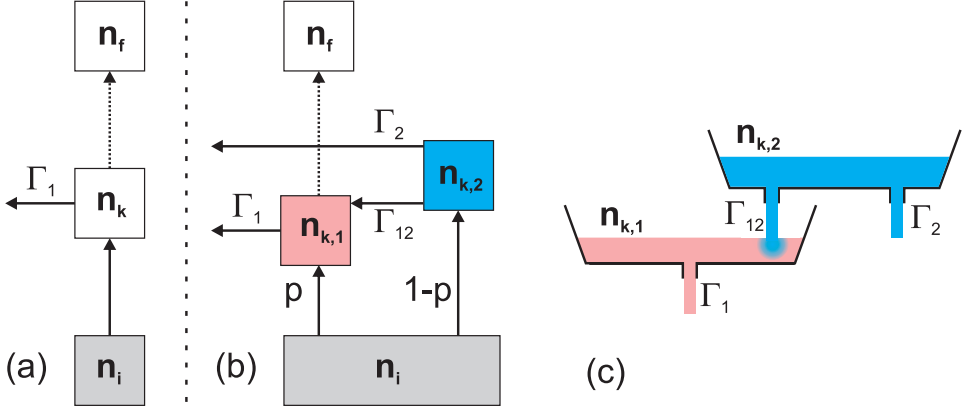


Figure 2.32: Diagram of a 3- and 4-level system with initial, intermediate and final states i, k, f . (a) Decay scheme of a 3-level system. (b) Decay scheme of a 4 level system. The population in $n_{k,2}$ fills the probed population $n_{k,1}$ with a rate Γ_{12} . (c) Representation of the two intermediate states of a 4-level system by a system of coupled water reservoirs.

The XC function $F_{XC}(\tau)$ is obtained from the decay of hot electrons at large excess energies ($E - E_F > 2$ eV) since the excitation proceeds via virtual intermediate states without a finite lifetime. If the lifetime is infinitely small, the response function of the system is a δ function, $R_k(t) = \delta(t)$, and (2.49) reduces to the XC function in (2.48). For a 3-level system with finite lifetime of the intermediate state the response function is given by

$$(2.50) \quad R_1(t) = \Theta(t) n_1^{(0)} e^{-\Gamma_1 t} \quad \text{with} \quad \Gamma_1 = \frac{1}{\tau_1} \quad ,$$

which describes the exponential decay of the initial population density $n_1^{(0)} = n_1(t=0)$ of the intermediate state k with a lifetime of τ_1 . $\Theta(t)$ denotes the Heaviside function. The description of the population dynamics in the QWSs with a 3-level system is only correct if a *single* QWS is populated by the pump laser field. This condition is not always fulfilled, the Pb layers exhibit several unoccupied QWS that can be coupled to each other, and dispersing states can present intra-band decay channels. This situation can be modeled by a 4-level system with two intermediate states, shown schematically in Fig. 2.32.

The populations in the two coupled intermediate states k_1 and k_2 decay with rates Γ_1 and Γ_2 , respectively, into the ground state. Additionally, the second state k_2 is coupled with a rate Γ_{12} to the intermediate state k_1 . Neglecting the optical coupling of k_1 and k_2 by the laser field, the rate equations for the population densities are:

$$(2.51) \quad \dot{n}_1(t) = -\Gamma_1 n_1(t) + \Gamma_{12} n_2(t)$$

$$(2.52) \quad \dot{n}_2(t) = -(\Gamma_{12} + \Gamma_2) n_2(t)$$

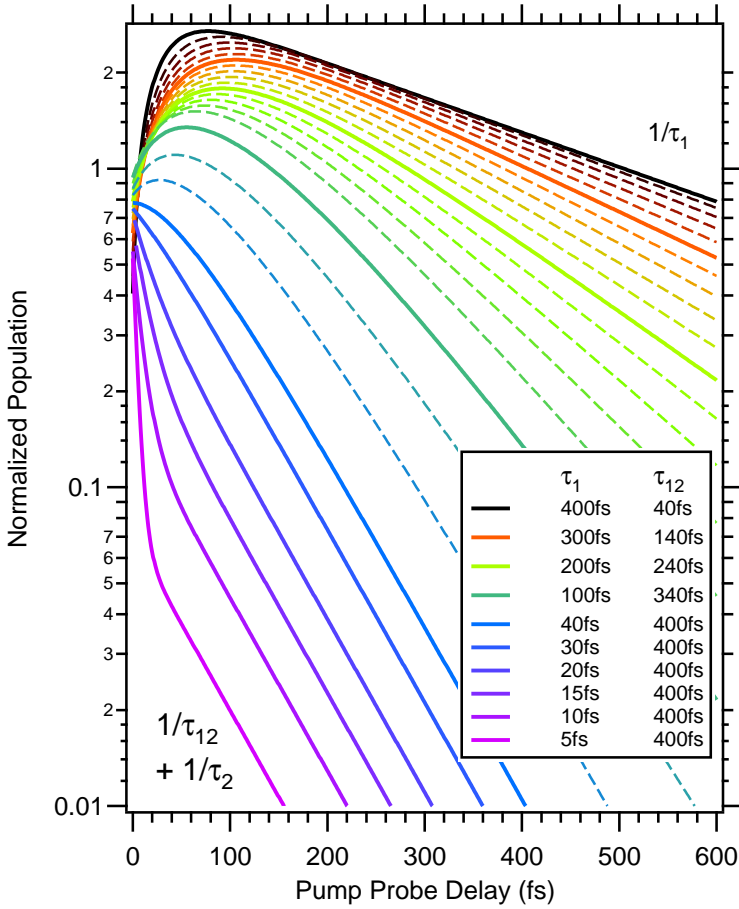


Figure 2.33: Response function of a 4-level system (2.54) for different ratios of τ_1 to τ_{12} and constant $10n_1^{(0)} = n_2^{(0)}$ and $\tau_2 = 100$ fs. For large τ_1 and small τ_{12} a delayed rise of the population is encountered (upper curves). The opposite case of small τ_1 and large τ_{12} leads to a bi-exponential decay. The slopes at later delays are given by Γ_1 and $\Gamma'_2 = \Gamma_{12} + \Gamma_2$, respectively.

The coupled rate equations replace equation (2.45) and are solved analytically to yield the response functions $R_1(t)$ and $R_2(t)$ of both intermediate states:

$$(2.53) \quad R_1(t) = \Theta(t) \left(n_1^{(0)} e^{-\Gamma_1 t} + n_2^{(0)} C (e^{-\Gamma_1 t} - e^{-\Gamma'_2 t}) \right)$$

$$(2.54) \quad R_2(t) = \Theta(t) \left(n_2^{(0)} e^{-\Gamma'_2 t} \right) \quad \text{with}$$

$$\Gamma'_2 = \Gamma_{12} + \Gamma_2 \quad \text{and} \quad C = \frac{\Gamma_{12}}{\Gamma'_2 - \Gamma_1} \quad ,$$

where Γ'_2 describes the total decay rate of the second intermediate state k_2 . The population densities at $t = 0$ are given by $n_1^{(0)}$ and $n_2^{(0)}$, respectively.

Fig. 2.32(c) depicts a simple analogy of the coupled 4-level system. The populations n_1 and n_2 are represented by fluid levels in the two water reservoirs, the decay channels are given by openings at the bottom of the reservoirs. The flow speed ($\dot{n}_x(t)$) is proportional to the opening (Γ_x) and the fill level (n_x), in accordance with (2.51) and (2.52). The lower lying reservoir n_1 is refilled by the flow Γ_{12} from the higher lying reservoir n_2 . This refilling is also influenced by the flow Γ_2 out of the higher lying reservoir. This influence of Γ_2 on the refilling of n_1 allows to obtain informations on the population decay n_2 , which might not be directly probed.

The description of a 4-level system utilizes 5 free parameters ($n_1^{(0)}$, $n_2^{(0)}$, Γ_1 , Γ_2 , Γ_{12}) and thus requires a careful and critical interpretation of the results. However, there are two limiting cases for the response function $R_1(t)$, which can be clearly distinguished as discussed in Fig. 2.33. (I) A delayed rise of the n_1 population is observed for $\Gamma_1 < \Gamma'_2$, which results in $C < 0$ in (2.53). After a delayed population build up due to scattering $k_2 \rightarrow k_1$, the subsequent decay proceeds at a rate Γ_1 . This decay mode is similar to the radioactive decay of a parent nuclide into a daughter product [MK94]. (II) A bi-exponential decay of n_1 is observed for $\Gamma_1 \ll \Gamma_{12}$ and thus $C > 0$. The fast initial decay is determined by Γ_1 and the slope of the subsequent decay is given by $\Gamma'_2 = \Gamma_2 + \Gamma_{12}$. Finally, for $\Gamma_2 = \Gamma_{12} = 0$ the response function (2.50) of the 3-level system is obtained.

2.4.7 Time- and Angle-Resolved Photoemission Spectroscopy

Time- and angle-resolved photoemission spectroscopy (tr-ARPES) is a relatively new experimental technique that was first described in the mid 1980's [Fuj84, Fan92, Hai95]. It provides unique information about non-equilibrium dynamics of the occupied band structure. Compared to purely optical pump-probe schemes, tr-ARPES has the advantage to detect these transient signals directly in reciprocal space. Thus it is free of any model dependent assumptions because it combines the measurement of the single particle spectral function $A(k, \omega)$ in the frequency domain with information about collective excitation modes in the time domain. This can be summarized by an extended spectral function $A(k, \omega, \Delta t)$, which is measured in a tr-ARPES experiment. Part of this thesis work deals with the observation of a collective CDW excitation mode in a strongly correlated material (chapter 7).

The tr-ARPES scheme employs fairly strong pump pulses in the range from $F_{\text{pump}} = 40 \mu\text{Jcm}^{-2}$ to $F_{\text{pump}} = 2 \text{mJcm}^{-2}$ to perturb the occupied band structure by excitation of a significant amount of carriers¹¹. The subsequent UV laser pulse with photon energies larger than the sample work function probe the transient band structure below E_F as well as the excited carriers above E_F . This is depicted in Fig. 2.34(a).

Fig. 2.34 discusses the excitation and subsequent equilibration of the transient electron population around E_F . Before arrival of the pump laser pulse, the electron distribution is characterized by a thermal Fermi-Dirac distribution with an electronic temperature T_{el} equal to the macroscopic sample temperature $T_0 = T_{\text{el}}$. At time

¹¹Typically a few % of the electrons at E_F are excited, which is several orders of magnitude larger than the excitation densities reached in 2PPE. Lisowski et al. [Lis04a] discuss excitation densities of 18% of the electrons at E_F .

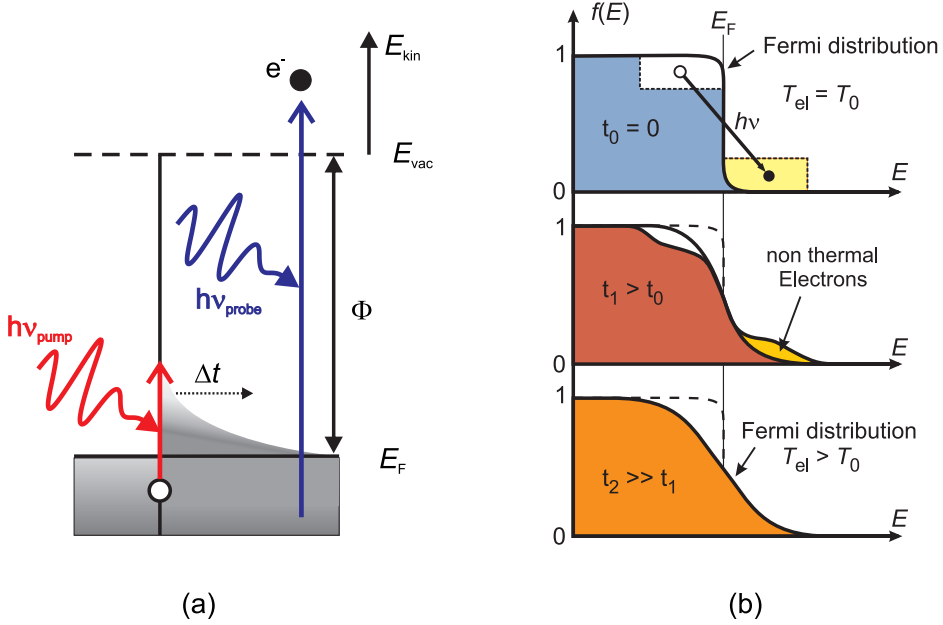


Figure 2.34: (a) Time-resolved photoemission. An intense pump pulse with 1.5 eV photon energy creates a significant¹¹ population of hot electrons above E_F . The time-delayed UV pulse with $h\nu = 6$ eV probes both the transient change of the occupied band structure as well as the short lived population of states above E_F . (b) Sketch of the time-dependent distribution function and of the thermalization process [Lis05a]. The excitation around time zero projects part of the equilibrium electron distribution, which initially is described by a Fermi-Dirac distribution of temperature T_0 , into states above E_F . Inelastic scattering of these excited carriers reestablishes a Fermi-Dirac distribution at a higher temperature $T_{el} > T_0$.

zero, the pump pulse excites electrons into unoccupied states above E_F and creates a transient non-thermal electron distribution, which is not described by a Fermi-Dirac statistic. Due to inelastic e-e and e-ph scattering this non-thermal distribution evolves within 10 – 100 fs [Fan92, Ret02, Lis04a] into a Fermi-Dirac distribution of higher electronic temperature $T_{el} > T_0$, where the electronic temperature can reach several 1000 K [Fan92, Ret02, Lis04a]. This whole process is termed thermalization.

The electronic system is still not equilibrated with the phonon system, which acts as heat bath. Further e-ph scattering equilibrates the electron and phonon system on time scales of > 1 ps, depending on excitation density and the e-ph coupling strength. The whole sequence of excitation and thermalization may be described within a so-called two-temperature model [Ani74, Ret02] that treats the electronic and phononic systems as coupled heat baths. However, a precise description requires an explicit consideration of transport processes as well [Ret02, Lis04a, Lis05a].

The high excitation densities in the tr-ARPES experiments and the associated high electronic temperatures can have drastic impact on the occupied band structure. On the one hand, the sudden drop of electron density around E_F changes the Coulomb

interaction due to an change of the number of electrons and the associated screening. Since the ion cores react to the surrounding electronic potential, this can lead to the excitation of collective modes in the time domain such as coherent phonons [Bov04, Bov06, Bov07, Lis05b, Per06, Lou07, Per07, Per08, Sch08]. On the other hand, tr-ARPES measures the single particle spectral function, just as conventional ARPES does. The unique capability of tr-ARPES now is the simultaneous observation of these two complimentary regimes, as it allows to directly monitor the change of the single particle spectral function in the time domain upon collective excitation of correlated modes.

The tr-ARPES data is evaluated according to the outline presented for time-resolved 2PPE. Vertical cuts along the energy axis yield single spectra as function of pump-probe delay, which then, for example, can be fitted with Lorentzian peaks and a Fermi-Dirac distribution. This yields parameters such as the transient peak amplitude, width and position as well as the electronic temperature. Horizontal cuts along the pump-probe axis result in XC traces that characterize the transient population of occupied and unoccupied states.

3 Experimental Details

To study the ultrafast electron dynamics in low-dimensional metallic structures with femtosecond time-resolved one- and two-photon photoemission, it is necessary to combine femtosecond laser spectroscopy with epitaxial growth of metal films in situ.

The amplified Ti:Sa laser system provides ultrashort laser pulses to excite and subsequently probe the transient evolution of the sample band structure by two-photon photoemission (2PPE) as well as by time- and angle-resolved photoemission spectroscopy (tr-ARPES). The epitaxial Pb/Si(111) samples for the 2PPE investigations were prepared by metal evaporation and characterized with low energy electron diffraction (LEED) and photoemission spectroscopy (PES) in an ultrahigh vacuum chamber. The TbTe₃ crystals for the tr-ARPES measurements were grown and characterized by Ian Fisher and Zhi-Xun Shen and coworkers from the Stanford University as part of our collaboration. The transient one- and two-photon photoemission spectra are collected with a electron time-of-flight (TOF), where the in-coupled laser pulses generate the photoelectrons.

A vital part of this work was to design, implement and commission a novel *position-sensitive* electron time-of-flight (pTOF) spectrometer, which is tailored to deal very efficiently with k -dependent anisotropic electron dynamics. Such anisotropic electron dynamics are important for one- and two-dimensional band structures in low-dimensional, strongly correlated materials. This part of the thesis is described in chapter 4. The hard- and software components are listed in appendix G.

3.1 Laser Setup

The first main building block of the time-resolved photoemission setup is the commercially available amplified laser system (Coherent) as sketched in 3.1. A 18 W¹ Verdi continuous wave (cw)-laser (V-18) [Coh07] pumps a Mira seed oscillator (Mira 900-B) [Coh93] and a regenerative amplifier (RegA) (RegA 9050) [Coh97]. The RegA pulses (800 – 830 nm, 300 kHz, 5 μ J/pulse, 55 fs after compression) can drive two optical parametric amplifiers (OPAs), which are tunable in the visible (VIS) and infrared (IR) spectral range. Subsequent second harmonic generation (SHG) extends the accessible spectral range further into the ultraviolet (UV). The RegA pulses can alternatively supply the optical path for tr-ARPES with 205 nm probe and 820 nm pump pulses in the μ J range and overall < 100 fs time resolution.

The operation principle of the laser system as well as more specific design considerations of the optical paths are summarized in appendix E. More details regarding the generation and control of femtosecond laser pulses can be found in [Dem03, Rul98, Boy92, Tre02], the manuals [Coh07, Coh93, Coh97, Coh94], and in previous thesis works [Kno97, Den99, Hot99, Gah04, Lis05a, St07].

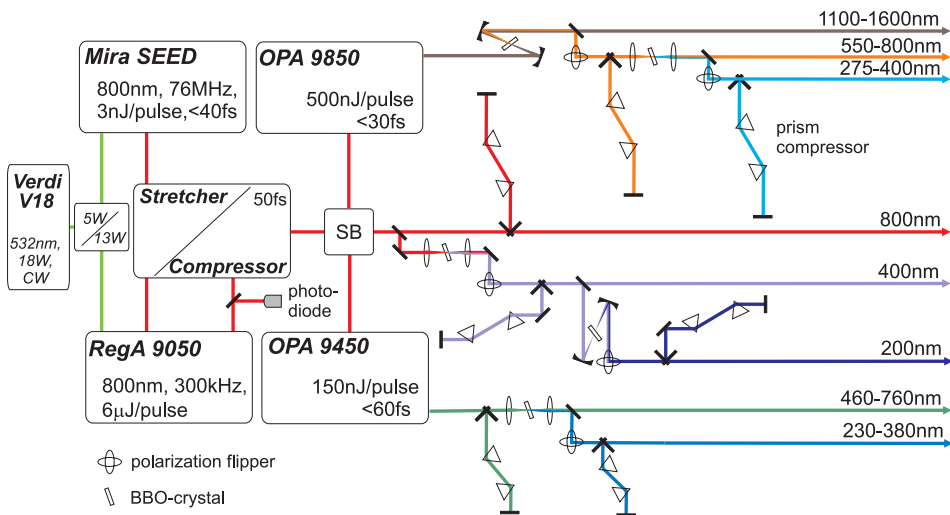


Figure 3.1: Optical path of the femtosecond laser system. A 18 W Verdi cw-laser (V-18) pumps a Mira seed oscillator and a regenerative amplifier (RegA 9050). The RegA pulses can drive two OPAs or alternatively supply the tr-ARPES optical path. Thus, the laser system is quasi-continuously tunable in the range from 200 – 1600 nm. See appendix E for details.

¹The V-18 Verdi laser replaced a 5 W V-5 Verdi laser for pumping the Mira oscillator and a 10 W V-10 Verdi laser for pumping the RegA amplifier in January 2007. This increased the cw power by 80%.

3.1.1 Generation and Amplification of fs-Laser Pulses

The amplified fs-laser system with two different tunable OPAs enables bichromatic 2PPE experiments in which the photon energies of pump and probe pulse can be chosen independently. This allows to populate intermediate states via resonant optical excitation or non-resonant transitions. For the 2PPE experiments it is also necessary to avoid direct photoemission and adapt the maximum photon energy to the sample work function. The OPA 9450 (visible optical parametric amplifier (VIS-OPA)) [Coh94] delivers tunable VIS pulses (460 – 760 nm, 55 fs at 150 nJ/pulse); the OPA 9850 (infrared optical parametric amplifier (IR-OPA)) [Coh94] generates ultrashort infrared pulses (1100 – 1600 nm, 30 fs at 500 nJ/pulse). The range of photon energies is then further extended into the UV by SHG in β -barium-borate (BBO) crystals. Frequency doubling of the VIS-OPA output yields 230 – 380 nm. The VIS-OPA was used in the 2PPE experiments on Pb/Si(111) and 4×1 -In/Si(111) due to its easier handling and tunability.

Alternatively, the RegA output can be used for tr-ARPES at 820 nm pump and 205 nm probe wavelength (6 eV probe energy). The pump pulse duration is given by the RegA pulses of 55 fs, the probe pulses are limited to about 80 fs pulse duration. The upgraded¹ RegA system provides up to 1 μ J pumping power at the position of the sample. This excitation regime allows to trigger collective many-body dynamics like optically induced ultrafast phase transitions in highly correlated materials [Per06, Per08, Sch08] and high- T_c superconductors [Kor06, Per07]. The photon flux in the 205 nm probe beam is in the order of 10^{13} photons/s and thus comparable with third generation synchrotron undulator light sources [Kor06]. This facilitates an efficient characterization of the occupied band structure at 6 eV photon energy. The tr-ARPES path was used in the experiments on Pb/Si(111) and TbTe_3 .

3.1.2 Pulse Incoupling

The next step is the incoupling of the laser pulses into the ultrahigh vacuum (UHV) chamber and establishment of spatial and temporal overlap of pump and probe beam in the focus of the acceptance cone of the TOF. A detachable breadboard houses the delay stage (Physik Instrumente), the focusing optics, a pinhole for finding the spatial overlap, a fast photodiode to constrict the temporal overlap, and a charge coupled devices (CCD) camera (The ImagingSource) to capture beam profiles, see Fig 3.2. The computer-controlled delay stage, which delays the probe pulse with respect to the pump pulse with < 0.5 fs precision and repeatability, is positioned in the VIS path of the time-resolved experiments. The tunability of the OPA system as well as photon energies in the range of ~ 200 nm do not permit the use of commercial high-reflection dichroic mirrors. The Aluminum mirrors, which are used in the UV path, however, have a reflectivity of 80%. This leads to significant intensity losses and calls for a minimal number of UV mirrors.

Pump and probe beam are independently focused onto the sample surface by two lenses. Both beams are adjusted to equal size for the 2PPE experiments (see Fig. 3.3) to suppress the uncorrelated background in the 2PPE spectra. For the tr-ARPES experiments the probe beam is adjusted to be smaller than the pump beam to ensure a homogeneously excited sample and to avoid broadening of the spectra, which can

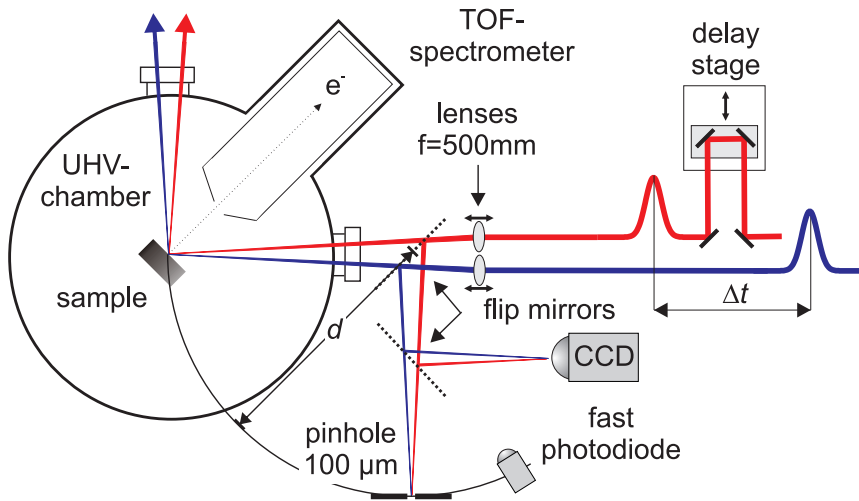


Figure 3.2: Incoupling of the pump and probe beams into the UHV chamber. The time-correlated beams, which are delayed on a delay stage, are independently focused onto the sample in front of the TOF entrance aperture by two lenses. The spatial overlap is established in a pin hole outside the chamber. The beam profiles are acquired in a UV sensitized CCD camera. The temporal overlap is constricted with a fast photodiode.

occur on inhomogeneous sample surfaces. The incoupling geometry is quasi-collinear to similarly avoid interferometric conditions and minimize the temporal broadening due to a non-collinear geometry. The sample is brought to the nominal distance of 3 mm in front of the entrance aperture of the TOF. The visible beam, which is observed with an optical microscope equipped with a CCD camera, is first aligned to fix the beam position in the focus of the acceptance cone of the TOF. The single color 2PPE count rate can additionally be used to align the beam in case of a homogeneous, defect free surface.

The focus position of the pump beam is transferred via a flip mirror to a pin hole of 100 μm diameter. The pinhole is positioned at exactly the same distance d to the flip mirror as the sample surface, see Fig. 3.2. The position of the pin hole itself is determined by maximization of the power transmitted through the pinhole. The UV beam, which is visualized with optical brightener on paper cards, is aligned to also be transmitted through the pinhole, which ensures the spatial overlap on the sample. A second flip mirror directs the beams to CCD camera. The CCD chip has been sensitized for UV radiation by removing the entrance window of the CCD chip. The CCD image is used to determine the pump and probe beam profiles and thus the laser fluence, see Fig. 3.3. The intense laser beams are dimmed with neutral density filters to avoid damage of the CCD.

The temporal overlap of the pump and probe pulse is initially checked with an ultrafast photodiode and a broadband oscilloscope with regard to a time reference

signal from the RegA. The coarse overlap to within 1 cm optical path length difference, corresponding to 10 ps time difference, is adjusted with the mirror positions on the optical table. The correlated 2PPE signal is found comparably easy by fast scanning the delay stage in a range of ± 10 ps and monitoring the 2PPE signal, which increases by up to three orders of magnitude at zero delay. The spatial overlap is then maximized by fine tuning of the laser pointing with the incoupling mirrors.

To find the correlated tr-ARPES signal is, however, a much more difficult task as a very small spectral changes in the order of $10^{-3} - 10^{-5}$ have to be detected. This can not be accomplished by scanning the delay and monitoring the count rate, but requires to sample spectra for each delay and (manually) search for a signature of hot electrons in the unoccupied states, or binding energy shifts in the occupied band structure. Experience has shown that TaS₂ is best suited for the overlap search in tr-ARPES experiments [Per06, Per08], due to a well-resolved hot electron signal and long-lived coherent phonon modes which modulate the bands near E_F . In a typical search for temporal overlap in a tr-ARPES experiment the delay is scanned in the range of ± 20 ps and 400 spectra have to be acquired, see appendix E for details.

3.1.3 Pulse Characterization

The wide tunability of the laser setup requires several optical spectrometers to characterize the spectral properties of the beams. The VIS and UV spectra from the VIS-OPA can be acquired anywhere on the laser table with a computer-controlled fiber-optic grating-spectrometer (B&M), see Fig. 3.4. The IR spectra are measured with a separate IR laser spectrometer (APE Wavescan). The 205 nm pulses are characterized with a grating monochromator (LOT-Oriel ANDOR). Recently, the RegA setup was equipped with a so-called Grenouille, which allows the simultaneous determination of beam profiles, spectral profiles and a frequency-resolved optical grating trace in the wavelength range 1100 – 700 nm. This allows a very efficient alignment of the stretcher-compressor where the pulse duration and the spectral profile are optimized simultaneously. Details can be found in [Tre02, Tre07].

The beam profiles from the CCD camera are evaluated by a fit of two Gaussian beam profiles, as shown in Fig 3.3. This yields the full width at half maximum (FWHM) of the beams, which are typically 100 – 150 μm . The laser fluence is calculated from the transmission of the incoupling window $T = 0.95$, the cw power P , the laser repetition rate $R \approx 300$ kHz, the FWHM a and b of the laser spot, and the azimuth and polar (manipulator) angles α and β according to

$$(3.1) \quad F = \frac{TP \cos \alpha \cos \beta}{R \pi ab}$$

The manipulator angle β (45° in normal emission) takes the elliptic projection of the beam profiles onto the sample surface into account. The angle α is only non-zero for the tr-ARPES experiments on TbTe₃, which used slanted posts with $\alpha = 45^\circ$, see chapter 3.3.2. Typical fluences in the 2PPE experiments are in the range of 1 – 2 $\mu\text{J}/\text{cm}^2$ for the UV and 20 – 60 $\mu\text{J}/\text{cm}^2$ for the VIS beam. The fluence of the 800 nm IR beam in the tr-ARPES experiments was in the range of 0.1 – 3 mJ/cm^2 .

The evaluation of the electron dynamics in the transient spectra requires precise knowledge of the zero pump-probe delay as well as the temporal laser pulse shape and

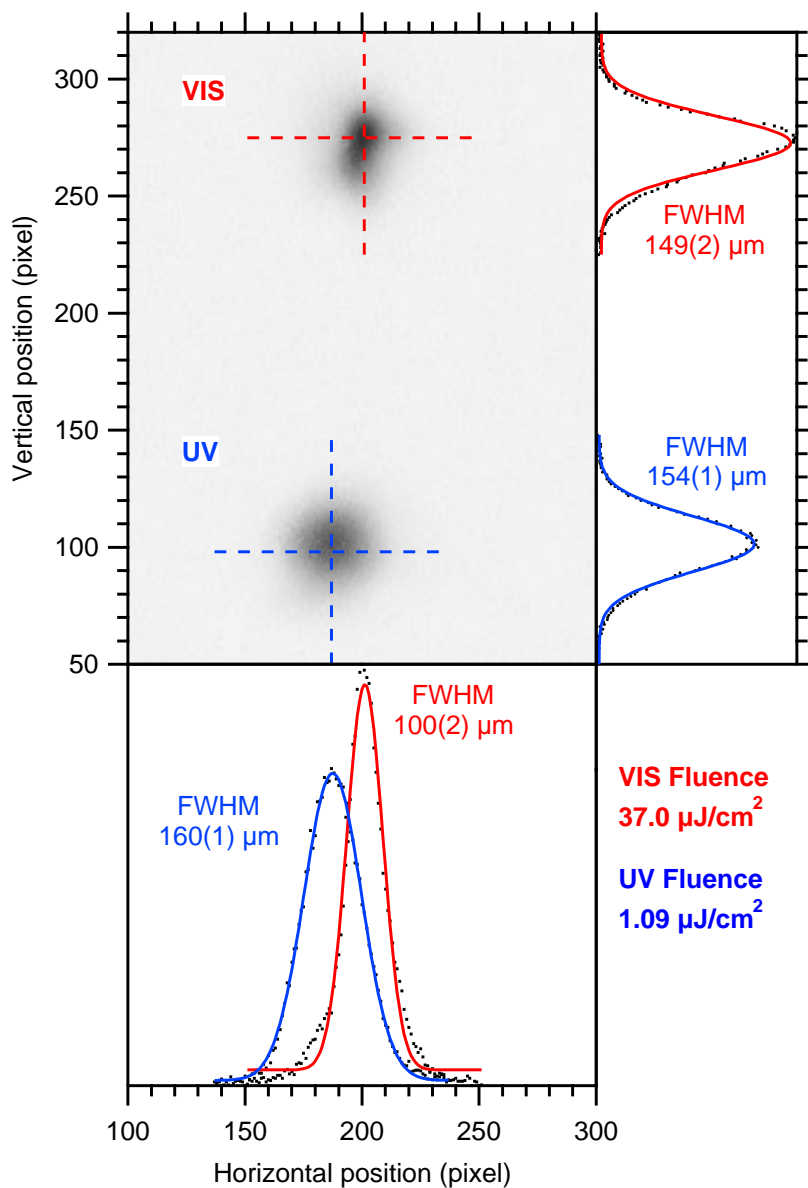


Figure 3.3: Typical beam profiles in the 2PPE experiments. The fluences for both the VIS pump beam (red) and the UV probe beam are indicated.

pulse duration. This is obtained from a cross correlation (XC) of the 2PPE signal from pump and probe pulse on the sample in the UHV chamber. This procedure is much more direct and reliable than the (optical) determination of the pulse characteristics on the laser table.

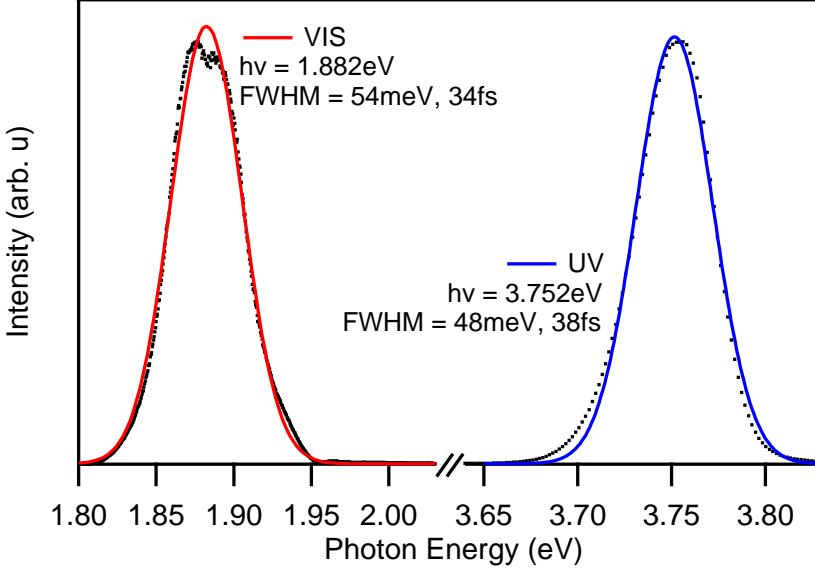


Figure 3.4: Typical laser spectra of the VIS-OPA output and the frequency doubled UV pulses. The mean photon energy as well as the FWHM with the corresponding Fourier limit from equation (3.6) are given.

The XC of the laser pulses is conveniently obtained on single crystal surfaces that exhibit an occupied surface state, like Cu(111). The photoemission process proceeds via a direct two-photon process if the photon energies are chosen to avoid any resonant transitions into real intermediate states. The virtual intermediate state involved in the direct two-photon process is only populated for an infinitesimal amount of time. The measured intensity XC $F_{XC}(t)$, which corresponds to the convolution of both the pump and probe transient intensities $I_1(t)$ and $I_2(t)$

$$(3.2) \quad F_{XC}(t) = \int_{-\infty}^{+\infty} dt' I_1(t) I_2(t - t')$$

can be approximated with an intensity auto correlation (AC) $F_{AC}(t)$ of two identical pulses if pump and probe are of comparable duration [Rul98]. For the commonly used Gaussian and sech^2 pulse shapes² this gives:

$$(3.3) \quad F_{XC}(t) \cong F_{AC}(t) = \begin{cases} \frac{3(x \cosh x - \sinh x)}{\sinh^3 x} & \text{sech}^2 \text{ pulse shape} \\ e^{-x^2} & \text{Gaussian pulse shape.} \end{cases}$$

²Normally, ultrafast oscillators generate sech -pulses, whereas fs-amplifiers deliver Gaussian pulse profiles.

The characteristic time $x = t/T$ is connected to the FWHM of the AC trace in the time domain $\Delta\tau$

$$(3.4) \quad \frac{\Delta\tau}{T} = \begin{cases} 2\sqrt{\ln 2} & \text{sech}^2 \\ 2 \operatorname{asech}\left(\frac{1}{\sqrt{2}}\right) & \text{Gaussian.} \end{cases}$$

Interestingly, the ultrafast community has agreed to use the more optimistic sech^2 pulse shape [Rul98] as this results in the shortest pulse duration. The laser pulse duration is defined as the FWHM of the intensity profile in the time domain Δt for a given FWHM $\Delta\tau$ of an AC trace:

$$(3.5) \quad \Delta t \Delta\tau = \begin{cases} 1.543 & \text{sech}^2 \\ 1.414 & \text{Gaussian.} \end{cases}$$

The temporal width in the time domain Δt can be compared to the spectral bandwidth in the frequency domain, defined as FWHM of the laser spectrum $\Delta\nu$. This can serve to verify that the laser pulses are Fourier-limited, i.e. that all laser modes are coherently coupled and contribute to the pulse, see Fig. E.3 in appendix E. The time-bandwidth product then is constant and given by:

$$(3.6) \quad \Delta\nu \Delta t = \text{const} = \begin{cases} 0.3148 & \text{sech}^2 \\ 0.4413 & \text{Gaussian.} \end{cases}$$

If the surface under investigation lacks an occupied surface state, the hot electron signal at energies $E - E_F \geq 2$ eV can still be used in a comparable fashion. At intermediate state energies $E - E_F \geq 2$ eV the excited electron lifetime is ≤ 10 fs, which does not show up in a peak shift or broadening of the XC traces because the laser pulse duration exceeds 40 fs. Thus the lifetime is negligible compared to the pulse duration and equation (3.3) may be applied.

3.2 Ultra High Vacuum Chamber

The study of well-defined single crystal surfaces requires to work in ultrahigh vacuum (UHV) conditions of $p \lesssim 10^{-10}$ mbar to minimize the adsorption of rest gas atoms. The time to build up a monolayer (ML) coverage is ~ 10 h at 10^{-10} mbar but only a few seconds at 10^{-6} mbar [Zan88]. The photoelectron spectroscopy requires that the mean free path of the photoemitted electrons is large compared the drift distance in the TOF spectrometer.

The whole UHV setup is firmly mounted to the air-damped laser table to ensure stable beam pointing. The vacuum chamber is separated by a gate valve into two independently pumped vessels of preparation and spectrometer level as sketched in Fig. 3.5. The chamber is also equipped with a sample transfer and storage system (not shown), which allows to exchange samples without breaking the UHV conditions. A high sample throughput is especially relevant for the work with Silicon samples, which degrade rapidly upon flashing, and TbTe_3 , where the surface is prepared by cleavage of single crystals in UHV. All pumps of the UHV system are lubricant-free to avoid any hydrocarbon contaminations.

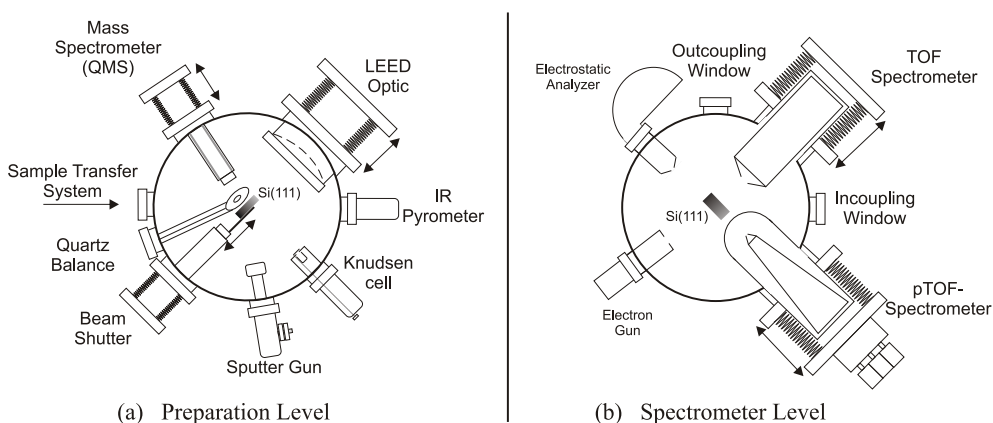


Figure 3.5: UHV chamber with tools for surface preparation and characterization. In- and outcoupling windows are made from UV-transmitting MgF_2 . Both TOF spectrometers can be retracted to work at the same laser focus.

The preparation level is evacuated to $7 \cdot 10^{-11}$ mbar by a turbo-molecular pump (Pfeiffer) connected down stream to a turbo pump (Pfeiffer), which is combined with a four-stage membrane pump unit (Pfeiffer). The preparation level is equipped with various tools for surface preparation and characterization. For the growth of ultrathin metal films several tools have been used: a low energy electron diffraction (LEED) optic (Specs) to characterize the symmetry and surface quality, a home-built, water-cooled Knudsen cell for metal evaporation, a Quartz balance (Inficon) for the calibration of the evaporation rate, a retractable shutter to block parts of the metal vapor, and an IR pyrometer (Impac) for the measurement of high sample

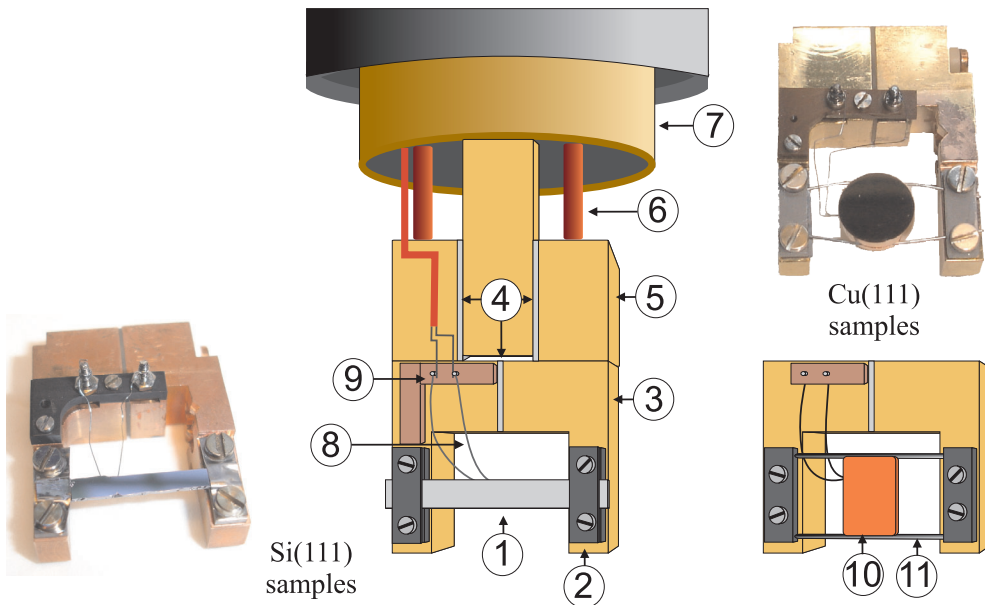


Figure 3.6: Drawings and photographs of the sample holder and sample boats for crystal transfer. (1) Silicon wafer. (2) Ta-mount. (3) Transferable sample boat. (4) Sapphire plates. (5) Gold-plated Cu-blocks (fixed to the cryostat). (6) Current leads. (7) Cryostat. (8) Thermocouple. (9) Thermocouple connection. (10) Cu(111) single crystal. (11) Ta wires.

temperatures of $T > 1000$ K [Tim93]. Additionally, the preparation level is equipped with tools for preparing metal single crystal surfaces, such as a sputter gun (Specs), an electron bombardment heater, a gas dosing system with pinhole- and leak-dosers, and a quadrupole mass spectrometer (QMS) (MKS Instruments) for the residual gas analysis.

The spectrometer level is pumped down to $< 3 \cdot 10^{-11}$ mbar by a Titanium sublimation pump (Riber) and an ion getter pump (Riber) when the gate valve is closed. With open gate valve a pressure of $< 5 \cdot 10^{-11}$ mbar in the spectrometer level is ensured. The main items in the spectrometer level are the conventional electron TOF spectrometer and the pTOF, compare to chapter 4.

The manipulator is equipped with a 400 mm long Helium-flow-cryostat (CryoVac), which connects the upper preparation level with the lower spectrometer level. The stationary part of the sample holder is mounted to the cryostat, which is housed in a differentially pumped rotation feed through that allows a 360° rotation of the sample. The manipulator can laterally move by ± 12.5 mm and vertically by 400 mm. All three manipulator axes are equipped with stepper motors, which allow to move

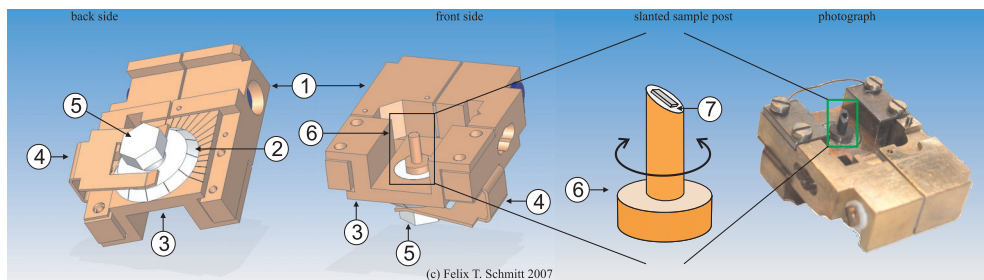


Figure 3.7: Drawings and photograph of the slanted sample posts that were used for the tr-ARPES measurements on TbTe_3 . Left panel: Back side from where the goniometer is accessed. Center panel: Front side housing the sample. Right panel: Close-up on the slanted sample post made from phosphor-bronze. (1) exchangeable sample boat (2) Al goniometer for in-plane rotation (3) insertion device to connect the sample post and sample boat (4) CuBe springs to hold goniometer setup in place (5) Hex nut to rotate the sample post in-plane (6) sample post (7) small single crystal on the slanted sample post.

the sample with $\pm 10 \mu\text{m}$ precision. The sample can be cooled to $< 100 \text{ K}$ with liquid N_2 . Liquid He cooling allows to reach 40 K sample temperature. The Si and Cu(111) single crystal samples were annealed with direct current heating of the sample in the sample boat. The TbTe_3 samples were cleaved *in situ* and did not require any further treatment.

The sample holder is shown in Fig. 3.6. All sample holder parts are manufactured from non-magnetic materials like Aluminum (Al), Copper (Cu), Titanium (Ti), Tantalum (Ta), and ceramics to ensure the absence of magnetic fields for the TOF measurements. The left hand side depicts a rectangular Silicon wafer mounted between two Ta sheets in the exchangeable sample boat. The right hand side shows the exchangeable sample boat, which is equipped with a Cu(111) single crystal mounted in between two Ta wires. Both parts of the sample boat are electrically insulated but thermally well connected to the cryostat by 0.5 mm thick Sapphire plates. W/Rh (Type C) thermocouple wires were used in the experiments with Pb/Si(111). The non-magnetic W/Rh alloy thermocouple wires tolerates temperatures of $T > 2000 \text{ K}$ and thus is well suited for the Si preparation. The sample transfer requires a customized thermocouple connection to avoid contact potentials.

The sample boat is a versatile design [Lis05a] as it accommodates wafer samples, commercial single metal crystals as well as smaller single crystals on a small post. Such single crystal samples of only a few mm^2 size, like TbTe_3 and BSSCO, can be glued by vacuum-compatible epoxy-glues onto a post shown in Fig. 3.7, which was designed and built by Felix Schmitt from the Stanford University in the context of our collaboration. The post can be slanted and is freely rotated by the screw driver, which is installed for the sample transfer. Thereby the geometric restriction of angle-resolved photoemission spectroscopy (ARPES) at low photon energies can be overcome and wave vectors of up to 0.5 \AA^{-1} at $h\nu = 6 \text{ eV}$ in any direction of the Brillouin zone become accessible (See chapters 4 and 7). All measurements on TbTe_3 were performed with 45° slanted posts.

3.2.1 Conventional Time-of-Flight Electron Spectrometer

One of the key elements of the time-resolved photoemission setup is the electron time-of-flight (TOF) spectrometer, where the correlated pump and probe beams are overlapped in time and space and TOF electron spectra are recorded in an angle resolved manner as function of pump-probe delay. This section briefly discusses the conventional electron TOF, which was built in the Fritz-Haber-Institute of the Max-Planck-Gesellschaft and extensively described by Knoesel and Hotzel [Kno97, Hot99]. However, the basic concepts of electron TOF measurements discussed here will be the foundation for the pTOF spectrometer that is described in chapter 4.

The conventional electron TOF spectrometer, as shown in Fig. 3.8 consists of a field free Al drift tube with a 1.5 mm large aperture at the conical flight tube tip and a chevron stack of 40 mm micro channel plate (MCP) for single electron detection. After a drift length of 297 mm the electrons transverse a first grid and are accelerated with +15 V toward a second grid at +570 V in front of the MCPs. The second grid supplies the energy necessary to launch an electron avalanche in the channels of the MCPs, which are biased at +2.1 kV.

Each electron launches an electron avalanche that results in a charge cloud of $10^6 - 10^7$ electrons. The voltage signal from the charge cloud can be outcoupled with a capacitor (i) at an anode structure on the back of the MCPs that gathers the charge cloud or (ii) directly at the MCPs since the electron avalanche results in a sudden voltage drop across the MCPs. The voltage pulses with a few mV amplitude and a few ns pulse duration are amplified in a broadband amplifier (Ortec) directly after the outcoupling.

All parts of the setup like the flight tube, tip and grids are coated with Graphite (Contact Chemie) to ensure a homogeneous work function of ~ 4.3 eV. The whole TOF spectrometer is housed in a 2 mm μ -metal casing to shield residual magnetic fields, which influence the electron trajectories and thus the TOF at the low kinetic electron energies of a few eV. The shield has cut-outs for the manipulator and the laser

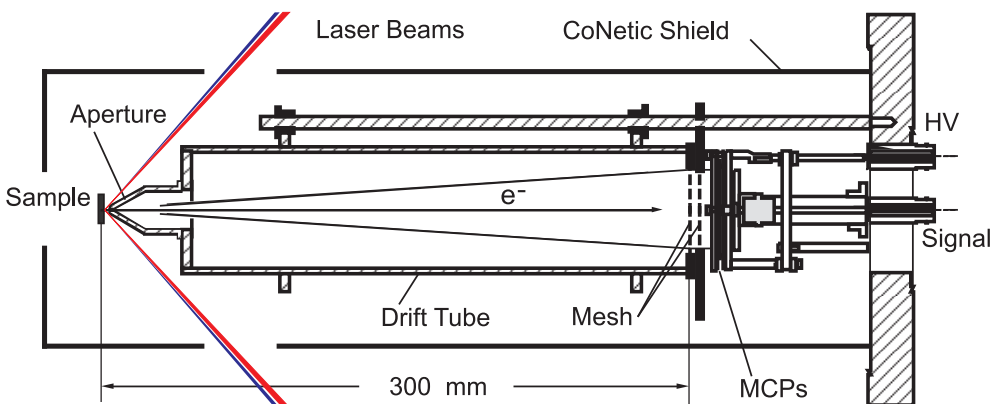


Figure 3.8: Convectional electron TOF spectrometer with 300 mm drift length and 40 mm diameter MCPs after [Kno97].

beam entering with 45° angle, as seen in Fig. 3.8. The opening for the manipulator allows to rotate the sample by $\pm 40^\circ$ and thus enables angle-resolved studies in k -space.

3.2.2 Data Acquisition

The data is acquired and analyzed in real time using two different computer systems: One high-performance work station is exclusively dedicated to the novel pTOF spectrometer, which produces a significant data stream of up to 14 MByte/s. This part of the data acquisition and analysis is discussed in chapter 4. The second computer acquires the TOF data of the conventional electron spectrometer and controls all other electronic instruments.

The TOF is determined from the time difference of a start signal from a fast photodiode in the optical beam path and a stop pulse that is outcoupled from the MCPs. A fast discriminator and amplifier (Ortec) generates nuclear instrumentation module (NIM) pulses that serve as start pulses. The typical width of the NIM start signal is 10 ns and the root-mean-square (rms) jitter of the leading edge amounts to 50 ps. The outcoupled signals from the MCPs show a broad distributions of amplitudes and thus have to be discriminated in a constant-fraction-discriminator (CFD).

The start and stop pulses are fed into a multi event time-to-digital converter (TDC) (FAST Comtech) and sampled with 250 ps resolution and 38bit sample depth. 13bits of the measurement interval in the FAST card are used to sort the TOF into 8192 equidistant bins of 250 ps width, which results in an overall discretization error of < 500 ps. The multihit capability of the FAST card allows to sample multiple events within one laser cycle of $> 3.3 \mu\text{s}$ duration without electronic deadtime. Nonetheless, the electronic deadtime of the CFD amounts to 10 ns and presents a bottle neck. In principle, this can introduce systematic distortions of the peak shape due to saturation of the TOF spectra. However, such distortions have not been observed. The multihit capability leads to a situation where the maximal measurable count rate is practically only limited by space charging in the laser focus, see chapter 2.4.3.

The measuring computer is equipped with a multi-functional data acquisition card (National Instruments, NI), which combines eight differential A/D converters, two D/A converters, two 24bit counters, eight logic channels and ten programmable digital channels. The measurement software is based on the graphical NI LabView 6.x front end to acquire the TOF spectra, actuate and coordinate the manipulator, the laser beam shutters, and the delay stage.

For time-resolved studies, the optical path length of the visible beam is controlled by a delay stage (Physik Instrumente). Typically, the time-resolved 2PPE measurements consist of 100 – 200 single spectra at subsequent delays, whereas the tr-ARPES data sets generally are larger and comprise up to 400 transient spectra. The computer drives the delay stage to each predefined delay step and spectra are acquired for typically 500 – 1000 ms. Two mechanical laser shutters in the beam paths block the pump and probe beam separately after each delay scan and acquire spectra of the uncorrelated background. The delay scan is repeated up to 100 times and the transient spectra are averaged to obtain high signal-to-noise (S/N) ratios significantly better than 1000 : 1 after background subtraction.

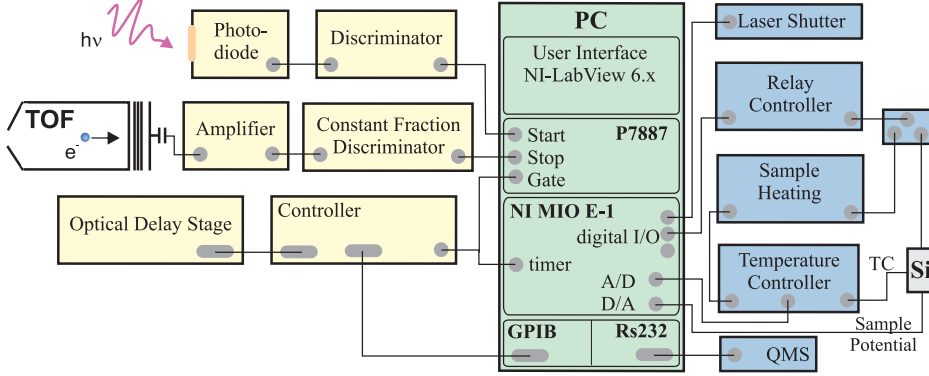


Figure 3.9: Electronic signal processing in the time-resolved experiments.

The achievable S/N level limits the physical questions that can be addressed and thus is of high importance for the time-resolved experiments. The S/N ratio in general is determined by the counting statistics $\delta N = 1/\sqrt{N}$ of each transient spectra at a given delay. Specifically, this is a function of many parameters such as the long-term (> 1 h) stability of the manipulator and the laser jitter. The influence of these instabilities can be partly compensated by increasing the number of delay scans. However, fine structures in the spectra will be washed out due to mechanical and optical fluctuations and the maximum time for a delay scan is limited by the lifetime of the sample in UHV. The sample quality itself also influences the S/N ratio as very flat and homogeneous samples tend to have only a low uncorrelated background. Rougher and inhomogeneous samples can create a significant amount of secondary electrons due to excitation of surface enhanced plasmons, which lowers the S/N ratio.

In the time-resolved experiments, the count rates of 20 – 300 kHz were maximized up to the space charge limit by adjusting the laser fluence and monitoring the position of the high-energy cutoff at the Fermi edge, which reacts very sensitively to space charging. Here, space charge induced shifts at E_F of up to 20 meV were tolerated. This weak space charging can be neglected compared to the finite energy resolution of the TOF spectrometer and the significant laser bandwidth, but ensures the highest possible counting statistics.

3.2.3 Data Analysis

The TOF t from the photoemission event to the arrival at the detector is directly correlated to the kinetic energy E_{kin} of these non-relativistic³ electrons:

$$(3.7) \quad E_{\text{kin}} = \frac{m_e}{2} \left(\frac{L}{t} \right)^2 = 2.4828 \text{ eV ns}^2 \text{ mm}^{-2} \cdot \frac{L^2}{t^2},$$

³The kinetic energy is small compared to the energy equivalent of the electron mass $m_e c^2 \gg E_{\text{kin}}$.

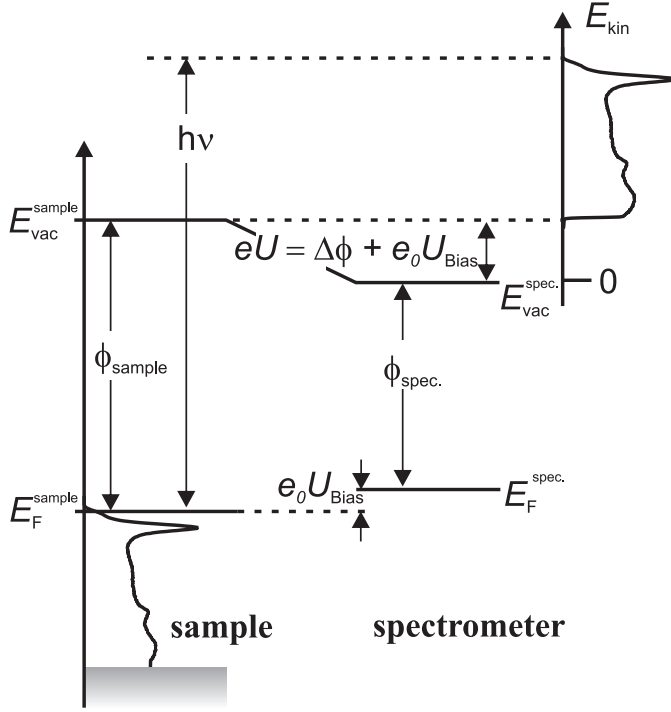


Figure 3.10: Potential gradients between sample and spectrometer. The spectrometer is permanently grounded, whereas the sample can be biased with a voltage U_{bias} , which is important to adjust the difference of vacuum energies for angle-resolved TOF measurements. The kinetic energy is always measured with respect to the vacuum level of the spectrometer. The vacuum level of the sample defines the low-energy cutoff.

where L is the constant, field-free drift distance. The electrons have to overcome the potential barrier $e_0 U$ due to the difference of sample and spectrometer work function, Φ_{sample} and $\Phi_{spec.}$, respectively, as well as an applied bias voltage U_{bias}

$$(3.8) \quad e_0 U = \Phi_{sample} - \Phi_{spec.} + e_0 U_{bias} \quad .$$

Fig. 3.10 shows a potential diagram between sample and spectrometer. The angle-resolved detection of the photoelectrons requires to offset the difference of vacuum energies ($U = 0$) by applying a bias voltage of $e_0 U_{bias} = -(\Phi_{sample} - \Phi_{spec.})$ to ensure a field free region between the sample and the spectrometer and thus unperturbed electron trajectories.

The TOF signal of the electrons is measured from the start pulse of a fast photodiode in the laser beam path and the stop pulse from the MCPs of the spectrometer. This time t' differs by a constant offset t_0 from the actual TOF t because the optical and electric signals need different propagation times to the timing device. Using

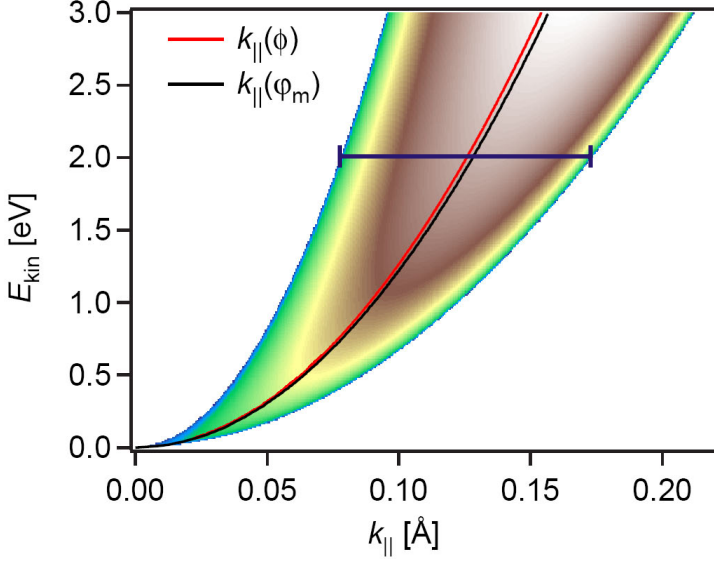


Figure 3.11: Effective $k_{||}$ -acceptance as function of kinetic electron energy E_{kin} due to the averaging over conventional TOF spectrometer after [Gah04].

equations (3.7) and (3.8) yields:

$$(3.9) \quad E_{\text{kin}} = \frac{m_e}{2} \left(\frac{L}{t - t_0} \right)^2 - (\Phi_{\text{sample}} - \Phi_{\text{spec.}}) - e_0 U_{\text{Bias}}$$

Here, the initial acceleration due to the potential barrier U is approximated to occur instantaneously and also the final acceleration at the grids in front of the MCPs is neglected. However, these simplifying assumptions are empirically well justified [Hot99]. The timing offset t_0 is obtained from a so-called bias series by adjusting t_0 as a free parameter in a series of spectra that were taken at different bias voltages. In the variable transformation from TOF to kinetic energy $t \rightarrow E$ the change of intensities has to be taken into account:

$$(3.10) \quad \frac{dN}{dE} = \frac{dN}{dt} \left| \frac{dE}{dt} \right|^{-1} = \frac{dN}{dt} \frac{t^3}{m_e L^2}$$

The energy resolution of the TOF spectrometer is, according to equation (3.7), energy dependent and mainly determined by the timing accuracy, uncertainty of the drift length and imperfections of the spectrometer work function. This is discussed in detail in the context of the new position-resolving TOF spectrometer, see chapter 4.1.4. Hotzel estimates the absolute error to be $\Delta E = 13 - 19$ meV for kinetic energies of $E_{\text{kin}} = 0.5 - 2.5$ eV [Hot99]. However, the time-resolved spectra do not exhibit such fine structures due to the convolution with the laser bandwidth of < 50 meV. The low-energy cutoff at the secondary edge is only influenced by the homogeneity of the sample and thus can serve as a measure for the energy resolution of the spectrometer.

The k -space resolution is determined by the acceptance angle of the spectrometer, which is calculated from the diameter of the MCPs and the drift tube length to be 7.6° . This opening angle still allows precise angle-resolved measurements [Hot00, Gah02, Kir05, Per07, Sch08]. However, the spectra will be averaged over the acceptance angle, which also results in spectral broadening in case of dispersing states. As seen in Fig. 3.11, this averaging over the acceptance angle thus leads to an effective $k_{||}$ -acceptance as function of kinetic electron energy as estimated by Gahl [Gah04]. For a peak at $E_{\text{kin}} = 2$ eV and a sample rotation angle of 10° the peak is centered around 0.12 \AA^{-1} but has been averaged in the range $0.08 - 0.17 \text{ \AA}^{-1}$ as indicated by the blue bar in Fig. 3.11. This is one of the motivations to develop a position-resolving electron TOF spectrometer, which allows to efficiently determine the photoemission angles with high precision, see chapter 4.

3.3 Sample Preparation

3.3.1 Preparation of Ultrathin Epitaxial Metal Films

The time-resolved spectroscopic investigation of quantized electronic states in ultrathin epitaxial metal films requires to grow structures with low defect densities. This is because electron-defect scattering events at corrugated interfaces may alter the total observed decay rate.

Silicon Preparation

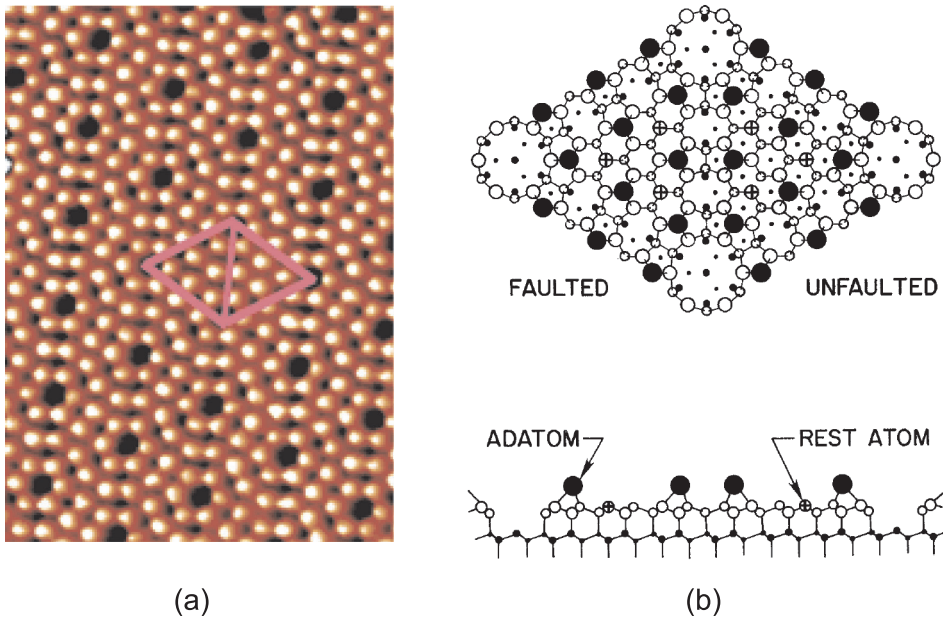


Figure 3.12: Silicon 7×7 reconstruction. (a) Atomically resolved STM image [Tao04]. (b) Ball and stick model of the reconstructed surface [Bol93].

The semiconducting Si substrate is chosen for the study of the ultrafast electron dynamics in ultrathin metal films since (i) it facilitates the energetic confinement of the metal electrons in the region of the global Si bandgap, see chapter 2.1.2, and (ii) it minimizes the absorption of light with a photon energy below the direct bandgap [Lan76]. The light absorption of the substrate leads to excited carriers, which can scatter into the unoccupied states of the metal film. Furthermore, the preparation of Si under UHV conditions is a well documented [Hat00], technically exploited process on which large parts of the semiconductor industry rely. This ensures the availability of high quality wafer substrates, which do not require any additional preparation steps, except the cutting of the wafers to their final size.

The Si samples are cut from Boron p-doped single-sided polished 4 inch wafers with $500 \mu\text{m}$ thickness and a specific resistance of $\sim 15 \Omega\text{cm}$ (MaTeck). The wafers are

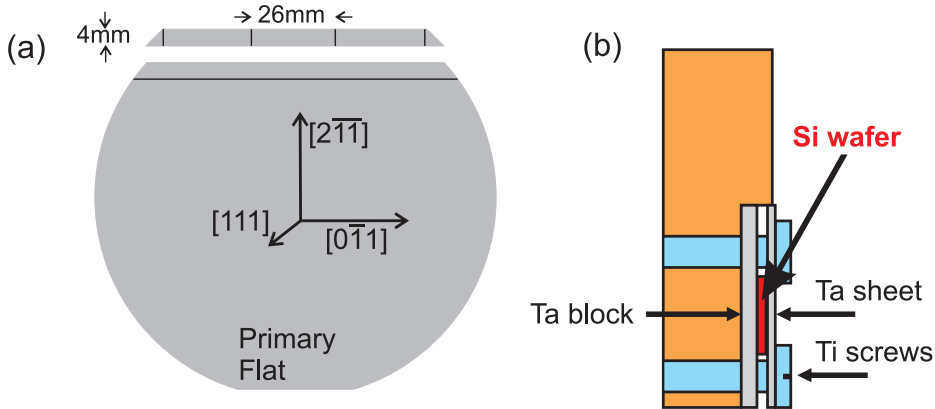


Figure 3.13: (a) The wafer samples of $26 \times 4 \text{ mm}^2$ size are cut from commercial p-doped 4 inch Si wafers. (b) Side view of the sample boat. The Si wafer is mounted between Ta pieces and fixed with Ti screws.

cut to the desired size of $26 \times 4 \text{ mm}^2$ in a customized Polyethylene box, which allows to precisely transfer the crystal orientation as indicated by the primary wafer flat to the Si samples, see Fig. 3.13. The polished side of the wafer disk is cut along a ruler from the backside with a diamond pen. The $< 4 \text{ mm}$ wide stripes are then trimmed to a length of $22 - 26 \text{ mm}$. The resistance of the samples at room temperature amounts to $2 \text{ k}\Omega$, which thus are well suited for PES studies. The Si samples are mounted in the sample boat between a 2 mm Ta block and a 0.1 mm Ta sheet that can be pressed onto the samples and ensures a good electric contact. The thermocouple, which is important for the low temperature metal deposition, is either clamped in between the Ta block and the sample boat or is glued to the back of the Silicon crystal with a UHV-compatible ceramic glue (Kager Industrieprodukte Ultra-Temp 516).

The Si surface reacts very sensitively to contamination by forming undesired reconstructions with metals like Chromium, Nickel and Cobalt. Hence, it is necessary to avoid such metals in the sample holder design and the preparation process. The cutting produces small Si dust particles that are removed by blowing with dry and clean N_2 gas or rinsing with ultrapure deionized water. Finally, the sample boats are transferred via the load lock into the sample magazine and backed at 110 C° for $> 12 \text{ h}$ to ensure UHV conditions upon transfer.

The surface of the Si samples is prepared by direct current heating that leads to the formation of the famous 7×7 -Si(111) reconstruction. Upon annealing in the temperature range $600 - 900 \text{ C}^\circ$ the Si(111) surface forms the 7×7 reconstruction [Bin82, Bin83, Ham86] with 49 surface atoms per unit cell, shown in Fig. 3.12. This allows to minimize the free surface energy by saturation of the dangling bonds of the unreconstructed 1×1 surface. For that purpose a relatively high voltage of $U \approx 150 \text{ V}$ is applied to the sample in a current limited mode ($I \leq 0.01 \text{ A}$) to slowly heat the sample. The rising temperature creates exponentially more free carriers and leads to a sudden decrease of the resistivity and thus an increasing current and temperature,

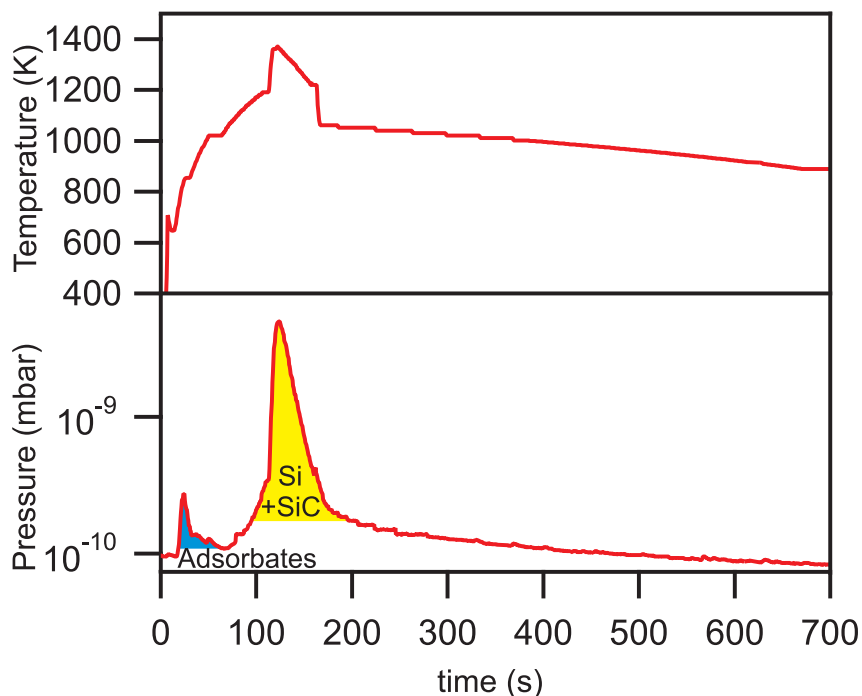


Figure 3.14: Temperature and pressure transients during the initial 7×7 -Si(111) preparation. The pressure rise at ~ 700 K is due to the desorption of adsorbates, whereas the pressure peak at > 1200 K stems from the desorption of Si and SiC at high temperatures.

as seen in Fig. 3.14. This is termed the "ignition" of the sample as one switches from the voltage to the current controlled section of the preparation cycle.

The temperature is raised stepwise to 1200 K where the several μm thick SiO_2 layer, which protects commercial Si wafers, is desorbed. Then the sample is flashed for < 10 s to 1400 K to sublime the uppermost Si layers and SiC contaminations. The pressure rise during the flash indicates the cleanliness of the Si substrate and should be below $5 \cdot 10^{-9}$ mbar, see Fig. 3.14. After flashing, the temperature is quenched with > 5 K/s to 1200 K and then slowly lowered by -1 K/s to 970 K. The slow cooling of the surface leads to the formation of the 7×7 -Si(111) reconstruction, which can be annealed for ~ 30 min at 970 K to form large defect free terraces. Normally, about five of these preparation cycles are required for a negligible pressure increase. The Si samples degrade upon flashing and are discarded after typically 10-15 flashing cycles.

The long range quality of the clean 7×7 -Si(111) reconstruction is inspected with LEED. Fig. 3.15 shows a LEED image of the 7×7 reconstruction. The six intermediate spots along the three high symmetry directions evidence the seven-fold reconstructed structure. The sharp spots and the low inelastic background indicate a good surface quality. The LEED images are evaluated quantitatively to yield the next neighbor distance

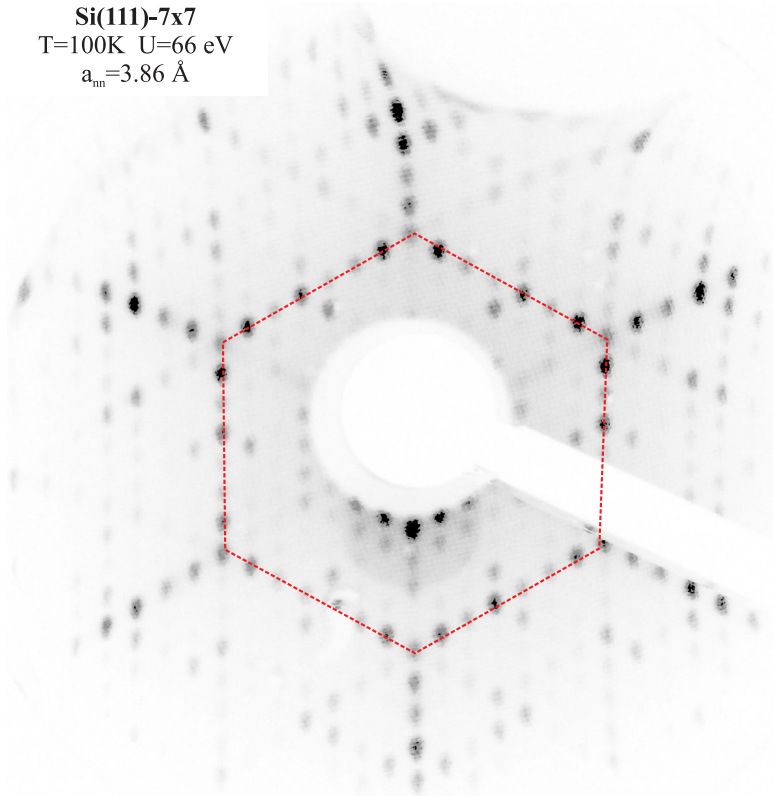


Figure 3.15: LEED image of the 7×7 -Si(111) reconstruction. The reciprocal 1×1 zone is indicated and the 6 intermediate spots are well visible. The slight distortions at the upper edge of the image are introduced by imperfectly shielded magnetic fields in the preparation level of the UHV chamber.

$$(3.11) \quad a_{nn} = \frac{hD}{2s \sin \alpha_0 \sqrt{2m_e E_{\text{kin}}}} \quad ,$$

where D is the full diameter of the LEED image, s is the distance of the first order spots from the center of the image, $2\alpha_0$ is the full opening angle of the LEED optic, and E_{kin} the kinetic energy of the impinging electrons. For the Si(111)- 7×7 reconstruction, the experimentally determined next neighbor distance of $a_{nn} = 3.86 \text{ \AA}$ is in good agreement to the theoretical value of 3.84 \AA , see chapter 2.1.2.

The 7×7 reconstruction extends over three atomic layers and introduces a buckling of the surface. Thus, metal films grown directly on the 7×7 reconstruction tend to be rough and, of course, are not ideally suited for the study of the electron dynamics. This problem can be overcome by the formation of an intermediate metal-Si reconstruction that serves as a wetting layer and reduces the significant lattice mismatch. This allows to grow epitaxial films that are well suited for PES [Upt04b, Upt04a, Upt05, Dil06, Dil07].

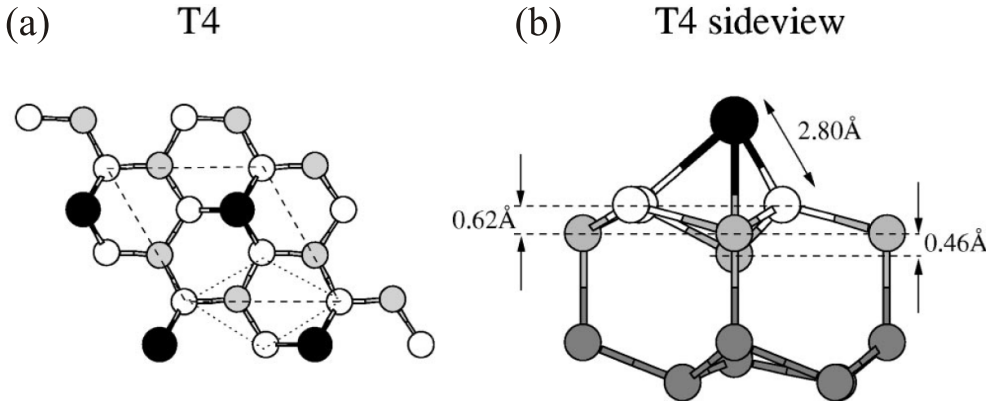


Figure 3.16: Schematic drawing of the β - $(\sqrt{3} \times \sqrt{3})R30^\circ$ -Pb/Si(111) reconstruction [Cha03] that serves as a smooth wetting layer for the epitaxially grown Pb film on top. The adsorption site with minimal energy is found to be of T4 symmetry and the next neighbor distance is calculated to be 7.0 Å.

Formation of a Wetting Layer

Generally, the adsorption of a few ML of metal atoms onto a semiconductor surface will induce a reconstruction of the surface due to the directional long range interaction of the covalent semiconductor bonds and the dangling bonds associated with an unreconstructed surface [Mön01]. Specifically for Pb/Si(111), numerous well ordered low coverage phases have been observed depending on coverage and substrate temperature using reflection high energy electron diffraction (RHEED) and LEED [Hor99, Pet99b, Ste06], scanning tunneling microscopy (STM) [Sle99, Sle00, Hup02a, Bri05, Bri07] (compare to the formation of the devil's staircase phases presented in chapter 2.1.3), PES [Car92, Kar92, Dud04, Cho07] and density functional theory (DFT) [Hup02b, Cha03]. The β - $(\sqrt{3} \times \sqrt{3})R30^\circ$ -Pb/Si(111) reconstruction is most interesting for the subsequent growth of epitaxial Pb films on Si.

Fig. 3.16 visualizes the $(\sqrt{3} \times \sqrt{3})R30^\circ$ -Pb/Si(111) reconstruction in a ball and stick model [Cha03]. This reconstruction has received significant attention in the literature as it can serve as a well defined model system for the study of the Schottky barrier formation [Lou76, Lou77, Hes90, Car92, Kar92], see chapter 2.1.2. It can be noted that the literature does not clearly distinct between the densely packed α - $(\sqrt{3} \times \sqrt{3})R30^\circ$ -Pb/Si(111) with $4/3$ ML nominal coverage and the β - $(\sqrt{3} \times \sqrt{3})R30^\circ$ -Pb/Si(111) with $1/3$ ML nominal coverage, where the later is being used as wetting layer.

Pb with a melting point of 600.6 K [Kit04, Ash76, Web08] is well suited for the evaporation under UHV conditions using a Knudsen cell. The Knudsen cell was designed and built in the Fritz-Haber-Institute of the Max-Planck-Gesellschaft and consists of a Boron Nitride crucible that is surrounded by heating coils and enclosed by a water cooled Cu aperture. All heated parts of the Knudsen cell are surrounded by a water cooled shielding to ensure low outgasing of the setup. This allows to operate the Knudsen cell at $p < 5 \cdot 10^{-10}$ mbar. The evaporation temperature of 790 – 840 C°

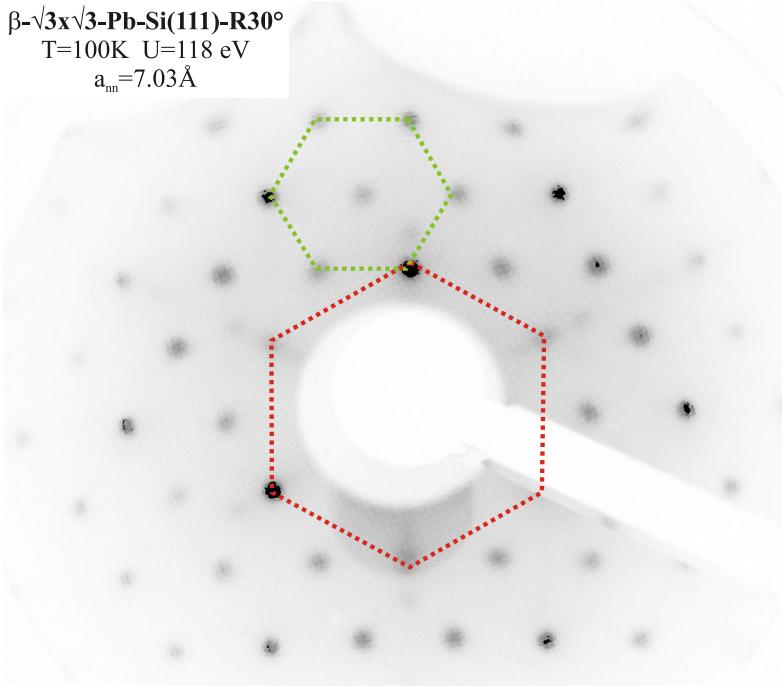


Figure 3.17: LEED image of the $\beta\text{-}(\sqrt{3}\times\sqrt{3})\text{R30}^\circ\text{-Pb/Si(111)}$ reconstruction. The 30° tilted reciprocal $\sqrt{3}\times\sqrt{3}$ zone is indicated (green) along with the 1×1 unit cell (red).

of the Knudsen cell is controlled by a PID controller (WEST Industries) within an accuracy of ± 0.5 K. Typical evaporation rates are 0.7 ML/min, which were constant within a few % variation. The emission rate of the cell at the sample position is monitored with a retractable Quartz balance⁴.

To form the $\beta\text{-}(\sqrt{3}\times\sqrt{3})\text{R30}^\circ\text{-Pb/Si(111)}$ reconstruction, 2 – 3 ML Pb are deposited onto the freshly flashed $7\times 7\text{-Si(111)}$ reconstruction at a substrate temperature of 100 K. After deposition, the surface assumes a 1×1 hexagonal symmetry as the Pb adatom diffusion is hindered at temperatures < 130 K [Hup01]. Then the sample is heated to ~ 600 K to desorb excess Pb and introduce enough free energy to form the $\beta\text{-}(\sqrt{3}\times\sqrt{3})\text{R30}^\circ\text{-Pb/Si(111)}$ reconstruction. This annealing step is performed directly in front of the LEED optic to follow the formation of the reconstruction in real time.

Fig. 3.17 shows the LEED image of the $\beta\text{-}(\sqrt{3}\times\sqrt{3})\text{R30}^\circ\text{-Pb/Si(111)}$ reconstruction after cooling the sample to 100 K. The unreconstructed 1×1 unit cell (red) and the reconstructed $\sqrt{3}$ unit cell (green) are indicated. Again, the sharp spots and the

⁴The Quartz balance is a water-cooled Quartz crystal vibrating at its eigen-frequency. The adsorption of atoms induces a change of the crystal mass and thus of the eigen-frequency that can be measured with high precision. Using the surface mass density of the evaporated metal, the eigen frequency is converted to a film thickness. To obtain an tenfold higher precision of the film thickness reading, only the tenth of the metal density is used in the evaluation. This results in 0.1 Å thickness resolution.

low inelastic background indicate a long range order with low defect density. The experimentally determined next neighbor distance of $a_{\text{nn}} = 7.03 \text{ \AA}$ is in good agreement with the expected value of 7 \AA for the reconstruction with $1/3 \text{ ML}$ nominal coverage. The long-range quality of the $(\sqrt{3} \times \sqrt{3})\text{R}30^\circ\text{-Pb/Si(111)}$ reconstruction is of importance for the subsequent preparation of the epitaxial Pb films, which extend over a macroscopic length of $\sim 10 \text{ mm}$ and thus require an excellent film quality.

Preparation of Smooth Pb Wedges

On the $(\sqrt{3} \times \sqrt{3})\text{R}30^\circ\text{-Pb/Si(111)}$ reconstruction wedges of epitaxial Pb layers with hexagonal symmetry are grown. The use of wedges allows (i) to perform very efficient and consistent measurements of several different ML coverages on a single sample surface [Kaw99] and (ii) to study nearly exactly integer ML coverages with little adatoms. The later is important for the investigation of femtosecond electron dynamics in ultrathin metal film since excess Pb adatoms introduce additional scattering channels [Rot02, Wei02b, Rot04] that may the electron-electron (e-e) scattering processes.

The preparation scheme of the Pb wedges is shown in Fig. 3.18 and exemplified for a typical Pb wedge of 8 – 13 ML thickness assuming an evaporation rate of 1 ML/min. At the beginning, the whole sample, which offers 10 mm of usable space, is placed for 8 min in the center of the Pb evaporation cone and 8 ML are grown on top of the $(\sqrt{3} \times \sqrt{3})\text{R}30^\circ\text{-Pb/Si(111)}$ reconstruction. Then the sample is retracted behind the shutter with a speed of 2 mm/min and 10 μm step width. Thus, after a time of 13 min only the right side of the sample is still exposed to the Pb beam, resulting in a film thickness of 8 ML at the left and 13 ML at the right side of the sample with a quasi-continuous thickness variation in between.

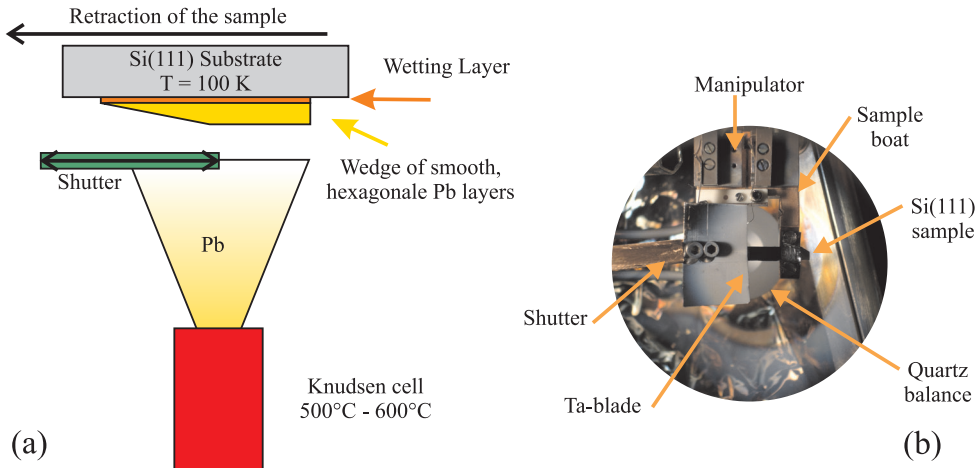


Figure 3.18: The homogeneous Pb wedges are prepared by evaporation of Pb from a Knudsen cell. (a) A retractable shutter blocks part of the Pb vapor such that a lateral movement of the sample results in a continuous variation of the dosing time and a wedge with atomic resolution. (b) photograph of the setup in UHV, the individual parts are labeled.

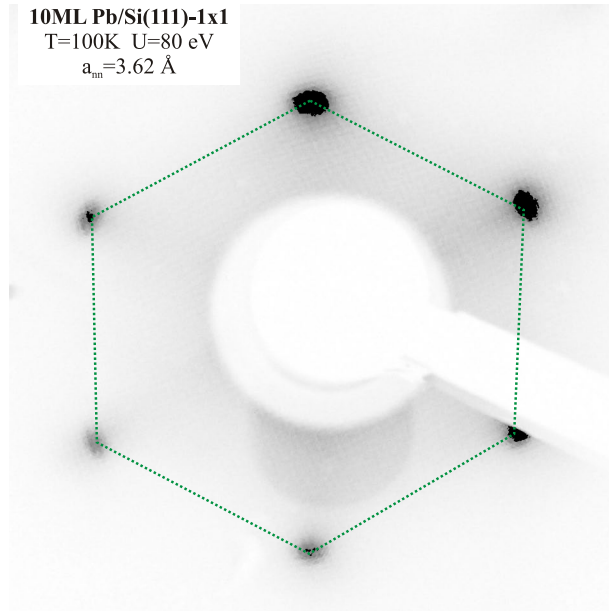


Figure 3.19: LEED image of 10 ML Pb/Si(111)-(1×1) film. The hexagonal 1×1 unit cell is indicated.

The whole preparation procedure, including the formation of the $\sqrt{3}$ reconstruction, is performed at a substrate temperature of < 100 K to quench the Pb adatom diffusion on the surface [Hup01]. These diffusion processes lead to the formation of the so-called "magic" island heights, compare to chapter 2.1.3, and hinder the growth of smooth epitaxial films. Also the photoemission experiments were performed at < 100 K to avoid the rupture of unstable film thicknesses below 10 ML coverage [Zha98, Zha05]. This allows to also study ultrathin film with only 1 ML coverage above the wetting layer.

In the preparation of the wedges, the laser spot size of $\sim 100 \mu\text{m}$ has to be taken into account. The spot size limits the final spatial resolution in the photoemission experiments and thus the achievable coverage resolution. To avoid a crosstalk of subsequent coverages, which smears out the discrete nature of the quantum well states (QWSs), shallow wedges with a slop of < 0.5 ML/mm have been prepared. This leads to an effective thickness resolution of < 0.05 ML/spectrum, when single spectra are acquired at a spatial separation of $100 \mu\text{m}$, comparable to the laser spot size. The final calibration of the coverage distribution as function of the sample position is crosschecked by comparison of the binding energies of the occupied QWSs to a DFT calculation [Wei02a], as detailed in chapter 5.3.

The long range order and symmetry of the Pb/Si(111)-(1×1) surface was inspected with LEED, as shown in Fig. 3.19. The LEED image exhibits a three-fold surface symmetry. The next neighbor distance of $a_{\text{nn}} = 3.62 \text{ \AA}$ is larger than the bulk Pb value of 3.50 \AA , which might be explained by the slight distortions observed in the LEED image.

3.3.2 Preparation of TbTe_3

The TbTe_3 samples for the tr-ARPES studies have been grown and characterized in the groups of I. R. Fisher and Z.-X. Shen from the Stanford University in the context of our collaboration. This section briefly reviews the growth procedure of the binary alloy and discusses the cleavage of TbTe_3 under UHV conditions.

Crystal growth of TbTe_3

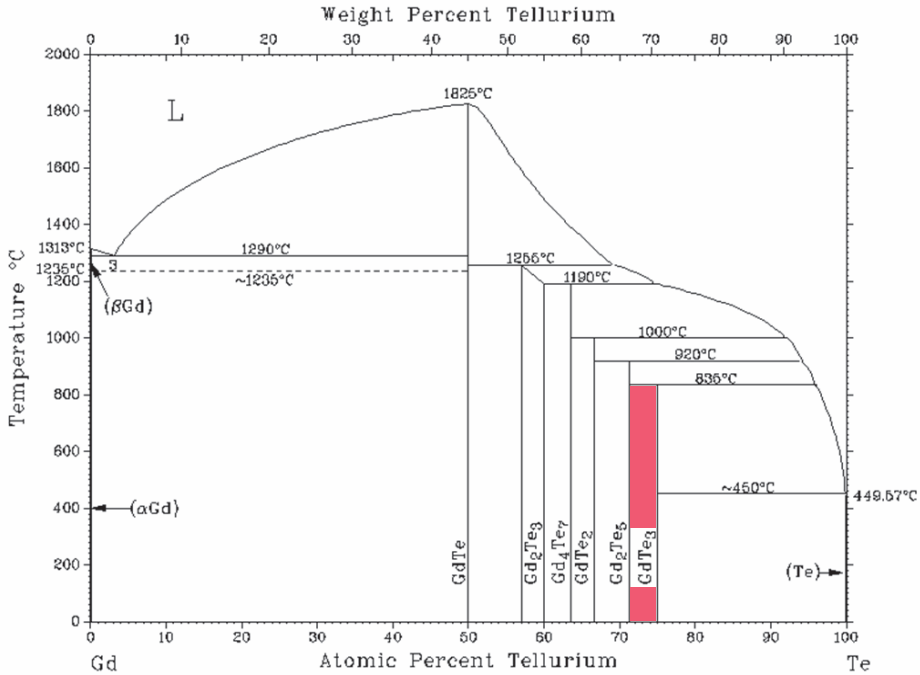


Figure 3.20: The phase diagram of Gd_xTe_y according to [Mas96]. The marked area indicates the region for the formation of GdTe_3 . L indicates the liquid phase.

Large RTe_3 crystals (R = rare earth element) are grown via a self-flux technique by slow cooling of a binary R and Te melt [Shi05, Ru06b]. Fig. 3.20 shows an exemplary phase diagram of Gd_xTe_y as function of the Te concentration [Mas96]. The marked area indicates the Tritelluride phase, which forms across almost the entire rare earth series except for Eu and Yb . As expected from the stoichiometry of RTe_3 , 71 – 75 atomic percent of Te are required to crystallize GdTe_3 below 835 °C. The resulting crystals are typically flat, according to the layered structure of RTe_3 , and a few mm^2 in size as shown in Fig. 2.16. The crystals are soft like layered Graphite and require careful handling since most members of the rare earth series easily oxidize. Thus the crystals were handled in a N_2 purged glove-box during the preparation procedure and stored under UHV conditions in the sample magazine.

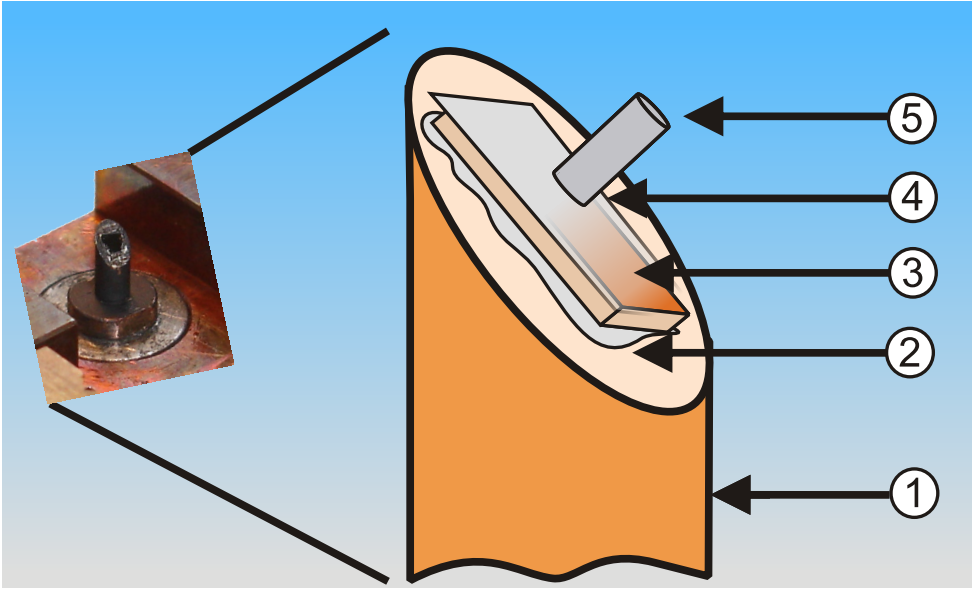
Cleavage of TbTe_3 

Figure 3.21: Preparation procedure for the cleavage of TbTe_3 under UHV conditions. (1) 45° slanted post. (2) Ag-epoxy glue. (3) TbTe_3 single crystal. (4) The sapphire plate is fixed with Ag-epoxy glue to the sample. (5) The ceramic cleavage pin is glued with Varian Torr Seal to the sapphire plate. Not shown: The cleavage pin is fixed with a Ta wire to the sample boat. The front side of the sample boat is coated with Graphite.

To obtain a clean, well-ordered and macroscopically homogeneous surface for the tr-ARPES studies, the TbTe_3 crystals were cleaved under UHV conditions. The TbTe_3 crystals are oriented and mounted to break along the b -axis, compare to Fig. 2.18, exposing a flat Te plane. The preparation of the TbTe_3 crystals for the cleavage involves two steps: First, the symmetry of the crystals has to be analyzed with Laue diffraction and second, the oriented crystals have to be mounted precisely on the slanted post, see Fig. 3.7. From the Laue pattern the relative orientations of the a , c -plane, see chapter 2.2.3, can be inferred. This allows to align the TbTe_3 single crystal on the slanted post. This alignment is crucial to reach the outer regions of the Brillouin zone at the low photon energies used in the tr-ARPES experiments, see chapter 7.

The mounting of a crystal on a slanted post, Fig. 3.7, requires about 5 steps, as detailed in Fig. 3.21. The TbTe_3 single crystal (3) is glued with silver-epoxy glue (Polytec PT EPO-TEK-H20E) (2) on the 45° slanted post from Phosphor bronze (1). The silver-epoxy glue is a good electric and thermal conductor due microscopic silver particles. This ensures the absence of surface charging in the ARPES experiments. At this point, the orientation of the high symmetry crystal axis with respect to the sample post can be checked again with Laue diffraction and realigned if necessary,

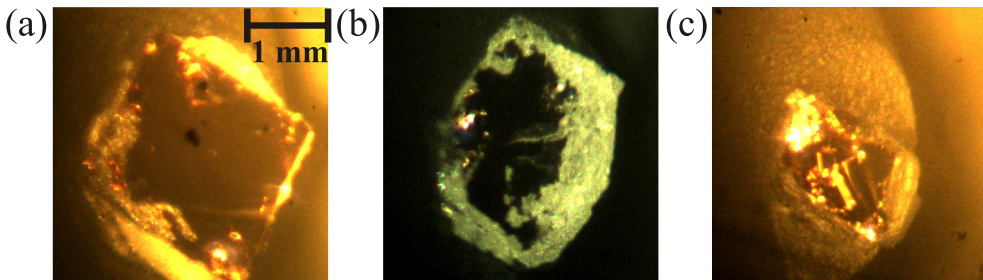


Figure 3.22: Microscope images of different TbTe_3 samples on the slanted sample post. (a) Almost ideal cleave (The black spot in the image center are due to dust on the microscope objective.) with a flat surface indicated by the homogeneous reflection. The crystal surface is only buckled at the very edge. (b) Too little of this samples was left on the post to be measured. (c) A severely buckled surface is observed by the twinkling of the crystal. Both the samples in (b) and (c) were not suited for the tr-ARPES measurements.

resulting in a precise alignment. On top of the attached sample a 0.5 mm thick sapphire plate (4) is glued with silver-epoxy glue. This sapphire plate distributes the forces of the cleavage process evenly across the soft crystal and thus minimizes the buckling of the cleaved surface. Then the ceramic cleavage pin (5) is glued to the sapphire plate with high-strength Varian Torr Seal. The different glues locate the predetermined break point in the TbTe_3 crystal. The cleavage pin is fixed with a 1 mm diameter Ta wire (not shown) to the sample boat (i) to avoid the cleavage pin to fall onto the gate valve, blocking the access to the spectrometer level, and (ii) to be able to recycle the remains of the TbTe_3 on the sapphire plate. Finally, the whole front of the sample boat is coated with Graphite (Contact Chemie) to ensure a homogeneous work function and avoid the charging of the sample in the ARPES experiments. The sample boats were then transferred into the sample magazine, where they were baked at 110 C° for $> 12\text{ h}$.

The quality of the cleave is inspected with an optical microscope and ARPES. In Fig. 3.22 typical microscope images of a nearly ideal cleave (a) and insufficient cleaves (b) and (c) are shown. In some cases, the crystal did not stick sufficiently well to the sample post and the remaining pieces of the samples were too small for angle-resolved investigations (b). In other cases the (layered) crystal surface was too buckled for the tr-ARPES measurements (c). A buckling of the surface not only smears out the band structure due to loss of angular resolution, but also generates large amounts of secondary photoelectrons due to plasmon excitation at the rough interface. Since a large uncorrelated pump-only background covers the small changes in the transient band structure, samples with a buckled surface were discarded as well. These high requirements on the surface quality for tr-ARPES were only met by every $5 - 10^{\text{th}}$ cleave.

4 Position-Sensitive Electron Time-of-Flight Spectrometer

To study the ultrafast dynamics with photoemission techniques in low-dimensional materials exhibiting anisotropic band structures requires to resolve the photoelectron spectra along different directions in k -space. On the one hand, the angular resolution can be introduced in a conventional photoemission setup by rotating the sample with respect to the spectrometer axis. On the other hand, modern imaging techniques enable angle-resolved photoemission studies without change of the sample geometry. Moreover, imaging techniques allow a simultaneous detection of *both* in-plane electron momenta and hence facilitate the efficient determination of the band structure along *all* in-plane directions.

This chapter introduces a novel electron time-of-flight (TOF) photoelectron spectrometer, which is based on such an imaging technique. The position-sensitive electron time-of-flight (pTOF) spectrometer is developed to simultaneously analyze low energy electrons photoemitted from solid surfaces in an energy- and angle-resolved manner. To achieve this, a field free drift tube with an acceptance angle of $\pm 11^\circ$ perpendicular to the spectrometer axis is combined with 2D position-sensitive detection of photoelectrons, which is realized by a micro channel plate (MCP) stack and a delay-line anode for position encoding. Here, the design considerations and principles of operation including analysis of multiple events per light pulse are presented. The last part discusses the actual performance of the pTOF spectrometer, which is demonstrated by photoemission from a Cu(111) single crystalline surface by ultraviolet (UV) femtosecond laser pulses at 6.2 eV photon energy.

4.1 Design Considerations

Angle-resolved photoelectron spectroscopy using UV radiation is a well established experimental technique to study the bulk and surface electronic structure of solids [Kev92, Hüf95]. Femtosecond time- and angle-resolved two-photon photoemission (2PPE) spectroscopy has contributed significantly during the last two decades to the understanding of elementary scattering processes and relaxation dynamics in excited electronic states on solid surfaces [Fau95, Pet97b, Ech04, Zhu04, Fau07]. In particular, angle-resolved 2PPE has proved to be a powerful tool for the study of ultrafast intra- and inter-band relaxation dynamics in image potential states of clean and adsorbate-covered metal surfaces [Hot00, Kir05, Wei02b, Güd05]. Moreover, the band dispersion of localized and delocalized excited states and the respective energy relaxation dynamics have been probed at metal-molecule interfaces by angle-resolved 2PPE spectroscopy directly in the time domain [Mil02a, Ge98, Gah02].

More recently, time- and angle-resolved photoemission spectroscopy (tr-ARPES) has emerged [Ani74, Fan92, Hai95] as a promising tool for the study of non-equilibrium phenomena in metals [Lis05b, Bov06, Bov07, Lou07]. Since tr-ARPES measures the single particle spectral function directly in the time domain, it is well suited to address effects of strong electron-electron correlation, the electronic coupling to other degrees of freedom, and collective excitation modes of such a coupled system [Per06, Per07, Per08]. Most of these phenomena occur in materials with a highly anisotropic band structure, making k -resolved studies necessary to sample the presumably anisotropic electron dynamics in the relevant parts of the band structure. The work on 4×1 -In/Si(111) and TbTe_3 , see chapters 6 and 7, highlights the need for an efficient, simultaneous detection of both in-plane momentum components. Since the nesting driven charge density wave (CDW) in TbTe_3 gaps out certain parts of the Fermi Surface (FS), the analysis of the ground state properties and collective CDW excitation modes can only proceed in the adequate parts of the band structure, which are not accessible in normal emission [Sch08].

Conventionally, such angle-dependent studies are performed by rotating the sample with respect to the spectrometer axis, which is only applicable to spectrometers with sufficiently small acceptance angles. In general, such angle-resolved measurements can only be performed at the pivotal point of the sample manipulator and are difficult to perform on inhomogeneous samples such as the Pb/Si(111) wedges studied in chapter 5. This approach yields an individual spectrum per photoemission angle, i.e. for one particular electron momentum parallel to the surface [Hüf95]. Two commonly used experimental approaches for the angle-resolved energy analysis of photoelectrons are electrostatic energy analyzers, which are compatible with quasi-continuous light sources, and electron TOF spectrometers [Lan73, Kno97, Hot99, Lis04a] requiring pulsed light sources.

Recently introduced electrostatic analyzers enable very efficient simultaneous angle- and energy-resolved measurements as the angular distribution of the photoelectrons can be dispersed onto a 2D detector: Thereby the photoelectron emission intensity is recorded as function of one angle after energy selection in the hemisphere. The electrostatic lens system used for the imaging may be adapted to electrons of low kinetic energies which makes these imaging-type hemispherical analyzers very well

suiting for angle-resolved 2PPE spectroscopy using laser light sources [Spe, Gd05]. In this approach, the dispersion of photoelectrons along one of the two independent directions of the 2D detector represents the kinetic energy. The dispersion along the second direction refers to the angular dependence of the photoemission intensity along a selected in-plane direction x of the sample surface and yields the band dispersion with momentum k_x . To analyze the second in-plane electron momentum component k_y requires to rotate the sample and to record a series for various (but fixed) values of k_y . The schematic experimental geometry and the kinematic parameters measured in an angle-resolved photoemission experiment are shown in Fig. 4.3 Also, the dynamic range of 1 : 4000 of the established 2D electrostatic analyzers is limited by the 12 bit precision of the employed charge coupled devices cameras [Spe].

Here, a 2D imaging detector is combined with the conventional TOF concept to obtain a 2D pTOF spectrometer. This instrument analyzes the kinetic electron energy E_{kin} along *both* in-plane electron momenta k_x and k_y of electronic Bloch states in a solid. This spectrometer allows to map out the respective band dispersions of occupied and unoccupied electronic states with angle-resolved photoemission spectroscopy (ARPES) and 2PPE. Since both in-plane momentum components and the kinetic energy of each photoelectron is determined simultaneously in a "single shot", no rotation of the sample or the spectrometer is required. Particularly for systems exhibiting a highly anisotropic band structure, as for example in CDW materials like RTe₃ or quasi-1D nanowires [Yeo99, Rg07], a simultaneous analysis of two perpendicular directions in the surface plane is advantageous. Furthermore, the electronic discrimination of the signals allows to reach signal-to-noise (S/N) ratios of 1 : 10⁵ and better.

The first concept of a pTOF electron spectrometer for angle-resolved photoemission was introduced by Haight et al. [Hai88] using a 64 sector anode. However, the parallel signal processing and data analysis involved did not favor a widespread use of this particular technique. The implementation of a pTOF spectrometer has become more practicable with the development of modern concepts of high-performance charged-particles imaging techniques [Oel01, Jag02c, Jag02a, Jag02b, Hat04, Cos05, Roe], which have been developed for and successfully used widely in cold target recoil ion momentum spectroscopy (COLTRIMS) [Ull03]. The concept of an angle-resolved TOF spectrometer was already successfully employed in coincidence studies of electrons photoemitted from a Cu(111) surface [Hat04, Hat08]. However, the spectrometer from Ref. [Hat04] is optimized for acceptance of electrons in 2π solid angle by use of a projection method. Very recently, a photoelectron microscope in combination with an imaging energy filter for momentum resolved photoelectron detection has been reported as well [Kr08].

Here, a pTOF electron spectrometer is presented, which was especially designed and constructed to facilitate the high-resolution analysis of low-energy electrons with a few eV kinetic energy. The presented pTOF spectrometer design includes the required hardware and software for data analysis to cope with multi-hit events. This makes the developed pTOF an ideal tool for the investigation of ultrafast electronic phenomena in solids and at their surfaces probed by femtosecond laser light sources.

4.1.1 Hardware Implementation

Fig. 4.1 shows a schematic drawing of the pTOF spectrometer with a sketch of the electronic data acquisition. The geometric parameters of the setup are a field free drift tube of length $z = 200$ mm combined with a chevron-mounted MCP stack of 80 mm active diameter. The acceptance angle spans $\pm 11^\circ$ when the pTOF spectrometer axis is oriented parallel to the surface normal. Rotating the sample by 11° with respect to the spectrometer axis allows to extend the maximum acceptance to $\theta = 22^\circ$ in one particular direction. The opening of the entrance aperture of 1.9 mm is carefully matched to the sample-aperture distance of 3.0 mm and the acceptance angle. The drift tube itself is made from vacuum-compatible aluminum to avoid remanent magnetic fields in the drift region. The aperture and the inside of the drift tube are graphite-coated to achieve a homogeneous work function of the pTOF spec-

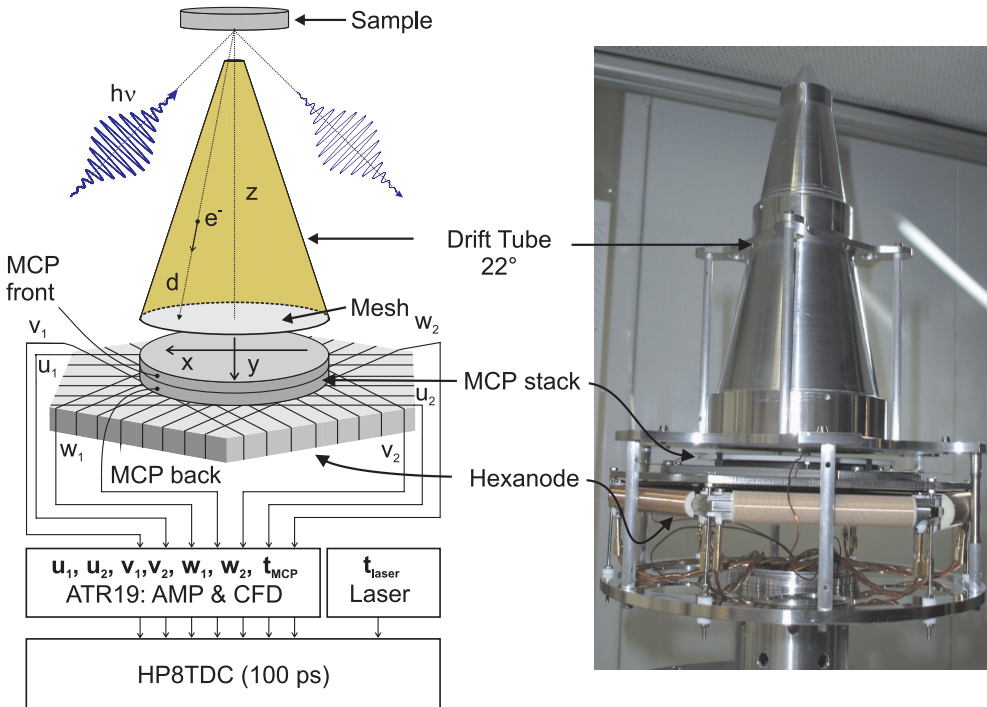


Figure 4.1: (a) Schematic drawing of the pTOF electron spectrometer. A partially absorbed light pulse generates photoelectrons which propagate through a field-free flight tube. They are detected by a two-dimensional position-sensitive detector based on a microchannel plate (MCP) stack and a delay line anode. The mesh shields the flight tube from the electric fields applied to the detector. The six timing signals from the three wire layers, the MCP and the light source are amplified (AMP) and digitized in constant-fraction-discriminators (CFD) to be recorded by a time-to-digital-converter (TDC). (b) Photograph of the fully assembled pTOF spectrometer without the μ -metal housing.

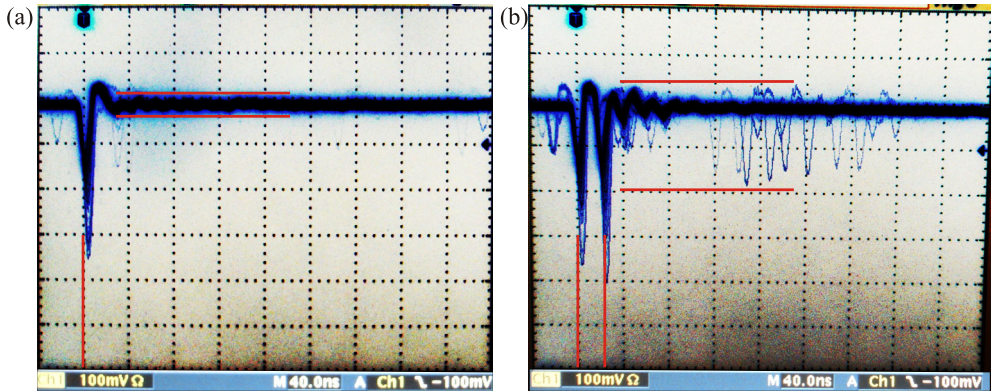


Figure 4.2: Oscilloscope screens of the analog TOF signal after amplification but before digitization in the CFD. (a) A matched impedance results in a single peak that leads to a well defined trigger (green line). The ringing of the signal, indicated by two limiting red lines, can be neglected. (b) Identical conditions as in (a) but with $10\ \Omega$ impedance mismatch. A spurious peak is generated at a distance of 30 ns due to a reflection at the outcoupling circuit. Also the ringing has increased significantly, the original pulse can not be discriminated from reflections.

trometer as the kinetic electron energy is directly referenced to the vacuum level of the surrounding, see Fig. 3.10.

The 2D impact positions and TOF of the photoelectrons are recorded by a 2D position-sensitive detector based on a commercially available delay-line readout concept (RoentDek, [Jag02c, Roe]). Each electron hit is amplified by a Chevron MCP stack and the resulting electron cloud is collected by three meandering anode wires rotated by 60° with respect to each other. The analysis of the signal propagation times across the wire structure yields the in-plane positions. The MCP front is biased with +300 V to attract the electrons after traversing the field free drift tube. The MCP back is biased with +2500 V to yield the voltage required for charge amplification of 2200 V across the MCP stack. The anode wires have the highest positive potential with +3000 V to attract the charge cloud emitted from the MCPs. Additionally, the holder is floating at +2750 V to expand the charge cloud in between the MCPs and anode wires. The whole spectrometer setup is placed in a μ -metal housing (SAM Products) of 1.5 mm thickness to prevent deflection of the photoelectrons by residual magnetic fields (not shown in Fig. 4.1).

The signals from the MCP backside and the six anode wires are carefully coupled out by individual electronic circuits, which yield a voltage pulse of a few meV amplitude and 1 – 2 ns width for each detected electron. The matching of the impedance of the Lecher wires of $Z \approx 120\ \Omega$ to the outcoupling circuits is crucial, especially for the analysis of multiple events. Fig. 4.2 shows two oscilloscope screens of the TOF signal coupled out from the MCP back for the case of perfect and imperfect impedance matching. An impedance mismatch results in spurious peak replicas and increases the ringing of the signal at later times, which results in a situation where the original hits can hardly be discerned from fake signals due to reflections.

The subsequent electronic devices process six anode signals from the three wire layers of the Hexanode, the MCP signal t_{MCP} , and a time-reference signal t_{laser} from the laser light source. The out-coupled analog signals are first fed to broad-band amplifiers, which are combined on-board with constant-fraction-discriminators (CFDs) (ATR19, RoentDek) to digitize the signals. The digitization in the combined amplifier/CFD is another important step to obtain clean and reliable position and timing information. For an ideal analog signal without any noise the amplifier levels are high and the thresholds for the discrimination are low to be sensitive to weak hits. As the S/N ratio is finite in reality, the amplifier levels are carefully lowered and the CFD thresholds are raised to avoid triggering on reflections but still obtain a high detection efficiency.

The digital signals from the CFDs are sent to an eight-channel PC-based multi-stop time-to-digital converter (TDC) (TDC8HP PCI card, RoentDek) with < 100 ps time resolution and 25 ps least-significant-bit, which is run in common start mode. The eight timing signals are processed online in real-time by customized C++-based routines, which utilize LabView 8.x and Igor Pro 6.x as front-end software. Additionally, the raw data may be saved into a list-mode-file format for later off-line analysis, see section 4.2.

4.1.2 Principle of Operation

A typical photoelectron emission geometry at a solid surface is sketched in Fig. 4.3. The sample surface plane is defined as the xy -plane and the surface normal is oriented along z . Photons of energy $h\nu$ are incident under an angle φ with respect to the surface normal and thus photoelectrons of momentum \vec{k} are emitted. The out-of-plane angle θ of photoemission is defined with respect to the surface normal and the in-plane emission angle ϕ with respect to a high-symmetry crystal axis. The experimentally measured quantities are the photoemission angles θ and ϕ , and the kinetic energy E_{kin} , which are determined by analysis of the TOF, as detailed in chapter 3.2.1.

The drift distance in equation (3.9) is replaced by $d = \sqrt{x^2 + y^2 + z^2}$ to account for the elongated flight distance in off-normal emission¹. Explicitly, the kinetic energy is a function of the position coordinates (x, y) and the TOF t :

$$(4.1) \quad \begin{aligned} E_{\text{kin}}(t, x, y) &= \frac{m_e d^2}{2(t - t_0)^2} = \frac{m_e (r^2 + L^2)}{2(t - t_0)^2} \\ &= 2.4828 \text{ eV ns}^2 \text{ mm}^{-2} \cdot \frac{x^2 + y^2 + L^2}{(t - t_0)^2} \quad , \end{aligned}$$

where $r^2 = x^2 + y^2$ denotes the electron position on the detector and $z = L$ the length of the drift tube. Normally, the spectrometer axis is oriented parallel to the surface normal and the lateral positions x and y are thus determined by the polar and azimuthal emission angles θ and ϕ via

¹In the conventional TOF spectrometer without position analysis this correction is omitted and the actual flight distance d is underestimated by $1/\cos\theta$ with the consequence of a systematic error in the energy determination. The systematic error, however, amounts to 1.8% for the opening angle of 3.5° and thus can be neglected.

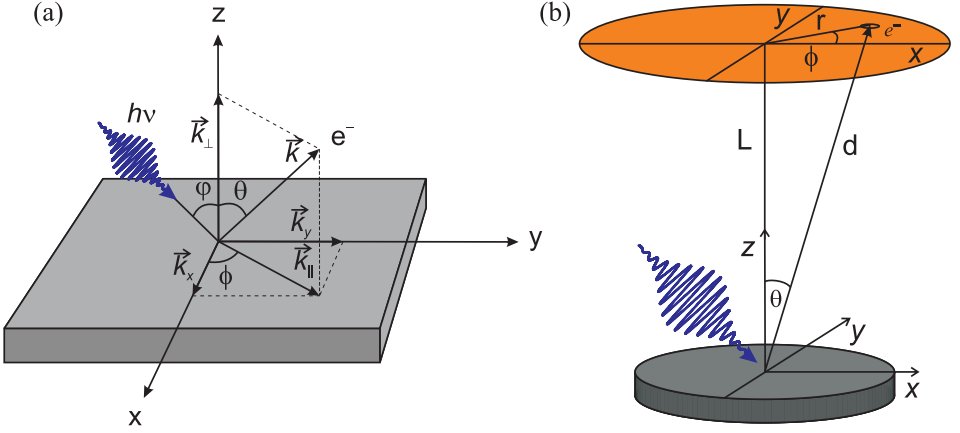


Figure 4.3: (a) Sketch of the experimental geometry and kinematic parameters in an angle-resolved PES experiment, $h\nu$: photon energy, φ : angle of incidence, θ and ϕ : out-of-plane and in-plane photoemission angle, \vec{k} : momentum of the photoelectron, k_{\parallel} and k_{\perp} : in- and out-of-plane electron momenta. (b) Position-resolved detection of the photoelectron after traversing the field free drift tube of length L .

$$(4.2) \quad \tan \theta = \frac{\sqrt{x^2 + y^2}}{z}$$

$$(4.3) \quad \tan \phi = \frac{y}{x} .$$

The electron wave vectors k_x and k_y are calculated from the x - and y -component of the electron velocity, respectively:

$$(4.4) \quad \begin{aligned} \vec{k}_{\parallel}(x, y, t) &= \begin{pmatrix} k_x \\ k_y \end{pmatrix} = k_{\parallel} \begin{pmatrix} \cos \phi \\ \sin \phi \end{pmatrix} = \frac{m_e}{\hbar(t - t_0)} \begin{pmatrix} x \\ y \end{pmatrix} \\ &= 0.8638 \text{ \AA}^{-1} \text{ ns mm}^{-1} \cdot \frac{1}{t - t_0} \begin{pmatrix} x \\ y \end{pmatrix} \\ k_{\parallel} &= \sqrt{k_x^2 + k_y^2} . \end{aligned}$$

4.1.3 Time-of-Flight Analysis

The acquisition and analysis of the TOF is slightly different to the conventional concept, presented in chapter 3.2.3 where only the offset t_0 due to different signal propagation times had to be taken into account. The HP8TDC-PCI board is triggered in a common-start mode by the MCP signal to only record actual² electron hits. The

²If the laser pulse would serve as trigger input it would create large amounts of empty data. Assuming a laser repetition rate of 300 kHz and an event rate of 30 kHz only 10% of the data comprise factual events.

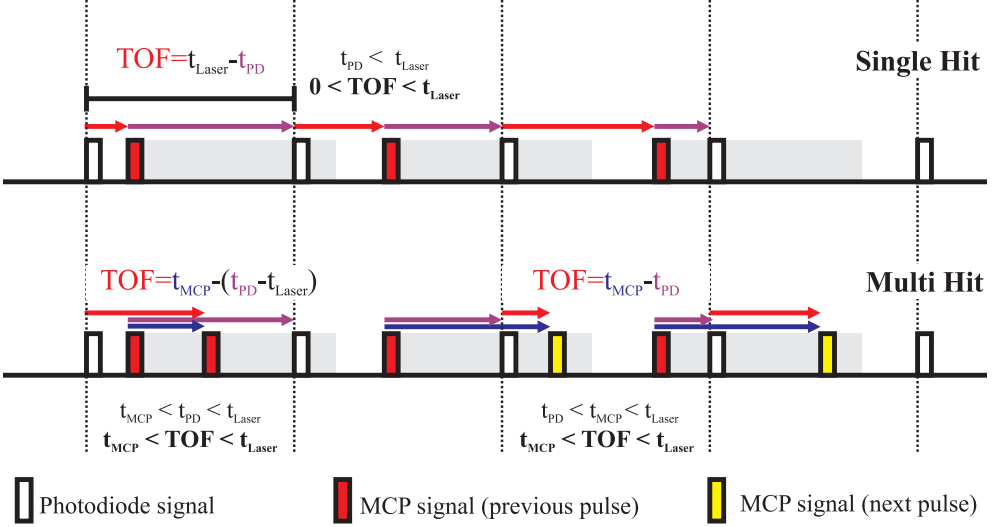


Figure 4.4: Analysis of the TOF in the pTOF spectrometer. The MCP signal serves as trigger for the TDC and the timing of the subsequent laser pulse is recorded. Top: The time-of-flight TOF for single hits is calculated from the difference of the laser cycle duration t_{Laser} and the arrival time of the next laser pulse t_{PD} . Bottom: The occurrence of multiple hits per events makes a distinction of cases necessary since the second hit can stem from the next laser pulse. The gray shaded area indicates the duration of the armed trigger, which is chosen slightly shorter than t_{Laser} . The vertical lines indicate the arrival time of the laser pulse at the sample.

reference signal from the photodiode thus samples the time difference to the *next* laser pulse. The correct TOF with respect to the laser pulse that photoemitted the electron is obtained from the inverse laser repetition rate t_{Laser} , which has to be known precisely³, as discussed in Fig. 4.4. Additionally, multiple events per laser cycle result in detection of electrons from the *subsequent* laser pulse and lead to a distinction of cases for the electron time-of-flight TOF

$$(4.5) \quad \text{TOF} = \begin{cases} t_{\text{MCP}} - (t_{\text{PD}} - t_{\text{Laser}}) & \text{for } t_{\text{MCP}} < t_{\text{PD}} \\ t_{\text{MCP}} - t_{\text{PD}} & \text{for } t_{\text{MCP}} \geq t_{\text{PD}} \end{cases}$$

The duration of the armed trigger frame as well as the trigger dead time is defined to be slightly below the time of a laser cycle t_{Laser} corresponding to inverse laser repetition rate.

³The laser repetition rate is continuously logged using a LabView interface. This allows to reach an relative uncertainty of $< 10^{-5}$ for t_{Laser} .

4.1.4 Energy and Momentum Resolution

The overall experimental accuracy Δt in the TOF analysis and the drift length L ultimately determine the achievable energy resolution:

$$(4.6) \quad \Delta E_{kin} = \sqrt{\left(\frac{dE}{dt}\right)^2 \Delta t^2 + \left(\frac{dE}{dr}\right)^2 \Delta r^2} \approx \sqrt{\frac{8E_{kin}^3}{m_e} \frac{\Delta t}{L}}.$$

Here, the uncertainty of the in-plane position determination $\Delta r \approx 0.2$ mm, which in turn is determined by Δt , see section 4.1.5, can be neglected compared to the timing uncertainty Δt . Hence, the energy resolution is largely determined by the precision of the TOF measurement as the length of the drift tube is fixed by the geometrical considerations regarding the acceptance angle. The length of the drift tube is a trade-off between a preferably high acceptance angle and a drift length still enabling an energy resolution ≤ 10 meV.

The precision of the TOF measurement itself is determined by both the jitter of the electronic start pulse from the laser source and the accuracy of the stop pulse from the MCP. The timing signal from the laser source is generated by a fast photodiode with < 100 ps signal rise time and a root-mean-square (rms) jitter of 50 ps. The accuracy of the MCP signal is limited to 100 ps by the bandwidth of the amplifiers and the TDC resolution such that the overall resolution of the TOF analysis is estimated to be ~ 200 ps. This translates into an energy resolution of $\Delta E \approx 5$ meV at $E_{kin} = 2$ eV, shown as thick solid line in Fig. 4.5. A more conservative estimate of $\Delta E \approx 10$ meV at $E_{kin} = 2$ eV includes imperfections of the work function of the spectrometer, uncertainties of the drift distance z , and the unaccounted acceleration of the electrons in-between the grid and MCP stack.

In Fig. 4.5(a), ΔE_{kin} is depicted as a function of E_{kin} for various time resolutions $\Delta t \leq 1$ ns and for a constant drift length $d = 200$ mm as employed in the pTOF spectrometer. For example at $E_{kin} < 4$ eV the energy resolution can be kept well below 10 meV, provided that the time resolution is better than 0.2 ns. Time-resolved photoemission experiments can not necessarily benefit from a much higher energy resolution as the spectral bandwidth of the femtosecond laser pulses amounts to typically 10 – 50 meV.

The momentum resolution $\Delta k_{||}$ depends on the accuracy of the lateral position determination Δr and the temporal resolution of the TOF measurement Δt and can be estimated from equations (4.1) and (4.4) to be:

$$(4.7) \quad \Delta k_{||} \approx k_{||} \sqrt{\left(\frac{\Delta r}{z}\right)^2 + \frac{2E_{kin}}{m_e} \left(\frac{\Delta t}{z}\right)^2}.$$

With a conservative estimate for the position resolution of $\Delta r \approx 0.2$ mm and a time resolution of $\Delta t \approx 200$ ps the maximum error of the momentum coordinates amounts to $\Delta k_{||} \leq 0.002 \text{ \AA}^{-1}$ for all momenta $k_{||} \leq 1 \text{ \AA}^{-1}$ and kinetic energies $E_{kin} \leq 10$ eV. The absolute error of the momentum determination as function of E_{kin} and $k_{||}$ is indicated in Fig 4.5(b) as gray scale intensity. For example, for an emission angle of 22° and a kinetic electron energy of $E_{kin} = 2$ eV the maximum parallel momentum is given by $k_{||} = 0.2714 \text{ \AA}^{-1}$ with a momentum resolution of $\Delta k_{||} = 3.1 \cdot 10^{-4} \text{ \AA}^{-1}$.

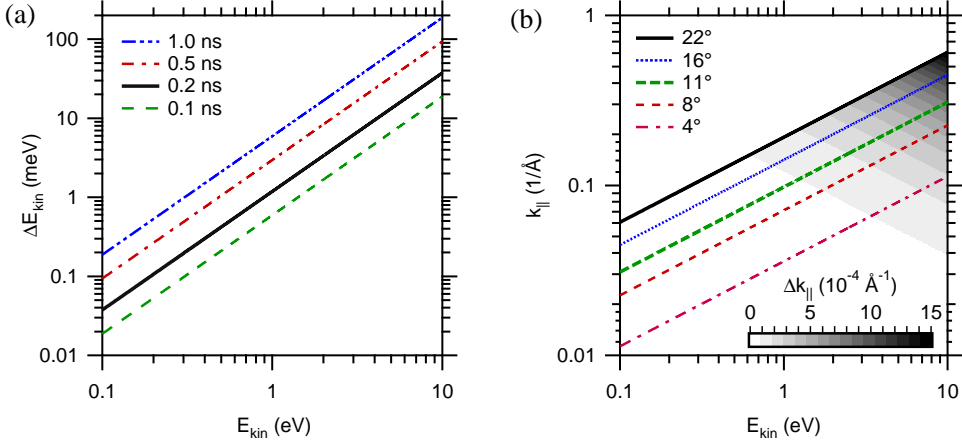


Figure 4.5: (a) Energy resolution ΔE_{kin} as a function of E_{kin} as given by equation (4.6) for various time resolutions $\Delta t \leq 1$ ns and constant drift length $d = 200$ mm. The thick solid line represents the energy resolution expected for a typical time resolution $\Delta t = 0.2$ ns of the pTOF spectrometer (see text). (b) Accessibility of the parallel wave vector k_{\parallel} as a function of E_{kin} for various acceptance angles θ_{max} of the spectrometer. The thick solid curve ($\theta_{\text{max}} = 22^\circ$) shows the geometric limit of the developed pTOF spectrometer (see text). The momentum resolution as given by equation (4.7) is indicated by the underlying gray scale and is $< 0.002 \text{ \AA}^{-1}$ for all kinetic energies and momenta plotted.

Typical kinetic electron energies for a 2PPE experiment are $E_{\text{kin}} = 1$ eV, 2 eV and 4 eV, which allow to access $k_{\parallel} < 0.19 \text{ \AA}^{-1}$, 0.27 \AA^{-1} and 0.38 \AA^{-1} , respectively. At first glance, the accessible region of k -space seems to be confined to the center of the Brillouin zone. The option to rotate the sample or use slanted sample posts, however, extends the range of operation toward the Brillouin zone boundaries.

4.1.5 Delay-Line Anode

Several designs of two-dimensional anodes for the position read-out of MCPs have been established, but only few of them are capable to analyze multihit events⁴, which is crucial for laser-induced photoemission spectroscopy using amplified femtosecond laser pulses. One concept is the delay-line read-out for position determination, implemented in the pTOF spectrometer.

The working principle is shown in Fig. 4.6 for a simplified single wire layer and summarized in the following (for further details see [Sob88, Jag02a]). The amplified charge cloud from the MCP stack, which is generated upon impact of a single photoelectron, is collected by parallel wound wire layers of the delay-line anode structure. Upon impact it produces two charge pulses counter-propagating toward the ends of the respective wire. Each layer consists of a pair of copper wires, the so called "reference wire" and "signal wire", which generally is kept at a slightly more positive

⁴A multihit event occurs when more than one electron is detected within one laser cycle of a few μs .

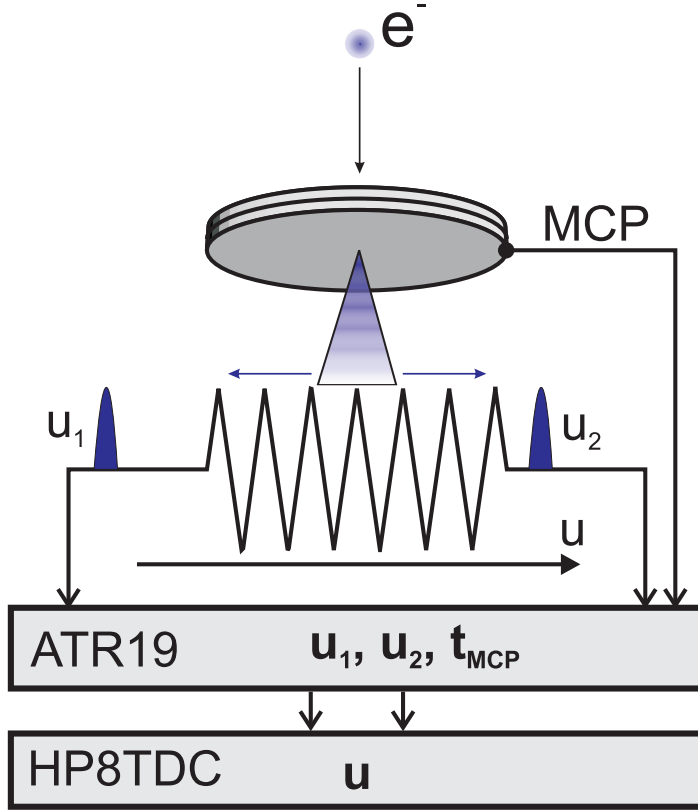


Figure 4.6: Position encoding in 1D using a delay line anode. The electron cloud e from the MCP is collected on the signal wire and two current pulses u_1 and u_2 propagate to the wire ends. The hit position is determined from the propagation time difference of the two signals measured with respect to the MCP signal.

voltage (~ 50 V) than the reference wire to collect the electron cloud. The ends of reference and signal wires of each layer are bundled in Lecher-wires and connected to the electrical feedthroughs. The difference of currents in signal and reference wire is then coupled out via a current transformer to yield a short voltage pulse at the respective wire end. The spatial position U along one wire is determined by the difference between the timing signals u_1 and u_2 of each wire end, which are referenced to the MCP signal t_{MCP} as time-zero:

$$(4.8) \quad U = c_u [(u_1 - t_{MCP}) - (u_2 - t_{MCP})] \quad ,$$

where c_u is the effective signal propagation speed perpendicular to the meandering wire structure. The signal propagate along the wire with a speed of $2/3 c$ but due to the meandering wire structure, the effective propagation speed is reduced to the order of ns/mm, which can be accurately measured with modern timing instruments.

The charge cloud is expanded in-between the MCP stack and the anode structure and covers several wires of a layer. These overlapping signals increase the position

resolution by interpolation of the center-of-mass of the charge cloud. Thus the position resolution is not limited by the ~ 1 mm spacing between the wires of a layer but by the product of time resolution Δt and the propagation velocity c_u . For the pTOF setup with MCPs of 80 mm diameter the propagation speed is of the order of 0.7 mm/ns. The overall time resolution is mainly limited by the electronic timing precision of 100 ps, which enables a position resolution < 0.2 mm and thus a corresponding angular resolution of $\Delta\theta < 0.06^\circ$. In fact, this high angular resolution can compete with state-of-the-art hemispherical electron analyzers, which also reach $< 0.1^\circ$ angular resolution.

To determine the position in two dimensions a second delay-line structure has to be implemented in the perpendicular direction to form a cross-type anode. This is sufficient for the position determination of single hits but has serious disadvantages in multihit operation [Jag02c]. This limited multihit capability may be overcome by introduction of a third layer, which gives the anode a hexagonal shape and the name Hexanode. As shown in Fig. 4.1, three independent and mutually isolated wire layers are wound at an angle of 120° to each other. This makes it necessary to project the hexagonal in-plane coordinates U , V and W of each layer onto the Cartesian in-plane coordinates x and y . Explicitly, the Cartesian coordinates x and y are calculated from the hexagonal coordinates according to

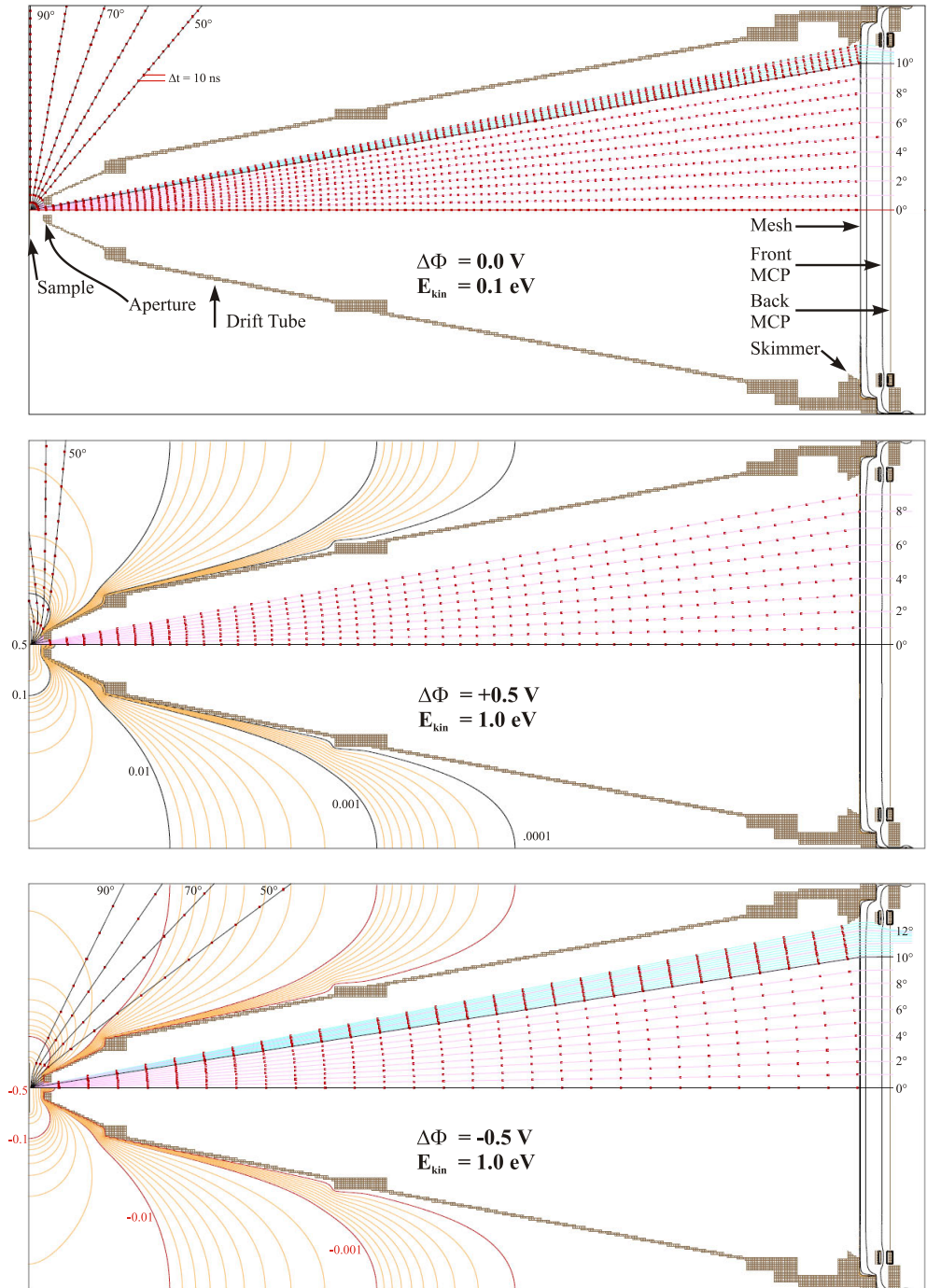
$$(4.9) \quad \begin{aligned} x_{uv} &= U & y_{uv} &= \frac{U - 2V}{\sqrt{3}} \\ x_{uw} &= U & y_{uw} &= \frac{2W - U}{\sqrt{3}} \\ x_{vw} &= V + W & y_{vw} &= \frac{W - V}{\sqrt{3}}, \end{aligned}$$

when the x direction is defined to coincide with the U hexagonal coordinate [Jag02c]. This coordinate transformation directly expresses the redundancy of the Hexanode design as the x and y position can be inferred from any two of the hexagonal coordinates independently.

4.1.6 Trajectory Simulations

This section discusses numerical simulations of the electron trajectories in the pTOF spectrometer, which have been performed with the SimIon 7.0 software package from the Idaho National Engineering and Environmental Laboratory. The simulations are intended to optimize the geometry of the drift tube aperture and estimate the effects of a finite difference $\Delta\Phi$ of sample and spectrometer vacuum levels. The trajectory simulations were carried out by assuming a certain potential difference of

Figure 4.7 (*facing page*): Numerical electron trajectory simulations with SimIon 7.0. (a) The electron trajectories are straight lines for aligned vacuum levels of sample and spectrometer, and the effective acceptance angle is given by the geometrical acceptance angle of $\pm 11^\circ$. (b) A positive vacuum energy difference decelerates the electrons and thereby decreases the effective acceptance angle to 9° on the MCPs. (c). A negative vacuum energy difference accelerates the electrons and therefor increases the effectively sampled angular spread to 12° .



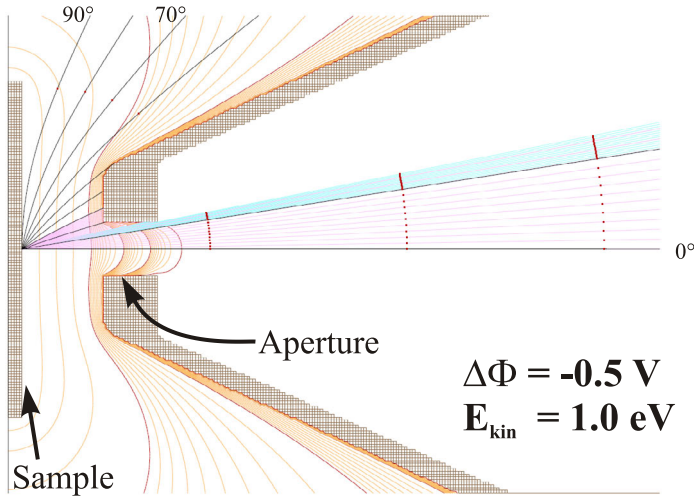


Figure 4.8: Close-up of the trajectories at the aperture where a finite vacuum energy difference forms an electron lens in the aperture. Shown for a negative (forward) bias voltage.

sample and spectrometer and calculating the spatial potential distribution assuming a cylindrical symmetry of the pTOF drift tube assembly. The potential grid had a step size of 0.1 mm in each direction. The refined self-consistent potential then is used to propagate the electrons in small discrete time steps.

In Fig. 4.7 three exemplary sets of trajectory simulations are shown for different vacuum energy differences $\Delta\Phi = \Phi_{\text{spec.}} - \Phi_{\text{sample}} + e_0 U_{\text{bias}}$, as indicated. The upper panel depicts the situation for equal vacuum levels of sample and spectrometer and a kinetic electron energy of 0.1 eV. The electrons are emitted at emission angles ranging⁵ from 0° up to 90° and the TOF of the electrons is encoded by timestamps at a distance of 10 ns. The electrons propagate on straight lines since no electrostatic potential alters the trajectories. The 90° emission cone emitted from the sample is blocked by the aperture at the tip and the angular spread of the electrons in the drift tube spans 11°. Then the electrons traverse the mesh and are accelerated by the electric field of the front MCP, biased at +300 V. Here, the skimmer at the outer edge of the drift tube is important to avoid electrons being deflected and thereby deteriorating the angular resolution, as detailed below.

The center panel of Fig. 4.7 depicts the simulation for a vacuum energy difference $\Delta\Phi = +0.5$ eV, which decelerates the electrons, and a kinetic electron energy of 1.0 eV, typical for time-resolved studies at low photon energies. The equi-potential lines are indicated in a logarithmic fashion with the numerical values given in eV. Compared to the case of no vacuum energy difference, the deceleration decreases the spread of the electron trajectories from 11° to 9°. The bottom panel of Fig. 4.7 shows the opposite arrangement with a vacuum energy difference of $\Delta\Phi = -0.5$ eV, which accelerates the electrons toward the spectrometer, and a kinetic electron energy

⁵Due to the cylindrical mirror symmetry electron emission in the range from 0° to -90° has been omitted.

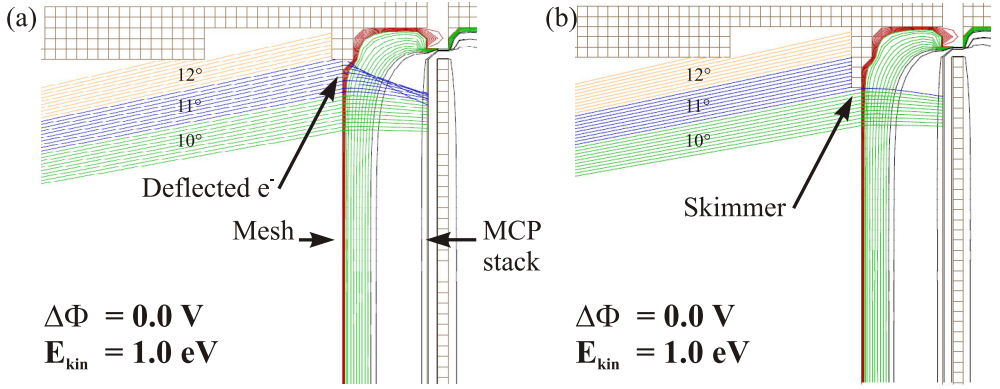


Figure 4.9: Close-up of the trajectories at the outer edge of the MCPs. (a) Electrons passing at the outer edge of the mounting of the mesh can be deflected and decrease the angular resolution. (b) The sharp edged skimmer blocks the outer electron beam and prevents deflections without sacrificing the 11° acceptance angle.

of 1.0 eV. The equi-potential lines exhibit the same symmetry and shape but with reversed sign. Due to the acceleration of the electrons, the angular spread increases from 11° to 12° .

Focusing on the aperture of the drift tube, a close up in Fig. 4.8 shows 1 eV electrons traversing the drift tube tip. Here, a negative vacuum energy difference is discussed, a case which is commonly encountered for negatively biased samples, compare to Fig. 3.10. The equi-potential lines indicate that the space in between the sample and the tip of the TOF can be approximated by a plate capacitor configuration. This allows to (i) minimize the effects of a finite vacuum energy difference and (ii) apply analytical corrections for the electron trajectories in the case of such differences [Hen08]. The close up also highlights the electrostatic electron lens that forms in the aperture itself. Here, the optimization of the diameter and the depth of the aperture are important. The simulations result in a minimum field penetration for an aperture diameter of 1.9 mm and a depth of the hole of 2.0 mm, which still allows an efficient electron transmission at a fixed sample-tip distance of 3 mm.

The panels (a) and (b) of Fig. 4.9 discuss the electron skimmer at the outer edge of the mesh in front of the MCP stack. These simulations were performed for electrons with 1 eV kinetic energy and no vacuum energy difference. As depicted in Fig. 4.9(a), electrons with $\sim 11^\circ$ photoemission angle passing the outer edge of the drift tube hit the mounting ring of the mesh, which deflects some electrons toward the center of the MCPs. This results in loss of spatial resolution and worsens the S/N ratio, and hence has to be avoided. Without sacrificing the 11° acceptance angle of the pTOF, a sharp edged electron skimmer is introduced as mount for the mesh. Its sharp edge skims the outer part of the electron emission cone without allowing deflection.

4.2 Software Implementation

The underlying principle of data acquisition connects the electron time-of-flight t with the two position coordinates (x, y) for each event to yield the kinetic energy $E_{\text{kin}}(x, y, t)$ and parallel momentum $\vec{k}_{\parallel}(x, y, t)$, see equations (4.1) and (4.4). This requires to store and process each event separately. Only after analysis the data can be sorted into histograms, the so-called binning.

The real-time analysis at event rates beyond 10 kHz is even more demanding and requires high-performance software, which is dedicated to the specific task of position calculations and kinematic conversions including the multihit analysis outlined below. Each event consists 136 Byte if 3 hits on 8 channels are acquired and creates fairly large data sets of 1.4 GByte per 10^7 events. This translates to a data rate of 14 MByte/s for an event rate of 100 kHz and storage and analysis of a single event must proceed in $< 10 \mu\text{s}$. This demanding real time analysis reaches the limits of the currently employed hard- and software.

Moreover, the statistic nature of the single particle counting in photoemission has to be considered. For a given number of counts N , the stochastic uncertainty is given by $\delta N = 1/\sqrt{N}$ which can be minimized by acquiring large data sets. The pTOF distributes the counts over a 4-dimensional volume, which is spanned by energy, two momentum axes and pump-probe delay. Compared to the conventional TOF spectrometer the phase space is increased by a factor of ~ 1000 . The pTOF data sets can comprise more than $5 \cdot 10^8$ individual events, stored in ~ 10000 separate files, which require several 100 GByte storage space and significant amounts of volatile memory.

To fulfill the requirements on calculation speed and storage capacity, the the pTOF setup is equipped with a high-performance dual processor workstation and a TByte RAID system. Additionally, the data can be transported with large mobile hard disks.

4.2.1 The cEvent Class

To obtain a flexible high-performance implementation of the signal processing and storage, a C++ class was designed and implemented⁶. The C++ class `cEvent` provides all tools (i) to characterize, adjust and calibrate the signal input by means of control coordinates, to (ii) actuate external devices such as the laser beam shutters and the optical delay stage, and to (iii) perform all coordinate transformations to obtain angle- and time-resolved electron spectra in real time. The last point is of importance for the alignment of the laser beam in the focus of the acceptance cone of the pTOF. The separation of the back-bone functionality of the `cEvent` class from the front-end that submits the adjustable parameters, and retrieves and displays the processed data is necessary due to the high data rates and the large data volume. Additionally, the functionality of the `cEvent` class has to be implemented only once and can be used by different front ends, see next section 4.2.2.

The `cEvent` class first checks the validity of each registered event and proceeds to calculate the time and space coordinates from the TDC raw data, which finally yields

⁶The final implementation of the `cEvent` class as outlined here was realized in a marvelous fashion by Laurenz Rettig.

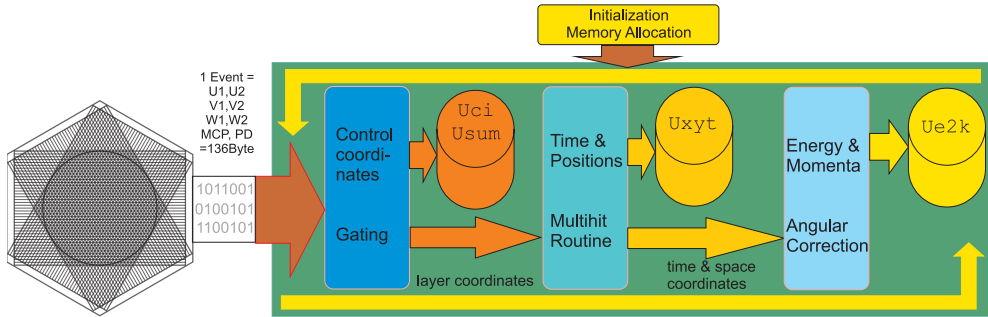


Figure 4.10: Working principle of the `cEvent` class. After initialization and memory allocation, each event is checked for its consistency using control coordinates. The time and space coordinates of valid hits finally yield the kinetic energy and parallel momenta. Different coordinates are saved to different data volumes.

the kinetic energy and the parallel momenta. The coordinates of each individual event then are sorted into separate three-dimensional histograms. The real and reciprocal space coordinates are binned into data volumes termed `Uxyt` and `Ue2k`, respectively. The bin sizes are fixed by the initialization procedure. On the one hand, larger bins result in less occupied memory and increase the counting statistics in each bin. On the other hand, the effective resolution decreases with increasing bin width. Generally, bin widths of 1 mm and 0.2 ns for the real space coordinates result in 200 MByte memory requirements for `Uxyt`. Bin widths of 0.002 \AA^{-1} and 5 meV for `Ue2k` are usually sufficient and result in 100 MByte memory requirements for each data set.

Fig. 4.10 depicts the signal processing of the `cEvent` class as outlined in the following. To begin the data acquisition several parameter sets are initialized as outlined below. A complete list of the pTOF parameters with a detailed description of their function is given in appendix F.

kinetic parameters supply calibration data for the detector and coordinates conversion.

binning parameters define the size of the data volumes by passing the smallest and largest bin, and the bin width.

gating parameters assign criteria for the validation of the events and gating of the coordinates, see below.

advanced parameters are necessary for the advanced multihit reconstruction, see chapter 4.2.3.

The initialization provides all parameters necessary for the data acquisition and analysis and allocates the volumes for storage of the processed data. Each event of 136 byte consists of the TDC hit register, containing the 32 bit timing information of 3 hits on 8 channels, a 32 bit counter array, summarizing the number of hits per channel, and a global 64 bit timestamp, used for the evaluation of the event rate.

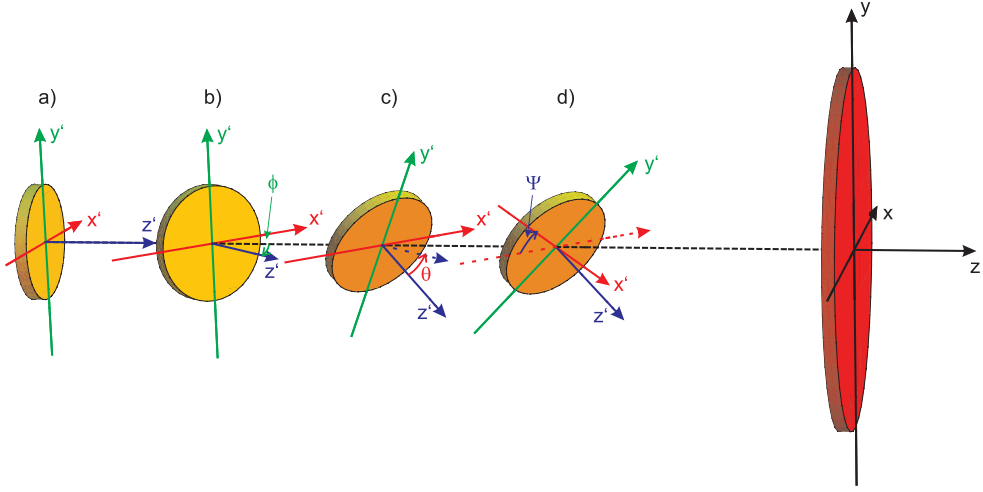


Figure 4.11: Relation of sample and pTOF coordinate system. The primed sample coordinate system (a) is first rotated about the y' axis by an angle ϕ , which corresponds to a rotation of the manipulator (b). Then the sample is tilted around the new x' axis by an angle Θ , which can be realized by a tilted mounting of the samples or a slanted sample post (c). Finally, the sample is rotated around the z' axis by an angle Ψ , which is an in-plane rotation of the sample and important for samples with anisotropic band structures (d). The unprimed coordinate system of the spectrometer is depicted at the right.

After the TDC raw data is transferred to the class, the control coordinates are calculated for a check of the data consistency. Among these the **consistency indicator** (CI) and the time-sum of each layer is determined. The CI is a 6 bit mask, in which each bit resembles one wire end of the Hexanode and indicates if a signal has been coupled out on the specific wire end. The bit mask thus displays on which channels signals were retrieved and which signals have been lost. The time-sum exploits that the total propagation time across a specific wire is constant. The time sum u_{sum} of, for example, the U layer is defined as

$$(4.10) \quad u_{\text{sum}} = (u_1 - t_{\text{MCP}}) + (u_2 - t_{\text{MCP}}) = \text{const}$$

for both timing signals u_1 and u_2 which are referenced to the MCP signal as time-zero, as indicated in Fig. 4.6. Then the time and space coordinates are calculated from the time information of each layer and the MCP signal. The calculation can proceed in two ways: If at least two signals from two layers have been retrieved, equations (4.8), (4.9) and (4.5) are used; otherwise an advanced multihit reconstruction routine is employed, see section 4.2.3. At this point, a gating can be applied, which sorts out the valid hits according to certain criteria such as the active MCP radius, the CI and the time-sums. The validated hits are saved into the U_{xyt} data volume.

After determination of the real space coordinates the reciprocal coordinates are calculated according to equations (4.1), (4.4) for each validated event. To take a rotation of the sample coordinate system into account, the full vacuum wave vector

$\vec{k} = (k_x, k_y, k_z)^T$ in the sample coordinate system is determined. The conventions regarding the axes orientation and sequence of rotations is discussed in Fig. 4.11. The three subsequent rotations are described with a rotation matrix

$$(4.11) \quad R = \begin{pmatrix} \cos \psi & \sin \psi & 0 \\ -\sin \psi & \cos \psi & 0 \\ 0 & 0 & 1 \end{pmatrix} \begin{pmatrix} 1 & 0 & 0 \\ 0 & \cos \theta & \sin \theta \\ 0 & -\sin \theta & \cos \theta \end{pmatrix} \begin{pmatrix} \cos \phi & 0 & -\sin \phi \\ 0 & 1 & 0 \\ \sin \phi & 0 & \cos \phi \end{pmatrix}$$

Here, a passive transformation is used, which rotates the coordinate system itself. The primed wave vector in the sample coordinate system is given by multiplication with the rotation matrix R :

$$(4.12) \quad \vec{k}' = \begin{pmatrix} k'_x \\ k'_y \\ k'_z \end{pmatrix} = R \cdot \begin{pmatrix} k_x \\ k_y \\ k_z \end{pmatrix}$$

The rotated parallel momentum components k'_x and k'_y , and the kinetic energy are binned into the `Ue2k` data volume. This evaluation algorithm is successively applied to each individual event.

After binning and saving of all events of a data set, the data volumes are sliced to obtain two-dimensional cuts that can be displayed as intensity matrices. This is realized by integration of the data volumes along one or more predefined directions and yields, for example, the band dispersion along a both in-plane directions $I(E, k_x)$ and $I(E, k_y)$, energy spectra $I(E)$ and constant energy surfaces $I(k_x, k_y)$ with $E = \text{const.}$ The global timestamp of each event is used to normalize all data volumes and slices to the count rate and the bin width of all dimensions⁸.

4.2.2 Igor Pro and LabView Front Ends

The measurement software is programmed with National Instruments LabView 8.5 and enables to control the TDC data, the storage of the raw TDC data to hard disk, the integration of the `cEvent` C++ class, and the display of the processed data in real time. The hardware driver interface and the `cEvent` class are implemented with a dynamic link library (.dll) that is called by LabView.

For data acquisition, the TDC hardware buffer is enabled and reads data for ~ 0.5 s. The data stream is processed in real time by the `cEvent` class and saved simultaneously to a binary list-mode-file (lmf) format, which is commonly used in high-energy physics. Slices of the multidimensional data volumes are extracted in between the acquisition cycles and displayed in the LabView front end, while the TDC hardware buffer continues to acquire data. The regions for the extraction of the sliced data can be defined interactively in the front end, which enables an actual analysis in real time. After finishing a measurement the extracted spectra can be saved to disk in a Wavemetrics IgorPro compatible binary file format (.ibw). Additionally,

⁷The k_z component describes the normal momentum component *in vacuum*, which must not be confused with the perpendicular momentum k_\perp *inside the crystal* that is generally not conserved in the photoemission process.

⁸An increase of the bin width at constant count rate leads to more counts in a each bin, which is accounted for by normalization to the bin width. This results in units of Hz/eV or Hz/Å⁻¹.

the LabView front end controls, displays and stores the conversion parameters and control coordinates.

To obtain time-resolved data sets, one instance of the `cEvent` class is created for each pump-probe delay point, which contains all events at the particular delay. Additionally, one instance of `cEvent` is defined for acquisition of uncorrelated background spectra. Then the optical delay stage is moved to the delays. Data is acquired for ~ 1 s at each delay point, which is transferred to the corresponding instance of the `cEvent` class and saved to a separate lmf for each delay. A typical time resolved measurement contains 100 delay points and can comprise more than 100 scans of the delay axis, which results in 10^4 lmf files and a data volume of a few 10 GByte, depending on the count rate. Angle-resolved cross correlation (XC) traces are obtained by integration of the photoemission yield in a k -space cube, $\{\Delta E, \Delta k_x, \Delta k_y\}$, as a function of pump-probe delay. The offline analysis may proceed either by loading the lmf files into the LabView front end and saving the processed data into the binary IgorPro .ibw format, or by using a separate command line tool. The command line tool is based on the `cEvent` class as well and generates IgorPro .ibw files but lacks any interactive controls and displays. Especially, the lack of the interactive slicing of the data volumes is a severe drawback. Therefore, an interactively controlled implementation of the `cEvent` class into an IgorPro plug-in (XOP) has been realized⁶.

4.2.3 Reconstruction of Multihit Events

The use of the pTOF spectrometer for photoemission experiments employing laser light sources with several 100 kHz repetition rate requires the ability to detect multihit events with more than one hit in a time range of ~ 100 ns. For illustration, consider two photoelectrons, which are emitted with the same kinetic energy and out-of-plane photoemission angle θ , but at a different in-plane angle ϕ , see Fig. 4.3. This could be a typical photoemission signature from an electronic state delocalized in the surface plane which gives rise to a sharp peak in the angle-resolved photoemission spectrum. Consequently, these two photoelectrons will hit the MCP at different positions at nearly the same time. The strength of the pTOF spectrometer with the Hexanode detector is to retrieve E_{kin} , k_x and k_y of two or even more hits. A fundamental concept for the multihit operation is based on the time-sums [Jag02a, Jag02c], which are defined as the total propagation time across a specific wire and thus are constant for each layer, see equation (4.10). The time-sum of a certain hit not only serves as a test if the signals on both ends of the anode wires have been coupled out consistently, but also provides the redundancy needed for the analysis of multihit events.

If two or more electrons hit the detector within the pulse-pair resolution $\Delta T < 10$ ns of the TDC system only one MCP signal is registered. In the following several different situations for multihit events are discussed: (i) If the TOF of both electrons differ by ΔT or more, the hits are easily disentangled if the positions are not identical. (ii) If the positions are identical their TOF difference must be larger than ΔT . Albeit this might at first glance look like a severe limitation, it is not a serious problem, since the analysis procedure clearly identifies such events by inconsistencies of timing and position signals and discards them. Thus, the following will focus on the case where the TOF is identical but the spatial positions are sufficiently different as defined below.

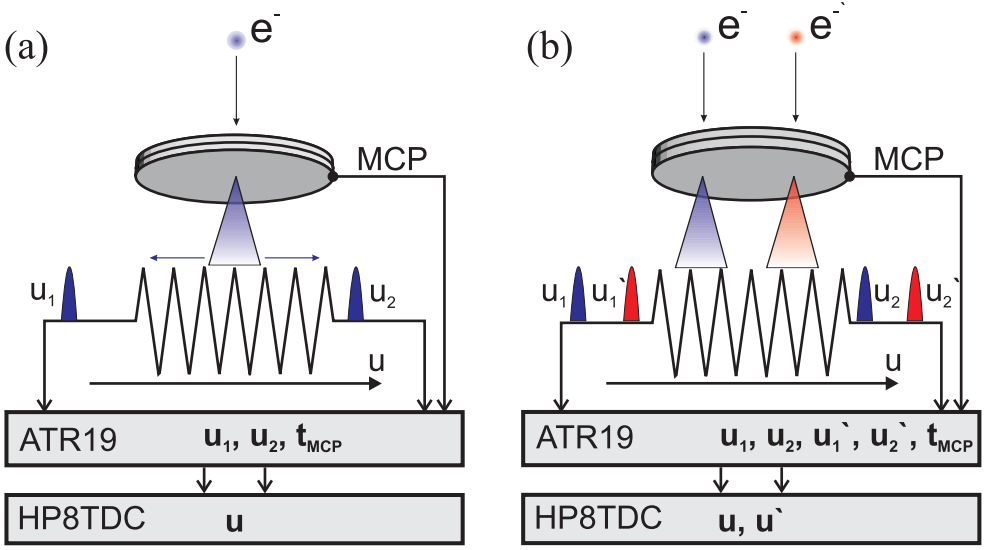


Figure 4.12: (a) One dimensional position determination in single hit limit. One electron cloud e is collected on the signal wire and two current pulses u_1 and u_2 propagate to the wire ends, which are directly analyzed to yield the position. (b) One dimensional position determination in multihit operation. Two electron clouds e and e' hit one layer of the delay-line anode at the same time but at different positions. The timing signals reaching the one end of the delay-line wire (u_1, u_1' or u_2, u_2') can be resolved as long as the time coordinates of the subsequent particles differ by the pulse-pair resolution of the detector system (see text).

Consider one layer of the delay-line detector where two electron clouds e and e' hit the detector at different positions, as shown in Fig. 4.12(b). Each electron produces two current pulses u_1, u_2 and u_1', u_2' , which propagate toward the two ends of the layer. If the arrival time of two electrons differs by less than the total propagation time across the layer, given by the time-sum, some of the signals may not be in the correct time order or some signals are lost due to temporal overlapping. The anode signals can be discriminated if the position coordinates of subsequent particles differ by more than the product of the effective signal propagation speed c_u and the pulse-pair resolution ΔT . The missing MCP timing signal t'_{MCP} is reconstructed from the time-sum u_{sum} of the specific layer:

$$(4.13) \quad t'_{MCP} = \frac{1}{2}(u_1' + u_2' - u_{\text{sum}}) \quad .$$

In this situation the pulse-pair dead time of the detector system can effectively be reduced to zero.

In the case of a conventional cross-type delay-line anode the lower limit on the particle distance of $c_u \cdot \Delta T \approx 7$ mm creates a cross-shaped region which is insensitive to multihit events [Jag02c]. The strength of the Hexanode design is the use of the additional information from the redundant third wire layer to reconstruct and verify hits, which are in too close spatial proximity on the other two wire layers to be retrieved [Jag02c]. Thus, the Hexanode design reduces the corresponding region

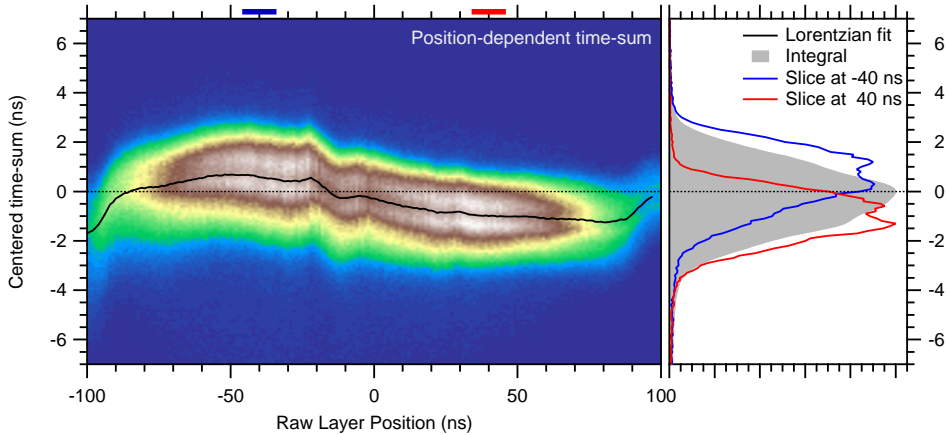


Figure 4.13: Dependence of the time-sum on the raw layer position in ns. As evidenced by the panel on the right side, the center of mass of the time-sum (gray area) is centered at 0 ns^9 , whereas the slices extracted at $\pm 40 \text{ ns}$ raw layer position (red and blue), as indicated by the color bars on top, are shifted. The position-dependence of the time-sums is corrected by fitting a Lorentzian line to the time-sums. The individual time-sums also exhibit a fine structure with two separate peaks that are averaged out in the center of mass of the time-sum.

insensitive to multihit events significantly to a circle of $\sim 7 \text{ mm}$ diameter [Jag02c]. Consequently, the severe limitation of a cross-shaped dead region is overcome as the third Hexanode layer adds the redundancy to extend the operation into the multihit regime beyond the limit of the electronic pulse-pair dead time.

The fundamental concept for the reconstruction of multihit events outlined so far can be extended even further to not only retrieve missing MCP signals but also reconstruct inconsistent or lost layer signals. This extended multihit reconstruction is accomplished by an advanced multihit reconstruction routine `Resort64.dll`, which was designed and programmed by Achim Czasch from RoentDek [Jag02a, Roe06]. As depicted in Fig. 4.12(b) the sequence of the out-coupled signals may be reversed at the respective wire ends such that the time-sums for both electrons e and e' are inconsistent. Consequently, both events are discarded in a single hit analysis. In a multihit analysis, the time-sums are used to recover the correct sequence of signals, leading to valid time-sums for both electron hits.

Another problem in the multihit operation are missing signals due to (i) overlapping of multiple signals within the dead time of the combined CFD-TDC chain, (ii) weak hits, (iii) reflections at the out-coupling devices. The advanced multihit reconstruction routine supplies 20 different methods to sort the valid hits and reconstruct missing signals. The first 14 methods are conservative: Starting from a fully recorded hit with all 6 anode signals and the MCP signal (method no. 0) to partly resolved hits with 5 anode signals and a missing MCP signal (method no. 13), only redundant information is used. Nevertheless, at high event rates in the regime of 100 kHz the sorting and reconstruction of the multihit events is important to obtain a high acquisition efficiency and avoid systematic distortion of the spectra. The more

advanced methods no. 14-20 are used for events where even more anode signals have been lost and are more speculative since no redundancy of the Hexanode is left to perform consistency checks. An extreme example is method no. 19 where only one signal from each layer and no MCP signal is available. Even though the standard single hit evaluation could neither determine the positions nor the TOF, the advanced reconstruction retrieves both in-plane positions and the TOF. Of course, these very advanced methods are risky as they tend to produce ghost hits and usually are not used for data evaluation.

The evaluation of the raw data with the advanced reconstruction routine requires to characterize the anode hardware in detail and supply this information to the reconstruction software, as detailed in appendix F. In order to recover the proper sequence of valid hits and discard reflections the maximum propagation times on each Hexanode layer, the electronic dead times of the anode and MCP channels, and, most importantly, the correction of the position dependence of the time-sums has to be known.

Fig. 4.13 depicts the time-sum⁹ of the W-layer as function of the raw position on the W-layer, given in ns. Evidently, the time-sum is not simple constant as suggested in equation (4.10) but depends on the position on the layer. This is explained by the different electric permeability ϵ of the ceramics that support the Cu wires of the anode structure, which slightly modulates the propagation speed in the wires. This variability of the time-sum has to be corrected since the advanced reconstruction routine relies on the precise knowledge of the time-sums. The correction is realized by fitting the center of the time-sum with a Lorentzian line as function of the raw layer position and passing the correction values to the advanced reconstruction algorithm.

⁹For numerical reasons, the time-sums are shifted to be centered around 0 ns in the advanced reconstruction algorithm.

4.3 Performance of the pTOF Spectrometer

The performance of the pTOF spectrometer is demonstrated with an energy- and angle-resolved study of electrons photoemitted from a Cu(111) surface by femtosecond laser pulses of 6.2 eV photon energy. The exemplary data set discussed in the following consists of 10^7 events and was recorded within 344 s. The experiment was carried out under ultra high vacuum (UHV) conditions with a base pressure $< 10^{-10}$ mbar. The Cu(111) surface was prepared by standard procedures of repeated cycles of Ar^+ sputtering at 700 eV ion energy for 5 min followed by annealing at a temperature of 700 K for 20 min [Mus82]. The good surface quality was confirmed by a sharp low energy electron diffraction (LEED) pattern with low background and a small line width of the Cu(111) surface state in the photoemission spectrum. The femtosecond laser system used here is described in chapter 3.1.1 and appendix E

The laser beam hits the Cu(111) sample at an incidence angle of $\varphi = 45^\circ$ with respect to the surface normal. The photoemitted electrons pass the entrance aperture and the field free drift region before the position-sensitive detector records the lateral positions and the TOF. The kinetic energy and in-plane momenta of the detected photoelectrons are analyzed based on the pTOF technique described in the previous section. To ensure unperturbed trajectories of the photoemitted electrons the vacuum energies of sample and pTOF spectrometer have to be carefully matched. The difference in vacuum energies of the Cu(111) sample with a work function of $\Phi = 4.90$ eV [Kno98a] and the graphite-coated pTOF spectrometer with a work function of ~ 4.4 eV was offset by applying a small bias voltage of +0.5 V from a battery to the sample.

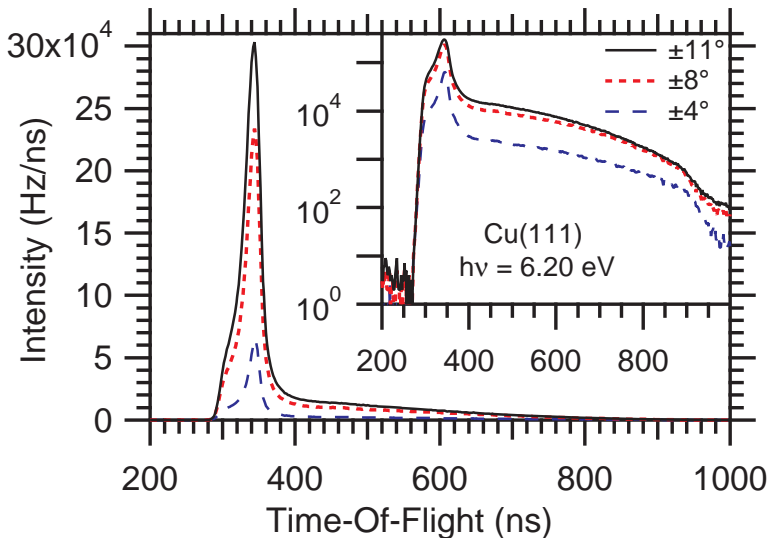


Figure 4.14: TOF electron spectra taken at $h\nu = 6.2$ eV at the Cu(111) surface integrated over various emission angles θ as indicated. The inset shows a logarithmic representation of the same data set.

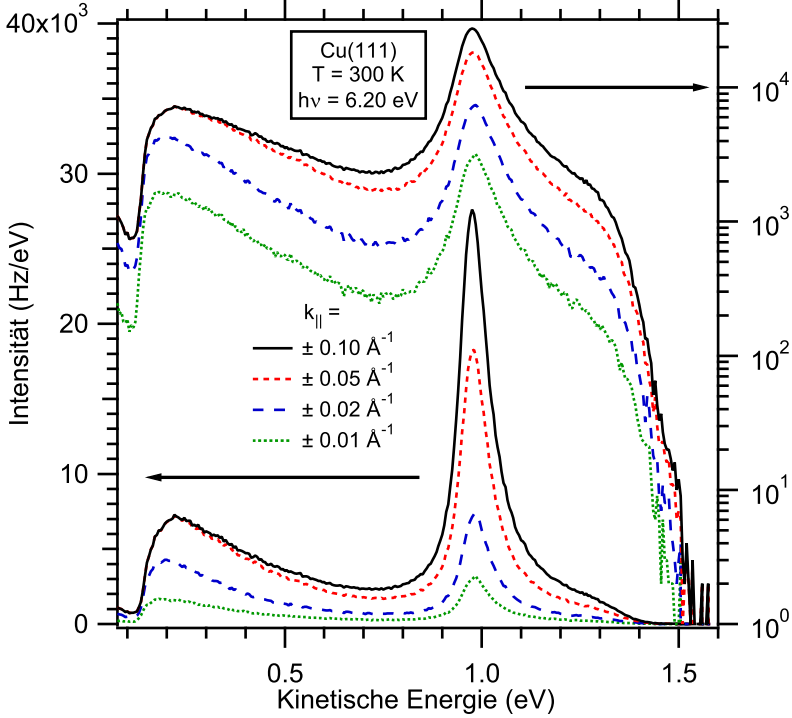


Figure 4.15: Photoelectron spectra integrated over circular regions in the $k_x k_y$ -plane as indicated. The right-hand scale with logarithmic intensity scale emphasizes the high- and low-energy cutoffs at the Fermi ($E_{\text{kin}} \approx 1.4$ eV) and secondary edge ($E_{\text{kin}} \approx 0.1$ eV), respectively. Please note the excellent S/N ratio of $> 10^4$ obtained in this measurement.

Fig. 4.14 shows TOF spectra integrated over various acceptance angles of $\pm 4^\circ$, $\pm 8^\circ$, and $\pm 11^\circ$, which corresponds to an effectively used MCP diameter of 26 mm, 54 mm and 70 mm. The different spectra were generated out of one data set by applying different cuts in the off-line analysis. The pronounced peak in the TOF spectrum between 300 ns and 400 ns, which is observable at all acceptance angles, originates from the occupied surface state of the Cu(111) surface. The sharp cutoff for < 300 ns corresponds to the fastest electrons at the Fermi level E_F . The signal at > 400 ns is due to secondary electrons of low kinetic energy, which have undergone elastic and inelastic scattering. In the following, we will focus on the well-defined surface state peak in the photoemission spectra and the features observed in the energy domain.

The binding energy and the band dispersion of the Cu(111) surface state have been extensively studied by direct photoemission [Rei01] and time-resolved 2PPE [Kno98a] spectroscopy. At a sample temperature of 300 K the binding energy of the surface state referenced to the Fermi level E_F is observed to be $E - E_F = -0.39(1)$ eV with a natural line width of $62(4)$ meV [Kno98a]. The band dispersion of the Cu(111) surface state is characterized by an effective electron mass of $m^* = 0.412(1) m_e$ [Rei01].

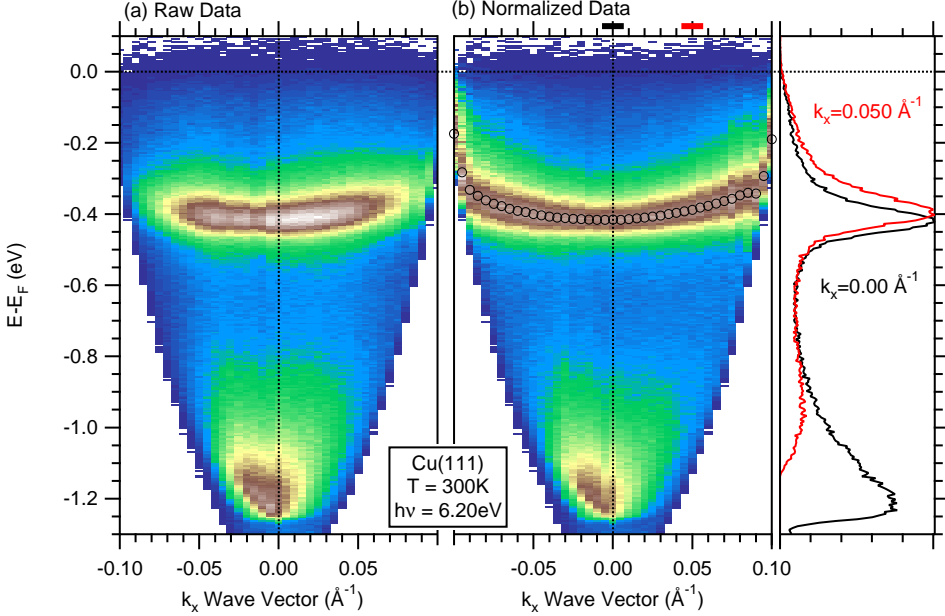


Figure 4.16: (a)/(b) Color-coded photoemission intensity as function of in-plane momentum k_x and kinetic energy E_{kin} generated by a $\Delta k_y = \pm 0.02 \text{\AA}^{-1}$ wide cut in the $k_x k_y$ -plane. A Lorentzian fit yields the positions of the peak maxima as indicated by open circles to guide the eye. The raw data in panel (a) is normalized to the peak intensity and yields the representation in panel (b). Right: Spectra extracted at normal, $k_x = 0.00 \text{\AA}^{-1}$, and non-normal emission, $k_x = 0.05 \text{\AA}^{-1}$, showing the dispersion of the Cu(111) surface state towards E_F .

In Fig. 4.15 kinetic electron energy spectra are shown, which have been averaged over circular regions of $k_{\parallel} \leq 0.01 \text{\AA}^{-1}$ up to 0.1\AA^{-1} in the (k_x, k_y) -plane as indicated. The low-energy cutoff at the secondary edge corresponds to the electrons of low kinetic energy which are barely excited above the vacuum level, whereas the high-energy cutoff is given by the electrons of high kinetic energy originating from E_F . The sample work function is calculated from the difference of low- and high-energy cutoff and the photon energy to be $\Phi = 4.945(10)$ eV. The observed 10%-90% width of ~ 10 meV of the secondary edge indicates a smooth and uncorrugated surface, which is corroborated by the sharp surface state. Since the width of the secondary edge is determined by the spectrometer resolution as well as the homogeneity of the work function, the spectrometer resolution can indeed be assumed to follow equation (4.6) without significant broadening due to imperfections of the pTOF.

The pronounced peak at a kinetic energy of $E - E_F \approx 1$ eV originates from the occupied surface state of Cu(111). A fit of a Lorentzian peak convoluted with a Gaussian instrument-function of 20 meV FWHM yields a binding energy of $E - E_F = -404(10)$ meV and a line width of $80(4)$ meV for $k_{\parallel} \leq \pm 0.01 \text{\AA}^{-1}$ (dotted line). This in agreement with previous work on Cu(111) at room temperature [Kno98a]. The binding energy rises to $E - E_F = -409(10)$ meV and the line broadens to

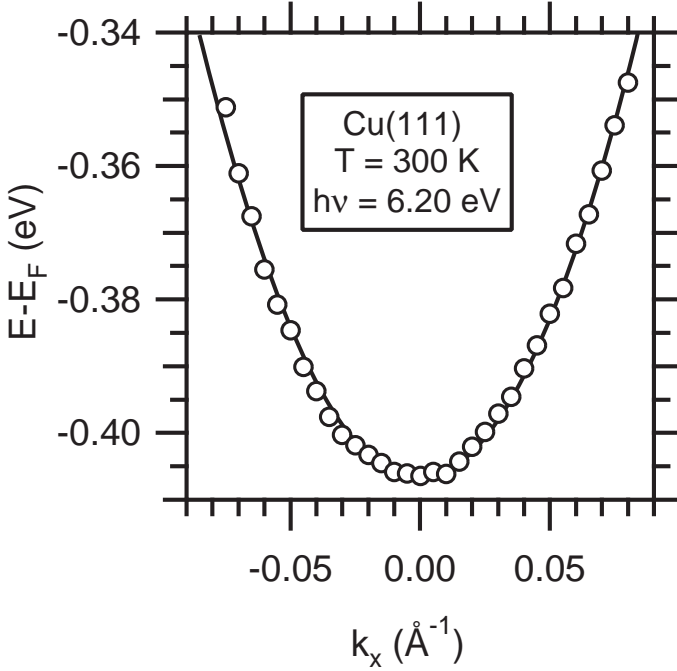


Figure 4.17: Dispersion of the Cu(111) surface state (\circ) with a fit of a free-electron parabola ($-$), which yields a binding energy at the band bottom of $E - E_F = -406(5)$ meV and effective electron mass of $m^* = 0.408(5) m_e$.

83(5) meV when the data is integrated over a circle with $k_{\parallel} = 0.1 \text{ \AA}^{-1}$ radius (solid line). Fig. 4.16 shows a color-coded plot of the photoemission intensity as function of binding energy and k_x wave vector, which was generated by a $\Delta k_y = \pm 0.02 \text{ \AA}^{-1}$ wide cut in the (k_x, k_y) -plane. In this specific experiment the maximum kinetic electron energy is given by $h\nu - \Phi \approx 1.3 \text{ eV}$, which allows to access parallel wave vectors with $k_{\parallel} \leq 0.1 \text{ \AA}^{-1}$, see Fig. 4.5. The raw data in Fig. 4.16(a) is normalized to the Lorentzian peak intensity to make the peak dispersion well visible in Fig. 4.16(b). Within the region of accessible momenta the Cu(111) surface state peak shows a dispersion which can be followed over the whole k -range. Significant deviation from the expected parabola are only revealed for $|k_x| \geq 0.09 \text{ \AA}^{-1}$, corresponding to the outermost parts of the circular detector. The origin of this deviation is currently under investigation. In principle, these distortions could be explained by electron deflection at the skimmer or in the drift tube itself, compare to section 4.1.6.

In Fig. 4.17 the surface state dispersion of the data set in Fig. 4.16 is analyzed. The peak positions of the surface state (open circles) were determined by a Lorentzian line fit of the energy spectra for all discrete wave vectors with $|k_x| < 0.09 \text{ \AA}^{-1}$. Due to a slight misalignment of the Cu(111) crystal surface with respect to the pTOF axis, the dispersion curve had to be shifted by $k_x = +0.0045 \text{ \AA}^{-1}$ to yield the minimum of the parabola at $k_x = 0 \text{ \AA}^{-1}$. This small misalignment of the crystal actually underlines the high resolution that can be obtained with the pTOF spectrometer as deviations in the order of a few $< 10^{-2} \text{ \AA}^{-1}$ can be identified and quantified. A least square fit of a free-electron parabola (solid line) yields a binding energy at the band bottom of $E - E_F = -406(5)$ meV and an effective electron mass of $m^* = 0.408(5) m_e$, in good agreement to literature values [Kno98a, Rei01].

4.3.1 Comparison to Conventional TOF Spectrometer

The performance of the pTOF spectrometer is further evaluated by comparison to the results from the conventional TOF spectrometer described in chapter 3.2.2. The angle-resolved measurements on the identical Cu(111) single crystal with the conventional TOF were realized by rotating the sample in front of the TOF spectrometer. Fig. 4.18 shows the angle resolved spectra for emission angles of $\pm 20^\circ$ in a waterfall plot and as color-coded photoemission yield. In this representation, the photoemission angles can be assigned to the parallel wave vectors only for specific kinetic energies. For the kinetic energy of the Cu(111) surface state, the accessible range is given by $k_{\parallel} = \pm 0.2 \text{ \AA}^{-1}$

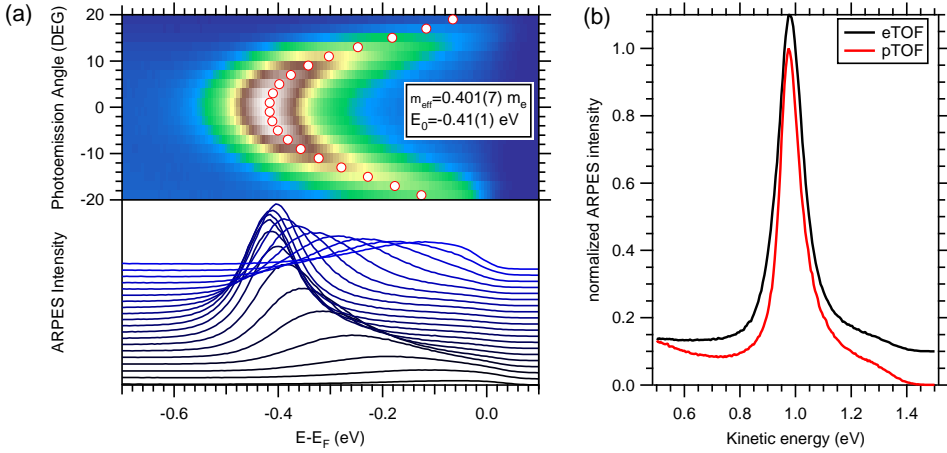


Figure 4.18: (a) Dispersion of the Cu(111) surface state measured with the conventional TOF spectrometer described in chapter 3.2.2. The rotation of the sample by $\pm 20^\circ$ with respect to the spectrometer axis allows to access parallel momenta of up to 0.2 \AA^{-1} at 1 eV kinetic energy, see Fig. 4.5. (b) Lineshapes of the Cu(111) surface state at $k_{\parallel} = 0 \text{ \AA}^{-1}$ acquired with the conventional TOF (black) and the novel pTOF (red). To account for the slightly different bias voltages in both experiments, the TOF spectrum was shifted by 83 meV.

The linewidth of the Cu(111) surface state of $106(5) \text{ meV}$ at normal emission increases to $286(10) \text{ meV}$ at an emission angle of 20° . Fitting the surface state dispersion with a free electron parabola yields an effective electron mass of $m^* = 0.401(7)m_e$ and a binding energy of $E - E_F = -0.410(10) \text{ eV}$ at the minimum of the parabola. These values are in good agreement with literature [Kno98a, Rei01] and the values determined with the pTOF. The smaller linewidth of the pTOF spectra is evidenced in Fig. 4.18(b) and indicates a superior energy resolution of the pTOF, which is explained by the significantly better timing accuracy of the TDC¹⁰.

The slightly smaller background of the conventional TOF at low kinetic energies might be ascribed to different surface roughness due to different sample preparation

¹⁰The HP8TDC card from RoentDek enables 100 ps resolution with 25 ps least-significant bin, whereas the FAST card that is utilized in the conventional electron TOF spectrometer operates with 250 ps resolution.

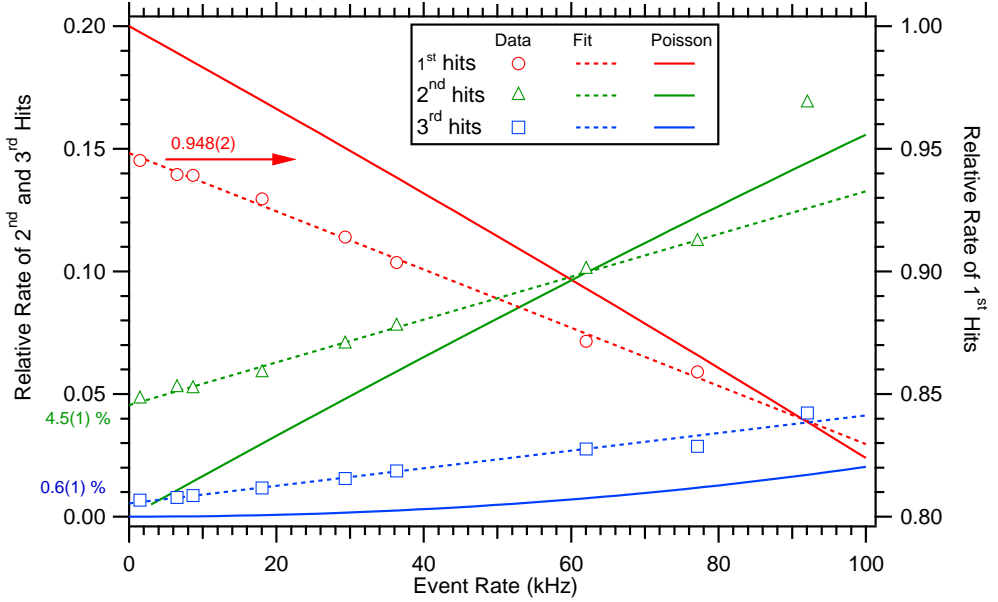


Figure 4.19: Distribution of multihit events with 1, 2, and 3 hits per event as function of the event rate. The solid curves represent the results of a stochastic model based on a Poisson-distributed photoemission probability. The dashed curves are linear extrapolations of the multihit probability at low event rates. Here, the finite ratio of multihits in the limit of vanishing event rate is surprising.

at different days. Nevertheless, the S/N ratio obtained with the pTOF spectrometer is better than 10^4 as evidenced in Fig. 4.15 and hence ideally suited to detect small transient changes in the spectra. Furthermore, The comparison of Fig. 4.16 and Fig. 4.18(a) emphasizes the superior angular resolution of the pTOF spectrometer. The seemingly small angular acceptance of the pTOF spectrometer of $\pm 11^\circ$ can be extended by rotation of the sample, compare to Fig. 4.11.

4.3.2 Discussion of the Multihit Capability

As detailed in section 4.2.3, the ability to detect and analyze multihit events with more than one particle arriving in one laser cycle, is crucial for laser-based photoemission. The data set analyzed above comprises 10^7 events and was recorded within 344 s at an event rate of 29 kHz and a laser repetition rate of 300 kHz. The advanced multihit analysis software was able to detect $10.245 \cdot 10^6$ individual hits in this data set, of which $7.259 \cdot 10^6$ (70.9%) hits could be analyzed by the 14 redundant reconstruction methods described in section 4.2.3. These valid hits are composed out of $6.643 \cdot 10^6$ (91.5%) first hits, $585 \cdot 10^3$ (8.1%) second hits and $29 \cdot 10^3$ (0.4%) third hits. In total a significant multihit rate of 8.5% is observed which emphasizes the importance of multihit detection, even though in average only every tenth laser pulse photoemits an electron at this specific event rate.

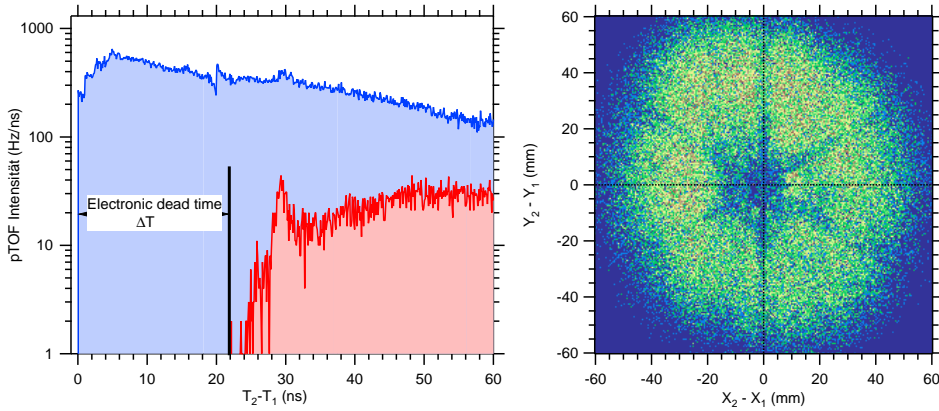


Figure 4.20: (a) Semi-logarithmic plot of the TOF correlation function $\text{CorT}_{12} = T_2 - T_1$ with (blue) and without (red) the advanced reconstruction routine. (b) The photoemission intensity as function of the in-plane position correlation $\text{CorXY}_{12} = \{X_2 - X_1, Y_2 - Y_1\}$ is depicted within the electronic dead time ΔT_{dead} . The sections of the Hexanode, which are insensitive for multihits within ΔT_{dead} , are indicated by yellow lines.

To analyze the multihit capability in more detail, the probability of multihit events was systematically studied by variation of the event rate¹¹ upon changing the laser fluence. Fig. 4.19 shows the relative hit rates as function of the event rate, which underline the importance of the multihit analysis as event rates of ~ 100 kHz leads to a fraction of $\sim 20\%$ multihits. A single hit analysis would have to discard this significant fraction of events and thus is inefficient. Focusing on low event rates of < 30 kHz, the occurrence of double hits is surprising since in average only every 10^{th} laser pulse photoemits an electron. Extrapolating the data for < 90 kHz to the limit of vanishing event rate yields a ratio of $94.(8)\%$ single hits and $4.5(1)\%$ second hits. Hence, a stochastic Poisson model systematically overestimates the single hit probability and underestimates the double hit probability. This counterintuitive behavior could be explained by laser fluctuations that significantly increase the event rate for a few μs but are not detected by a standard rate meter with a time constant of > 1 ms. Another explanation involves the correlation of two photoemission events. Here, the energy of an absorbed electron or photon is shared between *two* emitted electrons. Such two-electron emission events are studied with Auger coincidence electron spectroscopy [Haa78, Bar96, Kir95], which focuses on so-called $(e, 2e)$ reactions, whereas two electron photoemission spectroscopy investigates $(\gamma, 2e)$ reactions [Her98, Hat04, Hat08]. The study of these phenomena requires to determine the mesoscopic temporal structure of the laser pulses and perform coincidence analysis of the energy-sharing in double hit events. However, the detailed study of these multihit events is beyond the scope of the present work.

¹¹Only hits, which have been recorded on at least two of the three anode layers, were analyzed to ensure a reliable data set

The multihit capabilities, as discussed in chapter 4.2.3, rely to a large extent on the redundant Hexanode design with three wire layers and the time-sum based reconstruction of multihit events beyond the electronic dead time. To exemplify these advantageous capabilities, the TOF correlation function $\text{CorT}_{12} = T_2 - T_1$ is plotted in Fig. 4.20(a) for a data set acquired with 29 kHz event rate. Here, T_1 and T_2 denote the TOF of the first and second electron, respectively. Without the advanced reconstruction routine (red), no second hit can be recorded within the total electronic dead time of the digitizing electronics of $\Delta T_{\text{dead}} \approx 22$ ns. In contrast, the time-sum based multihit reconstruction (blue) not only recovers hits within the electronic dead time $\text{CorT}_{12} < \Delta T_{\text{dead}}$, but also increases the number of valid hits for $\text{CorT}_{12} > \Delta T_{\text{dead}}$ by almost an order of magnitude. The latter is explained by the reconstruction of missing and mixed up anode signals, which is provided by the advanced reconstruction routine [Roe06].

Fig. 4.20(b) shows the spatial correlation function $\text{CorXY}_{12} = \{X_2 - X_1, Y_2 - Y_1\}$ of the in-plane position $\{X_1, Y_1\}$ and $\{X_2, Y_2\}$ of the first and second hit, respectively. The hits depicted were exclusively reconstructed within the electronic dead time ΔT_{dead} . The ~ 7 mm wide sections of each Hexanode layer, which are insensitive to multihits within ΔT_{dead} , are indicated by yellow lines. The Hexanode is only "blinded" in the center, in the outer regions the third redundant layer can supply the necessary information for the reconstruction.

Conclusions

In conclusion, a novel position-sensitive TOF electron spectrometer was designed, implemented and tested, which enables simultaneous energy- and angle-resolved photoemission experiments by pulsed laser sources. The spectrometer is capable to record the in-plane impact position along with the TOF of the photoemitted electrons and thereby determines the complete electron velocity vector in "a single shot". The two-dimensional detector allows determining both polar and azimuthal photoemission angles with high precision and can perform angle-resolved experiments without any compromise in energy resolution. Furthermore, the complete hard- and software implementation of the spectrometer is optimized to analyze multihit events, which is crucial for laser-based photoemission experiments. The capabilities of the pTOF spectrometer enable efficient investigations of ultrafast electron relaxation dynamics in low-dimensional materials surfaces that regularly exhibit anisotropic quasi-2D and quasi-1D band structures. A first experiment employing the pTOF spectrometer for time-resolved 2PPE investigates the k -dependence of hot electron lifetimes in quasi-1D metallic nanowires in $4\times 1\text{-In/Si}(111)$ and is presented in chapter 6.

5 Ultrafast Dynamics in Quantized Pb/Si(111) Bands

The quantum well states (QWSs) (or subbands) in epitaxial Pb films on Si(111) present a quasi-2D model system. The *occupied* QWSs have been studied by laser-induced photoemission spectroscopy (PES) at 6 eV photon energy. The binding energies of the QWS were found in good agreement with density functional theory (DFT) calculations for a freestanding Pb slab. The *unoccupied* QWS in Pb/Si(111) have been investigated with monochromatic two-photon photoemission (2PPE) at a photon energy of ~ 4 eV. Up to four unoccupied QWSs as well as an image potential state (IPS) are identified and analyzed as a function of Pb thickness. In contrast to the occupied QWSs, the binding energy of the unoccupied QWSs systematically deviates from DFT calculations, which suggests to improve the theoretical modeling by taking the Si substrate explicitly into account. Furthermore, an oscillation of the work function with a period of 2 ML was observed as a function of film thickness, which correlates nicely with the oscillatory electron density at the Fermi level E_F determined from the photoemission spectra.

The ultrafast electron dynamics in the unoccupied QWS of Pb/Si(111) has been investigated by femtosecond time-resolved 2PPE. Using 1.9 eV photon energy for optical excitation electron-hole pairs are formed in the Pb film and in the Si substrate. The hot electron population in the QWS exhibits a bi-exponential decay. The slower decay component with decay times of 130 fs and 900 fs is attributed to delayed filling of the states in the adlayer due to electronic relaxation in the Si(111) substrate. The faster decay of 5 – 140 fs is caused by electron-electron (e-e) scattering in the Pb film. At a first glance, the extracted decay times increase toward E_F as predicted by the Fermi liquid theory (FLT). However, by investigation of the quantized electronic structure more detailed insight into scattering among defined subbands has been gained. The simultaneous decay and rise in the two lowest unoccupied QWS is attributed to inter-subband scattering. Thereby, the importance of inter-subband decay in low-dimensional metallic systems is demonstrated in addition to intra-subband scattering processes considered in FLT and derived descriptions. Moreover, the decay times of the lowest unoccupied quantum well state (luQWS) due to e-e scattering in the metal film exhibits a strong modulation as function of film thickness with a period of 2 ML. The coverage dependent decay times are compared to the predications of FLT for two and three dimensional electron systems. Interestingly, the modulation of the lifetimes can be understood within 3D FLT by consideration of the quantized binding energies of the QWS and the phase space available for scattering.

Finally, first studies of the ultrafast dynamics in the occupied part of the quantized Pb/Si(111) band structure were carried out with time-resolved PES employing intense 1.5 eV pump pulses with absorbed fluences in the order of $100 \mu\text{J}/\text{cm}^2$. The shift of the occupied QWS binding energies on a 100 fs timescale is compared to a simulation within the two temperature model (2TM). The transient *increase* of the binding energy points to an ultrafast hardening of the Pb crystal structure due to a quasi-instantaneous change of the screening in the metal film. Moreover, an oscillation of the

binding energy of the highest occupied quantum well state (hoQWS) at a frequency of 2.2 THz was resolved, which coincides with a peak in the phononic density of states (DOS) due to a longitudinal phonon along the Γ -L film direction. Thus, the binding energy modulation is assigned to the excitation of a coherent phonon in the film direction. This work highlights the importance of electron-phonon (e-ph) coupling in solids, where (i) incoherent e-ph scattering leads to an equilibration of the energy content in the electronic and phononic subsystem and (ii) coherent e-ph coupling drives a coherent phonon mode by a dispersive excitation mechanism.

Experimental Details

The experimental setup and the preparation procedures have been described in detail in chapter 3. In brief, epitaxial Pb films are grown as wedges (chapter 3.3.1) under ultrahigh vacuum (UHV) conditions in two steps after substrate preparation. First, the Si(111)- 7×7 surface reconstruction is formed. Second, the dangling Si bonds are partially saturated by preparation of the β -($\sqrt{3} \times \sqrt{3}$)R30°-Pb/Si(111) reconstruction. Subsequently, Pb was evaporated from a Knudsen cell and epitaxial Pb(111) wedges are grown. During preparation and photoemission experiments, the temperature was kept at 100 K to avoid island formation and surface diffusion [Hup01]. The evaporation rate was monitored by a Quartz balance and crosschecked after deposition by comparison of the observed binding energies of occupied QWS with DFT calculations from Wei and Chou [Wei02a]. The coverage scale derived from analysis of the PES data then was transferred to the 2PPE experiments by overlapping the laser for 2PPE on exactly the same spot on the sample. This procedure results in an intrinsically correlated coverage scaling for both the PES and 2PPE experiments.

For laser based PES, photons with $h\nu = 6.0$ eV are generated by frequency quadrupling the output of a mode-locked amplified Ti:Sapphire laser system at 300 kHz repetition rate (chapter 3.1.1 and appendix E). Laser pulses at 5.3 eV photon energy were produced by frequency-doubling the output of an optical parametric amplifier (OPA) driven by the regenerative amplifier (RegA). For bichromatic 2PPE experiments the RegA output drives an OPA operating in the visible (VIS) spectral range and its tunable signal output is frequency doubled in a β -barium-borate crystal to generate the second harmonic in the ultraviolet (UV) spectral range. The time-correlated pairs of VIS and UV laser pulses are focused into the UHV chamber and spatially overlapped on the Pb film. For 2PPE spectroscopy the pulses overlap in time. For time-resolved 2PPE spectroscopy $h\nu_1$ and $h\nu_2$ are delayed with respect to each other by a controlled variation in the optical path length.

The photoelectron yield was detected by an electron time-of-flight (TOF) spectrometer (chapters 3.2.2 and 3.2.3). From the kinetic energy E_{kin} the binding energy referenced to the Fermi level $E - E_F = E_{kin} + \Phi - h\nu$ was calculated¹, where Φ denotes the work function and $h\nu$ the probe photon energy.

¹The binding energy scale in conventional PES is defined to be positive for bound states below E_F . However, to obtain a consistent binding energy scale for initial states at $E - E_F < 0$ and intermediate states at $E - E_F > 0$ in PES and 2PPE, respectively, the term "binding energy" describes the energy of a given state with respect to E_F .

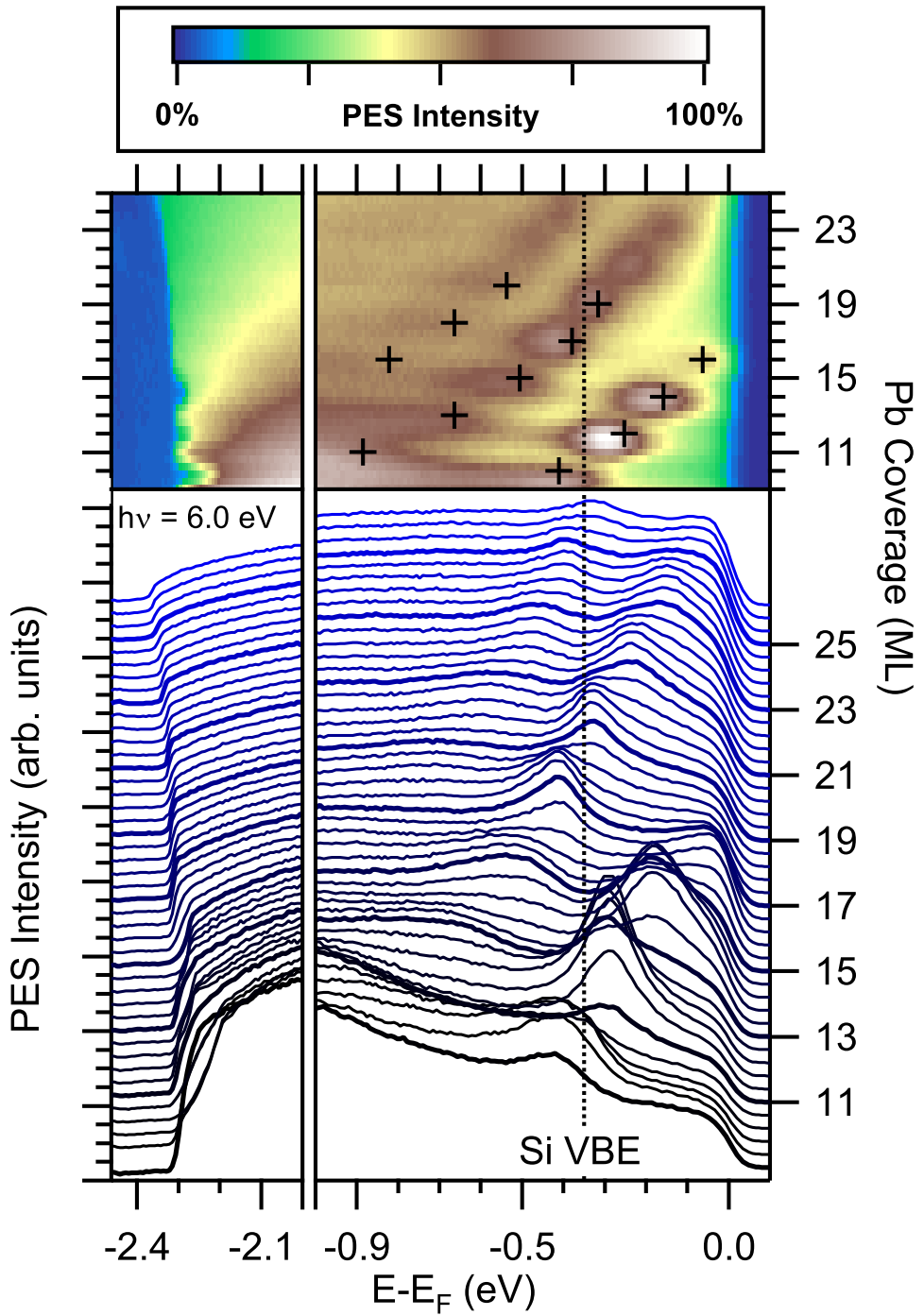
5.1 Structure of the Occupied QWS

In Fig. 5.1 photoemission spectra of a Pb wedge with a slope of 4.0 ML/mm are displayed as spectra from 9 – 26 ML coverage (lower panel) which were taken at $h\nu = 6.0$ eV with a lateral resolution of 100 μm by moving the sample in front of the TOF spectrometer. The upper panel shows a color-coded representation of the photoemission intensity. The data exhibit a series of occupied QWSs dispersing with coverage, where particularly sharp states are observed in the energy range of the indirect band gap of the Si substrate as indicated by the upper valence band edge (VBE) at $E - E_F = -0.35$ eV [Dil06]. These QWSs are *energetically* located in the indirect Si band gap and are thus *spatially* confined to the Pb film as the wave function of the QWS cannot penetrate into the substrate. At energies $E - E_F < -0.35$ eV much broader quantum well resonances (QWRs) are observed which are degenerate with occupied Si bands. These states are more prominently seen in Fig. 5.4 discussed further below. The theoretical results for the QWS binding energies from a DFT calculation of Wei and Chou [Wei02a] for a free standing Pb film of variable thickness are displayed as crosses in the color-coded plot of the photoemission yield. Clearly, the DFT data agree well for all three branches of occupied QWSs observed experimentally.

The left panel of Fig. 5.1 focuses on the low-energy cutoff of the photoemission spectra which is a direct measure of the global sample work function. In PES, the global work function - rather than the local one - is accessible due to the macroscopic spot size of the incident light. Contributions from different patches of the surface are averaged which results in a finite width of the low-energy cutoff. Nevertheless, below a coverage of 16 ML a work function modulation is clearly observed that vanishes above 16 ML. The work function oscillations are discussed in detail in section 5.1.1.

In order to perform a proper analysis of the data it is necessary to take the finite laser spot size into account. On a wedge with a slope of 4.0 ML/mm as in Fig. 5.1, the laser spot size of 150 μm averages over a coverage distribution of 0.6 ML nominal width. The observation of pronounced QWS peaks and work function modulations at low coverage is not hindered by the averaging process which is evident from the contrast of the PES intensity at subsequent monolayers. The intensity of the QWS peaks exhibits a pronounced oscillation with film thickness: For an even film thickness of 10 ML a high photoemission intensity is observed below E_F , which is significantly reduced at 11 ML and reappears at 12 ML coverage. As the coverage increases to more than 20 ML, the averaging within the laser spot size reduces the contrast of the discrete QWSs and the peaks merge into a continuous branch of QWSs. The absence of the work function modulation for a coverage exceeding 16 ML is explained by

Figure 5.1 (*facing page*): Photoemission spectra of Pb/Si(111) for various thickness observed on a Pb wedge of 4.0 ML/mm slope using 6.0 eV photon energy. The right panel shows a series of discrete QWS dispersing with Pb coverage. The silicon valence band edge (VBE) is indicated. The upper panel displays the identical data in a false-color representation. The QWS binding energies (+) from a DFT calculation [Wei02a] are included. In the left panel the modulation of the low-energy cutoff is highlighted which is a direct measure of the global work function of the Pb film.



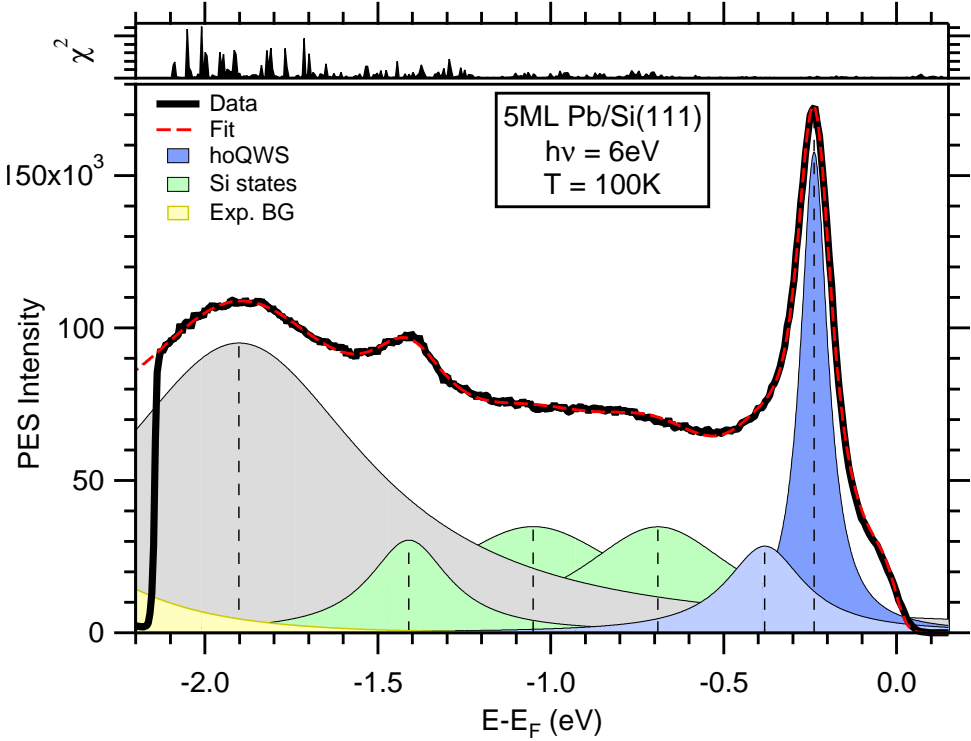


Figure 5.2: Exemplary fit of the PES spectra for 5 ML Pb/Si(111) with 6 Lorentzian lines. The χ^2 function is indicated in the upper panel. The highest occupied QWS (hoQWS) presents a sharp peak (blue) at $E - E_F = -0.24$ eV and the asymmetric line shape is explained by patches with 3 ML coverage that give rise to a hoQWS peak at $E - E_F = -0.38$ eV. The green shaded peaks indicate Si states that are discussed in the context of the work function oscillations in section 5.1.1.

neighboring patches of ± 1 ML in the laser spot which give an averaged contribution and broaden the secondary edge. The decrease of the work function by 110 meV for > 16 ML and the broadening of the QWS peaks point to a roughening of the Pb films at these coverage.

The PES spectra are further analyzed by fitting a number of Lorentzian lines to the spectra, which are convoluted with a Fermi-Dirac distribution of temperature $T = 100$ K and a Gaussian instrument function of 50 meV width. Additionally, an exponential decaying background due to scattered secondary electrons can be taken into account. An exemplary fit for 5 ML Pb/Si(111) with 6 Lorentzian lines is shown in Fig. 5.2. Clearly, the fit results in an excellent description of the spectra evidenced by the χ^2 function in the upper panel. The hoQWS presents a sharp peak at $E - E_F = -0.24$ eV (blue). The asymmetric line shape is explained by patches with 3 ML coverage that give rise to an additional weak hoQWS peak at $E - E_F = -0.38$ eV (light blue). Four more Lorentzian lines are considered to

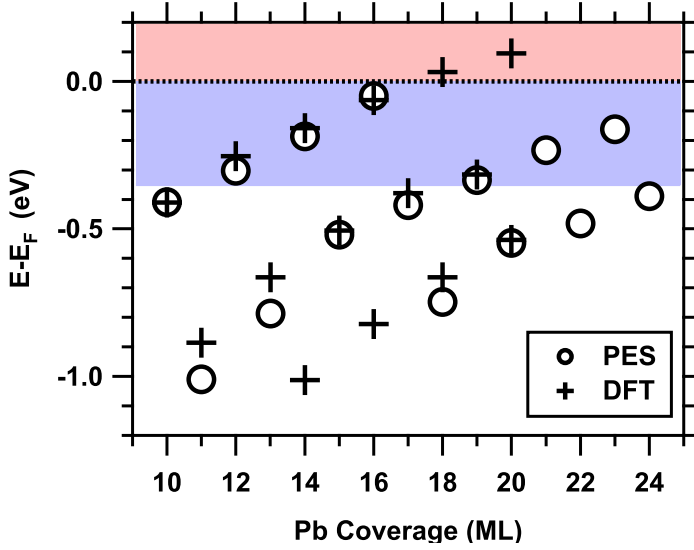


Figure 5.3: QWS binding energies as function of coverage as observed by PES and calculated by DFT [Wei02a]. The experimental QWS binding energy were determined from the peak maxima in the photoemission spectra and the error is given by the size of the symbols (\circ). The gray shaded area indicates the fundamental Si band gap.

describe the whole spectrum appropriately. Three peaks are assigned to states of the Si substrate (green). Due to the comparably small photon energy of $h\nu = 6$ eV the mean free path of the photoelectrons amounts to several 10 \AA , compare to Fig. 2.25 and thus also features from the band structure of the underlying substrate can be sampled. The weak peaks at $E - E_F = -0.70$ eV, -1.05 eV and -1.40 eV can be seen more prominently in Fig. 5.4, where an even lower photon energies of $h\nu = 5.3$ eV facilitates their observation. The peak at $E - E_F = -1.90$ eV is not assigned to any specific state and serves only to describe the spectrum completely. Finally, it is noted that the exponentially decaying secondary electron background (yellow) does not play a major role in these PES spectra, which supports a high crystalline quality of these epitaxial films.

In Fig. 5.3 the binding energies determined from the fitting procedure of the photoemission spectra are compared to the DFT calculation from Ref. [Wei02a] and are generally in good agreement. Some deviations, especially of the QWRs, which are not confined by the Si band gap, might be attributed to the influence of the Si interface. In a phase-accumulation model, see chapter 2.1.1, electrons of the Pb film are confined by the vacuum barrier and the barrier due to the energy gap of the substrate, such that reflection at the interfaces results in two energy-dependent phase shifts at the film surface and the film-substrate interface, given by ϕ_s and ϕ_i , respectively. These phase shifts have to fulfill the Bohr-Sommerfeld quantization rule, see equation (2.2). The presence of the Si interface results in an additional phase shift of the QWS wave function due to a finite penetration of the wave function into the substrate which in turn alters their eigen-energies.

As a result the QWS binding energies observed in very thin films of < 10 ML tend to be larger than predicted by vacuum slab models as the penetration of the wave function into the substrate effectively generates a wider quantum well. Especially the quantum well resonances at $E - E_F < -0.35$ eV experience this effective widening of the potential well, which results in a significant increase of the binding energy compared to a freestanding Pb slab. Turning to the QWSs confined in the narrow energy region of the Si band gap $E - E_F > -0.35$ eV one notices that discrete states are observed in the uppermost branch only at coverage of 10, 12, 14, 16 ML, and in the lower branch at 17, 19, 21, 23 ML, respectively.

This special feature of the Pb/Si(111) QWSs is explained by the influence of the Fermi wave vector k_F along the L- Γ direction, where the quantization occurs. The periodicity of QWSs crossing the Fermi level is calculated according to equation (2.9) to be $\Delta\Theta = \pi/(k_F d) = 2.24$ ML, see chapter 2.1.2. This means that initially a QWS is expected to cross the Fermi level at every 2 ML because locally only discrete, integer numbers of ML are possible. The small difference between 2.24 ML and 2.0 ML generates a beating effect such that at 4×2.24 ML = 9.0 ML the hoQWS is expected at *odd* and not at *even* coverage and vice versa. Exactly this odd-even switching behavior is found here as the hoQWS are observed at even coverage from 10 ML to 16 ML, each separated by 2 ML. For a coverage > 17 ML the hoQWS can only be supported in a Pb film with odd number of monolayers which is manifested by the series of QWS from 17 to 23 ML.

In this context it is interesting to note an PES study of uniform Pb films on Si(111) [Zha05], where this odd-even switching is reported for 13 ML and 22ML film thickness. The results presented here show an odd-even switching at a film thickness of 16 ML, which are in excellent agreement with the theoretical work of reference [Wei02a] where a switching is predicted for 7 and 16 ML as well as with previous results from PES [Dil04]. In the comparison of QWSs binding energies from different work an odd numbered film thickness difference of 1 or 3 ML is frequently encountered. This is explained by a variable thickness of the wetting layer ranging from 1 – 3 ML [Hup01] and different ways how studies of Pb clusters take the wetting layer into account [Jia07]. For example, the formation of the "magic islands" heights is explained by a minimization of the DOS at E_F , which is realized when the hoQWS is far from E_F . The "magic islands" occur at absolute thicknesses of 15 and 17 ML (including the wetting layer) [Ote02], which agrees well to the large distance of the hoQWS from E_F analyzed here. Summarizing, the occurrence of QWS occupation with a period of 2.24 ML provides a natural explanation for the specific stability of even and odd numbered film thicknesses, on account of the principle of total energy minimization [Pag99, Pag02].

5.1.1 Workfunction Oscillations

An oscillatory behavior of the work function as a function of film thickness in ultrathin metal films has long been predicted by calculations employing a jellium model [Sch76] and was experimentally confirmed for the case of Ag/Fe(100) [Pag02]. Qualitatively, the surface dipole is modulated due to a change of the electron spill-out of the hoQWS wave function. For Pb/Si(111), the work function oscillation was theoretically re-

investigated recently by a DFT calculation of a freestanding Pb slab [Wei02a]. In this work, a pronounced oscillation of the global sample work function as a function of film thickness was resolved, which is directly correlated to the modulation of the electron density at the Fermi level. The use of Pb wedges allows to follow the work function modulation as the coverage is tuned quasi-continuously, as will be shown in the following.

For a more quantitative analysis of the thickness-dependent work function changes, Pb/Si(111) wedges with a reduced thickness gradient and thus increased coverage resolution have been prepared. This approach reduces the problem of averaging over different thicknesses by the finite laser spot size. The PES data taken on such a shallow wedge of 1.50 ML/mm slope are shown in Fig. 5.4 as spectra (bottom) and color-coded intensity plot (top). The decreased slope enhances the thickness resolution to 0.15 ML per spectrum and the QWSs at even film thickness of 10, 12, and 14 ML are well separated. The high contrast of the QWSs obtained is remarkable: For even thickness intense and sharp QWSs are observed in the region of the Si bandgap, which completely vanish at odd coverage, leaving only a continuous background from elastically and inelastically scattered electrons. The pronounced Fermi edge observed for all film thicknesses indicates the metallic character of the surface and the presence of an intact Pb film. This proves that indeed the averaging due to the finite laser spot size of the scanned region can be neglected. For such a sample a pronounced work function oscillation is observed in the low-energy cutoff in Fig. 5.4 which is followed over the entire wedge.

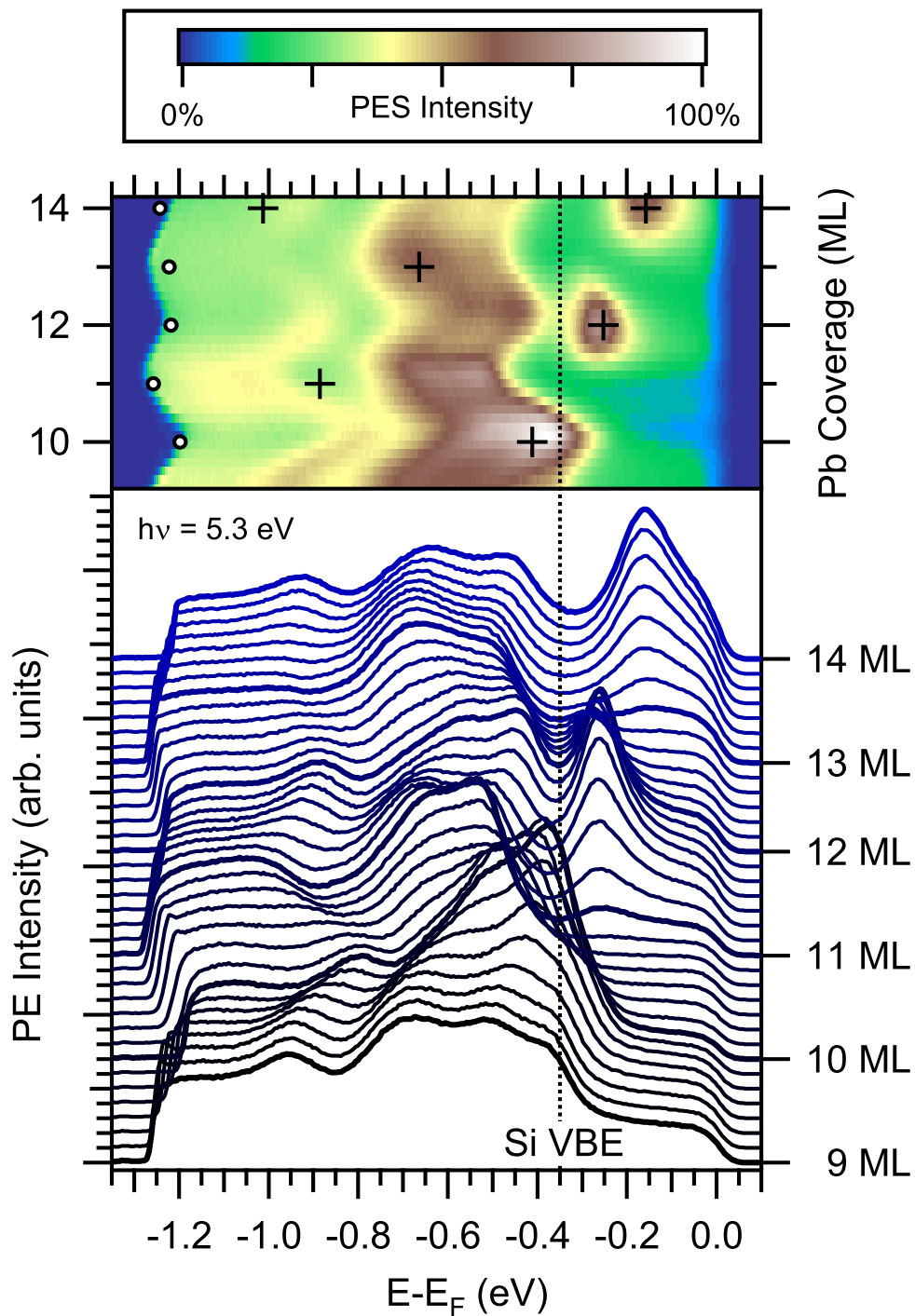
The work function as function of film thickness obtained from the spectra shown in Fig. 5.1 and Fig. 5.4 is plotted in the lower panel of Fig. 5.5(a) in comparison to the theoretical values of Ref. [Wei02a]. Not only is the periodicity of the experimentally determined oscillations in good agreement with the DFT calculation, but also the amplitude of the modulation matches fairly well the calculated data. The work function oscillations are further analyzed by fitting a phenomenological function [Wei02a] to the data:

$$(5.1) \quad \Phi(\Theta) = \frac{A|\sin(k_F d \Theta + \phi_0)| + B}{\Theta^\alpha} + C \quad ,$$

where A , B , C , α , and ϕ_0 are constants. The coverage Θ is in this description a continuous variable as used in jellium models [Sch76]. For fixed interlayer spacing d the fit yields the Fermi wave vector k_F , which determines the period of the work function modulation. The denominator Θ^α expresses the decreasing contribution of each newly occurring QWS such that for $\Theta \rightarrow \infty$ the modulations disappear. The exponent $\alpha \approx 1$ is determined in agreement with other reports [Sch76, Wei02a].

The results of the fit of the PES and DFT data are displayed in Fig. 5.5(a) as solid and dashed lines, respectively. At first sight, a continuous change of the work function

Figure 5.4 (*facing page*): Photoemission spectra of Pb/Si(111) measured at 5.3 eV photon energy on a wedge with 1.5 ML/mm slope. The Si valence band edge (VBE), the QWS binding energies (+) and work function modulation (o) calculated by DFT [Wei02a] are indicated.



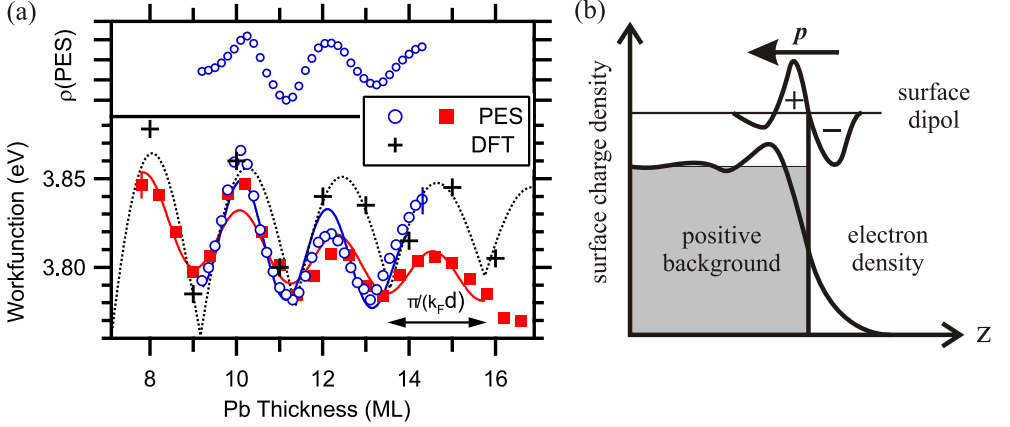


Figure 5.5: (a) Work function oscillations as a function of film thickness observed in the Pb wedges on Si(111) deduced from the photoemission spectra of Fig. 5.1 (■) and Fig. 5.4 (○). The measured data was offset by +186 meV (■) and -183 meV (○) in order to match the theoretical prediction from DFT [Wei02a]. The solid and dashed lines are fits of equation (5.1) to the data points convoluted with a Gaussian function taking into account the finite laser spot size. The upper panel shows the PES intensity $\rho(\text{PES})$ integrated over the region $E - E_F > -0.35$ eV of the Si bandgap. (b) Sketch of the electron spill-out at the film-vacuum interface, which gives rise to a surface dipole p . Hence, the modulation of the electron density due to the periodic occurrence of the QWSs results in oscillations of the work function.

as in a jellium model might appear counterintuitive because the coverage increases locally in integer steps of 1 ML. The experimental observations are explained by the layer-by-layer growth of the films and the finite resolution of the laser spot. As the coverage Θ is increased on a sub-monolayer scale, a fraction $0 \leq x \leq 1$ of the probed region has a higher thickness which exhibits a different work function. These different surface patches are averaged within the laser spot. For example, a $\Theta + x$ ML film consists of fraction $1 - x$ patches with Θ ML and x patches with $\Theta + 1$ ML thickness. The work function of a $\Theta + x$ ML film therefore is the weighted arithmetic average of the work functions of a Θ and $\Theta + 1$ ML film.

Fitting a convolution of equation (5.1) and a Gaussian instrument function for 7.8 – 15.8 ML and 9.2 – 14.0 ML results in periods of 2.2(1) ML and 2.0(1) ML for the steep wedge in Fig.5.1 and the shallow wedge in Fig.5.4, respectively. These periods suggests that the work function modulation is directly linked to the periodic modulation of density of states at the Fermi level by the hoQWS. The comparison of the position of the maxima of the work function with the appearance of the hoQWS reveals that a confined QWS close to the Fermi level coincides with a maximum of the work function. This is corroborated by a qualitative model of the electron spill-out of the QWS wave function at the Pb-vacuum interface. The work function of a metal surface depends on two basically independent contributions of the chemical potential μ and the surface dipole barrier D [Lan70, Lan71, Leu03]:

$$(5.2) \quad \Phi = -\mu + D = -\mu - \frac{e\hat{n} \cdot \vec{p}}{\epsilon_0}$$

Here, \hat{n} is a unit vector normal to the surface and \vec{p} polarization vector, which points from the negative to the positive charge spill-out and usually is oriented toward the crystal. Since the chemical composition of the surface is constant throughout the wedge, the surface dipole contribution must be modulated by the occurrence of the QWSs. The electron wave functions decay exponentially into the vacuum, which leads to a redistribution of charges at the surface and so-called Friedel oscillations [Fri54], as depicted in Fig 5.5(b). An electron that traverses the metal-vacuum interface therefor is attracted by the uncompensated positive charges of the ion cores and repelled by the electronic excess charge density. This results in a linear scaling of the work function with the dipole barrier D .

The penetration of a plane wave function Ψ of an electron with energy $E < V_0$ at a rectangular potential barrier with height V_0 is given by [Nol04]:

$$(5.3) \quad \Psi(z) \propto \exp(-z\sqrt{V_0 - E}) \quad .$$

Thus, a hoQWS close to E_F experiences a small barrier and will have a significant electron spill-out into the vacuum which increases the surface dipole and thereby creates a large work function. The opposite situation of a hoQWS far from E_F generates a small electron spill-out with a small surface dipole and a small work function. This interpretation of the work function in terms of electron density at E_F is supported by the electron density analyzed by PES. In the upper panel of Fig. 5.5(a) the photoemission yield $\rho(\text{PES})$ integrated in the region of the Si bandgap ($E - E_F > -0.35$ eV) is shown as function of coverage for the shallow wedge. A maximum (minimum) of the electron density appears, which corresponds exactly to the maximum (minimum) of the work function measured for the more shallow wedge (◦). The amplitude of this modulation is observed in the electron density and can be linked directly to the magnitude of the work function oscillation.

Interestingly, there are conflicting reports in the literature regarding the precise microscopic connection of the work function oscillations and the occurrence of the hoQWS close to E_F . Ma et al. and Jia et al. [Ma07, Jia07] observed oscillations in a scanning tunneling spectroscopy (STS) study of the surface reactivity of O_2 on Pb/Si(111) and interpreted this as Φ modulation. The authors argue that *"The closer the hoQWS is to the Fermi energy, the smaller the value of the local work function is"* and explain *"The higher the film density of states near the Fermi level, the lower the potential for electrons to escape, and hence the lower the work function."* This argumentation, however, might confuse the spill-out of a given hoQWS with the spill-out at E_F . Only in a recent publication [Zha08] the authors reconsider their interpretation.

To elucidate this point, a simple plane wave model of the spill-out at a rectangular potential barrier according to equation (5.3) is depicted in Fig. 5.6. To model the Pb-vacuum interface barrier a potential depth of $V_0 = 10$ eV is assumed and the Fermi level is fixed at 6 eV, which corresponds to a constant chemical potential and results in $\Phi = 4$ eV, comparable to the Pb bulk value. The plane wave function at $z < 0$ are matched at $z = 0$ to the exponentially decaying wave functions on the vacuum side. The left panel depicts the electron density for the hoQWS at 11 ML and 12 ML with the measured binding energy of $E - E_F = -0.90$ eV and $E - E_F = -0.25$ eV, respectively. Clearly, for the hoQWS close to E_F the spill-out S increases, which is

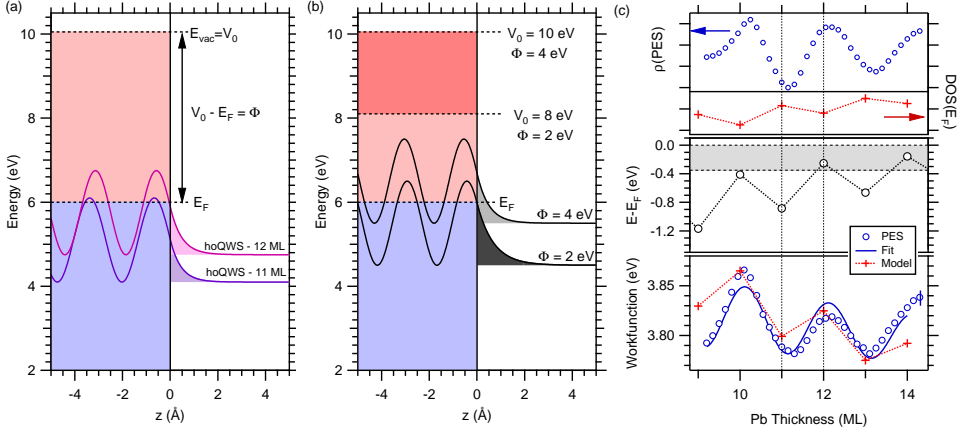


Figure 5.6: Modeling the work function oscillations as extracted from PES by the spill-out of the hoQWS. (a) A hoQWS far from E_F (11 ML) results in a smaller electron spill-out than a hoQWS close to E_F (12 ML). A larger (smaller) spill-out induces a larger (smaller) surface dipole contribution to Φ . (b) A large (small) Φ induces a small (large) electron spill-out at E_F , which is shown for an exaggerated example. Thus, the $\text{DOS}(E_F)$ modulation is a secondary effect caused by the change of Φ . (c) The Φ modulations (bottom) due to the spill-out of the hoQWS are calculated from the experimental binding energies (central) and agree nicely with the PES data. In contrast, the $\text{DOS}(E_F)$ (top) exhibits a qualitatively opposite behavior compared to the electron density from PES. Thus the $\text{DOS}(E_F)$ can not explain the origin of the Φ oscillations. See text.

evaluated by integration

$$(5.4) \quad S = \int_0^{\infty} dz \Psi(z)^2 \quad .$$

Going from 11 to 12 ML the spill-out in the model increases by 17%, whereas the experimentally determined Φ increases by 1% from 3.782 eV to 3.819 eV. Φ is estimated within the model by assuming a linear scaling with the spill-out

$$(5.5) \quad \Phi \propto S/\Theta + C$$

similar to equation 5.1.1 The modeled workfunction is depicted in the lower panel of Fig. 5.6(c). Although the simple model calculation is not self-consistent and the QWS induced surface dipole is treated as small perturbation, the odd-even behavior of Φ is nicely explained by the measured energetic positions of the hoQWSs (central panel) and the associated DOS (upper panel).

In the STS measurements under discussion [Jia07, Ma07] the $\text{DOS} \pm 5 - 10$ meV around E_F is sampled and thereby the DOS for a fixed energy $E = E_F$ is evaluated. Fig. 5.6(b) depicts the effect of a work function change on the $\text{DOS}(E_F)$. Here, an exaggerated example of $\Phi = 2$ eV and 4 eV is shown since the effect on the $\text{DOS}(E_F)$ is fairly small (1%) for the actual workfunction variation of 1%. Within this model of a potential barrier, a larger (smaller) work function results in an small

(large) $\text{DOS}(E_F)$. The $\text{DOS}(E_F)$ is modeled as a function of coverage employing the experimental hoQWS positions and $V_0 = 10$ eV to determine the surface dipole contribution to Φ due to the spill-out of the hoQWS according to equations (5.3), (5.4) and (5.5). The modeled $\text{DOS}(E_F)$ is compared to the measured electron density $\rho(\text{PES})$ in the top panel of Fig. 5.6(c). A hoQWS far from E_F results in a large $\text{DOS}(E_F)$, which is in accordance to the STS studies. However, the electron density $\rho(\text{PES})$ and the modeled $\text{DOS}(E_F)$ show a qualitatively opposite behavior. This leads to the conclusion that the spill-out at E_F does not induce the observed work function oscillations. Rather, the modulation at E_F is a secondary effect that is caused by the opposed spill out of the hoQWS and the associated Φ modulation.

Summarizing, the hoQWS close to (far from) E_F induces a large (small) electron spill-out, which leads to a large (small) surface dipole contribution and a large (small) workfunction. In turn, the large (small) work function gives rise to an small (large) electron spill out at E_F . In this respect the microscopic mechanism of the oscillatory surface reactivity of O_2 on Pb/Si(111) reported in [Ma07, Jia07, Zha08] is surprising since the reactivity scales with the DOS only a few meV around E_F , whereas the QWSs themselves interact indirectly by modulation of the electron spill-out at E_F and do not contribute directly to the bonding.

5.1.2 Substrate Contributions

As pointed out in the context of the fitting procedure in Fig. 5.2, the increased bulk sensitivity due to the low kinetic energy of < 1 eV of the photoelectrons generated by the laser allows the observation of electronic states of the Si substrate. Clearly, additional peaks below the Si VBE are observed in Fig. 5.2 and Fig. 5.4. In Fig. 5.7(a), the oscillating binding energies of the states at $E - E_F \approx -0.9$ eV (A), -0.6 eV (B) and -0.5 eV (C) are obtained from a Lorentzian line fit and displayed as solid lines. These peaks can not be assigned to any QWSs because the binding energy of these states is modulated and these features are observed at all film thicknesses. Furthermore, they exhibit no intensity modulation as function of film thickness.

Fig. 5.7(b) compares the modulated binding energies of the three states to the workfunction modulations and the DOS at E_F as determined by PES. Notably, the oscillations of the binding energies have an about three times larger amplitude than the work function oscillations and correlate nicely to $\rho(\text{PES})$, where a large DOS induces a peak shift towards E_F . The significant modulation of the binding energies with the characteristic 2 ML period suggests that the peaks A, B and C originate from hybridized interface states or Si bulk states, which experience an oscillatory interaction with the metallic DOS.

The observed binding energies are compared to the data from angle-resolved photoemission spectroscopy (ARPES) experiments at the clean 7×7 -Si(111) surface, where three non-dispersing surface state bands are observed at $E - E_F = -0.5$ eV (S1), -0.9 eV (S2) and -1.5 eV (S3) [Uhr85, Nor86]. The S1 state is associated with adatom and back-bond states, whereas the S2 state stems from the rest atoms [Los00, Bar06]. In contrast to the S3 state, the S1 and S2 states strongly interact with adsorbates and are quenched² by the adsorption of 1 ML Pb [Wei92, Dil06]. This comparison suggests

²The ARPES study in [Wei92] was performed at $h\nu = 21.2$ eV and thus is more surface sensitive than the measurements at $h\nu = 5 - 6$ eV presented here.

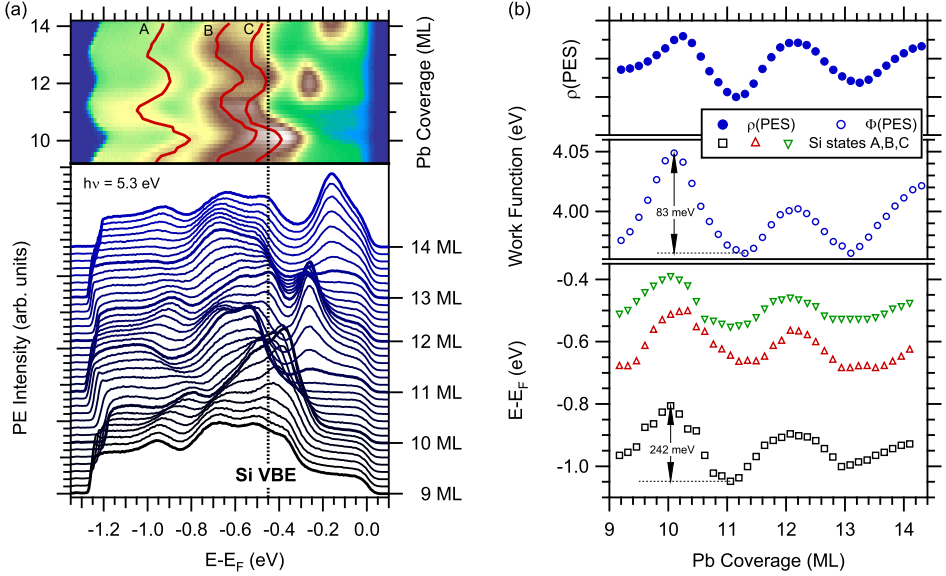


Figure 5.7: (a) PES spectra of 9 – 14 ML Pb/Si(111) as in Fig. 5.4 with three alleged Si states A,B and C indicated. (b) The modulation of the binding energies of Si states (bottom) has about three time larger amplitudes than the Φ oscillations (center). The binding energy oscillations are in-phase with the DOS at E_F (top).

that the peaks A and the double peak structure B,C might be derived from hybridized S2 and S1 states, respectively, which form at the $(\sqrt{3} \times \sqrt{3})R30^\circ$ -Pb/Si(111) reconstruction or at the boundary of the epitaxial Pb film. This assignment is consistent with peak at $E - E_F = -1.4$ eV observed in the spectrum of Fig. 5.2 being derived from the S3 state.

Turning to the fundamental physical mechanism that causes the binding energy modulations, the "attractive" interaction of the presumed Si states with the QWSs is surprising, where a large DOS due to the occurrence of a confined hoQWS in the Si bandgap shifts the binding energies towards E_F . Considering the qualitative behavior of a metal/p-semiconductor contact in the Schottky-Mott picture (see chapter 2.1.2) an increase of electron density in the metal increases the work function due to the enlarged electron spill-out and results in smaller band bending and vice versa, see Fig.2.6. At least qualitatively this can explain the modulations; of the Si states by a periodically modified band bending. This argumentation, however, can not account quantitatively for the observed binding energy modulations, which are about three times larger than the work function oscillations. In this respect, energy conservation would be violated, which points to a more evolved mechanism that enhances the binding energy modulations significantly. Other possible explanations could involve the modulation of the hybridization of the Si states with Pb bands due the modulated DOS around E_F .

To resolve the issue of the modulated Si states, a first principle calculation of the Pb/Si(111) band structure is desirable, which takes the substrate and the reconstructed interface explicitly into account. As discussed in the following, the odd-even behavior of the unoccupied QWS deviates significantly from a DFT calculation of a free-standing Pb slab [Wei02a] and an *ab initio* study of the full Pb/Si(111) structure would facilitate the understanding of the unoccupied band structure as well. If, however, a first principle study can take the long range effects of the semiconductor depletion layers and the associated band bending into account has yet to be investigated.

5.2 Structure of the Unoccupied QWS

The unoccupied electronic structure of Pb/Si(111) is investigated by single color 2PPE spectroscopy using UV laser pulses. The photon energy of $h\nu_2 = 3.75$ eV is chosen to be just below the sample workfunction, see section 5.1.1, which allows to investigate most³ bound unoccupied electronic states in Pb/Si(111). Before turning to the detailed assignment of the unoccupied states, the fitting procedures and background subtraction are discussed.

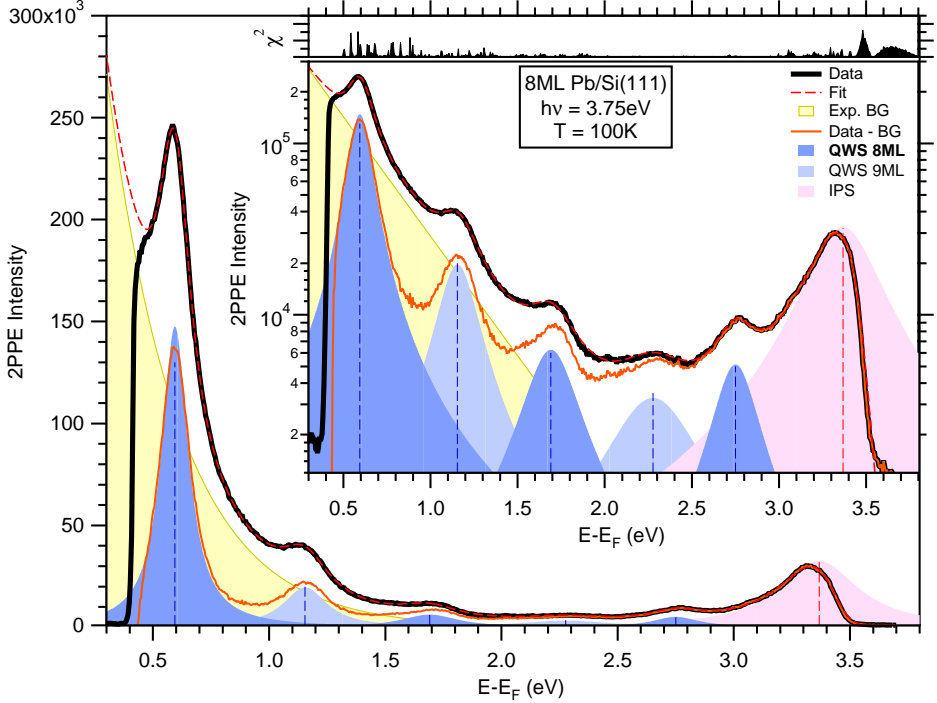


Figure 5.8: 2PPE spectrum for 8 ML Pb/Si(111) with linear and logarithmic intensity scaling. The experimental data (black line) is well described by a fit (red dashed line) of six Lorentzian peaks, an exponentially decaying background (yellow) of secondary electrons and a Fermi-Dirac distribution that is convoluted with a Gaussian instrument function. The fit of several subsequent 2PPE spectra from a single wedge allows a clear identification of the unoccupied QWS (blue) even though the crosstalk of neighboring coverage leads to additional features in the 2PPE spectrum. Moreover, an IPS in front of the Pb(111) surface is identified (pink). To further enhance the odd-even contrast, the exponential background is subtracted to yield background corrected 2PPE spectra (orange line). The χ^2 function is indicated.

In Fig. 5.8 an exemplary 2PPE spectrum for 8 ML Pb/Si(111) is shown in linear and logarithmic intensity scaling. The spectrum exhibits a series of six peaks of

³At odd coverages $\Theta > 8$ ML the hoQWS is located only slightly above E_F and is difficult to access with 2PPE, especially due to the work function oscillations.

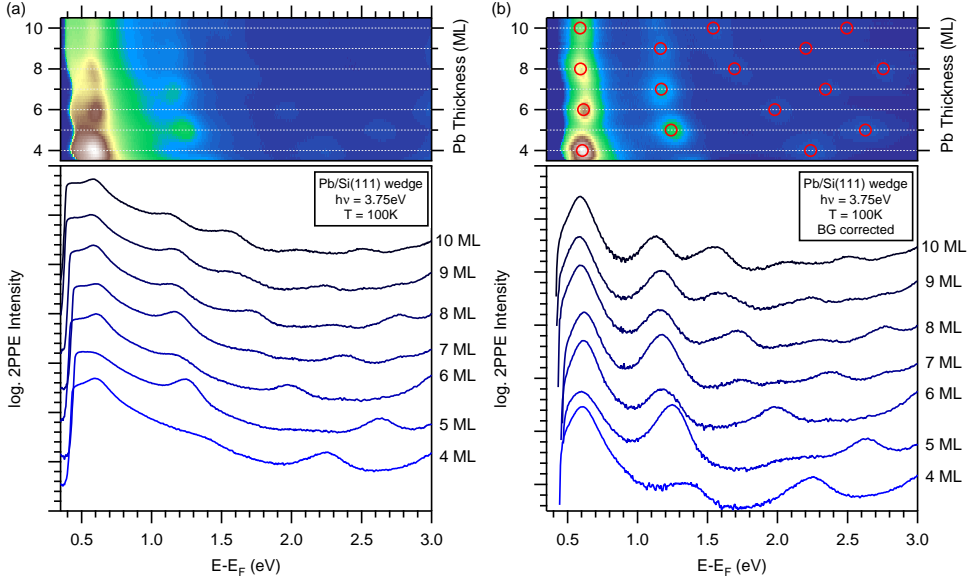


Figure 5.9: Background correction of the 2PPE spectra for a Pb/Si(111) wedge with 1.5 ML/mm slope ranging from 4 to 9 ML. The upper panels show the color coded 2PPE intensity of the spectra shown in a semi-logarithmic waterfall plot in the lower panel. (a) The original data already show a well visible odd-even contrast of neighboring coverages. (b) Subtraction of the exponentially decaying background enhances the contrast even further and allows a clear assignment of the QWS dispersion with coverage. The open circles indicate the Lorentzian peak position from the fit.

which five are identified as unoccupied QWSs of the Pb $6p_z$ band. The sixth peak $E - E_F = 3.44$ eV is attributed to an IPS in front of the Pb(111) surface. The 2PPE data are described very well by a fit of six Lorentzian peaks, an exponentially decaying background and a Fermi-Dirac distribution that is convoluted with an Gaussian instrument function of 50 meV width. The Gaussian function takes both the limited resolution of the electron spectrometer (~ 10 meV) and the bandwidth of the laser pulses (~ 40 meV) into account. Compared to the PES data from the occupied QWSs the exponentially decaying background due to scattered electrons is much more significant and of the order of the peak intensity itself. Therefore, the original data is fitted and the exponential background⁴ is subtracted. This allows to enhance the contrast of the spectra and highlights the odd-even behavior expected for the unoccupied QWSs. The number of five QWSs peaks is explained by a cross-talk of subsequent coverages that occurs even for the shallow wedges of 1.5 ML/mm slope, corresponding to 0.15 ML/spectrum resolution, see Fig. 5.12.

The crosstalk of neighboring coverages, however, does not prevent a clear as-

⁴The concept of an energy-dependent background subtraction is comparable to the background subtraction algorithms introduced by Shirley [Shi72] and Tougaard [Tou93] which are frequently used in x-ray photoemission spectroscopy.

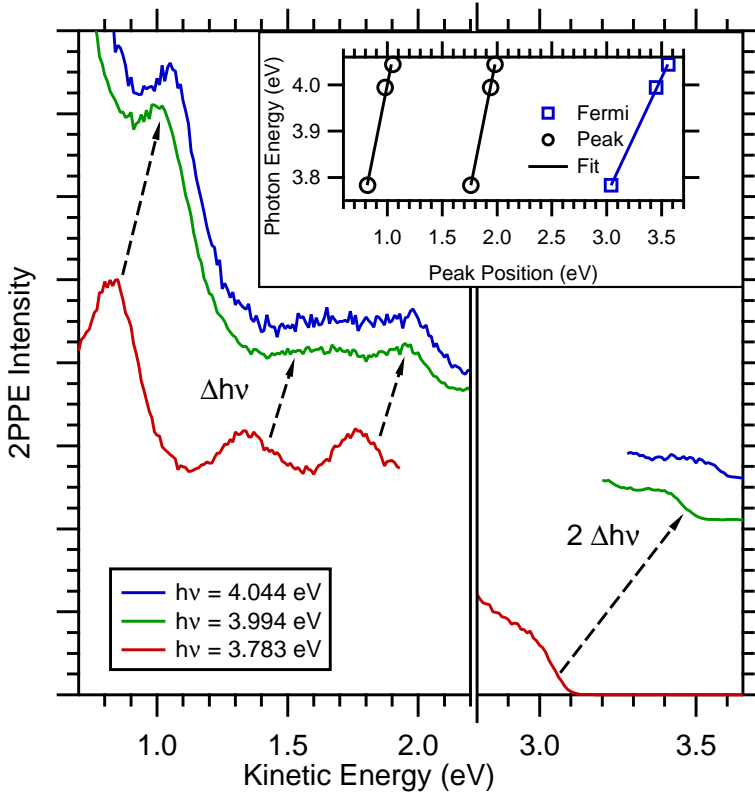


Figure 5.10: Photon energy dependence of two unoccupied QWS and the cutoff at the Fermi level. The unoccupied QWS present real intermediate states, which shift with the photon energy difference of $\Delta h\nu$, whereas the Fermi edge shifts with $2\Delta h\nu$, which indicates photoemission via virtual intermediate states. The IPS at 3.0 – 3.3 eV is omitted in this representation.

signment of the QWSs binding energies since the Pb/Si(111) wedges exhibit a high contrast of subsequent states that is even more enhanced after subtraction of the exponential background, as discussed in Fig. 5.9. The systematic treatment of several subsequent 2PPE spectra at different film thicknesses makes this fitting procedure robust and enables to unambiguously identify the dispersion of all QWSs peaks with coverage. As shown in Fig. 5.9(a) already the raw 2PPE data exhibit a well visible odd-even contrast. However, the weak QWSs at $E - E_F > 1.5$ eV are only barely visible, even in a logarithmic intensity scaling. Fitting the sequence of spectra from the wedge and subtracting the coverage dependent exponential background results in the background corrected spectra in Fig. 5.9(b). Now, all states at all coverages can be clearly discerned and the pronounced odd-even contrast becomes evident.

To verify that the considered QWSs are in fact unoccupied real intermediate states it is important to analyze the photon energy dependence of the intermediate state

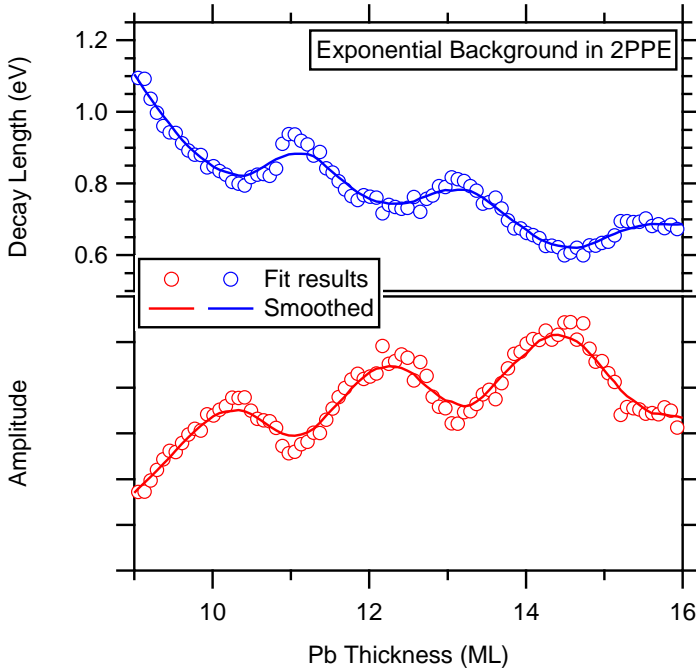
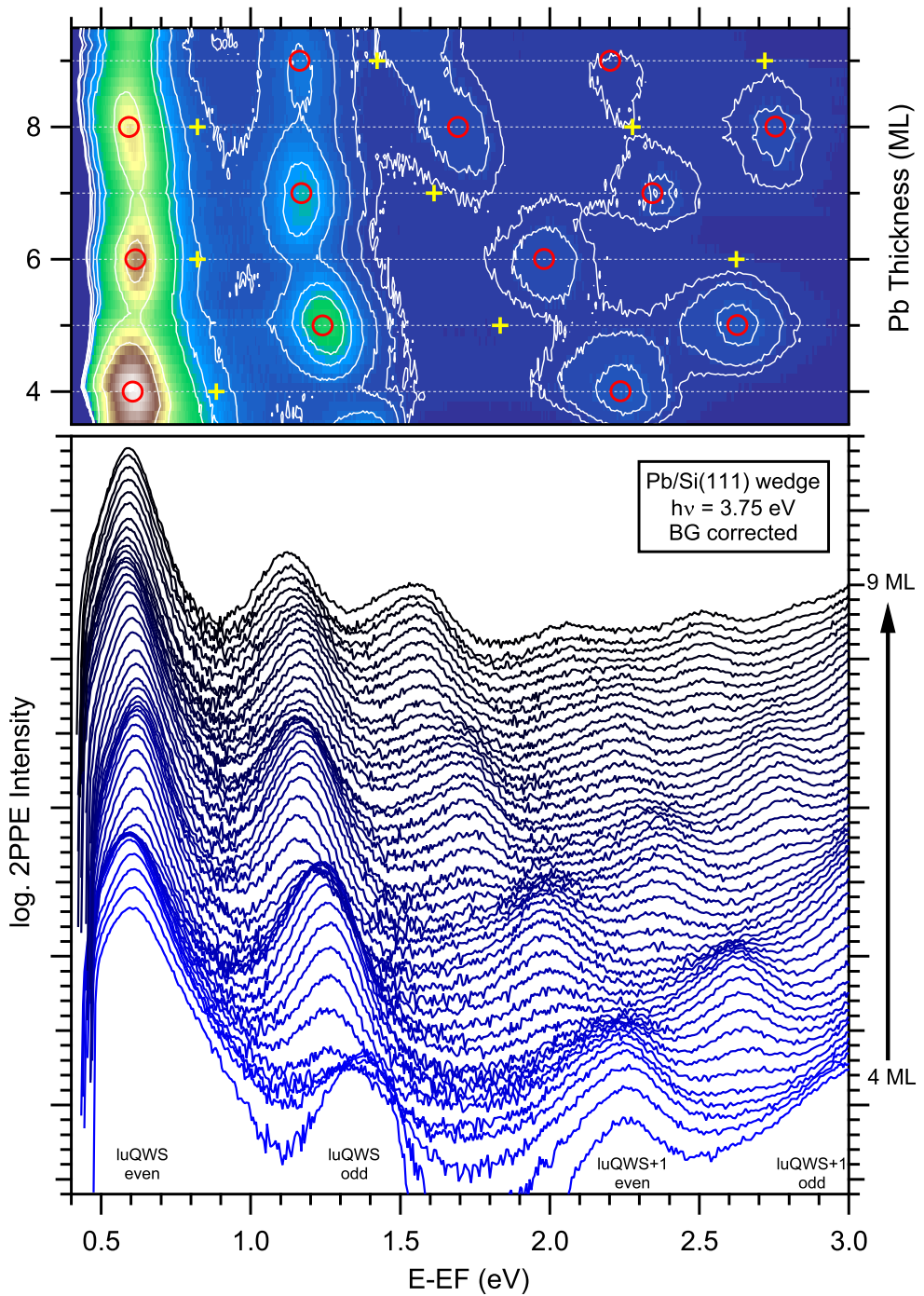


Figure 5.11: Coverage dependence of the exponential background as determined from a sequential fit of a Pb/Si(111) wedge. The amplitude increases for thicker films and the decay length shrinks, which points to an roughening of the wedge at larger thicknesses. Moreover, the amplitude and decay length (in the energy domain) exhibit a 2 ML oscillation, which is characteristic for Pb/Si(111). The solid lines indicate a box-car smoothing with 1.5 ML width.

peaks. As detailed in chapter 2.4.4, the photon energy dependence provides information on how an intermediate state is populated. Fig. 5.10 shows monochromatic 2PPE spectra for 10 ML Pb/Si(111) taken at three different photon energies. The inset depicts the peak shift of two unoccupied QWSs and the cutoff at the Fermi edge as of function of photon energy. The QWSs shift with $0.9(1) \Delta h\nu$, which thus present real intermediate state that are not resonantly populated. In contrast, the

Figure 5.12 (*facing page*): Monochromatic 2PPE spectra on logarithmic intensity scale recorded with $h\nu = 3.75$ eV at $T = 100$ K for an ultrathin Pb/Si(111) wedge with 1.5 ML/mm slope. The upper panel shows the linear 2PPE intensity as false color plot. The exponential background due to secondary electrons has been subtracted and enhances the odd-even contrast. The peak positions resulting from the fits are indicated by open circles and the contour lines emphasize the weaker QWSs at higher energies. The binding energies from a DFT calculation of a free-standing Pb slab are appended as yellow crosses [Wei02a], which, however, deviate by as much as 0.5 eV from the experimental values in this coverage range.



Fermi edge shifts with $2.0(1)\Delta h\nu$, which indicates that the 2PPE proceeds via virtual intermediate states by the simultaneous absorption of two photons.

Interestingly, the exponential background due to secondary electrons shows a pronounced coverage dependence given in Fig. 5.11. With increasing coverage the amplitude of the background increases and the decay length shrinks, which points to a roughening of the wedge at higher coverages, similar to the data presented in Fig. 5.1. The characteristic 2 ML period might indicate an aspect of the electronic growth mode typical for Pb/Si(111) since the even coverages exhibit a larger background amplitude than the odd coverages. Although the films were grown at $T = 100$ K to minimize the influence of adatom diffusion and the occurrence of "magic island heights" [Hup01] the surface diffusion might not be completely quenched. In this case, Pb layers with odd coverage are energetically more favorable than those with even coverage because the total energy of the system is minimal for the hoQWS being far from E_F , compare to section 5.1. This electronic growth mechanism can explain why the even coverages appear to be rougher than the odd coverages. The coverage dependent secondary electron background, however, is subtracted for the determination of the peak positions and thus can be neglected for the discussion of the binding energies.

In Fig. 5.12 the background corrected 2PPE spectra from Fig. 5.9 for a Pb/Si(111) wedge with 1.5 ML/mm slope and a film thickness ranging from 4 to 9 ML are compiled and shown as a function of intermediate¹ state energy $E - E_F$. The spectra exhibit a series of four peaks, which disperse toward E_F as function of coverage and evidence a pronounced odd-even behavior by the high contrast of peaks at subsequent coverages. Apparently, the unoccupied DOS exhibits the same characteristic 2 ML odd-even behavior found for the occupied DOS.

The weakly dispersing branch of peaks at $E - E_F = 0.6$ eV for even coverages and 1.2 eV for odd coverages is assigned to the luQWS. This state is confined in the global Si bandgap to the Pb layer for even coverages. The next higher lying luQWS+1 presents a strongly dispersing branch of peaks at $E - E_F = 1.2 - 2.3$ eV and $2.2 - 2.6$ eV for even and odd coverages, respectively. This state and all higher lying QWS, such as luQWS+2 appearing at $E - E_F = 2.7$ eV for 8 ML, are degenerate with Si bulk bands. Compared to the results from a DFT calculation of a free-standing Pb slab [Wei02a], which are given by yellow crosses in Fig. 5.12, the measured peak positions of all four QWSs branches deviate as much as 0.5 eV. This systematic disagreement to DFT, which is significantly larger than both the bandwidth and the separation of the four QWS branches, is remarkable since DFT was well suited to describe the occupied states. Possible explanations for this discrepancy are investigated in the next section, where a comprehensive overview of the quantized occupied and unoccupied band structure in Pb/Si(111) is presented and discussed.

In addition, the $n = 1$ image potential state in front of the Pb/Si(111) surface at $E - E_F = 3.3 - 3.4$ eV⁵ is identified, see Fig. 5.8. The assignment is based on the fact that the considered IPS is (i) pumped with the UV light $h\nu_2$ in the time-resolved

⁵The absolute value of the work function is somewhat different for each wafer prepared, which is attributed to different pinning positions of E_F . Since the IPSs are fixed to the vacuum level such work function fluctuations alter the binding energy of the IPSs with respect to E_F and lead to a relatively large uncertainty of 100 meV on this energy scale. Compare also to Fig. 5.20.

experiments, (ii) detected at all thicknesses, (iii) does not disperse with coverage, and (iv) shows a binding energy of $E - E_V = -0.76(5)$ eV⁵ with respect to the vacuum level E_V , which agrees with the value expected for the first IPS [Ech04]. The origin of the IPSs is well understood. In brief, the polarization generated in the surface plane by an electron in front of the surface leads to an attractive potential that asymptotically approaches E_V . The image potential gives rise to a series of bound Rydberg-like IPSs converging toward E_V . The IPSs are localized in front of the metal surface while being delocalized parallel to the surface plane [Hot00, Ber01, Ber02, Rot02, Rot04, Roh05]. The IPSs serve as model system for the electron dynamics in 2D *in front* of the metal surface. Considerable theoretical [Ech78, Smi85, Smi89, Smi90, Ech00, Ech04] and experimental [Hul85, Pad92, Fau95, Oga96b, Wol96, Pet97b, Pet97a, Wol99, Wei02b, Zhu04, Gd05, Gd07, Fau07] efforts resulted in a coherent description of the electron dynamics, which is governed by the concepts of wave function overlap with bulk states. However, a detailed analysis of the IPSs is beyond the scope of the present work, which focuses on the electron dynamics of QWSs *confined in* the metal film.

5.3 Overview of the Quantized Pb/Si(111) Band Structure

The preparation of several wedges allows to generate a precise overview of the quantized electronic structure of Pb/Si(111) as function of coverage. In Fig. 5.13 four different wedges are combined in an intensity map for the coverage range of 1 – 16 ML. The occupied band structure was investigated with PES at $h\nu = 6$ eV, whereas the unoccupied band structure was probed with 2PPE at $h\nu = 3.7 - 3.8$ eV on the identical wedge. This quasi-simultaneously measurement with PES and 2PPE allows a highly reliable correlation of the occupied and unoccupied band structure. Additionally, the binding energies of the QWSs as extracted from a fit of the spectra (\circ) are depicted in Fig. 5.13 in combination with results ($+$) of a density functional calculation of a bare Pb slab [Wei02a]. Due to the restriction that the photon energy in 2PPE must not exceed the workfunction a small part of the unoccupied DOS below $E - E_F = 0.4$ eV is not accessible.

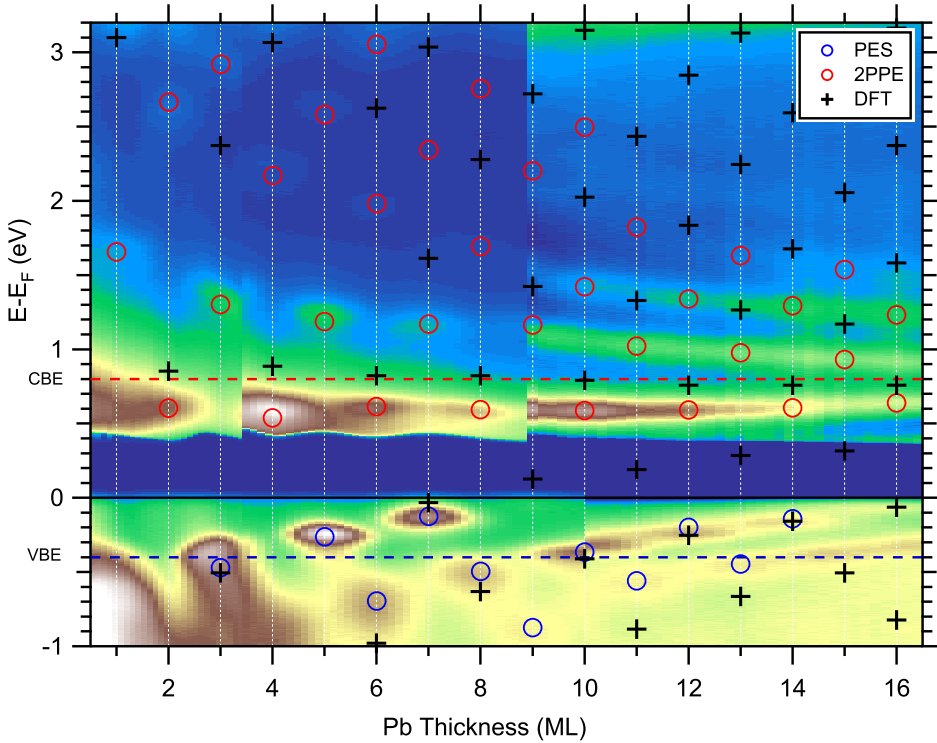


Figure 5.13: Overview of the quantized Pb/Si(111) band structure. The occupied states at $E - E_F < 0$ were mapped out with PES, whereas the unoccupied states at $E - E_F > 0$ were studied with monochromatic 2PPE. Circles represent the results of a Lorentzian peak fit of the data and crosses the binding energies from a DFT calculation [Wei02a], which, however, deviate systematically for the unoccupied states. The CBE at ~ 0.8 eV and the VBE at ~ -0.4 eV are indicated.

The use of low thickness gradients for the Pb/Si(111) wedges minimizes the crosstalk of neighboring coverages and gives rise to a remarkably high contrast of subsequent coverages, which allows a clear identification of the dispersion of both the occupied and unoccupied QWS as function of Pb thickness. The work function oscillations are reflected in the modulated low-energy cutoff of the 2PPE spectra at ~ 0.4 eV. Only at higher coverages the contrast reduces, probably due to a roughening of the films, which is also evidenced by the vanishing work function oscillations.

Such correlated measurements of the occupied and unoccupied states were carried out for several different wedges. The peak positions as extracted from a Lorentzian line fits (not shown, see exemplary fit in Fig. 5.8) are compiled in Fig. 5.14 for seven different wedges that partially overlap. The data points for different wedges scatter only little and are consistent within the experimental resolution, corresponding to the symbol size. The observed binding energies of the hoQWS, luQWS, luQWS+1, and luQWS+2 are compiled in table 5.1. In Fig. 5.14 the binding energies from DFT calculation [Wei02a] are connected with dashed lines to emphasize the 2 ML odd-even behavior of the hoQWS, luQWS, luQWS+1, and luQWS+2. Additionally, the branches of equal Bohr-Sommerfeld quantum number n are indicated, which follow from a comparison of the experimental and DFT data to a phase accumulation model, see chapter 2.1.1.

Beginning the discussion at $\Theta = 1$ ML, the luQWS exhibits a broad peak at $E - E_F = 1.66(5)$ eV since this state with $n = 2$ is degenerate with unoccupied Si bands and presents a QWR. With increasing coverage the quantum well grows wider and the luQWS shifts towards E_F . For 2 ML the $n = 2$ state has crossed the conduction band edge (CBE) and is found as truly confined QWS at $E - E_F = 0.60(5)$ eV. For 3 ML this state has shifted below E_F and thus has turned into an occupied QWS at $E - E_F = -0.39(5)$ eV. At 4 ML the state with $n = 2$ has moved out of the substrate bandgap and is located at $E - E_F = -0.97(5)$ eV as broad QWR. At higher coverages the $n = 2$ state is fully degenerate with occupied Si bands and cannot be resolved anymore. As the film thickness is further increased, more and more unoccupied QWS appear, which shift to lower energies and turn into occupied QWS below E_F . This behavior is emphasized in Fig. 5.14 by the thin dashed green lines that indicate constant Bohr-Sommerfeld quantum numbers n .

One fundamental property of the Pb/Si(111) quantum well system is the pronounced odd-even oscillation with a period of 2 ML for the states close to E_F , see chapter 2.1.2 and 2.1.3. These odd-even oscillations lead to a drastic redistribution of the electron density for two neighboring coverages and a decisively different electronic structure for odd and even film thicknesses. At small layer thicknesses, the hoQWS is confined in the substrate bandgap close to E_F for odd coverages, whereas at even coverages the hoQWS is located below the VBE. As the coverage increases the branches of QWS shift to higher energies, which expresses the slight deviation of the periodicity from the ideal integer value of 2 ML. The shift to higher energies with coverage can be understood by a slightly larger period than 2 ML, where the film thicknesses are slightly smaller than required for a constant binding energy at E_F . This mismatch of the oscillation period to 2 ML creates a 9 ML beating period of the odd-even behavior, see section 5.1.

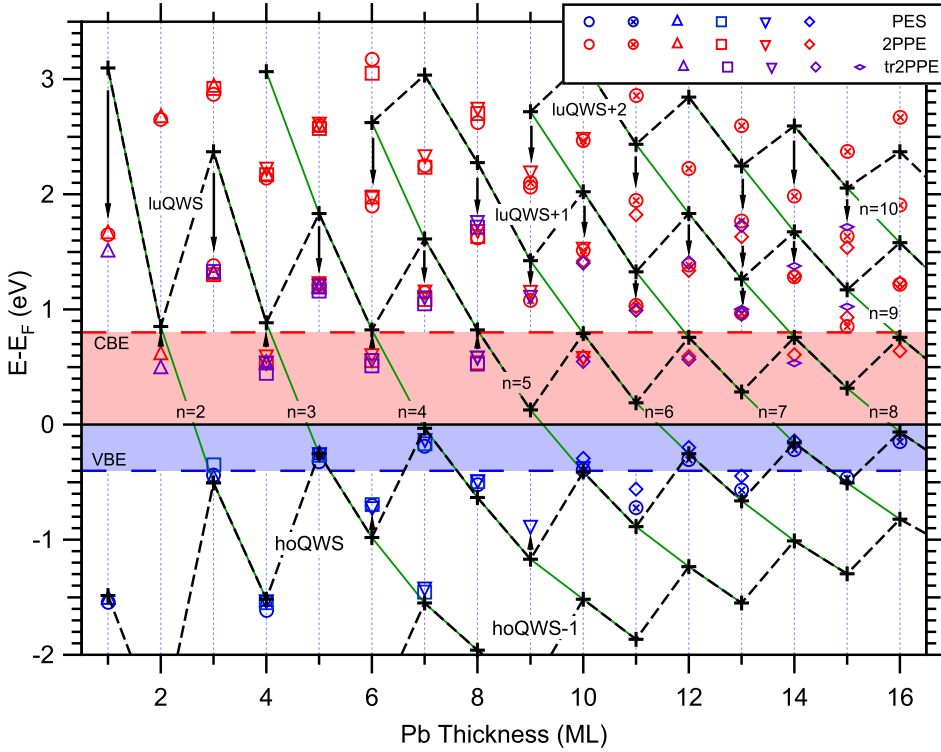


Figure 5.14: Compilation of the QWS binding energies for seven different wedges as indicated by different symbol shapes, which were investigated with PES, monochromatic 2PPE and bichromatic time-resolved 2PPE. A DFT calculation (+) of free-standing slab [Wei02a] systematically predicts too high energies for the unoccupied QWSs, which deviate by as much as 1.5 eV from the experimental values at low coverage, as indicated by arrows. The green lines connect QWSs with the same Bohr-Sommerfeld quantum number n . The shaded area symbolizes the global Si bandgap.

The experimentally determined energies of the occupied QWSs that are confined to the global Si bandgap agree very well to the results of a DFT calculation of a free-standing Pb slab. Only the QWR, which are degenerate with Si bands, exhibit somewhat too large energies as discussed in section 5.1. Since the DFT calculation does not take the Si substrate into account, the deviation can be explained by the penetration of the QWS wave functions into the substrate, which generates an effectively wider well and thus enlarges the binding energies.

Turning to the unoccupied states, more severe deviations of experiment and theory are encountered. Focusing on the luQWS, the experimentally determined energies are systematically overestimated by DFT. When the luQWS is confined by the global Si bandgap the deviations are slight and amount to 100 – 200 meV. In contrast, the discrepancy becomes much larger when the luQWS is degenerate with Si bands and can be as large as 1.5 eV at 1 ML. Clearly, the deviations decrease as the film

thickness increases but do not vanish completely in the investigated coverage range. The overestimation of the energies by DFT is a general trend that is encountered for all higher lying states, such as luQWS+1 and luQWS+2, which are degenerate with Si bands at all coverages.

Here, the fact is considered that DFT calculations for *unoccupied* states can lead to deviations because the electronic structure is optimized for the occupied states. Moreover, luQWS and luQWS+1 are degenerate with the Si conduction band and the respective interaction is not considered in the calculation. As the deviation between experiment and theory increases for smaller film thickness where interface effects become more pronounced the interaction of Pb with the Si substrate is considered to be the dominating effect. This is evidenced by the oscillatory behavior of the binding energy deviation of the luQWS. Only a slight and coverage-independent discrepancy is encountered for even coverages, when the state is confined by the substrate bandgap, whereas at odd coverages, when the state is degenerate with Si bands, the deviations are much larger. In the Si band gap such a hybridization is suppressed as the Pb wave function is damped exponentially into Si and the approximation of the Pb film on Si(111) by a freestanding Pb slab apparently holds. The systematic overestimation of the binding energies of the unoccupied QWS indicates that the potential above E_F is in fact lower than described by the image potential assumed in the calculation of the bare slab. Here, an extended DFT calculation including the reconstructed interface and the substrate itself would be helpful to obtain better agreement of theory and experiment for this important quantum well model system.

Θ (ML)	hoQWS			InQWS			InQWS+1			InQWS+2		
	$E - E_F$ (eV)	Δ (meV)	n	$E - E_F$ (eV)	Δ (meV)	n	$E - E_F$ (eV)	Δ (meV)	n	$E - E_F$ (eV)	Δ (meV)	n
1	-1.52(90)	160(50)	1	1.66(5)	250(50)	2	2.78(5)	230(70)	3			
2				0.60(5)	320(30)	2						
3	-0.39(5)	180(10)	2	1.30(5)	220(20)	3	2.91(5)	100(50)	4			
4	-0.97(8)	740(90)	2	0.53(5)	140(20)	3	2.22(5)	280(20)	4			
5	-0.24(1)	90(10)	3	1.24(2)	140(20)	4	2.63(5)	320(50)	5			
6	-0.71(5)	590(50)	3	0.614(5)	109(5)	4	1.98(3)	190(30)	5	3.17(5)	230(50)	6
7	-0.12(1)	140(10)	4	1.17(2)	160(20)	5	2.34(5)	580(50)	6			
8	-0.48(2)	240(20)	4	0.59(1)	110(10)	5	1.69(2)	280(20)	6	2.82(5)	340(50)	7
9	-0.88(5)	690(90)	4			5	1.10(3)	280(30)	6	2.06(5)	310(50)	7
10	-0.37(1)	130(10)	5	0.59(1)	120(10)	6	1.42(2)	128(20)	7	2.52(3)	320(20)	8
11	-0.56(5)	450(50)	5			6	1.02(2)	120(20)	7	1.95(5)	420(50)	8
12	-0.22(3)	220(30)	6	0.59(1)	120(10)	7	1.34(2)	120(20)	8	2.23(3)	160(30)	9
13	-0.45(5)	290(50)	6			7	0.97(2)	160(20)	8	1.77(2)	280(20)	9
14	-0.15(3)	180(30)	7	0.61(1)	170(10)	8	1.29(2)	210(20)	9	2.00(3)	260(50)	10
15	-0.37(3)	180(30)	7			8	0.94(2)	170(20)	9	1.64(5)	280(50)	10
16	-0.05(5)	100(50)	8	0.64(1)	150(10)	9	1.23(2)	240(20)	10	1.91(3)	300(40)	11

Table 5.1: Binding energies $E - E_F$, linewidth (FWHM) Δ and associated Bohr-Sommerfeld quantum numbers n of the highest occupied (hoQWS), the lowest unoccupied (luQWS) and the next higher lying (InQWS+1 and InQWS+2) quantum well states for a coverage of 1 – 16 ML. For odd coverages $\Theta \geq 9$ ML the luQWS can not be accessed with 2PPE due to the restriction of the photon energy $h\nu < \Phi$.

Conclusions

In summary, quantum size effect in Pb/Si(111) were investigated by laser-based PES at UV photon energies of 5 – 6 eV. The observed binding energies of the occupied QWS and the modulation of the global sample work function are found in excellent agreement with recent results from a DFT calculation [Wei02a] of a freestanding Pb film. The work function oscillation predicted for a quantum well system which is highly decoupled from the substrate was resolved with high accuracy. The analysis of the photoemission spectra as function of coverage confirms that the work function modulation is governed by the modulation of electron density below E_F and the electron spill-out of the QWS wave function into the vacuum. Additionally, the low kinetic energy of the photoemitted electrons permitted the detection of electronic states of the Si substrate. These states exhibit a modulation of the binding energy which is correlated to the oscillation of the electron density at the Fermi level induced by the QWSs.

The unoccupied electronic structure of the QWSs in ultrathin Pb films on Si(111) has been investigated by 2PPE. Up to three QWSs above E_F and their dispersion with film thickness are identified, which all exhibit a pronounced odd-even behavior. The respective binding energies are in agreement with DFT calculations of a free-standing Pb film for large thicknesses (~ 20 ML). At lower thickness the energies are systematically overestimated by DFT, most likely due to interaction with the Si substrate not taken into account by the calculation.

This work highlights the large capabilities of laser based PES with the advantages of high photon flux at small spot sizes in conjunction with increased bulk sensitivity. Furthermore, the use of ultrashort laser pulses adds femtosecond time resolution to the experimentally accessible dependencies. In the next section, femtosecond time-resolved 2PPE is utilized to further the understanding of energy relaxation dynamics of electrons photoexcited into *unoccupied* QWS. The well understood electronic structure which is readily controlled by variation of the film thickness makes Pb/Si(111) an ideal candidate for the investigation of electron dynamics at the crossover from 3D to 2D.

5.4 Ultrafast Electron Dynamics of the Unoccupied QWS

Scattering of excited electrons in metals occurs on femtosecond timescales due to (i) the large phase space for e-e scattering and (ii) efficient screening of the hole related to the electron by the underlying elementary excitation of an electron-hole (e-h) pair. Since in metals the electron-ion interaction is weak the electron scattering rates Γ can reasonably well be approximated by the free electron model [Pin66]. This holds in particular for simple metals like Al, Na, or K where Γ is dominated by e-e scattering, shows a weak momentum dependence, and follows approximately a quadratic energy scaling with respect to the Fermi level E_F , $\Gamma_{e-e} \sim (E - E_F)^2$, as predicted by FLT [Pin66, Chu06a, Chu06b]. In principal, this scaling also holds for noble metals like Cu, Ag, and Au. However, it has been shown by *ab initio* calculations using the *GW* approximation for the self energy of the excited quasi-particle that the contribution of the *d*-band electrons to screening of the e-e interaction leads to an increase of the electron lifetimes $\tau_{e-e} = \hbar/\Gamma_{e-e}$ compared to the free electron gas description [Cam99, Chu06a]. In transition metals the larger number of final states in e-e scattering due to *d*-bands close to E_F reduces τ_{e-e} . In addition, a pronounced dependence on the electron momentum is encountered [Kno00, Lad03, Chu06a, Chu06b, Zhu05, Mön06]. The underlying mechanism of the energy relaxation within FLT are discussed in detail in chapter 2.3.1 and appendix C.

Experimental access to hole lifetimes is facilitated by photoelectron spectroscopy which measures the hole lifetime through the spectral line width [Ger01]. Ballistic electron emission spectroscopy can be employed in combination with a sophisticated theory to analyze electron lifetimes [Lad03]. Time-resolved 2PPE on the other hand monitors the decay of an excited electron population directly in the time domain [Pet97b]. By two time-delayed femtosecond laser pulses hot electrons are first excited into bound intermediate states and subsequently photoemitted into vacuum states, see Fig. 5.15, right. Electron lifetimes have been studied intensively by 2PPE in noble and transition metals [Sch94, Pet97a, Cao98, Kno98b, Pet99a, Aes00, Lis04b, Mer04] and a comprehensive understanding has been developed by joined experimental and theoretical efforts for image potential states on noble metal surfaces, see references [Wei02b, Ech04, Zhu04] and references therein. Up to now, the electron dynamics in simple metals have not been investigated by 2PPE on a comparable level, albeit individual Cs adatoms adsorbed on single crystal Cu surfaces have received considerable attention [Bau99, Pet00a, Pet00b]. On the other hand, thin film structures on insulating or semiconducting substrates have been shown to be important to limit transport effects that complicate the analysis of electronic lifetimes [Kno98b, Aes00, Lis04b]. Thus, a promising approach to provide experimental data for simple metals is to prepare thin films and to study the ultrafast electron dynamics as a function of film thickness in order to analyze electronic scattering in the crossover regime between two and three spatial dimensions.

Thin films of *sp*-metals like Al and Pb grown epitaxially on semiconducting substrates, e.g. Si(111) [Aba01, Upt04b, Upt04a, Dil06, Kir07] present interesting systems to study ultrafast electron dynamics since the electron confinement leads to the formation of well-defined occupied and unoccupied QWS, as presented in the previous

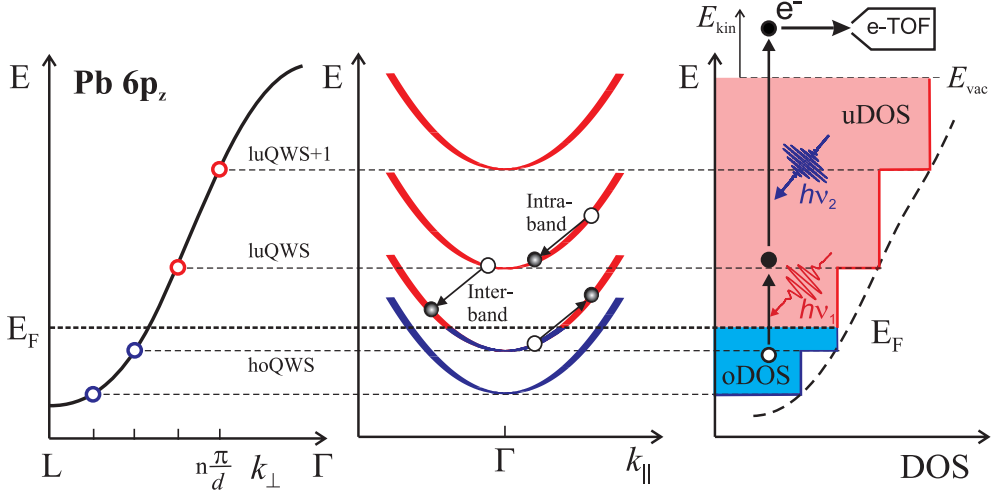


Figure 5.15: Left: QWS formation by quantization of the respective bulk valence band in a free-electron like metal (solid line). Allowed values of k_{\perp} (\circ) are determined by the film thickness. Center: Idealized dispersion of QWS within the film plane, i.e. along k_{\parallel} . e-e scattering processes among the subbands are indicated. Right: Simplified quantized DOS in a two-dimensional system. The 2PPE process involving the lowest unoccupied QWS (luQWS) is indicated. Excitation of electron-hole pairs occurs by absorption of a VIS laser pulse $h\nu_1$. The excited electron is photoemitted by a UV laser pulse $h\nu_2$ and analyzed by an electron time-of-flight spectrometer

section 5.3. The respective wave functions are confined to the film and occur at specific electron momenta k_{\perp} along the film normal which results in a quantization of the free-electron like band in the direction perpendicular to the film plane, as illustrated in Fig. 5.15, left. Within the film plane these confined states remain delocalized and the quantization leads to formation of subbands dispersing along parallel electron momentum k_{\parallel} , see Fig. 5.15, center and comprehensive reviews by Chiang [Chi00] and Milun et al. [Mil02b].

A first study on ultrafast electron dynamics in unoccupied QWS has been reported by Ogawa et al. [Oga02] who investigated the system Ag/Fe(001). Albeit this system is well known for its excellent electron confinement to the Ag film from photoelectron spectroscopy under equilibrium conditions [Chi00], the lifetimes observed by Ogawa et al. are below 10 fs for QWS at 1.0 – 1.6 eV above E_F . Since these are considerably shorter lifetimes than in bulk Ag a non-perfect electron confinement originating from additional decay channels at the interface has been concluded by the authors. A qualitative difference between the Ag/Fe(001) and Pb/Si(111) systems is found in the character of the substrate band gap that facilitates electron confinement. The total band gap in Si requires inelastic scattering processes if an electron in a QWS is transferred to the substrate. In case of Fe(001) elastic scattering is sufficient as an orientation band is responsible for electron confinement. Considering e-e scattering confined to the adlayer, hot electrons can only decay through intra-subband scattering

to the bottom of a particular subband or by inter-subband scattering to a lower lying subband. Due to energy and momentum conservation both these processes are accompanied by generation of an electron-hole pair in the vicinity of E_F as depicted in Fig. 5.15, center.

This chapter reports on results of time-resolved 2PPE and investigates the decay of hot electrons in thin Pb films grown epitaxially on Si(111) as wedges. The Pb/Si(111) wedges enables investigation of the electron dynamics at quasi-integer film thickness, which is highly important to minimize the influence of additional scattering processes at a possibly corrugated interface. This careful experimental procedure allows to identify the electronic relaxation processes in the metallic adlayer as the fastest decaying component of 30 – 140 fs. Additionally, a delayed rise (~ 70 fs) of the electron population in the luQWS is observed. This behavior is attributed to inter-subband scattering from the next higher lying luQWS+1. A second slower decay component 130 – 900 fs is assigned to relaxation of photoexcited carriers in the Si substrate. Moreover, the lifetime of the luQWS shows an oscillatory behavior with the characteristic 2 ML period of Pb/Si(111), which correlates nicely to the phase space available for e-e scattering. Interestingly, the lifetime in the quasi-2D luQWS coincide rather well with the predictions from FLT in 3D.

5.4.1 Coverage Dependence of the Schottky Barrier

To be able to utilize the high dynamic range of the TOF spectrometer of $> 10^5$ for the analysis of the population decay it is necessary to perform a background correction. The constant uncorrelated background due to 2PPE by the pump and probe pulse alone is subtracted from the time-resolved 2PPE data. In the course of this procedure it becomes evident that the pump pulse lifts the band bending at the Pb/Si interface and creates so-called flat-band conditions by excitation of carries in the semiconducting substrate which lead to a surface photo voltage (SPV).

In Fig. 5.16(a) the background subtraction of the bichromatic time-resolved 2PPE data and the coverage dependence of the SPV is discussed. The raw 2PPE data, which was integrated around the time-zero delay, is composed of two parts: The spectrum for energies $E_K < 1.8$ eV is dominated by the correlated 2PPE signal, whereas the 2PPE intensity at higher energies is due to photoemission of the UV probe pulse only, exposing a pronounced peak from the IPS. This high-energy part of the raw 2PPE data exhibits a rigid shift of ~ 100 meV compared to the UV only signal. To subtract the background properly the energy scale of the UV only signal is corrected by the amount of SPV measured at the high-energy cutoff of the uncorrelated signal for time-zero delay and added to the VIS only data. This constant background spectrum (BG) then is subtracted from the raw 2PPE data for all delays and yields the background corrected correlated 2PPE spectrum (2PPE-BG). The background corrected spectra exhibit signal-to-noise (S/N) ratios better than 10^3 and allow a reliable discussion of weakly coupled decay channels that present only small fractions of the transient signal.

This significant spectral shift of the UV component is explained by the presence of the VIS pump pulse which excites carriers of the Si substrate. As depicted in Fig. 5.17, the excited electrons and photoholes are separated by the electric field of

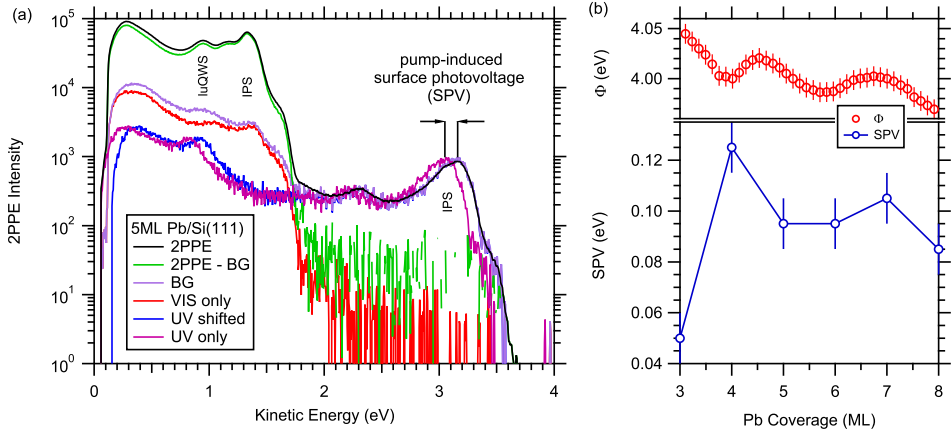


Figure 5.16: (a) The uncorrelated background (BG) is subtracted from the bichromatic 2PPE spectra with a S/N ratio of 10^5 to yield the correlated 2PPE spectra (2PPE-BG). The uncorrelated background stems from monochromatic 2PPE of the VIS pump and UV probe pulse only. The UV only signal is shifted with respect to the 2PPE signal by a pump-induced SPV, which compensates the surface band bending. (b) The coverage dependence of the SPV follows a Schottky-Mott behavior for $\Theta < 6$ ML, where a large workfunction induces a small band-bending and thus a small SPV. For larger film thicknesses the correlation of Φ and SPV is reversed.

the hole depleted near surface region and completely compensate the hole depletion of the p-semiconductor for sufficiently high excitation densities. Hence, flat bands form up to the surface without any band-bending. Since the positions of the VBE

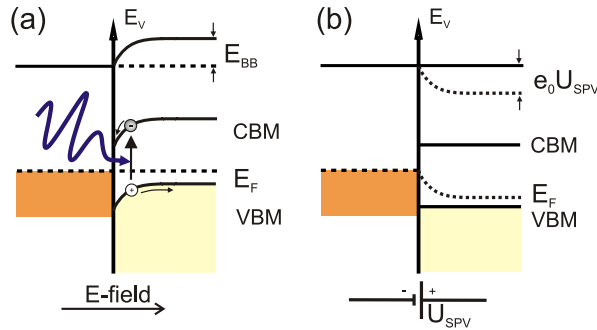


Figure 5.17: (a) The pump pulse excites carriers of the p-Si substrate from the VB to the CB, where charge separation occurs due to the electric field in the space charge region, which induces the surface band-bending E_{BB} . (b) For sufficiently high excitation densities the hole depleted surface charge region is compensated completely by the photoholes and flat conduction and valence bands form up to the surface. Due to energy conservation the Fermi level inside the semiconductor is shifted by $e_0 U_{SPV}$.

and CBE with respect to E_F are fixed inside the bulk by the intrinsic dopant concentration the Fermi and the vacuum level are shifted by the amount of the SPV e_0U_{SPV} . Metaphorically speaking, the Pb/Si(111) acts as simple photovoltaic device that absorbs photon energy and separates the e-h pairs at an interface. Please note that the decay of the SPV proceeds on a timescale of several 100 ns [Wid03] such that these experiments with 300 KHz laser repetition rate lead to steady-state conditions of the SPV.

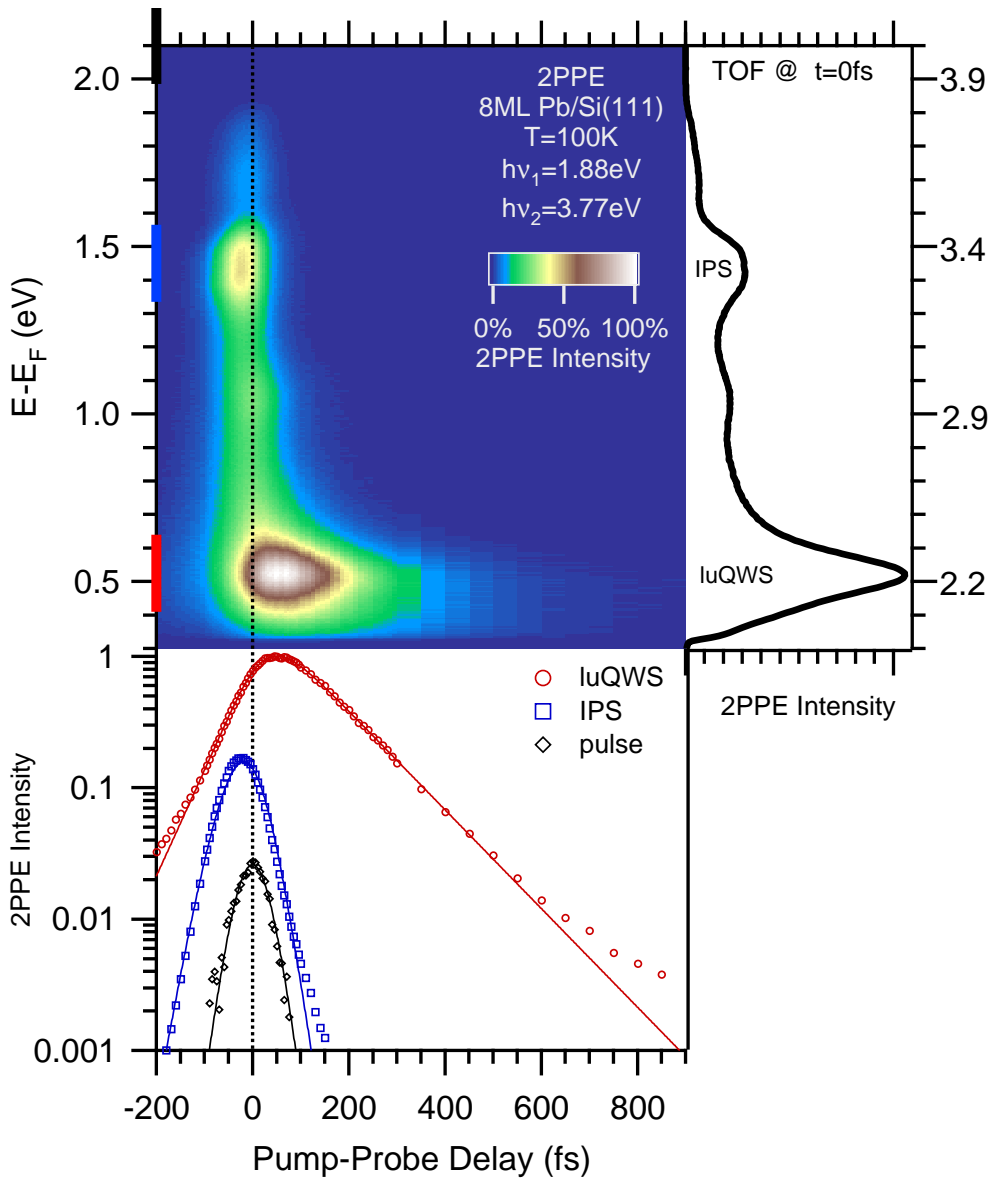
The coverage dependent analysis of the pump-induced photovoltage is shown in Fig. 5.16(b) and reveals an interesting behavior. The SPV was explained in the Schottky-Mott model of interfacial charge transfer. As detailed in chapter 2.1.2, a large workfunction metal will induce a small band-bending and vice versa. In fact, for layer thicknesses of < 5 ML this Schottky-Mott behavior is observed. Going from 3 to 4 ML, the work function drops by ~ 50 meV and the SPV increased by ~ 75 meV. At higher coverages, however, the correlation of Φ and SPV is reversed and does not follow the predications of the Schottky-Mott theory anymore. Since the SPV depends on the incident pump fluences if the hole depletion layer is not fully compensated, this discrepancy might be resolved by future fluence dependent studies.

5.4.2 Population Decay Times

The ultrafast electron dynamics in Pb/Si(111) is studied with time-resolved 2PPE. For this purpose the UV probe pulse with $h\nu_2 = 3.77$ eV is time-delayed with respect to the visible pump pulses with $h\nu_1 = 1.88$ eV and 2PPE spectra are measured as a function of time delay t . In the central panel of Fig. 5.18 the 2PPE intensity is shown as a function of time delay and intermediate state energy in an exemplary false color map for 8 ML Pb/Si(111). The left energy axis is valid for peaks that are probed with the UV pulse $h\nu_2$ such as the luQWS, whereas the right energy axis describes the intermediate state energy for states that are probed with the VIS pulse $h\nu_1$, e.g. the IPS. The different energy scales are discussed in detail in chapter 2.4.4.

The right part of the figure shows a 2PPE spectrum integrated over t from -110 to 200 fs, exhibiting a peak from the luQWS at $E - E_F = 0.52$ eV. In addition to the luQWS a second state is observed at higher energy at $E - E_F = 3.35$ eV. The analysis of the time-dependent intensity corroborates the assignment as $n = 1$ IPS in front of the Pb(111) surface with a binding energy of $E - E_V = -0.74$ eV with respect to the vacuum level E_V . Since the origin and the dynamics of the IPS are well-understood the following discussion focuses on the electron relaxation in the unoccupied QWS.

Figure 5.18 (*facing page*): A false color representation of the 2PPE intensity as a function of pump-probe delay and intermediate state energy $E - E_F$ is given in the center panel. The vertical color bars indicate the energy windows in which the intensity was integrated to monitor the time dependence of the 2PPE intensity. Three spectral features are analyzed in the bottom panel, which are attributed to the luQWS, an IPS, and high-energy electrons. The time-dependence of the latter allows a good estimate of the laser pulse duration. Note that the IPS is excited with the UV pulse $h\nu_2$ and thus its energy is given by the right energy scale to be $E - E_F = 3.35$ eV, respectively $E - E_V = -0.74$ eV. Solid lines are fits following a rate equation model, see text and chapter 2.4.6. These spectral signatures are also seen in the 2PPE spectrum integrated from -110 to 200 fs, given in the right panel.



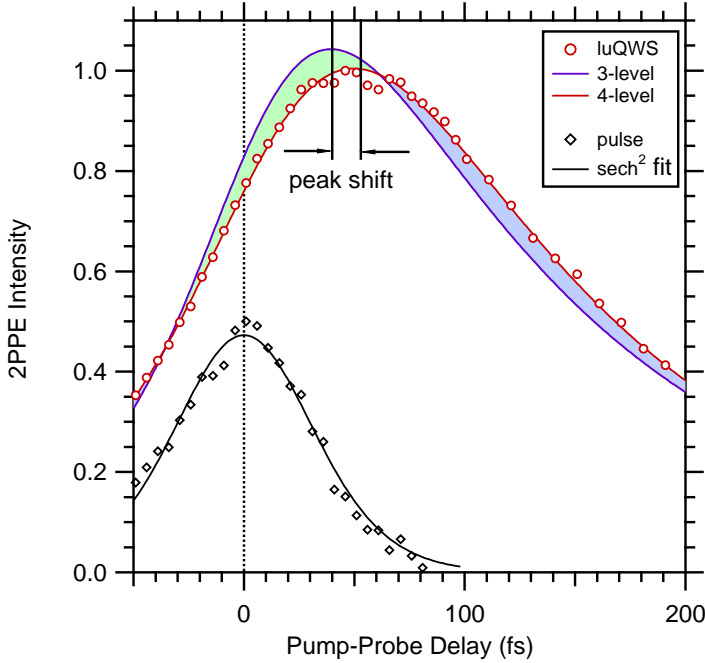


Figure 5.19: Fitting the transient population in the luQWS with a single exponential decay, corresponding to a 3-level system, predicts the peak maximum at too early delays and does not describe the XC shape appropriately. In contrast, the rate equation model of a 4-level system from chapter 2.4.6 describes the data excellently at all delays.

The bottom panel of Fig. 5.18 shows cross correlation (XC) traces, which have been integrated over the energy regions indicated by the color bars on the left. As detailed in chapter 3.1.3, the laser pulse duration is inferred according to equation (3.4) from the XC trace of the hot electron distribution for $E - E_F > 1.8$ eV to be 54(4) fs. The peak maximum of the IPS occurs at formally negative delays -8 fs, which indicates that the IPS population is build up by the UV pulse $h\nu_2$ and probed by the VIS pulse $h\nu_1$. Modeling of the XC trace of the IPS according to equations (2.49) and (2.50) by convolution of the laser pulse's temporal profile and a single exponential decay results in an IPS decay time $\tau = 20(5)$ fs. This decay constant is of the same order as, e.g., in Cu(111) [Ech04] and corroborates the assignment as IPS.

The XC trace of the luQWS, however, can not be satisfactorily be described by a single exponential decay as seen in Fig. 5.19. As explained in chapter 2.4.6, a single exponential decay is expected for a non-resonantly pumped state that is only weakly coupled to other states. The fit result for a single exponential decay corresponding to a 3-level system predicts the peak maximum at too early delay of 40 fs and underestimates the intensity for later delays. Especially the disagreement of the position of the peak maximum is a strong indication that the underlying model is not correct. In contrast, the XC trace of the luQWS exhibits a broad flat-top shaped peak maximum ranging from 30 to 80 fs. This XC shape indicates that part of the

intermediate state population in luQWS (state no. 1) is build up at later delays by scattering from another state (state no. 2). Since the simpler 3-level system fails to describe the transient population in luQWS a coupling of luQWS to other features of the Pb/Si(111) band structure has to be assumed. In fact, modeling the data with the 4-level approach discussed in chapter 2.4.6 describes the experimental data very well for all delays and over two orders of magnitude in the dynamics range, see solid line in Fig. 5.18 and Fig. 5.19. For this data set the fit results in $\tau_1 = 123(5)$ fs for the decay of luQWS (no. 1) at later times and a characteristic time $\tau_{12} = 26(5)$ fs for the delayed rise. Since the 4-level rate equation system incorporates another intermediate state (no. 2) its lifetime of $\tau_2 = 102(5)$ fs can be determined as well.

Before turning to the detailed physical interpretation of these numerical results the pronounced coverage dependence of the XC traces of luQWS has to be considered. The coverage dependence makes it necessary to adapt the numerical parameters of the 4-level rate equation model as well as the interpretation of the physical meaning of the free fitting parameters. The strong and characteristic odd-even modulation of the decay times of the luQWS in Pb/Si(111) as extracted by fits of the 4-level rate equation model from chapter 2.4.6 is discussed in the following.

5.4.3 Coverage Dependence of the Decay Times

In Fig. 5.20 the time-resolved 2PPE intensity is compared for a neighboring even and odd coverage of 4 and 5 ML, respectively. In agreement to the results of section 5.3, the luQWS is located in the Si bandgap for an even coverage and degenerate with Si bands for an odd coverage. The oscillatory position of luQWS with respect to the substrate bandgap has drastic consequences on the observed electron dynamics. As discussed for the case of 8 ML in Fig. 5.18, the transient population luQWS exhibits a delayed intensity rise. The subsequent decay proceeds on a timescale of ~ 100 fs for even coverages and does not depend strongly on the film thickness. This is opposed to the case of an odd layer thickness where a biexponential decay is resolved, which occurs on a timescale of 5 – 35 fs and 90 – 300 fs, respectively, where both time constants increase monotonously with the odd number of layers.

The description of the population decay by the 4-level rate equation model presented in chapter 2.4.6 is flexible enough to allow the description of both decay modes - delayed rise and biexponential decay - consistently within one model, see Fig. 2.33. As given by the set of coupled differential equations (2.51) and (2.52), the model assumes that the directly probed population $n_1(t)$ of state no. 1 decays with a time constant $\tau_1 = 1/\Gamma_1$ and is coupled by a rate constant $\Gamma_{12} = 1/\tau_{12}$ to the population n_2 of state no. 2, which itself decays on a timescale $\tau_2 = 1/\Gamma_2$. The analytic solutions in equations (2.53) and (2.54) allow to distinct two limiting cases:

(I) A delayed rise of the n_1 population is observed for $\Gamma_1 < \Gamma'_2 = \Gamma_{12} + \Gamma_2$, resulting in $C < 0$ in (2.53). After a delayed population build up due to scattering $|2\rangle \rightarrow |1\rangle$, the subsequent decay proceeds at a rate Γ_1 . For an even number of layers these boundary conditions were used to describe the XC traces of luQWS. In the following, only the parameters for the observed decay τ_1 and the delayed rise τ_{12} , which can be directly read off the XC traces, are discussed in detail and τ_2 is treated as auxiliary parameter in the fitting procedure.

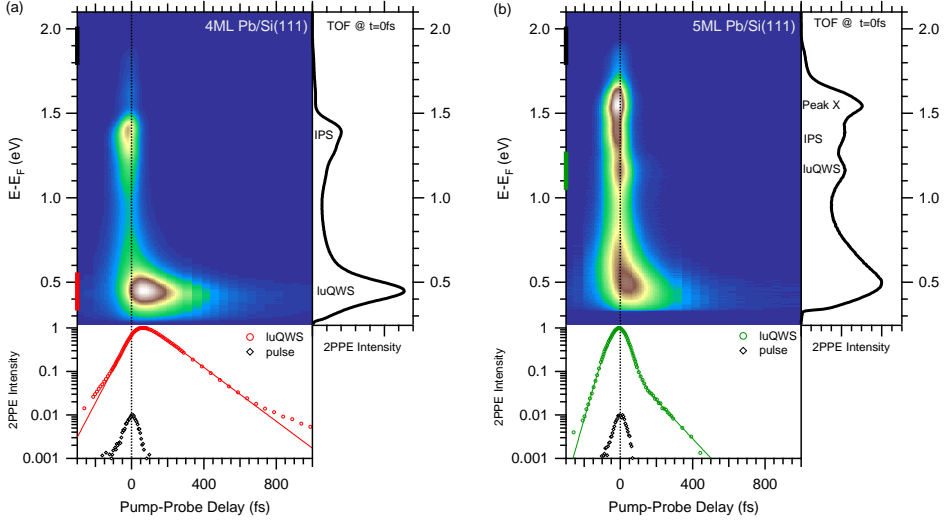


Figure 5.20: The time-resolved 2PPE intensity is compared for (a) an even coverage of 4 ML and (b) an odd film thickness of 5 ML. At $\Theta = 4$ ML the luQWS presents a delayed rise and subsequently a comparably slow decay constant of ~ 100 fs as opposed to the decay at 5 ML, where a about three times faster biexponential decay is resolved. (See text.) The difference of the low-energy cutoff is due to the oscillatory work function, which also affects the binding energy of the IPS with respect to E_F . The peak X in (b) is assigned to an unoccupied QWS that is pumped with UV and probed with VIS.

(II) A bi-exponential decay of n_1 is observed for $\Gamma_1 \ll \Gamma_{12}$ and thus $C > 0$. The fast initial decay is determined by Γ_1 and the slope of the subsequent decay is given by $\Gamma'_2 = \Gamma_2 + \Gamma_{12}$. All XC traces of luQWS at an odd number of layers were fitted under this restriction. Here, the directly accessible parameters τ_1 and $\tau_2^{\text{odd}} = 1/(\tau_{12}^{-1} + \tau_2^{-1})$ are reviewed.

In Fig. 5.21 the XC traces of the luQWS for an odd and even number of layers are compared. Clearly, for an odd coverage both contributions τ_1 and τ_2' exhibit a pronounced coverage dependence, whereas the XC traces for an even number of layers show only little variation. For an even coverage an additional decay component τ_B is observed at $t > 800$ fs. This component amounts only to $\sim 1\%$ of the total intensity in luQWS and is attributed to scattering of excited carriers of the Si substrate. A detailed discussion of this contribution is given in section 5.4.6.

Focusing on the interpretation of the fit results, e-e scattering in the ultrathin Pb film is considered to be the dominating channel of energy relation, compare to chapter 2.3. The necessity to use the more evolved 4-level model to describe the transient population of luQWS points to additional decay channels operative in the quantum well system. Nevertheless, it seems safe to assume that e-e scattering within the metal film itself will induce the fastest decaying component. Thus in the following the lifetime τ_1 is interpreted as decay time due to e-e scattering τ_{e-e} for all even and odd coverages. The other observed decay channels τ_2' , and τ_{12} then are linked to (i)

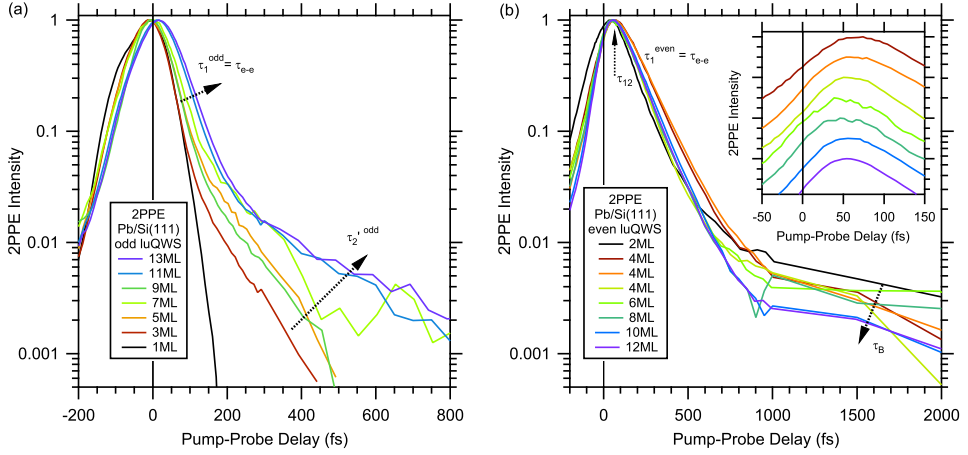
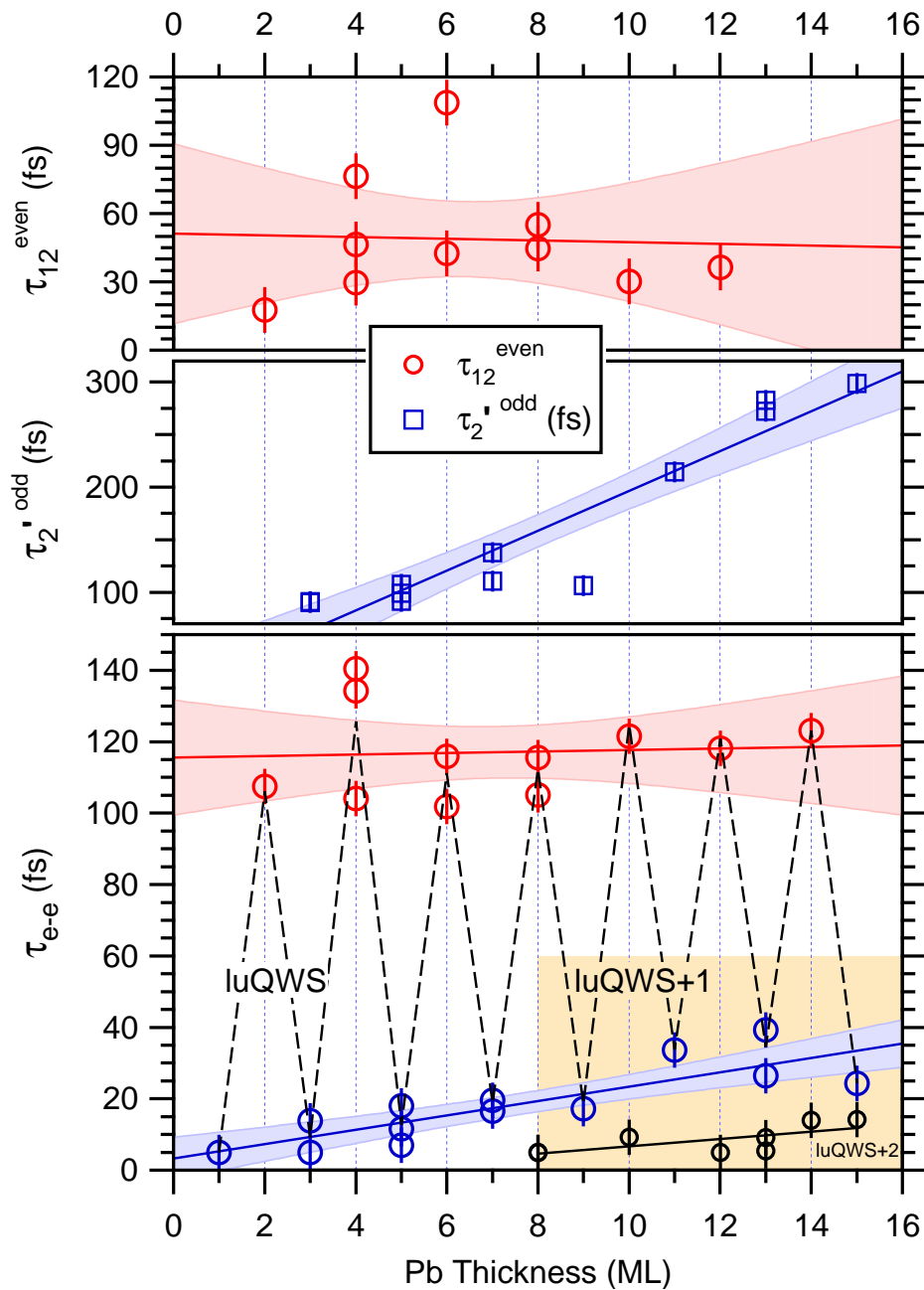


Figure 5.21: Comparison of the XC traces for (a) odd and (b) even coverage. All XC traces for odd coverage, where luQWS is degenerate with the Si bands, consistently exhibit a biexponential decay where both components show a well-resolved coverage dependence. In contrast, all XC traces for even coverage, where luQWS is located in the Si bandgap, present a delayed rise and a slower decay that does not depend strongly on the coverage. At later delays of $t > 800$ fs an additional decay component τ_B is encountered for the even luQWS, which is discussed in chapter 5.4.6. Please note the different scaling of the pump-probe delay axis for both type of traces.

intra-subband and (ii) inter-subband scattering within the quantum well system, and (iii) additional contributions from the optically excited Si substrate.

Fig. 5.22 summarizes the coverage dependence of the different decay constants. The lower panel depicts $\tau_1 = \tau_{e-e}$, which shows a strong oscillatory behavior of the e-e scattering rate with respect to odd and even film thicknesses. The contrast observed in the lifetime of subsequent states is remarkable: Going from $\Theta = 5$ ML to 6 ML the lifetime τ_{e-e} increases by a factor of 8 from 13(5) fs to 111(5) fs. Increasing the coverage further to 7 ML results in a decrease to 19(5) fs again. As indicated by the solid lines, which are linear fits to the data, only the decay constants for odd coverages exhibit an noticeable variation with coverage, see Fig. 5.21. For the odd coverages τ_{e-e} increases continuously from 5(5) at 1 ML to 35(5) fs at 15 ML and the second decay constant $\tau_2^{\text{odd}} = 1/(\tau_{12}^{-1} + \tau_2^{-1})$ observed in the biexponential XC traces of luQWS

Figure 5.22 (*facing page*): Coverage dependence of the decay constants for the fastest decay channel $\tau_1 = \tau_{e-e}$, the lifetime of the 2nd decay contribution $\tau_2^{\text{odd}} = 1/(\tau_{12}^{-1} + \tau_2^{-1})$, and τ_{12}^{even} for odd and even coverages, respectively. The dashed line shows the average value of τ_{e-e} for different wedges and highlights the strong odd-even contrast of subsequent layers. The solid lines are linear fits as guide for the eye and the shaded areas indicate a 90% confidence interval. The lifetime errors are given by vertical lines. Please note that for odd coverages of $\Theta \geq 9$ ML luQWS+1 is observed since luQWS is too close to E_F to be accessible with 2PPE, compare to Fig. 5.14.



rises from 90(10) to 295(10) fs. In contrast, τ_{e-e} for even coverages is rather constant at ~ 110 fs. The rise time τ_{12} of the signal in luQWS scatters more than the other fit parameters, however, within in the large error bars of the linear fit, this value can be approximated to be constant around ~ 50 fs. Fig. 5.22 also depicts the lifetime of the higher lying luQWS+2 for coverages $\Theta \geq 8$ ML. The XC of this state is well described by a single exponential decay, see equation (2.50), although its lifetime in the range of 5 – 15 fs is at the lower limit of the accessible decay constants.

At this point, the comparison to electron lifetimes analyzed by time-resolved 2PPE for unoccupied QWS in Ag/Fe(001) [Oga02] is of interest. Here, the lifetimes were smaller than 10 fs. The lifetimes determined here for Pb/Si(111) in a comparable energy interval above E_F are considerably larger than this value. Since Ag and Pb both exhibit *sp*-bands in the relevant energy range, the substrate or the interface is responsible for these differences in the lifetimes. Generally speaking, the presented results suggest that an orientation band gap as in Fe(001) confines electrons to a considerably weaker degree than a total band gap. Elastic scattering associated with the electron transfer from the adlayer to the substrate appears to be the decisive process that limits the residence time of hot electrons in QWS on substrates with orientation band gaps. This is because elastic electron transfer is facilitated at the interface due to the break of symmetry and defects arising from lattice mismatch. On the other hand, the efficient electron confinement by the global Si bandgap in Pb/Si(111) allows to resolve the population decay due to inelastic e-e scattering in the metal film. Also, the density of states of the substrate may play a role in the comparison of metallic and semiconducting substrates. This suggests more systematic studies comparing QWS from the same material on different substrates. The current study would be complemented nicely by a time-resolved investigation of electron decay in Pb/Cu(111).

5.4.4 Comparison to Fermi Liquid Theory

Before proceeding to the analysis of the additional components τ_{12}^{even} , and τ_2^{odd} , the fast decay times attributed to the decay within the metal film due to e-e scattering $\tau_1 = \tau_{e-e}$ are compared to FLT. The details of this description and especially the dimensionality dependence of the quasi-particle lifetime are discussed in chapter 2.3.1 and appendix C. The discussion follows the pioneering work of Quinn and Ferrell [Qui58] and more recent analysis of Vignale et al. [Giu05, Qia05, Qia06]. In fact, it will be shown that FLT accounts nicely for the observed coverage dependence of τ_1 , although no evidence for a 2D behavior in the e-e scattering is revealed. In Fig. 5.23 the individual data points of τ_{e-e} are plotted versus the binding energy of the particular state. In general, the observed lifetimes increase toward E_F and follow the prediction from FLT, which justifies the assignment $\tau_1 = \tau_{e-e}$ a posteriori.

Employing the 3D bulk electron density of $13.2 \cdot 10^{28} \text{ m}^{-3}$ [Kit04] in equation (C.11) yields the gray line, which describes the data surprisingly well without any free parameters. Only at energies $E - E_F > 1.1$ eV, where luQWS is degenerate with the Si substrate, FLT predicts too large lifetimes. This discrepancy may be understood by the influence of the Si band structure that offers additional decay channels for the energy relaxation of the hot electrons and hence reduces the lifetimes in this energy

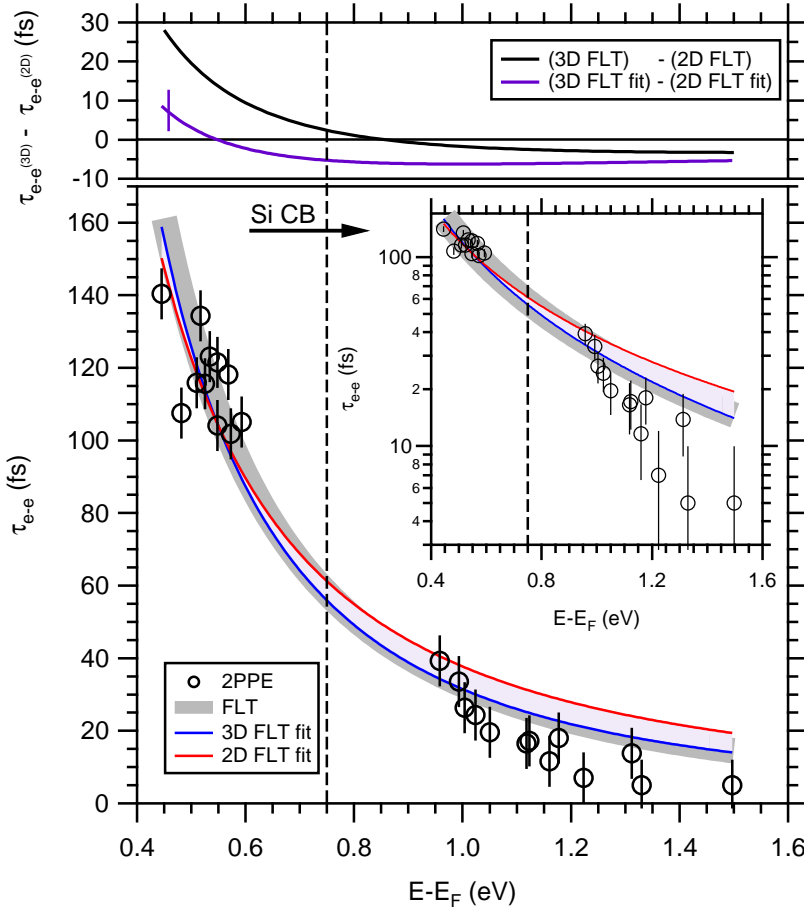


Figure 5.23: The data points (2PPE) of τ_{e-e} for luQWS as shown in Fig. 5.22 are plotted versus the binding energy of the respective state. The inset depicts a semi-logarithmic representation of the data and the Si CBE is indicated. Employing the bulk Pb electron density yields the gray line (FLT) and describes the general trend of the data satisfactorily without any free parameters. Solid lines show fits with the FLT scaling laws for a 3D and 2D electron gas, where the electron density is used as free parameter. The upper panel compares the experimentally determined deviation from 3D FLT behavior to the expectation from FLT. In conclusion, the binding energy dependence can be rationalized within 3D FLT and does not show an explicit 2D behavior.

region. In contrast, at small excess energy above E_F the QWS is confined in the metal film by the Si bandgap and hot electron relaxation may only proceed via e-e scattering to unoccupied bands of the metal, see Fig. 5.15. Thus, FLT for bulk Pb describes the main trend reasonably and can explain the coverage dependence of τ_{e-e} observed in Fig. 5.22. This is in agreement with a recent STS study on the quantum well system of Yb(111)/W(110) [Weg05].

For the luQWS in the Si bandgap only a weak dispersion of the binding energy with the even coverage is observed, compare to Fig.5.14. Hence, a quasi constant e-e scattering rate of the even luQWS is expected by FLT due to the constant phase space available for scattering. In contrast, the upper branch of the odd luQWS disperses strongly toward E_F with increasing film thickness. Thus, the phase space available for energy relaxation processes decreases as well and results in an increase of the lifetime for the odd luQWS in agreement to FLT. In this discussion the screened Coulomb interaction for both odd and even luQWS is approximated to be constant as function of coverage and thus does not introduce any additional thickness dependence of the electron lifetimes. However, it can not be excluded that the screened Coulomb interaction differs for the odd and even branches of QWS and contributes to the deviation of the lifetimes at large excess energies. This is because the luQWSs observed at large excess energies stem from films of only a few ML thickness. In this quasi-2D limit the screening might be reduced and promote more intense e-e scattering leading to shorter lifetimes.

To further analyze if the well-confined quantum well system of Pb/Si(111) exhibits any signs for a dimensionality dependence of the observed decay times, the scaling laws for a 3D and 2D Fermi liquid are compared to the data in Fig. 5.23. The hot electron lifetimes in a 3D and 2D Fermi liquid are expected to scale with the excess energy $\xi = E - E_F$ of the quasi-particle with respect to E_F as $\tau_{e-e}^{(3D)} \propto \xi^{-2}$ and $\tau_{e-e}^{(2D)} \propto \ln(1/\xi)^{-1} \xi^{-2}$. These results are derived in appendix C. In brief, the quadratic scaling with the excess energy ξ expresses energy and momentum conservation of the phase space available for scattering. The logarithmic correction for the 2D case is a consequence of the structure of the screened Coulomb interaction in 2D.

Accordingly, the data is fitted with equations (C.11) and (C.17) from appendix C, where the electron density n is used as a free fit parameter. The fits result in an electron density of $n^{(3D)} = 12.6(5) \cdot 10^{28} \text{ m}^{-3}$ and $n^{(2D)} = 4.3(3) \cdot 10^{19} \text{ m}^{-2}$ for 3D and 2D FLT respectively. The fitted electron densities agree reasonably well to the values calculated in chapter 2.1.2 from the lattice parameter and the number of valence electrons of $n^{(3D)} = 13.2 \cdot 10^{28} \text{ m}^{-3}$ and $n^{(2D)} = 3.77 \cdot 10^{19} \text{ m}^{-2}$. However, the relative deviation of 13% for the 2D case and 5% for the 3D case does not favor the description by 2D FLT. One might be surprised by the good description of the data by 3D as well as 2D FLT. As discussed in the context of Fig. 2.23 in chapter 2.3.1, a pronounced dimensionality dependence of the hot electron lifetimes is expected for excess energies of $< 0.4 \text{ eV}$ above E_F . This weaker dimensionality dependence in the energy regime of $E - E_F > 0.4 \text{ eV}$ discussed here leads to only minor differences of the fits in Fig. 5.23.

Following the introduction in chapter 2.3.1, the difference of the fits for the 3D and 2D FLT scaling laws are plotted in the upper panel of Fig. 5.23 and compared to the difference of the parameter-free description employing the calculated 3D and 2D electron densities. As discussed in Fig.2.23 such a difference plot should reveal any explicit 2D behavior in the electron dynamics of Pb/Si(111). However, the 2D scaling law fails to deliver a better description than the ordinary 3D case. At small binding energies $E - E_F < 0.8 \text{ eV}$ virtually no difference of the 3D and 2D case are encountered. Moreover, at higher energies where the 3D FLT scaling law predicted slightly too large decay times, 2D FLT does even worse and overestimates the lifetimes

by a factor of more than two. This qualitative disagreement and the rather large deviation of the 2D electron density points to the fact that the electron dynamics in Pb/Si(111) are governed by a 3D behavior, although the discrete 2D band structure and the well-resolved lifetimes evidences a high degree of confinement in the surface plane.

The absence of a clear experimental proof for explicitly 2D behavior of the e-e scattering dynamics is surprising and points to a conceptual problem. The theoretical discussion in chapter 2.3.1 and appendix C is valid only for ideal 2D confinement. In fact, the actual QWSs in Pb/Si(111) are confined to a high extend perpendicular to the film as indicated by the formation of sharp, discrete QWSs in the unoccupied band structure. In fact, this point motivated the time-resolved studies on Pb/Si(111) with its high degree of confinement in the global substrate band gap. These sharp QWSs, however, do not imply the complete absence of any coupling in the film direction. Inspecting the derivation of the lifetime in 3D and 2D reveals that the qualitatively different structure of the screened Coulomb interaction mainly determined the different scaling laws in equations (2.29) and (2.30). The good description of the data achieved with 3D FLT might point to a rather 3D screened Coulomb interaction. Calculating the screening wave vectors from equation (C.4) yields $k_s^{(3D)} = 3.45 \text{ \AA}^{-1}$ and $k_s^{(2D)} = 3.78 \text{ \AA}^{-1}$, which corresponds to screening lengths of $\lambda_s^{(3D)} = 2\pi/k_s = 1.82 \text{ \AA}$ and $\lambda_s^{(2D)} = 1.67 \text{ \AA}$. Compared to a thickness of 2.86 \AA for 1 ML these values indicate that already a free-standing Pb(111) film of 1 ML thickness exhibits a 3D type of screening. Moreover, for thin layers of only a few ML thickness also the Si substrate may contribute to the screening in the metal film. Summarizing, with respect to the scattering of hot electrons, the quantum well system of Pb/Si(111) retains a 3D character and should be regraded as quasi-3D as far as the energy relaxation due to e-e scattering is concerned.

Returning to Fig. 5.22 one notices the scattering of the data points of τ_{e-e} at the same film thickness but measured in different Pb/Si(111) wedges. For example, at $\Theta = 4 \text{ ML}$ three different wedges have been evaluated and yield decay times ranging from 104(5) fs to 140(5) fs that are incompatible to each other within the error bars. As shown in Fig. 5.24, the scattering of these individual data points is not due to erroneous data or insufficient fits, but are explained by slight variations of the binding energy of luQWS observed for different wedges. The luQWS observed on wedge "A" for 4 ML is located at $E - E_F = 0.45 \text{ eV}$ and exhibits a decay time $\tau_{e-e} = 140 \text{ fs}$. The $\sim 35 \text{ fs}$ smaller decay time for the luQWS from wedge "C" is explained by the 100 meV larger distance of this particular luQWS to E_F . Hence, the phase space available for scattering increases and the lifetime decreases in accordance with 3D FLT. This close correlation of the binding energy and the observed decay times proves the predicative power of 3D FLT in Pb/Si(111). The variation of the binding energy of luQWS for nominally identical coverages might be introduced by modulations of the pinning position of the Fermi level on each wafer prepared. However, no systematic dependence on the preparation procedure was resolved.

Since time-resolved 2PPE spectroscopy provides simultaneous access to the linewidth in the frequency domain *and* the population decay in the time domain, it is inter-

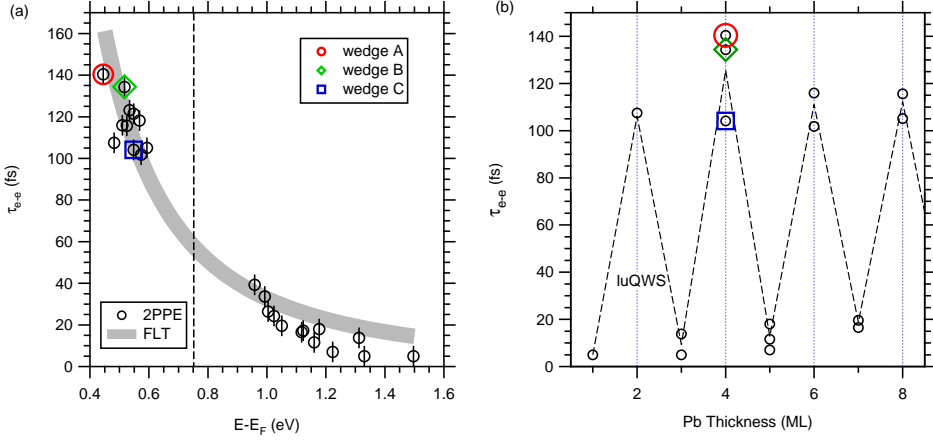


Figure 5.24: The different values of τ_{e-e} observed at nominally identical coverage but for different wedges are explained within 3D FLT by slight variations of the binding energy of the particular luQWS. As the distance to E_F increases, the associated change of the phase space available for scattering increases as well and the lifetime of the state decreases.

esting to compare the linewidth⁶ to the lifetimes. In Fig. 5.25 the spectral linewidth Γ_s of the luQWS is compared to the reciprocal lifetime $\Gamma_1 = \hbar/\tau_1$, given in units of meV. The linewidth Γ_s is extracted from a Lorentzian fit of the spectra, see Fig. 5.8. The linewidth in 2PPE spectroscopy is a time-dependent quantity that can be used to resolve elastic scattering processes that induce dephasing [Fau95, Wei02b]. For the linewidth analysis of the monochromatic 2PPE spectra outlined here a constant contribution of 50 meV due to spectral broadening in the 2PPE process and a finite spectrometer resolution was subtracted.

According to the definition of the spectral function in equation (2.34), the full width at half maximum (FWHM) is related to the linewidth as $2\Gamma_s = \text{FWHM}$. In fact, linewidth and reciprocal lifetime are nicely correlated for the whole wedge up to 8 ML, although the small values of τ_1 for the odd coverages introduces a significant error in Γ_1 . The reciprocal lifetime, however, can not fully account for the observed linewidth since $\Gamma_s > \Gamma_1$ is consistently observed over the whole wedge. On average the inverse lifetime is ~ 40 meV smaller than the linewidth. In other words, the peak is broadened by scattering processes that do not contribute to the population decay. Here, elastic and quasi-elastic scattering processes, as discussed in section 2.3, are considered since they contribute to the linewidth by dephasing but do not induce a population decay. Compared to typical dephasing rates of 20 – 40 meV analyzed in IPS model systems such as Cu(111) [Kno98a], the value of 40 meV for a dephasing contribution to the linewidth in Pb/Si(111) seems reasonable. Possible origins for the dephasing processes are quasi-elastic e-ph and electron-defect scattering events.

⁶To illustrate this point the 2PPE data from the wedge discussed in Fig. 5.9 is used since it exhibits a most pronounced odd-even contrast, indicating a well-ordered Pb/Si interface with only little Pb adatoms that contribute to an inhomogeneous broadening.

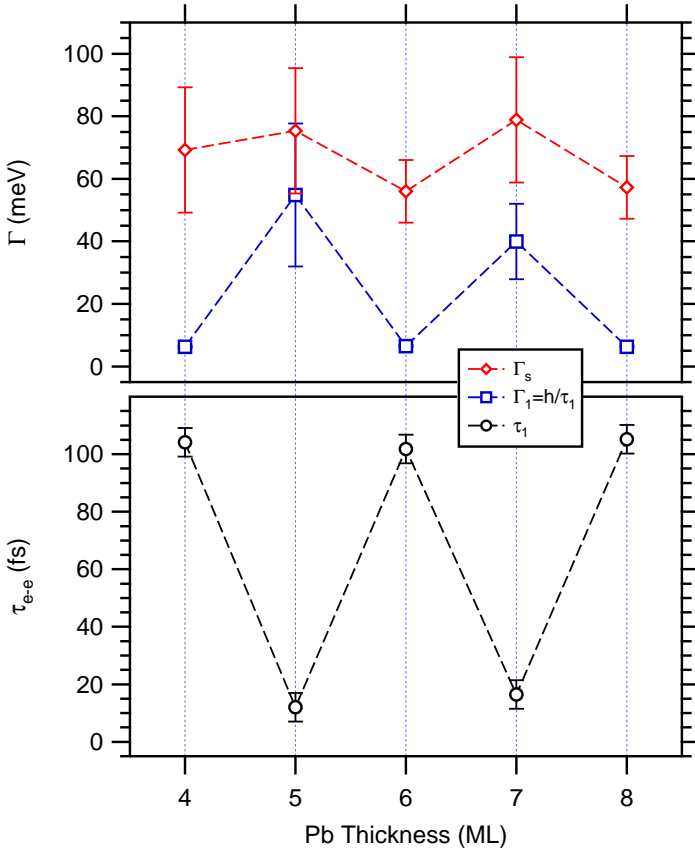


Figure 5.25: The upper panel compares the reciprocal lifetime $\Gamma_1 = \hbar/\tau_1$ of the luQWS to the spectral linewidth Γ_s determined by a Lorentzian fit (see Fig. 5.8) of the monochromatic 2PPE spectra from Fig. 5.9.

Very recently, the coverage dependence of the linewidth of the unoccupied QWS in Pb/Si(111) was analyzed with variable temperature STS [Hon08]. Brun et al. estimate the e-ph and defect scattering contribution to be about 50 meV [Bru08], which is in good agreement with the evaluation outlined here. To investigate these effects in more detail, however, requires to perform temperature dependent and time-resolved 2PPE studies, which allow to disentangle the contributions from e-ph and defect scattering. Also, a time-dependent analysis of the linewidth can elucidate the dephasing contributions to the lifetime in more detail. Nevertheless, the comparison of reciprocal lifetime and linewidth underlines the importance of time-resolved studies in general. Additional broadening mechanism may be operative that inhibit the direct transformation $\Gamma = 1/\tau$ when the lifetime of the hot electron population is concerned. Hence, the reliable access to ultrafast electron dynamics and the underlying microscopic scattering processes, as presented in the following, is greatly facilitated by investigations directly in the time-domain.

5.4.5 Interband vs. Intraband Scattering

Up to here, the contribution of the fast initial decay τ_1 to the energy relaxation in the unoccupied QWS was explained by e-e scattering $\tau_1 = \tau_{e-e}$. In the following, possible scenarios for the origin of the delayed rise feature τ_{12}^{even} in the XC traces of luQWS are reviewed. As suggested in Fig. 5.15, the underlying microscopic scattering processes in the quantized Pb/Si(111) band structure are assumed to be given by inter- and intra-subband scattering. The biexponential decay in luQWS with the second component τ_2^{odd} at odd coverages and the additional decay component τ_B at even coverages is attributed to scattering of photoexcited carriers from the Si substrate and discussed in section 5.4.6.

As presented in chapter 2.4.6 and in the context of Fig. 5.21, the rate equation model of a 4-level system is employed to analyze the XC traces. The rate equation model assumes a coupling of the probed state no. 1, e.g. luQWS, to a second state no. 2. On the one hand, this second state is given by luQWS at $k_{\parallel} \neq 0$ for the case of intra-subband scattering. Here, the hot electron population from outer regions of the Brillouin zone decays toward the band minimum at the Γ -point. Since these scattering processes take a finite amount of time, the population at the band bottom is build up on the timescale of the intra-subband scattering. On the other hand, higher lying states such as the luQWS+1 can couple to the lower lying luQWS. Then the energy relaxation toward E_F of hot electrons in these higher lying QWS can result in inter-subband scattering with the consequence of a delayed rise of the electron population in the luQWS.

For the distinction of inter- and intra-subband scattering in the luQWS, it is important to consider the photon energy of the pump pulse and the dispersion of the higher lying luQWS+1 with coverage since this determines if the luQWS+1 can be populated and thus transfer population to the lower lying luQWS due to inter-subband scattering. The quantized band structure in Fig. 5.14 evidences that at the employed pump photon energy of $h\nu < 1.9$ eV the luQWS+1 can only be populated for coverages $\Theta \geq 8$ ML. If inter-subband luQWS+1 \rightarrow luQWS would be the only contribution to the delayed rise in luQWS, then the delayed rise should be absent below this crossover coverage of 8 ML. The comparison of the XC traces for odd and even coverages in Fig. 5.21, however, does not indicate a decisive change of the shape of the XC traces at this crossover coverage. A closer investigation of the shape of the peak maximum in the inset of Fig. 5.21 reveals that the flat-top shaped peak maximum is especially pronounced for low coverages - in opposition to the expectations for inter-subband scattering. Also, the results for τ_{12} presented in Fig. 5.22 do not exhibit an abrupt change at 8 ML. These observations indicate that the delayed rise in the luQWS might be dominated by scattering with the subband itself and inter-subband scattering presents a smaller contribution.

The detailed investigation of intra-subband scattering processes requires angle- and time-resolved measurements, which, however, have to be carried out yet. The use of the Pb/Si(111) wedges proved to be very important for the reliable discussion of the population decay times without complications due to scattering at corrugated interfaces. But for angle-resolved investigations the macroscopically wedged and thus inhomogeneously prepared surface presents a severe problem because the rotation axis

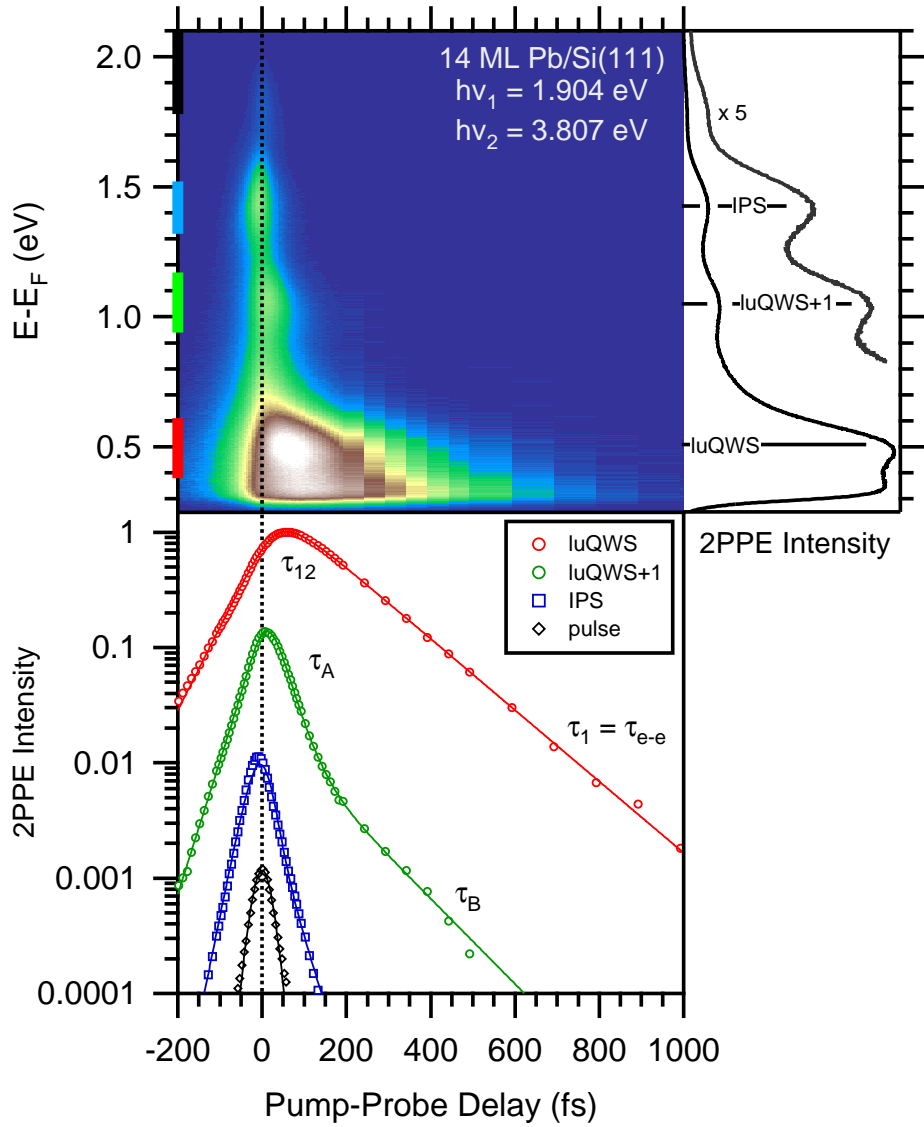
of the sample then defines a single coverage, which is not necessarily integer. One option to overcome this conceptual limitation is to use the position-sensitive electron time-of-flight (pTOF) spectrometer presented in chapter 4 and perform future angle- and time resolved 2PPE studies without rotation on wedged Pb/Si(111) samples.

Although the inter-subband channel $\text{luQWS}+1 \rightarrow \text{luQWS}$ can be ruled out for lower coverages where $\text{luQWS}+1$ is not populated by the pump laser pulse, the possibility remains that the delayed rise at even coverages of $\Theta \geq 8$ ML is - at least partially - induced by scattering from the higher lying to the lower lying state, $\text{luQWS}+1 \rightarrow \text{luQWS}$. To investigate the inter-subband scattering in Pb/Si(111) the time-resolved 2PPE data is analyzed for a 14 ML film where luQWS is situated well in the Si band gap and $\text{luQWS}+1$ is degenerate with Si states as shown in Fig. 5.26. For this preparation, the workfunction of $\Phi = 4.09$ eV allows to access both the luQWS and the $\text{luQWS}+1$.

The XC traces of luQWS and $\text{luQWS}+1$ show a complex behavior as seen in the bottom panel of Fig. 5.26. The electron decay in luQWS is characterized by a delayed rise of the intermediate state population which leads to a broad peak maximum extending from 30 fs to 85 fs, while $\text{luQWS}+1$ lacks a delayed rise and presents a biexponential decay. The similarity to the case of lower coverages where only luQWS could be populated evidences that the type of decay observed - delayed rise or biexponential decay - depends only on the energetic position of the respective state and not its rank within the hierarchy of the unoccupied QWS. In Fig. 5.14 and Fig. 5.22 it was discussed that for an crossover coverage of $\Theta > 8$ ML the unoccupied QWS at odd coverage turns from the luQWS into the $\text{luQWS}+1$. This change of the rank in the hierarchy of the unoccupied QWSs, however, does not change the characteristic shape of a biexponential decay. This is also seen in Fig. 5.21, where the slope of the second contribution in the biexponential decay changes with coverage, but the shape of the XC is essentially constant. To describe both QWS consistently the rate equation model is used to take inter-subband scattering from $\text{luQWS}+1$ to luQWS into account. This is done by interpreting the population density $n_1(t)$ as the transient population of luQWS and $n_2(t)$ as the population in $\text{luQWS}+1$ in equations (2.53) and (2.54), respectively⁷.

⁷Please note that for this particular assignment of the states to the transient populations equation (2.54) describes a single exponential decay and does not account for the second decay channel in $\text{luQWS}+1$.

Figure 5.26 (*facing page*): False color representation of the 2PPE intensity as a function of pump-probe delay and intermediate state energy $E - E_F$ is given in the center panel. The vertical color bars indicate the energy windows in which the intensity was integrated to monitor the time dependence of the 2PPE intensity. Four spectral features are analyzed (bottom panel) and attributed to luQWS , $\text{luQWS}+1$, an IPS, and high-energy electrons. Note that the IPS is excited with the UV pulse $h\nu_2$ and thus its energy is given by $E - E_F = 3.33$ eV, respectively $E - E_V = -0.76$ eV. Solid lines are fits following a rate equation model. The laser pulse duration is inferred from the transient hot electron distribution for $E - E_F > 1.8$ eV to be 34(5) fs, see chapter 3.1.3. For this preparation, the lifetime of the IPS is determined to be 24(5) fs in agreement with data presented in Fig. 5.18. These spectral signatures are also seen in the 2PPE spectrum integrated from -65 to 200 fs, given in the right panel.



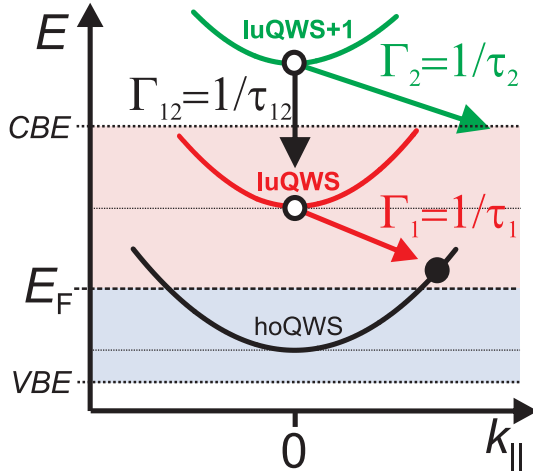


Figure 5.27: Visualization of the rate equations (2.51) and (2.52) for an inter-subband scattering mode. Γ_1 and Γ_2 quantify the depopulation rates of luQWS and luQWS+1 via scattering to unoccupied states. Γ_{12} accounts for the intra-subband scattering luQWS+1 \rightarrow luQWS.

These two coupled differential equations describe the transient population $n_1(t)$ and $n_2(t)$ of luQWS and luQWS+1, respectively, as sketched in Fig. 5.27. Γ_1 accounts for the decay of the excited electron population of luQWS to e.g. unoccupied states of the metal film near E_F . Γ_{12} describes the delayed filling of luQWS due to inter-subband scattering from luQWS+1. Γ_2 summarizes all decay channels of luQWS+1, which are not associated with the inter-subband transition luQWS+1 \rightarrow luQWS. These decay channels may involve scattering to unoccupied states of the Si substrate as well as inter-subband scattering to unoccupied states at $k_{||} \neq 0$ within the metal film. The total decay rate, which is directly observed in the fast initial decay of luQWS+1, is defined as $\Gamma'_2 = \Gamma_{12} + \Gamma_2$. The case $\Gamma'_2 > \Gamma_1$ results in $C > 0$ and equation (2.53) describes a delayed population build up in luQWS and subsequent decay at a rate Γ_1 . Thus the coupled rate equation model connects the decay rate Γ'_2 observed in the initial decay of luQWS+1 with the population build up in luQWS.

For luQWS the fit of the rate equation model results in $\tau_1 = \hbar/\Gamma_1 = 142(5)$ fs for the decay and a characteristic rise time of $\tau_{12} = 54(5)$ fs, which gives an excellent description of the data as shown in Fig. 5.26. Turning to luQWS+1, the population decay is analyzed⁸ by a biexponential decay resulting in a fast decay time of $\tau_A = 30(5)$ fs and a slow one of $\tau_B = 135(10)$ fs. As a test of the rate equation model the experimentally determined decay time τ_A of luQWS+1 is compared to the total decay time τ'_2 calculated within the rate equation model:

$$(5.6) \quad \tau'_2 = \frac{\tau_{12} \tau_2}{\tau_{12} + \tau_2} .$$

⁸In fact, the XC trace of luQWS+1 was analyzed by the identical 4-level rate equation model such that $\tau_A \equiv \tau_1$ and $\tau_B \equiv \tau'_2 = 1/(\tau_{12}^{-1} + \tau_2^{-1})$. However, to avoid confusion with the parameters for luQWS a different nomenclature was chosen.

In this equation, the decay constants τ_{12} and τ_2 measured for the luQWS determine the lifetime τ'_2 expected for luQWS+1. For a consistent description of inter-subband scattering luQWS+1 \rightarrow luQWS the calculated total decay time τ'_2 of luQWS+1 is expected to be identical to the decay time τ_A as observed in the experiment. Within errors bars the calculated value of $\tau'_2 = 35(10)$ fs indeed matches the experimentally determined decay time $\tau_A = 30(5)$ fs. Thus, the delayed population build-up in luQWS on a timescale τ_{12} and the simultaneous decay of luQWS+1 with $\tau'_2 = \tau_A$ are indeed compatible with the proposed inter-subband scattering from luQWS+1 to luQWS. This numerical analysis, however, is just a necessary condition for inter-subband scattering and does not prove it directly. Future angle- and time-resolved 2PPE investigations will be able to disentangle the underlying microscopic processes of inter- and intra-subband scattering in the important thin film model system of Pb/Si(111).

5.4.6 Substrate Contributions

At this point, the slower decay component τ_B ⁹ observed in the biexponential decay of the luQWS is reviewed. The XC traces in Fig. 5.21 and the fit results in Fig. 5.22 show a faster, thickness dependent contribution of $\tau_B = 90 - 300(10)$ fs for odd coverages. The longer lifetime $\tau_B = 0.9(1)$ ps for even coverages is thickness independent, but the amplitude of this contribution decreases with increasing coverage, compare to Fig. 5.21. This biexponential decay of luQWS indicates scattering from higher lying states or states at equal energy, which are significantly longer lived than luQWS. These states could be localized either in the Pb film or in the substrate. The pump-photon energy $h\nu_1$ is not sufficient to populate any higher lying states in the film, such as luQWS+2 or any IPS by one-photon processes. Thus, the decay process described by τ_B is attributed to scattering of photoexcited electrons from the Si substrate to the unoccupied QWS in the metal film.

This brings up the question of the photo-generated carrier density in Si under the employed excitation conditions with typical fluences of up to $65 \mu\text{J}/\text{cm}^2$. Since pump pulses at 1.9 eV photon energy were used, indirect transitions and two photon absorption in Si [Sjo98] are responsible for the absorption as indicated in Fig. 5.28(b). An experimental analysis of the carrier density would require a systematic temperature and fluence dependence, which is out of the scope of the present study. Nevertheless, a comparison with earlier studies at similar photon energy and one order larger fluence [Gol94, Jeo96] suggests that sizable densities are generated. Please note that the population attributed to scattering from Si is considerably smaller than the photo-generated population in the Pb film and amounts to a few parts per thousand.

The following argumentation focuses on the comparison of the luQWS at 5 and 6 ML, as shown in Fig. 5.28, since no additional relaxation processes in the Pb film have to be taken into account as no higher lying QWS can be populated by the pump pulse, but such excitations do occur in the substrate. To explain the pronounced odd-even dependence of τ_B the position of the luQWS with respect to the Si bands and scattering from the bulk Si conduction band (CB) into the Pb film is considered.

⁹In this section the second decay constant τ'^{odd} from section 5.4.3 is termed τ_B to unify the nomenclature at this point.

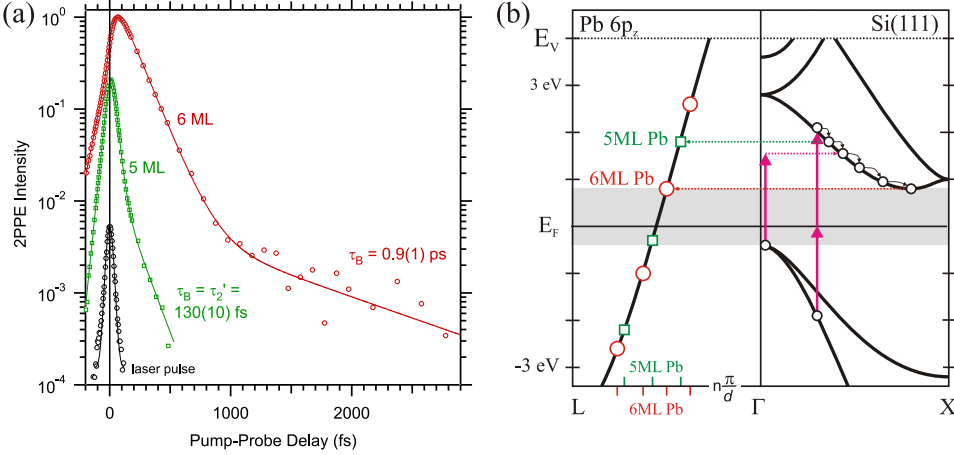


Figure 5.28: XC traces of luQWS for 5 ML (\circ) and 6 ML films (\square), which both exhibit a biexponential decay. The decay component τ_B at later delays is assigned to scattering of photoexcited electrons of the Si substrate to the unoccupied QWS. The inset shows the quantized dispersion of the Pb- $6p_z$ QWS along k_\perp and the indirect Si bandgap along ΓX . A possible mechanism explaining the different time-scales analyzed for τ_B is depicted.

Hot electrons in Si relax in a cascade of electrons via phonon-mediated intra-band scattering toward the band bottom, see Fig. 5.28(b). In bulk Si the energy relaxation time is found to be ~ 250 fs [Sjo98, Sab02] in the low excitation regime and increases for high excitation densities [Sjo98]. The relaxation time on the Si(100) surface is reported to be larger [Wei04, Wei05, Voe04]. Subsequent energy relaxation at the Si surface proceeds via formation of surface excitons in the Si band gap on a time scale of 5 ps [Wei04, Wei05]. Thus the specific binding energies of luQWS at different thickness with respect to the Si CB can explain the two time scales observed for τ_B . In case of 5 ML the luQWS is degenerate with the Si CB. The relaxation of hot electrons through intraband decay on a few 100 fs timescale in Si is monitored indirectly by means of electrons that scatter quasi-elastically into the luQWS located in the Pb film. This serves as a reasonable scenario to explain τ_B of about 130 fs for luQWS at 5 ML.

In contrast, for 6 ML luQWS resides in the Si band gap. Electrons scattered into luQWS might originate from electrons near the CB minimum in Si, where they exhibit a significantly longer lifetime. This scattering into the Pb adlayer might serve as an explanation for $\tau_B = 0.9(1)$ ps encountered for the 6 ML film. On the basis of these data it cannot be decided unambiguously whether the decay in Si or the scattering to the Pb film is the step that determines τ_B , although the coverage dependence of τ_B for the odd layers favors the first alternative. As the intraband decay in the Si CB is mediated by electron-phonon scattering it is rather likely that the ~ 1 ps timescale observed for 6 ML is determined by the decay in Si. Moreover, this timescale agrees with earlier reports reasonably well [Wei04, Voe04]. One could expect that the long lifetimes at the Si CB bottom leads to an even slower decay. However, the presence

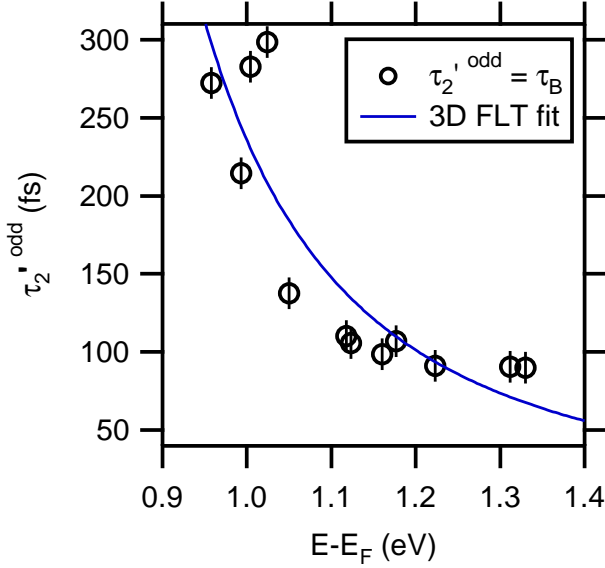


Figure 5.29: The energy dependence of the second component in the biexponential decay of the luQWS at odd coverages, $\tau_2'^{\text{odd}}$, can be modeled by the 3D FLT scaling law from equation (C.11) when the electron density n and the band bottom E_0 is used as a free fit parameter. This results in an electron density comparable to bulk Pb, which is combined with an energy reference of $E_0 = 0.62$ eV, comparable to the lower CBE.

of the metal facilitates energy gain of the excited electrons by their transfer to the metal film where they can decay to the Fermi level. Thereby, exciton formation in the region near the interface is quenched. Further insight is expected from future temperature-, fluence- and angle-dependent studies.

Furthermore, this Pb/Si interface scattering model might explain the coverage dependence of the second component⁹ in the biexponential decay at odd coverages $\tau_B \equiv \tau_2'^{\text{odd}}$ presented in Fig. 5.22. The different coverage dependence for odd and even film thicknesses was mainly determined by the fact that the unoccupied QWS at even coverage exhibit a quasi-constant binding energy of $E - E_F \approx 0.6$ eV, whereas the unoccupied QWS at even coverage disperse toward E_F with increasing film thickness. Qualitatively, the decreasing distance to E_F decreases the phase space available for the relaxation of the hot electron population and thus enlarges the lifetime. As the film thickness increases the luQWS moves toward the CBE of the Si substrate and thus samples an increasing lifetime of the photoexcited carriers with approaching the Si band bottom. To investigate this argument in more detail the lifetime $\tau_2'^{\text{odd}}$ is plotted as function of the excess energy in Fig. 5.29.

The lifetimes for large excess energies of > 1.1 eV are constant at ~ 100 fs and increase sharply with decreasing excess energy, which can be explained by a decrease of phase space. The qualitative behavior of the lifetimes resembles the expectation from FLT, see section 5.4.4. In fact, the dispersion of the lifetimes can be described by a 3D FLT fit according to equation (C.11). To achieve this, the reference to the

Fermi energy E_F , which has been fixed to $E_F = 0$ for the evaluation of $\tau_1 = \tau_{e-e}$, is replaced by a free fit parameter E_0 . In this model, the curvature of the energy dependence of the lifetimes is determined by n , whereas E_0 denotes the excess energy for which the lifetimes diverge due to an vanishing phase space.

The resulting fit is shown in Fig. 5.29 as solid line and yields a valence electron density of $n = 14(1) \cdot 10^{28} \text{ cm}^{-3}$ and $E_0 = 0.62(10) \text{ eV}$. The electron density is comparable to the bulk electron density of $13.2 \cdot 10^{28} \text{ cm}^{-3}$, whereas the energy reference coincides with the lower CBE of the Si substrate at $E - E_F \approx 0.7 \text{ eV}$. Thus, the second component τ_2^{odd} in the biexponential decay of the luQWS at odd coverages samples properties of both the substrate and the metal film. On the one hand, the coincidence of the fitted position of the band bottom E_0 with the lower Si CBE indicates that the phase space for the decay of the second component is governed by the band structure of the Si substrate. Considering the decay of hot electrons in the substrate, the lifetimes are expected to show a pronounced increase upon approaching the band bottom. On the other hand, the close resemblance of the fitted electron density with the value for bulk Pb points to a screening contribution to the lifetimes that is governed by the electron density in the metal film. Here, interface effects such as the band bending and the pinning of the Fermi level may serve as an example how the electron density in the metal directly influences the band structure at the metal/semiconductor interface. This might be an indication that the component τ_2^{odd} stems from a metal-induced state at the Pb/Si interface that is energetically referenced to the lower CBE of the substrate but otherwise governed by the electron density of the metal film. However, a first principle study, which takes the substrate with the reconstructed Pb/Si interface into account could contribute to a precise microscopic understanding of these different contributions in Pb/Si(111). Also, time-resolved studies of the electron dynamics at other well-defined metal/semiconductor interfaces might complement these investigations nicely.

Conclusions

The ultrafast electron dynamics in unoccupied quantum well states in ultrathin Pb films on Si(111) has been investigated by fs-time-resolved 2PPE. The transient populations of two QWSs above E_F are analyzed as function of film thickness and binding energy. The energy dependence of the fast initial decay times in the two unoccupied QWSs of 5 – 140 fs are assigned to e-e scattering within the metal film and agree surprisingly well with 3D FLT. Additional decay processes observed on longer timescales with decay times of 90 – 300 fs and ~ 900 fs are attributed to the decay of hot carriers in the Si substrate which are probed in 2PPE because hot electrons scatter from Si into the Pb film. Although the quantized Pb/Si(111) band structure indicates a high degree of electron confinement, which is corroborated by the well-resolved lifetimes, no explicitly 2D behavior of the scattering rates was revealed. Furthermore, to describe all observed transient populations quantitatively it is necessary to account for the quantization of the electronic system. The analysis of the simultaneous population decay and build-up in the two adjacent subbands favors inter-subband scattering from the higher lying luQWS+1 into the lower lying luQWS. The comprehensive analysis demonstrates that the quantization has to be considered explicitly for a description of electron dynamics in the quantum well subbands. Future angle-resolved investigations are expected to lead to a more comprehensive analysis of intra- and inter-subband scattering. Thereby the influence of (i) the quantization in the quasi-2D band structure and (ii) of the Si substrate on e-e scattering rates might be analyzed directly in the time domain.

5.5 Ultrafast Dynamics of the Occupied QWS

This section deals with the ultrafast electron dynamics of the *occupied* QWS in Pb/Si(111) that was investigated with time- and angle-resolved photoemission spectroscopy (tr-ARPES) far from thermal equilibrium¹⁰. The experimental details of the tr-ARPES experiments are explained in chapter 3.1 and appendix E. This tr-ARPES study was carried out on a 10 ML Pb/Si(111) film by pumping the system with infrared (IR) pulses of $h\nu_1 = 1.50$ eV photon energy and probing the transient band structure at a UV photon energy of $h\nu_2 = 6.00$ eV. The IR pump pulses present a pulse duration of 55 fs, whereas the UV probe pulse are slightly longer with 80 fs due to non-linear effects in the quadrupling process, see appendix E. The XC of pump and probe pulses results in an overall time resolution of 100 fs. Three different regimes for the absorbed fluence were studied: $F_1 = 40 \mu\text{Jcm}^{-2}$, $F_2 = 130 \mu\text{Jcm}^{-2}$ and $F_3 = 210 \mu\text{Jcm}^{-2}$.

These fluences are below the damage threshold of Pb/Si(111) as no irreversible spectral changes were encountered. The use of even higher pump fluences was inhibited by 3- and 4-photon absorption processes that created a large pump-induced background. This was because these measurements have not been carried out on a wedged sample. Hence, the film thickness slightly deviated from an integer value and plasmon excited at islands and step edges might lead to this limitation of the achievable S/N ratio.

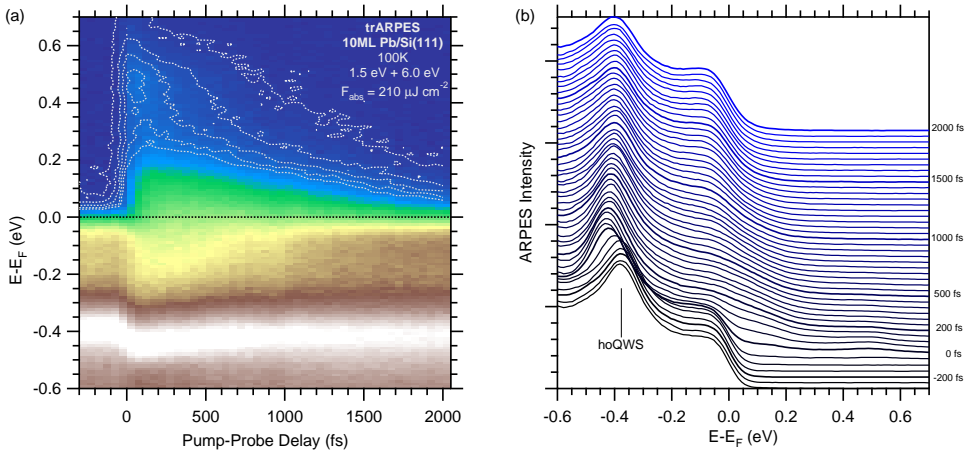


Figure 5.30: tr-ARPES spectra of 10 ML Pb/Si(111) for an absorbed fluence of $F_3 = 210 \mu\text{Jcm}^{-2}$. (a) False color plot of photoemission intensity at the Γ -point as function of pump-probe delay. The hot electron distribution above E_F is emphasized by the contour lines. The binding energy of the hoQWS at $E - E_F \approx -0.4$ eV shifts instantaneously within the pump pulse duration. (b) Transient spectra as function of pump-probe delay as indicated on the right side.

¹⁰The analysis of the peak shift and the simulation with the 2TM outlined in section 5.5.1 was performed by Laurenz Rettig.

Such a tr-ARPES measurement for 10 ML Pb/Si(111) is presented in Fig. 5.30. The hot electron distribution reaches up to 1.5 eV above E_F and persists up to 2 ps due to the strong excitation of the electronic system, where a few % of the electrons below E_F are excited. For the largest fluence F_3 , the spectral weight of the hot electron distribution at $0 < E - E_F < 1.5$ eV corresponds to 6% of the spectral weight below E_F . Besides the hot electron distribution, the most pronounced effect is a transient shift of the binding energy of the hoQWS at $E - E_F \approx -0.4$ eV away from E_F . The waterfall plot in Fig. 5.30(b) evidences that this binding energy shift occurs on an ultrafast timescale around zero pump-probe delay.

Before turning to the detailed analysis of the transient binding energy of the occupied QWS, the unoccupied QWS is briefly compared to the results from the previous section 5.3. As indicated by the contour lines in Fig. 5.30(a) and evidenced by the semi-logarithmic representation in Fig. 5.31, the luQWS is populated by the IR pump pulse and subsequently probed with the UV pulse. The binding energy of $E - E_F = 0.50$ eV observed with tr-ARPES fits nicely into the scheme of the quantized band structure in Fig. 5.14 analyzed with 2PPE. At the end of this chapter, the electron dynamics of the luQWS measured by tr-ARPES is compared to the results from 2PPE.

5.5.1 Simulation with the 2-Temperature Model

The next section discusses the behavior of the excited carriers to investigate the reason for the binding energy shift of the hoQWS in detail. Fig. 5.31(a) shows spectra of the hot electron distribution that were normalized to the intensity of the hoQWS for various pump-probe delays on a semi-logarithmic scale. At zero delay (topmost curve) the excited electrons are distributed non-thermally, which is indicated by the discrete spectral structure above E_F . In Fig. 5.31(b) the non-thermal part of the spectrum at zero delay is compared to a spectrum before excitation. The electron distribution follows a Fermi-Dirac distribution up to E_F , which is given by the temperature T_0 before excitation. These electrons originate from unexcited parts of the DOS that have not yet participated in the e-e scattering with hot electrons. With increasing pump-probe delay the excess energy of the hot electrons above E_F is transferred via e-e scattering to the cold part of the electronic subsystem. This process is described as thermalization of the hot electron distribution [Fan92, Lis04a]. After ≈ 200 fs the electron distribution is characterized by a Fermi-Dirac distribution again, which exhibits a significantly increased transient temperature $T_{el} \gg T_0$ that may rise up to 1000 K, depending on the applied fluence.

With increasing time the excess energy is transferred from the electronic subsystem to the phononic subsystem via e-ph scattering. This lowers the electronic temperature and raises the lattice temperature such that after a few ps both subsystems have equilibrated. This process can be described phenomenologically in the 2TM [Ani74, Ret02, Lis05a, Bov07]. This model treats the electronic and phononic subsystem as two coupled heat baths. The exciting laser field transfers its energy to the electronic heat bath and heats it. At the same time the electronic excess energy is redistributed due to electron diffusion and transferred to the phononic heat bath via e-ph scattering of hot electrons. The energy densities of the electron subsystem U_{el} and of the lattice

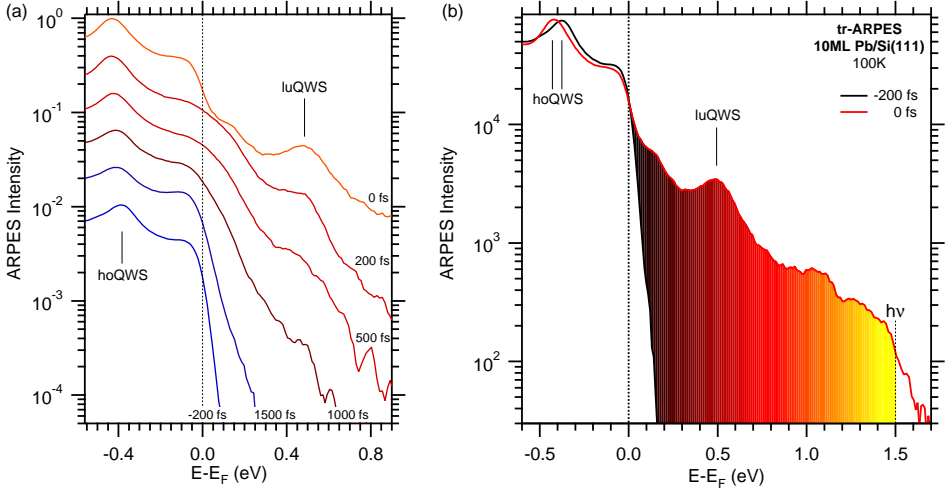


Figure 5.31: (a) PES spectra for various pump-probe delays on a semi-logarithmic scale. The non-thermal electron distribution around zero pump-probe delay has equilibrated at 200 fs. Even after 2 ps the surface has not yet relaxed as evidenced by the peak shift of the hoQWS. The spectrum at zero delay exhibits a peak from the luQWS at $E - E_F = 0.50$ eV. (b) The transient energy density is evaluated by integration of the excess energy times the PES intensity as highlighted by the color scale. Please note that the two small peaks observed at $E - E_F \approx 0.2$ eV and 1.1 eV are attributed to photoemission from neighboring coverages and initial state effects, respectively.

subsystem U_{ph} are determined by a set of coupled differential equations [Lis05a]:

$$(5.7a) \quad \frac{dU_{\text{el}}}{dt} = \underbrace{\frac{\partial}{\partial z} \left(\kappa_e \frac{\partial}{\partial z} T_{\text{el}} \right)}_{\text{diffusion}} - \underbrace{H(T_{\text{el}}, T_{\text{ph}})}_{\text{e-ph coupling}} + \underbrace{S(z, t)}_{\text{optical excitation}}$$

$$(5.7b) \quad \frac{dU_{\text{ph}}}{dt} = +H(T_{\text{el}}, T_{\text{ph}}) .$$

The energy densities U_{el} and U_{ph} are connected via the respective heat capacities to the temperatures of the electron and the lattice subsystem. The different contributions are discussed in detail in reference [Lis05a]. Fig. 5.32 shows the results of simulation within the 2TM for the electron and lattice temperature at the surface of a Pb single crystal. The numerical parameters used are given in table 5.2.

The ultrafast dynamics can be separated into two regimes: Within the first 150 fs most of the excess energy is stored in the electronic subsystem since the electrons absorb the light. Thus, effects occurring within the first 100 fs are likely to be induced by the interaction with the non-equilibrium electron distribution. At later times the energy is transferred to the lattice and thermally induced effects dominate. After ≈ 1200 fs both temperatures have equilibrated. However, since the Pb/Si interface most probably presents a barrier for the electronic diffusion the actual e-ph relaxation

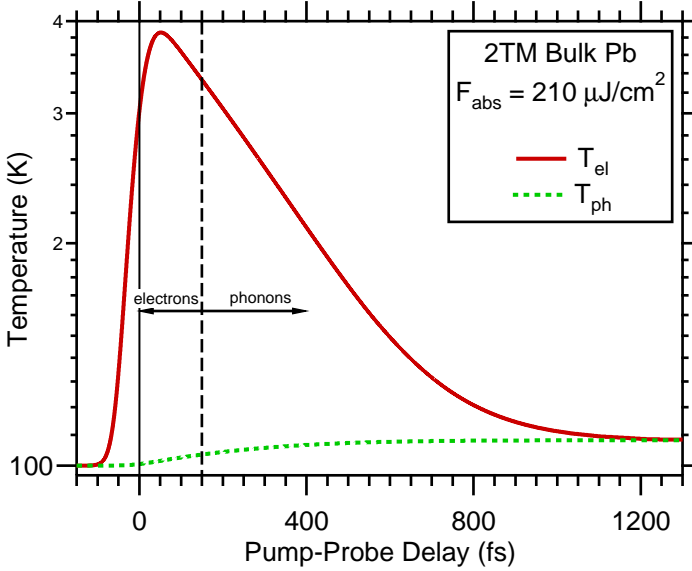


Figure 5.32: The transient electronic temperature T_{el} and lattice temperature T_{ph} at the surface of a Pb bulk crystal were calculated for an absorbed fluence $F_3 = 210 \mu\text{Jcm}^{-2}$ within the 2TM. Within the first 150 fs almost all excess energy is stored in the electronic subsystem and processes occurring on this time scale are dominated by electronic effects. After ≈ 1200 fs the electronic and phononic temperatures have equilibrated

in the thin film system of Pb/Si(111) will be slower than in the 2TM simulation.

Due to the pronounced non-thermal electron distribution the concept of an electronic temperature is not well-defined and has to be replaced by a more meaningful measure of the internal energy that remains valid under non-equilibrium conditions. This is achieved by introduction of the electronic excess energy U_{el} , which is well-defined at all times [Lis05a]. The electronic heat capacity γ_e provides the connection to the temperature [Kit04]:

$$(5.8) \quad U_{\text{el}} = c_e T_{\text{el}} = \frac{1}{2} \gamma_e T_{\text{el}}^2$$

e-ph coupling constant	g_{inf}	1.23 [Bro90]	$10^{17} \text{ Wm}^{-3}\text{K}^{-1}$
electronic heat capacity	γ_{el}	163.1 [Kit04]	$\text{Jm}^{-3}\text{K}^{-2}$
electronic heat conductivity	κ_0	35.3 [Kit04]	$\text{Jm}^{-1}\text{K}^{-1}$
Debye temperature	Θ_{D}	105 [Kit04]	K
mass density	ρ	11340 [Kit04]	Kgm^{-3}
optical penetration depth	δ	20.5 [Lan76]	nm
absorbed fluence	F_{abs}	210	μJcm^{-2}

Table 5.2: Material constants used for the 2TM simulation shown in Fig. 5.32.

This quantity is experimentally determined by integration of the photoemission signal times the excess energy [Lis05a]:

$$(5.9) \quad U_{\text{el}} \propto \int_0^{h\nu} I_{\text{PES}}(E)|E|dE$$

The shaded area in Fig. 5.31(b) resembles this integral, where the excess energy is indicated by the false color coding. The constant energy density before excitation due to a finite sample temperature is subtracted in the evaluation of the energy density U_{el} .

The transient electronic energy density is shown in the central panel of Fig. 5.33 as function of pump-probe delay for the three laser fluences used. After a steep increase on the timescale of the laser pulse duration, which is shown in the lower panel, the excess energy peaks at ≈ 150 fs. Subsequently, the electronic excess energy is dissipated to the lattice subsystem. The timescale for the relaxation of the electronic excess energy is significantly longer than the results of the 2TM simulation in Fig.5.32 suggest and takes longer than the investigated delay interval of 2 ps.

The transient shift of the binding energy of hoQWS, which was extracted from a Lorentzian line fit of the spectra, is depicted in the upper panel of Fig. 5.33. The comparison of the peak shift and electronic energy density underlines the electronic origin of the peak shift, which exhibit a close correlation for the first 100 fs. The binding energy change relaxes to its equilibrium value on a timescale of 500 fs for $F_1 = 40 \mu\text{Jcm}^{-2}$ and 1 ps for $F_3 = 210 \mu\text{Jcm}^{-2}$ toward its initial position. The equilibrium binding energy of hoQWS, however, is not reached after 1 ps and the peak continues to be slightly shifted. After one laser repetition cycle of 3.3 μs the system is back to equilibrium and can be excited again.

As discussed in Fig. 5.32 this ultrafast peak shift occurs on a timescale of ~ 100 fs, which points to an electronically induced effect as most of the excess energy is stored in the electronic subsystem¹¹. The ion cores are too massive to couple on this timescale to the external perturbation. Furthermore, the sign of the peak shift is interesting. After excitation the hoQWS peak shift away from E_F toward *larger binding energies*, which corresponds to an *energetic stabilization* of this state due to the pump pulse. This behavior is opposed to the naive idea that the excess energy in the electronic system weakens the bonds and thus decreases the binding energy. A similar peak shift was also encountered for the surface state of the Gd(0001) surface for comparable excitation densities [Bov07]. Here, the binding energy shift occurs on a somewhat slower timescale of ~ 200 fs and thus is explained by a combined influence of electronic and phononic effects. Also, for fluences of $> 60 \mu\text{Jcm}^{-2}$ and delay times > 500 fs the opposite sign of the peak shift toward E_F , e.g. smaller binding energies, is observed for Gd. This behavior is not encountered for the QWS of Pb/Si(111) and ascribed to thermal effects such as the lattice expansion in Gd.

¹¹The surface photovoltage (SPV) that was discussed in the context of section 5.4.1 can not explain this phenomenon since the SPV leads to a rigid shift of the whole spectrum. This is not observed here as Si bands at lower energy and the low-energy cut-off remain at constant energy. Also the SPV is known to relax on a significantly longer timescale of ~ 100 ns [Wid03].

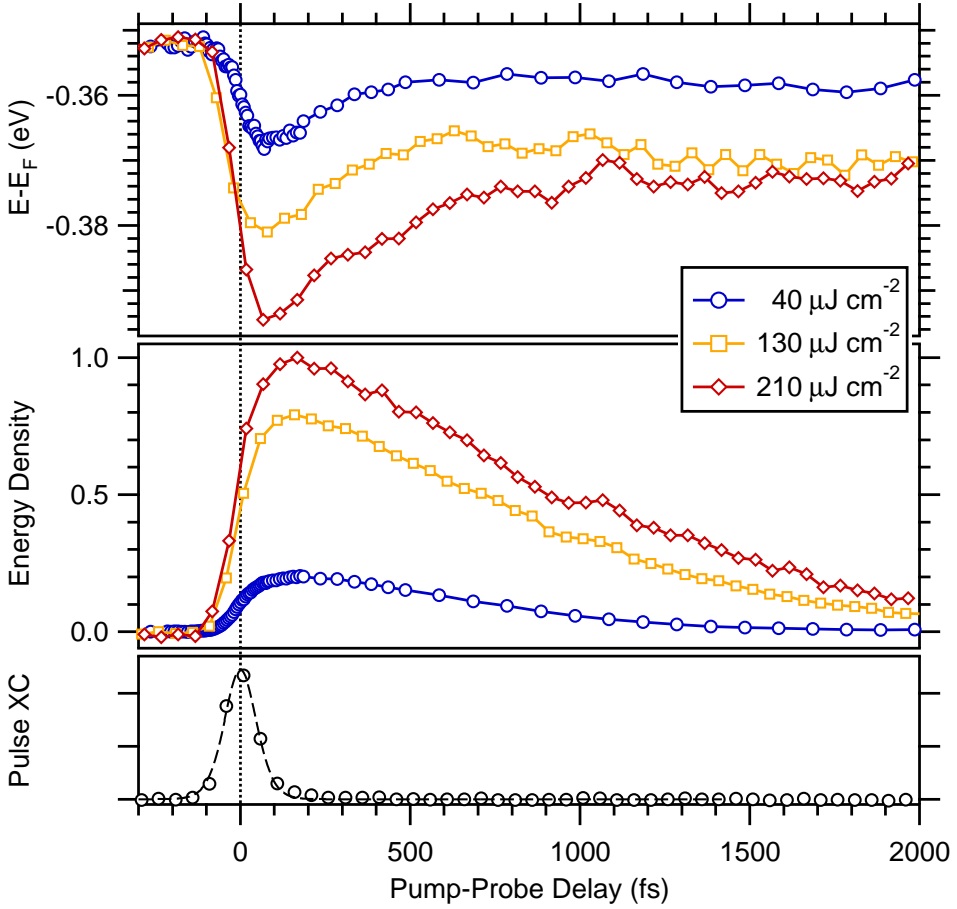


Figure 5.33: Comparison of the energy density according to equation 5.9 and the shift of the peak maximum of the hoQWS determined by a Lorentzian line fit as function of pump-probe delay. The shift of the peak maximum occurs on the timescale of the optical excitation regardless of the fluence. After 2 ps the initial excitation has not yet decayed and the hoQWS still is shifted from its equilibrium position. The lower panel depicts the laser pulse XC that was inferred from the hot electron population at $E - E_F = 1.5$ eV and results in 80(10) fs overall time resolution.

The transient peak shift in Pb/Si(111) to a larger binding energy can be explained - at least qualitatively - by an increase of the ion core potential due to photo-doping. The intense pump beam excites a significant amount of a few % the valence electrons into unoccupied parts of the band structure and creates the same amount of holes below E_F . The reduced density of valence electrons results in an decrease of the electronic screening of the ion cores and thus enlarges the ion potential. This increased potential then is observed as an increase of the binding energy. Recent calculations by Recoules et al. [Rec06] reveal an increasing binding energy of the d -bands in Au

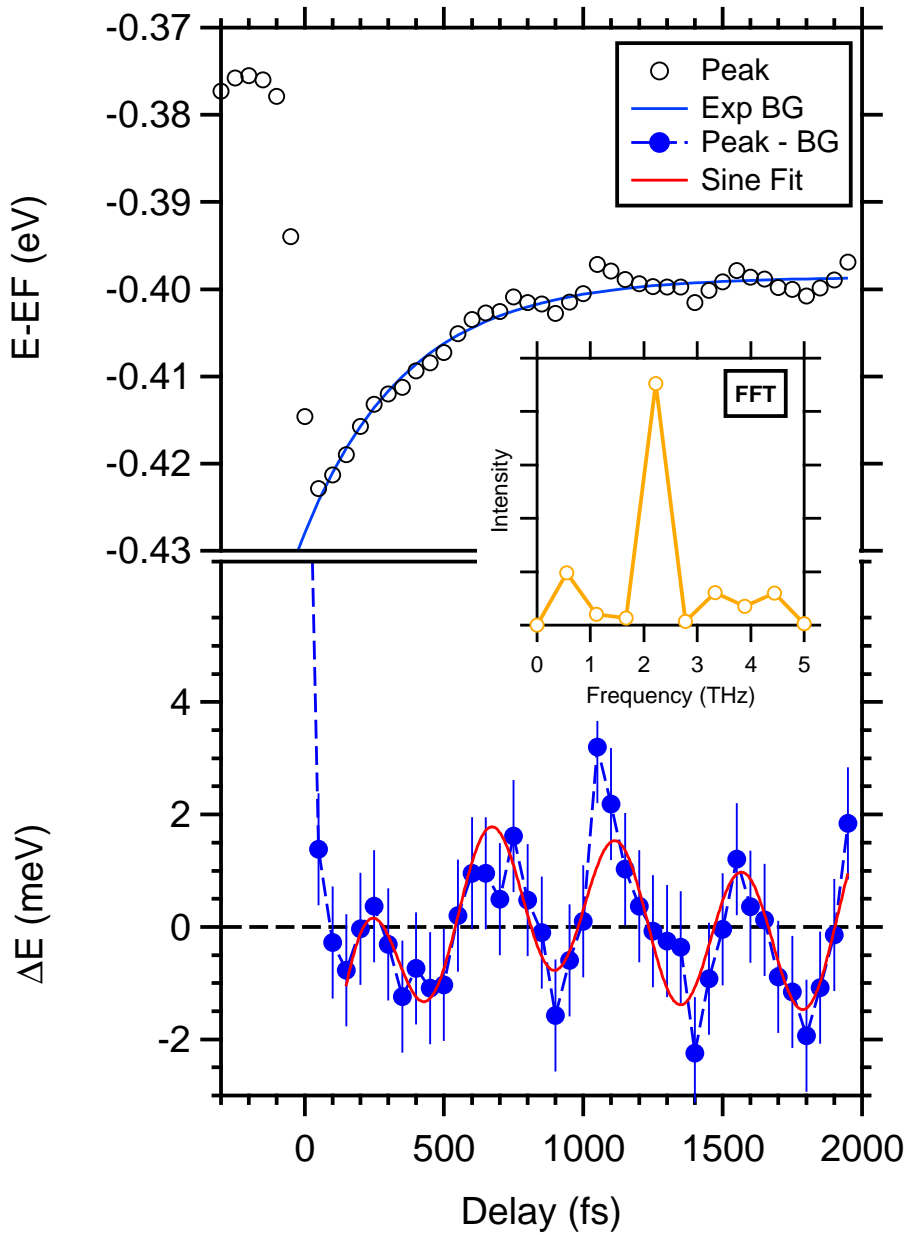
with increasing electronic temperature, which is explained by a decrease of screening. This stabilizes the lattice and increases the Debye temperature, which gives rise to a higher melting point. Recent investigations of the ultrafast melting of Au using time-resolved electron diffraction [Ern08] succeeded to observe this effect experimentally and corroborate the scenario introduced here.

5.5.2 Coherent Phonon Modes in Pb/Si(111)

A closer investigation of the transient spectra of the hoQWS for the largest applied fluence $F_3 = 210 \mu\text{Jcm}^{-2}$ reveals an oscillation of the binding energy, which is attributed to the interaction with a coherent phonon in the following. The upper panel of Fig. 5.34 shows the transient peak position of the hoQWS together with a fit of an exponential function, which describes the continuous relaxation of the peak position toward the equilibrium value. This fitted background (BG) is subtracted to highlight the binding energy oscillations ΔE as shown in the lower panel of Fig. 5.34. After the steep drop at 0 fs a modulation of the binding energy sets in after ~ 100 fs and persists up to 2 ps. In order to evaluate the frequency of the oscillation a sine function with frequency ν and phase ϕ together with a third order polynomial is fitted to the transient variation ΔE . The resulting fit is shown by a solid line in the lower panel of Fig. 5.34 and yields a period of 460 fs, corresponding to a frequency of $\nu = 2.18(5)$ THz and a phase of $\phi = 0.47(5)\pi$. To confirm the fitting results, the transient variation ΔE is Fourier transformed for the time interval 0.15 – 2 ps and is depicted in the inset of Fig. 5.34. The Fourier spectrum exhibits a well-resolved peak at a frequency of 2.2(1) THz.

This brings up the question of the origin of the binding energy oscillation. Here, e-ph interaction is considered to be the dominating effect. The 2TM discussed above describes incoherent e-ph interaction, where the electronic excess energy excites acoustical phonons with the result that the crystal is heated. Besides this incoherent e-ph interaction, coherent lattice motions can be induced by an excitation of the electronic system. The underlying physical mechanism as sketched in Fig. 5.35 is introduced briefly in the following, a more detailed reasoning is found in [Dek00, Bov07]. The ultrafast optical excitation with a photon of energy $h\nu$ suddenly changes the electronic screening of the ion cores and thereby induces a force on the lattice that initiates the motion of the nuclei. A resonant optical transition projects the system onto the excited state potential energy surface, which is determined by the screening in the excited electronic state. Since the new equilibrium position Q_0^* on the excited potential energy surface is displaced from the ground state equilibrium position Q_0 a coherent

Figure 5.34 (*facing page*): Top: The binding energy of the hoQWS reveals a modulation for the largest $F_3 = 210 \mu\text{Jcm}^{-2}$. Subtracting an exponential function (BG) yields the modulation ΔE in the lower panel. Fitting a sine function (solid line) to ΔE results in an oscillation frequency of $\nu = 2.18(5)$ THz and a phase of $\phi = 0.47(5)\pi$. Inset: The Fourier transformation (FFT) of the binding energy variation ΔE reveals a sharp peak at $\nu = 2.2(1)$ THz, which coincides with a maximum of the DOS in the phonon band structure [Row69, Lan76, Sav96].



wave packet motion is launched, provided that the exciting pump pulse $h\nu$ is shorter than the period of the phonon mode. The oscillating nuclei positions in turn affect the renormalization of the electronic band structure and thus can modulate the amplitude, linewidth and binding energy of a quasi-particle peak in the electronic spectrum. This resonant mechanism is termed displacive excitation of coherent phonons (DECP) [Che91, Lob01] and can also be described as resonant coherent Raman scattering [Gar96]. Off-resonant Raman excitation provides a scenario with the impulsive excitation of coherent phonons (IECP). Ideally, the quasi-instantaneous displacement of the lattice coordinates leads to a cosine phase for the DECP mechanism. In contrast, the IECP exhibits a sine phase with a linear increase of the amplitude after the excitation. The distinction of these two regimes, however, requires a photon energy dependent analysis [Gar96]. Such coherent phonons have been intensively investigated in semiconductors, semimetals and high-TC superconductors by femtosecond optical pump-probe experiments [Cho90, Che91, Gar96, Has96, Lob01, Has03] and ultrafast x-ray diffraction methods [ST03, Bar04]. Typical frequencies for the coherent phonons are of the order of THz. Coherent phonons in bulk metals have been observed only recently in *d*-wave transition metals [Has05]. Also, the lanthanide systems of Gd(0001) and Tb(0001) present coupled coherent phonon-magnon modes at about 3 THz that was examined with time-resolved PES [Bov04, Bov06, Bov07] and magneto-optical methods [Mel08]. Interestingly, coherent phonons have not been observed in *sp*-metals yet. This is explained by an efficient screening of the photoholes by the delocalized *sp*-bands [Bov07], which results in marginal changes of the excited state potential energy surface and a low excitation efficiency.

The elastic properties of Pb were investigated early in the 1960's using neutron diffraction [Bro61, Bro62] and superconducting tunneling [Row69]. Pb was the first material to present experimental evidence for a Kohn anomaly in the phonon spectrum [Koh59, Wol62, Bro61, Ste67] due to the large e-ph coupling constant in bulk Pb of $\lambda = 1.55$ [Sav96]. The coverage dependence of the e-ph coupling in Pb/Si(111) was studied in the context of the modulation of the superconductivity transition temperature [Guo04]. This analysis indicates that the e-ph coupling constant λ in the ultrathin Pb films is subject to a quantum size effect. The difference of λ for subsequent layers can be as large as 30% and is - besides the oscillatory DOS at E_F - one of the driving forces of the modulated superconductivity transition temperature. The phonon spectrum of Pb exhibits a pronounced peak at ~ 2.2 THz [Lan76, Row69] that is attributed to a longitudinal phonon mode along the Γ -L direction [Sav96].

In fact, not only the frequency of the longitudinal phonon of 2.2 THz at the L-point coincides perfectly with the observed binding energy oscillation, but also the direction of the phonon matches the film direction. Also, the phase of $\phi = 0.47(5)\pi$ extracted from the sine fit in Fig. 5.34 agrees well to the value of $\pi/2$ expected for the DECP mechanism shown in Fig. 5.35. The transient energy densities analyzed in Fig. 5.33 and their comparison to the modeled energy densities from Fig. 5.32 indicate that the Pb/Si interface presents a barrier for the energy transport. This barrier preserves the non-equilibrium conditions for > 2 ps as evidenced by the transient peak shift and the energy density. Thus, the ultrathin film with efficient confinement of the excitation energy and the large e-ph coupling in Pb might induce the displacive excitation of a longitudinal optical phonon mode, leading to the collective binding energy modulation

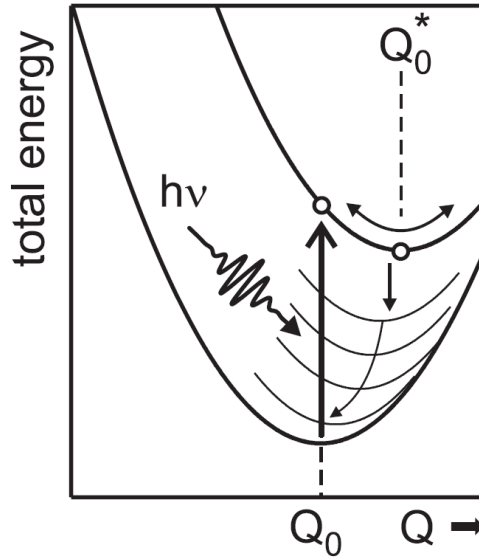


Figure 5.35: Sketch of ground state and excited state potential energy surface along the lattice coordinate Q with equilibrium positions Q_0 and Q_0^* , respectively. The resonant absorption of a photon with $h\nu$ changes the electronic screening quasi-instantaneously and projects the system onto the excited potential energy surface. A coherent phonon wave packet motion is launched due to the displaced equilibrium positions. The excited system relaxes toward the ground state due to dissipation and incoherent scattering process [Bov07].

at 2.2 THz. However, also the quantized band structure itself might play a role in the excitation mechanism.

A detailed investigation of the binding energy modulations will be the scope of future work. The analysis of the oscillation phase favors a DECP mechanism, which, however, requires a resonant optical transition that was not directly observed in this study at the Γ -point. To confirm the scenario outlined here, k -resolved 2PPE studies are necessary that investigate the excitation process for different pump photon energies and positions in the Brillouin zone. Such an analysis will contribute to a comprehensive understanding of the optical coherent phonon mode observed here. The oscillatory e-ph coupling suggest to perform future coverage-dependent 2PPE studies on wedged Pb/Si(111) sample. This also minimizes the surface roughness, allowing higher excitation densities and might enable a clearer observation of the coherent phonon mode in Pb/Si(111).

5.5.3 Population Decay in the Unoccupied Bands

The intense pump pulse employed in tr-ARPES creates a transient hot electron distribution in the *unoccupied* part of the band structure. The well-defined electronic structure of the QWSs in Pb/Si(111) above and below E_F allows to follow the decay of the transient population in the lowest unoccupied quantum well state (luQWS) and compare the dynamics to the results from time-resolved 2PPE, see chapter 5.4.3.

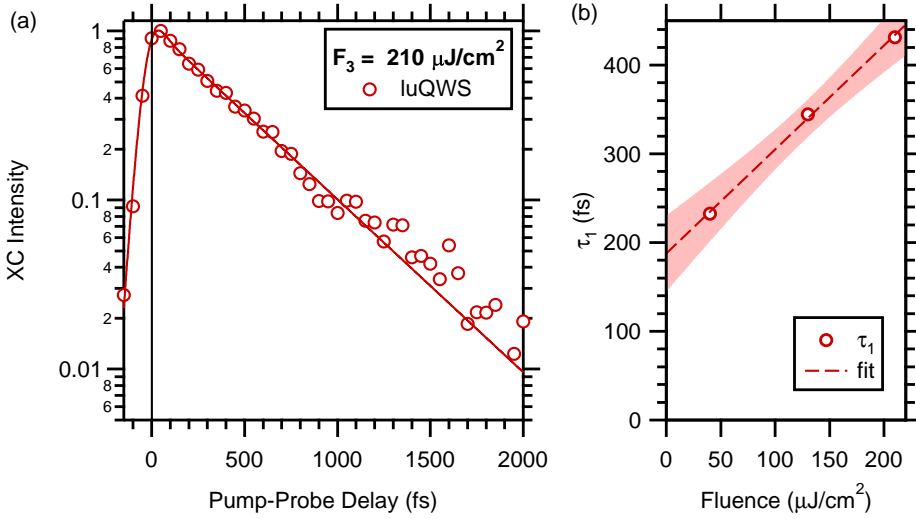


Figure 5.36: (a) XC trace of the lowest unoccupied QWS at 10 ML Pb/Si(111) analyzed by tr-ARPES. The population decay is described by a single exponential decay that is indicated by a solid line. (b) Compared to the results from 2PPE the decay time τ_1 analyzed here is fluence dependent. The shaded area indicates a 90% confidence interval of the linear fit.

In Fig. 5.31(a) the population decay of the luQWS at $E - E_F = 0.50$ eV is directly evident in the spectra up to a delay of 1 ps. The clear observation of the luQWS also in tr-ARPES suggest the comparison of the lifetimes analyzed by 2PPE for the regime of low excitation densities of $\sim 10^{-4}$ and tr-ARPES, which is performed at significantly higher excitation densities of up to 6%. The population decay in the luQWS is analyzed in Fig. 5.36 for the largest fluence F_3 . Due to the longer UV probe pulses the delayed rise of the transient population is not resolved here and the population decay is characterized by a single exponential decay. The decay is quantitatively analyzed by a fit of the 3-level response function from equation (2.50) and yields a decay time of $\tau_1 = 420(15)$ fs. Compared to the results from 2PPE the decay time analyzed for this fluence is about a factor three larger. Moreover, the decay times exhibit a pronounced fluence dependence, which is shown in Fig. 5.36(b). The decay time τ_1 observed in tr-ARPES scales linearly with increasing fluence. Extrapolating the values for a vanishing fluence $F = 0$ yields an axis intercept at $\tau_1(F = 0) = 190(42)$ fs. Although this value still is about 1.4 times larger than the results from 2PPE it is compatible within the error bars.

The pronounced fluence dependence of the population decay time τ_1 of the luQWS can be explained by the high excitation density of a few % achieved in this tr-ARPES experiment. This excitation density is more than two orders of magnitude higher than in the 2PPE experiments discussed in the previous section 5.4. For the discussion of the 2PPE experiments it was assumed that the excited electron density is small enough that (i) the interaction of the excited electrons themselves can be neglected and (ii) the band structure is not perturbed by the excited electrons and thus presents a fixed

stage for the electron dynamics. Both these arguments break down at the investigated excitation densities and hence, the excited electrons may interact with each other and also the band structure changes temporarily as evidenced by the transient binding energy shift of the hoQWS.

Thus, it is important to distinguish between the population decay in the single particle limit, i.e the lifetimes, as studied with 2PPE and the dynamics of an excited electron distribution, i.e. an effective population, accessible with tr-ARPES. Under the excitation conditions discussed here, a non-thermal excited electron distribution is created by intense pump pulse at 0 fs, which relaxes within ~ 200 fs via e-e scattering to form a thermalized hot electron distribution that is described by a Fermi-Dirac distribution function, see Fig. 5.31. As sketched in Fig. 5.15 the relaxation of the hot electron population proceeds via inelastic e-e scattering with cold electrons in the Fermi sea and the creation of secondary e-h pairs around E_F . Hence, electrons scatter in and out of the observation window at a fixed energy in the course of the thermalization process. At later delays the decrease of the hot electron population is dominated by e-ph scattering and the transfer of electronic excess energy to the lattice subsystem. If the population decay at later times is dominated by e-ph coupling, a non-exponential decay of the hot electron population due to the cooling of the Fermi-Dirac distribution can be expected. In this respect, the good description of the population decay by a single exponential decay in Fig. 5.36(a) for $t < 1000$ fs is interesting. The deviations encountered at $t > 1000$ fs might indicate the contribution from e-ph coupling to the population decay.

Conclusions

Time-resolved 2PPE enabled the detailed study of the ultrafast single particle electron dynamics in the limit of low excitation densities around $\ll 10^{-2}$. tr-ARPES extends the investigation into a regime of high excitation densities in the order of a few %, where collective excitations of the electronic system may be observed. Summarizing, the investigation of the ultrafast non-equilibrium dynamics in Pb/Si(111) revealed a transient binding energy stabilization of the hoQWS and a periodic modulation of the energy shift that is attributed to a coherent lattice motion. The creation of a significant amount of e-h pairs of up to 6% gives rise to a quasi-instantaneous change of the electronic screening of the ion cores. The resulting increase of the ion potential leads to an ultrafast energetic stabilization of the hoQWS, which was resolved by a transient increase of the binding energy occurring within the time-resolution of 100 fs. The analysis of the transient energy density corroborates the correlation of the binding energy shift to the excitation of the electronic system. After ~ 100 fs the binding energy relaxes toward its equilibrium value due to e-ph scattering. A detailed investigation of the transient binding energy revealed a modulation with a characteristic frequency of 2.2 THz. This frequency coincides with a peak in the phonon spectrum of Pb that originates from a longitudinal phonon along the [111] direction. This favors the assignment of the modulation to a coherent phonon mode along the [111] film direction. In this respect coherent and incoherent e-ph coupling in metals has been addressed: On the one hand, the redistribution of the excess energy in the electronic system is governed by incoherent e-ph scattering processes. The thermalization process leads to an equilibration of the energy content of the electronic and phononic subsystems and the relaxation of the peak shift. On the other hand, the optical excitation of a coherent phonon mode highlights the collective excitation of the electron and lattice subsystem, leading to a modulation of the binding energy with a well-defined phase with respect to the instant of excitation.

This work introduces tr-ARPES as a promising tool for the study of non-equilibrium phenomena beyond the single particle approximation at solid state surfaces. The next chapter will take this idea and extend it to the observation of collective charge density excitations in a strongly correlated electron system directly in k -space.

6 Electron Dynamics in In/Si(111)

This chapter presents a angle- and time-resolved two-photon photoemission (2PPE) study of quasi-1D, self-assembling Indium nanowires on Si(111) using the position-sensitive electron time-of-flight (pTOF) technique described in chapter 4. The 4×1 -In/Si(111) reconstructions leads to chain formation along the $[1\bar{1}0]$ -direction of the Si substrate that give rise to a quasi-1D band structure [Yeo99]. This creates the interesting situation where the potential anisotropy of the hot electron dynamics can be studied with respect to the directions of the metallic wires on the surface [Rüg07]. From simple considerations of the metallic density of states (DOS) and the wave function overlap parallel and perpendicular to the nanowires an asymmetry of the hot electron lifetimes can be expected. The more intense scattering of the hot electrons along the atomic chains is estimated to lead to shorter lifetimes of the hot electron distribution along the wires compared to the lifetime perpendicular to wires, where the scattering is less intense. In the previous chapters, the ultrafast dynamics in the quasi-2D model systems of ultrathin metal films of Pb/Si(111) (chapter 5) and in the quasi-1D system of RTe₃ (chapter 7) were studied. The investigation the k -resolved electron dynamics of 4×1 -In/Si(111) presented here, extends the study of the dimensionality dependence of the hot electron dynamics further in the quasi-1D regime.

The wealth of information that is obtainable with the pTOF technique is first analyzed in the spectral domain. Here, several different presentations of the photoelectron distribution in the 2D band structure are discussed. For an extensive analysis of the electron dynamics in the time domain, the transient spectral intensities are evaluated in the accessible part of the Brillouin zone and summarized in energy- and k -resolved maps of the hot electron lifetime. These obtained k -dependent lifetime maps allow the simultaneous analysis of the electron dynamics along any in-plane direction. The analysis of the asymmetry in the lifetime maps regarding the scattering of hot electrons parallel and perpendicular to the nanowires, however, could not resolve an unambiguous asymmetry in the hot electron lifetimes in the vicinity of the Γ -point and at binding energies essentially degenerate with the Si substrate. This result is explained by the fact that the quasi-1D character of the 4×1 -In/Si(111) band structure is most pronounced at the Brillouin zone boundary, whereas this investigation was carried out at the zone center. Future investigations will focus on lower energies and other regions of the Brillouin zone where the anisotropy of the band structure is strongest and pronounced effects also on the hot electron lifetime can be expected, see Fig. 6.2 and Fig. 6.3.

6.1 Ground State Properties of 4×1 -In/Si(111)

The 4×1 -In/Si(111) reconstruction forms metallic nanowires that can be regarded as a prototypical quasi-1D system since it exhibits a strongly anisotropic band dispersion depending on the in-plane orientation with respect to the nanowires. First studies indicating quasi-1D bands in 4×1 -In/Si(111) were performed with angle-resolved photoemission spectroscopy (ARPES) [Abu95, Yeo99] and inverse photoemission spectroscopy (IPES) [Hil97, Hil99]. The 4×1 -In/Si(111) surface undergoes a reversible phase transition at low temperatures that doubles the periodicity of the surface reconstruction to 8×2 observed with scanning tunneling microscopy (STM) [Par04, Lee06] that is accompanied by the opening of a bandgap at the Fermi Surface (FS) as evidenced by ARPES data [Yeo99, Gal01, Yeo02, Ahn04, Cra06, Sun08]. This phase transition is assigned to a Peierls metal-to-insulator transition that is driven by the nesting of the quasi-1D FS along the direction of the nanowires, see chapter 2.2 for details on the Peierls mechanism. The phase transition in In/Si(111) and the electronic ground state properties of the metallic nanowires were studied intensely by numerous techniques such as reflectance anisotropy spectroscopy (RAS) [Ped98, Fle04, Fle05], low energy electron diffraction (LEED) [Oef93, Sar97, Gal01, Lee02, Lee06], STM [Kra97, Ryj01, Uch02, Kur05], reflection high-energy positron diffraction (RHEPD) [Has07, Fuk08, Has08]. The In/Si(111) surface has also received significant attention from theory [Cho01, Miw01, Nak01, Sri04, Cho05a, LL05, Tsa05, Gon06, LL06, Rii06, Yeo06, Yag07].

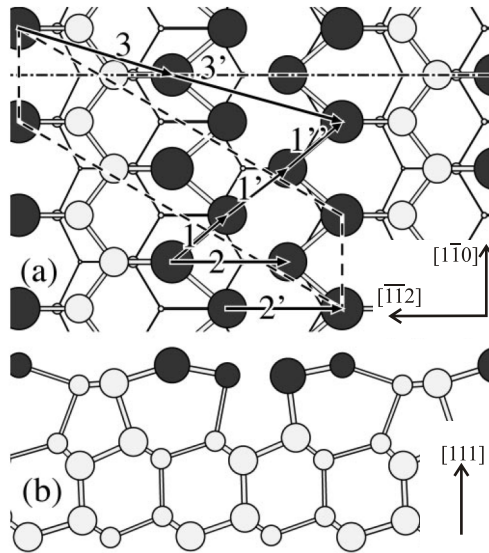


Figure 6.1: Ball and stick model of the 4×1 -In/Si(111) reconstruction after [Bun99]. (a) Top view of the 4×1 reconstructed surface. Two zig-zag chains of In atoms run along $[1\bar{1}0]$ and form the metallic nanowires. In the perpendicular direction $[\bar{1}12]$ the In chains are separated by a Si stripe. (b) Side view of the 4×1 surface. The in- and out-of-plane symmetry directions are indicated.

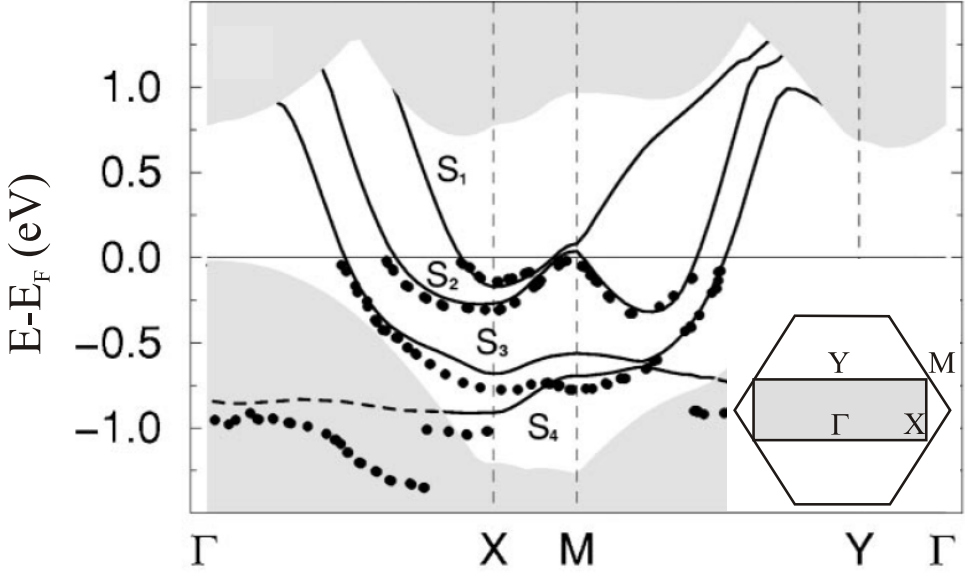


Figure 6.2: Surface band structure of 4×1 -In/Si(111) calculated within DFT. Shaded areas indicate the projected bulk-band structure. Filled circles represent the ARPES data from [Abu95]. The inset shows the surface Brillouin zone for the rectangular 4×1 unit cells with the hexagonal 1×1 unit cell as a reference.

The detailed structure of the 4×1 and 8×2 phases and the microscopic correlation of the real space and electronic structure in the course of the Periel's transition are still debated in literature [Bun99, Kum00, Gon06, Rii06, Yeo06, Fuk08]. Nevertheless, the quasi-1D structure of the 4×1 -In/Si(111) reconstruction was revealed by surface x-ray diffraction (SXRD) [Bun99], which will be used in the following as the underlying structure model for 4×1 -In/Si(111). A ball and stick model of the 4×1 -In/Si(111) surface is shown in Fig. 6.1 as top and side view. The metallic chains are built from two zig-zag rows of In atoms that run along $[1\bar{1}0]$. In total the atomic chain is 4 In atoms wide, corresponding to ~ 7 Å, and each chain is separated by a Silicon strip of ~ 6 Å width from the other chains. The inter-chain separation amounts to ~ 13 Å [Bun99, Cho01, Miw01].

Turning to the electronic structure, the results of a density functional theory (DFT) calculation [Cho01] are depicted in Fig. 6.2 along the high symmetry directions parallel and perpendicular to the nanowires. The subbands S_1 to S_4 are derived from In orbitals and form the FS in In/Si(111). As indicated by the 4×1 unit cell in Fig. 6.2, the nanowires run along the Γ -X direction, which is reflected by the parabolic dispersion of the bands. In the X-M direction perpendicular to the nanowires the bands retain a more localized character with less dispersion.

Focusing on the results from ARPES, a photoemission intensity map at E_F of the nesting region in 4×1 -In/Si(111) [Sun08] is shown in Fig. 6.3. In accordance with the calculated band structure in Fig. 6.2 and earlier ARPES studies [Yeo99, Gal01, Yeo02] the FS is formed by three subbands, termed m_1 , m_2 , and m_3 here. These subbands

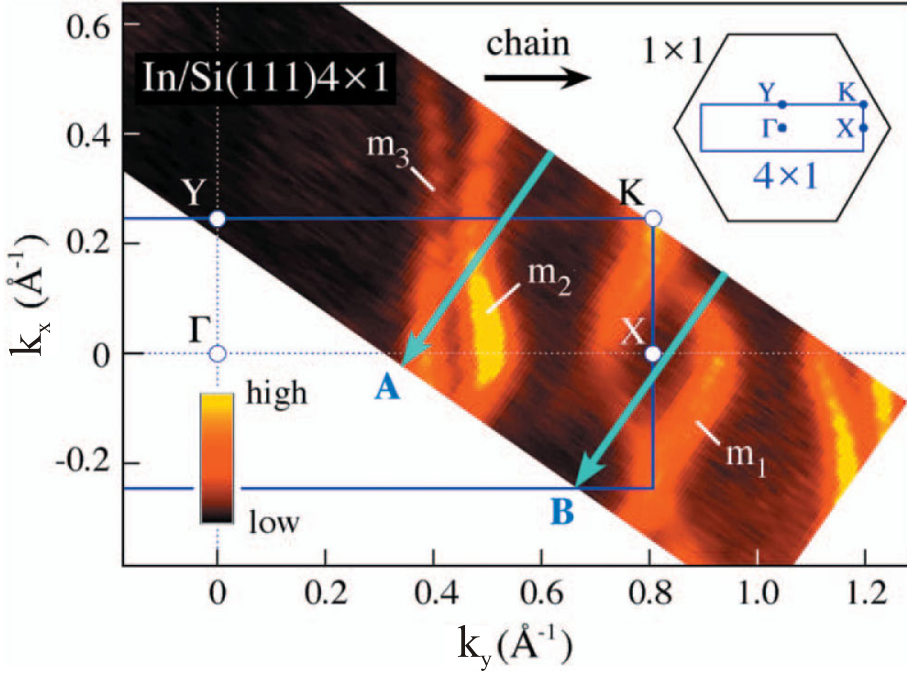


Figure 6.3: Photoemission intensity map of the quasi-1D FS in 4×1 -In/Si(111). The subbands m_1 , m_2 , and m_3 exhibit an anisotropic dispersion: A nearly free electron dispersion is encountered along the wires in ΓX -direction (k_y), whereas the bands perpendicular to the wires in ΓY direction (k_x) remain localized with constant energy. Taken from [Sun08].

disperse strongly parallel to the direction of the atomic chains, Γ -X (k_y) and remain rather localized with a weak dispersion perpendicular to the wires Γ -Y (k_x). Thus, the band structure of 4×1 -In/Si(111) resembles a parabolic trench that runs along the ΓY direction and a slice of the band structure at constant energy results in a quasi-1D rectangular FS.

Up to now, the electron dynamics in the 4×1 -In/Si(111) reconstruction have not been investigated directly in the time domain. However, there exists a very recent electron energy loss spectroscopy (EELS) study, which claims non-Fermi liquid theory (FLT) behavior of low energy plasmon excitations in 4×1 -In/Si(111) [Hwa07, Liu08]. Hwang et al. observed an anomaly of the scaling law of the plasmon energy-momentum dispersion $\omega(q)$ in 4×1 -In/Si(111) which can not be understood on the basis of FLT. Although the quasi-1D electron system of 4×1 -In/Si(111) does not exhibit signs of a spin-charge separation expected for the so-called Luttinger liquid [Lut61, Lut63, Med92, Voi95], the authors explain this anomaly with the nearly perfect 1D band structure. The well-understood equilibrium band structure of 4×1 -In/Si(111) and the strongly anisotropic quasi-1D band dispersion that stems from the linear structure of the self-assembling metallic chains qualifies 4×1 -In/Si(111) as an excellent candidate for anisotropic scattering rates of hot electrons.

6.2 Experimental Details

The preparation of the 4×1 -In/Si(111) reconstruction is similar to the preparation of the Pb/Si(111)- $(\sqrt{3}\times\sqrt{3})$ -R 30° reconstruction described in chapter 3.3.1. In brief, the n-doped Si substrate is flashed to 1470 K to obtain a clean surface. Immediately after the flash, the temperature is quenched within a few seconds to ~ 1200 K and then slowly lowered to 970 K to obtain the 7×7 -Si surface reconstruction. About 2 ML In are evaporated from Knudsen cell onto the Si substrate at room temperature, which then is annealed to $\sim 500^\circ\text{C}$ to form the 4×1 -In/Si(111) reconstruction [Hil97, Kra97, Hil99]. The annealing step is performed in front of the LEED optic to follow the formation of the reconstruction in real time. All measurements of In/Si(111) were performed at $T = 300$ K to avoid the formation of the 8×2 phase at lower temperatures.

The finite spot size of the incident laser pulses requires the preparation of a single domain 4×1 -In/Si(111) reconstruction, which allows to address the electron dynamics along specific high symmetry directions along and perpendicular to the nanowire structure. To achieve a single domain surface reconstruction, the wafer samples are cut with a slight misalignment of $|\alpha| < 4^\circ$ with respect to the [111] surface normal. A miscut toward the $[\bar{1}\bar{1}2]$ direction generates steps in the Si substrate that run along the perpendicular $[1\bar{1}0]$ direction. These steps in the substrate break the three-fold symmetry of the Si(111) surface and predefine a direction for the growth of the In nanowires. Please note that the 4×1 -In/Si(111) reconstruction forms self-assembled nanowires on flat terraces and does not decorate the step edges, as does Gold on vicinal Si(111) surfaces [Seg99, Los01, SP04, Teg05, Rüg07].

In this context the three-fold symmetry of the Si(111) surface has to be observed as this leads to two inequivalent miscuts. For a miscut angle $\alpha > 0$ the direction perpendicular to the steps is given by $[\bar{1}\bar{1}2]$ and a single-domain 4×1 -In/Si(111) re-

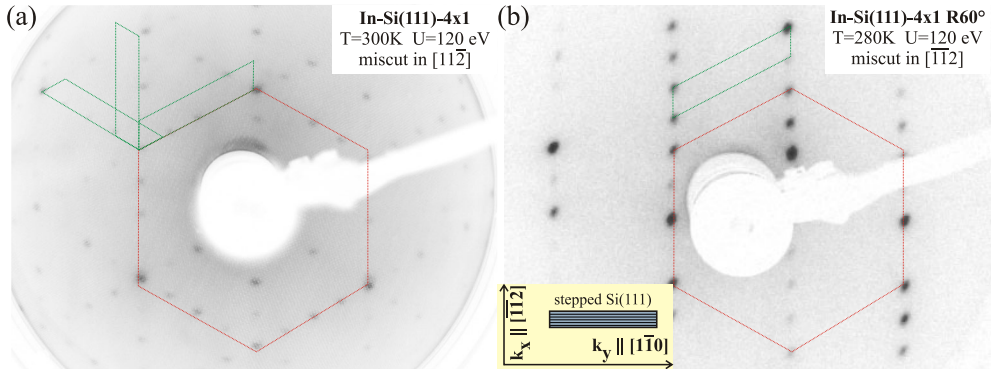


Figure 6.4: LEED images of 4×1 -In/Si(111) with the hexagonal 1×1 Si unit cell (red) and the 4×1 reconstructed surface cell (green) in reciprocal space. (a) multi-domain 4×1 reconstruction obtained on a sample with miscut along $[11\bar{2}]$. (b) Single domain 4×1 reconstruction prepared on a wafer with miscut along $[\bar{1}\bar{1}2]$. The inset shows a Si wafer with step rows indicated by horizontal lines and the coordinate system used throughout the text.

construction with single steps can be achieved by the quenching of the sample temperature [Lin98]. In the case $\alpha < 0$ the steps are perpendicular to the $[11\bar{2}]$ direction and tend to form triple steps [Lin98]. In Fig. 6.4 the consequence of the different miscut directions for the 4×1 -In/Si(111) reconstruction is illustrated by LEED images. The image in Fig. 6.4(a) was obtained on a sample that was miscut in the $[11\bar{2}]$ direction, whereas the LEED image in Fig. 6.4(b) was taken from a sample with a miscut along the $[\bar{1}\bar{1}2]$ direction. Clearly, the miscut along $[11\bar{2}]$ produces a multi domain reconstruction, where all three symmetry directions of the Si(111) surface are present. In contrast, the miscut along $[\bar{1}\bar{1}2]$ yields a single domain reconstruction [Ste93] that is well suited for photoemission studies [Hil97, Hil99, Gal01]. Therefore, the present study was performed on Si(111) samples with a miscut of $\alpha = 3^\circ$ toward the $[\bar{1}\bar{1}2]$ direction.

The preparation of the stepped Si(111) surface requires consideration of step migration and step bunching [Lat89, Gol91, Vie98, Yan96]. These processes are induced by the current that passes the Si sample under direct current heating conditions. Since step migration and step bunching can lead to undesired irregular step ensembles, such processes are avoided by mounting the samples such that the $[1\bar{1}0]$ direction along the wires is parallel to the direction of current flow. The homogeneity of the LEED images over several mm ensured the presence of a well-ordered single domain 4×1 -In/Si(111) reconstruction without significant step bunching.

6.3 Time- and Angle-Resolved 2PPE

Before turning to the experimental results, the data acquisition and analysis for the time- and angle-resolved 2PPE data set as presented in the following are discussed. Such a time- and angle-resolved 2PPE study can be considered as 4-dimensional spectroscopy that addresses the energy E , both in-plane electron momenta k_x, k_y and the pump-probe delay t . The time- and angle-resolved 2PPE data set that is analyzed in the following was recorded using the pTOF technique described in chapter 4. The data set was acquired within 13 h and consists of 101 delay points with 172 individual scans of each delay point. Including the data for the background subtraction due to 2PPE from the pump and probe pulses only, this results in 17544 separate list-mode-files (lmfs) for the storage of the unprocessed raw data, see chapter 4.2. The raw data in the lmfs occupied 35286 MByte on disk and comprised $2.6 \cdot 10^8$ individual events. The analysis of the kinetic energy and the in-plane electron momenta as function of pump-probe delay, which includes the advanced multihit reconstruction described in chapter 4.2.3, used ~ 8 h of CPU time on a 3 GHz workstation. The comprehensive analysis of the electron dynamics presented in the form of lifetime maps additionally required to perform $\sim 5 \cdot 10^5$ individual least square fits of the transient intensity for each $\{E, k_x, k_y\}$ bin, see Fig. 6.7.

First, the electronic structure at the Γ -point and the influence of the fs laser irradiation is analyzed. Fig. 6.5(a) depicts monochromatic 2PPE spectra of 4×1 -In/Si(111) that have been acquired at a photon energy of $h\nu = 4.210$ eV in normal emission at room temperature using the conventional electron time-of-flight (TOF) spectrometer described in chapter 3.2.1. In this experiment, the incident ultraviolet (UV) pulse energy was varied to monitor the shift of the spectra with fluence. Such a measurement allows to verify flat-band conditions, in which the photoexcited carriers compensate the adsorbate-induced band bending at the surface, compare to chapter

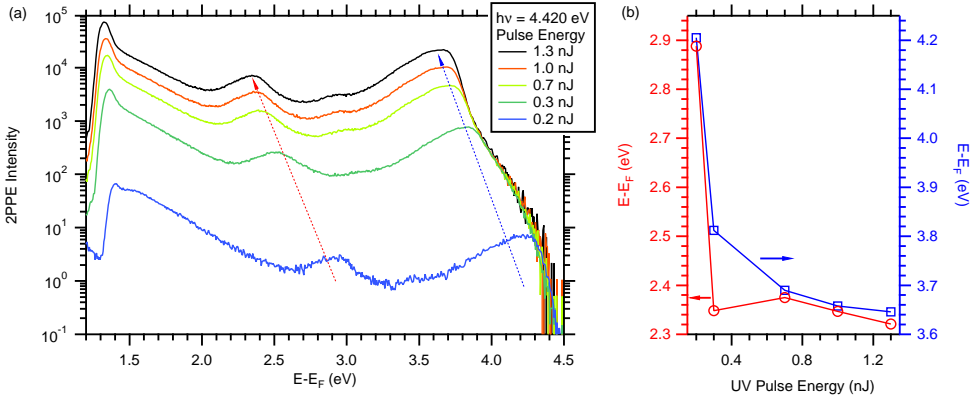


Figure 6.5: (a) Monochromatic 2PPE spectra of 4×1 -In/Si(111) for various pulse energies as indicated. The high-energy cutoff stays at constant energy, whereas as the two peak shift toward E_F with increasing pulse energy. (b) The analysis of the peak shift reveals two regimes.

2.1.2 and 5.4.1. The peak shift of the two spectral features at $E - E_F \approx 2.3$ eV and $E - E_F \approx 3.6$ eV (for 1.3 nJ pulse energy) is analyzed as a function of pulse energy in Fig. 6.5(b). Here, two different regimes are noticeable. For pulse energies > 0.7 nJ quasi-flat band conditions are reached, where the peak shift with increasing excitation density is comparably small, although the peak continues to shift by ~ 70 meV. Also, the shift does not saturate at the highest investigated fluence. For lower pulse energies of < 0.3 nJ the peak shift is very pronounced and amounts to ~ 0.5 eV. This is about half the energy of the global Si bandgap and thus presents a considerable shift of the energy scales.

These observations are different to the case of Pb/Si(111), where the whole spectrum shifted rigidly, which could be qualitatively explained in a Schottky-Mott picture of interfacial charge transfer, compare to Fig. 5.16. In the case of 4×1 -In/Si(111), only the discrete peaks change in energy, whereas the high-energy cutoff, indicating a Fermi-Dirac distribution, stays at constant energy. Also, the low-energy cutoff at the secondary edge exhibits a fluence dependent shift of ~ 200 meV, which, however, does not follow the shift of the peaks. Since these investigations have been carried out at very low count rates of $\ll 10$ kHz, corresponding to a $\ll 3\%$ probability for the emission of one electron per pulse, space charging effects can be ruled out. The fluence dependent shift of the low-energy cutoff at the secondary edge introduces a relatively large uncertainty of the work function in the order of ± 300 meV. The uncertainty of the work function also contributes to the error of the intermediate energy scale $E - E_F$.

The observed change of the energy references can be explained by the excitation of free carriers in the Si substrate, resulting in a change of band bending that is associated with the charge transfer across the In/Si interface. In this respect, the underlying physical mechanism is comparable to the case of Pb/Si(111), see chapter 5.4.1. The qualitatively different behavior of the low- and high-energy cutoffs compared to Pb/Si(111), however, requires a different explanation. In this respect, the choice of n-doped Si wafers might not have been optimal. Recent reports on the fluence dependent shift of the energy reference in Si(100) [Wei04, Wei05] indicate that flat band conditions can be reached over a wide range of fluences using p-doped Si wafers, as was the case for Pb/Si(111). In the case of n-doped Si wafers, significantly different energy references can occur due to defect induced pinning at the surface. Thus, n-doped Si wafers might induce a strong change of the energy reference under the excitation conditions created by the amplified fs laser pulses since the In/n-Si Schottky contact presents a barrier for electron transfer from the semiconductor to the metal.

For the time-resolved studies, however, certain minimum count rates in the order of kHz have to be achieved in order to record statistically significant data sets. This is especially important for the operation of the pTOF spectrometer that distributes the counts in a 3D variable space, see chapter 4. Thus, the energy reference in the time-resolved experiments actually depends on the fluence and can introduce a significant uncertainty regarding the transformation of the kinetic energy scale to a binding energy scale $E - E_F$, compare to chapter 3.2.3. As the analysis in Fig. 6.5 evidences, this uncertainty can be as large as 0.5 eV. Nevertheless, the population decay of the hot electrons can safely be studied using the pTOF concept since the time-of-flight,

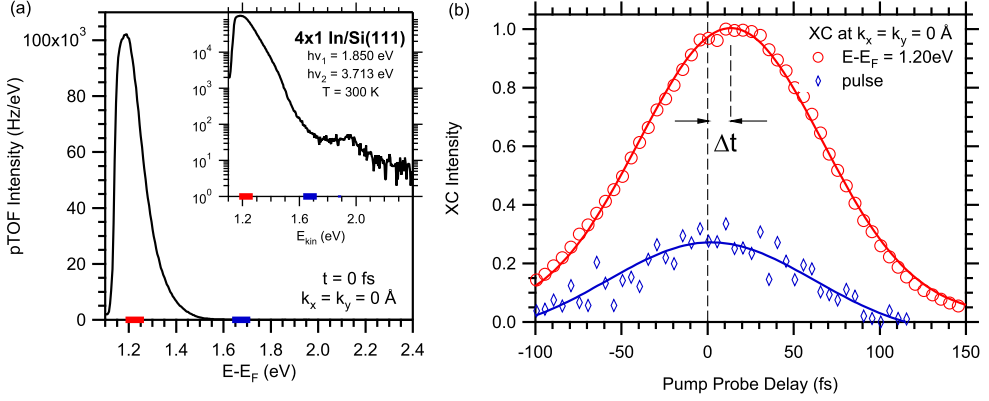


Figure 6.6: (a) Bichromatic 2PPE spectrum of 4×1 -In/Si(111) at the Γ -point, i.e. at $k_x = k_y = 0$. The inset depicts the spectrum on a logarithmic intensity scale. The horizontal color bars indicate the energies at which the XC traces in (b) were integrated over. (b) The XC traces of the electrons close to the low-energy cutoff at $E - E_F = 1.1$ eV exhibit a shift of the intensity maximum of Δt with respect to the hot electron distribution at higher energies of 1.7 eV. The latter may serve as measure for the zero pump-probe delay. Thus, the peak shift Δt indicates a finite lifetime of the electrons at $E - E_F < 1.6$ eV.

which determines the kinetic energy and the in-plane momenta k_x and k_y , is not affected by deviations of the energy reference. Only the interpretation of the energy scales as binding energy has to proceed very carefully. Additionally, the time-resolved data sets provide an independent way to reference the energy scales. As was discussed in chapter 2.4.4, see Fig. 2.29, the correlated 2PPE signal exhibits a high-energy cutoff that indicates the pump photon energy on the appropriate intermediate state energy scale $E - E_F$. Thus, the energy reference can be established by determination of the cutoff energy, where the correlated 2PPE signal vanishes.

In Fig. 6.6(a) a bichromatic 2PPE spectrum at zero pump-probe delay is shown. The spectrum was acquired on the 4×1 -In/Si(111) surface at room temperature using the pTOF spectrometer and cut out of the 3D data volume at the Γ -point. The inset depicts a semi-logarithmic representation of the same data set. The energy scale above the Fermi level $E - E_F$ was gauged by determining the cutoff energy where the correlated signal vanishes. Then the energy scale was shifted such that the cutoff energy coincides with the pump photon energy of $h\nu_1 = 1.850$ eV on the intermediate energy scale $E - E_F$. The correlated 2PPE spectrum in Fig. 6.6(a) does not exhibit any discrete peaks and resembles a hot electron distribution that decreases exponentially with increasing excess energy. The small feature at $E - E_F = 1.9$ eV is assigned to 2PPE from the UV probe pulse only.

Focusing on the dynamics of the hot electron population, cross correlation (XC) traces are extracted at different energies by integration of the transient photoelectron yield as function of pump-probe delay in the energy intervals marked by the horizontal color bars in Fig 6.6(a). The resulting XC traces are shown in Fig 6.6(b) for two representative energies. Identical to the approach followed for Pb/Si(111) in chapter

5.4, the pulse duration and the zero pump-probe delay are inferred from a XC traces directly at the high-energy cutoff of the correlated 2PPE signal at $E - E_F = 1.8$ eV. The low intensity at this intermediate state energy introduces statistical noise, which, however, does not hinder the evaluation of the XCs by fits of Gaussian functions, indicated by solid lines.

Turning to the XC trace acquired at lower energies of $E - E_F = 1.20$ eV, a shift of the peak maximum by Δt with respect to the zero pump-probe delay at $t = 0$ fs is observed. This peak shift indicates a finite lifetime of the hot electrons at these energies [Her96, Wol96, Wol97], compare also to Fig. 5.19. The pulse duration of ~ 70 fs in this experiment does not allow to reliably extract the lifetime of the hot electron distribution by fitting the XC traces with the response functions introduced in chapter 2.4.6. Therefore, the peak shift Δt of the XC traces with respect to the zero pump-probe delay is evaluated by a fit of a Gaussian function. This peak shift can serve as indicator of the hot electron lifetimes, however, it does not equal the hot electron lifetimes. On the other hand, the evaluation of the peak shift Δt avoids any assumptions about the exact line shape of the XC traces, which requires knowledge or hypothesis of the underlying microscopic scattering processes, and thus presents a more robust method.

The enormous amount of information supplied by the pTOF spectrometer in the form of 4D data volumes $\{E, k_x, k_y, t\}$ has to be selected and presented according to physical questions addressed. The evaluation of the 4D data sets is exemplified in Fig. 6.7, which shows 2D slices in k -space at zero pump-probe delay. Selecting a slice at constant in-plane momentum $k_x = 0$ yields the 2PPE intensity distribution as function of the perpendicular momentum k_y and intermediate state energy $E - E_F$ as shown on the left side of Fig. 6.7. Such a slice in the $\{E, k\}$ plane is appropriate to discuss the electronic structure and the electron dynamics along a certain direction. A slice of the 2PPE intensity at constant energy in the $\{k_x, k_y\}$, as shown in Fig. 6.7 on the right for $E - E_F = 1.20$ eV and 1.25 eV, is better suited to address the asymmetry of two perpendicular directions.

Although this slicing procedure reduces the data sets to 3D volumes, the transient evolution of the 2PPE intensity can only be examined in the form of animated intensity maps. To allow a more intuitive access to the k -resolved electron dynamics without the use of animations, the concept of a lifetime map is applied to the data [Mat08]. Such a lifetime map¹ is generated by extracting the transient intensity of each data point of the $\{E, k_x, k_y\}$ volume, as shown in the inset of Fig. 6.7, and determining the peak shift Δt of the peak maximum of the XC trace with respect to time zero. This procedure allows to visualize the electron dynamics along two axis in a 2D map of the peak shift distribution. Also, this procedure shifts the emphasis away from the spectral intensities and focuses on the dynamics of the intensity distribution.

The results of this evaluation scheme for the angle- and time-resolved 2PPE data obtained in 4×1 -In/Si(111) is shown in Fig. 6.8 and Fig. 6.9. In Fig. 6.8 the photoemission intensity as function of energy $E - E_F$ and the in-plane momenta k_x (a) and k_y (b) is shown. Both slices are centered at the Γ -point. Please note that the data was

¹Although the peak shift does not exactly equal the hot electron lifetimes, it is a very good indicator for lifetimes that are significantly shorter than the pulse duration [Her97] as is the case here. Thus, the term "lifetime map" is used instead of "peak shift map".

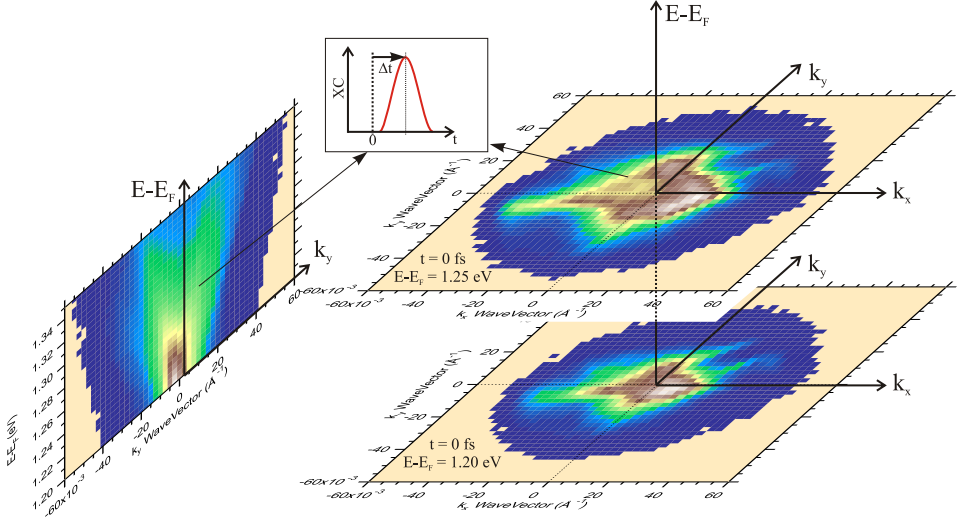


Figure 6.7: Different evaluation schemes in angle- and time-resolved 2PPE spectroscopy. The 3D data volumes of $\{E, k_x, k_y\}$ allow to select different 2D slices. Cuts at constant energy yield the in-plane electron intensity distributions along k_x and k_y , which are shown for $E - E_F = 1.20$ eV and 1.25 eV at zero pump-probe delay. The left side depicts a slice at constant $k_x = 0$, which results in an intensity distribution along E and k_y . The photoelectron intensity in each data point of the respective slices is a transient quantity that was determined for each delay point, see inset. According to this, the transient intensity can be evaluated separately for each $\{E, k_x, k_y\}$ point. This procedure yields, for example, a value of the peak shift for each data point, which can be plotted in a lifetime map, see Fig. 6.8 and Fig. 6.9.

not normalized in any way, compare to Fig. 4.16. In accordance with the spectrum shown in Fig. 6.6, which was obtained at the Γ -point, the angle-resolved photoelectron distribution is largely featureless and is ascribed to hot electrons rather than to well-defined intermediate states such as the quantum well states in Pb/Si(111). Also, the photoelectron distribution seems not decisively different for the k_y direction, which runs parallel to In nanowires, and the k_x direction, which is oriented perpendicular to the atomic chains.

Irrespective of this, the population dynamics of the hot electron distribution can be evaluated in k -space to yield lifetime maps. Fig. 6.8(a')/(b') show the peaks shift Δt for the same $\{E, k\}$ slices as given in the panels (a) and (b). The peak shift ranges from $\Delta t = 0 - 20$ fs, where $\Delta t = 0$ fs indicates a very short lifetime < 5 fs that could not be resolved with the pulse duration of 70 fs employed in this experiment. Comparing the peak shift at the Γ -point, i.e. at $k_x = k_y = 0$, with the peak shift in off-normal emission, a noticeable longer lifetime of the hot electron population at the Γ -point can be resolved. This is physically meaningful as inter- and intraband scattering is expected to lead to shorter lifetimes at $k_x \neq 0$ and $k_y \neq 0$. Focusing on a possible anisotropy of the peak shift with respect to the directions of the In nanowires, the comparison of the panels (a') and (b') in Fig. 6.8 seems to suggest a longer electron lifetime in the k_y direction, i.e. parallel to the nanowires.

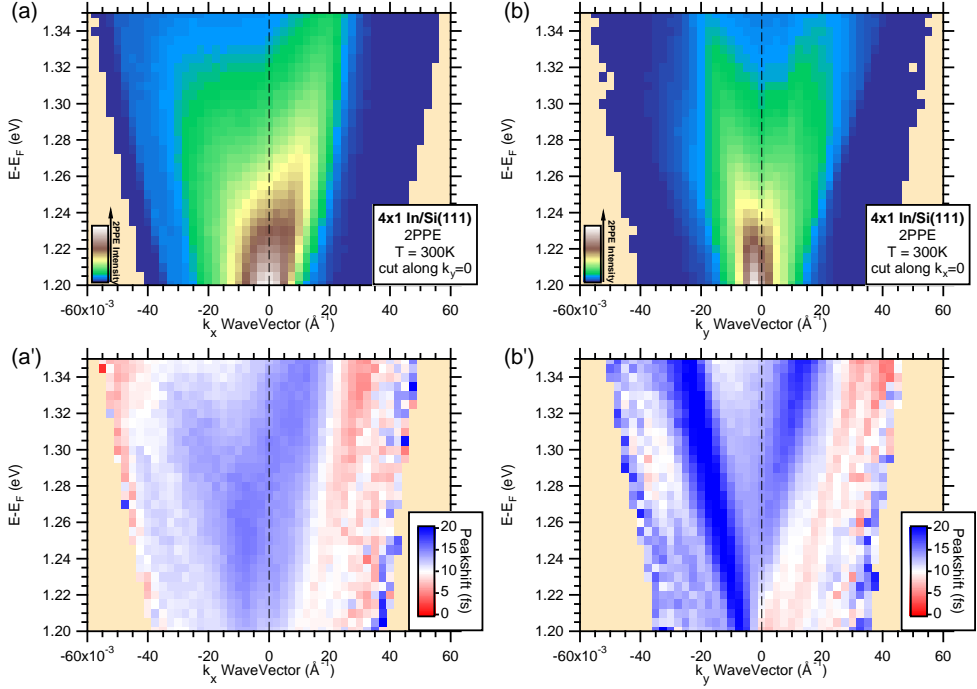


Figure 6.8: Color coded 2PPE intensity along the energy axis $E - E_F$ and both in-plane momenta k_x (a) and k_y (b) at zero pump-probe delay. Both slices are centered at the Γ -point. The peak shift as discussed in Fig. 6.6 was evaluated for each data point in the E, k planes and is shown in (a')/(b') as a lifetime map.

To investigate this anisotropy in more detail, slices in the $\{k_x, k_y\}$ plane at constant energy are evaluated in lifetime maps shown in Fig. 6.9. Such cuts in the $\{k_x, k_y\}$ plane allow to address the asymmetry of the hot electron lifetimes with respect to the high-symmetry directions of the 4×1 -In/Si(111) surface most efficiently. The upper panels (a) and (b) in Fig. 6.9 depict the 2PPE intensity in the $\{k_x, k_y\}$ plane for zero delay at constant energy of $E - E_F = 1.20$ eV and 1.25 eV, respectively. The 2PPE intensity is symmetrically centered around the Γ -point. The origin of the distortions in off-normal emission are currently under investigation. Nevertheless, the transient intensities can be evaluated to yield the lifetime maps at the same cut positions shown in the lower panels (a') and (b') of Fig. 6.9. Consistent with the data shown in Fig. 6.8 the peak shift is largest in the vicinity of the Γ -point and reduces in the outer regions of the accessible Brillouin zone. For the lifetime maps in Fig. 6.9 the assignment of asymmetries to the hot electron lifetimes is not straight forward. For example, in Fig. 6.9(b') at $k_x = 20 \cdot 10^{-3} \text{\AA}^{-1}$, $k_y = 20 \cdot 10^{-3} \text{\AA}^{-1}$ a small peak shift is detected. This is opposed to the position $k_x = -20 \cdot 10^{-3} \text{\AA}^{-1}$, $k_y = -20 \cdot 10^{-3} \text{\AA}^{-1}$, where a large peak shift is observed. This diagonal alignment of the structures in the lifetime map inhibits a direct assignment of the observed asymmetries to the high-symmetry directions defined by the nanowires.

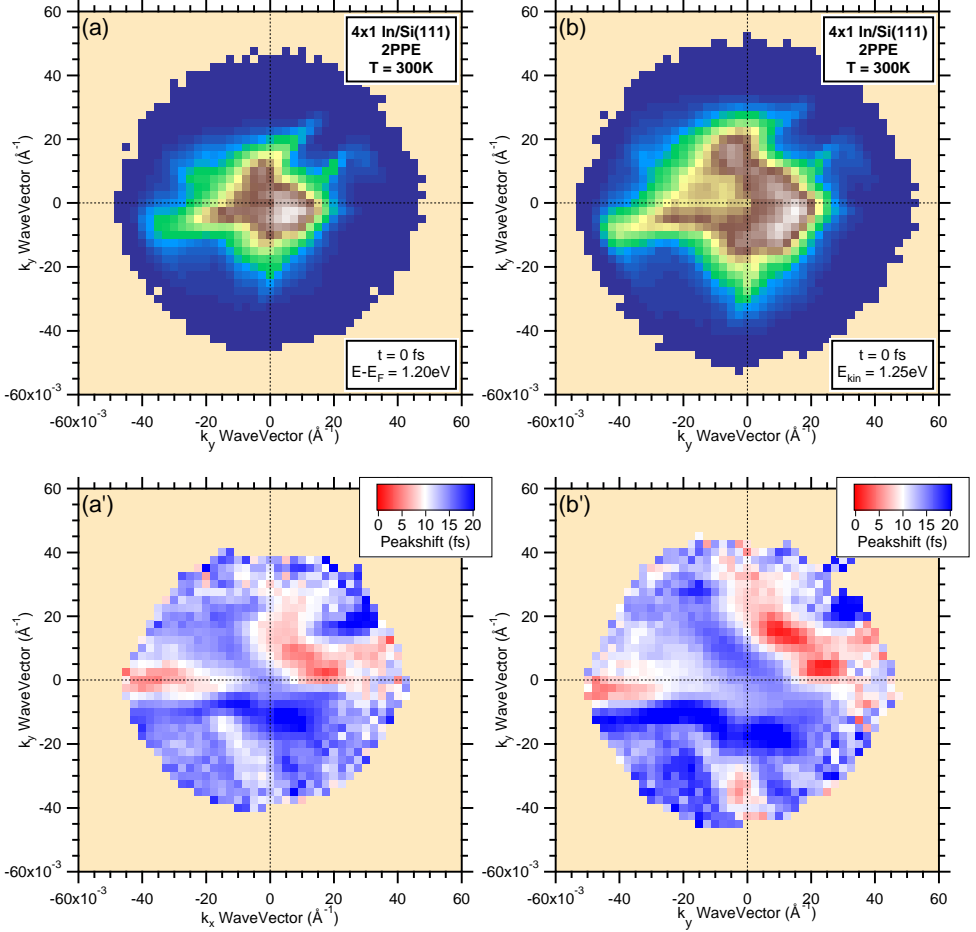


Figure 6.9: Color coded 2PPE intensity for constant energy $E - E_F = 1.20 \text{ eV}$ (a) and 1.25 eV (b) as function of the in-plane momenta k_x and k_y at zero pump-probe delay. The cuts are centered at the Γ -point. The peak shift was evaluated for each data point in the k_x, k_y planes and is shown in (a')/(b') in a corresponding lifetime map.

In order to implement a method for the systematic evaluation of the asymmetries of the peak shift, which does not rely on the eye of the evaluator, four regions of interest are defined as rectangular boxes in the $\{k_x, k_y\}$ plane. This is shown in the inset of Fig. 6.10. The k -boxes are oriented to integrate the peak shift² parallel and perpendicular to the nanowires in the outer regions of the accessible Brillouin zone. The resulting peak shift in the four regions of interest was evaluated as function of the

²Please note that it is fundamentally different to apply this integration to the k -resolved 2PPE intensity and then calculate the peak shift from an integrated XC trace as this puts the emphasis on the spectral intensities. In contrast, the averaging of the peak shift employed here depends only marginally on the spectral intensity.

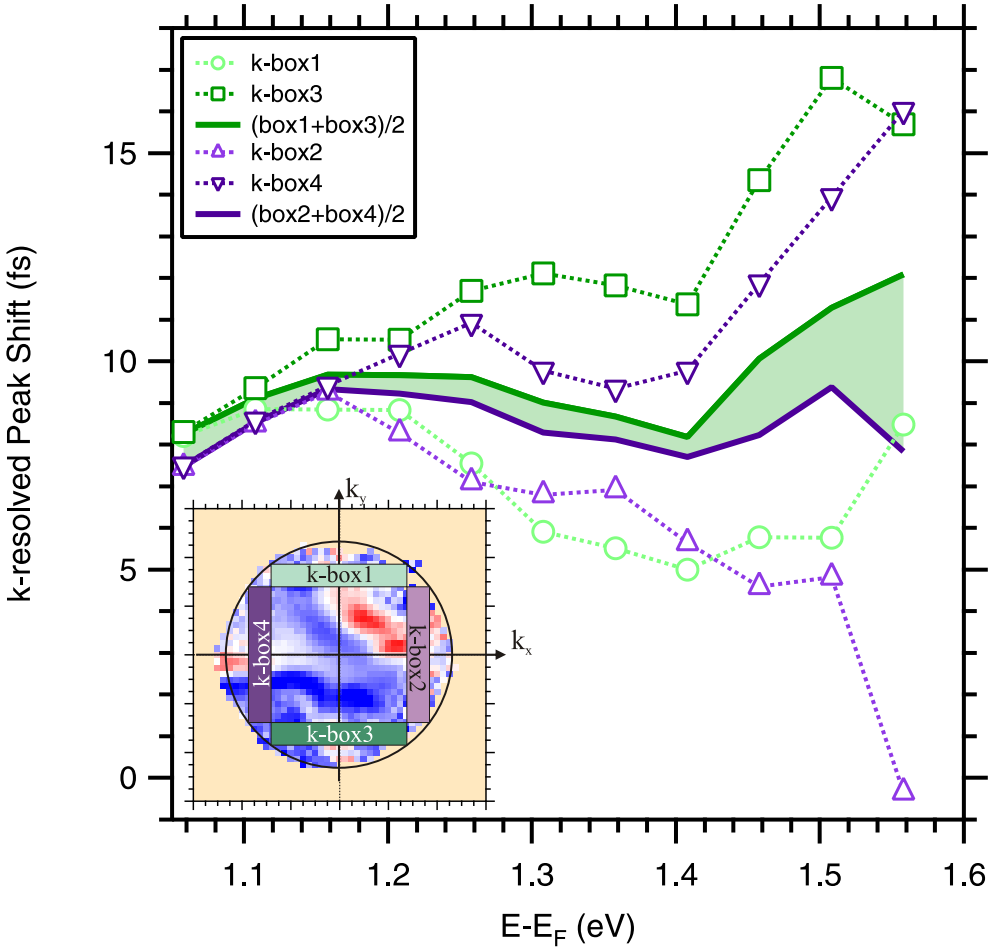


Figure 6.10: To search for asymmetries of the k -resolved lifetimes four boxes are defined at $\pm k_x$ and $\pm k_y$ in the outer regions of the accessible Brillouin zone. The peak shift (see Fig. 6.8) in each box is integrated and plotted as dashed lines and markers. The asymmetry along the different directions, however, vanishes when the averaged shift (solid lines) of the k -boxes no. 1 and no. 3, and the k -boxes no. 2 and no. 4, respectively, along the high symmetry directions of the 4×1 -In/Si(111) surface is evaluated.

energy $E - E_F$ at which the $\{k_x, k_y\}$ plane was extracted. The resulting integrated peak shifts are depicted in Fig. 6.10 by markers and dashed lines.

This evaluation clearly reflects the asymmetries that are present in the lifetime maps of Fig. 6.9. For example, k -box no. 1 samples a consistently smaller lifetime than k -box no. 4. Comparing these perpendicularly aligned regions of interest no. 1 and no. 4 along k_y and $-k_x$, respectively, an asymmetry of the hot electron lifetime becomes noticeable. The peak shift in box no. 1 in k_y direction is in the range of 5 – 9 fs, whereas the peak shift integrated over box no. 4 in $-k_x$ direction increases

with intermediate state energy $E - E_F$ from 7 to 16 fs. In the opposed quadrant in the k -boxes no. 2 and no. 3 along k_x and $-k_y$, respectively, this observation is reversed and the peak shift is small along k_x and large along $-k_y$. If the In nanowires are indeed responsible for the observed asymmetries of the hot electron lifetimes it is reasonable to expect that the sign of the in-plane direction should not influence the lifetimes. Rather one might expect that only the alignment with respect to the wire direction, i.e perpendicular or parallel to the atomic chains, affects the lifetimes. This argument can be investigated by averaging the lifetimes observed in the k -boxes along the high-symmetry directions $|k_x|$ and $|k_y|$. The averaged peak shifts of the regions of interest no. 1 and no. 3 along $|k_y|$, and no. 2 and no. 4 along $|k_x|$, respectively, are shown as solid lions in Fig. 6.10. Within the error bars of the peak shift determination, which amount to ± 2 fs, all asymmetries are averaged out and the curves are almost identical. Thus, it seems not reasonable to assign the asymmetries - that are clearly observed in the lifetime maps - to the influence of the quasi-1D band structure of 4×1 -In/Si(111).

These results suggest to focus future time- and angle-resolved 2PPE investigations on (i) lower energies, where the global Si bandgap facilitates the electron confinement which might lead to larger lifetimes, and (ii) on other regions of the Brillouin zone. In the nesting region of the Peierls metal-to-insulator transition, see Fig. 6.3, the band dispersion is more anisotropic than at the Γ -point and k -dependent anisotropies of the hot electron lifetime might be resolved. Also, the relatively low photon energies compared to other experiments [Yeo99, Sun08] might make this study rather sensitive to processes occurring in the Si substrate. Very recently conducted ARPES investigations of the occupied band structure in 4×1 -In/Si(111) at a photon energy of $h\nu = 6$ eV are dominated by negatively dispersing Si bands below E_F and point to a relatively large bulk sensitivity. Finally, the 4 atoms wide structure of the nanowires in 4×1 -In/Si(111) has to be considered. Hence, an excited electron has to propagate in average the distance of 2 atoms in the direction perpendicular to the nanowires before it is affected by the linear structure of the chains. If the hot electron scattering rates are very large the excited electron can decay before they have reached this limit and can "sample" the anisotropy of the band structure.

Conclusions

Summarizing, the quasi-1D model system of self-assembling metallic Indium nanowires in 4×1 -In/Si(111) was investigated with time- and angle-resolved 2PPE using the pTOF technique that allows to simultaneously address the electron dynamics along two perpendicular in-plane directions in the vicinity of the Γ -point. The transient 2PPE intensity is retrieved in the form of 4D data volumes that are spanned by the energy E , both in-plane electron momenta k_x, k_y , and the pump-probe delay t . These 4D data volumes are evaluated by determining the peak shift Δt with respect to zero pump-probe delay for each $\{E, k_x, k_y\}$ data point, which yields energy- and k -resolved lifetime maps. Near the Γ -point, the hot electron lifetimes in In/Si(111) amount to 4–17 fs at 1.1–1.5 eV above the Fermi level. The careful analysis of the lifetime distributions in the $\{k_x, k_y\}$ plane centered at the Γ -point, however, does not indicate an asymmetry of the hot electron lifetimes with respect to the high-symmetry directions parallel and perpendicular to the nanowires. Thus, it is proposed to conduct future investigations of the asymmetry of the hot electron dynamics in 4×1 -In/Si(111) at lower energies, where the hot electrons are confined in the global Si bandgap. Also the study of other regions of the Brillouin zone might be promising since the anisotropy of the band dispersion is more pronounced than at the Γ -point.

7 Time- and Angle-resolved Photoemission of TbTe₃

Obtaining insight into microscopic cooperative effects is a fascinating topic in condensed matter research since through self-coordination and collectivity, they can lead to instabilities with macroscopic impacts like phase transitions. Here, femtosecond time- and angle-resolved photoemission spectroscopy (tr-ARPES) is used to optically pump and probe TbTe₃, an excellent model system to study these effects. The strong infrared (IR) pump pulse drives a transient charge density wave (CDW) melting and excites collective lattice vibrations in TbTe₃, which are observed through their time-, frequency-, and momentum-dependent influence on the electronic band structure. Furthermore, the role of the observed collective vibration in the phase transition is identified and documented in the time domain. The information that is accessible with tr-ARPES will greatly enhance the understanding of all materials exhibiting collective phenomena.

Emerging phenomena are a major theme in modern physics. For example, in quantum matter, the emergence of order and collective modes associated with order are key areas to gain knowledge on electronic correlations and collective behavior. As model systems, CDW materials are among the well-established examples that have had a major impact on our understanding of quantum many-body problems [Grü94]. Recent efforts on RTe₃ (R = Rare Earth element) have identified it to be a quasi-1D model system to study Fermi Surface (FS) nesting driven CDW formation [DiM95, Gwe98, Bro04, Mal05, Kim06, Ru06b, Fan07, Bro08, Ru08]. The study of the electronic structure and FS of RTe₃ via angle-resolved photoemission spectroscopy (ARPES) has played a major role in developing the current knowledge [Gwe98, Bro04, Bro08, Moo08].

However, conventional ARPES can only provide very limited information on the collective excitations that are important to understand the nature of the many-body state. Important many-body collective modes, such as the CDW amplitude mode [Lit82], can only be detected e.g. by Raman spectroscopy [Soo81], which cannot be directly linked to the CDW gap modulation - the defining signature of the mode [Grü94]. tr-ARPES offers the capability to capture simultaneously the single particle (frequency domain) and collective (time domain) information, thus making it possible to directly probe the link between the collective modes and single particle states that form the charge density wave.

This chapter reports on fs tr-ARPES of TbTe₃¹. Absorption of IR fs laser pulses generates electron-hole (e-h) pairs driving collective phonon modes and thereby allowing an analysis of their impact on the electronic structure directly in the time domain. The amplitude mode of the CDW state (see chapter 2.2.2) is identified through an inspection of time- and k -dependent modulations of the single-particle spectral function

¹This work presents a collaboration with I. R. Fisher, Z. X. Shen and their coworkers from the Stanford University. The sample preparation and characterization in Stanford were performed in the group of I. R. Fisher. F. T. Schmitt from Shen's group in Stanford designed the slanted sample holder, mounted the samples, performed the ARPES study at the SSLR and evaluated the data.

$A(\omega, \vec{k}, t)$ in the CDW state. A is most susceptible to the excitation at the FS due to a divergence of the Lindhard response function $\chi(\vec{q})$ that was discussed in chapter 2.2. For sufficiently high excitation densities, an ultrafast melting of the charge ordered state is observed by closing of the CDW band gap through a transient recovery of the ungapped electronic dispersion which otherwise can only be observed above the CDW transition temperature.

Experimental Details

The angle-resolved photoemission spectroscopy (ARPES) experiments discussed in the following were performed at two complementary setups of synchrotron- and laser-based photoemission facilities, which are sketched in Fig. 7.1. Both ARPES experiments are comprised of ultrahigh vacuum chambers that allow to cleave and measure single crystals of TbTe_3 in situ at pressures always around or better than $4 \cdot 10^{-11}$ mbar, see chapter 3.2 and 3.3.2.

The high-resolution ARPES measurements were conducted at the Stanford Synchrotron Radiation Laboratory (SSRL), beam line 5-4, in the same geometry and conditions as described by Moore et al. [Moo08]. The incident light at 23 eV photon energy was polarized in the plane that is formed by the incident light direction and the analyzer axis, see Fig. 7.1(a). The light beam and the analyzer form a fixed 45° angle, and the crystal a -(c -) axis are in the same horizontal plane as the light beam, as indicated by the green arrow in Fig. 7.1(a). The presented measurements were taken with a Scienta R4000 analyzer with an angular resolution of 0.3° and an energy resolution of ~ 10 meV.

The fs time-resolved ARPES experiments were performed with the setup at the Freie Universität Berlin, which is described in detail in chapter 3.1.1 and appendix E. In brief, the sample is pumped by an intense IR pulse of 1.5 eV photon energy, a pulse energy of $0.5 \mu\text{J}$ and a pulse duration of 50 fs. The temporal evolution of the band structure is subsequently probed by 6 eV ultraviolet (UV) pulses with a duration of 80 fs and a pulse energy < 50 pJ. The overall time resolution of pump and probe pulses thus is given by 100 fs. Compared to conventional ARPES conducted typically at $h\nu = 20 - 200$ eV the photon energy of the fs UV laser pulses is with 6 eV rather

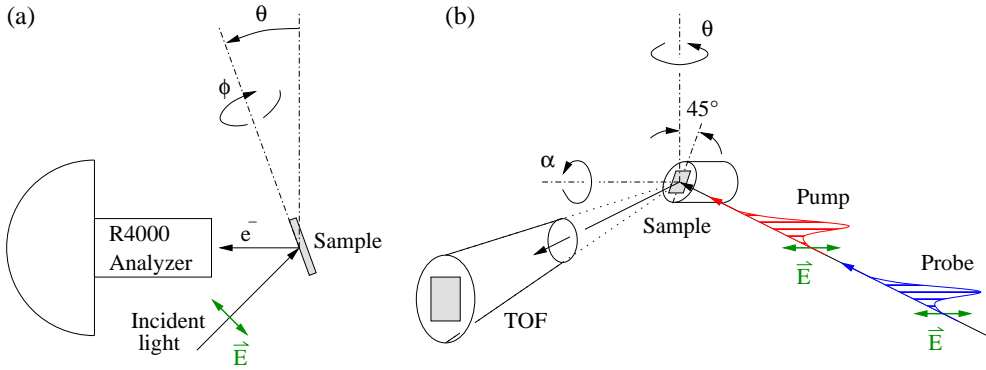


Figure 7.1: To access the Fermi surface, photoelectrons in a particular angular range are detected and analyzed by rotating the sample along the respective two indicated angles. The light polarization is marked by the green arrows. (a) Schematic of the ARPES setup at SSRL, Beam line 5-4 (top view) [Moo08]. (b) Scheme of the fs time-resolved ARPES setup at the Freie Universität Berlin. The IR pump pulse excites the system and precedes the UV probe pulse, which generates photoelectrons, by a defined time delay. The independent variation of the angles α and Θ and the use of a 45° slanted sample posts allows to access the whole Brillouin zone as discussed in Fig. 7.2.

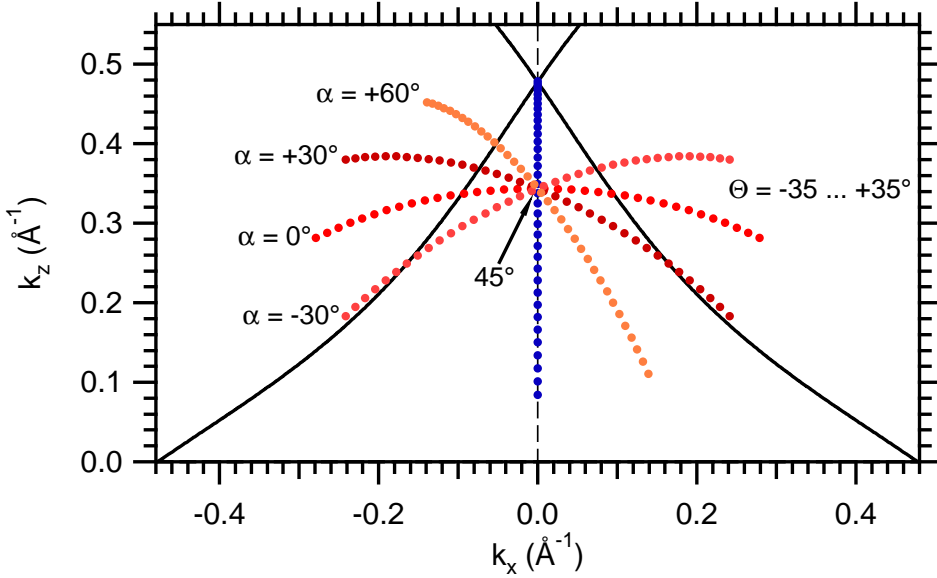


Figure 7.2: Scheme of the diamond-shaped FS of TbTe₃ (solid lines) together with various sample geometries (dots) in the tr-ARPES experiment, c.f. Fig. 2.18. The blue dots indicate the change of the region of interest with the slanting angle of the sample post. For a fixed slanting angle of 45°, the independent variation of the sample post rotation angle α and the manipulator angle Θ allows to access different locations (reddish dots) in the nesting region of the FS of TbTe₃.

small. Hence the accessible k -space region is limited, see chapter 2.4.3. To facilitate access to the FS of TbTe₃ a slanted sample holder was employed in the tr-ARPES experiments, see chapter 3.3.2. As shown in Fig. 7.1 the slanting angle of 45° is fixed, and the rotation of the sample post by an angle α and of the manipulator by an angle Θ allowed to perform angle-resolved measurements along trajectories that cross the FS. This is demonstrated in Fig. 7.2, where the diamond-shaped FS of TbTe₃ (solid lines), see chapter 2.2.3, is presented together with different tr-ARPES geometries (dots). Keeping $\alpha = 0$ and $\Theta = 0$ and changing the slanting angle of the sample post shifts the region of interest in the Brillouin zone away from the Γ -point (blue dots). For a constant slanting angle of 45°, the independent variation of α and the manipulator angle Θ from -35° to $+35^\circ$ allows to access various positions in the nesting region of the FS (reddish dots). The work function of TbTe₃ was determined from the low-energy cutoff and the photon energy to be 5.2 – 5.3 eV. A variation of 100 meV was observed for different cleaves and different samples and an average work function of $\Phi = 5.25$ eV was assumed throughout this work. For the angle-resolved detection, the difference of sample and spectrometer work function was offset by applying a bias voltage from a battery box. All time-resolved ARPES experiments were carried out well below the phase transition temperature T_{CDW} at $T = 100$ K unless stated otherwise.

7.1 Equilibrium Bandstructure of TbTe₃

Before turning to the ultrafast, photo-induced CDW dynamics in TbTe₃, the band structure in thermal equilibrium is analyzed with ARPES at photon energies of 23 eV and 6 eV for the ungapped metallic and the gapped CDW state. The coupled instability of the electron and lattice system that can lead to CDW formation in low-dimensional solids and the resulting band gap in the FS was discussed in chapter 2.2. The prototypical CDW compound TbTe₃ was introduced in chapter 2.2.3. In brief, TbTe₃ is a member of the RTe₃ family of compounds that exhibit a FS nesting driven CDW formation [DiM95, Mal05, Ru06b, Ru08, Moo08]. The band dispersion around E_F of the metallic state of RTe₃ can be described well by a tight binding (TB) model with weakly hybridized p_x - and p_z -orbitals in the Te-plane, which, together with a $\sqrt{2} \times \sqrt{2}$ -R45° reduction of the Brillouin zone due to the underlying RTe layer, leads to its diamond-like shape [Gwe98, Lav05, Bro04, Bro08, Moo08].

In Fig. 7.3 ARPES measurements at photon energies of 23 eV and 6 eV are compared for a temperature of 300 K and 100 K. As the transition temperature for TbTe₃ is $T_{\text{CDW}} = 335$ K [Ru08], the CDW gap at 300 K is almost closed and the FS in Fig. 7.3(a) exhibits the characteristic diamond-shaped topology that is well described by the TB model, including the back-folded shadow bands. Fig. 7.3(a') shows the FS of TbTe₃ for a temperature of 100 K, where the CDW gap extends throughout a significant part of the Brillouin zone. The FS observed here for the metallic and the charge ordered CDW state are in good agreement to previous ARPES studies on other members of the RTe₃ family [Bro04, Bro08]. The CDW gap is further analyzed by spectral cuts as a function of energy $E - E_F$ through the Brillouin zone, as indicated by red arcs in Fig. 7.3(a) and (a').

The photoemission intensity maps in Fig. 7.3(b) and (b') were extracted from interpolation of the ARPES data taken at a photon energy of 23 eV. They show a weakly dispersing p -like Te band at $E - E_F \approx -0.45$ eV and a p -like Te valence band (VB). The Te VB disperses from $E - E_F \approx -0.2$ eV through E_F above T_{CDW} , whereas it exhibits the CDW gap well below the phase transition temperature. As was discussed in chapter 2.2.3, the Te VB is derived from the in-plane $5p_x$ - and $5p_z$ -orbitals, which can be reproduced well by a TB model. Since the Te bands form the VB in RTe₃ they will be abbreviated with VB in the following. The figures Fig. 7.3(c) and (c') show the same spectral cuts across the Brillouin zone as in (b)/(b'), but were taken with the tr-ARPES setup using 6 eV fs laser probe pulses without optical pumping. In general, both ARPES measurements agree well, although the lower lying Te band exhibits some differences. Nevertheless, the dispersion of the Te VB and the opening of the CDW gap below T_{CDW} , is captured correctly by the ARPES measurement at $h\nu = 6$ eV.

A priori, this good correspondence is not self-evident since the photoemission signal might differ for both photon energies due to energy-dependent matrix elements and a different escape depth of the photoelectrons, compare to chapter 2.4. The good agreement of both experiments observed here, ensures that in tr-ARPES the same position in the Brillouin zone is probed as in conventional ARPES. Thus, the temporal evolution of the electronic band structure can be safely analyzed with tr-ARPES in the following.

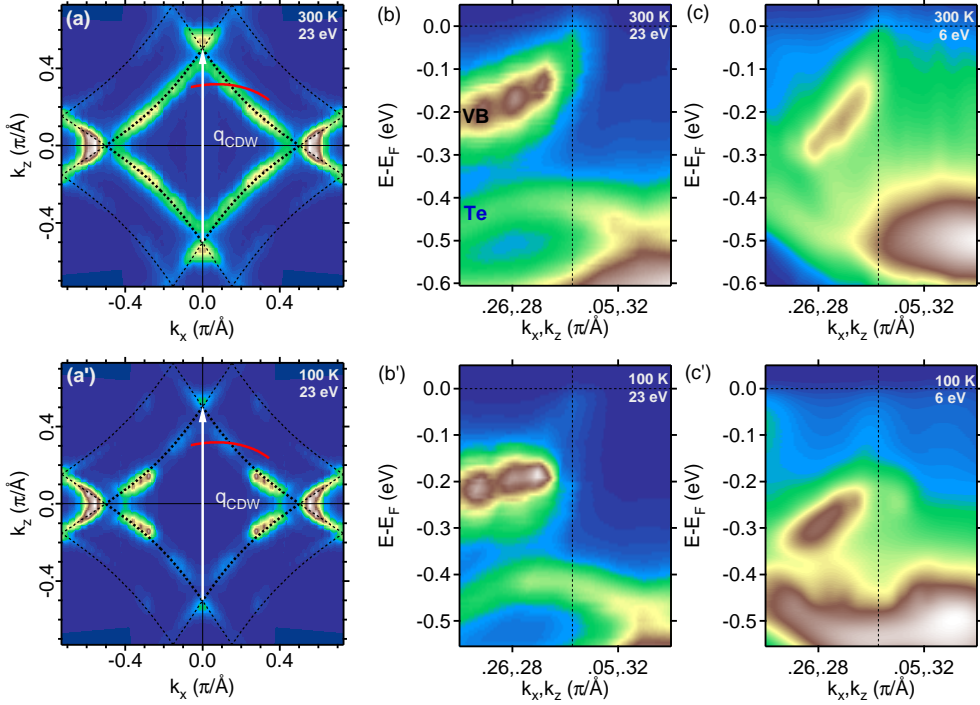


Figure 7.3: ARPES measurements taken at 300 K (upper row) and 100 K (lower row). The photoelectron intensity is encoded in a false color scale. (a)/(a') The Fermi surface (FS) maps along the in-plane directions k_x and k_z were obtained from ARPES of TbTe₃ by integrating an energy window of 20 meV centered at E_F . Also plotted are the tight binding model [Bro08] presented in chapter 2.2.3 (dotted lines), the back-folded shadow bands (thin dotted lines), and the CDW nesting vector q_{CDW} (white arrow) along the nesting direction k_z . (b)/(b') The spectral cuts along the in-plane directions as indicated were extracted by interpolation of the conventional ARPES data that have been measured at a photon energy of 23 eV. In (b) the localized Te band and the Te-derived VB are indicated. The Fermi energy and the Fermi wave vector are given by horizontal and vertical lines, respectively. (c)/(c') Identical spectral cuts using the tr-ARPES system at a probe photon energy of 6 eV. The position of the spectral cuts shown in (b)/(b') and (c)/(c') is marked in the FS plots (a)/(a') with a red curve. In fact, the ARPES data obtained at a photon energy of 23 eV and 6 eV, respectively, agree reasonably well.

For better orientation and to familiarize the reader with cuts through the FS typically done with ARPES, the TB band structure of RTe₃ and an example cut is presented in Fig. 7.4(a) and (b). The figures 7.4(c) and (d) show schematically the expected resulting electronic band structure in thermal equilibrium with (c) and without (d) a CDW gap, i.e. below and above T_{CDW} , respectively. Note that the bands have been cut off at the Fermi energy E_F in Fig. 7.4(a), and the resulting diamond is identical with the one seen in the FS plot in Fig. 7.3(a).

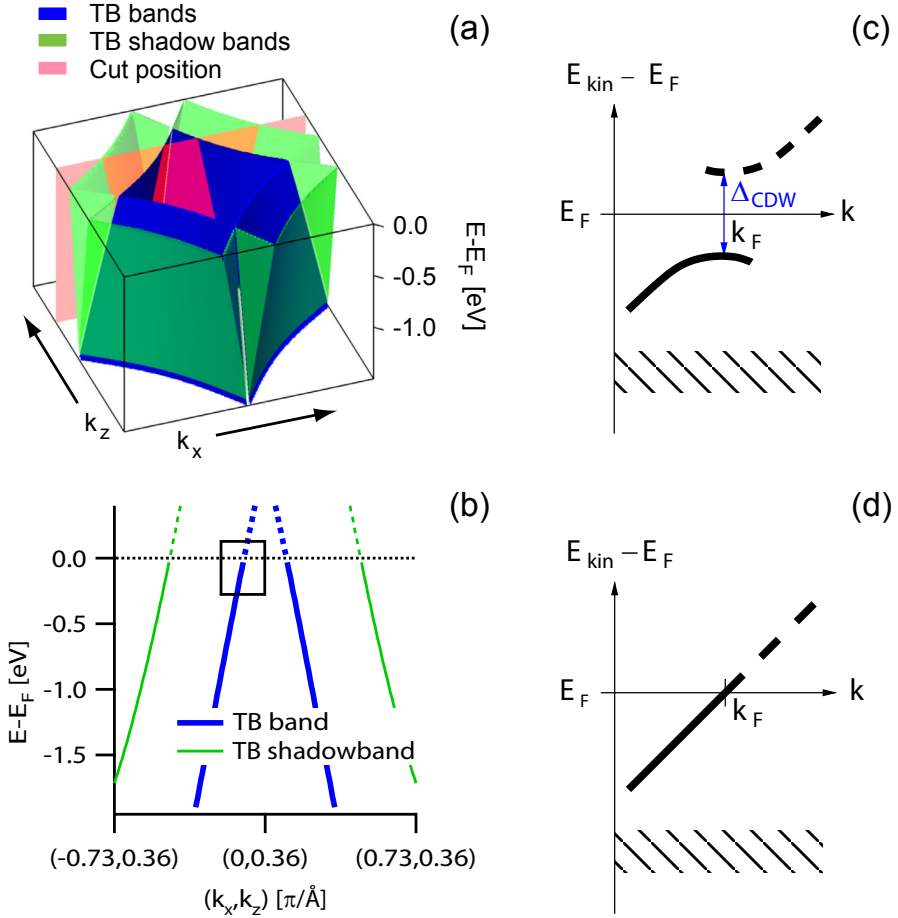


Figure 7.4: (a) Tight binding (TB) model of the VB (blue sheets) in $R\text{Te}_3$, including shadow bands (green sheets), plotted in dependence of k_x , k_z and binding energy $E - E_F$. The parameters for this calculation were taken from [Bro04]. An exemplary spectral cut in k -space is indicated by the red plane. (b) Band dispersion along the spectral cut indicated in (a). The black box marks the detail plots shown in panels (c) and (d). (c)/(d) Scheme of the resulting band structure with (c) and without (d) a CDW bandgap [Grü94]. The Fermi crossing of the electronic dispersion k_F and the maximum gap location Δ_{CDW} are marked.

7.2 Excitation of Collective Modes

In *tr*-ARPES, the CDW system is optically pumped with an IR laser pulse of 50 fs pulse duration and 1.5 eV photon energy. Subsequently, the transient band structure is probed after a variable delay by photoemission with an UV laser pulse of 80 fs duration and 6 eV photon energy, resulting in an overall time resolution of 100 fs. Thus, the time-dependent evolution of the electron occupation [Fan92, Lis04a, Bov07] and

the transient single-particle spectral function is probed [Per06, Lou07]. Pump-probe spectroscopy in general has contributed significantly to the understanding of non-equilibrium states of condensed matter and remarkable achievements have been made on ultrafast timescales. Regarding transitions from insulating to conducting states [Cav04, Cho05b] and analysis of collective modes [Dem99], optical spectroscopy was employed. To trace structural transitions, time-resolved diffraction techniques were established [Fri07, Bau07, vKS07]. However, the correlation of electronic structure and ionic motion is difficult to track by these methods as they are not sensitive to the momentum dependence of the electronic band structure. Therefore, tr-ARPES is used to probe the single particle spectral function $A(\omega, k)$ as well as to analyze collective excitations simultaneously [Per06, Lou07].

The following presentation will focus on two different regimes for the intensity of the perturbation of the CDW system. First, a relatively weak perturbation of the CDW system is discussed, where the energy absorbed from the IR pump pulse is insufficient to drive the system from the low-temperature CDW phase into a metallic state. In these weakly perturbative experiments, a transient binding energy oscillation of the Te-derived VB is observed, which is assigned to the collective excitation of the CDW amplitude discussed in chapter 2.2.2. This assignment is based on the characteristic fluence-, temperature- and k -dependence expected for the amplitude mode. In a next step, the fluence of the IR pump pulse is increased so far that an ultrafast breakdown of the charge ordered CDW state is observed by an closing of the CDW gap. In this regime, the system is driven from the gapped CDW state to an ungapped metallic state within ~ 100 fs.

7.2.1 Excitation of the CDW Amplitude Mode

The discussion starts out with tr-ARPES data that was acquired at a low incident fluence of $F_1 = 0.3 \text{ mJcm}^{-1}$ in the 1.5 eV pump beam. In Fig. 7.5(a) the photoelectron yield as function of energy $E - E_F$ and pump-probe delay t is given for a Brillouin zone position directly at the Fermi vector k_F (see Fig. 7.3)(a') and a temperature of 100 K well below the CDW phase transition temperature of $T_{\text{CDW}} = 335$ K [Ru08]. In Fig. 7.5(b), spectra before, at, and after the optical excitation are shown on a logarithmic intensity scale. Before the arrival of the pump pulse, the spectrum exhibits two peaks from the Te band and the VB at $E - E_F = -0.50$ eV and -0.25 eV, respectively, and a sharp Fermi-Dirac distribution around E_F . At zero time delay, the optical excitation with the IR pulse generates a non-thermal electron distribution, which is highlighted by the contour lines in panel (a), and populates an unoccupied state, which is identified in panel (b) by a peak at $E - E_F = 0.15$ eV. At $t = 0$ fs, however, the optical pumping has only minor influence on the occupied states and also the Fermi-Dirac distribution remains essentially unchanged around E_F . The continuous population of states above E_F occurs through electron-electron (e-e) scattering within the experimental time resolution of 100 fs, as under the excitation conditions used, inelastic e-e scattering is known to be the dominant relaxation process within the first few 100 fs [Fan92, Ret02, Lis04a, Bov07], see also chapter 5.5. These efficient scattering processes ensure that effects of a coherent polarization are negligible and indeed a transient electronic population is observed.

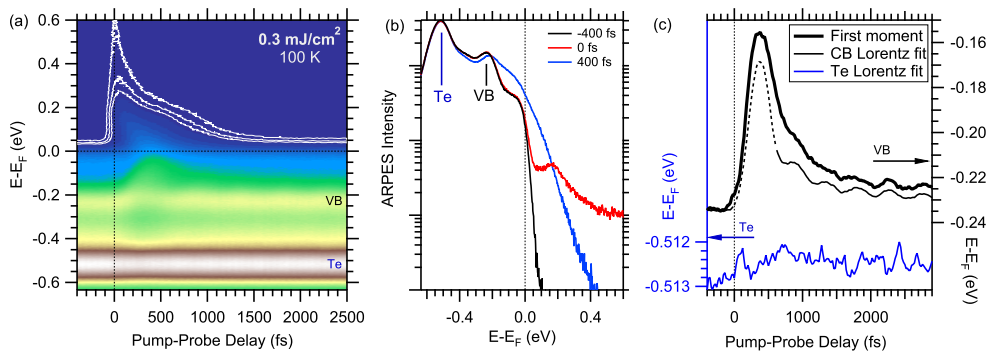


Figure 7.5: (a) Photoelectron intensity in a false color plot as a function of energy $E - E_F$ and pump-probe delay taken at k_F , $T = 100 \text{ K}$ and at a low fluence of 0.3 mJ/cm^2 . The white contour lines emphasize the hot electron distribution at higher energies. The Te band and the Te derived VB are indicated. (b) Spectra from (a) for selected delays on a logarithmic intensity scale. The peak at $E - E_F = 0.15 \text{ eV}$ in the unoccupied part of the band structure evidences the photo-doping at zero delay. (c) Transient binding energy of the Te band (blue) and the VB (black). Analysis was done by fitting Lorentzian lines to the Te (blue) and VB (black) states. For the VB, also the first statistical moment (i.e. center of mass) was determined (bold), which basically coincide with the results from the Lorentzian line fit. The dotted line describes where the Lorentzian is not capable to fit the line as satisfactorily as for later delays (see Fig. 7.6).

The photo-doping of the electronic part of the CDW state is evidenced by the discrete peak appearing at $E - E_F = 0.15 \text{ eV}$ for zero pump-probe delay. As a consequence the CDW amplitude is weakened as the electron redistribution changes the screening and the electron-phonon (e-ph) coupling. Within 400 fs the hot electron distribution has thermalized and the broadening of the Fermi-Dirac distribution indicates a significantly enhanced electron temperature $T_{el} \gg 100 \text{ K}$. In addition, the VB shows a considerable shift of its spectral weight toward E_F after pumping, which reaches its maximum at 400 fs (blue line in Fig. 7.5(b)). In Fig. 7.5(c) the analysis of the transient binding energies of the Te band and the VB is presented. The detailed methodology of the binding energy analysis is discussed in the context of Fig. 7.6. During the first $\sim 400 \text{ fs}$ the excess energy that was deposited by the IR pump pulse resides mainly in the electronic system, see also Fig. 5.32. Since T_{el} is enhanced with respect to the lattice temperature at these delays, the transient shift of the VB is attributed to the hot electron distribution [Per06, Lou07], compare to chapter 5.5. Electrons and phonons subsequently equilibrate through e-ph scattering within roughly 1 ps. At later delays, the analysis of the transient binding energy and center of mass reveals an oscillatory behavior, see Fig. 7.5(c). The oscillatory changes of the VB are well resolved and persist for several ps.

The evaluation of the oscillation frequency, which is detailed in the next paragraph, results in a frequency of $\Omega_{VB} = 2.3(5) \text{ THz}$. For the Te band, the changes are much weaker and a Fourier transformation (see Fig. 7.6) yields a periodic contribution at $\Omega_{Te} = 3.6(5) \text{ THz}$. Thus, the VB is clearly more susceptible to the optical excita-

tion. Before turning to the underlying physical mechanism that drives the collective oscillations in TbTe₃ in section 7.2.2, the analysis of the transient spectra and the extraction of the oscillation frequencies is presented.

Analysis of the Frequencies

In detail, the peak positions of both bands are analyzed by fits of two Lorentzian peaks as shown in Fig.7.6(a). To avoid additional assumptions about the exact line shape under these non-equilibrium conditions, also the first statistical moment, i.e. the center of mass of the spectra, was evaluated. For delays between 0 fs and 500 fs after pumping, the VB states are still too far out of equilibrium, which in turn results in significant errors bars of the Lorentzian line fits for these delays. Therefore, the delays between 0 fs and ~ 500 fs after pumping are excluded from the frequency analysis. The characteristic time of ~ 500 fs is assumed to be the relevant timescale for the hot electron distribution to relax via e-e scattering [Fan92, Ret02, Lis04a, Bov07]. The lower-lying Te band is not pumped out of equilibrium appreciably, and the Lorentz fits describe the data well throughout the whole pump-probe delay range, as can be seen in Fig. 7.6(a).

The oscillation frequencies of the Te band and the VB are evaluated by two different methods. On the one hand, the characteristic frequencies can be determined by

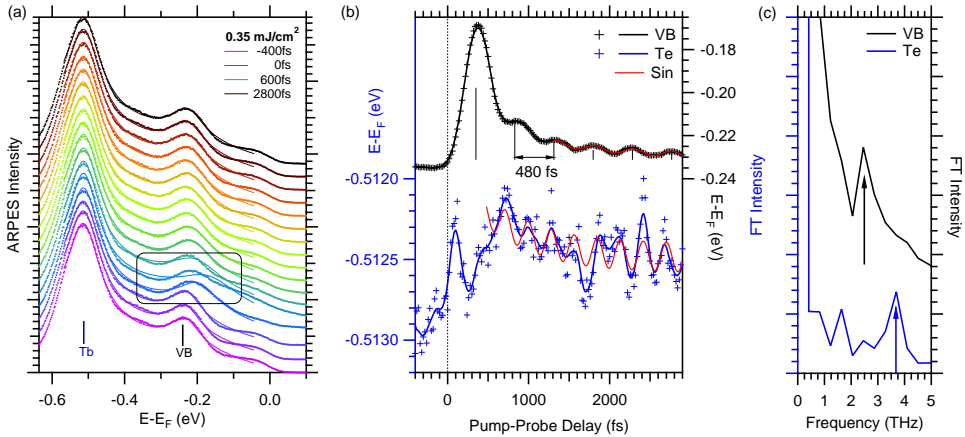


Figure 7.6: (a) Energy distribution curves (dots) for various pump-probe delays and a representative low pump power of 0.35 mJ/cm^{-2} . Included are fits of two Lorentzian peaks with linear background (solid lines). The black box serves as a guide to the eye, indicating the region in which the fit is not able to reproduce the data properly. (b) Parameters extracted from the spectra in (a), as already shown in Fig. 7.5. The red curves are sine fits with polynomial background. The Lorentzian peak position is plotted for the Te band (blue crosses) and VB (black crosses). The solid blue and black lines are the data smoothed by a Gaussian function of 90 fs FWHM. The constant oscillation period in the VB is indicated. (c) Fourier transformations of the transient binding energies in (b). The peaks at $\Omega_{\text{Te}} = 3.6(5)$ THz and $\Omega_{\text{VB}} = 2.3(5)$ THz in the Fourier spectrum of the Te band and the Te-derived VB, respectively, are indicated by arrows.

fitting a sine function to the transient binding energies as shown by the solid lines in Fig. 7.6(b). For the case of a relatively low fluence discussed here, the approximation of a single harmonic oscillation holds rather well. The vertical lines in Fig. 7.6 emphasize the constant period of ~ 480 fs of the binding energy oscillations in the VB. On the other hand, the frequencies can be extracted from a Fourier transformation of the transient energies, which is presented in Fig. 7.6(c). The fits of a sine model function, however, presumes that there is only one dominant, harmonic oscillation. Also, the criteria for determining the reliability of the sine fit is subject to the experimenter's view. For this reason, the frequency analysis was repeated by Fourier transforming the Lorentz fit positions (first statistical moment) for the same delays > 500 fs and plotting all the peaks found in Fourier space. An exemplary Fourier transformation of the data is shown in Fig. 7.6(c). For a consistent description, the frequency of the sine fit was discarded whenever the Fourier spectrum clearly showed more than one frequency.

This redundant analysis was repeated several times with slight variations in the methodology. Depending on the method of analysis, the frequencies scattered more or less strongly by up to ± 0.5 THz, since the total number of pump-probe delay points that were sampled restricts the accuracy in Fourier space. However, the results of two distinct frequencies at $\Omega_{\text{Te}} = 3.6(5)$ THz and $\Omega_{\text{VB}} = 2.3(5)$ THz, as presented in Fig. 7.6(c), were robustly reproduced, regardless which way of analysis was used.

7.2.2 Assignment of the Frequencies

The hot electron distribution and the peak shift of the VB seen in Fig. 7.5 evidences that the electronic part of the CDW decreases almost instantaneously due to photo-doping, i.e. the optical e-h pair excitations. This, then, initiates a movement of the ionic part of the CDW in order to compensate for the instantaneous change in electronic screening. Since the pulse duration is shorter than the oscillation period, a phase relation with respect to time zero is established [Dek00, Bov07]. When the CDW amplitude is above its equilibrium value, the ions will be driven back by a steep rise in the lattice strain energy. When the CDW amplitude is below, the steep loss of the energy gained from electron-phonon interaction will drive them back. The ions thus start to oscillate [Grü94]. This amplitude mode would then be excitable and directly observable with the tr-ARPES technique. Based on the data presented so far and those to follow, the 2.3 THz oscillation is attributed to the CDW amplitude mode. The tr-ARPES data directly reveals that the amplitude mode oscillation indeed drives the VB and thus causes the modulation of the CDW gap. Here, the modulation of the lower edge of the CDW gap in the occupied part of the band structure is directly monitored. For the upper edge of the CDW gap in the unoccupied band structure a π phase-shifted binding energy oscillation would be expected.

To strengthen the evidence leading to the assignment of the CDW amplitude mode to the oscillations of the VB, the fluence dependence of the frequencies observed in the Te band and the VB is analyzed for 100 K and 300 K, e.g. in the normal metallic state and the gapped CDW state. Fig. 7.7 summarizes these results and displays the observed frequencies for both bands as a function of fluence F . All frequencies in Fig. 7.7 were determined from a series of pump-power-dependent spectra taken

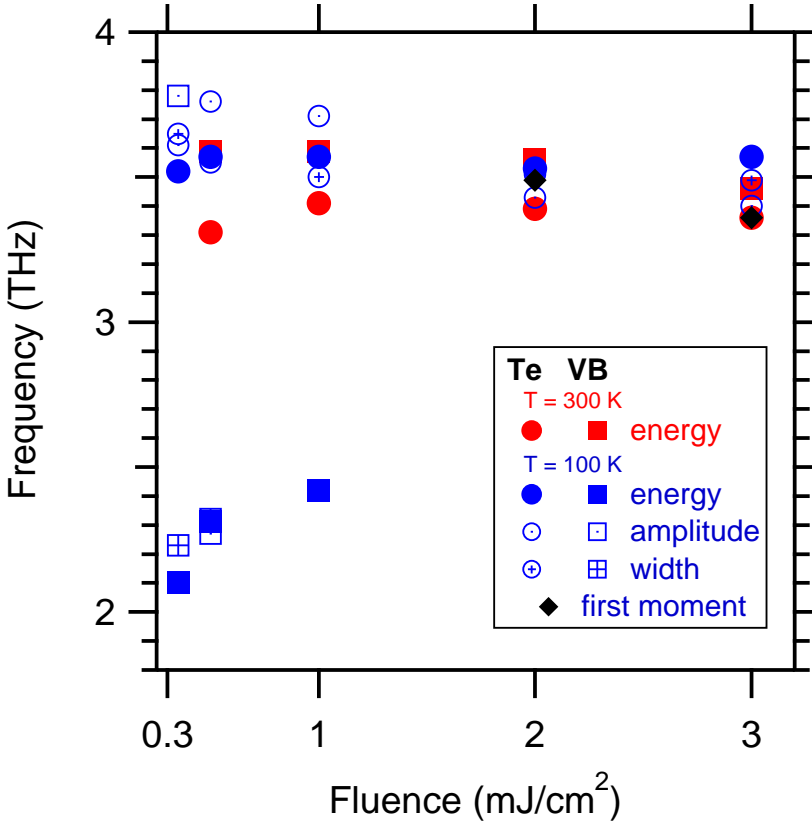


Figure 7.7: Fluence dependence of frequencies of the collective modes for 300 K and 100 K as a function of incident pump fluence. Circles represent the Te band, squares the VB. Solid symbols indicate an energy variation, symbols with a center dot an amplitude, and those with a center cross a line width variation. Frequencies have been determined after 500 fs. Diamonds give the frequency of the first statistical moment discussed in the figures 7.8 and 7.9.

at the point in the Brillouin zone where the CDW band crosses E_F in its normal state, as shown in Fig. 7.5(a). Note that the pump-induced oscillations affect the amplitude, line width and binding energy of the electronic states and thus presents a manifestation of the modulation in the all parts of the spectral function $A(\omega, k)$, which are the amplitude, and the real and imaginary part of the eigen-energy, see chapter 2.4.

The data in Fig. 7.7 evidences that at $T = 300$ K, where the CDW gap in TbTe₃ is almost closed, only the Te mode is observed and the ungapped VB exhibits no oscillations because thermodynamic fluctuations are expected to hamper excitation of the amplitude mode. The temperature dependence of the CDW amplitude is shown in Fig. 2.15(b) and allows to excite the amplitude mode only for sufficiently low temperatures $T < T_{CDW}$. The absence of oscillations in the VB for $T = 300$ K

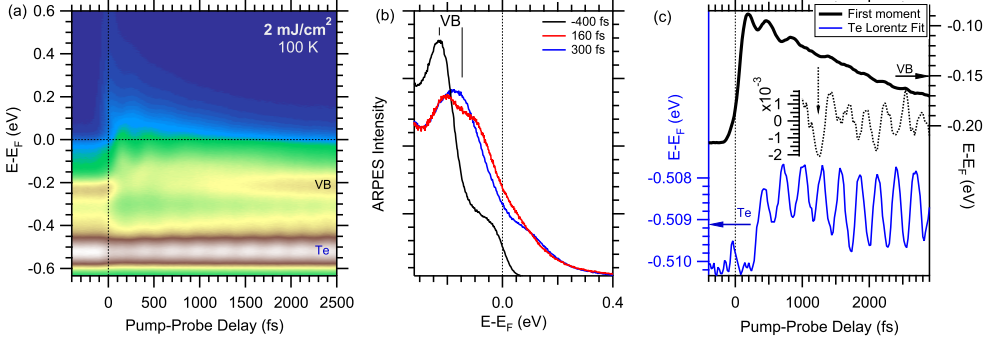


Figure 7.8: (a) Photoelectron intensity as a function of energy and delay taken under identical conditions as in Fig. 7.5, but a higher fluence of 2 mJ/cm^2 . (b) The spectra from (a) at selected delays on a linear intensity scale exhibit a shifting and splitting of the VB peak. (c) Transient binding energy of the Te band (blue) and the VB (black). The data was analyzed by fitting a Lorentzian peak to the Te band (blue). The strong perturbation does not allow to describe the VB peak with a Lorentzian (see Fig. 7.9) and therefore the first moment was determined (bold). A background was subtracted from the first moment to make the oscillations well visible (dashed).

again points to the 2.3 THz mode being the CDW amplitude mode. In contrast, at $T = 100 \text{ K}$ - well below T_{CDW} - two modes are identified for lower fluences of $F \leq 1 \text{ mJ/cm}^2$. Here, only the low frequency mode at 2.3 THz is observed in the VB. Moreover, this frequency regime is typical for the CDW systems [Tra83]. Also, recent Raman [Lav08] and time-dependent reflectivity [Yus08] studies come to the conclusion that the 2.3 THz mode is intimately connected to the formation of the CDW in RTe_3 . Interestingly, the presumed CDW amplitude mode is not observed for higher pump fluences of $F > 1 \text{ mJ/cm}^2$. This fluence regime is investigated in detail in next section, where evidence for an ultrafast melting of the frozen-in CDW phase is presented.

7.2.3 Ultrafast Melting of the CDW State

This section discusses tr-ARPES data that has been taken at an increased IR pump fluence of $F_2 = 2 \text{ mJ/cm}^2$ and presents further evidence consistent with the assignment of the CDW amplitude mode to the oscillations in the VB. Respective data are shown in Fig. 7.8, which were acquired under the same experimental conditions described in the context of Fig. 7.5, but for a higher fluence F_2 . Clearly, the impact of oscillations on the electronic states has increased compared to the regime of lower fluences shown in Fig. 7.5. Furthermore, the spectral function of the VB depends on the oscillation phase as seen from spectra given in Fig. 7.8(b). For a delay of 160 fs the VB peak is significantly broadened, whereas at 300 fs an additional splitting of the line is observed. However, these spectra suggest not a simple shift and broadening of the line, but a more complex transient state, that will be discussed in the following in terms of a strong perturbation of the CDW state. In this fluence regime, the variations of the VB peak, as shown in Fig. 7.8(c), are analyzed by determining the center

of mass, which accounts for the transfer of spectral weight and avoids assumptions of particular spectral line profiles, see Fig. 7.9. Compared to the weakly perturbative excitation presented in Fig. 7.5, the amplitude of the Te mode is increased, whereas the VB mode has changed qualitatively.

Analysis of the Frequencies

As will be discussed in the next section 7.2.4, a strongly perturbative regime is entered at high pump fluences of $\geq 1 \text{ mJ/cm}^2$ and drives an ultrafast phase transition. In this excitation regime, the system is not near equilibrium and the VB does not exhibit a symmetrical, Lorentzian line shape after pumping, see Fig. 7.9(a). In contrast to the case of a weak excitation presented in Fig. 7.6, the line shape of the VB does not recover it until 2 – 3 ps pump-probe delay and leads to unreliable Lorentz fits. Therefore, the first statistical moment of the spectrum in the region between 0.4 eV and 0 eV binding energy was computed. This quantity allows to extract frequency information for these high pump powers, since it does not rely on any model. The further frequency analysis proceeds with fits of sine functions and Fourier transformations to extract the frequencies the same way as described in the context of Fig. 7.6.

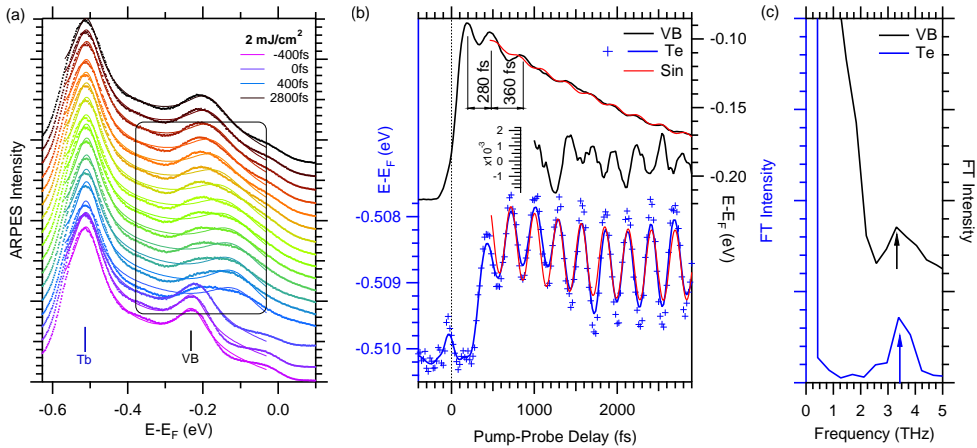


Figure 7.9: Energy distribution curves (dots) for various pump-probe delays and a representative high pump power of 2 mJ/cm^2 . Included are fits of two Lorentzian peaks with linear background (solid lines). The black box indicates the region in which the fit is not able to describe the position of the VB properly. Thus, the first statistical moment was determined for the VB. (b) Parameters extracted from the spectra in (a), as already shown in Fig. 7.8. The red curves are sine fits with polynomial background. The Lorentz position of the Te band (blue crosses) is plotted along with the data that was smoothed by a Gaussian function of 90 fs FWHM. The change of the oscillation period of the VB within the first 1 ps is highlighted. (c) Fourier transformations of the transient binding energies in (b). The peaks at 3.4(1) THz and 3.3(1) THz in the Fourier spectrum of the Te band and the VB, respectively, are indicated by arrows.

Focusing on the oscillations of the Te band, the oscillations are now well resolved and the frequency analysis yields $\Omega_{\text{Te}} = 3.6(1)$ THz, see Fig. 7.9(c). Recent results from Raman spectroscopy on RTe_3 [Lav08] indicate that this mode cannot be assigned to one of the four Raman-active A_{1g} modes predicted for the undistorted lattice. The frequencies observed by Raman spectroscopy do not correspond to the 3.6 THz mode observed in tr-ARPES. The modulation of the Te band probably results from the new lattice periodicity superimposed by the CDW [Lav08]. The Te oscillation is robustly present in all measurements, regardless of the position in the Brillouin zone, the temperature, or the pump power. However, the Te mode decreases and eventually vanishes with increasing temperature or pressure above T_{CDW} [Lav08]. In this respect, the Te mode is linked to the CDW through a change of the lattice periodicity, but does not evidence the excitation of the amplitude mode of the CDW itself.

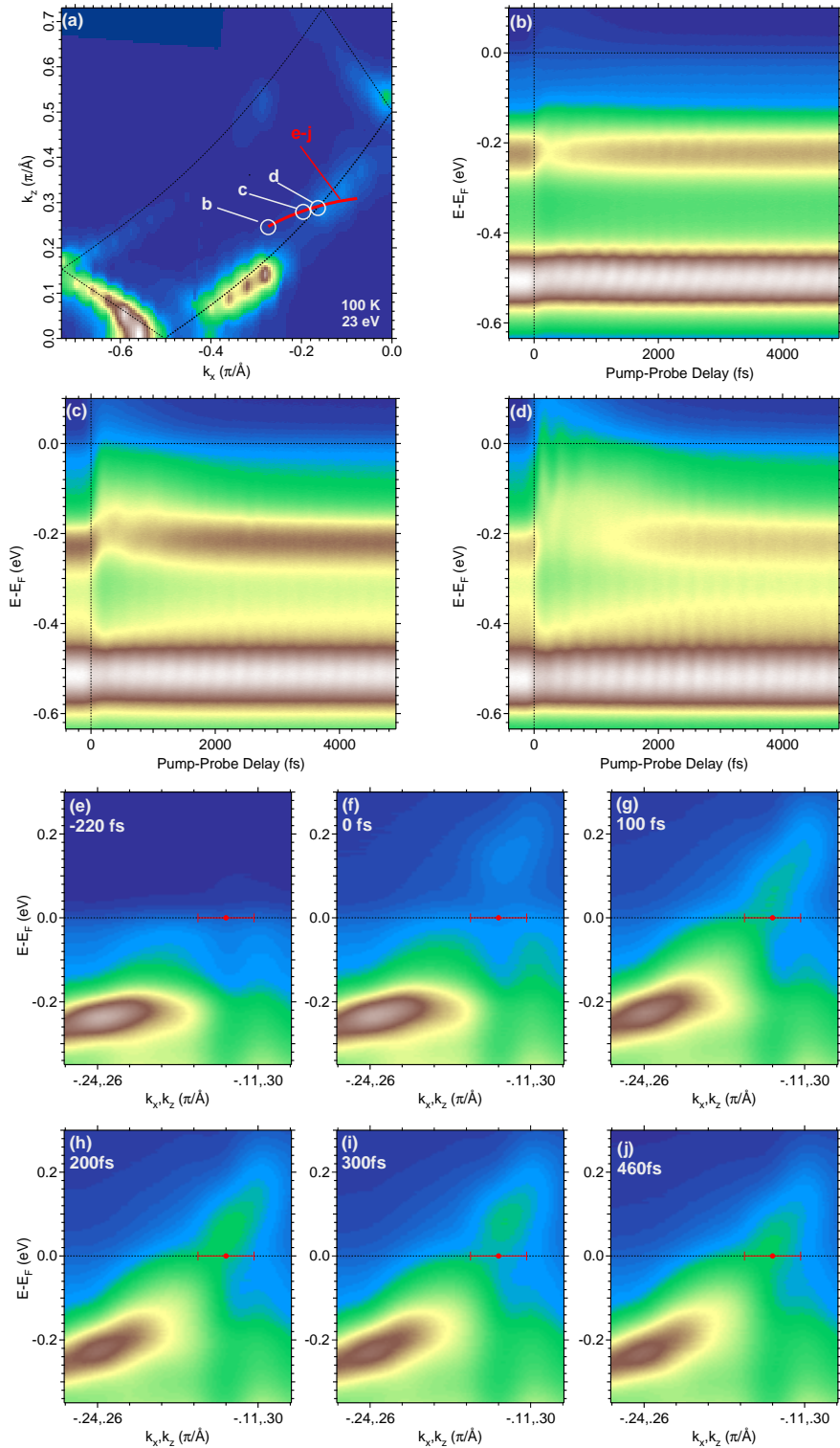
Turning to the VB mode in Fig. 7.9(b), its time evolution appears to be separated into two regimes. The first two pronounced oscillations display a different periodicity of 270 fs and 400 fs, respectively, which is indicated by vertical lines in Fig. 7.9(b). For the first ps, no phase correlation of the modes of the Te band and the VB is encountered. After 1 ps weak oscillations with a frequency of 3.6 THz appear, see inset of Fig. 7.9(b). In contrast to earlier delays, these oscillations after 1 ps are phase correlated, where the maxima in the VB oscillation tend to fall onto the minima of the transient Te binding energy. To investigate the impact of the strong excitation of e-h pairs on the CDW phase and the correlation of the oscillations of the Te band and the VB, the next section extends the analysis of the transient spectra into the CDW nesting region of the Brillouin zone.

7.2.4 Analysis in k -space

The tr-ARPES experiment provides an explicit link between the amplitude mode and CDW gap modulation via a momentum dependent analysis: In a nesting-driven CDW, the electrons are most susceptible to scattering by the CDW phonon wave vector q_{CDW} directly at the FS where the Lindhard response function $\chi(q)$ increases rapidly upon approaching k_F , see [Grü94] and chapter 2.2. Therefore, a modulation in the CDW amplitude and thus a modulation of the order parameter of the CDW phase transition, i.e. the gap magnitude Δ , is expected to influence the electronic band structure the strongest at or near k_F . This k -dependence should be present no matter if the system is perturbed weakly - i.e. the coherent amplitude mode oscillation is excited - or strongly - resulting in the ultrafast melting of the CDW state, as discussed in the following. In fact, tr-ARPES is able to provide this information.

Figure 7.10 (*facing page*): (a) Detail of the FS plot from Fig. 7.3(a') with positions (white circles) of time-resolved data shown in (b)-(d) and cut position (red line) of the photoelectron intensity as a function of energy and position (e)-(j) for $T = 100$ K and $F_2 = 2$ mJ/cm². k_F is marked in (e)-(j) by red dots.

7. Time- and Angle-resolved Photoemission of TbTe₃



In Fig. 7.10 such tr-ARPES data is presented. Fig. 7.10(a) defines the position in the Brillouin zone where the time-resolved data sets of Fig. 7.10(b)-(d) have been recorded under the conditions described in Fig. 7.8. As expected for the excitation of a nesting-driven CDW the tr-ARPES data in Fig. 7.10(b)-(d) establish a pronounced momentum dependent excitation of the electronic structure. While the VB energy does not vary in the data set of Fig. 7.10(b), which was acquired away from the FS, i.e. below k_F , the largest change of the VB indeed occurs directly at k_F , see Fig. 7.10(d). The momentum dependence of the Te band oscillation, however, is much less pronounced. This again corroborates the assignment of the VB mode to the amplitude mode of the CDW in TbTe₃.

In a next step, several tr-ARPES measurements at different positions in the Brillouin zone are combined to yield transient images of the band structure. This allows a momentum specific analysis of the electronic excitation and the response of the lattice in order to reveal the process of the ultrafast melting of the CDW state. Fig. 7.10(e)-(j) shows the momentum dependent data for selected delays as indicated. Starting out with the unperturbed equilibrium band structure for -220 fs, the same situation as depicted in Fig. 7.3(c') with the gapped CDW state is encountered. At a delay of 0 fs, where the leading edge of the IR pump pulse has already excited the electronic system due to e-h pair creation, the CDW gap is still preserved and the flat dispersion of the VB represents a localized state as prior to pumping. However, in the vicinity of k_F (red dots in Fig. 7.10(e)-(j)), an intensity increase at $E - E_F = 0.15$ eV is encountered. This peak coincides with the unoccupied state as observed in Fig. 7.5(b) and manifests an instantaneous photo-doping of the system, which drives the CDW amplitude mode at low excitation densities and initiates the break down of the CDW phase at higher fluences. At 100 fs when the pump pulse is already over and thus delayed with respect to the excitation and the occurrence of the photo-doped state above E_F , the CDW gap is closed and the dispersion of the VB resembles the quasi-free electron dispersion known from spectra taken at 300 K, i.e. the ungapped metallic state, see Fig. 7.3(c). For this reason, this excitation regime is termed "strongly perturbative" since the optical excitation results in an ultrafast melting of the charge ordered state. Remarkably, the conduction electrons recover their wavelike nature within the first 100 fs. In fact, the VB forms a free-electron like band despite the intense excitation and resulting intense scattering. Its dispersion can be followed well above E_F due to the photo-excited hot electron population. Moreover, the k -space cuts at later delays evidence the oscillations throughout the whole band structure. Going from a delay of 100 fs in Fig. 7.10(g) to 200 fs in Fig. 7.10(h) the hot electron intensity in the delocalized VB clearly increases, which is attributed to the creation of secondary e-h pairs in the vicinity of E_F in the thermalization process of the non-equilibrium electron distribution. Increasing the delay to 300 fs, as shown in Fig. 7.10(i), the continuous dispersion of the delocalized VB exhibits a discontinuity close to k_F , leading to the formation of a hot electron lobe in the unoccupied band structure. At a delay of 460 fs, when the thermalization process due to e-e scattering has established a defined electronic temperature and the hot electron distribution has relaxed toward E_F , the lobe has vanished again and the continuous dispersion in the VB is recovered. These time-resolved cuts of the band structure manifest that the modulations in the VB associated with the CDW state occur only at certain wave vectors in the CDW

nesting region and affirm the assignment of the modulations to the CDW amplitude mode.

The cuts of the transient band structure presented in Fig. 7.10(e)-(j) show the tr-ARPES data only for selected delays. In addition, the *animated movie file*² features all time frames of these cuts. This added information of the animated band structure in TbTe₃ showcase both the time-dependent closing of the CDW gap in the first ~ 100 fs as well as the ensuing oscillatory behavior in a striking manner. The bar to the right of the movie indicates the time difference between pump and probe laser pulse. Each movie frame features a false color plot of photoelectron intensity as a function of energy and Brillouin zone position, as indicated. The animation starts at a negative pump-probe delay before the arrival of the pump pulse, and proceeds toward increasing pump-probe delay in 20 fs time frames.

The animation in k -space allows to clearly identify a delay of the ultrafast melting of the CDW phase with respect to the photo-doping of the unoccupied parts of the band structure. The melting of the CDW phase is closely related to the mechanism of the CDW formation: Due to a coupling between lattice vibrations to the electrons, electronic energy is gained if a phonon with a wave vector q_{CDW} freezes in the crystal. This is because the phonon mode effectively nests two regions of the FS and presents a macroscopically occupied phonon mode, which leads to a charge density modulation. Upon cooling, this energy gain becomes larger than the energy loss from the lattice deformation and the system undergoes a phase transition into the CDW state. Because formation of the CDW requires freezing of a phonon, which is nothing else than nuclear motion, the inverse process of melting cannot proceed faster than the respective motion. Considering that photo-doping modifies the screened ion potential, such that it sustains a delocalized state, the ion cores still have to propagate to the potential minima in the presence of screening carriers, which explains the observed delay in the CDW melting. This result provides a direct and vivid demonstration of the electron-phonon interaction being the origin of the CDW formation.

This brings up the question whether the CDW phase transition is completed after the first 100 fs. Returning to the discussion of the strong perturbation case with $F_2 = 2$ mJ/cm² presented in Fig. 7.8 and Fig. 7.9 it was already mentioned earlier that the temporal evolution of the bands can be divided into two regimes according to the time delay. Between 1 – 3 ps, when the melting of the CDW phase is complete and the CDW amplitude mode - by definition - no longer exists, only the 3.6 THz Te phonon oscillation is observed. This is most clearly seen in the blown up dashed curve in Fig. 7.8(c) and Fig. 7.9(b) which exhibits a phase correlated oscillation of the VB and the Te band at the same frequency. For delays < 1 ps, the situation is more complex, as highlighted by the vertical lines in Fig. 7.9(b), which indicate the changing oscillation frequency. The time duration between the first two maxima is given by 280 fs, which corresponds to a frequency of 3.6 THz. Inspecting the duration between the second and third maximum yields a period of 360 fs (2.8 THz) and evidences a softening of the ion potential in the first 500 fs. At later times, the initial oscillation of the VB fades away and a weak modulation due to the coherent Te phonon is sampled in the VB.

²For the access to the supporting online material of reference [Sch08], which includes the k -space animation, *no* subscription to Science.org or AAAS should be necessary.

The mode associated with the oscillation of the VB is connected to the amplitude mode, but is not the same. While the CDW gap is closed at 100 fs due to the optical excitation of the electronic system, a transient "steady-state" of the coupled electron and lattice system outside the CDW phase has not been established yet. The ions experience a force due to the ultrafast change of the potential and start to oscillate in this new potential. At the same time the hot electron distribution relaxes the excess energy via incoherent e-ph scattering with the lattice subsystem. Since the ions are massive particles they cannot stop once excited and will continue to oscillate in the transient potential. Thus, one may expect the system to oscillate between a localized CDW state and a delocalized, molten CDW state in the course of the thermalization process to the transient equilibrium observed beyond 1 ps. Such a coupled electron and lattice dynamics goes beyond the Born-Oppenheimer approximation which assumes that the motion of the light electrons can be separated from the motion of the massive nuclei [Bor27].

Conclusions

Summarizing, the CDW model system of TbTe₃ was studied with fs time-resolved ARPES. The temperature-, fluence- and k_F -dependent analysis of the transient band structure in the CDW nesting region around k_F reveals an oscillation of the Te-derived VB, which is assigned the excitation of the amplitude mode of the CDW phase of TbTe₃. At the highest fluences investigated, the charge-ordered CDW melts within 100 fs, evidenced by the ultrafast closing of the CDW gap in the band structure at k_F and the transient recurrence of a nearly free electron dispersion.

The comprehensive analysis of the k -dependent coupled dynamics of the electron and lattice system in the prototypical CDW compound TbTe₃ has implications well beyond the specific material that was studied. Conventional ARPES offers superior energy and angle resolution and is able to detect the effect of collective modes in the form of dispersion kinks or spectral dips [Dam03]. The interpretation of their assignment and the impact on the low lying electronic structure, however, requires sophisticated theoretical calculations that often can only be done in the context of a particular model. tr-ARPES is still limited by the current technology in the accessible region of the Brillouin zone, and the energy-, and angle-resolution. Nevertheless, tr-ARPES is able to directly probe the transient interplay between collective modes and single particle states in theory-independent ways and thus is a valuable complement to conventional ARPES. Such tr-ARPES studies enable a direct access to the band structures in k -space and the femtosecond time resolution allows to monitor the elementary quasi-particle scattering processes occurring on an ultrafast time scale. The ability to simultaneously obtain single-particle information in the spectral domain and information about the collective excitations in the time-domain facilitates the understanding of such important phenomena as e-e correlation.

The insight gained here into the correlation of the electronic spectral function and collective modes establishes femtosecond time-resolved ARPES as a valuable tool for the study of many-particle and correlated electron physics. Specifically, the direct observation of collective modes via their interaction with the electronic band structure opens up the opportunity to gain insights on the central question of the quantum many body problem: the interplay between collective and individual properties.

8 Conclusions and Outlook

The present thesis investigated the ultrafast electron dynamics in low-dimensional materials. In such low-dimensional materials the confinement of the electronic wave functions to 2D and 1D can lead to quantum size effects (QSEs) that are important for the understanding of the macroscopic physical properties. Moreover, the electron confinement can lead to many-body phenomena, where electron-electron correlation and coupling to other quasi-particles such as phonons can result in the formation of broken-symmetry ground states like charge density wave (CDW) or superconducting phases. These fundamental questions are addressed with the investigation of well-defined quasi-2D and quasi-1D model systems such as ultrathin epitaxial metal films and a prototypical CDW compound using femtosecond time- and angle-resolved photoemission spectroscopy (PES) techniques.

Summarizing, the binding energies of the quasi-2D quantum well states (QWSs) in Pb/Si(111) are generally well-described by a model of a free-standing Pb slab. Deviations occur at low coverages for the unoccupied QWSs, which can be attributed to the influence of the substrate. The lifetime of the *unoccupied* QWSs due to inelastic electron-electron (e-e) scattering amounts to 5 – 140 fs and is governed by 3D Fermi liquid theory. Additional decay processes observed on longer timescales with decay times of 90 – 900 fs are attributed to the decay of hot carriers in the Si substrate due to hot electron scattering from Si into the Pb film. The strong thickness dependence of the quantized binding energies induces a 2 ML oscillation of the lifetimes by a modulation of the phase space. Moreover, the quantitative analysis of the transient populations requires to account for the quantization of the electronic system since the simultaneous population decay and build-up in the two adjacent subbands favors inter-subband scattering from the higher lying to the lower lying state. Time-resolved PES studies of the *occupied* QWSs in Pb/Si(111) revealed a transient binding energy stabilization occurring within the pulse duration of 100 fs. The intense optical excitation decreases the electronic screening of the ion cores quasi-instantaneously and results in an increase of the ion potential. Superimposed on the binding energy shift is a periodic modulation at a frequency of 2.2 THz that is attributed to the excitation of a coherent phonon mode in the [111] film direction. These results highlight the collective excitations of the phononic and electronic system, which are coupled by electron-phonon interaction.

The hot electron lifetimes in quasi-1D self-assembling metallic nanowires in 4×1-In/Si(111) were investigated with a novel position-sensitive electron time-of-flight (pTOF) technique that was developed in this work for efficient angle-resolved PES studies of low-dimensional materials with anisotropic band structure. The hot electron lifetimes in In/Si(111) amount to 4 – 17 fs at ~ 1 eV above the Fermi level. The energy- and momentum-dependent analysis of the lifetimes in the vicinity of the Γ -point, however, does not reveal an unambiguous anisotropy of the lifetimes that is correlated to the high-symmetry directions defined by the nanowires. This finding suggests to conduct future time- and angle-resolved investigations at lower energy in the substrate bandgap and in other parts of the Brillouin zone, where the anisotropy of the bands is more pronounced.

The collective excitations of electrons and phonons in the prototypical quasi-1D CDW compound of TbTe_3 and their k -dependence have been investigated with time- and angle-resolved PES. At moderate excitation densities, the valence band in the nesting region of the CDW reveals a coherent oscillation, which is observed exclusively for temperatures below the phase transition and in the nesting region of the CDW phase, i.e. where the Lindhard response function is largest. Hence, this mode is assigned to the coherent excitation of the amplitude mode of the CDW phase. High excitation densities lead to an ultrafast melting of the frozen-in CDW phase within 100 fs that was observed by a closing of the bandgap and a transient recurrence of the free electron-like dispersion of the bands around the Fermi level. This work presents the first time- and k -dependent study of the electronic structure in a solid and establishes this technique as a promising, novel tool for the study of correlation effects in condensed matter.

Future time-resolved investigations of the hot electron dynamics in the QWSs of Pb/Si(111) will focus on temperature- and angle-dependent studies of (i) intra- and intra-subband scattering in the quantized band structure and (ii) the contribution of electron-phonon coupling to the decay processes. In general, this work shows that the influence of the substrate due to transport can be minimized by the electron confinement in a global bandgap. This suggests to extend the time-resolved investigations to wide-bandgap QWS systems like Pb/SiC(0001) . The bandgap of single-crystalline graphite on silicon carbide extends several eV above and below the Fermi level [For98, Emt06] and thus provides a very high degree of electron confinement, resulting in strongly decoupled quasi-freestanding metal films that are well-suited for PES [Di107].

Time- and angle-resolved PES offers fascinating possibilities for the study of highly correlated materials. Specifically, temperature dependent studies and a systematic variation of the Lanthanide substituent R in the RTe_3 compounds might contribute to a precise microscopic understanding of the collective excitations in this prototypical CDW system. More generally, conventional and unconventional superconductors like Cuprates [Dam03] or Pnictides [Nor08] could be promising candidates to trigger a coupled electron and lattice dynamics that enables the study of the collective phenomena of superconductivity in the time domain.

Future experimental developments could include the implementation of an effectively larger acceptance angle in the pTOF spectrometer by applying electric extraction fields that accelerate and focus the photoelectrons toward the center of the detector [Hat04, Hat08]. For such an experimental scheme Hengstberger et al. [Hen08] employed an analytical method to retrieve the kinetic electron energy as well as the in-plane momentum. This procedure can be implemented into the pTOF concept and could refine the pTOF spectrometer to become an even more versatile tool. With respect to the analysis of the electron dynamics in $4\times 1\text{-In/Si(111)}$ in the form of energy and k -resolved lifetime maps, one might envision the extension of this concept to determine more complex quantities than the hot electron lifetime. This could be, for example, the extraction of an amplitude and frequency map in k -space for coherently excited phonons. The analysis of the k -dependence of the CDW

amplitude mode in TbTe_3 proves the demand for an angle-resolved analysis of the collective electron and lattice dynamics. Since the magnitude of the amplitude mode depends on the divergence of the Lindhard response at the Fermi vector, one might even speculate to extract the k -resolved Lindhard response function [Joh08] from the aspired coherent phonon amplitude maps in k -space.

A Abbreviations

1D	one dimension
2D	two dimensions
3D	three dimensions
2PPE	two-photon photoemission
2TM	two temperature model
AC	auto correlation
ARPES	angle-resolved photoemission spectroscopy
BBO	β -barium-borate
BCS	Bardeen-Cooper-Schrieffer
CB	conduction band
CBE	conduction band edge
CCD	charge coupled devices
CDW	charge density wave
CFD	constant-fraction-discriminator
CI	consistency indicator
CPA	chirped pulse amplification
cw	continuous wave
DECP	displacive excitation of coherent phonons
DFG	difference frequency generation
DFT	density functional theory
DOS	density of states
e-e	electron-electron
EELS	electron energy loss spectroscopy
e-h	electron-hole
e-ph	electron-phonon
IECP	impulsive excitation of coherent phonons
IR	infrared
IR-OPA	infrared optical parametric amplifier
FLT	Fermi liquid theory
FS	Fermi Surface
FWHM	full width at half maximum
GVD	group velocity dispersion
hoQWS	highest occupied quantum well state
IPS	image potential state
IPES	inverse photoemission spectroscopy

LEED	low energy electron diffraction
lmf	list-mode-file
luQWS	lowest unoccupied quantum well state
MCP	micro channel plate
ML	monolayer
NFE	nearly free electron gas
NIM	nuclear instrumentation module
OPA	optical parametric amplifier
PES	photoemission spectroscopy
PID	proportional integral differential
QMS	quadrupole mass spectrometer
QSE	quantum size effect
QWR	quantum well resonance
QWS	quantum well state
pTOF	position-sensitive electron time-of-flight
RAS	reflectance anisotropy spectroscopy
RegA	regenerative amplifier
RHEED	reflection high energy electron diffraction
rms	root-mean-square
SFG	sum frequency generation
SHG	second harmonic generation
S/N	signal-to-noise
SPV	surface photo voltage
STM	scanning tunneling microscopy
STS	scanning tunneling spectroscopy
SXRD	surface x-ray diffraction
TB	tight binding
TDC	time-to-digital converter
TOF	electron time-of-flight
tr-ARPES	time- and angle-resolved photoemission spectroscopy
UHV	ultrahigh vacuum
UV	ultraviolet
VB	valence band
VBE	valence band edge
VIS	visible
VIS-OPA	visible optical parametric amplifier
XC	cross correlation

B Free Electron Gas

The Fermi wave vector k_F and the Fermi energy E_F are determined by the filling of k -space with electrons and thus ultimately depend on the dimensionality d and the respective electron density $n^{(d)}$. This chapter summarizes the results of the free electron approximation.

Eigen-Energies

Starting point is the time-independent Schrödinger equation for a set of non-interacting electrons with eigen-energies E :

$$(B.1) \quad -\frac{\hbar^2}{2m} \Delta_{\vec{r}} \Psi(\vec{r}) = E \Psi(\vec{r}) \quad .$$

The solutions of the Schrödinger equation for a quasi-free particle are plane waves Ψ , which are normalized to a finite volume $V = L^d$ with the length L and d dimensions of the crystal under consideration:

$$(B.2) \quad \Psi(\vec{r}) = \frac{1}{\sqrt{V}} \exp(-i\vec{k} \cdot \vec{r}) \quad \text{and eigen-energies} \quad E = \frac{\hbar^2}{2m} \vec{k}^2 \quad .$$

With cyclic Born-von Karman boundary conditions in 3 dimensions

$$(B.3) \quad \Psi(\vec{r} + L\{m_1, m_2, m_3\}) = \Psi(\vec{r}) \quad \text{for} \quad m_i \in Z$$

one finds quantized wave vectors \vec{k} with the maximum wave vector \vec{k}_{max}

$$(B.4) \quad k_i = \frac{2\pi m_i}{L} \quad \text{for} \quad |2m_i| < N_\tau \quad \Rightarrow \quad k_{max} = \frac{\pi}{a}$$

where $a = L/N_\tau$ is the lattice constant of a simple cubic lattice.

Density of States in k -space

The k -space volume per point in d dimensions is reciprocal to the number of allowed k -states per unit volume in k -space:

$$(B.5) \quad \left(\frac{2\pi}{L}\right)^d \quad \Rightarrow \quad n_k^{(d)} = \left(\frac{L}{2\pi}\right)^d \quad .$$

Fermi energy E_F and Density of States

The energy levels are filled up to the Fermi level according to the Pauli principle

$$(B.6) \quad E_F = \frac{\hbar^2 k_F^2}{2m} \quad .$$

A solid with N_k k -states has $2N_k$ electronic states N due to the twofold degeneracy of the electron spin: $N = 2N_k$. For a large number of electronic states the volume of state space $\Omega^{(d)}$ can be approximated by a sphere of dimension d :

$$(B.7) \quad N = 2\Omega^{(d)} n_k^{(d)} \quad .$$

From this relation, the Fermi wave vector k_F is calculated. The dimension-less electron density parameter r_s is also given as it is used frequently throughout the theoretical literature. $n^{(d)}$ is given by the number of valence electrons per primitive unit cell of dimension d .

1 dimension

$$(B.8) \quad N = 2 \cdot 2k_F \frac{L}{2\pi} \quad \text{with} \quad n^{(1)} = \frac{N}{L} \quad \Rightarrow \quad \underline{k_F = \frac{\pi}{2} n^{(1)}}$$

$$r_s a_0 = \frac{1}{n^{(1)}} \quad \Rightarrow \quad \underline{r_s = \frac{1}{a_0} \frac{1}{n^{(1)}}}$$

2 dimensions

$$(B.9) \quad N = 2 \pi k_F^2 \frac{L^2}{4\pi^2} \quad \text{with} \quad n^{(2)} = \frac{N}{L^2} \quad \Rightarrow \quad \underline{k_F = (2\pi n^{(2)})^{\frac{1}{2}}}$$

$$\pi (r_s a_0)^2 = \frac{1}{n^{(2)}} \quad \Rightarrow \quad \underline{r_s = \frac{1}{a_0} \left(\frac{1}{\pi n^{(2)}} \right)^{1/2}}$$

3 dimensions

$$(B.10) \quad N = 2 \frac{4\pi k_F^3}{3} \frac{L^3}{8\pi^3} \quad \text{with} \quad n^{(3)} = \frac{N}{L^3} \quad \Rightarrow \quad \underline{k_F = (3\pi^2 n^{(3)})^{\frac{1}{3}}}$$

$$\frac{4\pi (r_s a_0)^3}{3} = \frac{1}{n^{(3)}} \quad \Rightarrow \quad \underline{r_s = \frac{1}{a_0} \left(\frac{3}{4\pi n^{(3)}} \right)^{1/3}}$$

Density of States in the Energy Domain

The density of states (DOS) in energy space of d dimensions $g^{(d)}(E)$ is derived using:

$$(B.11) \quad g^{(d)}(E) = \frac{\partial n^{(d)}(E)}{\partial E} \quad .$$

In the case $T = 0$, as discussed here, the ground state distribution function is given by a step function

$$(B.12) \quad f^{(0)}(E) = \begin{cases} 0 & \text{for } E > E_F \\ 1 & \text{for } E < E_F \end{cases}$$

The DOS $g^{(d)}(E)$ may be used to rewrite integrals from k - to E -space:

$$(B.13) \quad \int_{(d)} \frac{dk^3}{4\pi} F(E(\vec{k})) = \int dE f(E) g^{(d)}(E) F(E) \quad .$$

1 dimension

$$(B.14) \quad \begin{aligned} n^{(1)} &= \frac{N}{L} = \frac{2k}{\pi} = \frac{2}{\pi} \left(\frac{2mE}{\hbar^2} \right)^{\frac{1}{2}} \\ \Rightarrow g^{(1)} &= \frac{2}{\pi} \left(\frac{2m}{\hbar^2} \right)^{\frac{1}{2}} E^{-\frac{1}{2}} \end{aligned}$$

2 dimensions

$$(B.15) \quad \begin{aligned} n^{(2)} &= \frac{N}{F} = \frac{k^2}{2\pi} = \frac{mE}{\pi\hbar^2} \\ \Rightarrow g^{(2)} &= \frac{m}{\pi\hbar^2} = \text{const} \end{aligned}$$

3 dimensions

$$(B.16) \quad \begin{aligned} n^{(3)} &= \frac{N}{V} = \frac{k^3}{3\pi^2} = \frac{1}{3\pi^2} \left(\frac{2mE}{\hbar^2} \right)^{\frac{3}{2}} \\ \Rightarrow g^{(3)} &= \frac{1}{3\pi^2} \left(\frac{2m}{\hbar^2} \right)^{\frac{3}{2}} \sqrt{E} = \frac{3}{2} \frac{n^{(3)}}{E_F} \sqrt{\frac{E}{E_f}} \end{aligned}$$

C Landau Theory of Fermi Liquids

This chapter summarizes the results of the Landau theory of Fermi liquids for the inelastic electron-electron (e-e) scattering rate $\Gamma_{e-e} = 1/\tau_{e-e}$. The general description follows [Pin66, Giu05], whereas the explicit derivation of the scattering rate in 2D is taken from [Qia05, Qia06]. Finally, a short abstract of an *ab-initio* approach, the *GW*-approximation [Chu06a], for the calculation of Γ_{e-e} is presented.

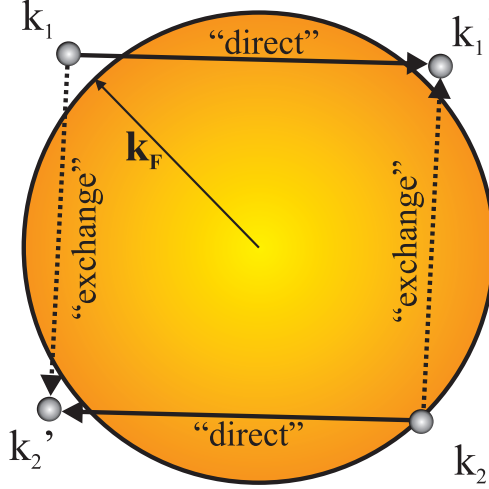


Figure C.1: Electron-electron scattering with direct (solid arrows) and exchange (dashed arrows) contribution.

The total inelastic scattering rate Γ_{e-e} has a direct contribution and an indirect "exchange" contribution as sketched in Fig. C.1.

$$(C.1) \quad \Gamma_{e-e} = \frac{1}{\tau_{e-e}} = \frac{1}{\tau_d} + \frac{1}{\tau_{ex}}$$

The direct term describes a hot electron \vec{k}_1 , which scatters with a cold electron \vec{k}_2 in the Fermi sea due to the screened Coulomb interaction W . This creates two quasi-particles \vec{k}_1' and \vec{k}_2' , and a quasi-hole \vec{k}_2 (solid arrows). An alternative pathway that leads to the same final state configuration is the "exchange" scattering (dashed arrows). In the following, it will be shown that in 3D only the direct term contributes to Γ_{e-e} , whereas in 2D also the "exchange" term has to be considered. Explicitly, the direct and the "exchange" scattering rates are given by two Golden-rule-like expressions

$$(C.2) \quad \frac{1}{\tau_d} = 2\pi \sum_{\vec{k}_2, \vec{q}} \sum_{\sigma'} W^2(\vec{q}) n_{k_2, \sigma'} [1 - n_{k_1', \sigma}] [1 - n_{k_2', \sigma'}] \\ \times \delta(\xi_{1, \sigma} - \xi_{2', \sigma} + \xi_{2, \sigma'} - \xi_{2', \sigma'})$$

and

$$(C.3) \quad \frac{1}{\tau_{\text{ex}}} = -2\pi \sum_{\vec{k}, \vec{q}} W(\vec{k}_1 - \vec{k}_2 + \vec{q}) W(\vec{q}) n_{k_2, \sigma} [1 - n_{k_1, \sigma}] [1 - n_{k_2, \sigma}] \\ \times \delta(\xi_{1, \sigma} - \xi_{2', \sigma} + \xi_{2, \sigma} - \xi_{2', \sigma}) \quad .$$

The second order perturbation approach is reflected in the quadratic dependence on the interaction potential W^2 . The conservation of energy and momentum is ensured by the δ functions. The transferred momentum is given with $\vec{q} = \vec{k}_1 - \vec{k}_2 = \vec{k}_1' - \vec{k}_2'$. The energy transferred in the scattering event is $E_q = \hbar^2 q^2 / (2m)$ and $\xi_{i, \sigma} = E_1 - E_F = \hbar^2 k_{i, \sigma}^2 / (2m) - E_F$ is the excess energy of the exited electron k_1' . The structure of (C.2) and (C.3) shows that the direct and "exchange" contribution tend to cancel each other.

The screened Coulomb interaction W is given by the Thomas-Fermi approximation with screening wave vector k_s

$$(C.4) \quad W(q) = \begin{cases} \frac{4\pi e_0^2}{q^2 + k_s^2} & \text{3D with } k_s = \sqrt{\frac{4k_F}{a_0}} \\ \frac{2\pi e_0^2}{\sqrt{q^2 + k_s^2}} & \text{2D with } k_s = \frac{2}{a_0} \end{cases}$$

Not only the screening vector k_s depends on the dimensionality, but also the structure of the interaction potential $W(q)$. This fact determines the dependence of the scattering rates on the electron density n and is the reason for the different scaling laws with respect to ξ . In 3D, the inelastic scattering rate scales with ξ^2 , whereas the calculation of the 2D case results in $\xi^2 \ln \xi^{-1}$. This logarithmic correction can be understood as direct consequence of $W(q)$ in two dimensions.

3 Dimensional Electron Liquid

The result for the inelastic e-e scattering rate in 3D calculated in the random phase approximation (RPA) is given by

$$(C.5) \quad \Gamma_{\text{e-e}}^{(3D)} = \frac{1}{\tau_{\text{e-e}}^{(3D)}} = \frac{2\sqrt{2} m_e^3 e_0^4}{\pi (4\pi \epsilon_0)^2 \hbar^7 k_F k_s^3} \frac{\pi^2 k_B^2 T^2 + \xi^2}{1 + e^{-\xi/k_B T}} F^{(3D)}(\lambda) \quad .$$

The Fermi energy E_F and the Fermi vector k_F in 3D are determined by the electron density, see appendix B,

$$(C.6) \quad E_F = \frac{\hbar^2 k_F^2}{2m_e} \quad \text{with } k_F = (3\pi^2 n)^{1/3} \quad ,$$

where $n = n^{(3D)}$ is the 3D electron density. The Thomas-Fermi screening vector in 3D is given with

$$(C.7) \quad k_s = k_{\text{TF}}^{(3D)} = \left(\frac{3e_0^2 n}{\epsilon_0 E_F} \right)^{1/2} = \left(\frac{2 \cdot 3^{1/3} e_0^2 m_e}{\pi^{4/3} \epsilon_0 \hbar^2} \right)^{1/2} n^{1/6} \quad \text{and } \lambda = \frac{2k_F}{k_s}$$

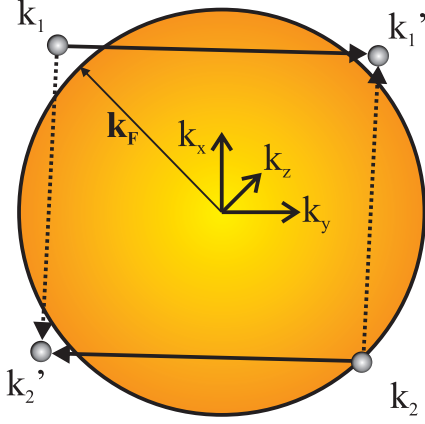


Figure C.2: Electron-electron scattering in 3D with direct (solid arrows) and exchange (dashed arrows) contribution. In 3D, only the direct term contributes to Γ_{e-e} and the scattering partners k_1 and k_1' are separated by $2k_F$ in phase space.

gives the ratio of Fermi to Thomas-Fermi vector. The $F(\lambda)$ function depends on the electron density via λ and summarizes the contributions for direct and indirect processes

$$(C.8) \quad F^{(3D)}(\lambda) = \underbrace{\frac{\lambda}{\lambda^2 + 1} + \tan^{-1} \lambda}_{\text{direct}} - \underbrace{\frac{1}{\sqrt{\lambda^2 + 2}} \left[\frac{\pi}{2} - \tan^{-1} \left(\frac{1}{\lambda} \frac{1}{\sqrt{\lambda^2 + 2}} \right) \right]}_{\text{exchange}}$$

For the case of high electron densities $r_s \rightarrow 0$ ($\lambda \rightarrow \infty$), which implies strong screening and justifies the weak coupling approximation a posteriori, the $F(\lambda)$ function becomes:

$$(C.9) \quad \lim_{\lambda \rightarrow \infty} F^{(3D)}(\lambda) = \frac{\pi}{2} \quad ,$$

which is determined only by the direct term (C.8). A typical scattering event in 3D is sketched in Fig. C.2 and involves two scattering partners that are separated by $2k_F$. Only the direct term (solid arrows) contributes to the leading order of Γ_{e-e} . Thus, in the limit of high electron densities, the exchange term can be neglected in 3D. For the experiments under discussion, the approximation of low temperatures $k_B T \ll \xi \ll E_F$ is well justified and leads to the famous result of Quinn and Ferrel [Qui58] with the $n^{-5/6} \xi^2$ scaling law

$$(C.10) \quad \Gamma_{e-e}^{(3D)} = \frac{1}{\tau_{e-e}^{(3D)}} = \frac{\sqrt{2} m_e^3 e_0^4}{\pi (4\pi\epsilon_0)^2 \hbar^7 k_F k_s^3} \xi^2 = \underbrace{\frac{e_0 m_e^{3/2}}{32 \cdot 3^{5/6} \pi^{2/3} \epsilon_0^{1/2} \hbar^4}}_{a^{(3D)}} n^{-5/6} \xi^2$$

Evaluating the constant prefactor $a^{(3D)}$ and converting the decay rate to the inelastic e-e lifetime yields τ_{e-e} , the expression that is compared to the two-photon photoemission (2PPE) data in chapter 5.4

$$(C.11) \quad \tau_{e-e}^{(3D)} [fs] = 499.164 n_{[10^{30} m^{-3}]}^{5/6} \xi_{[eV^2]}^{-2}$$

2 Dimensional Electron Liquid

The result for the inelastic e-e scattering rate in 2D for the case of low temperatures $k_B T \ll \xi \ll E_F$ is given by:

$$(C.12) \quad \Gamma_{e-e}^{(2D)} = \frac{1}{\tau_{e-e}^{(2D)}} = \frac{1}{4\pi\hbar E_F} \xi^2 \ln\left(\frac{2E_F}{\xi}\right) F^{(2D)}$$

The logarithmic correction to the ξ^2 scaling law in 3D was first derived by Chaplik [Cha71]. The Fermi energy and the Fermi vector in 2D are given by

$$(C.13) \quad E_F = \frac{\hbar^2 k_F^2}{2m_e} = \frac{\pi\hbar^2 n}{m_e} \quad \text{with} \quad k_F = (2\pi n)^{1/2} \quad ,$$

where $n = n^{(2D)}$ denotes the 2D electron density. The F -function summarizes the contributions from direct and "exchange" scattering

$$(C.14) \quad F^{(2D)} = \underbrace{4\overline{W}^2(0) + 2\overline{W}^2(2k_F)}_{\text{direct}} - \underbrace{\overline{W}^2(0) + 2\overline{W}(0)\overline{W}(2k_F)}_{\text{exchange}} \quad ,$$

where \overline{W} is the normalized [Qia06] screened Coulomb interaction in 2D. Evaluating the F -function for the limiting case of high electron densities $r_s \rightarrow 0$, respectively a weak e-e coupling, yields

$$(C.15) \quad \lim_{r_s \rightarrow 0} F^{(2D)} = 1 - \frac{1}{4} = \frac{3}{4} \quad .$$

The first term indicates the direct fraction and the second term the "exchange" fraction. The "exchange" term changes the absolute numerical result by 25% due to the properties of the 2D phase space and the screened Coulomb interaction. This fact demands more complicated calculations with explicit consideration of both contributions, which, however, has led to different results for the absolute value of the prefactor $a^{(2D)}$ in the theoretical literature [Cha71, Giu82, Qia05, Giu05]. For the comparison with experimental data, this work relies on the recent theoretical study of Qian et al. [Qia06, Giu05].

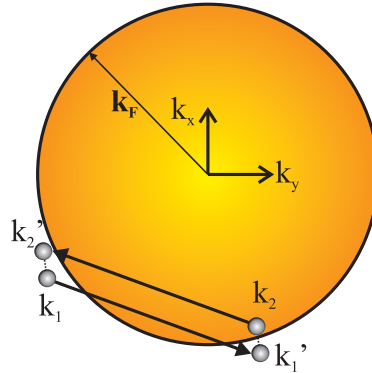


Figure C.3: Electron-electron scattering in 2D with direct (solid arrows) and exchange (dashed arrows) contribution. In 2D, also the "exchange" term contributes to Γ_{e-e} and the scattering partners \vec{k}_1 and \vec{k}_1 are much closer than $2k_F$ in phase space.

A typical e-e scattering process in 2D is indicated in Fig. C.3 and involves collisions that are close in phase space. This is in contrast to the 3D case, where the scattering partners are well separated in phase space and the "exchange" term does not contribute. The final result for the e-e scattering rate in 2D in the high-density low-temperature limit is:

$$(C.16) \quad \Gamma_{e-e}^{(2D)} = \frac{1}{\tau_{e-e}^{(2D)}} = \underbrace{\frac{3 m_e}{16\pi^2 \hbar^3} \ln \left(\frac{2\pi \hbar^2}{m_e} \right)}_{=a^{(2D)}} \frac{\xi^2}{n} \ln \left(\frac{n}{\xi} \right) .$$

Evaluation of the numerical constants leads to the expression, which is to be compared with the experimental data:

$$(C.17) \quad \tau_{e-e}^{(2D)} [fs] = 264.0 \frac{n_{[10^{20} m^{-2}]}}{\xi_{[eV^2]}^2 \ln \left(\frac{47.88 n_{[10^{20} m^{-2}]}}{\xi_{[eV]}} \right)}$$

The *GW* Approximation

The *GW* approximation employs the Greens function (*G*) formalism with the screened Coulomb interaction (*W*) to calculate the e-e scattering rate Γ_{e-e} [Ech00, Ech04, Pit04, Chu06a]. The reasoning is as follows: The quasi-particle energy is a complex quantity because the quasi-particle states are not eigen-states of the many-particle system. The imaginary part of the eigen-energy is a measure of energy and momentum transfer to the Fermi sea, where the scattering probability of two electrons is constrained by energy and momentum conservation, and the phase space. The *GW*-approximation projects the imaginary part of the eigen-energy onto the excited state and sums over the phase space of initial and final states. This allows to treat the band structure with, for example, surface states and orientation band gaps realistically.

In the *GW* approximation the e-e scattering rate Γ_{e-e} is expressed as projection of imaginary part of eigen-energy onto excited state wave function:

$$(C.18) \quad \Gamma_{e-e}(E_{k_1}) = -2 \int d\vec{r} \int d\vec{r}' \Psi_{k_1}^*(\vec{r}) \text{Im} \Sigma(\vec{r}, \vec{r}'; E_{k_1}) \Psi_{k_1}(\vec{r}')$$

The eigen-energy Σ is given by *W* and the phase space available for scattering

$$(C.19) \quad \text{Im} \Sigma(\vec{r}, \vec{r}'; E_{k_1}^-) = \sum_{\substack{E_{k_1}^- \geq E_{k_1}^-, \\ E_{k_1}^- \geq E_F}} \Psi_{k_1}^*(\vec{r}') \text{Im} W(\vec{r}, \vec{r}'; E_{\vec{q}}) \Psi_{k_1}(\vec{r}')$$

with $E_{\vec{q}} = E_{k_1}^- - E_{k_1}^-$ and the summation index ensures momentum conservation. The decay rate results in

$$(C.20) \quad \Gamma = -2 \sum_{E_{k_1}^-} \int d\vec{r} \int d\vec{r}' \Psi_{k_1}^*(\vec{r}) \Psi_{k_1}^*(\vec{r}') \text{Im} W(\vec{r}, \vec{r}'; E_{\vec{q}}) \Psi_{k_1}(\vec{r}') \Psi_{k_1}(\vec{r})$$

The screened Coulomb interaction *W* is given by the bare, unscreened Potential $v(\vec{r} - \vec{r}')$ and the Lindhard response function $\chi(\vec{r}_1, \vec{r}_2; E)$.

$$(C.21) \quad W(\vec{r}, \vec{r}'; E) = v(\vec{r} - \vec{r}') + \int d\vec{r}_1 \int d\vec{r}_2 v(\vec{r} - \vec{r}_1) \chi(\vec{r}_1, \vec{r}_2; E) v(\vec{r}_2 - \vec{r}')$$

D Optical Bloch Equations

The following quantum mechanical description of the two-photon photoemission process as 3-level system is based on discrete initial and intermediate states $|i\rangle$ and $|k\rangle$, respectively, which couple to a continuum of non-interacting final states $|f\rangle$.

Let $|i\rangle$, $|k\rangle$ and $|f\rangle$ be eigen-states of the unperturbed Hamilton Operator H_0 , then the time-dependent perturbing potential V , which couples the three states to each other, is given within the rotating wave approximation [Lou83] by

$$(D.1) \quad V(t, \tau) = \vec{\mu} \cdot \left(\vec{e}_1 A_1(t) e^{i\omega_1 t} + \vec{e}_2 A_2(t - \tau) e^{i\omega_2(t - \tau)} \right) \quad .$$

$\vec{\mu} = e\vec{r}$ is the dipole operator, \vec{e}_i are the polarization vectors of the two laser pulses with frequencies ω_i , A_i is the time-dependent envelope of the laser pulses, and τ denotes the pump-probe delay of the laser pulses.

The formulation of the quantum mechanical equations of motion is based on the phenomenological introduction of a dissipative term ρ_{diss} , which accounts for elastic and inelastic scattering processes that lead to dephasing and population decay, respectively. Within the density matrix formulation [CT99] follows:

$$(D.2) \quad \dot{\rho} = -\frac{i}{\hbar} [H_0 + V, \rho] + \dot{\rho}_{diss} \quad .$$

The diagonal elements of the density matrix ρ_{aa} resemble the population densities of the respective states, whereas the off-diagonal elements ρ_{ab} describe the coupling of the states to each other, where a and b denote the states i , k and f . The transition from the Schrödinger to the Dirac formulation

$$(D.3) \quad \tilde{\rho}_{ab} = \rho_{ab} e^{i(\omega_a - \omega_b)t} \quad V_{ab} = \frac{1}{\hbar} \langle a | V | b \rangle e^{i(\omega_a - \omega_b)t}$$

results in the optical Bloch equations [Lou83]

$$(D.4) \quad \dot{\tilde{\rho}}_{ab} = -i \sum_j V_{aj} \tilde{\rho}_{jb} + i \sum_j V_{jb} \tilde{\rho}_{aj} + (\dot{\tilde{\rho}}_{diss})_{ab} \quad .$$

The dissipative terms $(\tilde{\rho}_{diss})_{ab}$ are treated phenomenologically by (i) population decay due to inelastic scattering processes with an energy relaxation rate Γ_a and (ii) dephasing of the coherent polarization due to elastic scattering processes summarized by a dephasing rate Γ_{ab}^* . As seen in diagonal elements $\tilde{\rho}_{ik}$ and $\tilde{\rho}_{kf}$ in equation (D.5), the energy relaxation rate contributes with half its rate to the dephasing. To solve (D.4), an infinite lifetime of the final states is assumed and direct transitions from the initial to the final state are forbidden. Explicitly, for a 3-level system this results in a set of nine coupled differential equations:

$$\begin{aligned}
\text{(D.5)} \quad \dot{\tilde{\rho}}_{ii} &= iV_{ki}\tilde{\rho}_{ik} + cc. + \Gamma_k\tilde{\rho}_{kk} \\
\dot{\tilde{\rho}}_{ik} &= iV_{ik}(\tilde{\rho}_{ii} - \tilde{\rho}_{kk}) + iV_{fk}\tilde{\rho}_{if} - (\Gamma_{ik}^* + \frac{1}{2}\Gamma_k)\tilde{\rho}_{ik} \\
\dot{\tilde{\rho}}_{if} &= -iV_{ik}\tilde{\rho}_{kf} + iV_{kf}\tilde{\rho}_{ik} - \Gamma_{if}^*\tilde{\rho}_{if} \\
\dot{\tilde{\rho}}_{kk} &= (-iV_{ki}\tilde{\rho}_{ik} + iV_{fk}\tilde{\rho}_{kf}) + cc. - \Gamma_k\tilde{\rho}_{kk} \\
\dot{\tilde{\rho}}_{kf} &= iV_{kf}(\tilde{\rho}_{kk} - \tilde{\rho}_{ff}) - iV_{ki}\tilde{\rho}_{if} - (\Gamma_{kf}^* + \frac{1}{2}\Gamma_k)\tilde{\rho}_{kf} \\
\dot{\tilde{\rho}}_{ff} &= iV_{fk}\tilde{\rho}_{kf} + cc.
\end{aligned}$$

The three missing equations for the remaining off-diagonal elements are determined by the relation $\tilde{\rho}_{ab} = \tilde{\rho}_{ba}^*$. This equation set is used to simulate two-photon photoemission (2PPE) spectra by assuming a single occupied initial state and integration over the duration of excitation. The population in the final state then is proportional to the 2PPE signal. The pump-probe delay τ is included in the perturbation matrix elements V_{ab} .

The limiting case of a totally non-resonant excitation, which corresponds to vanishing off-diagonal elements in the density matrix, leads to a set of three classical coupled rate equations [Lou83], as discussed in chapter 2.4.6

$$\begin{aligned}
\text{(D.6)} \quad \dot{\rho}_{ii} &= -|V_{ik}(t, \tau)|^2 \rho_i + \Gamma_1 \rho_{kk} \\
\dot{\rho}_{kk} &= |V_{ik}(t, \tau)|^2 \rho_{ii} - |V_{kf}(t, \tau)|^2 \rho_{kk} - \Gamma_1 \rho_{kk} \\
\dot{\rho}_{ff} &= |V_{kf}(t, \tau)|^2 \rho_{kk} .
\end{aligned}$$

If the excitation mechanism is unclear, the classical rate equations give a lower limit of decay rates.

A detailed discussion of the two-photon photoemission process within the framework of the optical Bloch equations is given in [Wol99]. Wolf et al. also elucidate the polarization dependence of the 2PPE signal and give an analytical solution for the quantum mechanical equations (D.5).

E Generation and Amplification of fs-Laser Pulses

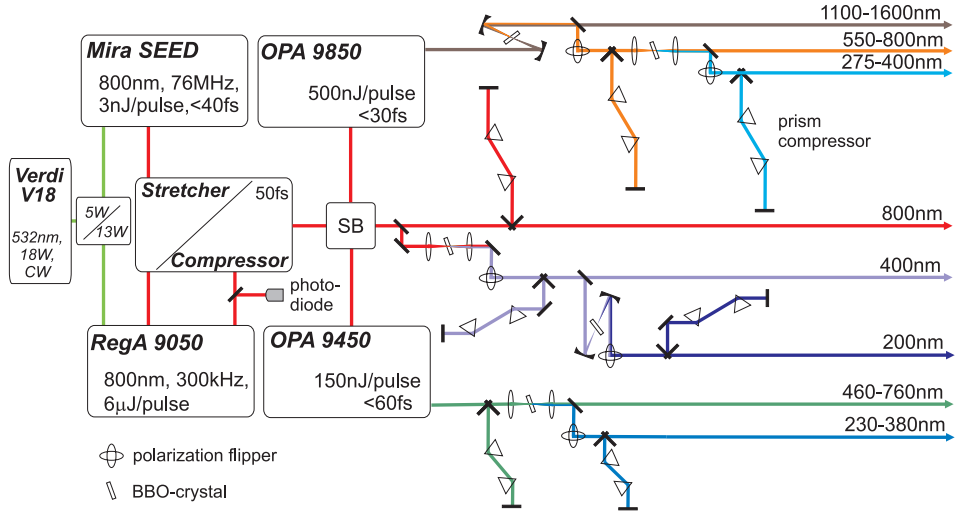


Figure E.1: Optical path of the femtosecond laser system. All components, which do not contribute to the pulse generation (mirrors, pin-holes, etc.), are omitted. A 18 W Verdi cw-laser (V-18) [Coh07] pumps the Mira seed oscillator [Coh93] and a RegA [Coh97]. The RegA pulses can drive two OPAs [Coh94] or alternatively supply the tr-ARPES optical path.

Mira 900-B Oscillator

The Mira 900-B seed oscillator [Coh93] is the starting point for the generation of ultrashort femtosecond laser pulses. The active laser material is a Titanium-doped Sapphire crystal (Ti:Sa with 0.1% Ti^{3+} in Al_2O_3). The long-lived ($\sim 3.3 \mu s$, [Mou92]) and spectrally broad vibronic fluorescence band (650 – 1130 nm [Mou86]) with a maximum at ~ 790 nm makes Ti:Sa an ideal material for the generation of intense ultrashort laser pulses. Also, the high damage threshold, the good heat conductivity and the high energy storage capacity [Dem03, Koe96] are important application aspects. The long-lived higher lying levels can very efficiently be pumped via a spectrally fully separated absorption band at 490 nm, see Fig. E.2. The Mira oscillator is pumped at 532 nm with 4 – 5 W continuous wave (cw)-power from a Verdi V-18 [Coh07]. The V-18 is a diode-pumped, frequency-doubled Nd:YVO₄ solid-state laser, which serves as global laser pump source and also supplies the regenerative amplifier E.

The femtosecond laser pulses are generated in a cavity, in which all the longitudinal resonator modes have a fixed phase relation and interfere constructively at one point. This mode-locking in the frequency domain builds up an ultrashort pulse in the time

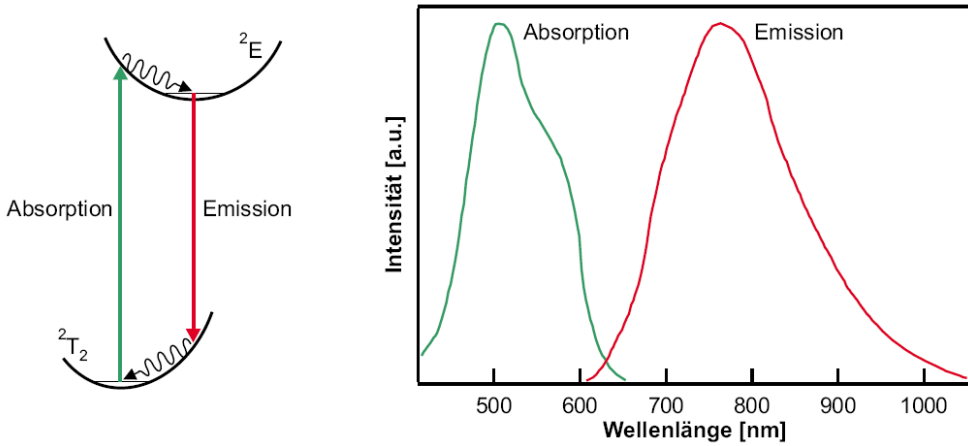


Figure E.2: Spectroscopic properties of Ti:Sa [Den99]. Left: Schematic energy levels of Ti^{3+} , which substitutes Al^{3+} in the sapphire. Right: Absorption- and emission spectra [Mou86] are broadened due to strong vibronic coupling of the energy levels.

domain. The time-bandwidth product for typical laser pulse shapes is given by

$$(E.1) \quad \Delta\nu \Delta t = \text{const} = \begin{cases} \frac{2 \ln 2}{\pi} & = 0.4413 \text{ Gaussian pulse shape} \\ \frac{2}{\pi^2} \text{sech}^{-1}\left(\frac{1}{\sqrt{2}}\right) & = 0.3148 \text{ sech}^2 \text{ pulse shape.} \end{cases}$$

Here, $\Delta\nu$ and Δt are the full width at half maximum (FWHM) of the laser spectrum and the pulse duration.

In order to achieve mode-locking, the non-linear intensity-dependence of the re-

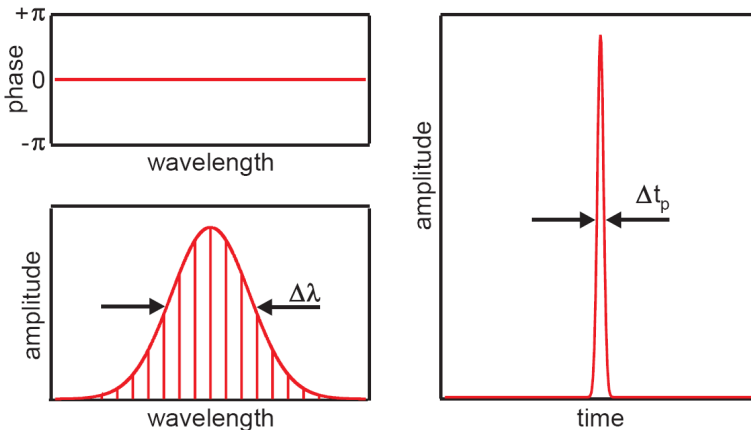
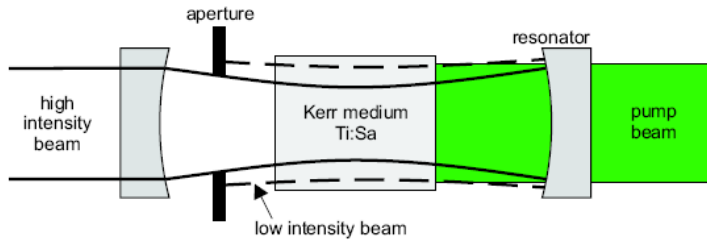


Figure E.3: Laser spectrum and amplitude for ideal coupling of the laser modes. The Gaussian spectral intensity and the flat phase in the frequency domain result in an ultrashort Gaussian pulse in the time domain, as time- and frequency-domain are connected via the Fourier transformation. Taken from [Den99].

(a) hard aperture mode locking



(b) soft aperture mode locking

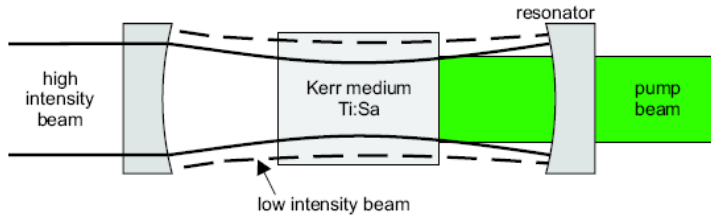


Figure E.4: Kerr-lens mode-locking. Short pulses of high intensity are generated by an intensity dependent amplitude modulation of the resonator mode. The self-focusing of the high intensity beam in the Kerr medium reduces the optical losses at the aperture (a) or leads to a better overlap of laser and pump beam (b). This favors short pulses until an equilibrium of pulse shortening and lengthening due to dispersion and gain narrowing of the laser medium is reached. Taken from [Wag06].

refractive index due to the optical Kerr-effect

$$(E.2) \quad n(\omega, I) = n_0(\omega) + n_2(\omega)I$$

is exploited in the so-called Kerr-lens mode-locking. The spatial variation of the laser intensity within the beam profile leads to a variation of the refractive index, such that the Kerr medium acts as a lens and focuses the beam according to the laser intensity. In Fig. E.4, so-called hard aperture mode-locking, where a solid aperture is set, and soft aperture mode-locking is shown. Usually, fs-oscillators employ soft aperture mode-locking, where the aperture is defined by the focus of the pump beam.

The theoretically achievable bandwidth of 100 nm for the Mira oscillator is reduced by spectral filtering to 30 nm bandwidth, which can efficiently be amplified in the regenerative amplifier (RegA). This enables to tune the central wavelength of the oscillator in the range from 750 to 850 nm. The Mira achieves a pulse energy of ~ 3 nJ at 800 nm central wave length and a repetition rate of 76 MHz of which 50% are coupled into the RegA and the other 50% intensity can drive oscillator based optical experiments.

RegA 9050 Regenerative Amplifier

The pulse energies required for higher order non-linear processes such as difference frequency generation (DFG), sum frequency generation (SFG) and second harmonic generation (SHG) are of the order of μJ , which can not be delivered by the oscillator. Thus, the oscillator pulses have to be amplified by three orders of magnitude, which is realized by the regenerative amplifier (RegA).

First, the oscillator pulses are stretched to a few 10 ps length in a so-called Stretcher to avoid damage of the Ti:Sa crystal inside the RegA and deterioration of the spatial beam profile. Second, the pulses are amplified in the Ti:Sa crystal of the RegA. Finally the spectral components are re-compressed to obtain a short pulse [Mar87]. Stretching and compression is achieved with a grating which separates the temporal components of the beam in space. This results in a so-called chirped beam with variable central frequency (color), which gives rise to the name chirped pulse amplification (CPA). The Ti:Sa crystal in the RegA is pumped by 12 W cw-power from a Verdi V-18 [Coh07] solid state laser. Initially, the quality of the laser cavity is reduced by an opto-acoustic modulator (Q-switch) to suppress spontaneous laser emission and induce a high population inversion in the Ti:Sa crystal. The cavity quality is increased after 3 μs and a single seed pulse from the oscillator is coupled in via a second opto-acoustic modulator (cavity-dumper), which then is amplified in 20-30 round trips in the cavity. Finally, the cavity-dumper refracts the amplified pulse out of the cavity, which is isolated from the oscillator cavity by a Faraday-isolator. Then the quality of the cavity is reduced again such that the gain medium can regenerate the population inversion. The synchronization of the in- and out-coupling of the pulses is handled by an external electronic circuit, which is controlled by fast photo diodes in the RegA.

With the V-18 Verdi pump laser source ¹ it is possible to pump the RegA with 12 W instead of the specified 10 W cw power and achieve 6 μJ pulse energy at 300 kHz repetition rate, which is equivalent to 1.8 W cw power. This presents an increase of 80% in cw power compared to the initial RegA setup [Gah04]. The RegA output is distributed to the optical parametric amplifiers (OPAs) for the two-photon photoemission (2PPE) experiments or the optical path for the time- and angle-resolved photoemission spectroscopy (tr-ARPES) experiments in a so-called switch box (SB), which is equipped with high reflection dichroic mirrors and dichroic beam splitters.

Optical Parametric Amplifier (OPA)

The tunability of the laser system from the infrared (IR) to the ultraviolet (UV) spectral regime is a crucial prerequisite to either selectively excite certain (resonant) optical transitions or to deliberately avoid such resonant excitations. To obtain tun-

¹The V-18 Verdi laser replaced a 5 W V-5 Verdi laser for pumping the Mira oscillator and a 10 W V-10 Verdi laser for pumping the RegA amplifier in January 2007. The V-18 runs at 16 – 17 W output power, which significantly enhances the lifetime of the IR pump diodes. The V-18 output is continuously split between Mira and RegA. Currently, the Mira is pumped with 4 W and the RegA with 12 – 13 W.

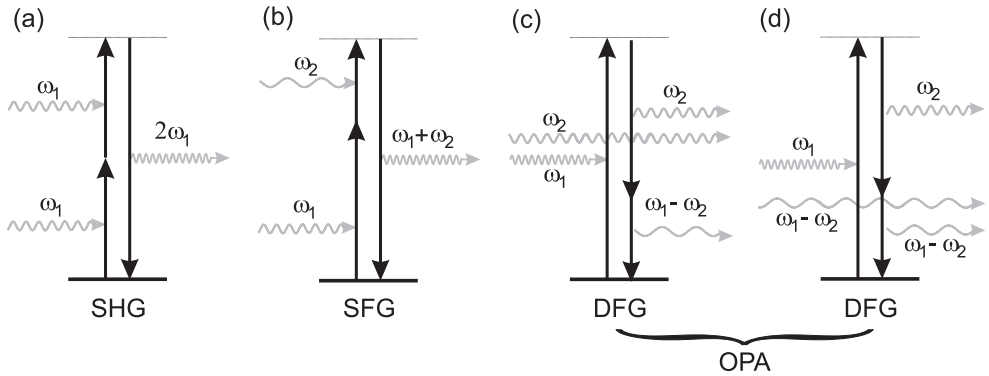


Figure E.5: Second order non-linear optical processes sketched in the frequency domain as virtual electron transitions with consideration of energy conversion. (a) Second harmonic generation (SHG), (b) Sum frequency generation (SFG), (c) & (d) Difference frequency generation (DFG). The OPA takes advantage of the mutual enhancement of processes (c) and (d).

able visible (VIS) and UV pulses the non-linear optical properties of matter at high electric field strength are utilized in an optical parametric amplifier (OPA).

The electric susceptibility becomes a function of the electric field strength $\chi = \chi(E)$ when the laser pulse intensity approaches the order of magnitude of local crystal fields. Thus, higher-order terms have to be considered in the macroscopic polarization $P(E)$ of an idealized loss-less medium:

$$(E.3) \quad P(t) = \varepsilon_0 \chi^{(1)} E(t) + \varepsilon_0 \chi^{(2)} E^2(t) + \varepsilon_0 \chi^{(3)} E^3(t) + \dots$$

$\chi^{(n)}$ defines the non-linear susceptibility of n -th order, which generally is given by a tensor of rank $(n + 1)$. Hence, irradiation of a non-linear crystal with light of two frequencies ω_1 and ω_2

$$(E.4) \quad \vec{E}(t) = \text{Re} \left\{ \vec{E}_1 e^{-i\omega_1 t} + \vec{E}_2 e^{-i\omega_2 t} \right\}$$

creates polarization components at the sum frequency ($\omega_1 + \omega_2$) and the difference frequency ($\omega_1 - \omega_2$) (Fig. E.5). However, macroscopic emission of light is only achieved when the microscopic light wave are in phase and interfere constructively. This corresponds to the conservation of photon momentum in the DFG and SFG processes:

$$(E.5) \quad \vec{k}(\omega_1 \pm \omega_2) = \vec{k}(\omega_1) \pm \vec{k}(\omega_2)$$

This phase-matching condition can be fulfilled in birefringent crystals by variation of the angle of incidence with respect to the crystal axes. Uniaxial β -barium-borate (BBO) crystals are used for the subsequent frequency-doubling and quadrupling (see Fig. E.1). The thickness of the BBO is limited by the group velocity dispersion (GVD), as a thicker crystal converts more light, but also introduces more dispersion to the beam and can reduce the bandwidth of the resulting pulse.

The OPA process exploits DFG to convert one photon (ω_1) with another photon of the seed pulse (ω_2) into two photons $\omega_3 = \omega_1 - \omega_2$ and ω_2 , Fig. E.5(c). The larger frequency is termed signal, the smaller frequency is called idler. Practically, this is realized by splitting the incoming RegA pulse in 50% pump and 50% seed power. The latter is focused into a sapphire crystal, where self-phase modulation creates so-called whitelight [Alf70]. The high field intensities modulate the light phase according to eq. (E.2)

$$(E.6) \quad \phi(t) = \omega \left(t - \frac{z n_0}{c} \right) - \underbrace{\frac{\omega z n_2}{c} I(t)}_{\text{non-linear contribution}}$$

and leads to a temporally and spectrally broadened whitelight continuum.

The difference frequencies ω_2 and ω_3 are chosen out of the whitelight continuum by the temporal delay of both pulses as well as the phase-matching angle in two passes of the spatially overlapping pump and seed beams. The photons created in the DFG process drive the complementary DFG process further, as sketched in Fig. E.5 (c) and (d), resulting in a quasi-exponential increase of intensity with crystal thickness.

In the visible optical parametric amplifier (VIS-OPA) a second BBO crystal is used to frequency-double the 800 nm RegA beam to 400 nm and use the second harmonic as pump beam. This leads to operation in the VIS at 460 – 760 nm for the signal beam. In the infrared optical parametric amplifier (IR-OPA) the 800 nm RegA pulses are directly used for the pump beam such that the signal output is in the IR 1100 – 1600 nm. The IR-OPA offers a large bandwidth of up to 100 nm, which is determined by the temporal overlap and phase-matching of the pump and the whitelight beam. Thus 30 fs pulse duration are achievable due to the decreased dispersion of the optical elements in the IR.

Optical Path for 2PPE

The optical path of the OPAs, as shown in Fig. E.1, consists of several prism compressors [For94], which compensate for the GVD of the optical elements like beam splitters, mirrors and lenses. The GVD compression allows to minimize the pulse duration at a certain position in the optical path, like a non-linear crystal for SHG or the sample position in the ultrahigh vacuum (UHV) chamber and ideally results in time-bandwidth limited laser pulses.

The output of the VIS-OPA is compressed in a prism compressor, focused by a lens into a BBO crystal to generate SHG light and recollimated by a second lens. A dichroic beam splitter separates the fundamental from the second harmonic, which is sent to a periscope to flip the polarization back² from s to p. This is due to the SHG process of type I which rotates the polarization axes in uni-axial crystals by 90° [Dem03]. The SHG light is then re-compressed in another prism compressor and sent to the UHV chamber.

²The light polarization in the experiments is chosen to be parallel with the plane of incidence and thus termed p.

The output of the IR-OPA is directly frequency doubled in a BBO crystal, sent through a prism compressor, frequency doubled and compressed a second time to obtain VIS and UV pulses as well.

Optical Path for tr-ARPES

Compared to the optical path for the 2PPE experiments, the optical path for tr-ARPES is simpler, see Fig. E.1, and consists of two subsequent non-linear processes of frequency doubling and quadrupling the RegA output in BBO crystals [Kat86, Joo91, Kou99]. However, the phase matching angle of BBO diverges at $h\nu \leq 205$ nm [Kat86]. The resulting chirp of third or higher order can not be easily compensated with prism compressors and may stretch the pulse duration significantly. To obtain the best temporal resolution, the fundamental seed wavelength from the Mira oscillator is tuned to higher wavelength of 820 – 830 nm, which requires the re-alignment of the RegA and the stretcher/compressor unit as well.

The first doubling crystal for the SHG process $820 \rightarrow 410$ nm is $500 \mu\text{m}$ thick and cut at $\Theta = 29.2^\circ$ phase matching angle. The BBO crystals have a anti-reflex coating that helps to protect the hygroscopic BBO crystals from the ambient humidity. The remains of the fundamental are separated by a dichroic mirror and the polarization of the SHG signal is flipped back to p in a periscope setup. The 410 nm pulses are recompressed in a fused silica GVD compressor and focused via a 200 mm focal length spherical mirror to minimize the chirp and chromatic aberration.

The second doubling crystal (from GVU) is especially designed for the fourth harmonic generation $410 \rightarrow 205$ nm with $50 \mu\text{m}$ thickness and $\Theta = 76.3^\circ$ phase matching angle. The thin crystal minimizes the dispersion and hence the higher order chirp. After flipping back the polarization to p, the intense 410 nm pulses are blocked in the dispersive section of the 205 nm prism compressor. The 205 nm probe beam is coupled directly into the chamber and the IR pump pulses are delayed via the optical delay stage.

In the 2PPE experiments, the prism compressors are easily aligned by maximizing a second order photoemission signal directly on the sample. For the alignment of the 205 nm compressor no higher order signal can be employed and thus the pulses can only be shortened once the temporal and spatial overlap has already been found. To find the tr-ARPES signal, however, is not straightforward as long as the 205 nm are not shortened. The overall efficiency of the fourth harmonic generation is of the order of 10^{-4} , which results in a photon flux in the order of 10^{13} photons/s in bandwidth window of ~ 7 meV width. This is comparable with the photon flux (not necessarily the brightness) of third generation synchrotron undulator light sources [Kor06]. Anyhow, the speed of data acquisition is not limited by the available photon flux, but by space charging effects, see chapter 2.4.3.

F Parameters for the pTOF-Software

This appendix describes the parameters of the pTOF-software, which are implemented in the `cEvent` C++ class. This list is part of the documentation of the TOF-software.

The parameters may be transferred either directly to the LabView front end or to the command line tool via a configuration file. The parameters are structured into four groups according as outlined in the following

kinetic Parameters

The `kinetic` parameter set contains all values for (i) the conversion of the raw timing information from the layer ends and the MCPs to the position and TOF coordinates, and (ii) the transformation of the real space coordinates to the reciprocal space. The `kinetic` parameters mostly comprise calibration values and hence are changed rarely once the system has been calibrated.

Parameter	Description	Unit
CalU CalV CalW	The signal propagation speeds v_{\perp} perpendicular to meandering anode wire structure	mm/ns
LayerOffsetW	Shift of the origin of the W-layer relative to the central crossing point of the U- and V-layer ¹	mm
dCenterX dCenterY	Shift of the crossing point of the three layers relative to the anode center	mm
InPlaneRotationAngle	Ψ -rotation along the high-symmetry axis in the sample plane relative to the spectrometer coordinate system (see Fig. 4.11)	Grad
SampleRotationAngle	ϕ -rotation of the manipulator relative to the spectrometer	Grad
SampleTiltAngle	Θ -tilt of the sample	Grad
zTOF	Length of the drift tube	mm
tLaser	Duration of one laser cycle, corresponding to the inverse laser repetition rate	ns
tOP	Time difference of the photodiode signal to the actual photoemission event (t_0)	ns

¹The shift of the W-layer is arbitrary and the other two layers could be shifted as well.

binning Parameters

The binning parameter determine the size of the data storage volumes. For each dimension the parameters **SmBin**, **LgBin** and **BinWidth** define the smallest bin, the largest bin and the binwidth. The following dimension are supported:

Parameters	Description	Unit
SmBinX LgBinX BinWidthX	x-coordinate	mm
SmBinY LgBinY BinWidthY	y-coordinate	mm
SmBinT LgBinT BinWidthT	Time-of-flight	mm
SmBinKX LgBinKX BinWidthKX	k_x -momentum	\AA^{-1}
SmBinKY LgBinKY BinWidthKY	k_y -momentum	\AA^{-1}
SmBinE LgBinE BinWidthE	Kinetic electron energy	eV
SmBinSums LgBinSums BinWidthSums	time-sums	ns
SmBinRaw LgBinRaw BinWidthRaw	Raw layer coordinates	ns
SmBinCorX LgBinCorX BinWidthCorX	x-coordinate of the correlation function	mm
SmBinCorY LgBinCorY BinWidthCorY	y-coordinate of the correlation function	mm
SmBinCorT LgBinCorT BinWidthCorT	Time-of-flight coordinate of the correlation function	ns

gating Parameters

The gating parameters supply several criteria for the evaluation of the hits:

Parameters	Description	Unit
HitMode	maximum number of hits per event	1-3
GatingFlag	Criteria for the evaluation of hits: 0 No Criterion 1 Time-sum gating 2 Radial gating 3 Radial and time-sum gating	0-3
MinSumU, MaxSumU MinSumV, MaxSumV MinSumW, MaxSumW	Minimal and maximal time-sum of valid hits	ns
MaxRadius	maximal MCP radius for valid hits	mm

Additionally, the following parameters define the integration boundaries for the slicing of the data volumes

Parameters	Description	Unit
MinX, MaxX	Integration boundaries along the x -coordinate	mm
MinY, MaxY	Integration boundaries along the y -coordinate	mm
MinT, MaxT	Integration boundaries along the time-of-flight axis	ns
MinKX, MaxKX	Integration boundaries along the k_x -coordinate	\AA^{-1}
MinKY, MaxKY	Integration boundary along the k_y -coordinate	\AA^{-1}
MinE, MaxE	Integration boundaries along the energy axis	eV
MinCorX, MaxCorX	Integration boundaries of the x -correlation coordinates	mm
MinCorY, MaxCorY	Integration boundaries of the y -correlation coordinates	mm
MinCorT, MaxCorT	Integration boundaries of the time-of-flight correlation coordinate	ns

advanced Parameters

The advanced parameters supply information for the advanced multihit hit reconstruction routine `resort64.dll`. These parameters can be regraded as extended Hexanode calibration values that are unique for each Hexanode.

Parameters	Description	Unit
<code>Use_Adv_Multihit</code>	Toggles the use of the advanced reconstruction routine	0/1
<code>DeltaSumU</code> <code>DeltaSumV</code> <code>DeltaSumW</code>	Shift of the time-sum signals with respect to the MCP signal	ns
<code>BaseWidthSumU</code> <code>BaseWidthSumV</code> <code>BaseWidthSumW</code>	Width of the time-sums	ns
<code>MaxRunTime</code>	largest propagation time on the anode layers	ns
<code>ActiveMCPradius</code>	Radius of the active MCP area	mm
<code>HP8TDCdeadtime</code>	Electronic dead time of the HP8TDC hardware	ns
<code>MCPdeadtime</code>	Electronic dead time of the MCP channel	ns
<code>GateLower</code> , <code>GateUpper</code>	lowest and highest reconstruction method to use ²	0-19
<code>USumUFile</code> <code>USumVFile</code> <code>USumWFile</code>	Path to the files containing the position-dependent time-sum correction	-

²The advanced reconstruction methods are described in detail in [Roe06]. The methods no. 0-13 are conservative and use only redundant information. The methods no. 14-19 are speculative as no redundant information from the Hexanode is available for crosschecks.

G Experimental Equipment

The following list summarizes the equipment for the two-photon photoemission and time- and angle-resolved photoemission spectroscopy experiments. Standard tools and simple custom devices are not listed.

Optical Setup

- Pump laser I: Coherent Verdi V5, Vanadate solid state diode laser [Coh99a]
- Pump laser II: Coherent Verdi V10, Vanadate solid state diode laser [Coh99b]
- Pump laser III: Coherent Verdi V18, Vanadate solid state diode laser [Coh07]
- Ti:Sa oscillator: Coherent MIRA Seed BRF [Coh93]
- Regenerative amplifier: Coherent RegA 9050 [Coh97]
- Stretcher/Compressor unit: Coherent EC 9150
- Optical-parametric amplifier 760 – 460 nm: Coherent OPA 9450
- Optical-parametric amplifier 1050 – 1600 nm: Coherent, OPA 9850
- Optical delay stage: Physik Instrumente PI-M505-4DG
- Auto-correlator I: APE Berlin 5050 Basic
- Auto correlator II: Swamp Optics Grenouille FROG device [Tre07]
- Power meter: Melles-Griot 13PEM001/J
- Beam profile camera: The Imaging Source DMK 21F04, 640×480 pixel, 8 Bit
- IR spectrometer: APE Berlin Wavescan
- VIS monochromator: B&M
- VIS spectrometer: Hamamatsu diode C4350
- UV spectrometer: LOT-Oriel MS 260i ANDOR-CCD detector
- Opto-mechanical components & optical elements: CVI Laser Optics, Layertec, Laser Components, Linos, New Focus, Newport, Spindler&Hoyer, Standa, Thorlabs

UHV Setup

- UHV chamber and manipulator: Vakuum-Anlagen-Bau (VAB), (no. 1.4335)
- Liquid Helium cryostat: CryoVac KONTI
- Turbo-molecular drag-pump (preparation level): Pfeiffer TMU 521UP, 500 l/s
- Drag pump (pre-pump): Balzers TPD 020, 15 l/s
- Membrane pump (pre-pump): Balzers TPC 015, 1 l/s
- Ion getter pump (spectrometer level): Riber PEG 2000 S
- Titanium sublimation pump (spectrometer level): Riber model 304
- Turbo-molecular pump (magazine): Pfeiffer TPD 240, 240 l/s
- Ionization gauge: Varian UHV-24 MultiGauge-Controller
- Pirani pressure gauge: Balzers TPR 010
- Quadrupole mass spectrometer: MKS Instruments, Spectra Satellite LM61
- Quartz balance: Inficon Deposition Monitor XTM/2
- IR pyrometer: Impac IS 5, 800 – 2500 C° and 650 – 1800 C°
- Conventional TOF spectrometer: Fritz-Haber Institut der MPG, Berlin
- Auger electron gun: Vacuum Generators LEG 63
- Auger electron analyzer: Vacuum Generators CLAM 2
- LEED optic: Specs, Berlin, ErLEED 150, 3 grid optic with 100 mm travel
- Sputter gun: Specs, Berlin
- Leak valve: Varian Variable Leak Valve 951-5106

- Knudsen cell: Fritz-Haber Institut der Max-Planck-Gesellschaft, Berlin
- PID controller: WEST Instruments 6100+
- Power supply for Si heating: EPS Germany EPA-250-16A
- Electronic ice-point: Newport Omega MCJ-C and MCJ-K
- Optical microscope: Spindler&Hoyer
- Microscope camera I: The Imaging Source DMK 21F04, 640×480 pixel, 8bit
- Microscope camera II: The Imaging Source DBK 21AF04, 640 × 480 pixel, 4×8bit

Data Acquisition

- Workstation: Dual-processor Pentium III 1.27 GHz, 1.75GB RAM
- Multifunction data acquisition card: National Instruments PCI-16MIOE-1
- Software: NI-Labview 6.1, NI-DAQ 6.1.1, NI-488.2M
- DC-motor controller, Physik Instrumente, C-844

The equipment for the conventional TOF spectrometer

- Ortec Fast-Timing preamplifier model VT 120 (stop pulses)
- Ortec pico-timing discriminator model 9307 (stop pulses)
- Ortec 100 MHz Discriminator, model 436 (start pulses)
- FAST ComTec time-to-digital converter p7887, 250 ps
- Ortec modular system bin, model 4001C
- Ortec Log/Lin rate meter, model 449

Position-Sensitive TOF Spectrometer

pTOF UHV Setup

- MCPs and position-sensitive anode: RoentDek 80 mm Hexanode
- HV feedthroughs: RoentDek and Vacom
- Housing and drift tube: Freie Universität Berlin
- μ -metal shielding: SAM Products
- Translation stage: Mc Allister BLT45-8 DN-150

pTOF Data Acquisition

- Workstation: Dual AMD Opteron processor 246, 64bit, 2.00 GHz, 2.00 GB RAM
- Multifunction data acquisition card: National Instruments, PCI-6251, DAQmx
- 2 dual channel HV supplies: iseg 2 × 4 kV, 3 mA
- 8 channel fast preamplifier & constant fraction discriminator: RoentDek ART19
- 8 channel time-to-digital converter: RoentDek HP8TDC 25 ps
- Software: Customized C++ classes with NI-Labview and Igor Pro front-ends

Bibliography

- [Aba01] L. Aballe, C. Rogero, P. Kratzer, S. Gokhale, & K. Horn. *Probing Interface Electronic Structure with Overlayer Quantum-Well Resonances: Al/Si(111)*. Physical Review Letters **87**, 15, 156801 (2001). DOI: 10.1103/PhysRevLett.87.156801. 146
- [Abu95] and Abukawa. *Surface Electronic Structure of a Single-Domain Si(111) 4×1 -In Surface: A Synchrotron Radiation Photoemission Study*. Surface Science **325**, 33 (1995). DOI: 10.1016/0039-6028(94)00693-8. 186, 187
- [Aes00] M. Aeschlimann, M. Bauer, S. Pawlik, R. Knorren, G. Bouzerar, & K. H. Bennemann. *Transport and dynamics of optically excited electrons in metals*. Applied Physics A **71**, 5, 485 (2000). DOI: 10.1007/s003390000704. 35, 146
- [Ahn04] J. R. Ahn, J. H. Byun, H. Koh, E. Rotenberg, S. D. Kevan, & H. W. Yeom. *Mechanism of Gap Opening in a Triple-Band Peierls System: In Atomic Wires on Si*. Physical Review Letters **93**, 106401 (2004). DOI: 10.1103/PhysRevLett.93.106401. 186
- [Alf70] R. R. Alfano & S. L. Shapiro. *Observation of Self-Phase Modulation and Small-Scale Filaments in Crystals and Glasses*. Physical Review Letters **24**, 592 (1970). DOI: 10.1103/PhysRevLett.24.592. 244
- [And65] J. R. Anderson & A. V. Gold. *Fermi Surface, Pseudopotential Coefficients, and Spin-Orbit Coupling in Lead*. Physical Review **139**, 5A, A1459 (1965). DOI: 10.1103/PhysRev.139.A1459. 13
- [Ani74] S. I. Anisimov, B. L. Kapeliovich, & T. L. Perelman. *Electron Emission from Metal Surfaces Exposed to Ultrashort Laser Pulses*. Soviet Physics JETP-USSR **39**, 375 (1974). 54, 86, 173
- [Ash76] N. W. Ashcroft & N. D. Mermin. *Solid State Physics*. Thomson Learning (1976). 8, 78
- [Bac76] C. E. Backus. *Solar Cells*. IEE Press Selected Reprint Series (1976). 13
- [Bar57a] J. Bardeen, L. N. Cooper, & J. R. Schrieffer. *Microscopic Theory of Superconductivity*. Physical Review **106**, 1, 162 (1957). DOI: 10.1103/PhysRev.106.162. 23
- [Bar57b] J. Bardeen, L. N. Cooper, & J. R. Schrieffer. *Theory of Superconductivity*. Physical Review **108**, 5, 1175 (1957). DOI: 10.1103/PhysRev.108.1175. 23
- [Bar96] R. A. Bartynski, E. Jensen, S. L. Hulbert, & C.-C. Kao. *Auger Photoelectron Coincidence Spectroscopy Using Synchrotron Radiation*. Progress in Surface Science **51**, 155 (1996). DOI: 10.1016/S0079-6816(96)00012-3. 114
- [Bar04] M. Bargheer, N. Zhavoronkov, Y. Gritsai, J. C. Woo, D. S. Kim, M. Woerner, & T. Elsaesser. *Coherent Atomic Motions in a Nanostructure Studied by Femtosecond X-ray Diffraction*. Science **306**, 1771 (2004). DOI: 10.1126/science.1104739. 180
- [Bar05] J. V. Barth, G. Costantini, & K. Kern. *Engineering Atomic and Molecular Nanostructures at Surfaces*. Nature **437**, 671 (2005). DOI: doi:10.1038/nature04166. 1
- [Bar06] I. Barke, Fan Zheng, A. R. Konicek, R. C. Hatch, & F. J. Himpsel. *Electron-Phonon Interaction at the Si(111)- 7×7 Surface*. Physical Review Letters **96**, 21, 216801 (2006). DOI: 10.1103/PhysRevLett.96.216801. 130
- [Bau99] M. Bauer, S. Pawlik, & M. Aeschlimann. *Decay dynamics of photoexcited alkali chemisorbates: Real-time investigations in the femtosecond regime*. Physical Review B **60**, 7, 5016 (1999). DOI: 10.1103/PhysRevB.60.5016. 146
- [Bau07] P. Baum, D.-S. Yang, & A. H. Zewail. *4D Visualization of Transitional Structures in Phase Transformations by Electron Diffraction*. Science **318**, 788 (2007). DOI: 10.1126/science.1147724. 208
- [Ber64a] C. N. Berglund & W. E. Spicer. *Photoemission Studies of Copper + Silver - Experiment*. Physical Review A **136**, 4A, 1044 (1964). DOI: 10.1103/PhysRev.136.A1044. 42

- [Ber64b] C. N. Berglund & W. E. Spicer. *Photoemission Studies of Copper + Silver - Theory*. Physical Review A **136**, 4A, 1030 (1964). DOI: 10.1103/PhysRev.136.A1030. 42
- [Ber01] W. Berthold, J. Gdde, P. Feulner, & U. Hfer. *Resonant Interband Scattering of Image-Potential States*. Applied Physics B **73**, 865 (2001). DOI: 10.1007/s003400100765. 39, 139
- [Ber02] W. Berthold, U. Hfer, P. Feulner, E. V. Chulkov, V. M. Silkin, & P. M. Echenique. *Momentum-Resolved Lifetimes of Image-Potential States on Cu(100)*. Physical Review Letters **88**, 5, 056805 (2002). DOI: 10.1103/PhysRevLett.88.056805. 39, 139
- [Bin82] G. Binnig, H. Rohrer, Ch. Gerber, & E. Weibel. *Tunneling Through a Controllable Vacuum Gap*. Applied Physics Letters **40**, 178 (1982). DOI: 10.1063/1.92999. 75
- [Bin83] G. Binnig, H. Rohrer, Ch. Gerber, & E. Weibel. *7x7 Reconstruction on Si(111) Resolved in Real Space*. Physical Review Letters **50**, 2, 120 (1983). DOI: 10.1103/PhysRevLett.50.120. 75
- [Bis06] F. Bisio, M. Nvlt, J. Franta, H. Petek, & J. Kirschner. *Mechanisms of High-Order Perturbative Photoemission from Cu(001)*. Physical Review Letters **96**, 8, 087601 (2006). DOI: 10.1103/PhysRevLett.96.087601. 44
- [Bog02] K. Boger, M. Roth, M. Weinelt, Th. Fauster, & P. G. Reinhard. *Linewidths in energy-resolved two-photon photoemission spectroscopy*. Physical Review B **65**, 7, 075104 (2002). DOI: 10.1103/PhysRevB.65.075104. 50
- [Bog04a] K. Boger, M. Weinelt, & Th. Fauster. *Scattering of Hot Electrons by Adatoms at Metal Surfaces*. Physical Review Letters **92**, 12, 126803 (2004). DOI: 10.1103/PhysRevLett.92.126803. 39
- [Bog04b] K. Boger, M. Weinelt, J. Wang, & Th. Fauster. *Scattering By Cu Adatoms Between Image-Potential Bands on Cu(001)*. Applied Physics A **78**, 2, 161 (2004). DOI: 10.1007/s00339-003-2312-4. 50
- [Bol93] J. J. Boland. *Scanning-Tunneling-Microscopy of The Interaction of Hydrogen With Silicon Surfaces*. Advances In Physics **42**, 2, 129 (1993). DOI: 10.1080/00018739300101474. 74
- [Bor27] M. Born & R. Oppenheimer. *Zur Quantentheorie der Molekeln*. Annalen der Physik **389**, 457 (1927). DOI: 10.1002/andp.19273892002. 219
- [Bov04] U. Bovensiepen, A. Melnikov, I. Radu, O. Krupin, K. Starke, M. Wolf, & E. Matthias. *Coherent Surface and Bulk Vibrations Induced by Femtosecond Laser Excitation of the Gd(0001) Surface State*. Physical Review B **69**, 23, 235417 (2004). DOI: 10.1103/PhysRevB.69.235417. 55, 180
- [Bov06] U. Bovensiepen. *Ultra-Fast Dynamics of Coherent Lattice and Spin Excitations at the Gd(0001) Surface*. Applied Physics A **82**, 395 (2006). DOI: 10.1007/s00339-005-3366-2. 55, 86, 180
- [Bov07] Uwe Bovensiepen. *Coherent and Incoherent Excitations of the Gd(0001) Surface on Ultrafast Timescales*. Journal of Physics: Condensed Matter **19**, 8, 083201 (2007). DOI: 10.1088/0953-8984/19/8/083201. 2, 55, 86, 173, 176, 178, 180, 181, 207, 208, 210, 211
- [Boy92] R. W. Boyd. *Nonlinear Optics*. Academic Press, San Diego, USA (1992). 58
- [Bri05] I. Brihuega, O. Custance, Rubn Prez, & J. M. Gmez-Rodrguez. *Intrinsic Character of the (3×3) to $(\sqrt{3} \times \sqrt{3})$ Phase Transition in Pb/Si(111)*. Physical Review Letters **94**, 4, 046101 (2005). DOI: 10.1103/PhysRevLett.94.046101. 78
- [Bri07] I. Brihuega, O. Custance, M. M. Ugeda, & J. M. Gmez-Rodrguez. *Defects in the $(\sqrt{3} \times \sqrt{3}) - (3 \times 3)$ Phase Transition in the Pb/Si(111) System*. Physical Review B **75**, 15, 155411 (2007). DOI: 10.1103/PhysRevB.75.155411. 78
- [Bro61] B. N. Brockhouse, K. R. Rao, & A. D. B. Woods. *Image of the Fermi Surface in the Lattice Vibrations of Lead*. Physical Review Letters **7**, 3, 93 (1961). DOI: 10.1103/PhysRevLett.7.93. 180
- [Bro62] B. N. Brockhouse, T. Arase, G. Caglioti, K. R. Rao, & A. D. B. Woods. *Crystal Dynamics of Lead. I. Dispersion Curves at 100K*. Physical Review **128**, 3, 1099 (1962). DOI: 10.1103/PhysRev.128.1099. 180

- [Bro90] S. D. Brorson, A. Kazeroonian, J. S. Moodera, D. W. Face, T. K. Cheng, E. P. Ippen, M. S. Dresselhaus, & G. Dresselhaus. *Femtosecond Room-Temperature Measurement of the Electron-Phonon Coupling Constant Γ in Metallic Superconductors*. Physical Review Letters **64**, 18, 2172 (1990). DOI: 10.1103/PhysRevLett.64.2172. 175
- [Bro04] V. Brouet, W. L. Yang, X. J. Zhou, Z. Hussain, N. Ru, K. Y. Shin, I. R. Fisher, & Z.-X. Shen. *Fermi Surface Reconstruction in the CDW State of CeTe₃ Observed by Photoemission*. Physical Review Letters **93**, 12, 126405 (2004). DOI: 10.1103/PhysRevLett.93.126405. 5, 7, 26, 28, 29, 30, 31, 201, 205, 207
- [Bro08] V. Brouet, W. L. Yang, X. J. Zhou, Z. Hussain, R. G. Moore, R. He, D. H. Lu, Z. X. Shen, J. Laverock, S. Dugdale, N. Ru, & I. R. Fisher. *ARPES Study of the Evolution of Band Structure and Charge Density Wave Properties in RTe₃ for R = Y, La, Ce, Sm, Gd, Tb and Dy*. <http://arxiv.org/abs/0801.2672>. 5, 26, 27, 28, 29, 30, 201, 205, 206
- [Bru08] C. Brun. EPFL - Institut de Physique des Nanostructures SB/IPN/LPS - BSP 420 (bat. Physique UNIL), 1015 Lausanne, Suisse. *private communication* (2008). 162
- [Bud00] K. Budde, E. Abram, V. Yeh, & M. C. Tringides. *Uniform, Self-Organized, Seven-Step Height Pb/Si(111)-(7x7) Islands at Low Temperatures*. Physical Review B **61**, R10602 (2000). DOI: 10.1103/PhysRevB.61.R10602. 15, 17
- [Bun99] O. Bunk, G. Falkenberg, J. H. Zeysing, J. Lottermoser, R. L. Johnson, M. Nielsen, F. Berg-Rasmussen, J. Baker, & R. Feidenhans'l. *Structure Determination of the Indium-Induced Si(111)-(4x1) Reconstruction by Surface X-Ray Diffraction*. Physical Review Letters **59**, 12228 (1999). DOI: 10.1103/PhysRevB.59.12228. 4, 186, 187
- [Cam99] I. Campillo, J. M. Pitarke, A. Rubio, E. Zarate, & P. M. Echenique. *Inelastic Lifetimes of Hot Electrons in Real Metals*. Physical Review Letters **83**, 11, 2230 (1999). DOI: 10.1103/PhysRevLett.83.2230. 35, 146
- [Cam00] I. Campillo, A. Rubio, J. M. Pitarke, A. Goldmann, & P. M. Echenique. *Hole Dynamics in Noble Metals*. Physical Review Letters **85**, 15, 3241 (2000). DOI: 10.1103/PhysRevLett.85.3241. 35
- [Cao98] J. Cao, Y. Gao, H. E. Elsayed-Ali, R. J. D. Miller, & D. A. Mantell. *Femtosecond Photoemission Study of Ultrafast Electron Dynamics in Single-Crystal Au(111) Films*. Physical Review B **58**, 16, 10948 (1998). DOI: 10.1103/PhysRevB.58.10948. 146
- [Car92] J. A. Carlisle, T. Miller, & T.-C. Chiang. *Photoemission Study of the Growth, Desorption, Schottky-Barrier Formation, and Atomic Structure of Pb on Si(111)*. Physical Review B **45**, 7, 3400 (1992). DOI: 10.1103/PhysRevB.45.3400. 78
- [Cav04] A. Cavalleri, Th. Dekorsy, H. H. W. Chong, J. C. Kieffer, & R. W. Schoenlein. *Evidence for A Structurally-Driven Insulator-To-Metal Transition in VO₂: A View from the Ultrafast Timescale*. Physical Review B **70**, 16, 161102 (2004). DOI: 10.1103/PhysRevB.70.161102. 208
- [Cha71] A. V. Chaplik. *Energy Spectrum and Electron Scattering Processes in Inversion Layers*. Soviet Physics JETP-USSR **33**, 5, 997 (1971). 36, 234
- [Cha02] S. H. Chang, W. B. Su, W. B. Jian, C. S. Chang, L. J. Chen, & T. T. Tsong. *Electronic Growth of Pb Islands on Si(111) at Low Temperature*. Physical Review B **65**, 245401 (2002). DOI: 10.1103/PhysRevB.65.245401. 15
- [Cha03] T.-L. Chan, C. Z. Wang, M. Hupalo, M. C. Tringides, Z.-Y. Lu, & K. M. Ho. *First-Principles Studies of Structures and Stabilities of Pb/Si(111)*. Physical Review B **68**, 4, 045410 (2003). DOI: 10.1103/PhysRevB.68.045410. 78
- [Cha06] T.-L. Chan, C. Z. Wang, M. Hupalo, M. C. Tringides, & K. M. Ho. *Quantum Size Effect on the Diffusion Barriers and Growth Morphology of Pb/Si(111)*. Physical Review Letters **96**, 22, 226102 (2006). DOI: 10.1103/PhysRevLett.96.226102. 17
- [Che89] J. R. Chelikowsky, T. J. Wagener, J. H. Weaver, & A. Jin. *Valence- and Conduction-Band Densities of States for Tetrahedral Semiconductors: Theory and Experiment*. Physical Review B **40**, 14, 9644 (1989). DOI: 10.1103/PhysRevB.40.9644. 11

- [Che91] T. K. Cheng, J. Vidal, H. J. Zeiger, G. Dresselhaus, M. S. Dresselhaus, & E. P. Ippen. *Mechanism for Displacive Excitation of Coherent Phonons in Sb, Bi, Te, and Ti₂O₃*. Applied Physics Letters **59**, 16, 1923 (1991). DOI: 10.1063/1.106187. 180
- [Chi00] T.-C. Chiang. *Photoemission Studies of Quantum Well States in Thin Films*. Surface Science Reports **39**, 7-8, 181 (2000). DOI: 10.1016/S0167-5729(00)00006-6. 7, 8, 9, 10, 147
- [Cho90] G. C. Cho, W. Kütt, & H. Kurz. *Subpicosecond Time-Resolved Coherent-Phonon Oscillations in GaAs*. Physical Review Letters **65**, 6, 764 (1990). DOI: 10.1103/PhysRevLett.65.764. 180
- [Cho01] J.-H. Cho, D.-H. Oh, K.S. Kim, & L. Kleinman. *Weakly Correlated One-Dimensional Indium Chains on Si(111)*. Physical Review B **64**, 235302 (2001). DOI: 10.1103/PhysRevB.64.235302. 186, 187
- [Cho05a] J. H. Cho, J. Y. Lee, & L. Kleinman. *Electronic Structure of One-Dimensional Indium Chains on Si(111)*. Physical Review B **71**, 8, 081310 (2005). DOI: 10.1103/PhysRevB.71.081310. 186
- [Cho05b] M. Chollet, L. Guerin, N. Uchida, S. Fukaya, H. Shimoda, T. Ishikawa, K. Matsuda, T. Hasegawa, A. Ota, H. Yamochi, G. Saito, R. Tazaki, S.-I. Adachi, & S.-Y. Koshihara. *Gigantic Photoresponse in 1/4-Filled-Band Organic Salt (EDO-TTF)₂PF₆*. Science **307**, 86 (2005). DOI: 10.1126/science.1105067. 208
- [Cho07] W. H. Choi, H. Koh, E. Rotenberg, & H. W. Yeom. *Electronic Structure of Dense Pb Overlayers on Si(111) Investigated Using Angle-Resolved Photoemission*. Physical Review B **75**, 7, 075329 (2007). DOI: 10.1103/PhysRevB.75.075329. 78
- [Chu06a] E. V. Chulkov, A. G. Borisov, J. P. Gauyacq, D. Sanchez-Portal, V. M. Silkin, V. P. Zhukov, & P. M. Echenique. *Electronic Excitations in Metals and at Metal Surfaces*. Chemical Reviews **106**, 10, 4160 (2006). DOI: 10.1021/cr050166o. 32, 35, 146, 231, 235
- [Chu06b] E. V. Chulkov, A. Leonardo, I. A. Nechaev, & V. M. Silkin. *Decay of Electronic Excitations in Bulk Metals and at Surfaces*. Surface Science **600**, 18, 3795 (2006). DOI: 10.1016/j.susc.2006.01.091. 146
- [Chu08] E. V. Chulkov. Donostia International Physics Center, 20018 San Sebastian/Donostia, Basque Country, Spain. *private communication* (2008). 35
- [Coh93] Coherent Laser Group. *Operator's Manual, The Coherent Mira 900-B Laser*. Coherent Inc., Santa Clara (1993). 58, 239, 251
- [Coh94] Coherent Laser Group. *Operator's Manual, The Coherent Modell 9800 Optical Parametric Amplifier*. Coherent Inc., Santa Clara (1994). 58, 59, 239
- [Coh97] Coherent Laser Group. *RegA 9050 System Operator's Manual, Preliminary Version 2.1*. Coherent Inc., Santa Clara (1997). 58, 239, 251
- [Coh99a] Coherent Laser Group. *Operator's Manual, Verdi V-2/V-5 Diode-Pumped Lasers*. Coherent Inc., Santa Clara (1999). 251
- [Coh99b] Coherent Laser Group. *Operator's Manual, Verdi V-8/V-10 Diode-Pumped Lasers*. Coherent Inc., Santa Clara (1999). 251
- [Coh07] Coherent Laser Group. *Operator's Manual, Verdi V-18 Diode-Pumped Lasers*. Coherent Inc., Santa Clara (2007). 58, 239, 242, 251
- [Cos05] G. Da Costa, F. Vurpillot, A. Bostel, M. Bouet, & B. Deconihout. *Design of A Delay-Line Position-Sensitive Detector with Improved Performance*. Review of Scientific Instruments **76**, 1, 013304 (2005). DOI: 10.1063/1.1829975. 87
- [Cra06] J. N. Crain & F. J. Himpsel. *Low-dimensional electronic states at silicon surfaces*. Applied Physics A **82**, 3, 431 (2006). DOI: 10.1007/s00339-005-3365-3. 186
- [CT99] C. Cohen-Tannoudji, B. Diu, & F. Laloe. *Quantenmechanik*. de Gruyter, Berlin, New York (1999). 237
- [Czo03] P. Czoschke, H. Hong, L. Basile, & T.-C. Chiang. *Quantum Oscillations in the Layer Structure of Thin Metal Films*. Physical Review Letters **91**, 226801 (2003). DOI: 10.1103/PhysRevLett.91.226801. 15, 18

- [Czo04] P. Czoschke, H. W. Hong, L. Basile, & T.-C. Chiang. *Quantum Beating Patterns Observed in the Energetics of Pb Film Nanostructures*. Physical Review Letters **93**, 3, 036103 (2004). DOI: 10.1103/PhysRevLett.93.036103. 15, 18
- [Dam03] A. Damascelli, Z. Hussain, & Z.-X. Shen. *Angle-Resolved Photoemission Studies of the Cuprate Superconductors*. Reviews of Modern Physics **75**, 473 (2003). DOI: 10.1103/RevModPhys.75.473. 2, 40, 220, 222
- [Dek00] T. Dekorsy, G. C. Cho, & H. Kurz. *Coherent Phonons in Condensed Media*, Vol. 76 of *Springer Topics in Applied Physics*. Springer-Verlag Berlin (2000). 178, 211
- [Dem99] J. Demsar, K. Biljakovic, & D. Mihailovic. *Single Particle and Collective Excitations in the One-Dimensional Charge Density Wave Solid $K_{0.3}MoO_3$ Probed in Real Time by Femtosecond Spectroscopy*. Physical Review Letters **83**, 800 (1999). DOI: 10.1103/PhysRevLett.83.800. 208
- [Dem03] W. Demtröder. *Laser Spectroscopy*. Springer, Berlin (2003). 58, 239, 244
- [Den99] D. Denzler. *Untersuchungen zur Ultrakurzzeitdynamik photostimulierter Oberflächenreaktionen und der Energielaxation in Metallen*. Diploma Thesis, Freie Universität Berlin (1999). 58, 240
- [Dil04] JH Dil, JW Kim, S Gokhale, M Tallarida, & K Horn. *Self-organization of Pb thin films on Cu(111) induced by quantum size effects*. Physical Review B **70**, 4, 045405 (2004). DOI: 10.1103/PhysRevB.70.045405. 3, 124
- [Dil06] J. H. Dil, J. W. Kim, Th. Kampen, K. Horn, & A. R. H. F. Ettema. *Electron Localization in Metallic Quantum Wells: Pb Versus In on Si(111)*. Physical Review B **73**, 16, 161308 (2006). DOI: 10.1103/PhysRevB.73.161308. 3, 16, 77, 120, 130, 146
- [Dil07] J. H. Dil, T. U. Kampen, B. Huelsen, T. Seyller, & K. Horn. *Quantum Size Effects in Quasi-Free-Standing Pb Layers*. Physical Review B **75**, 16, 161401 (2007). DOI: 10.1103/PhysRevB.75.161401. 77, 222
- [DiM95] E. DiMasi, M. C. Aronson, J. F. Mansfield, B. Foran, & S. Lee. *Chemical Pressure and Charge-Density Waves in Rare-Earth Tritellurides*. Physical Review B **52**, 20, 14516 (1995). DOI: 10.1103/PhysRevB.52.14516. 5, 26, 201, 205
- [Dud04] V. Dudr, N. Tsud, S. Fabik, M. Vondracek, V. Matolin, V. Chab, & K. C. Prince. *Evidence for Valence-Charge Fluctuations in the $\sqrt{3} \times \sqrt{3}$ -Pb/Si(111) System*. Physical Review B **70**, 15, 155334 (2004). DOI: 10.1103/PhysRevB.70.155334. 78
- [Ech78] P. M. Echenique & J. B. Pendry. *The Existence and Detection of Rydberg States at Surfaces*. Journal of Physics C **11**, 2065 (1978). DOI: 10.1088/0022-3719/11/10/017. 9, 139
- [Ech00] P. M. Echenique, J. M. Pitarke, E. V. Chulkov, & A. Rubio. *Theory of Inelastic Lifetimes of Low-Energy Electrons in Metals*. Chemical Physics **251**, 1-3, 1 (2000). DOI: 10.1016/S0301-0104(99)00313-4. 32, 35, 139, 235
- [Ech04] P. M. Echenique, R. Berndt, E. V. Chulkov, Th. Fauster, A. Goldmann, & U. Höfer. *Decay of Electronic Excitations at Metal Surfaces*. Surface Science Reports **52**, 7-8, 219 (2004). DOI: 10.1016/j.surfrep.2004.02.002. 32, 35, 45, 86, 139, 146, 152, 235
- [Ein05] A. Einstein. *Generation and Conversion of Light with Regard to a Heuristic Point of View*. Annalen der Physik **17**, 6, 132 (1905). DOI: 10.1002/andp.19053220607. 40
- [Emt06] K. V. Emtsev, Th. Seyller, L. Ley, A. Tadich, L. Broekman, J. D. Riley, R. C. G. Leckey, & M. Preuss. *Electronic Properties of Clean Unreconstructed 6H-SiC(0001) Surfaces Studied by Angle-Resolved Photoelectron Spectroscopy*. Surface Science **600**, 3845 (2006). DOI: 10.1016/j.susc.2006.01.094. 222
- [Ern08] R. Ernstorfer, M. Harb, C. T. Hebeisen, G. Sciaini, T. Dartigalongue, I. Rajkovic, M. Ligges, D. von der Linde, Th. Payer, M. Horn von Hoegen, F.-J. Meyer zu Heringdorf, S. Kruglik, & R. J. D. Miller. *Atomic View of the Photoinduced Collapse of Gold And Bismuth*. In *Ultrafast Phenomena XVI*. 2008) . 178

- [Fan92] W. S. Fann, R. Storz, H. W. K. Tom, & J. Bokor. *Direct Measurement of Nonequilibrium Electron-Energy Distributions in Subpicosecond Laser-Heated Gold Films*. Physical Review Letters **68**, 18, 2834 (1992). DOI: 10.1103/PhysRevLett.68.2834. 53, 54, 86, 173, 207, 208, 210
- [Fan07] A. Fang, N. Ru, I. R. Fisher, & A. Kapitulnik. *STM Studies of TbTe₃: Evidence for a Fully Incommensurate Charge Density Wave*. Physical Review Letters **99**, 4, 046401 (2007). DOI: 10.1103/PhysRevLett.99.046401. 5, 26, 29, 31, 201
- [Fau95] Th. Fauster & W. Steinmann. *Two-Photon Photoemission Spectroscopy of Image States*. Electromagnetic Waves: Recent Developments in Research, P. Halevi, Ed., Elsevier, Amsterdam **2**, 347 (1995). 2, 38, 45, 86, 139, 161
- [Fau07] Th. Fauster, M. Weimelt, & U. Höfer. *Quasi-Elastic Scattering of Electrons in Image-Potential States*. Progress in Surface Science **82**, 4-6, 224 (2007). DOI: 10.1016/j.progsurf.2007.03.007. 38, 39, 45, 86, 139
- [Fei83] P. J. Feibelman. *Static Quantum-Size Effects in Thin Crystalline, Simple-Metal Films*. Physical Review B **27**, 4, 1991 (1983). DOI: 10.1103/PhysRevB.27.1991. 17
- [Fei84] P. J. Feibelman & D. R. Hamann. *Quantum-Size Effects in Work Functions of Free-Standing and Adsorbed Thin Metal Films*. Physical Review B **29**, 12, 6463 (1984). DOI: 10.1103/PhysRevB.29.6463. 17
- [Feu78] B. Feuerbacher, B. Fitton, & R. F. Willis. *Photoemission and the Electronic Properties of Surfaces*. John Wiley (1978). 43
- [Fis08] I. R. Fischer. Geballe Laboratory for Advanced Materials, and Department of Applied Physics, Stanford University, USA. *private communication* (2008). 26
- [Fle04] K. Fleischer, S. Chandola, N. Esser, W. Richter, J. F. McGilp, W.G. Schmidt, S. Wang, W. Lu, & J. Bernholc. *Atomic Indium Nanowires on Si(111): The (4 × 1)-(8 × 2) Phase Transition Studied With Reflectance Anisotropy Spectroscopy*. Applied Surface Science **234**, 302 (2004). DOI: 10.1016/j.apsusc.2004.05.114. 186
- [Fle05] K. Fleischer, S. Chandola, N. Esser, & J. F. McGilp. *Optical Properties of Indium Nanowires - An Adsorption Study*. Physica Status Solidi B **242**, 13, 2655 (2005). DOI: 10.1002/pssb.200541155. 186
- [Fle07] G. Fleming & M. Ratner (Eds.). *Directing Matter and Energy: Five Challenges for Science and the Imagination*. US Department of Energy, Washington, DC (2007). 1
- [For94] R. L. Fork, O. E. Martinez, & J. P. Gordon. *Negative Dispersion Using Pairs of Prisms*. Optics Letters **9**, 5, 150 (1994). <http://www.opticsinfobase.org/abstract.cfm?URI=ol-9-5-150>. 244
- [For98] I. Forbeaux, J.-M. Themlin, & J.-M. Debever. *Heteroepitaxial Graphite on 6H-SiC(0001): Interface Formation through Conduction-Band Electronic Structure*. Physical Review B **58**, 24, 16396 (1998). DOI: 10.1103/PhysRevB.58.16396. 222
- [Frö54] H. Fröhlich. *On the Theory of Superconductivity: The One-Dimensional Case*. Proceedings of the Royal Society of London. Series A **223**, 296 (1954). DOI: 10.1098/rspa.1954.0116. 19
- [Fri54] J. Friedel. *Electronic Structure of Primary Solid Solutions in Metals*. Advances in Physics **3**, 12, 446 (1954). DOI: 10.1080/00018735400101233. 128
- [Fri07] D. M. Fritz, D. A. Reis, B. Adams, R. A. Akre, J. Arthur, C. Blome, P. H. Bucksbaum, A. L. Cavalieri, S. Engemann, S. Fahy, R. W. Falcone, P. H. Fuoss, K. J. Gaffney, M. J. George, J. Hajdu, M. P. Hertlein, P. B. Hillyard, M. Horn von Hoegen, M. Kammiller, J. Kaspar, R. Kienberger, P. Krejcik, S. H. Lee, A. M. Lindenberg, B. McFarland, D. Meyer, T. Montagne, E. D. Murray, A. J. Nelson, M. Nicoul, R. Pahl, J. Rudati, H. Schlarb, D. P. Siddons, K. Sokolowski-Tinten, Th. Tschentscher, D. von der Linde, & J. B. Hastings. *Ultrafast Bond Softening in Bismuth: Mapping A Solid's Interatomic Potential with X-Rays*. Science **315**, 633 (2007). DOI: 10.1126/science.1135009. 208
- [Fuj84] J. G. Fujimoto, J. M. Liu, E. P. Ippen, & N. Bloembergen. *Femtosecond Laser Interaction with Metallic Tungsten and Nonequilibrium Electron and Lattice Temperatures*. Physical Review Letters **53**, 19, 1837 (1984). DOI: 10.1103/PhysRevLett.53.1837. 53

- [Fuk08] Y. Fukaya, M. Hashimoto, A. Kawasuso, & A. Ichimiya. *Surface Structure of Si(111)-(8 × 2)-In Determined by Reflection High-Energy Positron Diffraction*. *Surface Science* **602**, 14, 2448 (2008). DOI: 10.1016/j.susc.2008.05.021. 186, 187
- [Gah02] C. Gahl, U. Bovensiepen, C. Frischkorn, & M. Wolf. *Ultrafast Dynamics of Electron Localization and Solvation in Ice Layers on Cu(111)*. *Physical Review Letters* **89**, 10, 107402 (2002). DOI: 10.1103/PhysRevLett.89.107402. 73, 86
- [Gah04] C. Gahl. *Elektronentransfer- und Solvatisierungsdynamik in Eis adsorbiert auf Metalloberflächen*. PhD Thesis, Freie Universität Berlin (2004). 58, 72, 73, 242
- [Gal01] O. Gallus, Th. Pillo, M. Hengsberger, P. Segovia, & Y. Baer. *A System with a Complex Phase Transition: Indium Chains on Si(111)*. *European Physical Journal B* **20**, 313 (2001). 4, 186, 187, 190
- [Gar96] G. A. Garrett, T. F. Albrecht, J. F. Whitaker, & R. Merlin. *Coherent THz Phonons Driven by Light Pulses and the Sb Problem: What is the Mechanism?* *Physical Review Letters* **77**, 3661 (1996). DOI: 10.1103/PhysRevLett.77.3661. 180
- [Gar07] D. R. Garcia, G.-H Gweon, S. Y. Zhou, J. Graf, C. M. Jozwiak, M. H. Jung, Y. S. Kwon, & A. Lanzara. *Revealing Charge Density Wave Formation in the LaTe₂ System by Angle Resolved Photoemission Spectroscopy*. <http://arxiv.org/abs/cond-mat/0703535v3> . 5, 26, 28
- [Güd05] J. Güdde & U. Höfer. *Femtosecond Time-Resolved Studies of Image-Potential States at Surfaces and Interfaces of Rare-Gas Adlayers*. *Progress in Surface Science* **80**, 49 (2005). DOI: 10.1016/j.progsurf.2005.10.003. 2, 86, 87, 139
- [Güd07] J. Güdde, M. Rohleder, T. Meier, S. W. Koch, & U. Höfer. *Time-Resolved Investigation of Coherently Controlled Electric Currents at a Metal Surface*. *Science* **318**, 5854, 1287 (2007). DOI: 10.1126/science.1146764. 139
- [Ge98] N.-H. Ge, C. M. Wong, R. L. Lingle Jr., J. D. McNeill, K. J. Gaffney, & C. B. Harris. *Femtosecond Dynamics of Electron Localization at Interfaces*. *Science* **279**, 202 (1998). DOI: 10.1126/science.279.5348.202. 45, 86
- [Ger01] A. Gerlach, K. Berge, A. Goldmann, I. Campillo, A. Rubio, J. M. Pitarke, & P. M. Echenique. *Lifetime of d holes at Cu surfaces: Theory and experiment*. *Physical Review B* **64**, 8, 085423 (2001). DOI: 10.1103/PhysRevB.64.085423. 34, 146
- [Gie85] K. Giesen, F. Hage, F. J. Himpsel, H. J. Riess, & W. Steinmann. *Two-Photon Photoemission via Image-Potential States*. *Physical Review Letters* **55**, 3, 300 (1985). DOI: 10.1103/PhysRevLett.55.300. 45
- [Gie87] K. Giesen, F. Hage, F. J. Himpsel, H. J. Riess, & W. Steinmann. *Binding Energy of Image-Potential States: Dependence on Crystal Structure and Material*. *Physical Review B* **35**, 3, 971 (1987). DOI: 10.1103/PhysRevB.35.971. 45
- [Gil90] T. L. Gilton, J. P. Cowin, G. D. Kubiak, & A. V. H. Gilton. *Intense Surface Photoemission: Space Charge Effects and Self-Acceleration*. *Journal of Applied Physics* **68**, 9, 4802 (1990). DOI: 10.1063/1.346137. 42
- [Giu82] G. F. Giuliani & J. J. Quinn. *Lifetime of a Quasiparticle in a Two-Dimensional Electron-Gas*. *Physical Review B* **26**, 8, 4421 (1982). DOI: 10.1103/PhysRevB.26.4421. 36, 234
- [Giu05] G. F. Giuliani & G. Vignale. *Quantum Theory of the Electron Liquid*. Cambridge University Press, Cambridge, U.K. (2005). 4, 157, 231, 234
- [Gol91] J. L. Goldberg, X.-S. Wang, J. Wei, N. C. Bartelt, & E. D. Williams. *Quantization of Terrace Widths on Vicinal Si(111)*. *Journal of Vacuum Science & Technology A* **9**, 1868 (1991). DOI: 10.1116/1.577536. 190
- [Gol94] J. R. Goldman & J. A. Prybyla. *Ultrafast Dynamics of Laser-Excited Electron Distributions in Silicon*. *Physical Review Letters* **72**, 1364 (1994). DOI: 10.1103/PhysRevLett.72.1364. 167
- [Gon06] C. Gonzalez, F. Flores, & J. Ortega. *Soft Phonon, Dynamical Fluctuations, and a Reversible Phase Transition: Indium Chains on Silicon*. *Physical Review Letters* **96**, 13, 136101 (2006). DOI: 10.1103/PhysRevLett.96.136101. 186, 187

- [Grü94] G. Grüner. *Density Waves in Solids*, Vol. 89 of *Frontiers in Physics*. Addison-Wesley (1994). 5, 7, 19, 20, 21, 22, 23, 24, 25, 30, 31, 37, 201, 207, 211, 215
- [GR05] S. Garrett-Roe, S.T. Shipman, P. Szymanski, M.L. Strader, A. Yang, & Harris C. B. *Ultrafast Electron Dynamics at Metal Interfaces: Intraband Relaxation of Image State Electrons as Friction*. *Journal of Physical Chemistry* **109**, 20370 (2005). DOI: 10.1021/jp051977z. 39
- [Guo04] Y. Guo, Y. F. Zhang, X. Y. Bao, T. Z. Han, Z. Tang, L. X. Zhang, W. G. Zhu, E. G. Wang, Q. Niu, Z. Q. Qiu, J. F. Jia, Z. X. Zhao, & Q. K. Xue. *Superconductivity Modulated by Quantum Size Effects*. *Science* **306**, 5703, 1915 (2004). DOI: 10.1126/science.1105130. 3, 7, 15, 18, 180
- [Gwe98] G.-H. Gweon, J. D. Denlinger, J. A. Clack, J. W. Allen, C. G. Olson, E. DiMasi, M. C. Aronson, B. Foran, & S. Lee. *Direct Observation of Complete Fermi Surface, Imperfect Nesting, and Gap Anisotropy in the High-Temperature Incommensurate Charge-Density-Wave Compound $SmTe_3$* . *Physical Review Letters* **81**, 4, 886 (1998). DOI: 10.1103/PhysRevLett.81.886. 5, 30, 201, 205
- [Haa78] H. W. Haak, G. A. Sawatzky, & T. D. Thomas. *Auger-Photoelectron Coincidence Measurements in Copper*. *Physical Review Letters* **41**, 26, 1825 (1978). DOI: 10.1103/PhysRevLett.41.1825. 114
- [Hai88] R. Haight, J. A. Silberman, & M. I. Lilie. *Novel System for Picosecond Photoemission Spectroscopy*. *Review of Scientific Instruments* **59**, 9, 1941 (1988). DOI: 10.1063/1.1140055. 87
- [Hai95] R. Haight. *Electron Dynamics at Surfaces*. *Surface Science Reports* **21**, 275 (1995). DOI: 10.1016/0167-5729(95)00002-X. 53, 86
- [Ham86] R. J. Hamers, R. M. Tromp, & J. E. Demuth. *Surface Electronic Structure of $Si(111)-(7 \times 7)$ Resolved in Real Space*. *Physical Review Letters* **56**, 18, 1972 (1986). DOI: 10.1103/PhysRevLett.56.1972. 75
- [Has96] M. Hase, K. Mizoguchi, H. Harima, S. Nakashima, M. Tani, K. Sakai, & M. Hangyo. *Optical Control of Coherent Optical Phonons in Bismuth Films*. *Applied Physics Letters* **69**, 17, 2474 (1996). DOI: 10.1063/1.117502. 180
- [Has03] M. Hase, M. Kitajima, A. M. Constantinescu, & H. Petek. *The Birth of a Quasiparticle in Silicon Observed in Time-Frequency Space*. *Nature* **426**, 51 (2003). DOI: 10.1038/nature02044. 180
- [Has05] M. Hase, K. Ishioka, J. Demsar, K. Ushida, & M. Kitajima. *Ultrafast Dynamics of Coherent Optical Phonons and Nonequilibrium Electrons in Transition Metals*. *Physical Review B* **71**, 18, 184301 (2005). DOI: 10.1103/PhysRevB.71.184301. 180
- [Has07] M. Hashimoto, Y. Fukaya, A. Kawasuso, & A. Ichimiya. *Surface Structure of $In/Si(111)$ Studied by Reflection High-Energy Positron Diffraction*. *Surface Science* **601**, 22, 5192 (2007). DOI: 10.1016/j.susc.2007.04.242. 186
- [Has08] M. Hashimoto, Y. Fukaya, A. Kawasuso, & A. Ichimiya. *Quasi-One-Dimensional In Atomic Chains on $Si(111)$ at Low Temperature Studied by Reflection High-Energy Positron Diffraction and Scanning Tunneling Microscopy*. *Applied Surface Science* **254**, 23, 7733 (2008). DOI: 10.1016/j.apsusc.2008.02.010. 186
- [Hat00] K. Hata, T. Kimura, S. Ozawa, & H. Shigekawa. *How to Fabricate Defect Free $Si(001)$* . *Journal of Vacuum Science Technology* **18**, 1933 (2000). DOI: 10.1116/1.582482. 74
- [Hat04] M. Hattass, T. Jalowy, A. Czasch, Th. Weber, T. Jahnke, S. Schössler, L. Ph. Schmidt, O. Jagutzki, R. Dörner, & H. Schmidt-Böcking. *A 2 Pi Spectrometer for Electron-Electron Coincidence Studies on Surfaces*. *Review of Scientific Instruments* **75**, 7, 2373 (2004). DOI: 10.1063/1.1765764. 87, 114, 222
- [Hat08] M. Hattass, T. Jahnke, S. Schössler, A. Czasch, M. Schöffler, L. Ph. H. Schmidt, B. Ulrich, O. Jagutzki, F. O. Schumann, C. Winkler, J. Kirschner, R. Dörner, & H. Schmidt-Böcking. *Dynamics of Two-Electron Photoemission from $Cu(111)$* . *Physical Review B* **77**, 16, 165432 (2008). DOI: 10.1103/PhysRevB.77.165432. 87, 114, 222

- [Haw87] P. Hawrylak. *Effective Mass and Lifetime of Electrons in a Layered Electron Gas*. Physical Review Letters **59**, 4, 485 (1987). DOI: 10.1103/PhysRevLett.59.485. 36, 37
- [Hen08] M. Hengsberger, F. Baumberger, H. J. Neff, T. Greber, & J. Osterwalder. *Photoemission momentum mapping and wave function analysis of surface and bulk states on flat Cu(111) and stepped Cu(443) surfaces: A two-photon photoemission study*. Physical Review B **77**, 8, 085425 (2008). DOI: 10.1103/PhysRevB.77.085425. 99, 222
- [Her96] T. Hertel, E. Knoesel, M. Wolf, & G. Ertl. *Ultrafast Electron Dynamics at Cu(111): Response of an Electron Gas to Optical Excitation*. Physical Review Letters **76**, 3, 535 (1996). DOI: 10.1103/PhysRevLett.76.535. 34, 50, 194
- [Her97] T. Hertel, E. Knoesel, A. Hotzel, M. Wolf, & G. Ertl. *Femtosecond Time-Resolved Photoemission of Electron Dynamics in Surface Rydberg States*. Journal of the American Vacuum Society **15**, 3, 1503 (1997). DOI: 10.1116/1.580570. 194
- [Her98] R. Herrmann, S. Samarin, H. Schwabe, & J. Kirschner. *Two Electron Photoemission in Solids*. Physical Review Letters **81**, 10, 2148 (1998). DOI: 10.1103/PhysRevLett.81.2148. 114
- [Hes90] D. R. Heslinga, H. H. Weitering, D. P. Vanderwerf, T. M. Klapwijk, & T. Hibma. *Atomic-Structure-Dependent Schottky-Barrier At Epitaxial Pb/Si(111) Interfaces*. Physical Review Letters **64**, 13, 1589 (1990). DOI: 10.1103/PhysRevLett.64.1589. 78
- [Hüf95] S. Hüfner. *Photoelectron Spectroscopy*. Springer, Heidelberg (1995). 2, 40, 43, 44, 86
- [Hil97] I. G. Hill & A. B. McLean. *Metallicity of In chains on Si(111)*. Physical Review B **56**, 15725 (1997). DOI: 10.1103/PhysRevB.56.15725. 186, 189, 190
- [Hil99] I. G. Hill & A. B. McLean. *Strongly Anisotropic Band Dispersion of an Image State Located above Metallic Nanowires*. Physical Review Letters **82**, 2155 (1999). DOI: 10.1103/PhysRevLett.82.2155. 186, 189, 190
- [Him02] F. J. Himpsel, K. N. Altmann, J. N. Crain, A. Kirakosian, J.-L. Lin, A. Liebsch, & V. P. Zhukov. *Photoelectron Spectroscopy of Atomic Wires*. Journal of Electron Spectroscopy and Related Phenomena **126**, 89 (2002). DOI: 10.1016/S0368-2048(02)00144-5. 34
- [Hon03] H. Hong, C.-M. Wei, M. Y. Chou, Z. Wu, L. Basile, H. Chen, M. Holt, & T.-C. Chiang. *Alternating Layer and Island Growth of Pb on Si by Spontaneous Quantum Phase Separation*. Physical Review Letters **90**, 076104 (2003). DOI: 10.1103/PhysRevLett.90.076104. 18
- [Hon08] I.-P. Hong, C. Brun, F. Patthey, & W.-D. Schneider. To be published (2008). 162
- [Hor84] K. Horn, B. Reihl, A. Zartner, D. E. Eastman, K. Hermann, & J. Noffke. *Electronic Energy Bands of Lead: Angle-Resolved Photoemission and Band-Structure Calculations*. Physical Review B **30**, 4, 1711 (1984). DOI: 10.1103/PhysRevB.30.1711. 12
- [Hor99] K. Horikoshi, X. Tong, T. Nagao, & S. Hasegawa. *Structural Phase Transitions of Pb-Adsorbed Si(111) Surfaces at Low Temperatures*. Physical Review B **60**, 13287 (1999). DOI: 10.1103/PhysRevB.60.13287. 78
- [Hot99] A. Hotzel. *Elektronendynamik der Adsorbatbedeckten Cu(111)-Oberfläche*. PhD Thesis, Freie Universität Berlin (1999). 58, 68, 72, 86
- [Hot00] A. Hotzel & M. Wolf. *Phonon-Mediated Intraband Relaxation of Image-State Electrons in Adsorbate Overlayers: N₂/Xe/Cu(111)*. Journal of Physical Chemistry B **104**, 35, 8438 (2000). DOI: 10.1021/jp000989b. 39, 73, 86, 139
- [Hul85] S. L. Hulbert, P. D. Johnson, N. G. Stoffel, W. A. Royer, & N. V. Smith. *Crystal-induced and image-potential-induced empty surface states on Cu(111) and Cu(001)*. Physical Review B **31**, 10, 6815 (1985). DOI: 10.1103/PhysRevB.31.6815. 139
- [Hup01] M. Hupalo, S. Kremmer, V. Yeh, L. Berbil-Bautista, E. Abram, & M. C. Tringides. *Uniform Island Height Selection in the Low Temperature Growth of Pb/Si(111)-(7 × 7)*. Surface Science **493**, 1-3, 526 (2001). DOI: 10.1016/S0039-6028(01)01262-6. 3, 7, 17, 79, 81, 119, 124, 138

- [Hup02a] M. Hupalo, , & M. C. Tringides. *Regular Nanocluster Networks on Pb/Si(111)-Pb- $\sqrt{3} \times \sqrt{3}$ at Low Temperatures*. Physical Review B **65**, 205406 (2002). DOI: 10.1103/PhysRevB.66.035325. 78
- [Hup02b] M. Hupalo, T.L. Chan, C. Z. Wang, K. M. Ho, & M. C. Tringides. *Atomic Models, Domain-Wall Arrangement, and Electronic Structure of the Dense Pb/Si(111)- $\sqrt{3} \times \sqrt{3}$ Phase*. Physical Review B **66**, 141410(R) (2002). DOI: 10.1103/PhysRevB.66.161410. 78
- [Hup03] M. Hupalo, J. Schmalian, & M. C. Tringides. *Devil's Staircase in Pb/Si(111) Ordered Phases*. Physical Review Letters **90**, 216106 (2003). DOI: 10.1103/PhysRevLett.90.216106. 3, 18
- [Hwa07] C. G. Hwang, N. D. Kim, S. Y. Shin, & J. W. Chung. *Possible Evidence of Non-Fermi Liquid Behaviour from Quasi-One-Dimensional Indium Nanowires*. New Journal Of Physics **9**, 249 (2007). DOI: 10.1088/1367-2630/9/8/249. 188
- [Iba90] H. Ibach & H. Lüth. *Festkörperphysik*. Springer, Berlin (1990). 13, 14
- [Int08] Intel. Homepage <http://www.intel.com/technology/silicon/index.htm>. 1
- [ITRfS07] ITRS International Technology Roadmap for Semiconductors. Homepage <http://www.itrs.net>. 1
- [Jac99] J. D. Jackson. *Classical Electrodynamics*. John Wiley & Sons, Inc. (1999). 10
- [Jag02a] O. Jagutzki, A. Cerezo, A. Czasch, R. Dorner, M. Hattass, M. Huang, V. Mergel, U. Spillmann, K. Ullmann-Pfeger, T. Weber, H. Schmidt-Böcking, & G. D. W. Smith. *Multiple Hit Readout of A Microchannel Plate Detector with A Three-Layer Delay-Line Anode*. Ieee Transactions on Nuclear Science **49**, 5, 2477 (2002). DOI: 10.1109/TNS.2002.803889. 87, 94, 104, 106
- [Jag02b] O. Jagutzki, J. S. Lapington, L. B. C. Worth, U. Spillman, V. Mergel, & H. Schmidt-Böcking. *Position Sensitive Anodes for MCP Read-Out Using Induced Charge Measurement*. Nuclear Instruments and Methods in Physics Research A **477**, 1-3, 256 (2002). DOI: 10.1016/S0168-9002(01)01843-5. 87
- [Jag02c] O. Jagutzki, V. Mergel, K. Ullmann-Pfeger, L. Spielberger, U. Spillmann, R. Dörner, & H. Schmidt-Böcking. *A Broad-Application Microchannel-Plate Detector System for Advanced Particle or Photon Detection Tasks: Large Area Imaging, Precise Multi-Hit Timing Information and High Detection Rate*. Nuclear Instruments and Methods in Physics Research A **477**, 244 (2002). DOI: 10.1016/S0168-9002(01)01839-3. 87, 89, 96, 104, 105, 106
- [Jak71] R. C. Jaklevic, J. Lambe, M. Mikkor, & W. C. Vassell. *Observation of Electron Standing Waves in a Crystalline Box*. Physical Review Letters **26**, 2, 88 (1971). DOI: 10.1103/PhysRevLett.26.88. 15, 17
- [Jal88] M. Jalochowski & E. Bauer. *Quantum Size and Surface Effects in the Electrical Resistivity and High-Energy Electron Reflectivity of Ultrathin Lead Films*. Physical Review B **38**, 8, 5272 (1988). DOI: 10.1103/PhysRevB.38.5272. 15, 17
- [Jal92a] M. Jalochowski, E. Bauer, H. Knoppe, & G. Lilienkamp. *Experimental Evidence for Quantum-Size-Effect Fine Structures in the Resistivity of Ultrathin Pb and Pb-In Films*. Physical Review B **45**, 13607 (1992). DOI: 10.1103/PhysRevB.45.13607. 15, 17
- [Jal92b] M. Jalochowski, H. Knoppe, G. Lilienkamp, & E. Bauer. *Photoemission from Ultrathin Metallic Films: Quantum Size Effect, Electron Scattering, and Film Structure*. Physical Review B **46**, 8, 4693 (1992). DOI: 10.1103/PhysRevB.46.4693. 15
- [Jeo96] S. Jeong, H. Zacharias, & J. Bokor. *Ultrafast carrier dynamics on the Si(100)- 2×1 surface*. Physical Review B **54**, R17300 (1996). DOI: 10.1103/PhysRevB.54.R17300. 167
- [Jia03] W. B. Jian, W. B. Su, C. S. Chang, & T. T. Tsong. *Vertical Friedel Oscillations in Interface-Induced Surface Charge Modulations of Ultrathin Quantum Islands*. Physical Review Letters **90**, 196603 (2003). DOI: 10.1103/PhysRevLett.90.196603. 15
- [Jia07] J. F. Jia, S. C. Li, Y. F. Zhang, & Q. K. Xue. *Quantum Size Effects Induced Novel Properties in Two-Dimensional Electronic Systems: Pb Thin Films on Si(111)*. Journal of the Physical Society of Japan **76**, 8, 082001 (2007). DOI: 10.1143/JPSJ.76.082001. 15, 124, 128, 129, 130

- [Joh08] M. D. Johannes & I. I. Mazin. *Fermi Surface Nesting and the Origin of Charge Density Waves in Metals*. Physical Review B **77**, 16, 165135 (2008). DOI: 10.1103/PhysRevB.77.165135. 5, 31, 223
- [Joo91] W. Joosen, H. J. Bakker, L. D. Noordam, H. G. Muller, & B. B. v. L. v. d. Heuvel. *Parametric generation in β -barium borate of intense femtosecond pulses near 800 nm*. Journal of the Optical Society of America B **8**, 2537 (1991). <http://www.opticsinfobase.org/abstract.cfm?URI=josab-8-12-2537>. 245
- [Kai01] R. A. Kaindl, M. Wurm, K. Reimann, M. Woerner, T. Elsaesser, C. Miesner, K. Brunner, & G. Abstreiter. *Ultrafast Dynamics of Intersubband Excitations in a Quasi-Two-Dimensional Hole Gas*. Physical Review Letters **86**, 1122 (2001). DOI: 10.1103/PhysRevLett.86.1122. 36
- [Kar92] C. J. Karlsson, E. Landemark, Y.-C. Chao, & R. I. G. Uhrberg. *Photoemission study of the Si(111)- 3×3 -Pb mosaic phase: Observation of a large charge transfer*. Physical Review B **45**, 11, 6321 (1992). DOI: 10.1103/PhysRevB.45.6321. 78
- [Kat86] K. Kato. *Second-Harmonic Generation to 2048 Å In β -Ba 2 O 4* . IEEE Journal of Quantum Electronics **22**, 1013 (1986). 245
- [Kaw99] R. K. Kawakami, E. Rotenberg, H. J. Choi, E. J. Escorcía-Aparicio, M. O. Bowen, J. H. Wolfe, E. Arenholz, Z. D. Zhang, N. V. Smith, & Z. Q. Qiu. *Quantum-Well States in Copper Thin Films*. Nature **398**, 132 (1999). DOI: 10.1038/18178. 80
- [Kev92] S.D. Kevan (Ed.). *Angle-Resolved Photoemission: Theory and Current Applications*. Elsevier, Amsterdam (1992). 40, 86
- [Kim06] H. J. Kim, C. D. Malliakas, A. T. Tomi, S. H. Tessmer, M. G. Kanatzidis, & S. J. L. Billinge. *Local Atomic Structure and Discommensurations in the Charge Density Wave of CeTe 3* . Physical Review Letters **96**, 22, 226401 (2006). DOI: 10.1103/PhysRevLett.96.226401. 5, 29, 201
- [Kir95] J. Kirschner, O. M. Artamonov, & S. N. Samarin. *Angle Resolved Energy Correlated Coincidence Electron Spectroscopy of Solid Surfaces*. Physical Review Letters **75**, 12, 2424 (1995). DOI: 10.1103/PhysRevLett.75.2424. 114
- [Kir05] P. S. Kirchmann, P. A. Loukakos, U. Bovensiepen, & M. Wolf. *Ultrafast Electron Dynamics Studied with Time-Resolved Two-Photon Photoemission: Intra- and Interband Scattering in C 6 F 6 /Cu(111)*. New Journal of Physics **7**, 113 (2005). DOI: 10.1088/1367-2630/7/1/113. 39, 73, 86
- [Kir07] P. S. Kirchmann, M. Wolf, J. H. Dil, K. Horn, & U. Bovensiepen. *Quantum Size Effects in Pb/Si(111) Investigated by Laser-Induced Photoemission*. Physical Review B **76**, 7, 075406 (2007). DOI: 10.1103/PhysRevB.76.075406. 7, 15, 17, 146
- [Kit04] Charls Kittel. *Introduction to Solid State Physics*. Wiley, London (2004). 8, 11, 12, 78, 157, 175
- [Kno96] E. Knoesel, A. Hotzel, T. Hertel, M. Wolf, & G. Ertl. *Dynamics of Photoexcited Electrons in Metals Studied with Time-Resolved Two-Photon Photoemission*. Surface Science **368**, 1-3, 76 (1996). DOI: 10.1016/S0039-6028(96)01032-1. 34
- [Kno97] E. Knoesel. *Ultrakurzzeit-Dynamik elektronischer Anregungen auf Metalloberflächen*. PhD Thesis, Freie Universität Berlin (1997). 58, 68, 86
- [Kno98a] E. Knoesel, A. Hotzel, & M. Wolf. *Temperature Dependence of Surface State Lifetimes, Dephasing Rates and Binding Energies on Cu(111) Studied with Time-Resolved Photoemission*. Journal of Electron Spectroscopy and Related Phenomena **88**, 577 (1998). DOI: 10.1016/S0368-2048(97)00178-3. 50, 108, 109, 110, 111, 112, 161
- [Kno98b] E. Knoesel, A. Hotzel, & M. Wolf. *Ultrafast Dynamics of Hot Electrons and Holes in Copper: Excitation, Energy Relaxation, and Transport Effects*. Physical Review B **57**, 20, 12812 (1998). DOI: 10.1103/PhysRevB.57.12812. 34, 146
- [Kno00] R. Knorren, K. H. Bennemann, R. Burgermeister, & M. Aeschlimann. *Dynamics of excited electrons in copper and ferromagnetic transition metals: Theory and experiment*. Physical Review B **61**, 14, 9427 (2000). DOI: 10.1103/PhysRevB.61.9427. 146

- [Koe96] W. Koehler. *Solid-State Laser Engineering*. Springer, Berlin (1996). 239
- [Koh59] W. Kohn. *Image of the Fermi Surface in the Vibration Spectrum of a Metal*. Physical Review Letters **2**, 9, 393 (1959). DOI: 10.1103/PhysRevLett.2.393. 21, 180
- [Koo34] T. Koopman. *Über die Zuordnung von Wellenfunktionen und Eigenwerten zu den Einzelnen Elektronen Eines Atoms*. Physica **1**, 104 (1934). DOI: 10.1016/S0031-8914(34)90011-2. 41
- [Kor06] J. D. Koralek, J. F. Douglas, N. C. Plumb, Z. Sun, A. V. Fedorov, M. M. Murnane, H. C. Kapteyn, S. T. Cundiff, Y. Aiura, K. Oka, H. Eisaki, & D. S. Dessau. *Laser Based Angle-Resolved Photoemission, the Sudden Approximation, and Quasiparticle-Like Spectral Peaks in Bi2Sr2CaCu2O8+δ*. Physical Review Letters **96**, 017005 (2006). DOI: 10.1103/PhysRevLett.96.017005. 41, 59, 245
- [Kor07] J. D. Koralek, J. F. Douglas, N. C. Plumb, J. D. Griffith, S. T. Cundiff, H. C. Kapteyn, M. M. Murnane, & D. S. Dessau. *Experimental Setup for Low-Energy Laser-Based Angle Resolved Photoemission Spectroscopy*. Review of Scientific Instruments **78**, 5, 053905 (2007). DOI: 10.1063/1.2722413. 41
- [Kou99] H. Kouta & Y. Kuwano. *Attaining 186-nm light generation in cooled beta-BaB2O4 crystal*. Optics Letters **24**, 17, 1230 (1999). DOI: doi:10.1364/OL.24.001230. 245
- [Krö08] B. Krömker, M. Escher, D. Funnemann, D. Hartung, H. Engelhard, & J. Kirschner. *Development of a Momentum Microscope for Time Resolved Band Structure Imaging*. Review of Scientific Instruments **79**, 5, 053702 (2008). DOI: 10.1063/1.2918133. 87
- [Kra97] J. Kraft, M. G. Ramsey, & F. P. Netzer. *Surface Reconstructions of In on Si(111)*. Physical Review B **55**, 5384 (1997). DOI: 10.1103/PhysRevB.55.5384. 186, 189
- [Kum00] C. Kumpf, O. Bunk, J.H. Zeysing, Y. Su, M. Nielsen, R.L. Johnson, R. Feidenhans'l, & K. Bechgaard. *Low-Temperature Structure of Indium Quantum Chains on Silicon*. Physical Review Letters **85**, 4916 (2000). DOI: 10.1103/PhysRevLett.85.4916. 4, 187
- [Kur05] S. Kurata & T. Yokoyama. *Interchain Coupling of Degenerated Quasi-One-Dimensional Indium Chains On Si(111)*. Physical Review B **71**, 12, 121306 (2005). DOI: 10.1103/PhysRevB.71.121306. 186
- [Lad03] F. Ladstädter, P. F. de Pablos, U. Hohenester, P. Puschnig, C. Ambrosch-Draxl, P. L. de Andrés, F. J. García-Vidal, & F. Flores. *Hot-Electron Lifetimes in Metals: A Combined Ab Initio Calculation and Ballistic Electron Emission Spectroscopy Analysis*. Physical Review B **68**, 8, 085107 (2003). DOI: 10.1103/PhysRevB.68.085107. 35, 146
- [Lan70] N. D. Lang & W. Kohn. *Theory of Metal Surfaces - Charge Density And Surface Energy*. Physical Review B **1**, 12, 4555 (1970). DOI: 10.1103/PhysRevB.1.4555. 17, 127
- [Lan71] N. D. Lang & W. Kohn. *Theory of Metal Surfaces - Work Function*. Physical Review B **3**, 4, 1215 (1971). DOI: 10.1103/PhysRevB.3.1215. 17, 127
- [Lan73] James E. Land & Wilhelm Raith. *Fine Structure of O2+ Measured by Electron Time-of-Flight Spectroscopy*. Physical Review Letters **30**, 6, 193 (1973). DOI: 10.1103/PhysRevLett.30.193. 86
- [Lan76] Landolt & Börnstein. *Numerical Data and Functional Relationships in Science and Technology*. New Series. Springer, Berlin (1976). 12, 74, 175, 178, 180
- [Lat89] A. V. Latyshev, A. L. Aseev, A. B. Krasilnikov, & S. I. Stenin. *Transformations on Clean Si(111) Stepped Surface During Sublimation*. Surface Science **213**, 157 (1989). DOI: 10.1016/0039-6028(89)90256-2. 190
- [Lau77] L. D. Laude & M. Wautelet. *Double-Beam Photoemission and Electronic-Structure of Tellurium*. Nuovo Cimento Della Societa Italiana Di Fisica B **39**, 2, 734 (1977). 45
- [Lav05] J. Laverock, S. B. Dugdale, Zs. Major, M. A. Alam, N. Ru, I. R. Fisher, G. Santi, & E. Bruno. *Fermi surface nesting and charge-density wave formation in rare-earth tritellurides*. Physical Review B **71**, 8, 085114 (2005). DOI: 10.1103/PhysRevB.71.085114. 5, 28, 31, 205

- [Lav08] M. Lavagnini, M. Baldini, A. Sacchetti, D. Di Castro, B. Delley, R. Monnier, J.-H. Chu, N. Ru, I. R. Fisher, P. Postorino, & L. Degiorgi. *Evidence for Coupling Between Collective State and Phonons in Two-Dimensional Charge-Density-Wave Systems*. <http://arxiv.org/abs/0806.1455v1>. 5, 26, 213, 215
- [Lee74] P. A. Lee, T. M. Rice, & P. W. Anderson. *Conductivity from Charge or Spin Density Waves*. *Solid State Communications* **14**, 703 (1974). DOI: 10.1016/0038-1098(74)90868-0. 25
- [Lee02] S. S. Lee, J. R. Ahn, N. D. Kim, J. H. Min, C. G. Hwang, J. W. Chung, H. W. Yeom, S. Ryikov, & S. Hasegawa. *Adsorbate-Induced Pinning of a Charge-Density Wave in a Quasi-1D Metallic Chains: Na on the In/Si(111)-(4×1) Surface*. *Physical Review Letters* **88**, 196401 (2002). DOI: 10.1103/PhysRevLett.88.196401. 186
- [Lee06] G. Lee. *Real-Space Visualization of the Phase Transition of the In/Si(111) System*. *Surface and Interface Analysis* **38**, 12-13, 1636 (2006). DOI: 10.1002/sia.2417. 186
- [Leu03] T. C. Leung, C. L. Kao, W. S. Su, Y. J. Feng, & C. T. Chan. *Relationship between surface dipole, work function and charge transfer: Some exceptions to an established rule*. *Physical Review B* **68**, 19, 195408 (2003). DOI: 10.1103/PhysRevB.68.195408. 127
- [Lin54] J. Lindhard. *On the Properties of a Gas of Charged Particles*. *Matematisk-Fysiske Meddelelser Kongelige Danske Videnskabernes Selskab* **28**, 8, 1 (1954). <http://www.sdu.dk/media/bibpdf/Bind21>
- [Lin98] J.-L. Lin, D.Y. Petrovykh, J. Viernow, F.K. Men, D.J. Seo, & F.J. Himpsel. *Formation of regular steps on Si(111)-7×7*. *Journal of Applied Physics* **84**, 255 (1998). DOI: 10.1063/1.368077. 190
- [Lin04] D. Lincota, J. F. Guillemolesa, S. Tauniera, D. Guimarda, J. Sixc-Kurdia, A. Chaumonta, O. Roussele, O. Ramdania, C. Huberta, J. P. Fauvarquea, N. Bodereauea, L. Parissia, P. Panheleuxa, P. Fanouillerea, N. Naghavia, P.P. Granda, M. Benfaraha, P. Mogensenb, & O. Kerreca. *Chalcopyrite Thin Film Solar Cells by Electrodeposition*. *Solar Energy* **77**, 725 (2004). DOI: 10.1016/j.solener.2004.05.024. 1
- [Lis04a] M. Lisowski, P. A. Loukakos, U. Bovensiepen, J. Stähler, C. Gahl, & M. Wolf. *Ultra-Fast Dynamics of Electron Thermalization, Cooling and Transport Effects in Ru(001)*. *Applied Physics A* **78**, 4-6, 165 (2004). DOI: 10.1007/s00339-004-2591-4. 53, 54, 86, 173, 207, 208, 210
- [Lis04b] M. Lisowski, P. A. Loukakos, U. Bovensiepen, & M. Wolf. *Femtosecond Dynamics and Transport of Optically Excited Electrons in Epitaxial Cu Films on Si(111)-7×7*. *Applied Physics A* **79**, 4-6, 739 (2004). DOI: 10.1007/s00339-004-2591-4. 35, 146
- [Lis05a] M. Lisowski. *Elektronen- und Magnetisierungsdynamik in Metallen untersucht mit zeitaufgelöster Photoemission*. PhD Thesis, Freie Universität Berlin (2005). 54, 58, 67, 173, 174, 175, 176
- [Lis05b] M. Lisowski, P. A. Loukakos, A. Melnikov, I. Radu, L. Ungureanu, M. Wolf, & U. Bovensiepen. *Femtosecond Electron and Spin Dynamics In Gd(0001) Studied by Time-Resolved Photoemission and Magneto-Optics*. *Physical Review Letters* **95**, 137402 (2005). DOI: 10.1103/PhysRevLett.95.137402. 55, 86
- [Lit82] P. B. Littlewood & C. M. Varma. *Amplitude Collective Modes in Superconductors and Their Coupling to Charge-Density Waves*. *Physical Review B* **26**, 9, 4883 (1982). DOI: 10.1103/PhysRevB.26.4883. 201
- [Liu08] C. Liu, T. Inaoka, S. Yaginuma, T. Nakayama, M. Aono, & T. Nagao. *Disappearance of the Quasi-One-Dimensional Plasmon at the Metal-Insulator Phase Transition of Indium Atomic Wires*. *Physical Review B* **77**, 20, 205415 (2008). DOI: 10.1103/PhysRevB.77.205415. 188
- [LL05] X. Lopez-Lozano, A. A. Stekolnikov, J. Furthmuller, & F. Bechstedt. *Band Structure and Electron Gas of In Chains on Si(111)*. *Surface Science* **589**, 1-3, 77 (2005). DOI: 10.1016/j.susc.2005.05.053. 186

- [LL06] X. Lopez-Lozano, A. Krivosheeva, A. A. Stekolnikov, L. Meza-Montes, C. Noguez, J. Furthmuller, & F. Bechstedt. *Reconstruction of Quasi-One-Dimensional In/Si(111) Systems: Charge- and Spin-Density Waves Versus Bonding*. Physical Review B **73**, 3, 035430 (2006). DOI: 10.1103/PhysRevB.73.035430. 186
- [Lob01] A. I. Lobad & A. J. Taylor. *Coherent Phonon Generation Mechanism in Solids*. Physical Review B **64**, 18, 180301 (2001). DOI: 10.1103/PhysRevB.64.180301. 180
- [Los00] R. Losio, N. Altmann, & F. J. Himpsel. *Fermi surface of Si(111)7×7*. Physical Review B **61**, 10845 (2000). DOI: 10.1103/PhysRevB.61.10845. 130
- [Los01] R. Losio, K. N. Altmann, A. Kirakosian, J.-L. Lin, Petrovykh, & F. J. Himpsel. *Band Splitting for Si(557)-Au: Is it Spin-Charge Separation?* Physical Review Letters **86**, 4632 (2001). DOI: 10.1103/PhysRevLett.86.4632. 37, 189
- [Lou76] S. G. Louie & M. L. Cohen. *Electronic Structure of a Metal-Semiconductor Interface*. Physical Review B **13**, 6, 2461 (1976). DOI: 10.1103/PhysRevB.13.2461. 78
- [Lou77] S. G. Louie, J. R. Chelikowsky, & M. L. Cohen. *Ionicity and the Theory of Schottky Barriers*. Physical Review B **15**, 4, 2154 (1977). DOI: 10.1103/PhysRevB.15.2154. 78
- [Lou83] R. Loudon. *Quantum Theorie of Light*. Oxford University Press, New York (1983). 50, 237, 238
- [Lou07] P. A. Loukakos, M. Lisowski, G. Bihlmayer, S. Bluegel, M. Wolf, & U. Bovensiepen. *Dynamics of the Self-Energy of the Gd(0001) Surface State Probed by Femtosecond Photoemission Spectroscopy*. Physical Review Letters **98**, 9, 097401 (2007). DOI: 10.1103/PhysRevLett.98.097401. 55, 86, 208, 209
- [Luh01] D.-A. Luh, T. Miller, J. J. Paggel, M. Y. Chou, & T.-C. Chiang. *Quantum Electronic Stability of Atomically Uniform Films*. Science **292**, 1131 (2001). DOI: 10.1126/science.292.5519.1131. 18
- [Luh02] D.-A. Luh, T. Miller, J. J. Paggel, & T.-C. Chiang. *Large Electron-Phonon Coupling at an Interface*. Physical Review Letters **88**, 25, 256802 (2002). DOI: 10.1103/PhysRevLett.88.256802. 10
- [Lut61] J. M. Luttinger. *Analytic Properties of Single-Particle Propagators for Many-Fermion Systems*. Physical Review **121**, 4, 942 (1961). DOI: 10.1103/PhysRev.121.942. 37, 188
- [Lut63] J. M. Luttinger. *An Exactly Soluble Model of a Many-Fermion System*. Journal of Mathematical Physics **4**, 9, 1154 (1963). DOI: 10.1063/1.1704046. 37, 188
- [Ma06] L.-Y. Ma, L. T.-., Z.-L. Guan, K. H., K. An, X.-C. Ma, J.-F. Jia, Q.-K. Xue, Y. Han, S. Huang, & F. Liu. *Quantum Size Effect on Adatom Surface Diffusion*. Physical Review Letters **97**, 26, 266102 (2006). DOI: 10.1103/PhysRevLett.97.266102. 15
- [Ma07] X. C. Ma, P. Jiang, Y. Qi, J.-F. Jia, Y. Yang, W. Duan, W.-X. Li, X. Bao, S. B. Zhang, & Q.-K. Xue. *Experimental Observation of Quantum Oscillation of Surface Chemical Reactivities*. Proceedings of the National Academy of Sciences **104**, 22, 9204 (2007). DOI: 10.1073/pnas.0611024104. 7, 15, 128, 129, 130
- [Mah70a] G. D. Mahan. *Angular Dependence of Photoemission in Metals*. Physical Review Letters **24**, 19, 1068 (1970). DOI: 10.1103/PhysRevLett.24.1068. 43
- [Mah70b] G. D. Mahan. *Theory of Photoemission in Simple Metals*. Physical Review B **2**, 11, 4334 (1970). DOI: 10.1103/PhysRevB.2.4334. 43
- [Mal05] C. Malliakas, S. J. L. Billinge, H. J. Kim, & M. G. Kanatzidis. *Square Nets of Tellurium: Rare-Earth Dependent Variation in the Charge-Density Wave of RETe3 (RE = Rare-Earth Element)*. Journal of the American Chemical Society **127**, 18, 6510 (2005). DOI: 10.1021/ja0505292. 5, 26, 28, 201, 205
- [Mal06] C. D. Malliakas & M. G. Kanatzidis. *Divergence in the Behavior of the Charge Density Wave in RETe3 (RE = Rare-Earth Element) with Temperature and RE Element*. Journal of the American Chemical Society **128**, 39, 12612 (2006). DOI: 10.1021/ja0641608. 28
- [Man02] A Mans, J. H. Dil, A. R. H. F. Ettema, & H. H. Weitering. *Quantum Electronic Stability and Spectroscopy of Ultrathin Pb Films on Si(111) 7 × 7*. Physical Review B **66**, 19, 195410 (2002). DOI: 10.1103/PhysRevB.66.195410. 18

- [Mar87] O. E. Martinez. *Design of high-power ultrashort pulse amplifiers by expansion and recompression*. IEEE Journal Of Quantum Electronics **23**, 1385 (1987). 242
- [Mas96] T. B. Massalski & H. Okamoto (Eds.). *Binary Alloy Phase Diagrams*. ASM International, Materials Park, OH, USA (1996). 82
- [Mat06] S. Mathias, M. Wiesenmayer, M. Aeschlimann, & M. Bauer. *Quantum-Well Wave-Function Localization and the Electron-Phonon Interaction in Thin Ag Nanofilms*. Physical Review Letters **97**, 23, 236809 (2006). DOI: 10.1103/PhysRevLett.97.236809. 3
- [Mat08] S. Mathias, M. Wiesenmayer, F. Deicke, A. Ruffing, L. Miaja-Avila, M. M. Murnane, H. C. Kapteyn, M. Bauer, & M. Aeschlimann. submitted to: Journal of Physics . 3, 36, 194
- [McR79] E. G. McRae. *Electronic Surface Resonances of Crystals*. Review of Modern Physics **51**, 3, 541 (1979). DOI: 10.1103/RevModPhys.51.541. 10
- [McR81] E. G. McRae & M. L. Kane. *Calculations on the Effect of the Surface Potential Barrier in Lead*. Surface Science **108**, 3, 435 (1981). DOI: 10.1016/0039-6028(81)90559-8. 10
- [Med92] V. Meden & K. Schönhammer. *Spectral Functions for the Tomonaga-Luttinger Model*. Physical Review B **46**, 15753 (1992). DOI: 10.1103/PhysRevB.46.15753. 37, 188
- [Mel08] A. Melnikov, A. Povolotskiy, & U. Bovensiepen. *Magnon-Enhanced Phonon Damping at Gd(0001) and Tb(0001) Surfaces Using Femtosecond Time-Resolved Optical Second-Harmonic Generation*. Physical Review Letters **100**, 24, 247401 (2008). DOI: 10.1103/PhysRevLett.100.247401. 180
- [Mer04] M. Merschedorf, C. Kennerknecht, & W. Pfeiffer. *Collective and single-particle dynamics in time-resolved two-photon photoemission*. Physical Review B **70**, 19, 193401 (2004). DOI: 10.1103/PhysRevB.70.193401. 146
- [Mil02a] A. D. Miller, I. Bezel, K. J. Gaffney, S. Garrett-Roe, S. H. Liu, P. Szymanski, & C. B. Harris. *Electron Solvation in Two Dimensions*. Science **297**, 5584, 1163 (2002). DOI: 10.1126/science.1073571. 45, 86
- [Mil02b] M. Milun, P. Pervan, & D. P. Woodruff. *Quantum Well Structures in Thin Metal Films: Simple Model Physics in Reality?* Reports on Progress in Physics **65**, 2, 99 (2002). DOI: 10.1088/0034-4885/65/2/201. 7, 8, 10, 147
- [Miw01] R. H. Miwa & G. P. Srivastava. *Atomic Structure, Electronic Structure and Image State for Si(111)-In(4 × 1) Nanowires*. Surface Science **473**, 123 (2001). DOI: 10.1016/S0039-6028(00)00960-2. 186, 187
- [MK94] T. Mayer-Kuckuk. *Kernphysik*. Teubner Studienbücher Physik, Stuttgart (1994). 53
- [Mön01] W. Mönch. *Semiconductor Surfaces and Interfaces*. Springer Series in Surface Science (2001). 13, 14, 78
- [Mön06] A. Mönnich, J. Lange, M. Bauer, M. Aeschlimann, I. A. Nechaev, V. P. Zhukov, P. M. Echenique, & E. V. Chulkov. *Experimental Time-Resolved Photoemission and Ab Initio Study of Lifetimes of Excited Electrons in Mo and Rh*. Physical Review B **74**, 035102 (2006). DOI: 10.1103/PhysRevB.74.035102. 35, 146
- [Moo01] G. Moos, C. Gahl, R. Fasel, M. Wolf, & T. Hertel. *Anisotropy of Quasiparticle Lifetimes and the Role of Disorder in Graphite from Ultrafast Time-Resolved Photoemission Spectroscopy*. Physical Review Letters **87**, 267402 (2001). DOI: 10.1103/PhysRevLett.87.267402. 36
- [Moo08] R. G. Moore *et al.* To be published (2008). 31, 201, 203, 205
- [Mot39] N. F. Mott. *The Theory of Crystal Rectifiers*. Proceedings of the Royal Society of London. Series A, Mathematical and Physical Sciences **171**, 944, 27 (1939). <http://www.jstor.org/stable/97313>. 13, 14
- [Mou86] P. F. Moulton. *Spectroscopic and Laser Characteristics of Ti-Al₂O₃*. Journal of the Optical Society of America B **3**, 1, 125 (1986). <http://www.opticsinfobase.org/abstract.cfm?URI=josab-3-1-125>. 239, 240

- [Mou92] P. F. Moulton. *Tunable Solid-State Lasers*. Proceedings of the IEEE **80**, 3, 348 (1992). DOI: 10.1109/5.135352. 239
- [Mus82] R.G. Musket, W. McLean, C.A. Colmenares, D.M. Makowiecki, & W.J. Siekhaus. *Preparation of atomically clean surfaces of selected elements. A review*. Applications of Surface Science **10**, 143 (1982). DOI: 10.1016/0378-5963(82)90142-8. 108
- [Nak01] J. Nakamura, S. Watanabe, & M. Aono. *Anisotropic Electronic Structure of the Si(111)-(4 × 1)In Surface*. Physical Review B **63**, 193307 (2001). DOI: 10.1103/PhysRevB.63.193307. 186
- [Naz93] M. K. Nazeeruddin, A. Kay, I. Rodicio, R. Humphry-Baker, E. Mueller, P. Liska, N. Vlachopoulos, & M. Graetzel. *Conversion of Light to Electricity by cis-X2bis(2,2'-Bipyridyl-4,4'-Dicarboxylate)Ruthenium(II) Charge-Transfer Sensitizers (X = Cl-, Br-, I-, CN-, and SCN-) on Nanocrystalline Titanium Dioxide Electrodes*. Journal of the American Chemical Society **115**, 14, 6382 (1993). DOI: 10.1021/ja00067a063. 1
- [Nol04] W. Nolting. *Grundkurs Theoretische Physik 5/1*. Springer, Berlin (2004). 8, 128
- [Nor86] J. E. Northrup. *Origin of Surface States on Si(111)(7 × 7)*. Physical Review Letters **57**, 1, 154 (1986). DOI: 10.1103/PhysRevLett.57.154. 130
- [Nor08] Michael R. Norman. *High-Temperature Superconductivity in the Iron Pnictides*. Physics **1**, 21 (2008). DOI: 10.1103/Physics.1.21. 222
- [Oef93] H. Oefner, S. L. Surnev, Y. Shapira, & F. P. Netzer. *In Overlayers on Si(111) (7 × 7): Growth and Evolution of the Electronic Structure*. Physical Review B **48**, 10940 (1993). DOI: 10.1103/PhysRevB.48.10940. 186
- [Oel01] A. Oelsner, O. Schmidt, M. Schicketanz, M. Klais, G. Schönhense, V. Mergel, O. Jagutzki, & H. Schmidt-Böcking. *Microspectroscopy and Imaging Using A Delay Line Detector in Time-Of-Flight Photoemission Microscopy*. Review of Scientific Instruments **72**, 10, 3968 (2001). DOI: 10.1063/1.1405781. 87
- [Oga96a] S. Ogawa & H. Petek. *Femtosecond Dynamics of Hot-Electron Relaxation in Cu(110) and Cu(100)*. Surface Science **357-358**, 585 (1996). DOI: 10.1016/0039-6028(96)00228-2. 34
- [Oga96b] S. Ogawa & H. Petek. *Two-Photon Photoemission Spectroscopy at Clean and Oxidized Cu(110) and Cu(100) Surfaces*. Surface Science **363**, 313 (1996). DOI: 10.1016/0039-6028(96)00153-7. 139
- [Oga02] S. Ogawa, H. Nagano, & H. Petek. *Optical Intersubband Transitions and Femtosecond Dynamics in Ag/Fe(100) Quantum Wells*. Physical Review Letters **88**, 11, 116801 (2002). DOI: 10.1103/PhysRevLett.88.116801. 3, 11, 36, 147, 157
- [Oga04] E. Ogando, N. Zabala, E. V. Chulkov, & M. J. Puska. *Quantum Size Effects in Pb Islands on Cu(111): Electronic Structure Calculations*. Physical Review B **69**, 15, 153410 (2004). DOI: 10.1103/PhysRevB.69.153410. 3, 18
- [Oga05] E. Ogando, N. Zabala, E. V. Chulkov, & M. J. Puska. *Self-Consistent Study of Electron Confinement to Metallic Thin Films on Solid Surfaces*. Physical Review B **71**, 20, 205401 (2005). DOI: 10.1103/PhysRevB.71.205401. 10
- [Ote02] R. Otero, A. L. Vázquez de Parga, & R. Miranda. *Observation of Preferred Heights in Pb Nanoislands: A Quantum Size Effect*. Physical Review B **66**, 115401 (2002). DOI: 10.1103/PhysRevB.66.115401. 3, 15, 18, 124
- [Pad92] D. F. Padowitz, W. R. Merry, R. E. Jordan, & C. B. Harris. *Two-Photon Photoemission as A Probe of Electron Interactions with Atomically Thin Dielectric Films on Metal Surfaces*. Physical Review Letters **69**, 24, 3583 (1992). DOI: 10.1103/PhysRevLett.69.3583. 45, 139
- [Pag99] J. J. Paggel, T. Miller, & T.-C. Chiang. *Quantum-Well States as Fabry-Pérot Modes in a Thin-Film Electron Interferometer*. Science **283**, 1709 (1999). DOI: 10.1126/science.283.5408.1709. 3, 124
- [Pag02] J. J. Paggel, C. M. Wei, M. Y. Chou, D.-A. Luh, T. Miller, & T.-C. Chiang. *Atomic-Layer-Resolved Quantum Oscillations in the Work Function: Theory and Experiment for Ag/Fe(100)*. Physical Review B **66**, 233403 (2002). DOI: 10.1103/PhysRevB.66.233403. 17, 124

- [Par04] S. J. Park, H. W. Yeom, S. H. Min, D. H. Park, & I.-W. Lyo. *Direct Evidence of the Charge Ordered Phase Transition of Indium Nanowires on Si(111)*. Physical Review Letters **93**, 106402 (2004). DOI: 10.1103/PhysRevLett.93.106402. 186
- [Ped98] F. Pedreschi, J. D. O'Mahony, P. Weightman, & J. R. Power. *Evidence of Electron Confinement in the Single-Domain, (4 × 1)-In Superstructure on Vicinal Si(111)*. Applied Physics Letters **73**, 15, 2152 (1998). DOI: 10.1063/1.122407. 186
- [Pee00] P. S. Peercy. *The Drive to Miniaturization*. Nature **406**, 1023 (2000). DOI: 10.1038/35023223. 1
- [Pei29] R. E. Peierls. *The kinetic theory of thermal conduction in crystals*. Annalen der Physik **3**, 8, 1055 (1929). DOI: 10.1002/andp.19293950803. 19
- [Pei30a] R. E. Peierls. *Regarding the Theory of Electric and Thermal Conductibility of Metals*. Annalen der Physik **4**, 2, 121 (1930). DOI: 10.1002/andp.19303960202. 19
- [Pei30b] R. E. Peierls. *Remarks on the theory of conductivity*. Annalen der Physik **5**, 2, 244 (1930). DOI: 10.1002/andp.19303970205. 19
- [Pei55] R. E. Peierls. *Quantum Theory of Solids*. Oxford University Press, New York (1955). 19
- [Pen76] J. B. Pendry. *Theory of Photoemission*. Surface Science **57**, 2, 679 (1976). DOI: 10.1016/0039-6028(76)90355-1. 43
- [Per06] L. Perfetti, P. A. Loukakos, M. Lisowski, U. Bovensiepen, H. Berger, S. Biermann, P. S. Cornaglia, A. Georges, & M. Wolf. *Time Evolution of the Electronic Structure of 1T-TaS₂ Through the Insulator-Metal Transition*. Physical Review Letters **97**, 067402 (2006). DOI: 10.1103/PhysRevLett.97.067402. 55, 59, 61, 86, 208, 209
- [Per07] L. Perfetti, P. A. Loukakos, M. Lisowski, U. Bovensiepen, H. Eisaki, & M. Wolf. *Ultrafast electron relaxation in superconducting Bi₂Sr₂CaCu₂O₈+ δ by time-resolved photoelectron spectroscopy*. Physical Review Letters **99**, 19, 197001 (2007). DOI: 10.1103/PhysRevLett.99.197001. 55, 59, 73, 86
- [Per08] L. Perfetti, P. A. Loukakos, M. Lisowski, U. Bovensiepen, M. Wolf, H. Berger, S. Biermann, & A. Georges. *Femtosecond Dynamics of Electronic States in the Mott Insulator 1t-Ta₂S₂ by Time Resolved Photoelectron Spectroscopy*. New Journal of Physics **10**, 5, 053019 (2008). DOI: 10.1088/1367-2630/10/5/053019. 55, 59, 61, 86
- [Pet92] G. Petite, P. Agostini, R. Trainham, E. Mevel, & P. Martin. *Origin of the High-Energy Electron Emission from Metals Under Laser Irradiation*. Physical Review B **45**, 12210 (1992). DOI: 10.1103/PhysRevB.45.12210. 42
- [Pet97a] H. Petek, A. P. Heberle, W. Nessler, H. Nagano, S. Kubota, S. Matsunami, N. Moriya, & S. Ogawa. *Optical Phase Control of Coherent Electron Dynamics in Metals*. Physical Review Letters **79**, 23, 4649 (1997). DOI: 10.1103/PhysRevLett.79.4649. 139, 146
- [Pet97b] H. Petek & S. Ogawa. *Femtosecond Time-Resolved Two-Photon Photoemission Studies of Electron Dynamics in Metals*. Progress in Surface Science **56**, 4, 239 (1997). DOI: 10.1016/S0079-6816(98)00002-1. 2, 34, 38, 45, 86, 139, 146
- [Pet99a] H. Petek, H. Nagano, & S. Ogawa. *Hole Decoherence of d Bands in Copper*. Physical Review Letters **83**, 4, 832 (1999). DOI: 10.1103/PhysRevLett.83.832. 146
- [Pet99b] A. Petkova, J. Wollschläger, H.L. Günter, & M. Henzler. *Formation of an intermediate 3 \times 3 phase from Pb on Si(111) at high temperature*. Journal of Physics: Condensed Matter **11**, 9925 (1999). DOI: 10.1088/0953-8984/11/49/310. 78
- [Pet00a] H. Petek, M. J. Weida, H. Nagano, & S. Ogawa. *Real-Time Observation of Adsorbate Atom Motion Above a Metal Surface*. Science **288**, 1402 (2000). DOI: 10.1126/science.288.5470.1402. 146
- [Pet00b] H. Petek, M.J. Weida, H. Nagano, & S. Ogawa. *Electronic relaxation of alkali metal atoms on the Cu(111) surface*. Surface Science **451**, 22 (2000). DOI: 10.1103/PhysRevLett.83.832. 146
- [Pfe00] O. Pfennigstorf, K. Lang, H.-L. Günter, & M. Henzler. *Electronic Transport in Ultrathin Epitaxial Pb Films on Si(111) Surfaces*. Applied Surface Science **162-163**, 537 (2000). DOI: 10.1016/S0169-4332(00)00247-6. 15, 17

- [Pfe02] O. Pfennigstorf, A. Petkova, H. L. Guenter, & M. Henzler. *Conduction Mechanism in Ultrathin Metallic Films*. Physical Review B **65**, 4, 045412 (2002). DOI: 10.1103/PhysRevB.65.045412. 15, 17
- [Pin66] D. Pines & P. Nozieres. *The Theory of Quatum Liquids*, Vol. I of *Advanced Book Classic Series*. W. A. Benjamin, Inc. (1966). 4, 7, 32, 33, 34, 146, 231
- [Pit04] J. M. Pitarke, V. P. Zhukov, R. Keyling, E. V. Chulkov, & P. M. Echenique. *Ultrafast Electron Dynamics in Metals*. ChemPhysChem **5**, 9, 1284 (2004). DOI: 10.1002/cphc.200301222. 32, 35, 235
- [Qia05] Z. X. Qian & G. Vignale. *Lifetime of A Quasiparticle in An Electron Liquid*. Physical Review B **71**, 7, 075112 (2005). DOI: 10.1103/PhysRevB.71.075112. 36, 157, 231, 234
- [Qia06] Z. Qian. *Lifetime of A Quasiparticle in An Electron Liquid. II*. Physical Review B **73**, 24, 245112 (2006). DOI: 10.1103/PhysRevB.73.245112. 36, 157, 231, 234
- [Qui58] J. J. Quinn & R. A. Ferrell. *Electron Self-Energy Approach to Correlation in a Degenerate Electron Gas*. Physical Review **112**, 3, 812 (1958). DOI: 10.1103/PhysRev.112.812. 33, 34, 157, 233
- [Rec06] V. Recoules, J. Clerouin, G. Zerah, P. M. Anglade, & S. Mazevet. *Effect of intense laser irradiation on the lattice stability of semiconductors and metals*. Physical Review Letters **96**, 5, 055503 (2006). DOI: 10.1103/PhysRevLett.96.055503. 177
- [Rei01] F. Reinert, G. Nicolay, S. Schmidt, D. Ehm, & S. Hüfner. *Direct Measurements of the L-Gap Surface States on the (111) Face of Noble Metals by Photoelectron Spectroscopy*. Physical Review B **63**, 11, 115415 (2001). DOI: 10.1103/PhysRevB.63.115415. 109, 111, 112
- [Rei05] F. Reinert & S. Hüfner. *Photoemission Spectroscopy - From Early Days to Recent Applications*. New Journal of Physics **7**, 97 (2005). DOI: 10.1088/1367-2630/7/1/097. 40
- [Ret02] B. Rethfeld, A. Kaiser, M. Vicanek, & G. Simon. *Ultrafast Dynamics of Nonequilibrium Electrons in Metals Under Femtosecond Laser Irradiation*. Physical Review B **65**, 21, 214303 (2002). DOI: 10.1103/PhysRevB.65.214303. 54, 173, 208, 210
- [Rüg07] T. K. Rügheimer, Th. Fauster, & F. J. Himpsel. *Unoccupied Electronic States in Atomic Chains on Si(557)-Au: Time-Resolved Two-Photon Photoemission Investigation*. Physical Review B **75**, 12, 121401 (2007). DOI: 10.1103/PhysRevB.75.121401. 4, 37, 87, 185, 189
- [Rif93] D. M. Riffe, X. Y. Wang, M. C. Downer, D. L. Fisher, T. Tajima, J. L. Erskine, & R. M. More. *Femtosecond Thermionic Emission from Metals in the Spacecharge-Limited Regime*. Journal of the Optical Society of America B **10**, 1424 (1993). <http://josab.osa.org/abstract.cfm?URI=josab-10-8-1424>. 42
- [Rii06] S. Riikonen, A. Ayuela, & D. Sanchez-Portal. *Metal-Insulator Transition in the In/Si(111) Surface*. Surface Science **600**, 18, Sp. Iss. SI, 3821 (2006). DOI: 10.1016/j.susc.2006.01.092. 186, 187
- [Roe] RoentDek Handels GmbH. *RoentDek Handels GmbH*. Frankfurt am Main. 3, 87, 89
- [Roe06] RoentDek Handels GmbH. *Software for RoentDek Hexanode*. Frankfurt am Main (2006). 106, 115, 250
- [Roh05] M. Rohleder, K. Duncker, W. Berthold, J. Gudde, & U. Hofer. *Momentum-resolved dynamics of Ar/Cu(100) interface states probed by time-resolved two-photon photoemission*. New Journal Of Physics **7**, 103 (2005). DOI: 10.1088/1367-2630/7/1/103. 139
- [Rot02] Manfred Roth, Martin Pickel, Wang Jinxiong, Martin Weinelt, & Thomas Fauster. *Electron Scattering at Steps: Image-Potential States on Cu(119)*. Physical Review Letters **88**, 9, 096802 (2002). DOI: 10.1103/PhysRevLett.88.096802. 39, 80, 139
- [Rot04] M. Roth, M. Pickel, M. Weinelt, & Th. Fauster. *Dynamics of Image-Potential States on Stepped Cu(001) Surfaces*. Applied Physics A **78**, 2, 149 (2004). DOI: 10.1007/s00339-003-2311-5. 39, 80, 139
- [Row69] J. M. Rowell, W. L. Mcmillan, & W. L. Feldmann. *Phonon Spectra in Pb and Pb40Tl60 Determined by Tunneling and Neutron Scattering*. Physical Review **178**, 3, 897 (1969). DOI: 10.1103/PhysRev.178.897. 178, 180

- [Ru06a] N. Ru, C. L. Condon, G. Y. Margulis, K. Y. Shin, J. Laverock, S. B. Dugdale, M. F. Toney, & I. R. Fisher. *Effect of Chemical Pressure on the Charge Density Wave Transition in Rare-earth Tritellurides $R\text{Te}_3$* . <http://arxiv.org/abs/cond-mat/0610319>. 26, 28, 29
- [Ru06b] N. Ru & I. R. Fisher. *Thermodynamic and Transport Properties of YTe_3 , Late_3 , and Cete_3* . Physical Review B **73**, 033101 (2006). DOI: 10.1103/PhysRevB.73.033101. 5, 26, 28, 29, 82, 201, 205
- [Ru08] N. Ru, C. L. Condon, G. Y. Margulis, K. Y. Shin, J. Laverock, S. B. Dugdale, M. F. Toney, & I. R. Fisher. *Effect of Chemical Pressure on the Charge Density Wave Transition in Rare-Earth Tritellurides $R\text{Te}_3$* . Physical Review B **77**, 3, 035114 (2008). DOI: 10.1103/PhysRevB.77.035114. 5, 26, 27, 28, 29, 30, 31, 201, 205, 208
- [Rul98] Claude Rullière. *Laser Spectroscopy*. Springer, Berlin (1998). 50, 58, 63, 64
- [Ryj01] S. V. Ryjkov, T. Nagao, V.G. Lifshits, & S. Hasegawa. *Phase Transition and Stability of $\text{Si}(111)\text{-}8\times 8$ " 2×2 "-In Surface Phase at Low Temperatures*. Surface Science **488**, 15 (2001). DOI: 10.1016/S0039-6028(01)01145-1. 186
- [Sab02] A. J. Sabbah & D. M. Riffe. *Femtosecond pump-probe reflectivity study of silicon carrier dynamics*. Physical Review B **66**, 16, 165217 (2002). DOI: 10.1103/PhysRevB.66.165217. 168
- [Sac06] A. Sacchetti, L. Degiorgi, T. Giamarchi, N. Ru, & I. R. Fisher. *Chemical Pressure and Hidden One-Dimensional Behavior in Rare Earth Tri-Telluride Charge Density Wave Compounds*. <http://arxiv.org/abs/cond-mat/0606451>. 26
- [Sar97] A. A. Saranin, E. A. Khramtsova, K. V. Ignatovich, V. G. Lifshits, T. Numata, O. Kubo, M. Katayama, I. Katayama, & K. Oura. *Indium-Induced $\text{Si}(111) 4 \times 1$ Silicon Substrate Atom Reconstruction*. Physical Review B **55**, 5353 (1997). DOI: 10.1103/PhysRevB.55.5353. 186
- [Sav96] S. Y. Savrasov & D. Y. Savrasov. *Electron-Phonon Interactions and Related Physical Properties of Metals from Linear-Response Theory*. Physical Review B **54**, 23, 16487 (1996). DOI: 10.1103/PhysRevB.54.16487. 178, 180
- [Sch38] W. Schottky. *Semi-Conductor Theory in Barrier Layers*. Naturwissenschaften **26**, 843 (1938). DOI: 10.1007/BF01774216. 13, 14
- [Sch76] F. K. Schulte. *Theory of Thin Metal-Films - Electron-Density, Potentials and Work Function*. Surface Science **55**, 2, 427 (1976). DOI: 10.1016/0039-6028(76)90250-8. 17, 124, 125
- [Sch91] R. W. Schoenlein, J. G. Fujimoto, G. L. Eesley, & T. W. Capelhart. *Femtosecond Relaxation Dynamics of Image-Potential States*. Physical Review B **43**, 6, 4688 (1991). DOI: 10.1103/PhysRevB.43.4688. 45
- [Sch94] C. A. Schmuttenmaer, M. Aeschlimann, H. E. Elsayed-Ali, R. J. D. Miller, D. A. Mantell, J. Cao, & Y. Gao. *Time-Resolved Two-Photon Photoemission from $\text{Cu}(100)$: Energy Dependence of Electron Relaxation*. Physical Review B **50**, 8957 (1994). DOI: 10.1103/PhysRevB.50.8957. 34, 146
- [Sch97] R. R. Schaller. *Moore's Law: Past, Present and Future*. IEEE Spectrum **34**, 52 (1997). DOI: 10.1109/6.591665. 1
- [Sch03] W. Schattke & M. A. Van Hove. *Solid-State Photoemission and Related Methods*. Wiley-VCH (2003). 41, 42, 43
- [Sch08] F. Schmitt, P. S. Kirchmann, U. Bovensiepen, R. G. Moore, L. Rettig, M. Krenz, J.-H. Chu, N. Ru, L. Perfetti, D. H. Lu, M. Wolf, I. R. Fisher, & Z.-X. Shen. *Effect of the Amplitude Mode and the Transient Melting of A Charge Density Wave on the Electronic Structure of TbTe_3* . Science **321**, 5896, 1649 (2008). DOI: 10.1126/science.1160778. 55, 59, 73, 86, 218
- [Sea79] M. P. Seah & W. A. Dench. *Quantitative Electron Spectroscopy of Surfaces: A Standard Data Base for Electron Inelastic Mean Free Paths in Solids*. Surface and Interface Analysis **1**, 2 (1979). DOI: 10.1002/sia.740010103. 41, 42

- [Seg99] P. Segovia, D. Purdie, M. Hengsberger, & Y. Baer. *Observation of Charge Collective Modes in One-Dimensional Metallic Films*. Nature **402**, 504 (1999). DOI: 10.1038/990052. 37, 189
- [She95] Z.-X. Shen & D. S. Dessau. *Electronic Structure and Photoemission Studies of LaTe Transition-Metal Oxides - Mott Insulators and High-Temperature Superconductors*. Physics Reports **253**, 1 (1995). DOI: 10.1016/0370-1573(95)80001-A. 40
- [Shi72] D. A. Shirley. *High-Resolution X-Ray Photoemission Spectrum of the Valence Bands of Gold*. Physical Review B **5**, 12, 4709 (1972). DOI: 10.1103/PhysRevB.5.4709. 134
- [Shi05] K. Y. Shin, V. Brouet, N. Ru, Z.-X. Shen, & I. R. Fisher. *Electronic Structure and Charge-Density Wave Formation in LaTe_{1.95} and CeTe_{2.00}*. Physical Review B **72**, 8, 085132 (2005). DOI: 10.1103/PhysRevB.72.085132. 26, 28, 82
- [Sho39] W. Shockley. *On the Surface States Associated with a Periodic Potential*. Physical Review **56**, 317 (1939). DOI: 10.1103/PhysRev.56.317. 10
- [Sjo98] T. Sjodin, H. Petek, & H. L. Dai. *Ultrafast carrier dynamics in silicon: A two-color transient reflection grating study on a (111) surface*. Physical Review Letters **81**, 25, 5664 (1998). DOI: 10.1103/PhysRevLett.81.5664. 167, 168
- [Sle99] J. Slezak, P. Mutombo, & V. Chab. *STM Study of A Pb/Si(111) Interface at Room and Low Temperatures*. Physical Review B **60**, 13328 (1999). DOI: 10.1103/PhysRevB.60.13328. 78
- [Sle00] J. Slezak, P. Mutombo, & V. Chab. *Temperature Study of Phase Coexistence in the System Pb on An Si(111) Surface*. Surface Science **454-456**, 584 (2000). DOI: 10.1016/S0039-6028(00)00273-9. 78
- [Smi85] N. V. Smith. *Phase Analysis of Image States and Surface States Associated with Nearly-Free-Electron Band Gaps*. Physical Review B **32**, 6, 3549 (1985). DOI: 10.1103/PhysRevB.32.3549. 10, 139
- [Smi88] N. V. Smith. *Inverse Photoemission*. Reports on Progress in Physics **51**, 9, 1227 (1988). DOI: 10.1088/0034-4885/51/9/003. 45
- [Smi89] N. V. Smith & C. T. Chen. *Distance of the Image Plan from Metal Surfaces*. Physical Review B **40**, 11, 7565 (1989). DOI: 10.1103/PhysRevB.40.7565. 139
- [Smi90] N. V. Smith & C. T. Chen. *Spectroscopic constraints on the potential barrier at metal surfaces*. Surface Science **247**, 133 (1990). DOI: 10.1016/0039-6028(91)90119-D. 139
- [Smo41] R. Smoluchowski. *Anisotropy of the Electronic Work Function of Metals*. Physical Review **60**, 9, 661 (1941). DOI: 10.1103/PhysRev.60.661. 17
- [Sob88] S. E. Sobottka & M. B. Williams. *Delay Line Readout of Microchannel Plates*. IEEE Transactions on Nuclear Science **35**, 348 (1988). DOI: 10.1109/23.12740. 94
- [Soo81] R. Sooryakumar & M. V. Klein. *Raman Scattering from Superconducting Gap Excitations in the Presence of A Magnetic Field*. Physical Review B **23**, 7, 3213 (1981). DOI: 10.1103/PhysRevB.23.3213. 201
- [SP04] D. Sánchez-Portal, S. Riikonen, & R.M. Martin. *Role of Spin-Orbit Splitting and Dynamical Fluctuations in the Si(557)-Au Surface*. Physical Review Letters **93**, 146803 (2004). DOI: 10.1103/PhysRevLett.93.146803. 189
- [Spe] Specs. Specs. Berlin. 3, 87
- [Sri04] G. P. Srivastava & R. H. Miwa. *Self-Organised Wires and Antiwires on Semiconductor Surfaces*. Applied Surface Science **235**, 3, 293 (2004). DOI: 10.1016/j.apsusc.2004.05.102. 186
- [ST03] K. Sokolowski-Tinten, Ch. Blome, J. Blums, A. Cavalleri, C. Dietrich, A. Tarasevitch, I. Uschmann, E. Förster, M. Kammler, M. Horn von Hoegen, & D. von der Linde. *Femtosecond X-ray Measurement of Coherent Lattice Vibrations Near the Lindemann Stability Limit*. Nature **422**, 287 (2003). DOI: 10.1038/nature01490. 180
- [Stä07] J. Stähler. *Freezing Hot Electrons - Electron Transfer and Solvation Dynamics at D₂O and NH₃ - Metal Interfaces*. PhD Thesis, Freie Universität Berlin (2007). 58

- [Ste67] R. Stedman, L. Almqvist, G. Nilsson, & G. Raunio. *Fermi Surface of Lead from Kohn Anomalies*. Physical Review **163**, 3, 567 (1967). DOI: 10.1103/PhysRev.163.567. 180
- [Ste93] J. L. Stevens, M. S. Worthington, & I. S. T. Tsong. 4×1 Reconstruction of Indium Deposited on Vicinal Si(111) Surfaces. Physical Review B **47**, 1453 (1993). DOI: 10.1103/PhysRevB.47.1453. 190
- [Ste06] S. Stepanovsky, M. Yakes, V. Yeh, M. Hupalo, & M. C. Tringides. *The Dense $\alpha - \sqrt{3} \times \sqrt{3}$ Pb/Si(111) Phase: A Comprehensive STM and SPA-LEED Study of Ordering, Phase Transitions and Interactions*. Surface Science **600**, 7, 1417 (2006). DOI: 10.1016/j.susc.2005.12.041. 18, 78
- [Su01] W. B. Su, S. H. Chang, W. B. Jian, C. S. Chang, L. J. Chen, & T. T. Tsong. *Correlation Between Quantized Electronic States and Oscillatory Thickness Relaxations of 2D Pb Islands on Si(111)-(7 \times 7) Surfaces*. Physical Review Letters **86**, 22, 5116 (2001). DOI: 10.1103/PhysRevLett.86.5116. 15, 17
- [Sun08] Y. J. Sun, S. Agario, S. Souma, K. Sugawara, Y. Tago, T. Sato, & T. Takahashi. *Cooperative Structural and Peierls Transition of Indium Chains on Si(111)*. Physical Review B **77**, 12, 125115 (2008). DOI: 10.1103/PhysRevB.77.125115. 4, 186, 187, 188, 199
- [Tao04] F. Tao & G. Q. Xu. *Attachment Chemistry of Organic Molecules on Si(111)-7 \times 7*. Accounts of Chemical Research **37**, 11, 882 (2004). DOI: 10.1021/ar0400488. 74
- [Teg05] C. Tegenkamp, Z. Kallassy, H. Pfnür, H.-L. Günter, V. Zielasek, & M. Henzler. *Switching Between One and Two Dimensions: Conductivity of Pb-Induced Chain Structures on Si(557)*. Physical Review Letters **95**, 17, 176804 (2005). DOI: 10.1103/PhysRevLett.95.176804. 37, 189
- [Tim93] P. J. Timans. *Emissivity of Silicon at Elevated Temperatures*. Journal of Applied Physics **74**, 6353 (1993). DOI: 10.1063/1.355159. 66
- [Tou93] S. Tougaard & C. Jansson. *Comparison of validity and consistency of methods for quantitative XPS peak analysis*. Surface and Interface Analysis **20**, 13, 1013 (1993). DOI: 10.1002/sia.740201302. 134
- [Tra83] G. Travaglini, L. Märke, & P. Wachter. *CDW Evidence in One-Dimensional K0.3MoO3 by Means of Raman Scattering*. Solid State Communications **45**, 289 (1983). DOI: 10.1016/0038-1098(83)90483-0. 213
- [Tre02] R. Trebino. *Frequency-Resolved Optical Gating: The Measurement of Ultrashort Laser Pulses*. Springer, Berlin (2002). 58, 61
- [Tre07] R. Trebino. *GRENOUILLE Model 8-20 User's Guide, Swamp Optics, LLC*. Trebino, R., Atlanta (2007). 61, 251
- [Tsa05] S. F. Tsay. *Atomic and Electronic Structure of the (4 \times 1) and (8 \times 2) In/Si(111) Surfaces*. Physical Review B **71**, 3, 035207 (2005). DOI: 10.1103/PhysRevB.71.035207. 186
- [Uch02] T. Uchihashi & U. Ramsperger. *Electron Conduction Through Quasi-One-Dimensional Indium Wires on Silicon*. Applied Physics Letters **80**, 22, 4169 (2002). DOI: 10.1063/1.1483929. 186
- [Uhr85] R. I. G. Uhrberg, G. V. Hansson, J. M. Nicholls, P. E. S. Persson, & S. A. Flodström. *Photoemission Study of the Surface and Bulk Electronic Structures of Si(111) 7 \times 7 and Si(111) $\sqrt{3} \times \sqrt{3}$:Al*. Physical Review B **31**, 6, 3805 (1985). DOI: 10.1103/PhysRevB.31.3805. 130
- [Ull03] J. Ullrich, R. Moshhammer, A. Dorn, R. Dörner, L. Ph. H. Schmidt, & H. Schmidt-Bocking. *Recoil-Ion and Electron Momentum Spectroscopy: Reaction-Microscopes*. Reports on Progress in Physics **66**, 9, 1463 (2003). DOI: 10.1088/0034-4885/66/9/203. 87
- [Upt04a] M. H. Upton, T. Miller, & T.-C. Chiang. *Absolute Determination of Film Thickness from Photoemission: Application to Atomically Uniform Films of Pb on Si*. Applied Physics Letters **85**, 7, 1235 (2004). DOI: 10.1063/1.1783019. 15, 18, 77, 146
- [Upt04b] M. H. Upton, C. M. Wei, M. Y. Chou, T. Miller, & T.-C. Chiang. *Thermal Stability and Electronic Structure of Atomically Uniform Pb Films on Si(111)*. Physical Review Letters **93**, 2, 026802 (2004). DOI: 10.1103/PhysRevLett.93.026802. 3, 15, 18, 77, 146

- [Upt05] M. H. Upton, T. Miller, & T.-C. Chiang. *Unusual Band Dispersion in Pb Films on Si(111)*. Physical Review B **71**, 3, 033403 (2005). DOI: 10.1103/PhysRevB.71.033403. 16, 77
- [Vie98] J. Viernow, J.-L. Lin, D. Y. Petrovykh, F. M. Leibsle, F. K. Men, & F. J. Himpsel. *Regular Step Arrays on Silicon*. Applied Physics Letters **72**, 948 (1998). DOI: 0.1063/1.120882. 190
- [Vil91] P. Villars & L. D. Calvert (Eds.). *Pearson's Handbook of Crystallographic Data for Intermetallic Phases*. American Society for Metals, Metals Park, OH, USA (1991). 26
- [Vil02] I. Vilfan, M. Henzler, O. Pfennigstorf, & H. Pfnür. *Anomalous Thickness Dependence of the Hall Effect in Ultrathin Pb Layers on Si(111)*. Physical Review B **66**, 241306 (2002). DOI: 10.1103/PhysRevB.66.241306. 3, 15, 18
- [vKS07] C. v. Korff Schmising, M. Bargheer, M. Kiel, N. Zhavoronkov, M. Woerner, T. Elsaesser, I. Vrejoiu, D. Hesse, & M. Alexe. *Coupled Ultrafast Lattice and Polarization Dynamics in Ferroelectric Nanolayers*. Physical Review Letters **98**, 25, 257601 (2007). DOI: 10.1103/PhysRevLett.98.257601. 208
- [Voe04] C. Voelkmann, M. Reichelt, T. Meier, S. W. Koch, & U. Höfer. *Five-Wave-Mixing Spectroscopy of Ultrafast Electron Dynamics at a Si(001) Surface*. Physical Review Letters **92**, 12, 127405 (2004). DOI: 10.1103/PhysRevLett.92.127405. 168
- [Voi95] J. Voit. *One-dimensional Fermi-liquids*. Reports on Progress in Physics **58**, 997 (1995). DOI: 10.1088/0034-4885/58/9/002. 37, 188
- [Wag06] Steffen Wagner. *State- and Time-Resolved Investigations of Energy Transfer Mechanisms in Femtosecond-Laser Induced Associative Desorption*. PhD Thesis, Freie Universität Berlin (2006). 241
- [Wau77] M. Wautelet & L. D. Laude. *Laser-Modulated Photoemission in Semiconductors*. Physical Review Letters **38**, 1, 40 (1977). DOI: 10.1103/PhysRevLett.38.40. 45
- [Web08] WebElements.com. *Webelements: The Periodic Table on the Web*. Winter, M., Sheffield, U.K. (2008). 8, 11, 12, 78
- [Weg05] D. Wegner, A. Bauer, & G. Kaindl. *Electronic Structure and Dynamics of Quantum-Well States in Thin Yb Metal Films*. Physical Review Letters **94**, 126804 (2005). DOI: 10.1103/PhysRevLett.94.126804. 3, 36, 158
- [Wei92] H. H. Weitering, A. R. H. F. Ettema, & T. Hibma. *Surface states and Fermi-level pinning at epitaxial Pb/Si(111) surfaces*. Physical Review B **45**, 16, 9126 (1992). DOI: 10.1103/PhysRevB.45.9126. 130
- [Wei02a] C. M. Wei & M. Y. Chou. *Theory of Quantum Size Effects in Thin Pb(111) Films*. Physical Review B **66**, 23, 233408 (2002). DOI: 10.1103/PhysRevB.66.233408. 3, 13, 15, 81, 119, 120, 123, 124, 125, 127, 132, 136, 138, 140, 141, 142, 145
- [Wei02b] M. Weinelt. *Time-Resolved Two-Photon Photoemission from Metal Surfaces*. Journal of Physics: Condensed Matter **14**, 43, R1099 (2002). DOI: 10.1088/0953-8984/14/43/202. 2, 39, 45, 80, 86, 139, 146, 161
- [Wei04] M. Weinelt, M. Kutschera, Th. Fauster, & M. Rohlfing. *Dynamics of Exciton Formation at the Si(100) c(4x2) Surface*. Physical Review Letters **92**, 12, 126801 (2004). DOI: 10.1103/PhysRevLett.92.126801. 168, 192
- [Wei05] M. Weinelt, M. Kutschera, R. Schmidt, C. Orth, T. Fauster, & M. Rohlfing. *Electronic structure and electron dynamics at Si(100)*. Applied Physics A **80**, 5, 995 (2005). DOI: 10.1007/s00339-004-3127-7. 168, 192
- [Wid03] W. Widdra, D. Bröcker, T. Giefel, I. V. Hertel, W. Krüger, A. Liero, F. Noack, V. Petrov, D. Pop, P. M. Schmidt, R. Weber, I. Will, & B. Winter. *Time-Resolved Core Level Photoemission: Surface Photovoltage Dynamics of the SiO₂/Si(100) Interface*. Surface Science **543**, 1-3, 87 (2003). DOI: DOI: 10.1016/j.susc.2003.07.005. 150, 176
- [Wol62] E. J. Woll & W. Kohn. *Images of the Fermi Surface in Phonon Spectra of Metals*. Physical Review **126**, 5, 1693 (1962). DOI: 10.1103/PhysRev.126.1693. 21, 180

- [Wol96] M. Wolf, E. Knoesel, & T. Hertel. *Ultrafast Dynamics of Electrons in Image Potential states on clean and Xe covered Cu(111)*. Physical Review B **54**, R5295 (1996). DOI: 10.1103/PhysRevB.54.R5295. 139, 194
- [Wol97] Martin Wolf. *Femtosecond dynamics of electronic excitations at metal surfaces*. Surface Science **377-379**, 343 (1997). DOI: 10.1007/s00339-004-3127-7. 194
- [Wol99] M. Wolf, A. Hotzel, E. Knoesel, & D. Velic. *Direct and Indirect Excitation Mechanisms in Two-Photon Photoemission Spectroscopy of Cu(111) And CO/Cu(111)*. Physical Review B **59**, 8, 5926 (1999). DOI: 10.1103/PhysRevB.59.5926. 50, 139, 238
- [Xu97] S. Xu, C. C. Miller, J. Cao, D. A. Mantell, M. G. Mason, A. A. Muentner, B. A. Parkinson, R. J. D. Miller, & Y. Gao. *Femtosecond Photoemission Study of Electron Relaxation in Two-Dimensional Layered Electron Systems*. Journal of Vacuum Science & Technology A **15**, 3, Part 2, 1510 (1997). DOI: 10.1116/1.580571. 36, 37
- [Yag07] Y. Yagi, A. Yoshimori, K. Kakitani, & H. Kaji. *Transformation to Soluble Model for Structural Phase Transition from (4×1) to (8×2) of In-Adsorbed Si(111) Surface*. Surface Science **601**, 6, 1642 (2007). DOI: 10.1016/j.susc.2007.01.047. 186
- [Yak04] M. Yakes, V. Yeh, M. Hupalo, & M. C. Tringides. *Self-Organization at Finite Temperatures of the Devil's Staircase in Pb/Si(111)*. Physical Review B **69**, 22, 224103 (2004). DOI: 10.1103/PhysRevB.69.224103. 18
- [Yan96] Y.-N. Yang, E.S. Fu, & E.D. Williams. *An STM study of current-induced step bunching on Si(111)*. Surface Science **356**, 101 (1996). DOI: 10.1016/0039-6028(96)00033-7. 190
- [Yao06] H. Yao, J. A. Robertson, E.-A. Kim, & S. A. Kivelson. *Theory of Stripes in Quasi-Two-Dimensional Rare-Earth Tellurides*. Physical Review B **74**, 24, 245126 (2006). DOI: 10.1103/PhysRevB.74.245126. 31
- [Yeh00] V. Yeh, L. Berbil-Bautista, C. Z. Wang, K. M. Ho, & M. C. Tringides. *Role of the Metal/Semiconductor Interface in Quantum Size Effects: Pb/Si(111)*. Physical Review Letters **85**, 5158 (2000). DOI: 10.1103/PhysRevLett.85.5158. 15
- [Yeo99] H. W. Yeom, S. Takeda, E. Rotenberg, I. Matsuda, K. Horikoshi, J. Schaefer, C. M. Lee, S. D. Kevan, T. Ohta, T. Nagao, & S. Hasegawa. *Instability and Charge Density Wave of Metallic Quantum Chains on a Silicon surface*. Physical Review Letters **82**, 4898 (1999). DOI: 10.1103/PhysRevLett.82.4898. 4, 87, 185, 186, 187, 199
- [Yeo02] H. W. Yeom, K. Horikoshi, H. M. Zhang, K. Ono, & R. I. G. Uhrberg. *Nature of the Broken-Symmetry Phase of the One-Dimensional Metallic In/Si(111) Surface*. Physical Review B **65**, 241307(R) (2002). DOI: 10.1103/PhysRevB.65.241307. 186, 187
- [Yeo06] H. W. Yeom. *Comment on "Soft Phonon, Dynamical Fluctuations, and a Reversible Phase Transition: Indium Chains On Silicon"*. Physical Review Letters **97**, 18, 189701 (2006). DOI: 10.1103/PhysRevLett.97.189701. 186, 187
- [Yus08] R. V. Yusupov, T. Mertelj, J.-H. Chu, I. R. Fisher, D. Mihailovic, *et al.* To be published (2008). 213
- [Zac98] M. G. Zacher, E. Arrigoni, W. Hanke, & J. R. Schrieffer. *Systematic Numerical Study of Spin-Charge Separation in One Dimension*. Physical Review B **57**, 6370 (1998). DOI: 10.1103/PhysRevB.57.6370. 37
- [Zan88] A. Zangwill. *Physics at Surfaces*. Cambridge University Press, Cambridge (1988). 41, 65
- [Zha98] Z. Zhang, Q. Niu, & C.-K. Shi. *Electronic Growth of Metallic Overlayers on Semiconductor Substrates*. Physical Review Letters **80**, 5381 (1998). DOI: 10.1103/PhysRevLett.80.5381. 3, 7, 17, 81
- [Zha05] Y.-F. Zhang, J.-F. Jia, T.-Z. Han, Z. Tang, Q.-T. Shen, Y. Guo, Z. Q. Qiu, & Q.-K. Xue. *Band Structure and Oscillatory Electron-Phonon Coupling of Pb Thin Films Determined by Atomic-Layer-Resolved Quantum-Well States*. Physical Review Letters **95**, 096802 (2005). DOI: 10.1103/PhysRevLett.95.096802. 15, 18, 81, 124
- [Zha08] Z. Zhang, Y.-F. Zhang, Q. Fu, H. Zhang, Y. Yao, T. Ma, D. Tan, Q.-K. Xue, & X. Bao. *Modulation of Surface Reactivity Via Electron Confinement in Metal Quantum Well Films: O₂ Adsorption on Pb/Si(111)*. Journal of Chemical Physics **129**, 1, 014704 (2008). DOI: 10.1063/1.2919992. 15, 128, 130

- [Zhu04] X.-Y. Zhu. *Electronic Structure and Electron Dynamics at Molecule-Metal Interfaces: Implications for Molecule-based Electronics*. Surface Science Report **56**, 1 (2004). DOI: 10.1016/j.surfrep.2004.09.002. 2, 38, 45, 86, 139, 146
- [Zhu05] V. P. Zhukov, E. V. Chulkov, & P. M. Echenique. *GW + T Theory of Excited Electron Lifetimes in Metals*. Physical Review B **72**, 15, 155109 (2005). DOI: 10.1103/PhysRevB.72.155109. 35, 146

Publications

Publications in the framework of this thesis

P. S. Kirchmann, M. Wolf, J. H. Dil, K. Horn, & U. Bovensiepen. *Quantum Size Effects in Pb/Si(111) Investigated by Laser-Induced Photoemission*. Physical Review B **76**, 7, 075406, (2007). DOI: 10.1103/PhysRevB.76.075406

P. S. Kirchmann, L. Rettig, D. Nandi, U. Lipowski, M. Wolf, & U. Bovensiepen. *A Time-of-Flight Spectrometer for Angle-Resolved Detection of Low Energy Electrons in Two Dimensions*. Applied Physics A-Materials Science & Processing **91**, 2, 211, (2008). DOI: 10.1007/s00339-008-4422-5

P. S. Kirchmann & U. Bovensiepen. *Ultrafast Electron Dynamics in Pb/Si(111) Investigated by Two-Photon Photoemission*. Physical Review B **78**, 3, 035437, (2008). DOI: 10.1103/PhysRevB.78.035437

P. S. Kirchmann & U. Bovensiepen. *Ultrafast Electron Dynamics in Quantum Well States of Pb/Si(111) Investigated by Two-Photon Photoemission*. In P. Corkum, S. De Silvestri, K. Nelson, E. Riedle, & R. Schoenlein (Eds.), *Ultrafast Phenomena XVI*, Springer Series in Chemical Physics. Springer-Verlag Berlin (2008)

F. Schmitt, P. S. Kirchmann, U. Bovensiepen, R. G. Moore, L. Rettig, M. Krenz, J.-H. Chu, N. Ru, L. Perfetti, D. H. Lu, M. Wolf, I. R. Fisher, & Z.-X. Shen. *Effect of the Amplitude Mode and the Transient Melting of A Charge Density Wave on the Electronic Structure of TbTe₃*. Science **321**, 1649, (2008) DOI: 10.1126/science.1160778

In Preparation

P. S. Kirchmann, L. Rettig, & U. Bovensiepen. *Oscillatory Quasi-Particle Lifetimes in Quantum Well States of Pb/Si(111)*.

L. Rettig, P. S. Kirchmann, & U. Bovensiepen. *Coherent Phonon Modes in Quantum Well States of Pb/Si(111) Observed by Time-Resolved Photoemission*.

Publications concerning other topics

P. S. Kirchmann, P. A. Loukakos, U. Bovensiepen, & M. Wolf. *Ultrafast Electron Dynamics Studied with Time-Resolved Two-Photon Photoemission: intra- and inter-band scattering in $C_6F_6/Cu(111)$* . *New Journal of Physics* **7**, 113, (2005). DOI: 10.1088/1367-2630/7/1/113

P. S. Kirchmann, P. Loukakos, U. Bovensiepen, M. Wolf, S. Vijayalakshmi, F. Hennies, A. Pietzsch, M. Nagason, A. Föhlisch, & W. Wurth. *Ultrafast Electron Dynamics in $C_6F_6/Cu(111)$ After Localized or Delocalized Excitation*. In: R. J. D Miller, A. M Weiner, P. Corkum and D. Jonas (Ed.), *Ultrafast Phenomena XV*, Vol. 88 of *Springer Series in Chemical Physics*. Springer-Verlag Berlin (2007)

S. Vijayalakshmi, A. Foehlich, P. S. Kirchmann, F. Hennies, A. Pietzsch, M. Nagasono, & W. Wurth. *Bond polarization and image-potential screening in adsorbed C_6F_6 on $Cu(111)$* . *Surface Science* **600**, 22, 4972, (2006). DOI: 10.1016/j.susc.2006.08.017

Academic Curriculum Vitae

The curriculum vitae is omitted in this online version due to data privacy.

Acknowledgements

Eine solche Arbeit ist immer ein Gemeinschaftsprojekt zu deren Gelingen viele Menschen beigetragen haben. Es ist mir daher eine Freude an dieser Stelle meinen Dank ausdrücken zu können.

Zunächst möchte ich mich in aller Aufrichtigkeit bei Martin Wolf bedanken. Seine Arbeitsgruppe zeichnete sich neben hervorragend ausgestatteten Laboren und exzellenten Mitarbeitern vor allem durch eine familiäre Atmosphäre aus, die ein Arbeiten auf höchstem Niveau ermöglichte. Die besonderen Freiheiten in der Gestaltung meiner Arbeit habe ich allezeit zu schätzen gewusst. Auch gab es immer genug Gelegenheiten, um kleine und große Probleme zu diskutieren, was angesichts seines detailreichen Wissens ein steter Gewinn war.

Uwe Bovensiepen danke ich für die vorbildlichste Betreuung, die sich ein Doktorand nur wünschen kann. Ich war mir seiner kritischen Unterstützung immer sicher, was mir sehr half meine Ideen in vielen intensiven Diskussionen mit ihm weiterzuentwickeln. Auch für die Möglichkeit an zahlreichen internationalen Konferenzen teilzunehmen bin ich sehr zu Dank verpflichtet.

Karsten Horn vom Fritz-Haber-Institut der Max-Planck-Gesellschaft danke ich für die hilfreichen Diskussionen zu den QWSs und den Austrittsrechts-Oszillationen. Ausserdem bedanke ich mich für die freundliche Bereitstellung des Cu(111) Einkristalls, der in den Messungen mit dem pTOF Spektrometer benutzt wurde, sowie der Knudsen-Zelle für die Pb- und In-Präparation.

I thank Z.-X. Shen and Ian Fisher and their coworkers from the Stanford University for the efficient and fruitful collaboration and the hospitality when I visited them. Especially, I acknowledge Rob Moore, who was very fast in sending new TbTe₃ samples across the ocean after we have wrecked the old ones.

Ganz besonderer Dank gebührt Felix T. Schmitt von der Stanford University. Ich schätze mich glücklich einen solch talentierten Experimentator und gründlichen Theoretiker getroffen zu haben. Die tr-ARPES Messungen an RTe₃ waren schon ein ganz besonderes Erlebnis!

Mit Julia Stähler und Marcel Krenz habe ich nicht nur zwei gute Kollegen, sondern auch liebe Freunde gefunden. Gerade in Zeiten, die besonders dunkel zu sein schienen, habt Ihr mein Laborleben wieder aufgeheitert. Dafür danke ich Euch sehr.

Die Zusammenarbeit mit Laurenz Rettig hat mich nachhaltig beeindruckt, da sich sein großes Programmier-talent mit herausragendem experimentellen Geschick vereint. Ohne ihn wäre ich vermutlich immer noch dabei, die Software für das pTOF Spektrometer zu schreiben. :-)

Sebastian Hagen danke ich für die zuverlässige Betreuung des Lasersystems, ohne ihn wäre manche Messung sicher nicht möglich gewesen. Ihm danke ich ebenso wie Michael Meyer, Felix Leyssner und Luca Perfetti für die äußerst angenehme Stimmung im 2PPE Labor. Es war immer wieder ein großer Spaß und eine vorzügliche Ablenkung vom Laboralltag sich mit Euch zu unterhalten oder auf Reisen zu gehen.

I like to acknowledge Dhananjay Nandi, who helped a lot in the practical implementation of the pTOF spectrometer. Auch danke ich Gerald Wigger und Tobias Bernhardt für ihre praktische Hilfe beim Aufbau der Maschine und die erhellenden Diskussionen über Elektronentrajektorien. Schließlich gebührt der Feinwerktechnik Dank für die präzise Ausführung des Spektrometers und so manch schneller Änderung. Achim Czasch von der RoentDek GmbH in Frankfurt danke ich für die ausdauernde Betreuung in der Entwicklungsphase und darüber hinaus.

Für den vorzüglich durchdachten Aufbau spreche ich meinen Vorgängern an der 2PPE Apparatur Cornelius Gahl und Martin Lisowski meinen Dank aus. Letzterem sowie unserem ehemaligen Laserexperten Panagiotis Loukakos aka dem "master of disaster", danke ich für den äußerst zuverlässig betriebenen Laser. Ihnen verdanke ich nicht zuletzt den Hinweis auf die Möglichkeit zeitaufgelöste Photoemission an Blei auf Silizium zu betreiben. Dafür bedanke ich mich - eine ausgezeichnete Idee!

Peter West gebührt Dank für die Hilfe in Computer-Angelegenheiten und Bereitstellung einer sauber funktionierenden Infrastruktur. Dietgard Mallwitz hat mehr als einmal den Bürokratie-Dschungel für mich gelichtet - danke sehr!

Also, I thank the students Anastasia Averina, Rashmish Kumar and Andreas Bodmeier for their help and the intercultural atmosphere they brought to the laboratory.

Hugo Dil is acknowledged for introducing me to the preparation of ultrathin epitaxial metal films. Also, I owe him for his remark "that the observed QWS binding energies fit much better to theory if you don't invert the coverage scale". I guess, he was right!

Sandhya Chandola von der Technischen Universität Berlin und Norbert Esser vom Institute of Analytical Sciences Berlin danke ich für die schnelle Bereitstellung von fehlgeschnittenen Si(111) Wafern. In solchen Situationen merkt man was für ein toller Wissenschaftsstandort Berlin ist!

I like to thank Xiao-Yang Zhu from University of Minnesota in Minneapolis for the very kind invitation to his group and the inspiring discussions on the future of solar energy. I always enjoyed your company.

Bei Martin Weinelt vom Max Born Institut in Berlin bedanke ich mich herzlich für die ausführlichen Erklärungen zu Metal/Halbleiter-Grenzflächen und Diskussionen über LEED und 2PPE.

Mit Michael Bauer von der Universität Kiel und Stefan Mathias von der Universität Kaiserslautern genoss ich anregende Diskussionen über Elektronenstreuung in niedrig-dimensionalen Bandstrukturen - vielen Dank.

Hajo Freund, Thomas Risse und Bettina Menzel von der International Max-Planck-Research School on "Complex Surfaces in Material Science" danke ich für die spannenden Exkursionen und die großzügige Bezahlung so mancher Dienstreise, vor allem aber dafür, mich mit so vielen verschiedenen Doktoranten bekannt gemacht zu haben.

Zum Abschluss möchte ich meinen Schwiegereltern Sylvia und Rudolf Werner danken, die mich vom Kauf des ersten Computers bis zum Ausdruck dieser Dissertation immer tatkräftig unterstützt haben.

Von meinen Freunden möchte ich allen voran Bülent Tayfur für die treue Unterstützung in den letzten Jahren, die nicht immer einfach waren, danken. Diese Freundschaft gab mir auch manches Mal die nötige Bodenhaftung, um nicht im Elfenbeinturm der Physik verloren zu gehen.

Meiner lieben Ehefrau Anke Werner kann ich kaum genug danken, all die Jahre merkwürdiger Arbeitszeiten und seltsamer Diskussionen nicht nur ertragen, sondern auch verstanden zu haben. Ich liebe Dich!